Quantenkondensation in Elektron–Loch–Photon–Systemen

Habilitationsschrift
zur Erlangung des akademischen Grades
doctor rerum naturalium habilitatus (Dr. rer. nat. habil.)
der Mathematisch-Naturwissenschaftlichen Fakultät
der Universität Rostock

vorgelegt von

Dirk Semkat, geb. am 16. Juli 1973 in Güstrow

aus Krakow am See

Rostock, 21. Februar 2017

urn:nbn:de:gbv:28-diss2018-0096-5

1. Gutachter: Prof. Dr. Heinrich Stolz, Universität Rostock
2. Gutachter: Prof. Dr. Frank Jahnke, Universität Bremen
3. Gutachter: Prof. Dr. Rolf Binder, University of Arizona

Tag des Kolloquiums: 08.01.2018

Adresse: Universität Rostock
Institut für Physik
18051 Rostock

Zusammenfassung

Die vorliegende Habilitationsschrift umfaßt eine Reihe von Arbeiten zu Gleichgewichts- und Nichtgleichgewichtseigenschaften von Elektron–Loch–Plasmen bzw. Exzitonengasen in hochangeregten Halbleitern mit besonderem Augenmerk auf Quantenkondensationsphänomenen wie der Bose–Einstein–Kondensation der Exzitonen. Zu diesen Arbeiten, die in Fachzeitschriften veröffentlicht wurden, hat der Verfasser dieser Schrift wesentliche Beiträge geleistet.

In den Arbeiten, die in engster Kooperation zwischen Theorie und Experiment entstanden, wird zum einen die Quantenkondensation in Elektron–Loch–Systemen aus dem Auftreten zeitlich langreichweitiger Ordnung in den Zweiteilchenkorrelationen abgeleitet und das Ionisationsgleichgewicht des partiell ionisierten Elektron–Loch–Plasmas analysiert. Zum anderen werden Methoden der Theorie ultrakalter Bosegase auf das Exzitonengas im Halbleiter übertragen und dessen Thermodynamik in einer druckinduzierten Potentialfalle in Hinblick auf das Auftreten von Bose–Einstein–Kondensation untersucht sowie die Dynamik laserangeregter Exzitonen in der Falle mittels quantenkinetischer Gleichungen beschrieben. Zudem wird ein theoretischer Zugang zur exzitonischen Lumineszenz erarbeitet. Wesentliches Augenmerk in allen Arbeiten lag auf der Frage nach den Bedingungen für das Auftreten des Kondensats und dessen experimentell beobachtbaren Signaturen.

Abstract

This habilitation thesis comprises of a series of papers on equilibrium and nonequilibrium properties of electron–hole plasmas and exciton gases, respectively, in highly excited semiconductors with special attention to quantum condensation phenomena like Bose–Einstein condensation of the excitons. To these works which have been published in scientific journals, the author of this thesis has contributed significantly.

In the papers which arose from a close cooperation between theory and experiment, on the one hand, quantum condensation in electron–hole systems is derived from the occurrence of time long-range order in the two-particle correlations and the ionisation equilibrium of the partially ionised electron–hole plasma is analysed. On the other hand, methods of the theory of ultracold bosonic gases are applied to the exciton gas in semiconductors and its thermodynamics in a strain-induced potential trap is investigated with respect to the occurrence of Bose–Einstein condensation as well as the dynamics of laser excited excitons in the trap is described using quantum kinetic equations. Moreover, a theoretical approach to the excitonic luminescence is developed. The main focus in all works lay on the question for the conditions of the occurrence of a condensate and its experimentally observable signatures.

Inhaltsverzeichnis

Kapitel 1

Zusammenfassung der Publikationen

1.1 Einleitung

Seit einigen Jahrzehnten hat das Ziel, ein Bose–Einstein–Kondensat (BEK) von Exzitonen, gebundener Zustände aus Elektronen und „Löchern“ in angeregten Halbleitern, nachzuweisen, Generationen von Halbleiterphysikern motiviert. Während dieser exotische Quantenzustand, in dem der Grundzustand eines Systems aus Boseteilchen (also Mikroteilchen mit ganzzahligem Spin) makroskopisch besetzt wird, bereits 1925 theoretisch vorhergesagt wurde [Ein25], vergingen bis zur experimentellen Realisierung noch 70 Jahre. Gelungen ist diese Realisierung in Gasen ultrakalter Natrium- [DMA$^+$95] bzw. Rubidiumatome [AEM$^+$95] bei Temperaturen von wenigen Nanokelvin. Seit den grundlegenden Arbeiten ist aber bekannt, daß die kritische Temperatur, unterhalb derer die Kondensation einsetzt, für ein System nicht wechselwirkender Teilchen umgekehrt proportional zu deren Masse ist. Experimentell sollte es also umso einfacher sein, die Bedingungen für die Kondensation durch Abkühlen des Systems zu erreichen, je leichter die entsprechenden Teilchen sind. Schon in den 1960er Jahren wurde daher vorausgesagt, daß Exzitonen, deren Masse etwa drei bis vier Größenordnungen kleiner als typische Atommassen sind, ein BEK bilden können [Mos62, BBB62]. Die kritischen Temperaturen sollten für bei optischer Anregung erreichbare Dichten im Bereich einiger bis einiger hundert Millikelvin liegen.

Trotz dieses großen Vorteils gegenüber atomaren Gasen und einer entsprechend

Der zusammenfassende Teil dieser Habilitationsschrift wurde gemäß den Regeln der traditionellen deutschen Rechtschreibung verfaßt.

großen Zahl von Experimenten an verschiedensten Exzitonensystemen blieb der entscheidende Durchbruch bisher aus – zumindest für das „anschaulichste“ System eines Gases direkter Exzitonen im Volumenhalbleiter („*bulk*“). Wenn es auch keinen Mangel an Erfolgsmeldungen für letzteres System gab (für einen Überblick siehe [Sno03]), können als gesichert bisher nur die Nachweise eines Kondensats von Polaritonen in einer optischen Kavität [KRK$^+$06] und von (räumlich) indirekten Exzitonen in gekoppelten Schichtsystemen [BGC02] gelten. Es gibt allerdings vielversprechende Indizien in den Messungen der Rostocker Arbeitsgruppe um Heinrich Stolz, die das Auftreten eines Kondensats zumindest als sehr wahrscheinlich erachten lassen [SNKS12], siehe dazu auch die Arbeit A.8. Jede experimentelle Erfolgsmeldung muß sich an den vier von David Snoke aufgestellten Kriterien [Sno03] für das Auftreten eines Bosekondensats messen lassen, um einen tatsächlich zweifelsfreien Nachweis darzustellen.

Eine der hauptsächlichen Schwierigkeiten, ein exzitonisches Kondensat in dreidimensionalen Halbleiterkristallen zu erzeugen und nachzuweisen, ist die Erzeugung ausreichend hoher Dichten (Kondensation sollte offensichtlich im Prinzip durch Abkühlung bei konstanter Teilchendichte oder durch Dichteerhöhung bei konstanter Temperatur erreicht werden). Eine Methode, diese Schwierigkeit zu umgehen, ist die Erzeugung einer Hertzschen Potentialfalle für die Exzitonen, bei der durch mechanischen Druck auf die Kristalloberfläche eine Verspannung im Kristall und damit eine Deformation der Bandstruktur hervorgerufen wird. Nichtsdestotrotz bietet der Weg der Dichteerhöhung keinesfalls die Gewißheit, sich der Kondensationsgrenze tatsächlich zu nähern. Diese Unsicherheit liegt zum einen darin begründet, daß es ohnehin unmöglich ist, beliebig hohe Exzitonendichten zu erzeugen – mit wachsender Dichte nimmt die effektive Ionisierungsenergie der Exzitonen, also der energetische Abstand zwischen Exzitonniveau und Bandkante, ab, so daß oberhalb einer kritischen Dichte nur noch freie Elektronen und Löcher existieren können (Mott–Effekt) [EKK76]. Zum anderen ist bei höheren Dichten ein Zweikörperzerfall relevant, bei dem von den zwei beteiligten Exzitonen eines rekombiniert und das andere die freiwerdende Energie in Form von thermischer Energie aufnimmt [SK14]. Dieser dem Auger–Effekt der Atomphysik ähnliche Effekt, der quadratisch mit der Dichte wächst, vernichtet also zum einen Exzitonen und heizt die verbleibenden auf und wirkt somit in zweifacher Hinsicht kontraproduktiv.

Eine weitere entscheidende Schwierigkeit beim Nachweis des exzitonischen BEK ist schlicht die Frage, woran dessen Auftreten überhaupt erkannt werden kann. Da Exzitonen als Quasiteilchen eine begrenzte Lebensdauer haben und ihr Zerfall (also

die Rekombination von Elektron und Loch) mit der Emission von Licht verbunden ist, liegt es nahe, in dieser Lumineszenz nach Signaturen eines Kondensates zu suchen. Dazu bedarf es genauer Vorstellungen, was für Signaturen zu erwarten sind, und ob diese im Experiment beobachtbar sein sollten.

Mit den beiden oben genannten Punkten sind zwei wesentliche Grenzpflöcke eingeschlagen, die das Arbeitsgebiet markieren – es spannt sich von der Frage nach den Existenzbedingungen der Exzitonen bis hin zu den optischen Signaturen, die ein mögliches exzitonisches Kondensat bewirken könnte. Dazwischen liegt das weite Feld der Quantenstatistik bzw. Thermodynamik des partiell ionisierten Elektron–Loch–Plasmas bzw. des Exzitongases, die Dynamik der Exzitonen in der Potentialfalle und ihre Kopplung an das Lichtfeld, d.h. die Theorie der Lumineszenz. Die zu der vorliegenden Arbeit zusammengefaßten Publikationen sollen ein klein wenig zum Verständnis der oben aufgeworfenen Probleme beitragen, ohne den Anspruch zu verfolgen, diese auch nur im entferntesten erschöpfend zu behandeln.

Die Publikationen lassen sich in drei inhaltlich sehr eng zusammenhängende Komplexe gliedern: Zum ersten die Theorie der Quantenkondensation im Elektron–Loch–Plasma, verbunden mit der Thermodynamik dieses Systems aus Ladungsträgern und ihrer gebundenen Zustände, der Exzitonen. Zum zweiten die Beschreibung der Gleichgewichts- und Nichtgleichgewichtseigenschaften des Exzitonengases und der Bose–Einstein–Kondensation der Exzitonen. Zum dritten die möglichen Signaturen des Kondensats im Lumineszenzspektrum im Rahmen einer Theorie der exzitonischen Lumineszenz. In dieser Zusammenfassung soll der erste Komplex im Fokus stehen. Der zweite Komplex wird nur kurz umrissen; eine umfassende Darstellung ist in zwei vom Autor dieser Habilitationsschrift betreuten bzw. mitbetreuten Arbeiten – der Diplomarbeit und der Dissertation von Siegfried Sobkowiak [Sob10, Sob14] – zu finden. Zum dritten Komplex gibt es erste theoretische und numerische Resultate, die ausführlich dargestellt werden.

Bevor der erste Komplex behandelt wird, sollen zunächst einige einführende Bemerkungen zum zu untersuchenden System, dem angeregten Halbleiter, und dem dabei im Fokus stehenden Material Kupferoxydul (Cu_2O) vorangestellt werden.

1.2 Der angeregte Halbleiter

1.2.1 Elektron–Loch–Bild. Exzitonen

Daß Halbleiter hinsichtlich ihrer elektrischen bzw. Wärmeleitfähigkeit zwischen Metallen (Leitern) und Isolatoren (Nichtleitern) stehen, hat zu ihrer Namensgebung geführt. Die Ursache hierfür liegt in der Bandstruktur der Festkörper. Während ein isoliertes Atom diskrete Energieniveaus besitzt, überlagern sich diese Niveaus bei den im Kristallgitter angeordneten Atomen des Festkörpers zu Energiebändern. Zwischen diesen Bereichen „erlaubter“ Energien liegen Lücken, also „verbotene“ Bereiche. Im einfachsten Modell eines Zweibandsystems entscheidet die Lücke zwischen Valenz- und Leitungsband, ob der Festkörper ein Metall ist (überlappende Bänder, Elektronen können sich frei im Leitungsband bewegen) oder ein Isolator (große Lücke, das Leitungsband ist leer). Ist die Bandlücke klein genug, daß sie z.B. durch thermische oder optische Anregung von Elektronen aus dem Valenzband überwunden werden kann, spricht man von einem Halbleiter. [1]

Beschreibt man den angeregten Halbleiter in diesem „Bandbild“, erhalten sämtliche physikalische Größen einen Index, der kennzeichnet, ob sich das Elektron im Valenz- (v) oder Leitungsband (*conduction band*, c) befindet. Eine alternative Beschreibung beruht auf der sehr anschaulichen Vorstellung, daß ein ins Leitungsband „angehobenes“ Elektron ein „Loch“ im Valenzband zurückläßt. Da eine negative Ladung „fehlt“, müßte dieses Loch eine positive Ladung tragen. Es liegt also durchaus nahe, neben den Elektronen die „Löcher“ als weitere Teilchensorte einzuführen. Dabei definiert man neben der Ladung $q_h = -q_e = +e$ (h für *hole*) die effektive Lochmasse $m_h = -m_v$. (Die „Masse“ eines Bandes kann formal als zweite Ableitung der Banddispersion nach der Wellenzahl definiert werden.) Somit besitzt die Dispersion der Löcher gerade die negative Krümmung der Dispersion der Valenzbandelektronen. In Effektivmassennäherung (Annahme parabolischer Bänder) ergibt sich für die Lochdispersion eine Parabel, die, genau wie die der Elektronen, nach oben geöffnet ist, aber eine andere Krümmung besitzt.

Die Vorteile dieses „Teilchenbildes“ liegen auf der Hand. Anstelle von Elektronen, die sich in verschiedenen Bereichen einer mehr oder weniger komplizierten Energiebandstruktur befinden, liegt nun ein System aus zwei ungleichnamig geladenen Teil-

[1] Zur Quantentheorie angeregter Halbleiter siehe z.B. [Zim88, HK04].

chenspezies vor. Die Bandstruktur findet sich „lediglich“ in den effektiven Massen beider Spezies wieder. Damit ist die Beschreibung des angeregten Halbleiters auf die Beschreibung eines Plasmas, des Elektron–Loch–Plasmas (ELP), zurückgeführt worden. Das einfachste Analogon, das sich hier spontan aufdrängt, ist das Wasserstoffplasma aus Elektronen und Protonen. (Eine aufgrund des Massenverhältnisses noch größere Analogie zum ELP besitzt das Elektron–Positron–Plasma.) Genauso wie sich im Wasserstoffplasma Protonen und Elektronen zu Wasserstoffatomen verbinden können (oder Positronen und Elektronen zu Positronien), können Elektronen und Löcher gebundene Zustände bilden, die als Exzitonen bezeichnet werden. Die Bildung gebundener Zustände hängt von den Zustandsgrößen des Plasmas wie Dichte und Temperatur ab.

Die wesentlichen Unterschiede zwischen ELP und Wasserstoffplasma bestehen im Massenverhältnis, das im ELP von der Größenordnung 1 (bis 10) ist, und in der Abschirmung der Coulombwechselwirkung „von außen“, also durch das Gitter. Letzterer Effekt führt zu einer relativen Dielektrizitätskonstante $\epsilon_r > 1$, die die Coulombwechselwirkung abschwächt. Das Exziton ist damit wesentlich größer als ein Wasserstoffatom (Bohrscher Radius etwa zehn- bis hundertfach größer als der des Wasserstoffs) und viel schwächer gebunden (exzitonisches Rydberg $R_X \approx (10^{-2}...10^{-3})R_H$).

Das beschriebene Modell des über viele Gitterplätze ausgedehnten Exzitons im Halbleiter wird auch als Wannier– bzw. Wannier–Mott–Exziton bezeichnet [Wan37]. Im Gegensatz dazu ist das Frenkel–Exziton [Fre31] an einem Gitterplatz lokalisiert, kleiner und stärker gebunden.

1.2.2 Kupferoxydul

Kupferoxydul (oder Kupfer(I)-oxid, Cu_2O) ist ein Material, das in der Halbleitertechnologie schon sehr lange bekannt ist. Bereits in den 1920er Jahren wurde es für den Bau von Gleichrichterdioden verwendet. In Kupferoxydul konnten 1952 erstmals die theoretisch bereits 1931 [Fre31] postulierten Exzitonen experimentell nachgewiesen werden [GK52, HK52]. In der Natur kommt Kupferoxydul in Form des Minerals Cuprit vor. Im Kristall bilden die Kupferatome ein kubisch flächenzentriertes (fcc) und die Sauerstoffatome ein kubisch raumzentriertes (bcc) Gitter, die um ein Viertel der Raumdiagonale gegeneinander verschoben sind.

Die Eigenschaften des Materials, seine Bandstruktur, die entsprechenden Spektralserien usw. sind in einer Vielzahl von Publikationen ausführlich dargestellt, für einen

Überblick siehe z.B. [Kli05, Bra10, San10] und für aktuelle Resultate siehe [SKG$^+$16]. Hier sollen nur einige der wesentlichen Fakten in aller Kürze wiederholt werden, die für das Verständnis der nachfolgend umrissenen Untersuchungen relevant sind.

Die Bandstruktur ist sehr komplex [Kli05]. Es existieren zehn Valenz- und vier Leitungsbänder. Betrachten wir nur die beiden energetisch höchstgelegenen Valenzbänder ($^2\Gamma_7^+$, $^4\Gamma_8^+$ nach der entsprechenden Symmetrie) und die beiden niedrigsten Leitungsbänder ($^2\Gamma_6^+$, $^4\Gamma_8^-$), ergeben sich vier verschiedene Möglichkeiten, ein Elektron anzuregen und ein Exziton zu erzeugen. Für jede dieser vier Möglichkeiten existiert ein exzitonischer Grundzustand und eine Serie angeregter Zustände, analog zur Rydberg–Serie beim Wasserstoff. Tatsächlich findet man im Absorptions- bzw. Emissionsspektrum vier Serien (gelb, grün, blau, violett) [NGS61, GSN61, DDM66], wobei die gelbe Serie durch Rekombination zwischen dem $^2\Gamma_6^+$–Leitungsband und dem $^2\Gamma_7^+$–Valenzband entsteht. Das gelbe 1S–Exziton ist das energetisch am niedrigsten liegende. Der Zustand zerfällt in das dreifach entartete Orthoexziton mit Gesamtdrehimpuls $J = 1$, das aus Spin–Singulettzuständen aufgebaut ist, und das Paraexziton mit $J = 0$, das aus Spin–Triplettzuständen besteht. Letzteres entspricht dem energetischen Grundzustand, während das Orthoexziton durch die Elektron–Loch–Austauschwechselwirkung um 12,12 meV höher liegt. Das gelbe 1S–Paraexziton liegt bei $E_{1S} = 151$ meV. Die angeregten Zustände bilden eine Rydberg–Serie mit einer wesentlich kleineren Rydberg–Energie von $R_X = 86$ meV [SKG$^+$16]. Grund für diese Diskrepanz sind sogenannte *Central–Cell*–Korrekturen (u.a. ist das Exziton aufgrund des kleinen Bohr–Radius' von 0,52 nm [Sch17], der mit der Gitterkonstante von 0,43 nm vergleichbar ist, eigentlich nicht mehr gut als Wannier–Exziton beschreibbar, zudem wird die Nichtparabolizität der Bänder relevant).

Das gelbe 1S–Paraexziton ist ein sehr vielversprechender Kandidat, wenn es um Erzeugung und Nachweis eines exzitonischen Bose–Einstein–Kondensates geht. Ein wichtiger Grund dafür ist die genannte hohe Bindungsenergie, die hohe kritische Temperaturen erwarten läßt. Desweiteren ist die Lebensdauer mit einigen hundert Nanosekunden recht hoch. Dies ist in der Tatsache begründet, daß der direkte Zerfall des Paraexzitons (ohne Assistenz eines Phonons) optisch in allen Ordnungen verboten ist. Im homogenen Volumenhalbleiter wäre das Paraexziton somit im Experiment nicht zugänglich. Durch den mit dem Aufbau einer Hertzschen Potentialfalle (s.o.) verbundenen Deformation der Bänder kommt es aber zu einer Mischung mit der grünen Serie, und der Übergang wird schwach erlaubt [KM75].

Einen umfassenden Überblick über die bereits mehr als 30 Jahre währenden ex-

perimentellen Studien zum Nachweis eines exzitonischen BEK in Kupferoxydul findet man in [SK14]. In jüngerer Zeit wird dieses Material von Gruppen in Rostock (H. Stolz *et al.*), Dortmund (M. Bayer *et al.*) und Kyoto (N. Naka *et al.*) (siehe hierzu z.B. [SBF$^+$11, SNKS12] und die Arbeit A.8) sowie in Tokio (M. Kuwata–Gonokami *et al.*) [YCKG11, YMFKG13] intensiv untersucht.

1.3 Das partiell ionisierte Elektron–Loch–Plasma

Die bei Anregung des Halbleiters „entstehenden“ bzw. „frei werdenden“ Elektronen und Löcher sind Fermionen. Motivierend für die vorliegenden Arbeiten war aber die Untersuchung von Quantenkondensationsphänomenen. Die kondensierenden Objekte müssen der Bose–Statistik genügen, es kann sich also nur um Paare von fermionischen Ladungsträgern handeln. Das primäre Ziel der eingangs erwähnten Experimente ist, ein Kondensat von Exzitonen, Bindungszuständen aus Elektronen und Löchern, nachzuweisen. Es sind daher zwei grundlegende Probleme zu untersuchen: Zum ersten stellt sich die Frage, ob bei gegebener Dichte und Temperatur überhaupt Exzitonen existieren können. Hierfür muß das Ionisationsgleichgewicht des Elektron–Loch–Plasmas untersucht werden, was im ersten Unterabschnitt erfolgt. Zum zweiten ist bekannt, daß auch ungebundene Ladungsträgerpaare kondensieren können, was die Frage nach einem einheitlichen theoretischen Zugang und einer möglichen gemeinsamen Phasengrenze der Quantenkondensation aufwirft. Diese Frage wird im zweiten Unterabschnitt untersucht.

1.3.1 Ionisationsgleichgewicht. Mott-Effekt

Die Thermodynamik des Elektron–Loch–Plasmas (ELP) ist ausführlich untersucht, hier sei auf Standardwerke wie [EKK76] und [Zim88] verwiesen. Einige Grundgedanken sollen hier nur kurz wiederholt werden.

Die Bildung von gebundenen Zuständen aus Elektronen und Löchern ist von der Dichte der angeregten Ladungsträger und ihrer Temperatur abhängig, also von den Zustandsgrößen des ELP. Wie auch in atomaren Plasmen wird sich ein Gleichgewicht zwischen Bildung und Zerfall der Bindungszustände ausbilden.

Aus der Plasmaphysik ist bekannt, daß dieses Gleichgewicht bei tiefen Temperatu-

ren in Abhängigkeit von der Dichte deutlich zu einem der beiden Grenzfälle – atomares Gas bzw. vollständig ionisiertes Plasma – verschoben ist. Im stark verdünnten System können sich aufgrund des großen mittleren Teilchenabstandes keine gebundenen Zustände bilden. Mit wachsender Dichte steigt dann der Anteil der Bindungszustände an, bis alle Ladungsträger gebunden sind. Wird die Dichte weiter erhöht, kommt der mittlere Teilchenabstand irgendwann in die Größenordnung des Bindungsabstandes bzw. unterschreitet ihn. Dann sind gebundene Zustände nicht mehr stabil und werden mehr oder weniger schlagartig aufgebrochen, so daß das System in den vollständig ionisierten Zustand übergeht.

In diesem – wie wir später diskutieren werden, drastisch vereinfachten – Bild gibt es also eine bestimmte, im allgemeinen temperaturabhängige Dichte, unterhalb derer nur gebundene Zustände und oberhalb derer nur freie Ladungsträger vorliegen können. Diese Dichte wird als Mott–Dichte bezeichnet, der zugehörige Übergang zum vollständig ionisierten Plasma als Mott–Übergang [ZKK$^+$78, HT78]. Begrifflich soll hier, wie in [KKER86, KSK05], der Mott–Effekt unterschieden werden. Dieser beschreibt den dem Mott–Übergang zugrundeliegenden spektralen Effekt des „Verschwindens“ des Bindungszustandes im Kontinuum bzw. Band.

Sowohl das spektrale als auch das thermodynamische Phänomen wurden für das Elektron–Loch–Plasma in den Arbeiten A.2, A.3, A.6 und A.8 sowie [SRK$^+$10, MRS$^+$11] untersucht. Im Mittelpunkt stand die Abgrenzung des Existenzbereichs der Exzitonen, also die Frage, ob bei einer gegebenen Dichte und Temperatur überhaupt Exzitonen vorliegen können. Dazu muß die Mott–Dichte in Abhängigkeit von der Temperatur $n_{\mathrm{Mott}}(T)$ bestimmt werden. Zum anderen ermöglicht die Untersuchung der Thermodynamik des Elektron–Loch–Plasmas die Bestimmung des Zusammenhangs zwischen chemischem Potential und Dichte, also $\mu(n)$ bzw. $n(\mu)$. Dieser Zusammenhang spielt bei der Untersuchung der Phasengrenze der Quantenkondensation eine wesentliche Rolle, siehe Abschnitt 1.3.2.

Erweitertes Quasiteilchenkonzept

Ausgangspunkt der Untersuchungen ist die Dichte der Ladungsträger, also der Elektronen bzw. Löcher. Im Rahmen des Formalismus der reellzeitigen Greenfunktionen [FW71, KKER86, KSK05] erhält man diese Größe als Wellenzahlintegral über die zeitdiagonale Einteilchen–Korrelationsfunktion $G_a^<$ der jeweiligen Teilchensorte ($a = e, h$).

Im Gleichgewicht ist diese Definition äquivalent zu

$$n_a(\{\mu_c\},T) = g_a \int \frac{\mathrm{d}^3\mathbf{k}}{(2\pi)^3} \int \frac{\mathrm{d}\omega}{2\pi} \, (-\mathrm{i}\hbar) G_a^<(\mathbf{k},\omega) = g_a \int \frac{\mathrm{d}^3\mathbf{k}}{(2\pi)^3} \int \frac{\mathrm{d}\omega}{2\pi} \, A_a(\mathbf{k},\omega) \, f_a(\omega) \,, \tag{1.1}$$

wobei g_a die Multiplizität der Bänder (inklusive Spinentartung) ist. Die Funktion $f_a(\omega)$ ist die Fermi–Verteilung, $f_a(\omega) = \left(\mathrm{e}^{(\hbar\omega-\mu_a)/k_\mathrm{B}T}+1\right)^{-1}$.

Die Spektralfunktion $A_a(\mathbf{k},\omega)$ ist durch den Imaginärteil der retardierten Einteilchen–Greenfunktion gegeben, $A_a(\mathbf{k},\omega) = -2\mathrm{Im}\, g_a^r(\mathbf{k},\omega)$, und läßt sich explizit durch die Beziehung [KSK05]

$$A_a(\mathbf{k},\omega) = \frac{\hbar\Gamma_a(\mathbf{k},\omega)}{\left(\hbar\omega - \frac{\hbar^2k^2}{2m_a} - \mathrm{Re}\Sigma_a^r(\mathbf{k},\omega)\right)^2 + \left(\frac{1}{2}\Gamma_a(\mathbf{k},\omega)\right)^2} \tag{1.2}$$

ausdrücken, wobei die Einteilchen–Dämpfung Γ_a durch die Selbstenergien $\Sigma_a^{\gtrless}$ gegeben ist,

$$\Gamma_a(\mathbf{k},\omega) = -2\,\mathrm{Im}\,\Sigma_a^r(\mathbf{k},\omega) = \mathrm{i}\left[\Sigma_a^>(\mathbf{k},\omega) - \Sigma_a^<(\mathbf{k},\omega)\right] \,. \tag{1.3}$$

Die Dichte (1.1) ist eine Funktion der Temperatur und der chemischen Potentiale aller Teilchenspezies. Letzterer Fakt wird später bei der Diskussion der Einteilchen–Dämpfung Γ_a offensichtlich. Im Einkomponentenfall ist es somit möglich, durch Inversion den Zusammenhang $\mu_a(n,T)$ zu gewinnen und die Thermodynamik des Elektron–Loch–Plasmas zu entwickeln.[2]

Der nächste Schritt wäre nun die Wahl einer Approximation für die Selbstenergie. Da hier insbesondere die Zusammensetzung des partiell ionisierten Plasmas von Interesse sein soll, wollen wir zunächst die allgemeine Form der Spektralfunktion (1.2) einer wesentlichen Näherung unterwerfen. Dazu soll der Fall schwacher Dämpfung der Einteilchenzustände betrachtet werden, d.h. $\Gamma_a \ll \mathrm{Re}\,\Sigma_a^r$. Dann kann die Spektralfunktion bezüglich Γ_a in eine Taylorreihe entwickelt werden. Bis zur ersten Ordnung lautet die Entwicklung [KKL84, ZS85, Zim88, KSK05]

$$\begin{aligned} A_a(\mathbf{k},\omega) &= 2\pi\hbar\,\delta\left(\hbar\omega - E_a(\mathbf{k})\right) \left\{1 + \frac{1}{\hbar}\frac{\partial}{\partial\omega}\mathcal{P}\int\frac{\mathrm{d}\bar{\omega}}{2\pi}\,\frac{\Gamma_a(\mathbf{k},\bar{\omega})}{\omega-\bar{\omega}}\bigg|_{\hbar\omega=E_a(\mathbf{k})}\right\} \\ &\quad -\Gamma_a(\mathbf{k},\omega)\,\frac{\partial}{\partial\omega}\,\frac{\mathcal{P}}{\hbar\omega - E_a(\mathbf{k})} \,, \end{aligned} \tag{1.4}$$

[2] Wie wir später sehen werden, gilt das auch im allgemeinen.

wobei $\mathcal{P}$ bedeutet, daß ein Integral über die Funktion im Sinne des Cauchyschen Hauptwertes zu verstehen ist. Die Quasiteilchenenergie $E_a(\mathbf{k})$ ist die Lösung der Dispersionsrelation

$$E_a(\mathbf{k}) = \frac{\hbar^2 k^2}{2m_a} + \mathrm{Re}\Sigma_a^r(\mathbf{k},\omega)\Big|_{\hbar\omega = E_a(\mathbf{k})} . \tag{1.5}$$

Die Entwicklung (1.4) wird oft als „erweiterte Quasiteilchennäherung“ (*extended quasiparticle approximation*) bezeichnet. Der Sinn dieser Bezeichnung ist offensichtlich: Die normale Quasiteilchennäherung wird durch den ersten Term auf der rechten Seite der Gleichung (1.4) beschrieben. Dieser Term enthält die Quasiteilchenpole. Die Dämpfung, bewirkt durch die Wechselwirkung zwischen den Quasiteilchen, wird im zweiten (*off-pole*) Beitrag berücksichtigt, der das Quasiteilchenbild somit in erster Ordnung auf gedämpfte Zustände erweitert.

Setzt man die Entwicklung (1.4) in die Gleichung für die Dichte (1.1) ein, erhält man

$$\begin{aligned} n_a(\{\mu_c\},T) &= g_a \int \frac{\mathrm{d}^3\mathbf{k}}{(2\pi)^3} f_a\left(E_a(\mathbf{k})\right) \\ &\quad - g_a \int \frac{\mathrm{d}^3\mathbf{k}}{(2\pi)^3} \int \frac{\mathrm{d}\omega}{2\pi} \left\{ \Gamma_a(\mathbf{k},\omega) \left[f_a(\omega) - f_a\left(E_a(\mathbf{k})\right)\right] \frac{\partial}{\partial\omega} \frac{\mathcal{P}}{\hbar\omega - E_a(\mathbf{k})} \right\} \\ &= n_a^0 + n_a^{\mathrm{corr}} . \end{aligned} \tag{1.6}$$

Die Gesamtdichte n_a teilt sich somit in einen Beitrag der freien n_a^0 und einen der korrelierten Quasiteilchen n_a^{corr} ein. Man beachte jedoch, daß auch die „freien“ Quasiteilchen über die renormierte Dispersion $E_a(\mathbf{k})$ durch Korrelationseffekte beeinflußt sind. Der korrelierte Anteil wird wesentlich durch die Dämpfung $\Gamma_a(\mathbf{k},\omega)$, also den Imaginärteil der Selbstenergie, bestimmt. Für diese Größe ist nun also eine geeignete Näherung zu wählen.

Da es um die Untersuchung von gebundenen Zuständen geht, kommt offensichtlich nur die T–Matrix– oder Leiter–Näherung für die Selbstenergie in Frage. Da andererseits aber auch die Abschirmung der Coulombwechselwirkung als kollektiver Effekt im System geladener Teilchen berücksichtigt werden muß, ist die Wahl der sogenannten abgeschirmten Leiternäherung für die Selbstenergie angebracht. [3]

[3] In dieser ist die T–Matrix durch eine Lippmann–Schwinger–Gleichung (bzw. Bethe–Salpeter–Gleichung) gegeben, in der die „Leitersprossen“ nicht wie in der gewöhnlichen Leiternäherung durch das Coulombpotential, sondern durch das dynamisch abgeschirmte Coulombpotential gegeben sind [KSK05], vgl. Gl. (1.75) im folgenden Abschnitt, wo auf diese Näherung noch eingegangen wird.

Betrachten wir nun die Verteilungsfunktion $f_a\left(E_a(\mathbf{k})\right)$. Die Dispersion ist, wie bereits erwähnt, durch Korrelationseffekte renormiert. Wir versuchen nun, diejenigen Korrelationen, die den Aufbau gebundener Zustände ermöglichen, herauszupräparieren. Das gelingt, indem die Verteilungsfunktion entwickelt wird [KKS93],

$$f_a\left(\epsilon_a + \mathrm{Re}\,\Sigma_a''\right) \approx f_a(\epsilon_a) + \mathrm{Re}\,\Sigma_a'' \frac{\mathrm{d}f}{\mathrm{d}\epsilon_a}\,, \tag{1.7}$$

wobei

$$\epsilon_a(\mathbf{k}) = \frac{\hbar^2 k^2}{2m_a} + \mathrm{Re}\,\Sigma_a^{\mathrm{RPA}}(\mathbf{k},\omega)\Big|_{\hbar\omega=\epsilon_a(\mathbf{k})} \tag{1.8}$$

die Quasiteilchenenergie in *random phase approximation* (RPA) inklusive der Hartree–Fock–Selbstenergie Σ_a^{HF} ist, und Σ_a'' alle höheren Leiterterme umfaßt. Letztere Terme sind auch für verschwindende Abschirmung konvergent und enthalten gerade die gebundenen Zustände.

Für die Dichte ergibt sich mit (1.1)–(1.8)

$$n_a(\{\mu_c\},T) = g_a \int \frac{\mathrm{d}^3\mathbf{k}}{(2\pi)^3}\, f_a(\epsilon_a(\mathbf{k})) + g_a \sum_b \int_{-\infty}^{\infty} \frac{\mathrm{d}\omega}{2\pi}\, n_{ab}^B(\omega)\mathrm{Im}\,F(\omega) \tag{1.9}$$

mit

$$F(\omega) = \mathrm{Sp}_{12}\left[\frac{\mathrm{d}}{\mathrm{d}\omega}\mathcal{G}_{ab}^r(\omega)T_{ab}^r(\omega)\right]. \tag{1.10}$$

$\mathcal{G}_{ab}^r$ ist die freie retardierte Zweiteilchen–Greenfunktion, die sich durch die Einteilchen–Korrelationsfunktionen $g_a^{\gtrless}$ darstellen läßt,

$$\mathcal{G}_{ab}^r(\omega) = \int \frac{\mathrm{d}\bar{\omega}}{2\pi} \int \frac{\mathrm{d}\bar{\bar{\omega}}}{2\pi} \frac{g_a^>(\bar{\omega})g_b^>(\bar{\bar{\omega}}) - g_a^<(\bar{\omega})g_b^<(\bar{\bar{\omega}})}{\omega - \bar{\omega} - \bar{\bar{\omega}} + \mathrm{i}\epsilon}. \tag{1.11}$$

Um die Formel (1.9) auszuwerten, wäre es nun nötig, die retardierte T–Matrix T_{ab}^r detailliert zu untersuchen. Im Falle schwacher Dämpfung ist es möglich, diese Größe in den Beitrag der gebundenen Zustände und den der Streuzustände zu zerlegen. Ersterer folgt aus der Bilinearentwicklung der T–Matrix [Zim88, KSK05, KKK$^+$84],

$$F^{\mathrm{bound}}(\omega) = \sum_{n,l} \pi(2l+1)\delta(\hbar\omega - E_{nl})\,,$$

wobei E_{nl} die Bindungsenergie des Niveaus bezeichnet, das durch die Quantenzahlen $\{n, l\}$ bestimmt ist. Die explizite Form des Streuanteils soll uns, wie später noch diskutiert wird, hier nicht interessieren. Wir können nun die Dichte in Bindungs- und Streuanteile aufspalten,

$$\begin{aligned} n_e(\mu_e, \mu_h, T) &= g_e \int \frac{\mathrm{d}^3\mathbf{k}}{(2\pi)^3} f_e(\epsilon_e(\mathbf{k})) + g_e g_h \sum_{nl} (2l+1) \int \frac{\mathrm{d}^3\mathbf{K}}{(2\pi)^3} \frac{1}{\mathrm{e}^{\beta\left(\frac{\hbar^2 K^2}{2M} + E_{nl} - \mu_e - \mu_h\right)} - 1} \\ &\quad + g_e \int_\Delta^\infty \frac{\mathrm{d}\omega}{2\pi}\, n_{eh}^B(\omega) \mathrm{Im}\, F(\omega) \end{aligned} \tag{1.12}$$

mit $\beta = (k_B T)^{-1}$. Der erste Term in (1.12) repräsentiert die Dichte der „freien“, d.h. unkorrelierten Quasiteilchen, der zweite die der gebundenen Zustände und der dritte die der (korrelierten) Streuzustände [Zim88, EKK76, KKS93]. Das Auftreten einer unteren Integrationsgrenze Δ im dritten Term mag zunächst befremden, impliziert die Aufteilung der Größe $F(\omega)$ (1.10) in Bindungs- und Streuanteile doch zunächst die Aufteilung der Frequenzintegration bei $\omega = 0$. Es ist aber gut bekannt [KKER86], daß die Band- (bzw. Kontinuums-)kante durch Vielteilcheneffekte in Abhängigkeit von Dichte und Temperatur abgesenkt wird. Dieser Effekt, der im folgenden noch detailliert untersucht wird, führt zu einer (negativen) unteren Grenze $\Delta = \Delta(\mu, T)$ für das Streukontinuum in $F(\omega)$.

Chemisches Bild. Ionisationsgrad

Im vorangegangenen Abschnitt haben wir das Elektron–Loch–Plasma beschrieben, indem die Konstituenten als gedämpfte Quasiteilchen in Streu- und Bindungszuständen betrachtet wurden. Diese Beschreibung wird üblicherweise als „physikalisches Bild“ bezeichnet. Es ist aber für manche Untersuchungen zweckmäßig, die gebundenen Zustände von Elektronen und Löchern als neue Quasiteilchen und damit als dritte Teilchensorte im System zu definieren. Diese neuen Quasiteilchen sind, wie bereits in der Einleitung erwähnt wurde, die Exzitonen. Dazu schreiben wir den Bindungsanteil der Dichte (1.12) als

$$n_{eh}^B\left(\frac{\hbar^2 K^2}{2M} + E_{nl}\right) = \frac{1}{z_e^{-1} z_h^{-1} \mathrm{e}^{\beta\left(E_{nl} + \frac{\hbar^2 K^2}{2M}\right)} - 1}\,, \tag{1.13}$$

wobei $z_a = \mathrm{e}^{\beta\mu_a}$ die Fugazitäten der Ladungsträger sind. Die neue Teilchensorte „Exziton“ wird durch die Definition ihrer Fugazität z_X mit

$$z_X = z_e z_h \mathrm{e}^{-\beta E_{nl}} = \mathrm{e}^{\beta\mu_X} \tag{1.14}$$

eingeführt, wobei die Verteilungsfunktion der Exzitonen durch die ideale Boseverteilung

$$n_X^B\left(\frac{\hbar^2 K^2}{2M}\right) = \frac{1}{z_X^{-1}\mathrm{e}^{\beta\frac{\hbar^2K^2}{2M}} - 1} \tag{1.15}$$

gegeben ist. Das System besteht nun aus drei Teilchensorten – den geladenen Elektronen und Löchern und den neutralen Exzitonen. Die Analogie zum partiell ionisierten Wasserstoffplasma ist wiederum offensichtlich; die Exzitonen spielen die Rolle der Wasserstoffatome. Diese Darstellung ist als „chemisches Bild“ bekannt.

An dieser Stelle muß angemerkt werden, daß der Übergang vom physikalischen ins chemische Bild nur dann sinnvoll ist, wenn die Dichte „sauber“ in Bindungs- und Streuanteile aufgespalten werden kann, was wiederum voraussetzt, daß Bindungszustände und Streukontinuum im Einteilchenspektrum „ausreichend“ voneinander separiert liegen. Das ist strenggenommen nur im Grenzfall verschwindender Dämpfung – ohnehin die Voraussetzung für die Gültigkeit der erweiterten Quasiteilchennäherung – und damit verschwindender Dichte gegeben, aber natürlich für nicht zu große Dichten auch in guter Näherung erfüllt. Andererseits wird eine wohldefinierte Unterscheidung von Bindungs- und Streuzuständen mit wachsender Dichte immer problematischer und ist – wie wir später noch sehen werden – in der Umgebung der Mott–Dichte nicht mehr sinnvoll [BKS99, PSMH00, SMTH00].

Vernachlässigen wir zunächst die dichteabhängige Verbreiterung der Bindungszustände, können wir die Gesamtelektronendichte im chemischen Bild als

$$\begin{aligned} n_e(\mu_e,\mu_h,\mu_X,T) &= g_e\int\frac{\mathrm{d}^3\mathbf{k}}{(2\pi)^3}\,f_e(\epsilon_e(\mathbf{k})) + g_e\int_\Delta^\infty\frac{\mathrm{d}\omega}{2\pi}\,n_{eh}^B(\omega)\mathrm{Im}\,F(\omega) \\ &\quad + g_e g_h\sum_{nl}(2l+1)\int\frac{\mathrm{d}^3\mathbf{K}}{(2\pi)^3}\,n_X^B\left(\frac{\hbar^2K^2}{2M}\right) \\ &= n_e^{\mathrm{QP}} + n_e^{\mathrm{scatt}} + n_X \end{aligned} \tag{1.16}$$

[vgl. Gl. (1.12)] schreiben, d.h. sie teilt sich in die Dichte der ungebundenen Elektronen in „freien“ und Streuzuständen ($n_e^{\mathrm{QP}} + n_e^{\mathrm{scatt}}$) und die der Exzitonen n_X ein.

Wir bezeichnen im folgenden die Dichten der ungebundenen Elektronen und Löcher durch n_e^* und n_h^* mit $n_h^* = n_e^*$ aufgrund der Elektroneutralität, wobei $n_e^* = n_e^{\mathrm{QP}} + n_e^{\mathrm{scatt}}$. Unser Elektron–Loch–System bildet ein partiell ionisiertes Plasma, das dem Ionisationsgleichgewicht

$$e + h \rightleftarrows X \tag{1.17}$$

unterliegt, wobei letzteres über die Definition der Fugazitäten der „neuen“ Teilchen, der Exzitonen (1.14), kontrolliert wird. Diese Relation ist äquivalent zu der bekannten thermodynamischen Bedingung für das chemische Gleichgewicht

$$\mu_X = \mu_e + \mu_h - E_{nl}\,. \tag{1.18}$$

Ein sinnvolles Maß zur Kennzeichnung der Plasmazusammensetzung ist der Ionisationsgrad, der durch

$$\alpha = \frac{n_e^*}{n_e} \tag{1.19}$$

definiert ist.

Die Gleichungen (1.14) oder (1.18) sind äquivalent zu dem aus der Untersuchung chemischer Reaktionen bekannten Massenwirkungsgesetz. Um hieraus eine Gleichung zu gewinnen, die die Plasmazusammensetzung beschreibt, wird üblicherweise angenommen, daß das System nichtentartet ist, d.h. daß die Ladungsträger der Boltzmann–Statistik genügen,

$$f_e(\mathbf{k}) = \mathrm{e}^{\beta\left(\frac{\hbar^2 k^2}{2m_e} - \mu_e\right)}\,, \tag{1.20}$$

wobei die chemischen Potentiale sich aus dem idealen Anteil und einer Wechselwirkungskorrektur zusammensetzen, $\mu_e + \mu_h = \mu_e^{\mathrm{id}} + \Delta\mu_e + \mu_h^{\mathrm{id}} + \Delta\mu_h = \mu_e^{\mathrm{id}} + \mu_h^{\mathrm{id}} + \Delta\mu_{eh}$, mit dem idealen chemischen Potential

$$\mu_e^{\mathrm{id}} = k_B T \ln n_e \Lambda_e^3\,. \tag{1.21}$$

Dann folgt aus (1.14) oder (1.18) eine Saha–Gleichung,

$$\frac{1-\alpha}{\alpha^2} = n_e \Lambda_{eh}^3 e^{-\beta(E_{nl} - \Delta\mu_{eh})}\,, \tag{1.22}$$

wobei die thermische Wellenlänge

$$\Lambda_{eh} = \sqrt{\frac{2\pi\hbar^2}{m_r k_B T}} \qquad \text{mit} \qquad m_r^{-1} = m_e^{-1} + m_h^{-1} \tag{1.23}$$

eingeführt wurde.

Üblicherweise sucht man den Ionisationsgrad α in Abhängigkeit von der Temperatur und der Gesamtelektronendichte. Gleichung (1.22) ist dann eine transzendente Gleichung zur Bestimmung von α, da $\Delta\mu_{eh} = \Delta\mu_{eh}(n_e^*, T) = \Delta\mu_{eh}(\alpha n_e, T)$ gilt.

Auch in diesem relativ einfachen Zugang verbleibt nun noch die Bestimmung der Größen $\Delta\mu_{eh}$ und E_{nl}. Wir wollen im folgenden das Problem etwas allgemeiner angehen. Unabhängig vom Grad der Entartung des Systems gilt Gl. (1.18), d.h.

$$\mu_X(n_X, T) = \mu_e(n_e^*, T) + \mu_h(n_h^*, T) - E_{nl}(n_e, T)\,. \tag{1.24}$$

Mit $n_e^* = n_h^* = \alpha n_e$ und $n_X = n_e - n_e^* = (1-\alpha)n_e$ liest sich diese Gleichung

$$\mu_X((1-\alpha)n_e, T) = \mu_e(\alpha n_e, T) + \mu_h(\alpha n_e, T) - E_{nl}(n_e, T)\,. \tag{1.25}$$

Der Zusammenhang $\mu_X((1-\alpha)n_e, T)$ folgt aus den Gleichungen (1.14) und (1.15), also durch Inversion von

$$n_X(\mu_X, T) = g_e g_h \int \frac{\mathrm{d}^3\mathbf{K}}{(2\pi)^3} \frac{1}{\mathrm{e}^{\beta\left(\frac{\hbar^2K^2}{2M} - \mu_X\right)} - 1}\,. \tag{1.26}$$

Das chemische Potential der ungebundenen Ladungsträger $\mu_a(n_a^*, T)$ $(a = e, h)$ ergibt sich in analoger Weise aus der Verteilungsfunktion, wenn der Dichteanteil der Streuzustände vernachlässigt wird,

$$n_a^*(\mu_a, T) = g_a \int \frac{\mathrm{d}^3\mathbf{k}}{(2\pi)^3} \frac{1}{\mathrm{e}^{\beta(\epsilon_a(\mathbf{k}) - \mu_a)} + 1}\,. \tag{1.27}$$

Das Weglassen der Streuzustände in allen folgenden Betrachtungen ist bei ausreichend tiefen Temperaturen in guter Näherung gerechtfertigt [KKS93].

Die Berechnung von μ_e und μ_h erfordert die Kenntnis der Quasiteilchendispersion der Ladungsträger $\epsilon_e(\mathbf{k})$ bzw. $\epsilon_h(\mathbf{k})$ in RPA, Gl. (1.8).

Wie am Anfang des Abschnitts kurz erwähnt wurde, liegt dem Mott–Effekt das

Verschwinden des Exzitons im Leitungsband (also des Bindungszustandes im Streukontinuum) bei hohen Dichten zugrunde. Die Bindungsenergie des Exzitons geht direkt in Gl. (1.25) ein. Es stellt sich die Frage, wie die Lage der Bandkante mit den bisher betrachteten Größen zusammenhängt, mit anderen Worten, wie man aus der k-abhängigen Quasiteilchendispersion eine k-unabhängige Größe gewinnen kann, die ein Maß für die untere Grenze des Streukontinuums darstellt. Es erscheint naheliegend, hierfür z.B. die Selbstenergie bei $k = 0$ oder aber eine über die Verteilung gemittelte Selbstenergie heranzuziehen. Ein besser fundiertes Bild der Kontinuumskante gewinnt man jedoch wie folgt [Zim88, KSK05]:

Wir betrachten die Quasiteilchendispersion (1.8). Die Größe $\mathrm{Re}\,\Sigma_a^{\mathrm{RPA}}(\mathbf{k},\omega)|_{\hbar\omega=\epsilon_a(\mathbf{k})}$ wird auch als Quasiteilchenverschiebung $\Delta_a(\mathbf{k})$ bezeichnet. Eine dazu korrespondierende, aber k-unabhängige, also „starre“ Verschiebung (*rigid shift*) Δ_a kann man definieren, indem man fordert, daß für beide Größen die gleiche Dichte folgt:

$$n_a(\mu_a,T) = g_a \int \frac{\mathrm{d}^3\mathbf{k}}{(2\pi)^3} \frac{1}{\mathrm{e}^{\beta\left(\frac{\hbar^2k^2}{2m_a}+\Delta_a(\mathbf{k})-\mu_a\right)}-1} \tag{1.28}$$

$$= g_a \int \frac{\mathrm{d}^3\mathbf{k}}{(2\pi)^3} \frac{1}{\mathrm{e}^{\beta\left(\frac{\hbar^2k^2}{2m_a}+\Delta_a-\mu_a\right)}-1}\,. \tag{1.29}$$

Offensichtlich entspricht der Integrand in der zweiten Zeile einer idealen Fermiverteilung mit dem chemischen Potential $\mu_a^{\mathrm{id}} = \mu_a - \Delta_a$, d.h. es gilt $\mu_a = \mu_a^{\mathrm{id}} + \Delta_a$. Die Größe $\Delta_a \equiv \Delta\mu_a$ stellt also den Korrelationsanteil des chemischen Potentials dar, und $\Delta\mu_{eh} = \Delta\mu_e + \Delta\mu_h$ ist offensichtlich ein gutes Maß für die dichte- und temperaturabhängige Verschiebung der Kontinuumskante.

Dann ist es möglich, anstelle der numerisch aufwendigen Berechnung der Quasiteilchendispersion der Ladungsträger in RPA und *vollständiger* Inversion der Gleichung (1.27) eine sogenannte *unvollständige* Inversion durchzuführen, indem das chemische Potential wie oben in idealen und Wechselwirkungsanteil zerlegt und nur bezüglich des idealen Anteils invertiert wird.

Die Bindungsenergie des exzitonischen Grundzustands E_{nl} mit $n = 1$ und $l = 0$ liegt über weite Dichtebereiche konstant bei -1 Rydberg. Diese Aussage folgt aus experimentellen Befunden [FSTU82], aber auch aus theoretischen – sowohl analytischen als auch numerischen – Berechnungen [KKK77, ZKK$^+$78, Ric07]. Der Grund dafür ist eine weitgehende Kompensation der Vielteilcheneffekte. Konkret kompensieren sich für tiefliegende Bindungszustände (kleine Hauptquantenzahl n) die Beiträge der Hartree–

Fock–Selbstenergie und des Phasenraumverbrauchs (*Pauli blocking*) zur Störungskorrektur erster Ordnung zur Bindungsenergie [KSK05]. Erst für höhere Dichten wird diese Kompensation zunehmend unvollständig.

Die einfachste Möglichkeit, den Ionisationsgrad eines Elektron–Loch–Plasmas auch bei tiefen Temperaturen, also im entarteten Regime, in dem die Saha–Gleichung nicht mehr gilt, zu berechnen, ist damit vorgegeben: Man verschaffe sich (a) einen Ausdruck für den Korrelationsanteil des chemischen Potentials $\Delta\mu_{eh}$ und berechne (b) die exzitonische Bindungsenergie E_{nl}, z.B. störungstheoretisch. Diese Größen setze man in die Gl. (1.25) ein und löse diese.

Für $\Delta\mu_{eh}$ können zwei Grenzfälle einfach berechnet werden, zum einen der nichtentartete (also der Grenzfall hoher Temperaturen)

$$\Delta\mu_{eh}^{\mathrm{D}} = \frac{1}{4\pi\epsilon_0\epsilon_r}\kappa e^2\,, \tag{1.30}$$

wobei κ der inverse Abschirmradius ist, $\kappa^2 = \frac{e^2}{\epsilon_0\epsilon_r k_B T}\left(\frac{\partial n_e}{\partial\mu_e} + \frac{\partial n_h}{\partial\mu_h}\right)$. In der Plasmaphysik ist dieser Grenzfall als Debye–Approximation bekannt, in der Halbleiterphysik als Coulombloch(*Coulomb hole*)–Approximation. Im Grenzfall tiefer Temperaturen ist $\Delta\mu_{eh}$ durch die Hartree–Fock–Selbstenergie gegeben:

$$\Delta\mu_{eh}^{\mathrm{HF}} = \frac{1}{2}\left(\Sigma_e^{\mathrm{HF}}(k=0) + \Sigma_h^{\mathrm{HF}}(k=0)\right)\,. \tag{1.31}$$

In beiden Grenzfällen (und nur in diesen!) gilt der *Rigid–Shift*–Ansatz (1.28) exakt. Zimmermann [Zim88] und Rösler *et al.* [RZR84] haben Formeln entwickelt, die zwischen den beiden Grenzfällen interpolieren. Alle diese Näherungen für $\Delta\mu_{eh}$ werden später noch diskutiert.

Zweiteilchenspektrum

Auf dem bisher beschriebenen Stand wurde die Theorie in der Arbeit A.2 dargestellt. In den Arbeiten A.3, A.6 und [SRK$^+$10, MRS$^+$11] sind wir noch zwei wesentliche Schritte darüber hinausgegangen.[4] Der erste dieser Schritte betrifft die Berechnung

[4] In den Arbeiten A.3 und [SRK$^+$10] wurde die Theorie weiterentwickelt und, wie in A.2, auf Zinkselenid (ZnSe) angewendet. Im Fokus von A.6 stand die Anwendung auf Cu_2O mit besonderem Augenmerk auf den möglichen Existenzbereich eines exzitonischen BEK. In der Arbeit [MRS$^+$11] wurde die Theorie auf GaAs/AlGaAs–Quantenfilmstrukturen angewendet und experimentell beobachtete Exzitonlinienverschiebungen erklärt.

der exzitonischen Bindungsenergie. Die Lage der Exzitonniveaus und der Bandkante kann experimentell durch spektral aufgelöste Messung der Lichtabsorption bestimmt werden. Die Absorption ist mit dem Imaginärteil der dielektrischen Funktion bzw. der Suszeptibilität χ verknüpft. Letztere Größe charakterisiert die dielektrischen Eigenschaften des Halbleiters und ist mit der Polarisation über die Beziehung

$$P(\omega) = \int \frac{\mathrm{d}^3\mathbf{k}}{(2\pi)^3}\, p(\mathbf{k},\omega) = \chi(\omega)\, E(\omega) \tag{1.32}$$

verbunden, d.h. für schwache Felder hängt die makroskopische Polarisation linear vom Feld ab. Die Größe $p(\mathbf{k},\omega)$, erzeugt durch einen Testpuls $E(\omega)$ und durch das Dipolmatrixelement d an den Halbleiter gekoppelt, genügt den bekannten Halbleiter–Bloch–Gleichungen (HBG), die in exzitonischen Einheiten als

$$\begin{aligned} &\{\omega - \mathbf{k}^2 - \Delta^{\mathrm{HF}}(\mathbf{k}) - \Sigma^r(\mathbf{k},\omega)\}\, p(\mathbf{k},\omega) \\ &+ \int \frac{\mathrm{d}^3\mathbf{q}}{(2\pi)^3} \{N(\mathbf{k}) V_{eh}(\mathbf{k}-\mathbf{q}) + \Theta(\mathbf{k},\mathbf{q},\omega)\}\, p(\mathbf{q},\omega) = N(\mathbf{k})\, \mathrm{d}\, E(\omega) \end{aligned} \tag{1.33}$$

darstellbar sind. Hier finden sich die oben erwähnten Vielteilcheneffekte, zum einen als Hartree–Fock(HF)–renormierte Ladungsträgerenergien $\Delta^{\mathrm{HF}}(\mathbf{k})$ und Phasenraumverbrauch (*Pauli blocking*) $N(\mathbf{k}) = 1 - f_e(\mathbf{k}) - f_h(\mathbf{k})$, zum anderen als Abschirmeffekte in der renormierten Wechselwirkungsmatrix $\Theta(\mathbf{k},\mathbf{q},\omega)$

$$\begin{aligned} \Theta(\mathbf{k},\mathbf{q},\omega) &= \Delta V^{\mathrm{eff}}(\mathbf{k},\mathbf{q},\omega) - \mathrm{i}\Gamma(\mathbf{k},\mathbf{q},\omega) \\ &= \sum_{a\neq b} \int \frac{\mathrm{d}\bar{\omega}}{2\pi} \frac{[1-f_a(\mathbf{k})] V_{ab}^{>}(\mathbf{k}-\mathbf{q},\bar{\omega}) + f_a(\mathbf{k})\, V_{ab}^{<}(\mathbf{k}-\mathbf{q},\bar{\omega})}{\hbar\omega - \epsilon_a(\mathbf{k}) - \epsilon_b(\mathbf{q}) - \hbar\bar{\omega} + \mathrm{i}[\Gamma_a(\mathbf{k}) + \Gamma_b(\mathbf{q})]/2}\,, \end{aligned} \tag{1.34}$$

deren Real- und Imaginärteile $\Delta V^{\mathrm{eff}}(\mathbf{k},\mathbf{q},\omega)$ bzw. $\Gamma(\mathbf{k},\mathbf{q},\omega)$ die effektive Wechselwirkung bzw. die sogenannte nichtdiagonale Dephasierung (*off-diagonal dephasing*) sind, und in der Interband–Selbstenergie $\Sigma^r(\mathbf{k},\omega)$

$$\begin{aligned} \Sigma^r(\mathbf{k},\omega) &= \Delta e^{sc}(\mathbf{k},\omega) - \mathrm{i}\Gamma(\mathbf{k},\omega) = \int \frac{\mathrm{d}^3\mathbf{q}}{(2\pi)^3}\, \Theta(\mathbf{q},\mathbf{k},\omega) \\ &= \Sigma_e^r(\mathbf{k},\omega-\epsilon_h) + \Sigma_h^r(\mathbf{k},\omega-\epsilon_e)\,, \end{aligned} \tag{1.35}$$

deren Real- und Imaginärteile $\Delta e^{sc}(\mathbf{k},\omega)$ bzw. $\Gamma(\mathbf{k},\omega)$ die renormierte Interband–Selbstenergie und die diagonale Dephasierung (*diagonal dephasing*) sind.

Die Quasiteilchenenergien $\varepsilon_a(\mathbf{k})$ und die Quasiteilchendämpfung $\Gamma(\mathbf{k},\omega)$ folgen aus

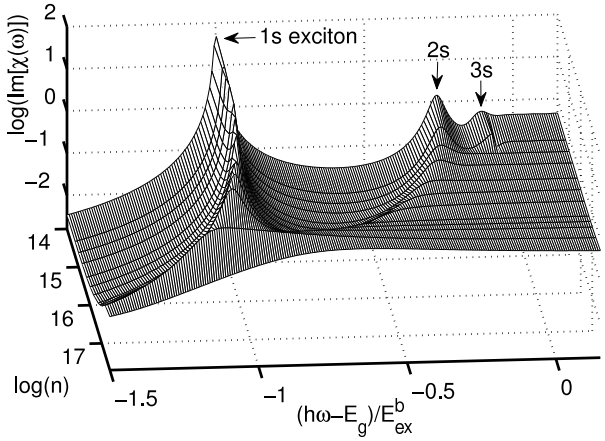

Abbildung 1.1: Imaginärteil der Suszeptibilität in Abhängigkeit von Ladungsträgerdichte $n[\mathrm{cm}^{-3}]$ und Energie. E_g ist die Bandlücke und E_ex^b ist die Energie des 1S–Paraexzitons. Abbildung entnommen aus A.3.

den Gln. (1.8,1.3) mit der RPA–Selbstenergie

$$\Sigma_a^{\gtrless}(\mathbf{k},\omega) \;=\; \int \frac{\mathrm{d}^3\mathbf{q}}{(2\pi)^3} \int \frac{\mathrm{d}\omega'}{2\pi}\, g_a^{\gtrless}(\mathbf{k}-\mathbf{q},\omega-\omega')\, V_{aa}^{\gtrless}(\mathbf{q},\omega')\,. \tag{1.36}$$

Die Korrelationsfunktionen des abgeschirmten Potentials $V_{ab}^{\gtrless}(\mathbf{q},\omega)$, die in den Gln. (1.34–1.36) auftauchen, sind mit der inversen retardierten dielektrischen Funktion $\varepsilon^{r^{-1}}(\mathbf{q},\omega)$ verbunden,

$$\begin{aligned} V_{ab}^{<}(\mathbf{q},\omega) &= 2\mathrm{i}\, V_{ab}(\mathbf{q})\, \mathrm{Im}\, \varepsilon^{r^{-1}}(\mathbf{q},\omega) n^B(\omega)\,, \\ V_{ab}^{>}(\mathbf{q},\omega) &= 2\mathrm{i}\, V_{ab}(\mathbf{q})\, \mathrm{Im}\, \varepsilon^{r^{-1}}(\mathbf{q},\omega) \left[1+n^B(\omega)\right]\,. \end{aligned} \tag{1.37}$$

$n^B(\omega)$ ist die Boseverteilung der elementaren Anregungen im Plasma (Plasmonen). Für $\varepsilon^{r^{-1}}(\mathbf{q},\omega)$ wurde die Lindhard–Funktion verwendet.

Die dreidimensionale Darstellung des Imaginärteils der Suszeptibilität in der Abb. 1.1 vermittelt einen Überblick über die Lage der exzitonischen Zustände und der Bandkante. Die Bindungszustände treten als mehr oder weniger scharfe Maxima hervor, die sich deutlich vom benachbarten plateauartigen Band abheben. Mit wachsender Dichte wandert die Bandkante zu niedrigeren Energien, die Bindungszustände ebenfalls, aber wesentlich schwächer, so daß sie nacheinander im Band verschwinden.

Belassen wir es zunächst bei diesem ersten Eindruck, extrahieren die quantitativen Informationen aus der Suszeptibilität (Exzitonenergie und Lage der Bandkante)

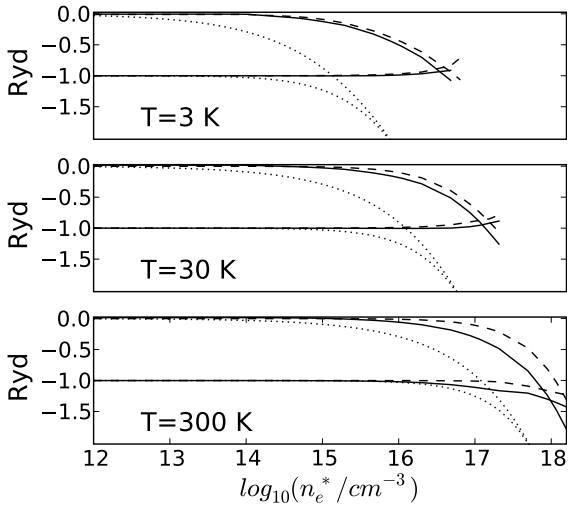

Abbildung 1.2: Zweiteilchenspektrum in Abhängigkeit von der Dichte in ZnSe: Bandkante (obere Kurven) und exzitonische Grundzustandsenergie (untere Kurven). Lösung der HBG (durchgezogene Linien), Lösung mit $\Theta(\mathbf{k},\mathbf{q},\omega)=0$ und $\Sigma^r(\mathbf{k},\omega)=0$ (Hartree–Fock–Approximation; gestrichelt), statische Grenze von $\Theta(\mathbf{k},\mathbf{q},\omega)$ and klassische Grenze für $\Delta e^{sc}(\mathbf{k},\omega)$ (Debye–Approximation; gepunktet). Ryd bezeichnet das exzitonische Rydberg. Abbildung entnommen aus A.3.

und vergleichen mit den oben erwähnten Grenzfällen (Debye bzw. Hartree–Fock), erhalten wir die in Abb. 1.2 dargestellte Dichteabhängigkeit von exzitonischem 1S–Grundzustand und Bandkante [A.3]. Hier ist noch einmal deutlich zu erkennen, daß sich die Bandkante stark und die Bindungsenergie schwach mit der Dichte verändern. Die Differenz aus beiden Energien stellt die effektive Ionisierungsenergie dar, die mit wachsender Dichte auf null abnimmt. Ist die Null erreicht, d.h. kreuzen sich Bandkante und Bindungsenergie, kann der gebundene Zustand nicht länger existieren, und das Exziton wird ionisiert. Dieser spektrale Effekt wird als Mott–Effekt bezeichnet, die entsprechende Dichte als Mott–Dichte.

Im Vergleich zur Lösung der Halbleiter–Bloch–Gleichungen (1.33) in RPA sind zusätzlich die Grenzfälle mit $\Theta(\mathbf{k},\mathbf{q},\omega)=0$ und $\Sigma^r(\mathbf{k},\omega)=0$ (Hartree–Fock–Approximation) sowie mit der statischen Grenze von $\Theta(\mathbf{k},\mathbf{q},\omega)$ und der klassischen Grenze für $\Delta e^{sc}(\mathbf{k},\omega)$ (Debye–Approximation) gezeigt. Während erstere Näherung den Verlauf der Energien und damit auch die Mott–Dichte im Vergleich zur vollen Rechnung bei tiefen Temperaturen relativ gut wiedergibt, überschätzt die Debye–Approximation die Vielteilcheneffekte drastisch und liefert selbst für Zimmertemperatur eine deutlich zu geringe Mott–Dichte.

Die zweite wesentliche Neuerung in der Arbeit A.3 bestand in der Berechnung der Quasiteilchenenergien der Ladungsträger durch selbstkonsistente Lösung der Gleichung für die retardierte Selbstenergie in Quasiteilchennäherung, die aus Gl. (1.36) folgt,

$$\Sigma_a^{\mathrm{RPA}}(\mathbf{k},\omega)\Big|_{\hbar\omega=\varepsilon_a(\mathbf{k})} = \Sigma_a^{\mathrm{HF}}(\mathbf{k}) + \int \frac{\mathrm{d}^3\mathbf{q}}{(2\pi)^3} \int \frac{\mathrm{d}\omega'}{2\pi} \frac{\left[1 - f^a(\varepsilon_a(\mathbf{q})) + n^B(\omega')\right] \hat{V}(\mathbf{k}-\mathbf{q},\omega')}{\varepsilon_a(\mathbf{k}) - \varepsilon_a(\mathbf{q}) - \omega' + \mathrm{i}\Gamma_a(\mathbf{q})/2}, \tag{1.38}$$

wobei die Größe $\hat{V}(\mathbf{q},\omega)$ mit den Korrelationsfunktionen des abgeschirmten Potentials, Gln. (1.37), durch $\hat{V}(\mathbf{q},\omega) = \mathrm{i}\left[V^{>}(\mathbf{q},\omega) - V^{<}(\mathbf{q},\omega)\right]$ verknüpft ist, gemeinsam mit der Gleichung für die Quasiteilchenenergie (1.8). Damit ist es möglich, die Gleichung für die Ladungsträgerdichte (1.27) *vollständig* zu invertieren, also das chemische Potential der Ladungsträger ohne die zusätzliche Näherung *unvollständiger* Inversion zu berechnen.

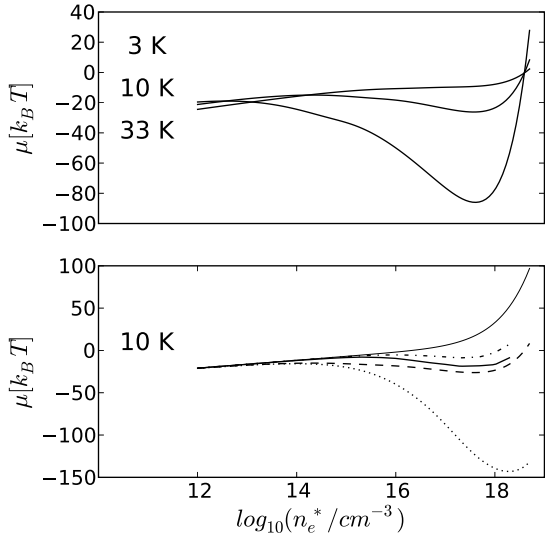

Abbildung 1.3: Summe der chemischen Potentiale von Elektronen und Löchern $\mu = \mu_e + \mu_h$ in Abhängigkeit von der Dichte in ZnSe. Obere Abbildung: μ^{RZR} für verschiedene Temperaturen T: 3 K (oben), 10 K (Mitte), 33 K (unten). Untere Abbildung: μ^{iter} entsprechend der selbstkonsistenten Lösung der Gln. (1.38) und (1.8) (fett durchgezogen), μ^{RZR} (gestrichelt), μ^{id} (dünn durchgezogen), μ^{HF} (Strich-Punkt), Debye–Approximation $\mu^{\mathrm{D}} = \mu_{\mathrm{e}}^{\mathrm{id}} + \mu_{\mathrm{h}}^{\mathrm{id}} - \Delta\mu_{\mathrm{eh}}^{\mathrm{D}}$ (gepunktet), für $T = 10$ K. Abbildung entnommen aus A.3.

Resultate dieser Rechnung sind in der Abbildung 1.3 (aus A.3) dargestellt, die im oberen Teil die Summe der chemischen Potentiale von Elektronen und Löchern über

der Dichte für verschiedene Temperaturen zeigt. Der Van–der–Waals–Bogen für tiefere Temperaturen kennzeichnet eine Instabilität $\partial\mu/\partial n \leq 0$ und kann Anzeichen eines Phasenübergangs sein. Im unteren Teil wird die selbstkonsistente Lösung mit Resultaten der unvollständigen Inversion der Dichtegleichung für eine feste Temperatur verglichen, wobei der Korrelationsanteil des chemischen Potentials $\Delta\mu_{eh}$ in verschiedenen Näherungen mitgenommen wurde: $\Delta\mu_{eh} = 0$ (μ^{id}), Hartree–Fock (μ^{HF}), Debye (μ^{D}) und nach der Interpolationsformel von Rösler, Zimmermann und Richert [RZR84] (μ^{RZR}). Allen Fällen mit Ausnahme des idealen ist das Auftreten eines Van–der–Waals–Bogens gemeinsam, wobei es quantitative Unterschiede gibt. Die deutlichste Abweichung zeigt der Debye–Fall.

Mott–Übergang

Wir haben nun alle Größen parat, um das Ionisationsgleichgewicht des ELP zu analysieren. Dazu ist die implizite Gleichung (1.25) für den Ionisationsgrad α zu lösen. Die Abbildung 1.4 illustriert die Lösung und zeigt die dabei auftretende Komplikation. Für eine vorgegebene Gesamtelektronendichte und Temperatur werden linke und rechte Seite von Gl. (1.25) über α aufgetragen. Der Schnittpunkt der Kurven kennzeichnet die Lösung. Aufgrund des Van–der–Waals–Bogens im chemischen Potential der Ladungsträger kann es aber für bestimmte Dichten und Temperaturen bis zu drei Schnittpunkte geben – die Lösung ist dann also mehrdeutig.

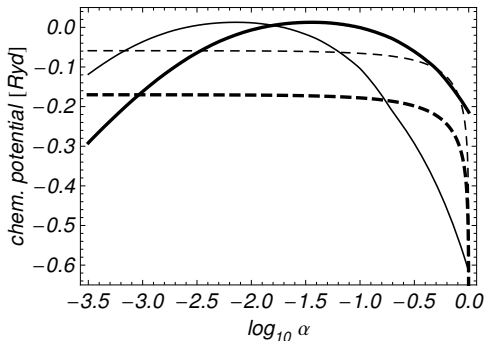

Abbildung 1.4: Graphische Lösung der Gl. (1.25): chemisches Potential der Exzitonen μ_X [linke Seite von (1.25); gestrichelt] und Summe der chemischen Potentiale von Elektronen und Löchern minus Bindungsenergie $\mu_e + \mu_h - E_1$ [rechte Seite von (1.25); durchgezogen] in Abhängigkeit von α für $T = 20$ K und zwei Dichten: $n_e = 10^{17}$ cm^{-3} (fett; eine Lösung für α) und $n_e = 5 \times 10^{17}$ cm^{-3} (dünn; drei Lösungen für α). Abbildung entnommen aus A.3.

Der Ionisationsgrad α ist in den Abbildungen 1.5 und 1.6 über der Gesamtelektronendichte dargestellt. Man erkennt das erwartete Verhalten: Bei höheren Temperaturen ist der Ionisationsgrad bei niedrigen Dichten etwa eins (die sogenannte Entropieionisation). Dieser Bereich ist bei tieferen Temperaturen zu noch deutlich niedrigeren Dichten verschoben und nicht mehr dargestellt. Im mittleren Dichtebereich fällt α auf null ab, um dann mehr oder weniger schlagartig (wieder) auf eins zu steigen. Dieser Übergang vom Exzitonengas zum vollständig ionisierten ELP wird als Mott–Übergang bezeichnet. Er kann, muß aber nicht von einem Phasenübergang begleitet sein [EKK76]. Im Bereich des Mott–Übergangs tritt bei tieferen Temperaturen die oben erwähnte Mehrdeutigkeit des Ionisationsgrades auf.

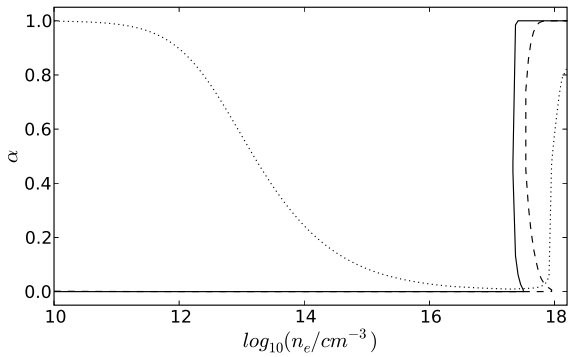

Abbildung 1.5: Ionisationsgrad α in Abhängigkeit von der Dichte für verschiedene Temperaturen T, Gl. (1.25): 2 K (durchgezogen), 10 K (gestrichelt) und 30 K (gepunktet). Abbildung entnommen aus A.3.

Hier wird in der Realität offensichtlich nicht die abgebildete Kurve durchlaufen, d.h. die mittlere Lösung ist instabil. Stattdessen könnte das Mehrdeutigkeitsgebiet als Koexistenzgebiet zweier Phasen (mit $\alpha = 0$ bzw. $\alpha = 1$) interpretiert werden [EKK76]. Eine ähnliche Interpretation (als Bistabilität und Hysterese) geben Snoke und Crawford [SC95].

Betrachtet man nun aber Abb. 1.6, in der verschiedene Approximationen miteinander verglichen werden, so wird deutlich, daß der Dichtebereich, in dem α mehrdeutig ist, immer weiter schrumpft, je besser die verwendete Näherung ist. Aus der Thermodynamik des Wasserstoffplasmas ist bekannt, daß die Berücksichtigung der Wechselwirkung der neutralen Atome untereinander das Mehrdeutigkeitsgebiet vollständig verschwinden lassen sollte [SK82].

Für einen abschließenden Überblick soll in Abb. 1.7 der Ionisationsgrad in Abhängigkeit von Dichte und Temperatur als Konturdiagramm gezeigt werden. Hier erkennt

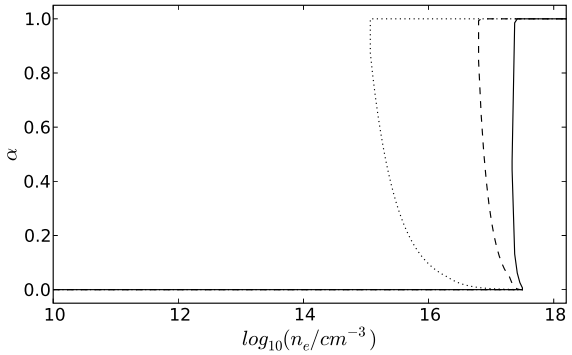

Abbildung 1.6: Ionisationsgrad α in Abhängigkeit von der Dichte, Gl. (1.25), für $T = 2$ K. Vergleich verschiedener Näherungen für das chemische Potential: μ^{iter} (durchgezogen), μ^{RZR} (gestrichelt) und Debye–Approximation μ^{D} (gepunktet). Abbildung entnommen aus A.3.

man noch einmal die *Dichteionisation* für konstante Temperatur, aber auch die *thermische Ionisation* für konstante Dichte. Das gestrichelt umrahmte Dreieck rechts unten zeigt den Bereich, in dem Bose–Einstein–Kondensation von Exzitonen möglich ist.

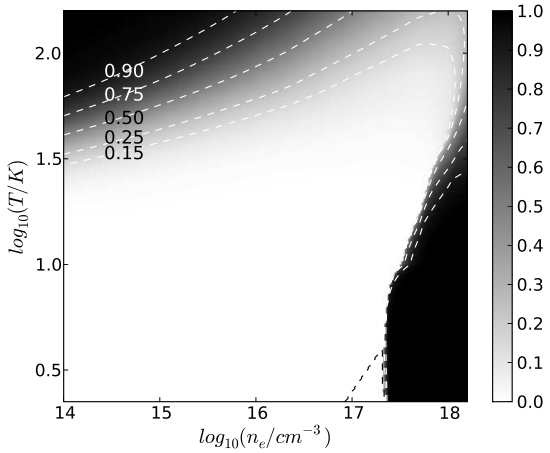

Abbildung 1.7: Isolinien des Ionisationsgrades in der Dichte–Temperatur–Ebene für ZnSe. Abbildung entnommen aus A.3.

In der Arbeit A.6 haben wir ein sehr ähnliches Resultat für den Ionisationsgrad in Cu_2O erhalten.[5] Besonders bemerkenswert war hier die Temperaturunabhängigkeit der Mott–Dichte bei tiefen Temperaturen bis hinauf zu etwa 60 K.

Können wir in Hinblick auf die Mehrdeutigkeit des Ionisationsgrades in bestimm-

[5] Andere Rechnungen zum Ionisationsgrad in Cu_2O auf ähnlichem Niveau sind dem Verfasser nicht bekannt.

ten Bereichen noch hoffen, daß sie durch verbesserte Näherungen – insbesondere die Berücksichtigung der Exziton–Exziton–Wechselwirkung – zum Verschwinden gebracht werden kann, wirft ein genauerer Blick auf die bisherigen Resultate ein weiteres Problem auf. Vergleicht man z.B. den mittleren Teil der Abb. 1.2 mit der gepunkteten Linie in Abb. 1.5, so fällt auf, daß der Schnittpunkt von Bandkante und Exzitonenergie bei etwa 10^{17} cm^{-3} liegt, der Übergang von $\alpha = 0$ auf $\alpha = 1$ aber erst bei etwa 10^{18} cm^{-3} erfolgt. Der Vergleich der anderen Temperaturen aus Abb. 1.2 mit Abb. 1.7 zeigt ähnliche Diskrepanzen. Wo aber liegt nun die Mott–Dichte? Wird sie durch den Mott–Effekt oder den Mott–Übergang definiert? Oder ist unser bisher entwickeltes Bild von diesem Phänomen falsch oder doch zumindest unzureichend?

Um diese Fragen zu klären, untersuchen wir noch einmal den Imaginärteil der Suszeptibilität, Abb. 1.1. Bisher hatten wir Exzitonenergien und Bandkante als beliebig scharfe Linien betrachtet. Offensichtlich sind aber die Exzitonniveaus durch die Dämpfung bei höheren Dichten deutlich verbreitert, und auch die Bandkante ist keinesfalls scharf und eindeutig von den Bindungszuständen trennbar. Die Niveauverbreiterung haben wir in der Arbeit [SRK$^+$10] in der spektralen Darstellung des Mott–Effekts analog zur Abb. 1.2 berücksichtigt. Zumindest für höhere Temperaturen wird aus dem Schnittpunkt aus Exzitonenergie und Bandkante eine Schnittlinie, die einen endlichen Dichtebereich überstreicht.

Eine eingehende Analyse der Problematik haben wir schließlich in der Arbeit A.8 vorgenommen. Die zugrundeliegende Fragestellung ist, ob und wie die Idee eines Schnitts zweier scharfer Linien auf die Verschmelzung einer Linie endlicher Breite mit einem nicht eindeutig separierbaren Kontinuum quantitativ übertragbar ist. Die Untersuchungen in A.8 haben zwar den Mott–Übergang in GaAs/GaAlAs–Quantenfilmsystemen zum Gegenstand, jedoch ist das Fazit aus den folgenden Überlegungen qualitativ auf Volumenhalbleiter wie Cu_2O übertragbar.

Das Exzitonniveau ist bereits für niedrigere Dichten keine scharfe Linie, siehe Abb. 1.8, linker Teil. Mit zunehmender Dichte wächst die Breite des Niveaus, besonders drastisch im für den Mott–Übergang relevanten Dichtebereich (Abb. 1.8, linker Teil), während die Peakintensität abnimmt. Betrachtet man zusätzlich die Absorption an der Bandkante (Abb. 1.8, rechter Teil), so fällt auf, daß die Bandkante vom Exzitonniveau nicht eindeutig trennbar ist, d.h. die Absorption fällt dazwischen nicht auf null ab. Wie kann nun ein Kriterium „Bandkante erreicht Exziton“ gefunden werden? Eine mögliche und sinnvolle Antwort hierauf, wie wir sie in A.8 gegeben haben, lautet: Man sucht die Stelle, wo das Niveau der Absorption an der Bandkante die Flanke des Ex-

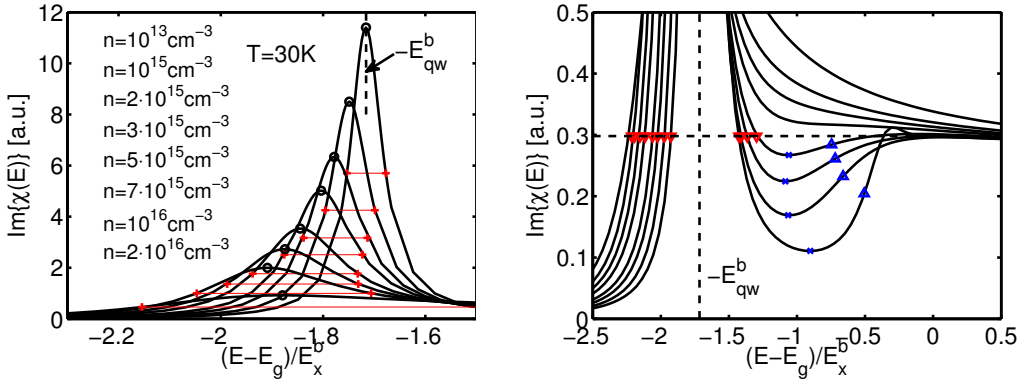

Abbildung 1.8: Imaginärteil der Suszeptibilität $\mathrm{Im}\,\chi$ in der exzitonischen (links) und der Bandkantenregion (rechts) bei $T = 50$ K für wachsende Ladungsträgerdichten in einer GaAs/GaAlAs–Quantenfilmstruktur. Absorptionsmaxima (links, ○) bzw. -halbmaxima (links, +), Halbwertsbreite (links, horizontale rote Linien), Absorptionsminima (rechts, ×) bzw. -halbminima (rechts, ▲), Exzitonenergie bei schwacher Anregung (vertikal gestrichelt), Niveau der Bandkantenabsorption (horizontal gestrichelt), Schnittpunkte mit der exzitonischen Absorption (▼). Abbildung entnommen aus A.8.

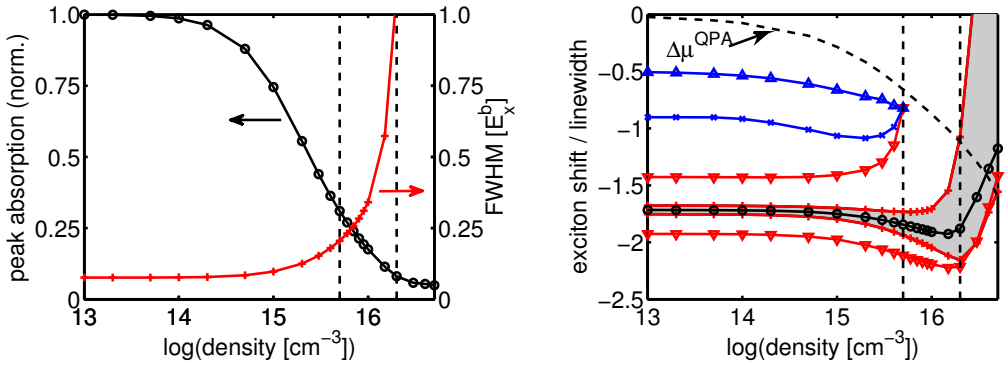

Abbildung 1.9: Links: Normiertes Absorptionsmaximum und Halbwertsbreite in Abhängigkeit von der Dichte, Marker siehe Abb. 1.8. Rechts: Exzitonenergie (○), Halbwertsbreite (+ und grau hinterlegte Fläche), Niveau, wo die exzitonische Absorption gleich der Bandkantenabsorption ist (▼), Absorptionsminima (×) bzw. -halbminima (▲). Abbildung entnommen aus A.8.

zitons schneidet [6] und betrachtet die Stelle minimaler Absorption (oder anschaulicher

[6] Betrachten wir den Energiebereich, der durch dieses Kriterium begrenzt wird (Abb. 1.9, rechter Teil), so kann für höhere Dichten von einem energetisch scharf definierten Exzitonniveau praktisch

die Stelle, wo die Bandkantenabsorption bzgl. des Minimums auf die Hälfte gefallen ist), die mit wachsender Dichte auf die obere Flanke des Exzitons zuläuft und sie genau dann erreicht, wenn das Minimum verschwindet (Abb. 1.9, linker Teil). Dort verschmilzt das Exzitonniveau ununterscheidbar mit der Bandkantenabsorption, und das Exziton „überlebt“ nur als Resonanz im Kontinuum. Diese Stelle sollte also eine untere Grenze für die Mott–Dichte markieren. Eine obere Grenze könnte dadurch definiert werden, daß der Korrelationsanteil des chemischen Potentials die obere Exzitonflanke (dann an der Stelle der Halbwertsbreite) erreicht (Abb. 1.9, rechter Teil).

Anstelle einer durch den Schnittpunkt zweier scharfer Linien klar definierten Mott–Dichte erhält man also einen Dichtebereich, in dem das Aufbrechen der Bindungszustände erwartet werden kann. Diese Unschärfe widerspiegelt die bekannte Tatsache, daß das chemische Bild – ohnehin nur für verschwindende Dichten exakt – im relevanten Dichtebereich, wo Bindungs- und Streuzustände nicht mehr eindeutig unterscheidbar sind, seine Gültigkeit verliert. Damit ist in diesem Bereich aber auch der Ionisationsgrad keine wohldefinierte Größe mehr. Formulierungen mit Blick auf den Mott–Übergang wie „schlagartiges Aufbrechen der Bindungszustände“ oder „Sprung im Ionisationsgrad von 0 auf 1“ sind daher immer unter Berücksichtigung einer prinzipiellen, durch Vielteilcheneffekte induzierten Unschärfe in der Dichte zu verstehen.

1.3.2 Theorie der Quantenkondensation

In den bisher vorgestellten Untersuchungen lag das hauptsächliche Augenmerk auf der Abgrenzung des Existenzbereichs der Exzitonen, ohne daß ein mögliches exzitonisches Kondensat explizit Berücksichtigung fand. Der Mott–Übergang in einem kondensierten Exzitonengas muß aber nicht automatisch zum Verschwinden der kondensierten Phase führen. Ein Kondensat ungebundener Elektron–Loch–Paare stellt natürlich nicht ein Bose–Einstein–Kondensat (BEK) im üblichen Sinne dar, sondern, analog zu den Cooper–Paaren beim Phänomen der Supraleitung, einen BCS-artigen Zustand [KK64, Clo65, HR68, Zim76]. Beide Formen können unter dem Oberbegriff der Quantenkondensation gemeinsam beschrieben werden. Andererseits unterscheiden sich die kondensierenden Objekte in ihrer physikalischen Natur deutlich, zudem sind nur die Grenzfälle sehr niedriger bzw. hoher Dichten streng als BEK bzw. BCS–Kondensat zu bezeichnen. (Wie wir im vorigen Abschnitt gesehen haben, ist das Exziton nur für sehr kleine Dichten ein wohldefinierter Zustand. Im BCS–Fall sollte die cooperpaar-

nicht mehr die Rede sein, so stark ist es durch Vielteilcheneffekte verbreitert.

bildende Wechselwirkung so schwach sein, daß der Paarradius groß gegen den mittleren Teilchenabstand ist [LZ12].) Von großem Interesse ist daher die Frage nach einer gemeinsamen Phasengrenze des Quantenkondensats auch im Übergangsbereich (*BEC–BCS crossover*). Bereits in [Eag69, Leg80, NSR85] wurde diese Frage untersucht und gezeigt, daß es einen nahtlosen Übergang („*smooth crossover*“) zwischen den Grenzfällen gibt. Im Halbleiter, wo die kondensierte Phase auch als exzitonischer Isolator bekannt ist, wurde die Phasengrenze z.B. für den druckinduzierten Halbleiter–Halbmetall–Übergang untersucht [BF06].

Unser Anliegen war es, einen allgemeinen Zugang zur Quantenkondensation auf dem Niveau der Ladungsträger zu finden. In den Arbeiten A.1 sowie [SKH09, KSH10] wurde eine Nichtgleichgewichtstheorie der Quantenkondensation in Fermisystemen mit Bindungszuständen im Rahmen der reellzeitigen Greenfunktionen entwickelt und diskutiert. Neben dem rein formalen Interesse an einer solchen Theorie motiviert zudem die Möglichkeit, die Phasengrenze des Quantenkondensats bestimmen zu können, d.h. die kritische Temperatur, unterhalb derer Kondensation auftritt. Im folgenden Abschnitt werden die Grundzüge dargelegt.

Nichtgleichgewichtstheorie. Time Long Range Order

Zur Beschreibung von Systemen geladener Fermiteilchen existieren wohlausgearbeitete Konzepte im Rahmen des Formalismus der reellzeitigen Greenfunktionen [FW71, EKK76, KKER86, HJ96, KSK05]. Da wir das Verhalten von Elektron–Loch–Paaren beschreiben wollen, ist das System auf der Zweiteilchenebene zu betrachten. Die Zweiteilchen–Greenfunktion G_{ab} ist definiert durch

$$(\mathrm{i}\hbar)^2\, G_{ab}(12,1'2') = \left\langle \mathrm{T}_{\mathcal{C}}\{\Psi_a(1)\Psi_b(2)\Psi_b^\dagger(2')\Psi_a^\dagger(1')\}\right\rangle , \tag{1.39}$$

wobei $1 = \{\mathbf{r}_1, t_1, s_1^{(3)}\}$ einen vollständigen Satz von Observablen und $\mathrm{T}_{\mathcal{C}}$ die Zeitordnung auf der zweizeitigen Keldysh–Kontur $\mathcal{C}$ [Kel64, KSK05] bezeichnet. Ψ_a ist der Feldoperator der Ladungsträgersorte a. Die verschiedenen Zweiteilchenfunktionen erhält man durch Positionierung der Zeitvariablen t_1, t_2, t_1', t_2' auf den beiden Ufern der Kontur. Wichtig ist z.B. die Zweiteilchen–Korrelationsfunktion $g_{ab}^<$

$$g_{ab}^<(12,1'2') \equiv g_{ab}^{++--}(12,1'2') = \frac{1}{(\mathrm{i}\hbar)^2}\left\langle \Psi_a^\dagger(1')\Psi_b^\dagger(2')\Psi_b(2)\Psi_a(1)\right\rangle , \tag{1.40}$$

die aus (1.39) folgt, indem t_1, t_2 auf dem oberen und t_1', t_2' auf dem unteren Ufer positioniert werden. Für gleiche Zeiten ist $g_{ab}^<$ äquivalent zur Zweiteilchen–Dichtematrix.

Im Normalfall ist davon auszugehen, daß in einem Vielteilchensystem alle binären Korrelationen für große Zeitdifferenzen abklingen, d.h. daß $G_{ab}(12, 1'2')$ verschwindet, wenn die Differenz aller gestrichenen und ungestrichenen Zeiten gegen unendlich geht, also $|\{t_1, t_2\} - \{t_1', t_2'\}| \to \infty$. Wenn das nicht der Fall ist, liegt eine *zeitlich langreichweitige Ordnung* vor (*time long range order*, TLRO). Die Struktur der Zweiteilchenfunktion ist dann offenbar

$$G_{ab}(12, 1'2') = \widehat{G}_{ab}(12, 1'2') + C_{ab}(12, 1'2')\,, \tag{1.41}$$

wobei für das asymptotische Verhalten

$$\lim_{|\{t_1,t_2\}-\{t_1',t_2'\}|\to\infty} \widehat{G}_{ab}(12, 1'2') = 0; \qquad \lim_{|\{t_1,t_2\}-\{t_1',t_2'\}|\to\infty} C_{ab}(12, 1'2') \neq 0 \tag{1.42}$$

gilt.

Das TLRO–Konzept wurde erstmals in den Arbeiten [KS69, RG71] für die Einteilchen–Korrelationsfunktion bzw. in [Sto75] für die Zweiteilchen–Korrelationsfunktion eingeführt und ausgearbeitet.

Aus der obigen Zerlegung der Zweiteilchenfunktion ergibt sich nun zwingend die Frage, unter welchen Bedingungen ein nichtverschwindendes C_{ab} existiert.

Zunächst betrachten wir die Bewegungsgleichung von $G_{ab}(12, 1'2')$, die Bethe–Salpeter–Gleichung (BSG), hier gegeben im sogenannten „Teilchen–Teilchen–Kanal“, die die Dynamik von Teilchenpaaren beschreibt. Sie kann in der Form

$$\begin{aligned} &\int_{\mathcal{C}} \mathrm{d}\bar{1}\, G_a^{-1}(1, \bar{1}) G_{ab}(\bar{1}2, 1'2') - \mathrm{i}\hbar \int_{\mathcal{C}} \mathrm{d}3\mathrm{d}\bar{1}\mathrm{d}\bar{2}\, G_b(2, 3) W_{ab}(13, \bar{1}\bar{2}) G_{ab}(\bar{1}\bar{2}, 1'2') \\ &= G_b(2, 2')\delta(1 - 1') \end{aligned} \tag{1.43}$$

geschrieben werden. Hier ist W_{ab} eine effektive Zweiteilchen–Wechselwirkung. Durch Feynman–Diagramme definiert, ist W_{ab} die Summe aller amputierten irreduziblen Zweiteilchendiagramme im Teilchen–Teilchen–Kanal. Gleichung (1.43) muß offensichtlich durch eine Gleichung für die Einteilchen–Greenfunktion, die Dyson–Gleichung, ver-

vollständigt werden,

$$\int\limits_{\mathcal{C}} \mathrm{d}\bar{1}\, \left[G_a^{0^{-1}}(1,\bar{1}) - \Sigma_a(1,\bar{1})\right] G_a(\bar{1},1') = \delta(1-1') \tag{1.44}$$

mit der freien inversen Einteilchen–Greenfunktion

$$G_a^{0^{-1}}(1,\bar{1}) = \left[\mathrm{i}\hbar\frac{\partial}{\partial t_1} + \frac{1}{2m_a}\left(-\mathrm{i}\hbar\nabla_1 - e_a\mathbf{A}(1)\right)^2 + \epsilon_a\right]\delta(1-\bar{1})\,.$$

Die allgemeine Lösung der BSG ist

$$G_{ab}(12,1'2') = \widehat{G}_{ab}(12,1'2') + \; F_{ab}(12)\; F^*_{ab}(1'2')\,, \tag{1.45}$$

wobei $\widehat{G}_{ab}(12,1'2')$ eine spezielle Lösung von (1.43) ist, die der Asymptotenbedingung

$$\lim_{|\{t_1,t_2\}-\{t_1',t_2'\}|\to\infty} \widehat{G}_{ab}(12,1'2') = 0 \tag{1.46}$$

genügt. Durch einen Vergleich der Lösungsstruktur (1.45) mit Gl. (1.41) kann der TLRO–Term identifiziert werden als $C_{ab}(12,1'2') = F_{ab}(12)F^*_{ab}(1'2')$. Die Funktion F_{ab} ist Lösung der homogenen Gleichung zu (1.43)

$$\int\limits_{\mathcal{C}} \mathrm{d}\bar{1}\, G_a^{-1}(1,\bar{1})F_{ab}(\bar{1}2) - \int\limits_{\mathcal{C}} \mathrm{d}\bar{2}\, G_b(2,\bar{2})D_{ab}(1\bar{2}) = 0\,, \tag{1.47}$$

mit der Abkürzung[7]

$$D_{ab}(12) = \mathrm{i}\hbar \int\limits_{\mathcal{C}} \mathrm{d}\bar{1}\mathrm{d}\bar{2}\, W_{ab}(12,\bar{1}\bar{2})F_{ab}(\bar{1}\bar{2})\,. \tag{1.48}$$

Für die Funktion D_{ab} folgt aus (1.43) und (1.47) unmittelbar die Integralgleichung

$$D_{ab}(12) = \mathrm{i}\hbar \int\limits_{\mathcal{C}} \mathrm{d}\bar{1}\mathrm{d}\bar{2}\mathrm{d}\bar{\bar{1}}\mathrm{d}\bar{\bar{2}}\, W_{ab}(12,\bar{1}\bar{2})G_a(\bar{1},\bar{\bar{1}})G_b(\bar{2},\bar{\bar{2}})D_{ab}(\bar{\bar{1}}\,\bar{\bar{2}})\,. \tag{1.49}$$

Die Funktion $D_{ab}(12)$ spielt offensichtlich eine zentrale Rolle bei der Bestimmung der TLRO–Anteile der Zweiteilchenfunktion.

Das oben eingeführte Konzept der zeitlich langreichweitigen Ordnung ist eng ver-

[7] Wir folgen der Notation von A.1. Man beachte, daß D nicht mit der Greenfunktion der Photonen (die hier nicht betrachtet wird) zu verwechseln ist.

bunden mit dem üblicherweise diskutierten Prinzip der räumlichen, „nichtdiagonalen“ langreichweitigen Ordnung (*off-diagonal long range order*, ODLRO), das Ausdruck des makroskopischen Ordnungszustandes im Quantenkondensat ist [PO56, Yan62]. ODLRO ist eine Eigenschaft der reduzierten Dichtematrizen, die sich im Zweiteilchenfall als

$$\varrho_{ab}(\mathbf{r}_1\mathbf{r}_2,\mathbf{r}_1'\mathbf{r}_2';t) = \widehat{\varrho}_{ab}(\mathbf{r}_1\mathbf{r}_2,\mathbf{r}_1'\mathbf{r}_2';t) + \Phi_{ab}(\mathbf{r}_1\mathbf{r}_2,t)\Phi_{ab}^*(\mathbf{r}_1'\mathbf{r}_2',t) \tag{1.50}$$

darstellen lassen, wobei $\widehat{\varrho}_{ab}$ verschwindet, wenn die Differenz aller gestrichenen und ungestrichenen *Orte* gegen unendlich geht. Φ_{ab} ist hier die Makrowellenfunktion des Kondensats, die aus der allgemeineren Funktion $F_{ab}(12)$ als Spezialfall für gleiche Zeiten folgt, $\Phi_{ab}(\mathbf{r}_1\mathbf{r}_2,t_1) = \mathrm{i}\hbar\, F_{ab}(12)|_{t_1=t_2}$. Da die Zweiteilchen–Dichtematrix durch $g_{ab}^<$ für $t_1 = t_2 = t_1' = t_2' = t$ gegeben ist, folgt aus (1.45) ODLRO, d.h. Quantenkondensation tritt auf, wenn Gl. (1.47) eine Lösung besitzt. Die zeitlich langreichweitige Ordnung TLRO ist somit das allgemeinere, übergeordnete Prinzip. Das Auftreten von TLRO in der Zweiteilchen–Korrelationsfunktion ist hinreichend für das Auftreten von Quantenkondensation im System.

Um die Struktur des TLRO–Beitrags näher zu untersuchen, betrachten wir zunächst die Einteilchen–Selbstenergie Σ_a in der Dyson–Gleichung (1.44). Diese Größe ist durch

$$\int\limits_{\mathcal{C}} \mathrm{d}\bar{1}\, \Sigma_a(1,\bar{1})G_a(\bar{1},1') = \sum_b \int\limits_{\mathcal{C}} \mathrm{d}2\, V_{ab}(1-2)G_{ab}(12,1'2^+) \tag{1.51}$$

mit $V_{ab}(1-2) = V_{ab}(\mathbf{r}_1-\mathbf{r}_2)\delta(t_1-t_2)$ und $t_2^+ = t_2+\epsilon$, $\epsilon\to 0$ definiert. Setzen wir die Lösungsstruktur (1.45) ein, findet man für $\Sigma_a(1,\bar{1})$ die Zerlegung $\Sigma_a(1,\bar{1}) = \widehat{\Sigma}_a(1,\bar{1}) + \Sigma_a^{\mathrm{LRO}}(1,\bar{1})$ mit der Selbstenergie der normalen Phase $\widehat{\Sigma}_a(1,\bar{1})$ und dem TLRO–Term $\Sigma_a^{\mathrm{LRO}}(1,\bar{1})$, wobei letzterer durch

$$\int\limits_{\mathcal{C}} \mathrm{d}\bar{1}\, \Sigma_a^{\mathrm{LRO}}(1,\bar{1})G_a(\bar{1},1') = \int\limits_{\mathcal{C}} \mathrm{d}2\, \Delta_{ab}(12)F_{ab}^*(1'2^+) \tag{1.52}$$

gegeben ist. In letzterer Beziehung wurde die sogenannte Gap–Funktion

$$\Delta_{ab}(12) = \mathrm{i}\hbar\, V_{ab}(1-2)F_{ab}(12) \tag{1.53}$$

eingeführt, die für die Beschreibung des Quantenkondensats eine zentrale Rolle spielt. Zu beachten ist, daß $\Delta_{ab}\neq 0$ nur für $a\neq b$ gilt, es gibt also kein Kondensat von Paa-

ren gleichartiger Teilchen. Unter Ausnutzung von Gl. (1.47) ist Σ_a^{LRO} explizit gegeben durch

$$\Sigma_a^{\mathrm{LRO}}(1,1') = \int\limits_{\mathcal{C}} \mathrm{d}2\mathrm{d}\bar{2}\, \Delta_{ab}(12) D^*_{ab}(1'\bar{2}) G_b(\bar{2},2^+)\,. \tag{1.54}$$

Oberhalb der kritischen Temperatur T_{crit} der Quantenkondensation sollte $\widehat{\Sigma}_a$ den einzigen Beitrag zur Selbstenergie darstellen, während für verschwindende Temperaturen Σ_a^{LRO} dominieren sollte. Bei endlichen Temperaturen unterhalb der kritischen wird jedoch eine signifikante Anzahl von Teilchen aus dem Kondensat angeregt sein, und beide Terme müssen Berücksichtigung finden.

Die Dyson–Gleichung auf der Keldysh–Kontur $\mathcal{C}$ erhält somit die Form

$$\int\limits_{\mathcal{C}} \mathrm{d}\bar{1}\, \left[G_a^{0^{-1}}(1,\bar{1}) - \widehat{\Sigma}_a(1,\bar{1}) - \Sigma_a^{\mathrm{LRO}}(1,\bar{1})\right] G_a(\bar{1},1') \;=\; \delta(1-1')\,. \tag{1.55}$$

Obwohl die Gleichung (1.55) gemeinsam mit (1.54) die Einteilcheneigenschaften des Systems vollständig beschreibt, ist oftmals eine Transformation vorteilhaft. Unter Verwendung von (1.52) läßt sich aus den Gleichungen (1.55) und (1.47) das folgende äquivalente Gleichungssystem für die beiden Funktionen G_a und F_{ab} ableiten:

$$\int\limits_{\mathcal{C}} \mathrm{d}\bar{1}\, \left[G_a^{0^{-1}}(1,\bar{1}) - \widehat{\Sigma}_a(1,\bar{1})\right] G_a(\bar{1},1') - \int\limits_{\mathcal{C}} \mathrm{d}2\, \Delta_{ab}(12) F^*_{ab}(1'2^+) \;=\; \delta(1-1'), \tag{1.56}$$

$$\int\limits_{\mathcal{C}} \mathrm{d}\bar{1}\, \left[G_b^{0^{-1}}(2,\bar{2}) - \widehat{\Sigma}_b(2,\bar{2})\right] F_{ab}(1\bar{2}) + \int\limits_{\mathcal{C}} \mathrm{d}\bar{2}\, G_a(1,\bar{1}) D_{ab}(\bar{1}2) \;=\; 0\,. \tag{1.57}$$

Die Gleichungen (1.56) und (1.57) verallgemeinern offensichtlich die bekannten Gorkow–Gleichungen [AGD65] in verschiedener Hinsicht: (i) Es sind Gleichungen für das Nichtgleichgewicht auf der Keldysh–Kontur und daher eine kompakte Darstellung der Gleichungen für die verschiedenen Keldysh–Komponenten. (ii) Die Näherung für W_{ab} bestimmt das Approximationsniveau der Theorie. (iii) Der Einfluß der normalen Phase wird durch $\widehat{\Sigma}$ berücksichtigt.

Schließlich soll noch einmal angemerkt werden, daß die erste Gorkow–Gleichung unmittelbar mit der Dyson–Gleichung übereinstimmt, während die zweite eine Konsequenz aus der Bethe–Salpeter–Gleichung für die Zweiteilchen–Greenfunktion darstellt.

Während die bisherigen Ableitungen noch weitgehend allgemein waren, soll nun

die Spezifik des Elektron–Loch–Plasmas, insbesondere der langreichweitigen Coulomb–Wechselwirkung, Berücksichtigung finden. Eine für Coulombsysteme angebrachte Näherung für die effektive Zweiteilchen–Wechselwirkung W_{ab} ist dadurch gegeben, diese Größe durch das dynamisch abgeschirmte Coulomb–Potential zu nähern:

$$W_{ab}(12,\bar{1}\bar{2}) = V^s_{ab}(1,2)\delta(1-\bar{1})\delta(2-\bar{2})\,, \tag{1.58}$$

wobei V^s durch die Integralgleichung

$$V^s_{ab}(1,2) = V_{ab}(1-2) + \sum_{cd}\int\limits_{\mathcal{C}} \mathrm{d}3\mathrm{d}4\, V_{ac}(1-3)\Pi_{cd}(34)V^s_{db}(4,2) \tag{1.59}$$

gegeben ist [KKER86]. Hier ist Π_{ab} die Polarisationsfunktion, die mit der Zweiteilchen–Greenfunktion durch

$$\Pi_{ab}(12,1'2') \;=\; L_{ab}(12,1'2') - \int\limits_{\mathcal{C}} \mathrm{d}3\mathrm{d}4\,\Pi_{ab}(13,1'3^+)V^s_{ab}(3,4)\Pi_{ab}(42,4^+2') \tag{1.60}$$

verknüpft ist, $L_{ab}(12,1'2') = G_{ab}(12,1'2') - G_a(1,1')G_b(2,2')$. Die Funktion $\Pi_{ab}(12)$ folgt aus der Beziehung $\Pi_{ab}(12) = \Pi_{ab}(12,1^+2^+)$. Die Approximation (1.58) definiert die bereits im vorangegangenen Abschnitt eingeführte *dynamisch abgeschirmte Leiternäherung* für die Zweiteilchen–Greenfunktion. Sie stellt das einfachste Schema dar, in einem System mit Coulomb–Wechselwirkung sowohl gebundene als auch Streuzustände zu beschreiben, wobei Coulombdivergenzen aus der Leitersumme beseitigt werden und der Einfluß der dynamischen Abschirmung auf Bindungs- und Streuzustände berücksichtigt wird. Die dynamisch abgeschirmte Leiternäherung enthält jedoch keine Drei- und Vierteilchenprozesse, so daß in ihrem Rahmen Ladungsträger–Exziton– bzw. Exziton–Exziton–Wechselwirkungen nicht beschrieben werden können.

Die Selbstenergie kann nun mit Hilfe des abgeschirmten Potentials ausgedrückt werden:

$$\Sigma_a(1,1') \;=\; \Sigma^{\mathrm{H}}_a(1,1') + \Sigma^s_a(1,1')\,, \tag{1.61}$$

$$\int\limits_{\mathcal{C}} \mathrm{d}\bar{1}\,\Sigma^s_a(1,\bar{1})G_a(\bar{1},1') \;=\; \sum_b \int\limits_{\mathcal{C}} \mathrm{d}2\, V^s_{ab}(1,2)\Pi_{ab}(12,1'2^+)\,, \tag{1.62}$$

wobei Σ^s_a die „abgeschirmte“ Selbstenergie und Σ^{H}_a den Hartree–Beitrag, also den des

mittleren Feldes, bezeichnen. In abgeschirmter Leiternäherung reduziert sich Π_{ab} auf

$$\Pi_{ab}(12,1'2') = L_{ab}(12,1'2') - \int\limits_{\mathcal{C}} \mathrm{d}3\mathrm{d}4\, G_a(1,3^+)G_b(3,1')V^s_{ab}(3,4)G_a(2,4^+)G_b(4,2')\,. \tag{1.63}$$

Der TLRO–Beitrag zu Π_{ab} stimmt offensichtlich mit dem zur abgeschirmten Leitersumme L_{ab} überein. Die Struktur der abgeschirmten Selbstenergie ist daher

$$\Sigma^s_a = \widehat{\Sigma}^s_a + \Sigma^{\mathrm{LRO}}_a\,, \tag{1.64}$$

wobei Σ^{LRO}_a wiederum durch Gl. (1.52) definiert ist, aber Δ_{ab} der Beziehung

$$\Delta_{ab}(12) = \mathrm{i}\hbar\, V^s_{ab}(1,2)F_{ab}(12) \tag{1.65}$$

genügt. F_{ab} ist Lösung der Gln. (1.47,1.48) mit W_{ab} gegeben durch (1.58). Der Vergleich von (1.65) mit (1.48) zeigt weiterhin, daß in dieser Näherung $D_{ab} = \Delta_{ab}$ gilt. Mit Hilfe von Gl. (1.49) erhält man nun eine Integralgleichung für die Gap–Funktion:

$$\Delta_{ab}(12) = \mathrm{i}\hbar \int\limits_{\mathcal{C}} \mathrm{d}\bar{1}\mathrm{d}\bar{2}\, V^s_{ab}(1,2)G_a(1,\bar{1})G_b(2,\bar{2})\Delta_{ab}(\bar{1}\bar{2})\,. \tag{1.66}$$

In dieser Weise ist es also möglich, die Theorie vollständig mit Hilfe des dynamisch abgeschirmten Potentials zu formulieren und somit die üblichen mit der Coulomb–Wechselwirkung verbundenen Probleme zu vermeiden.

Zur Untersuchung der Dynamik eines Teilchenpaares ist es oft hinreichend, die spezielle zweizeitige Funktion im Teilchen–Teilchen–Kanal

$$G_{ab}(12,1'2')\Big|_{\substack{t_1=t_2=t \\ t'_1=t'_2=t'}} = G_{ab}(\mathbf{r}_1\mathbf{r}_2t,\mathbf{r}'_1\mathbf{r}'_2t') \tag{1.67}$$

zu betrachten. Für diese lautet die TLRO–Bedingung

$$G_{ab}(\mathbf{r}_1\mathbf{r}_2t,\mathbf{r}'_1\mathbf{r}'_2t') = \widehat{G}_{ab}(\mathbf{r}_1\mathbf{r}_2t,\mathbf{r}'_1\mathbf{r}'_2t') + \frac{1}{(\mathrm{i}\hbar)^2}\,\Phi_{ab}(\mathbf{r}_1,\mathbf{r}_2,t)\Phi^*_{ab}(\mathbf{r}'_1,\mathbf{r}'_2,t')\,. \tag{1.68}$$

Im stationären Zustand hängt die zweizeitige Korrelationsfunktion nur von der (mikroskopischen) Relativzeit $\tau = t - t'$ ab, und wir können die Fouriertransformierte be-

trachten. Um die zum großkanonischen Dichteoperator korrespondierende Gleichgewichtslösung der BSG zu finden, muß weiterhin die Kubo–Martin–Schwinger–(KMS)–Bedingung

$$g_{ab}^{<}(\omega) = e^{-\beta(\hbar\omega-\mu_a-\mu_b)} g_{ab}^{>}(\omega) \tag{1.69}$$

erfüllt sein. Das erfordert für die Makrowellenfunktion

$$\Phi_{ab}(\mathbf{r}_1, \mathbf{r}_2, t) = e^{\frac{\mathrm{i}}{\hbar}(\mu_a+\mu_b)t} \Phi_{ab}(\mathbf{r}_1, \mathbf{r}_2)\,. \tag{1.70}$$

TLRO erzeugt dann einen zusätzlichen Term in der Spektraldarstellung von $g_{ab}^{<}$,

$$g_{ab}^{<}(\omega) = \; a_{ab}(\omega)\, \frac{\mathcal{P}}{e^{\beta(\hbar\omega-\mu_b-\mu_a)}-1} \; + 2\pi\delta(\hbar\omega-\mu_b-\mu_a)\; \Phi_{ab}\Phi_{ab}^{*}\,. \tag{1.71}$$

Eine zentrale Größe der abgeschirmten Leiternäherung (1.58) ist die T–Matrix, die mit G_{ab} über die Beziehung

$$T_{ab}(12,1'2') = V_{ab}^{s}(1,2)\delta(1-1')\delta(2-2') + V_{ab}^{s}(1,2)G_{ab}(12,1'2')V_{ab}^{s}(1'2') \tag{1.72}$$

verknüpft ist. TLRO in der Greenfunktion induziert dann auch TLRO in der entsprechenden T–Matrix:

$$T_{ab}(12,1'2') \;\; = \;\; \widehat{T}_{ab}(12,1'2') + \frac{1}{\mathrm{i}\hbar}\Delta_{ab}(12)\Delta_{ab}^{*}(1'2')\,. \tag{1.73}$$

Analog zu Gl. (1.71) erhält man im stationären Zustand auch einen zusätzlichen TLRO–Term in der Spektraldarstellung von $T_{ab}^{<}$:

$$T_{ab}^{<}(\omega) = 2\,\mathrm{Im}\,T_{ab}^{\mathrm{R}}(\omega)\frac{\mathcal{P}}{e^{\beta(\hbar\omega-\mu_b-\mu_a)}-1} + 2\pi\delta(\hbar\omega-\mu_b-\mu_a)\;\Delta_{ab}\;\Delta_{ab}^{*}\,. \tag{1.74}$$

Die abgeschirmte T–Matrix genügt der Vielteilchenform der Lippmann–Schwinger–Gleichung (LSG), die aus der Bethe–Salpeter–Gleichung folgt. Auf der Keldysh–Kontur hat die LSG die Form

$$\begin{aligned} T_{ab}(12,1'2') \;\; = \;\; & V_{ab}^{s}(1,2)\delta(1-1')\delta(2-2') \\ & +\mathrm{i}\hbar\int_{\mathcal{C}} \mathrm{d}\bar{1}\mathrm{d}\bar{2}\, V_{ab}^{s}(1,2)\, G_a(1,\bar{1})G_b(2,\bar{2})\, T_{ab}(\bar{1}\bar{2},1'2')\,. \end{aligned} \tag{1.75}$$

Damit folgt die Selbstenergie in abgeschirmter Leiternäherung explizit als

$$\begin{aligned}\widehat{\Sigma}_a(1,1') &= \pm \mathrm{i}\hbar \sum_b \int\limits_{\mathcal{C}} \mathrm{d}2\mathrm{d}\bar{2} \Big[\widehat{T}_{ab}(12,1'\bar{2}) \pm \delta_{ab} \widehat{T}_{ab}(12,\bar{2}1') \\ &\qquad - V^s_{ab}(1,2) G_a(1,1') G_b(2,\bar{2}) V^s_{ab}(1',\bar{2}) \Big] G_b(\bar{2},2)\,, \end{aligned} \tag{1.76}$$

sowie der TLRO–Anteil

$$\Sigma_a^{\mathrm{LRO}}(1,1') = \int\limits_{\mathcal{C}} \mathrm{d}2\mathrm{d}\bar{2}\, \Delta_{ab}(12) \Delta^*_{ab}(1'\bar{2}) G_b(\bar{2},2)\,. \tag{1.77}$$

Die optischen Eigenschaften des angeregten Halbleiters werden wesentlich durch die Polarisationsfunktion Π_{ab} bestimmt, deren TLRO–Beitrag daher auch angegeben werden soll. Wie bereits oben diskutiert, ist dieser Beitrag in abgeschirmter Leiternäherung gerade äquivalent zum TLRO–Anteil von G_{ab}, vgl. Gln. (1.41,1.45), d.h. man erhält für die zweizeitige Polarisationsfunktion

$$\Pi_{ab}^{\mathrm{LRO}}(12) = \Pi_{ab}^{\mathrm{LRO}}(12,1^+2^+) = F_{ab}(12)\; F^*_{ab}(12)\,. \tag{1.78}$$

Der TLRO–Beitrag ist wiederum in allen Keldysh–Komponenten gleich. Unter Berücksichtigung von

$$\Phi_{ab}(\mathbf{r}_1\mathbf{r}_2) = \int \mathrm{d}\bar{\mathbf{r}}_1 \mathrm{d}\bar{\mathbf{r}}_2\, \mathcal{G}^{\mathrm{R}}_{ab}(\mathbf{r}_1\mathbf{r}_2,\bar{\mathbf{r}}_1\bar{\mathbf{r}}_2;\omega)\Big|_{\hbar\omega=\mu_a+\mu_b} \Delta_{ab}(\bar{\mathbf{r}}_1\bar{\mathbf{r}}_2) \tag{1.79}$$

[vgl. Gln. (1.65,1.66)], erhält man im Quasigleichgewicht

$$\Pi_{ab}^{\mathrm{LRO}}(\mathbf{r}_1\mathbf{r}_2,\omega) = \left|\Phi_{ab}(\mathbf{r}_1\mathbf{r}_2)\right|^2 \cdot 2\pi\delta(\hbar\omega - \mu_a - \mu_b)\,. \tag{1.80}$$

Die verallgemeinerten Gorkow–Gleichungen für das Nichtgleichgewicht (1.56) und (1.57) erhalten in abgeschirmter Leiternäherung schließlich folgende Form:

$$\begin{aligned}&\left[\mathrm{i}\hbar\frac{\partial}{\partial t_1} + \frac{1}{2m_a}\left(-\mathrm{i}\hbar\nabla_1 - e_a\mathbf{A}(1)\right)^2 + \epsilon_a\right] G_a(1,1') - \int\limits_{\mathcal{C}} \mathrm{d}\bar{1}\, \widehat{\Sigma}_a(1,\bar{1}) G_a(\bar{1},1') \\ &- \int\limits_{\mathcal{C}} \mathrm{d}\bar{1} \Delta_{ab}(1\bar{1}) F^*_{ab}(1'\bar{1}) = \delta(1-1')\,, \end{aligned} \tag{1.81}$$

sowie

$$\left[\mathrm{i}\hbar\frac{\partial}{\partial t_1'} - \frac{1}{2m_b}\left(-\mathrm{i}\hbar\nabla_{1'} - e_b\mathbf{A}(1')\right)^2 - \epsilon_b\right] F_{ab}^*(11') + \int\limits_{\mathcal{C}} \mathrm{d}\bar{1}\, \widehat{\Sigma}_b^*(1',\bar{1})F_{ab}^*(1\bar{1})$$
$$- \int\limits_{\mathcal{C}} \mathrm{d}\bar{1}\Delta_{ab}^*(\bar{1}1')G_a(\bar{1},1) = 0\,. \tag{1.82}$$

Die Gleichungen (1.81,1.82) stellen die Grundgleichungen der Beschreibung des Nichtgleichgewichtsverhaltens des Elektron–Loch–Plasmas als quantenmechanisches Vielteilchensystem unter Einschluß des Quantenkondensats dar. Aus diesen Gleichungen folgen durch Positionierung der Zeiten auf der Keldysh–Kontur Gleichungen für die Korrelationsfunktionen $g_a^{\gtrless}$, die retardierten und avancierten Funktionen $g_a^{\mathrm{R/A}}$ sowie die Makrowellenfunktion Φ_{ab}, siehe A.1. Quantenkinetische Gleichungen im engeren Sinne, d.h. Gleichungen für die Wignerverteilung, folgen aus den zweizeitigen Gleichungen für $g_a^{\gtrless}$.

Lösung im thermodynamischen Gleichgewicht. BCS–Gleichungen

Im folgenden betrachten wir nun ein räumlich homogenes Elektron–Loch–Plasma im thermodynamischen Quasigleichgewicht. Dann hängen alle Zweiteilchenfunktionen nur von den mikroskopischen Variablen $t - t'$ und $\mathbf{r} - \mathbf{r}'$ ab, und es ist offensichtlich sinnvoll, die Fouriertransformation $t - t' \to \omega$, $\mathbf{r} - \mathbf{r}' \to \mathbf{k}$ durchzuführen. Zudem hat $\Delta_{ab}(\mathbf{k},t)$ die Struktur $\Delta_{ab}(\mathbf{k},t) = \mathrm{e}^{\frac{\mathrm{i}}{\hbar}(\mu_a+\mu_b)t}\Delta_{ab}(\mathbf{k})$. Es ist daher angebracht, die Ersetzung $F_{ab}^{\mathrm{R}}(\mathbf{k};t,t') \to \mathrm{e}^{-\frac{\mathrm{i}}{\hbar}(\mu_a+\mu_b)t}F_{ab}^{\mathrm{R}}(\mathbf{k};t-t')$ vorzunehmen. Wir erhalten dann für die retardierten bzw. avancierten Funktionen

$$\left[\hbar\omega - E_a(\mathbf{k}) - \widehat{\Sigma}_a^{\mathrm{R/A}}(\mathbf{k},\omega)\right] g_a^{\mathrm{R/A}}(\mathbf{k},\omega) - \Delta_{ab}(\mathbf{k})F_{ab}^{*\mathrm{A/R}}(-\mathbf{k},-\omega) = 1\,, \tag{1.83}$$

$$\left[\hbar\omega - E_b(\mathbf{k}) + \mu_a + \mu_b - \widehat{\Sigma}_b^{*\mathrm{A/R}}(-\mathbf{k},-\omega)\right] F_{ab}^{*\mathrm{R/A}}(\mathbf{k},\omega) + \Delta_{ab}^*(\mathbf{k})g_a^{\mathrm{A/R}}(-\mathbf{k},-\omega) = 0 \tag{1.84}$$

mit $E_{a/b}(\mathbf{k}) = \hbar^2k^2/(2m_{a/b})$. Diese Gleichungen lassen sich nun einfach lösen. Identifiziert man die Selbstenergie der kondensierten Phase mit

$$\Sigma_a^{\mathrm{LRO}}(\mathbf{k},\omega) = \frac{|\Delta_{ab}(\mathbf{k})|^2}{\hbar\omega + E_b(\mathbf{k}) - \mu_a - \mu_b + \widehat{\Sigma}_b^{*\mathrm{R}}(\mathbf{k},\omega)}\,, \tag{1.85}$$

folgt für g_a^{R}

$$g_a^{\mathrm{R}}(\mathbf{k},\omega) \;=\; \frac{1}{\hbar\omega - E_a(\mathbf{k}) - \widehat{\Sigma}_a^{\mathrm{R}}(\mathbf{k},\omega) - \Sigma_a^{\mathrm{LRO}}(\mathbf{k},\omega)}\,. \tag{1.86}$$

Mit der Lösung (1.85,1.86) hat man das wohlbekannte System der BCS–Gleichungen [AGD65, FW71] erhalten, hier nun verallgemeinert auf ein Zweikomponentensystem unter Einschluß der nichtkondensierten Phase. Die Spektralfunktion, die im thermodynamischen Gleichgewicht die Einteilcheneigenschaften des Vielteilchensystems vollständig beschreibt, folgt unmittelbar aus (1.86),

$$\begin{aligned} a_a(\mathbf{k},\omega) &= \frac{\Gamma_a(\mathbf{k},\omega)}{\Big[\hbar\omega - E_a(\mathbf{k}) - \mathrm{Re}\,\widehat{\Sigma}_a^{\mathrm{R}}(\mathbf{k},\omega) - \mathrm{Re}\,\Sigma_a^{\mathrm{LRO}}(\mathbf{k},\omega)\Big]^2 + \Big[\tfrac{1}{2}\Gamma_a(\mathbf{k},\omega)\Big]^2}\,, \\ \Gamma_a(\mathbf{k},\omega) &= 2\Big[\,\mathrm{Im}\,\widehat{\Sigma}_a^{\mathrm{R}}(\mathbf{k},\omega) + \mathrm{Im}\,\Sigma_a^{\mathrm{LRO}}(\mathbf{k},\omega)\Big]\,. \end{aligned} \tag{1.87}$$

Die Größe $\widehat{\Sigma}_a^{\mathrm{R}}$ folgt aus Gl. (1.76). Diese Näherung umfaßt sowohl die RPA–Selbstenergie als auch die Leiterterme höherer Ordnung und beschreibt daher zum einen kollektive Effekte wie die dynamische Abschirmung und zum anderen starke binäre Stöße und gebundene Zustände.

Eine entscheidende Vereinfachung ergibt sich unter der Annahme, daß die Dämpfung klein gegen die Renormierung der Energie ist, $\Gamma_a(\mathbf{k},\omega) < \mathrm{Re}\,\widehat{\Sigma}_a^{\mathrm{R}}(\mathbf{k},\omega)$. Dann kann die Spektralfunktion in eine Taylorreihe bezüglich Γ_a entwickelt werden, und in erster Ordnung entsteht die bereits im vorangegangenen Abschnitt diskutierte sogenannte „erweiterte Quasiteilchennäherung“ (*extended quasiparticle approximation*). Als Resultat für die Spektralfunktion erhält man nun

$$\begin{aligned} a_a(\mathbf{k},\omega) \;=\; & |u(\mathbf{k})|^2 \left\{ \left[1 + |u(\mathbf{k})|^2 \,\frac{1}{\hbar}\frac{\partial}{\partial\omega} \mathrm{Re}\,\widehat{\Sigma}_a^{\mathrm{R}}(\mathbf{k},\omega)|_{\hbar\omega = E_a^+(\mathbf{k})} \right] 2\pi\hbar\,\delta\Big(\hbar\omega - E_a^+(\mathbf{k})\Big) \right. \\ & \left. -\Gamma_a(\mathbf{k},\omega)\frac{1}{\hbar}\frac{\partial}{\partial\omega}\frac{\mathcal{P}}{\hbar\omega - E_a^+(\mathbf{k})} \right\} \\ & + |v(\mathbf{k})|^2 \left\{ \left[1 + |v(\mathbf{k})|^2 \,\frac{1}{\hbar}\frac{\partial}{\partial\omega} \mathrm{Re}\,\widehat{\Sigma}_a^{\mathrm{R}}(\mathbf{k},\omega)|_{\hbar\omega = E_a^-(\mathbf{k})} \right] 2\pi\hbar\,\delta\Big(\hbar\omega - E_a^-(\mathbf{k})\Big) \right. \\ & \left. -\Gamma_a(\mathbf{k},\omega)\frac{1}{\hbar}\frac{\partial}{\partial\omega}\frac{\mathcal{P}}{\hbar\omega - E_a^-(\mathbf{k})} \right\}\,, \end{aligned} \tag{1.88}$$

wobei $E_a^{\pm}$ die renormierten Dispersionsrelationen sind,

$$E_a^{\pm}(\mathbf{k}) = \left[\frac{1}{2}\{\varepsilon_a(\mathbf{k},\omega) - \varepsilon_b(\mathbf{k},\omega)\} \pm \sqrt{\varepsilon_{ab}^2(\mathbf{k},\omega) + |\Delta_{ab}(\mathbf{k})|^2}\right]_{\hbar\omega = E_a^{\pm}(\mathbf{k})} \tag{1.89}$$

mit $\varepsilon_a(\mathbf{k},\omega) = E_a(\mathbf{k}) - \mu_a + \mathrm{Re}\,\widehat{\Sigma}_a^{\mathrm{R}}(\mathbf{k},\omega)$ und $\varepsilon_{ab}(\mathbf{k},\omega) = \frac{1}{2}(\varepsilon_a(\mathbf{k},\omega) + \varepsilon_b(\mathbf{k},\omega))$.

Die spektralen Gewichte $u(\mathbf{k})$ und $v(\mathbf{k})$ sind durch

$$\begin{aligned} \left.\begin{array}{l} |u(\mathbf{k})|^2 \\ |v(\mathbf{k})|^2 \end{array}\right\} &= \frac{1}{1 - \frac{1}{\hbar}\frac{\partial}{\partial\omega}\mathrm{Re}\,\Sigma_a^{\mathrm{LRO}}(\mathbf{k},\omega)\Big|_{\hbar\omega = E_a^{\pm}(\mathbf{k})}} \\ &= \frac{1}{2}\left[1 \pm \frac{\varepsilon_{ab}(\mathbf{k},\omega)}{\sqrt{\varepsilon_{ab}^2(\mathbf{k},\omega) + |\Delta_{ab}(\mathbf{k})|^2}}\right]_{\hbar\omega = E_a^{\pm}(\mathbf{k})} \end{aligned} \tag{1.90}$$

mit $|u(\mathbf{k})|^2 + |v(\mathbf{k})|^2 = 1$ gegeben. Ist insbesondere $\Delta_{ab} = 0$, ist auch $v(\mathbf{k}) = 0$ und daher $u(\mathbf{k}) = 1$ in diesem Grenzfall.

Wenn die Anzahl der aus dem Kondensat angeregten Teilchen vernachlässigbar ist, gilt $\widehat{\Sigma}_a^{\mathrm{R}} \to 0$. Dann hat die Dispersionsrelation explizite Lösungen, die durch

$$E_a^{\pm}(\mathbf{k}) = \frac{1}{2}(e_a(\mathbf{k}) - e_b(\mathbf{k})) \pm \sqrt{e_{ab}^2(\mathbf{k}) + |\Delta_{ab}(\mathbf{k})|^2} \tag{1.91}$$

gegeben sind. Hier sind $e_{a/b}(\mathbf{k}) = E_{a/b}(\mathbf{k}) - \mu_{a/b}$ und $e_{ab}(\mathbf{k}) = \frac{1}{2}(e_a(\mathbf{k}) + e_b(\mathbf{k}))$ die Pole der Greenfunktion (1.86) für $\widehat{\Sigma}_a^{\mathrm{R}} \to 0$ und können als Quasiteilchenenergien interpretiert werden [Zim76, Sto75]. Die Funktionen $u(\mathbf{k})$, $v(\mathbf{k})$ folgen als Residuen der Pole. Offensichtlich kann die Einteilchenenergie nicht kleiner als $\Delta_{ab}(0)$ sein. Die angeregten Zustände des Systems sind also vom Grundzustand durch eine Energielücke (*gap*) getrennt, die gerade durch die Gap–Funktion gegeben ist. Die Spektralfunktion hat dann die einfache Form

$$a_a(\mathbf{k},\omega) = 2\pi\hbar\left[|u(\mathbf{k})|^2\ \delta\left(\hbar\omega - E_a^{+}(\mathbf{k})\right) + |v(\mathbf{k})|^2\ \delta\left(\hbar\omega - E_a^{-}(\mathbf{k})\right)\right]. \tag{1.92}$$

Gap–Funktion

Aus den bisherigen Darlegungen folgt offensichtlich, daß die Gap–Funktion Δ_{ab} die zentrale Größe in der Theorie darstellt. Sie bestimmt alle relevanten Größen des Quantenkondensats, wie Quasiteilchenenergie, spektrale Gewichte, Makrowellenfunktion

usw. Zu ihrer Berechnung gehen wir von Gl. (1.66) aus. In Fourierdarstellung folgt

$$\Delta_{ab}(\mathbf{k}) = \mathrm{i}\hbar \int \frac{\mathrm{d}^3\bar{\mathbf{k}}}{(2\pi)^3} V^s_{ab}(\mathbf{k}-\bar{\mathbf{k}}) \mathcal{G}^{\mathrm{R}}_{ab}(\bar{\mathbf{k}}, -\bar{\mathbf{k}}; \omega)\Big|_{\hbar\omega=\mu_a+\mu_b} \Delta_{ab}(\bar{\mathbf{k}})\,, \tag{1.93}$$

wobei V^s_{ab} hier und im folgenden das statisch abgeschirmte Coulomb–Potential bezeichnet. Der Propagator freier Teilchen $\mathcal{G}^{\mathrm{R}}_{ab}$ [vgl. Gl. (1.11)], der in der Gap–Gleichung auftritt, wird aus der Spektraldarstellung von $g^<_a$ und der Spektralfunktion (1.92) berechnet. Um jedoch die übliche Form der Gap–Gleichung zu erhalten, muß jeweils eine der Korrelationsfunktionen in (1.11) durch ihre Quasiteilchennäherung ersetzt werden [Zim88]. Durch diese Prozedur erhalten wir die nichtlineare Gap–Gleichung

$$\Delta_{ab}(\mathbf{k}) = \frac{e^2}{\epsilon_0\epsilon_r} \int \frac{\mathrm{d}^3\bar{\mathbf{k}}}{(2\pi)^3} \frac{1}{(\mathbf{k}-\bar{\mathbf{k}})^2+\kappa^2} \frac{\Delta_{ab}(\bar{\mathbf{k}})}{2\sqrt{(e_{ab}(\bar{\mathbf{k}}))^2+|\Delta_{ab}(\bar{\mathbf{k}})|^2}} \left[f(E^+_a(\bar{\mathbf{k}})) - f(E^-_a(\bar{\mathbf{k}}))\right]. \tag{1.94}$$

Diese Gleichung bestimmt die Gap–Funktion und damit den Ordnungsparameter der Quantenkondensation. Durch Vergleich der Gln. (1.94) und (1.65) kann die Makrowellenfunktion mit Hilfe der Gap–Funktion ausgedrückt werden. Es folgt unmittelbar

$$\Phi_{ab}(\mathbf{k}) \;=\; \frac{\Delta_{ab}(\mathbf{k})}{2\sqrt{(e_{ab}(\mathbf{k}))^2+|\Delta_{ab}(\mathbf{k})|^2}} \left[f(E^+_a(\mathbf{k})) - f(E^-_a(\mathbf{k}))\right]. \tag{1.95}$$

Mit Δ_{ab} aus Gl. (1.95) erhält man eine nichtlineare schrödingerartige Gleichung für die Makrowellenfunktion,

$$\left[e_a(\mathbf{k})+e_b(\mathbf{k})\right]\Phi_{ab}(\mathbf{k}) - \sqrt{\left[f(E^+_a(\mathbf{k})) - f(E^-_a(\mathbf{k}))\right]^2 - 4|\Phi_{ab}(\mathbf{k})|^2} \times \int \frac{\mathrm{d}^3\bar{\mathbf{k}}}{(2\pi)^3} V^s_{ab}(\mathbf{k}-\bar{\mathbf{k}})\Phi_{ab}(\bar{\mathbf{k}}) = 0\,. \tag{1.96}$$

Kritische Temperatur

Ein zentrales Problem in der Theorie der Quantenkondensation ist die Berechnung der kritischen Temperatur T_{crit} als Funktion des chemischen Potentials oder der Dichte. Letzterer Zusammenhang bestimmt die Phasengrenze des Kondensats. Da diese Grenze offensichtlich durch Verschwinden des *Gaps* definiert ist, muß sie aus der li-

nearisierten Form von Gl. (1.94) folgen:

$$\Delta_{ab}(\mathbf{k}) = -\frac{e^2}{\epsilon_0\epsilon_r}\int \frac{\mathrm{d}^3\bar{\mathbf{k}}}{(2\pi)^3}\frac{\hbar^2}{(\mathbf{k}-\bar{\mathbf{k}})^2+\hbar^2\kappa^2}\frac{\Delta_{ab}(\bar{\mathbf{k}})}{e_{ab}(\bar{\mathbf{k}})}\left[1-f(e_a(\bar{\mathbf{k}}))-f(e_b(\bar{\mathbf{k}}))\right]. \quad (1.97)$$

Diese Gleichung ist eine homogene Integralgleichung. Sie besitzt nur dann nichttriviale Lösungen, wenn die Koeffizientendeterminante des zu (1.97) äquivalenten Gleichungssystems verschwindet, d.h. man schreibt Gl. (1.97) in diskreter Form als

$$\Delta_i = \sum_j K_{ij}\Delta_j \qquad \text{bzw.} \qquad \sum_j (K_{ij}-\delta_{ij})\Delta_j = 0\,, \quad (1.98)$$

d.h. formal[8]

$$(\mathbf{K}-\mathbf{E})\vec{\Delta} = \vec{0}\,, \quad (1.99)$$

wobei $\mathbf{E}$ die Einheitsmatrix ist. Damit das homogene lineare Gleichungssystem (1.98) nichttriviale Lösungen besitzt, muß

$$\mathrm{Det}|\mathbf{K}-\mathbf{E}| = 0 \quad (1.100)$$

gelten. Da die Matrix $\mathbf{K}$ von der Temperatur und den chemischen Potentialen abhängt, liefert diese Bedingung den Zusammenhang $T_{\mathrm{crit}}(\mu_e,\mu_h)$, also die kritische Temperatur der Quantenkondensation in Abhängigkeit von den chemischen Potentialen der Ladungsträger.

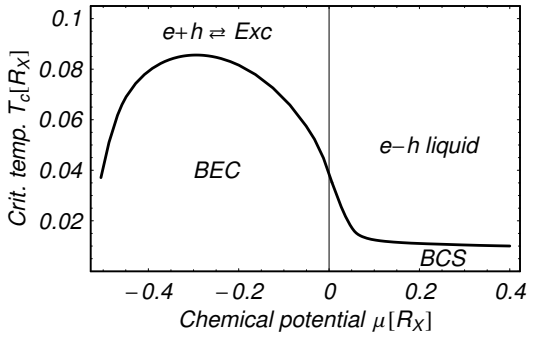

Abbildung 1.10: Kritische Temperatur als Funktion des chemischen Potentials der Ladungsträger. Abbildung entnommen aus A.1.

Für einen Modellhalbleiter mit gleichen Massen der Ladungsträger $m_e = m_h$ (was

[8] Zur Verdeutlichung werden hier ausnahmsweise Vektoren durch Pfeile gekennzeichnet.

für Kupferoxydul eine recht gute Näherung ist) haben wir $T_{\rm crit}(\mu)$ ($\mu = \mu_e = \mu_h$) in der Abb. 1.10 [A.1] dargestellt. Die Quantenkondensation setzt bei $\mu_e + \mu_h = -1\,R_X$ ein (also für $\mu_X = 0$, vgl. Gl. (1.25)), d.h. oberhalb davon gibt es eine endliche kritische Temperatur. Mit wachsendem μ erreicht $T_{\rm crit}$ ein Maximum, geht jedoch jenseits des Mott–Übergangs nicht gegen null! Das zeigt die Existenz eines Kondensats aus ungebundenen Elektron–Loch–Paaren, des BCS–Kondensats.

Die Bestimmung der Phasengrenze im Dichte–Temperatur–Diagramm, also der Abhängigkeit $T_{\rm crit}(n_e)$, erfordert die Untersuchung des Zusammenhangs zwischen Dichte und chemischem Potential und damit der Thermodynamik des Elektron–Loch–Systems. Dieses Thema ist im vorangegangenen Abschnitt im Zusammenhang mit dem Mott–Übergang ausführlich behandelt worden. Hier ist zu bemerken, daß wir die Thermodynamik in den Arbeiten A.1 und [SKH09, KSH10] auf dem Niveau eingebracht haben, wie es in A.2 vorgestellt wurde. Zusätzlich haben wir allerdings einen Punkt untersucht, der die Aufteilung der Dichte in Bindungs- und Streuanteile betrifft. Aufgrund der Erniedrigung der Ionisierungsenergie, die zum Aufbrechen der Bindungszustände führt, könnte man erwarten, daß der Bindungsanteil der Dichte für kritische Werte des Kopplungsparameters (hier der Dichte) Unstetigkeiten aufweist, nämlich genau dann, wenn ein Bindungszustand verschwindet. Aus der Plasmaphysik ist jedoch bekannt, daß diese Unstetigkeiten durch entsprechende Streuanteile kompensiert werden, so daß die Gesamtdichte stetig bleibt. Durch Anwendung des Levinson–Theorems in zweiter bzw. höherer Ordnung können genau diese Anteile herauspräpariert und zu den Bindungsanteilen transferiert werden [KSK05]. Der Rest des Streuanteils ist bei niedrigen Temperaturen vernachlässigbar. Für die Elektronendichte entsteht dann, verwendet man die Selbstenergie in *Rigid–Shift*–Approximation (vgl. Abschnitt 1.3.1) und beschränkt sich wiederum auf den 1S–Zustand, folgender Ausdruck:

$$\begin{aligned} n_e(\mu,T) &= (2s+1)\int \frac{\mathrm{d}^3\mathbf{k}}{(2\pi)^3}\frac{1}{\mathrm{e}^{\frac{1}{k_BT}(E(\mathbf{k})-\zeta_e)}+1} \\ &\quad +(2s+1)^2\int\frac{\mathrm{d}^3\mathbf{K}}{(2\pi)^3}\left[\frac{1}{\mathrm{e}^{\frac{1}{k_BT}\left(\frac{\hbar^2K^2}{2M}+I^{\rm eff}(\zeta,T)-\zeta_e-\zeta_h\right)}-1}\right. \\ &\quad \left.-\frac{1}{\mathrm{e}^{\frac{1}{k_BT}\left(\frac{\hbar^2K^2}{2M}-\zeta_e-\zeta_h\right)}-1}-\frac{M}{\hbar^2K^2}I^{\rm eff}(\zeta,T)\frac{1}{\mathrm{e}^{\frac{1}{k_BT}\left(\frac{\hbar^2K^2}{2M}-\zeta_e-\zeta_h\right)}-1}\right] \\ &= n_{\rm QP}(\zeta,T)+n_{\rm bound}(\zeta,T) \end{aligned} \tag{1.101}$$

mit $M = m_e + m_h$, wobei $\zeta = \mu + \Delta\mu^{\rm D}_{eh}/2$ das effektive chemische Potential bezeichnet

[für $\Delta\mu_{eh}^{\mathrm{D}}$ vgl. Gl. (1.30)] und für die Quasiteilchenenergie $E(\mathbf{k}) = \hbar^2 k^2/(2m_e) + \Sigma^{\mathrm{HF}}(k=0)/2$ gilt.

Die numerischen Untersuchungen haben jedoch gezeigt, daß der Einfluß der Korrekturterme (2. und 3. Term in der großen Klammer) klein ist, so daß wir sie in den nachfolgenden Arbeiten zum Ionisationsgleichgewicht nicht weiter betrachtet haben.

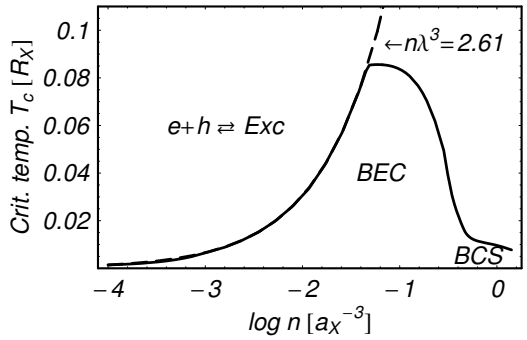

Abbildung 1.11: Phasengrenze des Quantenkondensats als Funktion der Dichte. Abbildung entnommen aus A.1.

Mit Hilfe des Zusammenhangs zwischen der Dichte der Ladungsträger und deren chemischen Potentialen können letztere Größen aus der impliziten Bestimmungsgleichung der kritischen Temperatur (1.100) eliminiert werden. Man erhält den Zusammenhang $T_{\mathrm{crit}}(n_e)$. Diese Größe ist in der Abb. 1.11 dargestellt.[9] Auffällig ist, daß die Phasengrenze über einen weiten Dichtebereich dem idealen Gesetz $n\Lambda^3 \approx 2{,}61$ folgt (Λ ist die thermische Wellenlänge). Der Übergang zwischen exzitonischem und BCS–Kondensat („*BEC–BCS crossover*“) erfolgt stetig, d.h. beide Grenzfälle sind durch eine gemeinsame Phasengrenze gekennzeichnet. Dieses Resultat ist im Einklang mit einer Reihe früherer Arbeiten auf diesem Gebiet, stellvertretend sei hier nur [BF06] genannt.

1.4 Das Exzitonengas in der Falle

In allen bisher besprochenen Arbeiten stand das Elektron–Loch–Plasma im Zentrum der Untersuchungen. Exzitonen wurden als Bindungszustände von Elektronen und Löchern auf der Zweiteilchenebene behandelt, während die Einteilchenebene den Ladungsträgern vorbehalten war. In einer Reihe von Arbeiten (A.4, A.5, A.8–A.11 sowie

[9] Die Abbildung ist aus A.1 entnommen, d.h. der Zusammenhang zwischen Dichte und chemischem Potential entspricht Gl. (1.101). Das Verhalten der Phasengrenze sollte jedoch auch bei verbesserter Thermodynamik (Arbeiten A.3 bzw. [SRK+10], siehe voriger Abschnitt) qualitativ unverändert bleiben.

[SSS+11]) haben wir einen alternativen Zugang zum Exzitonensystem verwendet. Die Exzitonen werden nun als strukturlose Teilchen aufgefaßt, d.h. ihr innerer Aufbau steht außerhalb der Betrachtungen. Die Exzitonen bilden also ein Gas neutraler Teilchen, in Analogie zu einem atomaren Gas.

Eine Limitierung dieses Bildes ist unmittelbar offensichtlich. Das Exziton als Elektron–Loch–Paar ist im Prinzip ein Dipol und erscheint nur aus sehr großem Abstand als neutrales „Punkt"–Objekt. Für höhere Dichten, also kleine mittlere Teilchenabstände, ist damit die Beschreibung als Gas neutraler Teilchen schon aus dem Grund nicht mehr möglich, da dann die innere Struktur als Ladungspaar für die Wechselwirkung relevant wird. Zudem haben wir im vorletzten Abschnitt gesehen, daß die Exzitonen aufgrund des Mott–Effekts bei höheren Dichten in ihre Konstituenten aufbrechen.

Eng verknüpft mit ersterem Punkt ist das Problem der Wechselwirkung zweier Exzitonen. Im Elektron–Loch–Bild haben wir keine Wechselwirkung der gebundenen Zustände untereinander betrachtet, die dort ja auf der Vierteilchenebene zu behandeln wäre. Ebensowenig haben wir die Wechselwirkung von Ladungsträgern mit Exzitonen berücksichtigt. Hier geht nun die Exziton–Exziton–Wechselwirkung bereits auf der Zweiteilchenebene ein. Zu ihrer Bestimmung müßte jedoch dennoch das Vierteilchenproblem (zwei Elektronen, zwei Löcher) gelöst werden. Eine häufig verwendete Näherung ist hier ein Kontaktpotential $V(\mathbf{r}-\mathbf{r}') = U_0\delta(\mathbf{r}-\mathbf{r}')$, deren Stärke durch die $s-$Wellen–Streulänge a_s gegeben ist, $U_0 = 4\pi a_s/M$. Darüber hinausgehende Zugänge zur Ableitung eines Exziton–Exziton–Wechselwirkungspotentials im Volumenhalbleiter sind bislang trotz vielversprechender Ansätze (siehe z.B. [OO01]) weitgehend erfolglos geblieben. Eine ausführliche Diskussion hierzu findet man in [CBMD08].

Die innere Struktur der Exzitonen bestimmt nicht nur die Wechselwirkung, sondern auch den Charakter der Spin–Statistik. So wie Exzitonen nur näherungsweise neutrale „Punktteilchen" sind, sind sie auch nur näherungsweise Bosonen [KK68].[10] Eventuelle Abweichungen von der Bose–Statistik sollten aber ebenfalls erst bei höheren Dichten relevant sein und sollen hier nicht betrachtet werden.

Die Beschreibung wechselwirkender Bosegase ist ein intensiv bearbeitetes Gebiet der Physik ultrakalter atomarer Gase [Gri96, DGPS99, BFBS00, PJ08]. Eine umfassende Darstellung findet man insbesondere in [GNZ09]. Die Zugänge und Methoden können unter Beachtung der Spezifik des Exzitonengases im Halbleiter – speziell in

[10] Zur Frage, ob Exzitonen als Bosonen beschrieben werden können oder nicht, findet man in der Literatur durchaus unterschiedliche Antworten, siehe z.B. [Sch03, Lai07].

Kupferoxydul – auf dieses System übertragen werden [BBH04].

Wie im einleitenden Abschnitt zu Kupferoxydul bereits erwähnt, besteht der 1S–Zustand der gelben Serie aus dem Paraexziton, das den energetischen Grundzustand darstellt, und dem dreifach entarteten Orthoexziton (dessen Komponenten im folgenden mit Ortho(+)-, Ortho(0)- und Ortho(−)exziton bezeichnet werden). Das zu beschreibende Bosegas ist also ein Mehrkomponentensystem. Die Anzahl der zu berücksichtigenden Komponenten ist durch den Charakter des Hertzschen Fallenpotentials festgelegt, das attraktiv für Para-, Ortho(+)- und Ortho(−)exziton, aber repulsiv für das Ortho(0)exziton ist. Letztere Spezies wird also aus der Falle verdrängt, so daß prinzipiell ein Dreikomponentensystem vorliegt.

1.4.1 Thermodynamik des Exzitonengases. Hartree–Fock–Bogoljubow–Popow–Theorie

In den Arbeiten A.4 und A.5 sowie in [SSS$^+$11] haben wir die Gleichgewichtseigenschaften des Exzitonengases in der Falle in Hinblick auf optische Signaturen eines Kondensats untersucht. Hierbei ging es in A.4 zunächst um den prinzipiellen Zugang zur Thermodynamik eines wechselwirkenden (Einkomponenten–)Exzitonengases über die Hartree–Fock–Bogoljubow–Popow–(HFBP–)Theorie und eine mögliche Signatur eines Kondensats im Lumineszenzspektrum. In A.5 und [SSS$^+$11] haben wir den Zugang auf ein Mehrkomponentensystem verallgemeinert, wobei in A.5 neben der Theorie wiederum die Suche nach möglichen spektralen Signaturen im Vordergrund stand, während in [SSS$^+$11] der Aspekt einer möglichen Phasenseparation der verschiedenen Exzitonenspezies untersucht wurde.

Der theoretische Apparat der HFBP–Theorie in seiner Anwendung auf ein mehrkomponentiges Exzitonengas sowie die Untersuchung der Signaturen im Lumineszenzspektrum wurden in der (vom Verfasser dieser Habilitationsschrift betreuten) Diplomarbeit von Siegfried Sobkowiak [Sob10] ausführlich dargestellt und diskutiert. Hier soll daher nur ein kurzer Überblick gegeben werden.

Ausgangspunkt der Untersuchungen ist der Hamiltonoperator eines K-komponenti-

gen Exzitonengases im großkanonischen Ensemble:

$$\begin{aligned}\mathcal{H} &= \sum_{i=1}^{K}\int \mathrm{d}^3\mathbf{r}\ \psi_i^\dagger(\mathbf{r},t)\left(-\frac{\hbar^2\nabla^2}{2M_i}+V_i(\mathbf{r})-\mu_i\right)\psi_i(\mathbf{r},t)\\ &+ \frac{1}{2}\sum_{i,j=1}^{K}\int \mathrm{d}^3\mathbf{r}\ h_{ij}\psi_i^\dagger(\mathbf{r},t)\psi_j^\dagger(\mathbf{r},t)\psi_j(\mathbf{r},t)\psi_i(\mathbf{r},t)\ ,\end{aligned} \tag{1.102}$$

wobei V_i die externen Potentiale der einzelnen Teilchensorten, μ_i deren chemischen Potentiale und M_i deren Massen sind. Die Matrix h_{ij} enthält die Wechselwirkungsstärken zwischen den Spezies, die durch die s–Wellen–Streulängen a_{ij}^s (siehe hierzu [SC01]) gegeben sind:

$$h_{ij} = 2\pi\hbar^2\left(\frac{1}{M_i}+\frac{1}{M_j}\right)a_{ij}^s\,. \tag{1.103}$$

Der Bose–Feldoperator ψ_i genügt der Heisenbergschen Bewegungsgleichung

$$\mathrm{i}\hbar\frac{\partial\psi_i(\mathbf{r},t)}{\partial t} = \left(-\frac{\hbar^2\nabla^2}{2M_i}+V_i(\mathbf{r})-\mu_i\right)\psi_i(\mathbf{r},t)+\sum_{j=1}^{K}h_{ij}\psi_j^\dagger(\mathbf{r},t)\psi_j(\mathbf{r},t)\psi_i(\mathbf{r},t)\,. \tag{1.104}$$

Zerlegen wir nun den Feldoperator ψ_i gemäß

$$\psi_i(\mathbf{r},t) = \Phi_i(\mathbf{r})+\widetilde{\psi}_i(\mathbf{r},t)\,, \tag{1.105}$$

in die skalare Wellenfunktion des Kondensats $\Phi_i(\mathbf{r}) = \langle\psi_i(\mathbf{r},t)\rangle = \langle\psi_i(\mathbf{r})\rangle$ und den Operator der thermischen Exzitonen $\widetilde{\psi}_i$, so können wir nach [Gri96] sehr allgemeine Bewegungsgleichungen für die letzteren beiden Größen ableiten. In diesen Gleichungen werden nun alle nichtdiagonalen Größen und Erwartungswerte $n_{ij}\equiv\Phi_j^*\Phi_i+\widetilde{n}_{ij}$, $m_{ij}\equiv\Phi_j\Phi_i+\widetilde{m}_{ij}$, $\widetilde{n}_{ij}=\langle\widetilde{\psi}_i^\dagger\widetilde{\psi}_j\rangle$ and $\widetilde{m}_{ij}=\langle\widetilde{\psi}_i\widetilde{\psi}_j\rangle$ für $i\neq j$ vernachlässigt. Es folgen effektive Einteilchengleichungen, in denen der Einfluß der jeweils anderen Teilchensorten in Form eines mittleren Feldes enthalten ist:

$$0 = \left(-\frac{\hbar^2\nabla^2}{2M_i}+V_i-\mu_i+h_{ii}\left(n_{ii}+\widetilde{n}_{ii}\right)+\sum_{j\neq i}h_{ij}n_{jj}\right)\Phi_i+\ h_{ii}\widetilde{m}_{ii}\Phi_i^*\,, \tag{1.106}$$

$$\mathrm{i}\hbar\frac{\partial\widetilde{\psi}_i}{\partial t} = \left(-\frac{\hbar^2\nabla^2}{2M_i}+V_i-\mu_i+2h_{ii}n_{ii}+\sum_{j\neq i}h_{ij}n_{jj}\right)\widetilde{\psi}_i+\ h_{ii}m_{ii}\widetilde{\psi}_i^\dagger\,. \tag{1.107}$$

Die Gleichung (1.106) stellt eine Verallgemeinerung der Gross–Pitajewski–Gleichung

dar. Die Bewegungsgleichung (1.107) kann mittels Bogoljubow–Transformation

$$\widetilde{\psi}_i = \sum_\sigma \left[u_i(\sigma) a_i(\sigma) \mathrm{e}^{-\mathrm{i}E_i(\sigma)t/\hbar} + v_i^*(\sigma) a_i^\dagger(\sigma) \mathrm{e}^{\mathrm{i}E_i(\sigma)t/\hbar} \right] \tag{1.108}$$

gelöst werden, wobei σ die Quasiteilchenzustände abzählt. Die Bogoljubow–Amplituden u_i und v_i erfüllen die Beziehung $\sum_\sigma [u_i(\sigma)^2 - v_i(\sigma)^2] = 1$. Das Spektrum der Elementaranregungen $E_i(\sigma)$ ist durch die Lösung des Eigenwertproblems

$$\begin{pmatrix} \mathcal{L}_i & h_{ii} m_{ii} \\ -h_{ii} m_{ii}^* & -\mathcal{L}_i \end{pmatrix} \begin{pmatrix} u_i(\sigma) \\ v_i(\sigma) \end{pmatrix} = E_i(\sigma) \begin{pmatrix} u_i(\sigma) \\ v_i(\sigma) \end{pmatrix} \tag{1.109}$$

gegeben, wobei

$$\mathcal{L}_i = -\frac{\hbar^2 \nabla^2}{2M_i} + V_i - \mu_i + 2h_{ii} n_{ii} + \sum_{j \neq i} h_{ij} n_{jj} \tag{1.110}$$

gilt.

Die Gleichungen (1.106) und (1.109) verallgemeinern die Hartree–Fock–Bogoljubow–(HFB–)Gleichungen auf den Mehrkomponentenfall. Die $3K$ Gleichungen koppeln über die Wechselwirkungsmatrixelemente h_{ij}.

Um ein „lückenloses“ (*gapless*) Anregungsspektrum zu garantieren, müssen die anomalen Mittelwerte $\widetilde{m}_{ii}$ in (1.106) und (1.109) weggelassen werden (Popow–Approximation; HFBP–Gleichungen). Man erhält

$$0 = \left(-\frac{\hbar^2 \nabla^2}{2M_i} + V_i - \mu_i + h_{ii} \left(n_{ii} + \widetilde{n}_{ii} \right) + \sum_{j \neq i} h_{ij} n_{jj} \right) \Phi_i \tag{1.111}$$

und

$$\begin{pmatrix} \mathcal{L}_i & h_{ii} \Phi_i^2 \\ -h_{ii} \Phi_i^{*2} & -\mathcal{L}_i \end{pmatrix} \begin{pmatrix} u_i(\sigma) \\ v_i(\sigma) \end{pmatrix} = E_i(\sigma) \begin{pmatrix} u_i(\sigma) \\ v_i(\sigma) \end{pmatrix} . \tag{1.112}$$

Da die Ausdehnung der Potentialfalle groß gegen den exzitonischen Bohrradius ist, können die Exzitonen als lokal homogenes System beschrieben werden, wobei die Ortsabhängigkeit nur durch das Fallenpotential eingeht (Lokaldichtenäherung). In diesem Fall können die HFBP–Gleichungen gelöst werden, und man erhält für die

Dichte $n_i^T \equiv \widetilde{n}_{ii}$ der thermisch angeregten Exzitonen

$$n_i^T(\mathbf{r}) = \int \frac{\mathrm{d}^3\mathbf{k}}{(2\pi)^3} \left[\frac{L_i(\mathbf{k},\mathbf{r})}{E_i(\mathbf{k},\mathbf{r})} \left(n_B(E_i(\mathbf{k},\mathbf{r})) + \frac{1}{2} \right) - \frac{1}{2} \right] \Theta\left(E_i(\mathbf{k},\mathbf{r})^2 \right) \tag{1.113}$$

mit der Bosefunktion $n_B(E) = [\exp(E/k_BT) - 1]^{-1}$. Das Anregungsspektrum E_i ist explizit gegeben durch

$$E_i(\mathbf{k},\mathbf{r}) = \sqrt{L_i(\mathbf{k},\mathbf{r})^2 - (h_{ii} n_i^c(\mathbf{r}))^2}\,, \tag{1.114}$$

$$L_i(\mathbf{k},\mathbf{r}) = \frac{\hbar^2 k^2}{2M_i} + V_i(\mathbf{r}) - \mu_i + 2h_{ii} n_i(\mathbf{r}) + \sum_{j\neq i} h_{ij} n_j(\mathbf{r})\,, \tag{1.115}$$

mit $n_i^c \equiv |\Phi_i|^2$ and $n_i \equiv n_{ii} = n_i^T + n_i^c$. Konsistent mit der Lokaldichtenäherung wendet man die Thomas–Fermi–Approximation auf die Gross–Pitajewski–Gleichung an, d.h. man vernachlässigt den Term der kinetischen Energie in (1.111). Dann folgt schließlich für die Dichte der kondensierten Exzitonen

$$\begin{aligned} n_i^c(\mathbf{r}) = \frac{1}{h_{ii}} \Bigg(& \mu_i - V_i(\mathbf{r}) - 2h_{ii} n_i^T(\mathbf{r}) - \sum_{j\neq i} h_{ij} n_j(\mathbf{r}) \Bigg) \\ & \times \Theta \Bigg(\mu_i - V_i(\mathbf{r}) - 2h_{ii} n_i^T(\mathbf{r}) - \sum_{j\neq i} h_{ij} n_j(\mathbf{r}) \Bigg)\,. \end{aligned} \tag{1.116}$$

Die über L_i und n_i^c gekoppelten Ausdrücke (1.113)–(1.116) sind selbstkonsistent zu lösen. Man erhält die räumlichen Dichteprofile der verschiedenen Exzitonenspezies in der Falle, jeweils zum einen die der thermisch angeregten bzw. zum anderen die der kondensierten Exzitonen.

Die Dichten der thermischen und kondensierten Exzitonen sind im Experiment nicht direkt, sondern nur über das bei der Rekombination von Elektron und Loch ausgestrahlte Licht zugänglich. Benötigt wird also eine Theorie der exzitonischen Lumineszenz, die die räumliche Dichteverteilung der Exzitonen in der Falle mit dem detektierten Licht verknüpft. Den aktuellen Stand dieser Theorie markieren die Arbeiten [HK83] und [SVG94]. Diese Arbeiten bestimmen die spektrale Intensität der Lumineszenz über Fermis Goldene Regel für den Zerfallsprozeß. Im allgemeinen Fall des phononassistierten Zerfalls ergibt sich für die Intensität

$$\begin{aligned} I_i(\mathbf{r},\omega) \propto\ & 2\pi |S_i(\mathbf{k}=0)|^2 \delta(\hbar\omega' - \mu_i) n_i^c(\mathbf{r}) \\ & + \sum_{\mathbf{k}\neq 0} |S_i(\mathbf{k})|^2 n_B(\hbar\omega' - \mu_i) A_i(\mathbf{r},\mathbf{k},\hbar\omega' - \mu_i)\,, \end{aligned} \tag{1.117}$$

wobei $S_i(\mathbf{k})$ die Exziton–Photon–Kopplung bezeichnet. Die Spektralfunktion ist durch die Bogoljubow–Amplituden u_i und v_i und die Quasiteilchendispersion aus Gl. (1.114) bestimmt:

$$A_i(\mathbf{r},\mathbf{k},\omega) = 2\pi\hbar\left[u_i^2(\mathbf{k},\mathbf{r})\delta(\hbar\omega - E_i(\mathbf{k},\mathbf{r})) - v_i^2(\mathbf{k},\mathbf{r})\delta(\hbar\omega + E_i(\mathbf{k},\mathbf{r}))\right] . \quad (1.118)$$

Das Auftreten des Kondensatsbeitrages, der durch den ersten Term in (1.117) gegeben ist, also eines intensiven, extrem schmalen Signals am chemischen Potential der jeweiligen Exzitonsorte, ist ganz erheblich von der Form der Exziton–Photon–Kopplung $S_i(\mathbf{k})$ abhängig. Der Zerfall des Paraexzitons findet direkt, also ohne Beteiligung eines Phonons statt, so daß die Emission aus Gründen der Energieerhaltung nur am Schnittpunkt von Exziton- und Photondispersion stattfinden kann, d.h. $S_i(\mathbf{k}) \propto \delta(k - k_0)$. Da das Kondensat aber durch $\mathbf{k} = \mathbf{0}$ gekennzeichnet ist, dürfte es überhaupt nicht emittieren. Strenggenommen gilt diese Aussage nur für ein homogenes System. Da aber selbst die Annahme lokaler Homogenität für das Exzitonengas in der Falle eine Näherung darstellt, kann eine wenigstens schwache direkte Lumineszenz des Kondensats nicht ausgeschlossen werden.

Die (parametrische) Ortsabhängigkeit des Beitrags der thermischen Exzitonen zur Intensität, manifestiert in der Ortsabhängigkeit der Spektralfunktion, entsteht durch das ortsabhängige Fallenpotential $V_i(\mathbf{r})$ und die Hartree–Fock–Renormierung $2h_{ii}n_i(\mathbf{r}) + \sum_{j\neq i} h_{ij}n_j(\mathbf{r})$.

Das Lumineszenzsignal bildet im wesentlichen die Dichteverteilung der Exzitonen in der Falle ab. Diese ist wiederum durch die minimale Energie $E_i(\mathbf{k} = \mathbf{0}, \mathbf{r})$ begrenzt, die im nichtkondensierten Fall durch das schwach renormierte parabolische Fallenpotential gegeben, bei Auftreten eines Kondensats aber gleich dem chemischen Potential und damit konstant ist. Damit scheint eine experimentell leicht verifizierbare Signatur des Kondensats gefunden – eine Abflachung der räumlich aufgelösten Lumineszenzlinie am chemischen Potential der entsprechenden Exzitonspezies, wie in der Arbeit A.4 vorgeschlagen wurde. Weitergehende Analysen und der Vergleich mit experimentellen Resultaten (veröffentlicht in A.8) haben allerdings gezeigt, daß dieser Effekt nicht beobachtbar ist, siehe unten mehr dazu.

Bei der Anwendung der Theorie auf das Exzitonengas in Kupferoxydul stand dessen prinzipiell mehrkomponentiger Charakter (Para- und zwei Sorten von Orthoexzitonen) und daraus resultierende Effekte im Mittelpunkt. Zum einen wurde untersucht,

wie ein Kondensat in einer oder mehreren Spezies die Linienform der Lumineszenz der anderen Komponenten beeinflußt. Das Augenmerk lag insbesondere auf charakteristischen Deformationen des (experimentell am besten untersuchten) Paraspektrums sowie in der Linienform sichtbaren Phasenseparationseffekten der Orthospezies. Beide genannten Effekte konnten demonstriert werden (siehe A.5 und [SSS$^+$11]) – allerdings nicht für den experimentell einzig realistischen Fall, daß (nur) ein Kondensat von Paraexzitonen vorliegt. Damit können derartige Phasenseparationseffekte als Signaturen eines Kondensats praktisch ausgeschlossen werden.

Die Arbeit A.8 gibt einen Überblick über die Forschung der Rostocker Arbeitsgruppe Stolz zur Kondensation von Exzitonen in Kupferoxydul, wobei die experimentellen Aktivitäten in Kooperation mit Nobuko Naka (Kyoto) und die theoretischen Untersuchungen wiederum – wie schon in den Arbeiten A.5 und [SSS$^+$11] – in Kooperation mit den Greifswalder Kollegen (Thomas Koch und Holger Fehske) durchgeführt wurden.

Im theoretischen Teil der Arbeit stand die Diskussion der spektralen Signaturen eines Kondensats im Mittelpunkt. Es wurde gezeigt, daß die für den kondensierten Fall in den vorigen Arbeiten vorhergesagte (und experimentell nicht beobachtete) Abflachung des räumlich aufgelösten Spektrums am chemischen Potential nur unter der Annahme eines komplett dunklen Kondensats sichtbar ist, aber bereits durch den Beitrag eines sehr schwach leuchtenden Kondensats so kaschiert wird, daß das Spektrum dann qualitativ nicht mehr vom unkondensierten Fall unterschieden werden kann.

Dafür konnten zwei andere wesentliche Signaturen identifiziert werden: Zum einen steigt die integrierte Gesamtintensität im wesentlichen linear mit der Leistung des anregenden Lasers, bevor sie bei einer bestimmten, temperaturabhängigen Leistung abrupt ihren Anstieg ändert. Die Leistung, bei der dieser Effekt auftritt, entspricht aber gerade der kritischen Exzitonendichte![11] Dieser „Knick“ in der Kurve, der offensichtlich durch das „Fehlen“ der Lumineszenz des Anteils kondensierter Exzitonen bedingt ist, bleibt qualitativ auch erhalten, wenn das Kondensat schwach leuchtet. Auch in den experimentell erhaltenen Kurven für die Gesamtintensität konnte der „Knick“ für einige Messungen nachgewiesen werden.

Zum anderen führt ein schwach leuchtendes Kondensat zu einer Modifikation des Profils der räumlich aufgelösten Lumineszenz. Der Beitrag der thermischen Exzitonen

[11] Der Nachweis der Temperaturabhängigkeit der kritischen Dichte, in A.8 noch nicht systematisch geführt, ist eines der Snokeschen Kriterien für den Nachweis der Kondensation [Sno03].

sollte im wesentlichen deren Verteilung abbilden, die in der Falle einem (asymmetrischen) Gauß–Profil entspricht. Jede Abweichung von einem solchen Profil sollte also ein Indikator für eine bimodale Verteilung (ein weiteres der Kriterien für den Nachweis eines BEK von Snoke [Sno03]) sein. Tatsächlich zeigt eine Reihe von Messungen einen zusätzlichen Beitrag zur Lumineszenz im Fallenzentrum. Damit konnten zwei Signaturen eines Kondensats nachgewiesen werden, die zwei der Kriterien von Snoke entsprechen.

Ein weiterer theoretischer Beitrag zu A.8 ist der Versuch, in einem ersten Ansatz Abweichungen vom globalen Gleichgewicht der Exzitonen in der Falle durch Einführung eines lokalen chemischen Potentials zu berücksichtigen. Mit diesem Ansatz konnte die bimodale Verteilung im kondensierten Fall in guter Übereinstimmung mit den experimentellen Befunden verifiziert werden. Die Annahme eines nur noch lokalen chemischen Gleichgewichts stellte zudem einen ersten Schritt hin zur Nichtgleichgewichtsbeschreibung des Exzitonengases dar, die im folgenden Abschnitt diskutiert werden soll.

In der Arbeit A.9, einem *Comment*, haben wir auf eine Arbeit von A. A. High *et al.* [HLR$^+$12] Bezug genommen und nachgewiesen, daß die dort vorgenommene Interpretation der experimentellen Resultate zu indirekten Exzitonen in CQW(*coupled quantum well*)–Strukturen nicht schlüssig und somit die Aussage, Kondensation nachgewiesen zu haben, nicht haltbar ist. Unsere Argumentation stützte sich zum einen auf die Anwendung der obigen Thermodynamik auf das genannte System, zum anderen konnten wir die in [HLR$^+$12] angewandte Technik der Verschiebungsinterferometrie (*shift interferometry*) analysieren und das dort experimentell erhaltene Interferenzmuster auch ohne Annahme eines Kondensats theoretisch reproduzieren.

1.4.2 Nichtgleichgewichtsbeschreibung

Die Modellierung des experimentell untersuchten Systems im Rahmen der Thermodynamik – sei das Gleichgewicht als global oder auch nur als lokal vorausgesetzt – ist aus verschiedenen Gründen nicht hinreichend. Durch den Laser werden Orthoexzitonen am Rand der Falle angeregt, diese bewegen sich in Richtung Fallenzentrum, wobei sie zu Paraexzitonen konvertieren. Während der Driftbewegung wechselwirken die Exzitonen mit Phononen, wodurch sie abkühlen. Alle diese Prozesse erfolgen nicht instantan. Insbesondere die Frage der Kühlung ist von höchstem Interesse. Man kann

zwar davon ausgehen, daß der Kristall (und damit die Phononen) die gleiche Temperatur wie das Heliumbad hat[12], wohingegen es unklar ist, ob die Exzitonen während ihrer endlichen Lebensdauer tatsächlich die Badtemperatur erreichen.

Ein wichtiges Instrument zur Beschreibung von Nichtgleichgewichtsprozessen sind sogenannte quantenkinetische Gleichungen, d.h. Gleichungen für die zeitliche Evolution einer Größe, die im wesentlichen die statistischen Eigenschaften eines Vielteilchensystems auf dem Einteilchenniveau enthält [HJ96, Bon98]. Diese Größe kann z.B. die zweizeitige Einteilchen–Korrelationsfunktion, die Wignerverteilung oder die Impulsverteilungsfunktion sein. In letzteren beiden Fällen wird die entsprechende Gleichung oft allgemein als (Quanten–)Boltzmann–Gleichung bezeichnet.

Die konkrete Form der Boltzmann–Gleichung hängt im wesentlichen von drei Fragestellungen ab: (i) Welches physikalische System soll untersucht werden? (ii) Unter welchen experimentellen Bedingungen (äußere Felder, Gradienten usw.) existiert das System? (iii) Auf welchen Zeitskalen spielen sich die zu untersuchenden Prozesse im System ab?

Die Beantwortung der Fragestellung (ii) bestimmt die Form der linken Seite der Gleichung, des sogenannten Driftterms. Dieser enthält neben der Zeitableitung die Wirkung äußerer Felder und Gradienten. Im allgemeinen Fall eines inhomogenen und anisotropen Systems in einem äußeren Potential $U(\mathbf{r},t)$ lautet die Boltzmann–Gleichung für die Wigner–Verteilung $f(\mathbf{r},\mathbf{p},t)$

$$\frac{\partial f(\mathbf{r},\mathbf{p},t)}{\partial t} + \frac{\mathbf{p}}{m}\cdot\nabla_{\mathbf{r}} f(\mathbf{r},\mathbf{p},t) - \nabla_{\mathbf{r}} U(\mathbf{r},t)\cdot\nabla_{\mathbf{p}} f(\mathbf{r},\mathbf{p},t) = I(\mathbf{r},\mathbf{p},t)\,. \tag{1.119}$$

Die rechte Seite der Gleichung, das sogenannte Stoßintegral $I(\mathbf{r},\mathbf{p},t)$ beschreibt den Einfluß der Wechselwirkung zwischen den Konstituenten des Systems („Stöße“), zudem Prozesse der Teilchenerzeugung und -vernichtung (Quell- bzw. Zerfallsterme). Welche Wechselwirkungen und weitere Prozesse Berücksichtigung finden müssen, wird durch das zu untersuchende System – hier also Exzitonen im angeregten Halbleiter – bestimmt. Darauf wird gleich noch einzugehen sein.

Der Fragestellung (iii) nach den Zeitskalen liegt die grundlegende Erkenntnis aus der statistischen Physik von Nichtgleichgewichtsprozessen zugrunde, daß im Zuge der Entwicklung eines Systems von einem Nichtgleichgewichtszustand ins Gleichgewicht

[12] Das sollte zumindest anfangs – bei schwachen Anregungsleistungen dauerhaft – gelten. Bei höheren Leistungen ist ein Aufheizen des Kristalls nicht ausgeschlossen.

(bzw. in einen stationären Zustand) die Relaxation verschiedene Stadien durchläuft, deren Zeitskalen im allgemeinen deutlich voneinander separieren [Bog46, Bon98]. Kurz zusammengefaßt ist das Anfangsstadium, die Domäne der Ultrakurzzeitphysik, durch den Aufbau der Korrelationen bestimmt, das kinetische Stadium durch die Relaxation der Einteilchen–Verteilungsfunktion hin zu einer (lokalen) Gleichgewichtsverteilung und schließlich das hydrodynamische Stadium durch die Relaxation makroskopischer Größen wie Dichte und Druck und durch Transportprozesse. Letzteres Stadium mündet in ein globales Gleichgewicht bzw. einen globalen stationären Zustand.

Bei der Beschreibung der Dynamik der Exzitonen in der Falle sollte das Anfangsstadium – dessen Untersuchung verallgemeinerte quantenkinetische Gleichungen jenseits der Boltzmann–Gleichung erfordern würde [Sem01, SB06] – nicht betrachtet werden. Der Fokus lag zum einen auf der Einstellung des lokalen Gleichgewichts (lokale Temperatur bzw. chemisches Potential) und zum anderen auf der Propagation der am Rande der Falle angeregten Exzitonen hin zum Fallenzentrum.

Zur Beschreibung der Kinetik bosonischer Gase bei tiefen Temperaturen existieren wohlausgearbeitete theoretische Zugänge, hervorgehoben sollen hier insbesondere die Arbeiten von Griffin *et al.* sein, siehe [GNZ09] und darin zitierte Literatur. Dieser Apparat war nun auf das Exzitonengas in der Falle anzuwenden, wobei die Spezifika des Halbleiters in die Theorie einzubringen waren. Das ist in den Arbeiten A.10 und A.11 erfolgt, eine exzellente und ausführliche Darstellung findet man in der (vom Verfasser dieser Habilitationsschrift mitbetreuten) Dissertation von Siegfried Sobkowiak [Sob14]. Hier soll es daher auch zu diesem Punkt nur einen kurzen Überblick geben.

Den Rahmen für die Untersuchungen bilden die aus der Theorie ultrakalter Atomgase wohlbekannten Zaremba–Nikuni–Griffin–(ZNG–)Gleichungen [ZNG99, GNZ09]. In diesem Formalismus genügt die Dynamik der kondensierten Teilchen einer verallgemeinerten Gross–Pitajewski–Gleichung der Form [vgl. Gl. (1.111)]

$$\mathrm{i}\hbar\frac{\partial\Phi(\mathbf{r},t)}{\partial t} = \left(-\frac{\hbar^2\nabla^2}{2M} + V_{\mathrm{ext}}(\mathbf{r}) + gn_c(\mathbf{r},t) + 2g\tilde{n}(\mathbf{r},t) - \mathrm{i}\,R_{\mathrm{ZNG}}(\mathbf{r},t)\right)\Phi(\mathbf{r},t)\,, \tag{1.120}$$

wobei $g \equiv h_{ii}$ ist und der Kopplungsterm $R_{\mathrm{ZNG}}(\mathbf{r},t)$ den Austausch von Exzitonen zwischen normaler und kondensierter Phase beschreibt. Die Evolution der thermischen Exzitonen wird durch eine Quanten–Boltzmann–Gleichung (1.119) beschrieben. Deren Stoßintegral ist für die Beschreibung der Dynamik des Exzitonengases um eine

Reihe von Beiträgen zu ergänzen, die der Spezifik des betrachteten Systems im Unterschied zum atomaren Gas Rechnung tragen. Die rechte Seite der Gleichung muß also neben (i) dem Beitrag der Stöße der thermischen Exzitonen untereinander und (ii) dem der Stöße zwischen thermischen und kondensierten Exzitonen auch Beiträge (iii) von Stößen mit Phononen und solche enthalten, die die Erzeugung und Vernichtung von Exzitonen beschreiben: (iv) die Rekombination, d.h. die endliche Lebensdauer, (v) den eingangs erwähnten augerartigen Zweikörperzerfall und (vi) die Erzeugung von Exzitonen durch Laseranregung.

Letzterer Prozeß kann im Experiment gepulst oder im Dauerstrich („*continuous wave*“, *cw*) erfolgen. Betrachtet wird hier die Dauerstrichanregung, bei der durch den Laser ständig Exzitonen „nachgeliefert“ werden, die entsprechend ihrer Lebensdauer zerfallen. Es ergibt sich ein stationärer Prozeß, ein globales Gleichgewicht kann sich in diesem Szenario nicht einstellen.[13] Das erste Stadium ist durch die Ausbildung des stationären Zustandes durch Relaxation der lasererzeugten Nichtgleichgewichtsverteilung ins lokale Gleichgewicht gekennzeichnet. Im zweiten Stadium erfolgt dann hydrodynamische Evolution, gekennzeichnet durch Konversionsprozesse zwischen Ortho- und Paraexzitonen und die Driftbewegung in Richtung Fallenzentrum.

Während des gesamten Evolutionsprozesses ist, wie bereits erwähnt, die Temperatur, d.h. die Dynamik des Abkühlprozesses, von besonderem Interesse. Im ersten Stadium erhält man durch die Lösung des gekoppelten Systems (1.119) und (1.120) das Resultat der Relaxation der anfänglichen lasererzeugten Nichtgleichgewichtsverteilung hin zum lokalen Gleichgewicht, also eine boseartige Verteilung mit jeweils orts- und zeitabhängiger Temperatur und chemischem Potential. Im Verlauf des Evolution zum Gleichgewicht ist die Größe „Temperatur“ naturgemäß nicht eindeutig definiert. Es ist aber möglich, über die Mittelung der kinetischen Energie über die Verteilungsfunktion (d.h. die kinetische Energie pro Teilchen) eine effektive Temperatur zu definieren, [14]

$$\frac{E}{N} = \frac{1}{n^T} \int \frac{\mathrm{d}^3 k}{(2\pi)^3} \frac{\hbar^2 k^2}{2M} f(\mathbf{k}, t) \equiv \frac{3}{2} k_\mathrm{B} T_\mathrm{eff} \,. \tag{1.121}$$

Bevor die Evolution dieser Größe betrachtet wird, muß obige Prämisse überprüft werden, ob innerhalb des ersten, zeitlich gut abgrenzbaren Stadiums lokales Gleichge-

[13] Bei gepulster Anregung werden keine Exzitonen „nachgeliefert“, und nach ausreichend langer Zeit sind die primär erzeugten zerfallen. Das globale Gleichgewicht entspricht dann dem unangeregten Halbleiter.

[14] Im nichtentarteten System im thermodynamischen Gleichgewicht gilt $T_\mathrm{eff} \equiv T$.

wicht erreicht wird. Tatsächlich zeigen die numerischen Resultate, daß eine lasererzeugte gaußförmige Anfangsverteilung innerhalb von einer Nanosekunde in eine Boseverteilung relaxiert, siehe hierzu Abb. 1 in der Arbeit A.10. Diese Relaxation erweist sich als ganz entscheidend durch Exziton–Exziton–Stöße bedingt. Auch die nachfolgende Thermalisierung des Exzitonengases wird durch diese stark begünstigt, insbesondere verhindern die Stöße einen oft als „Ausfrieren“ der Phononen bezeichneten Effekt[15], der zur Ausprägung einer Nichtgleichgewichtsverteilung und zu starker Herabsetzung der Abkühlungseffizienz führt (siehe Abb. 2 in der Arbeit A.10).

Die Evolution der effektiven Temperatur zeigt noch einmal die Bedeutung der Exziton–Exziton–Stöße für die Effizienz der Kühlung der Exzitonen bei tiefen Temperaturen des Heliumbades T_B, siehe Abb. 3 in der Arbeit A.10. Während sie aber bei Badtemperaturen von 0,5 K noch gewährleisten können, daß die Exzitonen innerhalb ihrer Lebensdauer von einigen hundert Nanosekunden die Badtemperatur tatsächlich erreichen, ist das bereits bei 0,1 K nicht mehr der Fall. Bei derartig tiefen Badtemperaturen muß man also davon ausgehen, daß die mittlere Temperatur des Exzitonengases in der Falle immer größer als T_B ist. Ob es aber Bereiche in der Falle – etwa im Zentrum – gibt, in denen die Exzitonen deutlich kälter sind und eventuell T_B erreichen, ist durch dieses Resultat noch nicht ausgeschlossen und wird im folgenden, hydrodynamischen Stadium untersucht.

Im hydrodynamischen Stadium ist die lokale Impulsverteilung bereits bekannt, so daß die Impulsvariable in der Boltzmann–Gleichung redundant ist. In diesem Fall ist es sinnvoll, zu sogenannten Momentengleichungen überzugehen, d.h. die Boltzmann–Gleichung jeweils über die $n-$te Potenz des Impulses[16] abzuintegrieren. Es entsteht ein gekoppeltes System für die Momente ($n = 0$: Teilchenzahl, $n = 1$: Impuls, $n = 2$: kinetische Energie usw.), also im Prinzip eine unendliche Hierarchie von Gleichungen. Allerdings kann unter der Bedingung der oben erwähnten Separation der Zeitskalen das System der ersten drei Gleichungen abgeschlossen werden, die Einführung der Boseverteilung mit lokalem chemischen Potential und lokaler Temperatur stellt gerade die Abschlußbedingung dar.

Von der Vielzahl der Resultate, die in der Arbeit A.11 publiziert wurden, soll hier nur eines hervorgehoben werden. Wir betrachten wiederum die Temperatur der Ex-

[15] Nur Exzitonen oberhalb einer durch die Schallgeschwindigkeit v_s bestimmten Energieschwelle $E \geq E_0 = mv_s^2/2$ können über Stokes- und Anti-Stokes-Streuung mit akustischen Phononen wechselwirken, darunter nur über Anti-Stokes-Streuung. Das führt zur Ausbildung eines Plateaus bei niedrigen Wellenzahlen und einer steilen Hochenergieflanke in der Verteilungsfunktion.

[16] im Allgemeinen mit einem Vorfaktor versehen, z.B. bei $n = 2$: $p^2/2M$

zitonen, diesmal im stationären Regime und räumlich aufgelöst, dazu auch die Dichteverteilung in der Falle, siehe Abb. 2 in A.11. Wie zu erwarten, ist das Dichteprofil gaußförmig mit dem Maximum im Fallenzentrum. Dort befindet sich bei nicht zu tiefen Bad- (bzw. Kristall- oder Phonon-)Temperaturen T_B auch das Minimum der Exzitonentemperatur T_X (je länger der Weg in die Falle, desto mehr Zeit steht zum Abkühlen zur Verfügung), und $T_X(r=0) \gtrsim T_B$. Bei sehr tiefer Badtemperatur (und hoher Exzitonendichte im Zentrum) aber bleibt T_X deutlich oberhalb T_B, und das Minimum liegt außerhalb des Fallenzentrums.

Neben der bereits oben diskutierten herabgesetzten Kühlungseffizienz bei tiefen Temperaturen liegt die Ursache für dieses Verhalten in einem Zweikörperzerfall, bei dem ein Exziton ionisiert wird und das zweite die freiwerdende Bindungsenergie in Form von kinetischer Energie erhält. Dieser Effekt, aufgrund der Parallelen zum Auger–Effekt der Atomphysik oft als Auger–Zerfall bezeichnet, führt zu einem lokalen Temperaturmaximum im Fallenzentrum und behindert das Anwachsen der Dichte dort. Er ist damit für das Erreichen der Kondensationsbedingungen in zweifacher Hinsicht kontraproduktiv. Über den Wert der Rate für diesen Prozeß herrscht noch große Unsicherheit, verschiedene theoretische Zugänge [KBW96, KB96, JW06] und experimentelle Befunde [OGW99, WOW00, YIMKG10, SNKS12] differieren um mehrere Größenordnungen. Da von der Größe der Rate aber abhängt, ob bei vorgegebenen experimentellen Parametern die Bedingungen für die Kondensation erreicht werden können, laufen hierzu intensive theoretische Untersuchungen [SS17].

1.5 Lumineszenzspektrum der Exzitonen

Die experimentelle Untersuchung des Exzitonengases in der Falle beruht auf der Messung des beim Zerfall der Exzitonen ausgesendeten Lichts, der sogenannten Lumineszenz. Für einen direkten Vergleich der theoretischen Resultate zur Thermodynamik und Hydrodynamik des Exzitonengases mit den experimentellen Befunden ist es also nötig, die Zerfallslumineszenz einer gegebenen Exzitonenverteilung beschreiben zu können.

Von besonderem Interesse sind Signaturen des Kondensats, die in dem Licht, das die Exzitonen bei ihrer Rekombination aussenden, experimentell beobachtbar sein sollten. Dabei wäre der schlagende Beweis – die „*smoking gun*“ – natürlich der Nach-

weis der Kohärenz des Lichts.[17] Daher sollte die Theorie in der Lage sein, die Kohärenzfunktionen erster bzw. zweiter Ordnung berechnen zu können. Zum anderen sollten aber auch eindeutige Signaturen bereits im Spektrum der Lumineszenz der thermischen Exzitonen auffindbar sein, wie wir im vorangegangenen Abschnitt gesehen haben. Das Spektrum – also die frequenzaufgelöste Lumineszenz – kann im Experiment ortsaufgelöst detektiert werden. Die Ortsabhängigkeit wird im wesentlichen durch die Potentialfalle bewirkt, in der die Exzitonen im Experiment gefangen werden. Zum anderen erfolgt die Anregung der Exzitonen bereits inhomogen, nämlich nur im Bereich des Laserspots (außerhalb der Falle). Der Laser kann, wie bereits beschrieben, gepulst oder im Dauerstrich betrieben werden, wobei letztere Methode einen stationären Nichtgleichgewichtszustand des Exzitonensystems erzeugt. Die Theorie muß also ein inhomogenes System beschreiben können, das sich im Allgemeinen im Nichtgleichgewicht befindet.

Wie einleitend bereits erwähnt, kann der exzitonische Grundzustand, das $1S-$Paraexziton, nur aufgrund der druckinduzierten Verspannung (die die Potentialfalle aufbaut) direkt, d.h. ohne Beteiligung von Phononen, rekombinieren, ansonsten ist dieser Übergang in allen Ordnungen verboten. Das hierbei ausgesendete Licht ist Gegenstand der in diesem Abschnitt beschriebenen Untersuchungen, die in der Arbeit A.12 publiziert wurden.

Frühere theoretische Zugänge zur exzitonischen Lumineszenz [HK83, SVG94] beruhten im Wesentlichen auf Fermis Goldener Regel, d.h. einem Exziton–Photon–Kopplungsanteil des Hamilton–Operators, der nur „normale“ Terme umfaßt, also solche, die die Erzeugung eines Photons bei gleichzeitiger Vernichtung eines Exzitons und den umgekehrten Prozeß beschreiben. Um aber mit der Bogoljubow–Beschreibung der Exzitonen konsistent zu sein, müssen auch anomale Exziton–Photon–Kopplungsterme einbezogen werden. Damit kann der Polaritoneffekt auf sehr allgemeine Weise berücksichtigt werden. Im Gegensatz zu Systemen in Mikrokavitäten koppeln die Exzitonen in der Potentialfalle an freie Photonmoden. Die Exziton–Photon–Wechselwirkung ist dann inhärent ein Quasigleichgewichtsproblem, und der strahlende Zerfall der Exzitonen sollte über transiente polaritonartige Zustände erfolgen.

Andere Zugänge betrachten unter Verzicht auf eine Bosonisierung direkt die Kopplung des Lichtfeldes an die Ladungsträger. Genannt werden soll hier der Zugang über

[17] Es ist nicht trivialerweise klar, daß das Kondensat – ein kohärenter Zustand – auch kohärentes Licht emittiert (genauer: wie sich die Kohärenz des Teilchensystems auf die Photonen überträgt), jedoch gemäß [FRTM98, Lai98, LO02] zu erwarten.

gekoppelte Halbleiter–Bloch– und Halbleiter–Lumineszenzgleichungen von S. W. Koch *et al.* Eine ausführliche Darstellung findet man in [KJHK99].

1.5.1 Grundgrößen und Bewegungsgleichungen

Zentrale Größe bei der Untersuchung der exzitonischen Lumineszenz ist die Feld–Feld–Korrelationsfunktion [Gla63]

$$G_{\mathrm{EE}}(\mathbf{r}_1,t_1;\mathbf{r}_2,t_2)=\left\langle E^{(-)}(\mathbf{r}_2,t_2)E^{(+)}(\mathbf{r}_1,t_1)\right\rangle\,, \tag{1.122}$$

wobei $E^{(\pm)}$ die positiven bzw. negativen Frequenzanteile des elektrischen Feldes bezeichnet,

$$\mathbf{E}^{(+)}(\mathbf{r},t)=\int\limits_0^\infty \mathrm{d}\omega\,\mathrm{e}^{-\mathrm{i}\omega t}\,\mathfrak{E}(\mathbf{r},\omega)\,,\qquad \mathbf{E}^{(-)}(\mathbf{r},t)=\int\limits_{-\infty}^0 \mathrm{d}\omega\,\mathrm{e}^{-\mathrm{i}\omega t}\,\mathfrak{E}(\mathbf{r},\omega)\,, \tag{1.123}$$

und das Feld parallel zu einem (zunächst beliebigen) Einheitsvektor $\mathbf{e}$ polarisiert sein soll,

$$E^{(+)}(\mathbf{r},t)=\mathbf{e}^*\cdot\mathbf{E}^{(+)}(\mathbf{r},t)\,,\qquad E^{(-)}(\mathbf{r},t)=\mathbf{e}\cdot\mathbf{E}^{(-)}(\mathbf{r},t)\,. \tag{1.124}$$

Aus der Feld–Feld–Korrelationsfunktion kann zum einen die Intensität (bzw. das ortsaufgelöste Spektrum) der Lumineszenz gewonnen werden,

$$I(\mathbf{r},\omega,T)=\frac{c\varepsilon}{2}\int\limits_{-\infty}^{\infty}\mathrm{d}\tau\,\mathrm{e}^{-\mathrm{i}\omega\tau}\,G_{\mathrm{EE}}\left(\mathbf{r},T+\frac{\tau}{2};\mathbf{r},T-\frac{\tau}{2}\right)\,, \tag{1.125}$$

zum anderen die Kohärenzfunktion erster Ordnung [Gla63],

$$g_1(\mathbf{r}_1,t_1;\mathbf{r}_2,t_2)=\frac{G_{\mathrm{EE}}(\mathbf{r}_1,t_1;\mathbf{r}_2,t_2)}{\sqrt{G_{\mathrm{EE}}(\mathbf{r}_1,t_1;\mathbf{r}_1,t_1)G_{\mathrm{EE}}(\mathbf{r}_2,t_2;\mathbf{r}_2,t_2)}}\,. \tag{1.126}$$

Dabei ist $\varepsilon=\varepsilon_0\varepsilon_r$ die Dielektrizitätskonstante und $c=c_0/\sqrt{\varepsilon_r}$ die Lichtgeschwindigkeit im Medium (c_0 ist die Vakuumlichtgeschwindigkeit).

Das elektrische Feld $\mathbf{E}$ ist in Coulomb–Eichung durch $\mathbf{E}(\mathbf{r},t)=-\frac{\partial}{\partial t}\mathbf{A}(\mathbf{r},t)$ mit dem

Vektorpotential $\mathbf{A}$ verknüpft, welches in 2. Quantisierung durch

$$\mathbf{A}(\mathbf{r},t) = \frac{1}{\sqrt{V}} \sum_{\lambda,\mathbf{q}} \sqrt{\frac{\hbar}{2\epsilon_0 \omega_q}} \mathbf{e}_{\lambda,\mathbf{q}} \mathrm{e}^{\mathrm{i}\mathbf{q}\cdot\mathbf{r}} \left[\hat{a}_{\mathbf{q},\lambda}(t) + \hat{a}^\dagger_{-\mathbf{q},\lambda}(t)\right] \tag{1.127}$$

gegeben ist [SW02]. Hier sind $\hat{a}^\dagger$ und $\hat{a}$ die Erzeugungs- bzw. Vernichtungsoperatoren der Photonen, $\mathbf{e}_{\lambda,\mathbf{q}}$ die Polarisations–Einheitsvektoren (Moden $\lambda = 1, 2$), $\hbar\omega_q$ ist die Photonenergie mit $\omega_q = cq$ und V das Systemvolumen.

Bilden wir die zeitliche Ableitung von (1.127) und setzen das Resultat in die Definition von G_{EE} (1.122) ein, erhalten wir

$$G_{\mathrm{EE}}(\mathbf{r}_1,t_1;\mathbf{r}_2,t_2) = \frac{\hbar}{2\varepsilon V} \sum_{\mathbf{q},\mathbf{q}'} \frac{1}{\sqrt{\omega_q \omega_{q'}}} \mathrm{e}^{-\mathrm{i}(\mathbf{q}'\cdot\mathbf{r}_2 - \mathbf{q}\cdot\mathbf{r}_1)} (1+\cos\vartheta) \left\langle \dot{\hat{a}}^\dagger_{\mathbf{q}'}(t_2) \dot{\hat{a}}_{\mathbf{q}}(t_1) \right\rangle . \tag{1.128}$$

Hierbei haben wir

$$\sum_{\lambda,\lambda'} \mathbf{e}_{\lambda,\mathbf{q}} \cdot \mathbf{e}_{\lambda',\mathbf{q}'} = 1 + \cos\vartheta \tag{1.129}$$

mit $\vartheta = \measuredangle(\mathbf{q},\mathbf{q}')$ ausgenutzt.

Um den Erwartungswert $\left\langle \dot{\hat{a}}^\dagger_{\mathbf{q}}(t_1) \dot{\hat{a}}_{\mathbf{q}'}(t_2) \right\rangle$ in Gl. (1.128) näher zu bestimmen, müssen wir die Bewegungsgleichung der Photonerzeuger bzw. -vernichter untersuchen,

$$\mathrm{i}\hbar\, \dot{\hat{a}}_{\mathbf{q}}(t) = -\left[\hat{H}, \hat{a}_{\mathbf{q}}(t)\right] . \tag{1.130}$$

Der Hamiltonoperator $\hat{H}$ des Systems setzt sich aus den Beiträgen der freien Exzitonen im Fallenpotential (V_{ext}) $\hat{H}_{\mathrm{X}}$, der Photonen $\hat{H}_{\mathrm{ph}}$, der Exziton–Exziton–Wechselwirkung $H_{\mathrm{X-X}}$ und der Exziton–Photon–Wechselwirkung $H_{\mathrm{X-ph}}$ zusammen, $\hat{H} = \hat{H}_{\mathrm{X}} + \hat{H}_{\mathrm{ph}} + \hat{H}_{\mathrm{X-X}} + \hat{H}_{\mathrm{X-ph}}$. Der exzitonische Anteil $\hat{H}_{\mathrm{X}} + \hat{H}_{\mathrm{X-X}}$ kann, wie bisher, mittels Bogoljubow–Transformation $\hat{B}_{\mathbf{q}} = u_{\mathbf{q}}\hat{b}_{\mathbf{q}} + v^*_{-\mathbf{q}}\hat{b}^\dagger_{-\mathbf{q}}$ diagonalisiert werden, d.h.

$$\begin{aligned} \hat{H}_{\mathrm{B}} = \hat{H}_{\mathrm{X}} + \hat{H}_{\mathrm{X-X}} &= \sum_{\mathbf{q}} \left(\frac{\hbar^2 q^2}{2m} + V_{\mathrm{ext}} - \mu \right) \hat{B}^\dagger_{\mathbf{q}} \hat{B}_{\mathbf{q}} + \frac{U_0}{2V} \sum_{\mathbf{qpk}} \hat{B}^\dagger_{\mathbf{p+q}} \hat{B}^\dagger_{\mathbf{k-q}} \hat{B}_{\mathbf{p}} \hat{B}_{\mathbf{k}} \\ &= \sum_{\mathbf{q}} E_{\mathbf{q}} \hat{b}^\dagger_{\mathbf{q}} \hat{b}_{\mathbf{q}} . \end{aligned} \tag{1.131}$$

Hier sind $\hat{B}^\dagger$, $\hat{B}$ ($\hat{b}^\dagger$, $\hat{b}$) die Erzeuger bzw. Vernichter der Exzitonen (Bogolonen), μ deren chemisches Potential und U_0 deren Wechselwirkungsstärke (unter der Annahme

eines Kontaktpotentials). Die Dispersion der Bogolonen ist durch $E_q = \sqrt{L_q^2 - U_0^2 n_c^2}$ mit $L_q = \frac{\hbar^2 q^2}{2m} + V_{\text{ext}} - \mu - 2U_0(n_c + n_T)$ gegeben, wobei n_c die Kondensatsdichte und n_T die Dichte der thermisch angeregten Zustände sind (siehe vorangegangener Abschnitt). Man beachte, daß das externe Fallenpotential ortsabhängig ist, damit auch die Dichten und die Dispersion!

Für die Exziton–Photon–Wechselwirkung $H_{\text{X-ph}}$ gehen wir vom Ausdruck in minimaler Kopplung aus [GA07],

$$\hat{H}_{\text{X-ph}} = -\frac{e}{m_0} \sum_j \hat{\mathbf{A}}(\hat{\mathbf{r}}_j) \cdot \hat{\mathbf{p}}_j + \frac{e^2}{2m_0} \sum_j |\hat{\mathbf{A}}(\hat{\mathbf{r}}_j)|^2 \,, \tag{1.132}$$

wobei m_0 die freie Elektronmasse und $\hat{\mathbf{r}}_j$ bzw. $\hat{\mathbf{p}}_j$ Ort und Impuls des j-ten Elektrons sind. In die Formel (1.132) wird nun die Heisenbergsche Bewegungsgleichung $\mathrm{i}\hbar\hat{\mathbf{p}}_j = m_0[\hat{\mathbf{r}}_j, \hat{H}_{\text{x}}]$ eingesetzt. Dabei wird der Ortsoperator in Bogolon–Wellenfunktionen $\Psi_{\mathbf{q}}^B$ entwickelt [GA07]:

$$\hat{\mathbf{r}}_j = \sum_{\mathbf{q}} \langle 0|\, \hat{\mathbf{r}}_j \,|\Psi_{\mathbf{q}}^B\rangle\, \hat{b}_{\mathbf{q}} + \sum_{\mathbf{q}} \langle \Psi_{\mathbf{q}}^B|\, \hat{\mathbf{r}}_j \,|0\rangle\, \hat{b}_{\mathbf{q}}^\dagger + \sum_{\substack{\mathbf{q},\mathbf{q}' \\ \mathbf{q}\neq\mathbf{q}'}} \sum \langle \Psi_{\mathbf{q}}^B|\, \hat{\mathbf{r}}_j \,|\Psi_{\mathbf{q}'}^B\rangle\, \hat{b}_{\mathbf{q}}^\dagger \hat{b}_{\mathbf{q}'} \,. \tag{1.133}$$

Der letzte Term auf der rechten Seite von Gl. (1.133) wird im folgenden weggelassen, da wir nur an Übergängen vom Bogoljubow–Grundzustand (dem Kondensat) in angeregte Zustände (bzw. umgekehrt) interessiert sind. Wenn wir nun mit Hilfe der Entwicklung (1.133) den Kommutator $[\hat{\mathbf{r}}_j, \hat{H}_{\text{x}}]$ berechnen und für das Vektorpotential $\hat{\mathbf{A}}$ die Normalmodenentwicklung (1.127) (mit $\hat{a}_{\mathbf{q},\lambda} \equiv \hat{a}_{\mathbf{q}}$) einsetzen, erhalten wir schließlich für den gesamten Hamiltonoperator $\hat{H} = \hat{H}_{\text{X}} + \hat{H}_{\text{ph}} + \hat{H}_{\text{X-ph}}$

$$\begin{aligned} \hat{H} \;=\; & \sum_{\mathbf{q}} E_{\mathbf{q}} \hat{b}_{\mathbf{q}}^\dagger \hat{b}_{\mathbf{q}} + \sum_{\mathbf{q}} \hbar\omega_{\mathbf{q}} \hat{a}_{\mathbf{q}}^\dagger \hat{a}_{\mathbf{q}} \\ & + \mathrm{i} \sum_{\mathbf{q}} C_{\mathbf{q}} (\hat{a}_{\mathbf{q}} + \hat{a}_{-\mathbf{q}}^\dagger)(\hat{b}_{-\mathbf{q}} - \hat{b}_{\mathbf{q}}^\dagger) + \sum_{\mathbf{q}} D_{\mathbf{q}} (\hat{a}_{-\mathbf{q}} + \hat{a}_{\mathbf{q}}^\dagger)(\hat{a}_{\mathbf{q}} + \hat{a}_{-\mathbf{q}}^\dagger) \,, \end{aligned} \tag{1.134}$$

mit der Exziton–Photon–Kopplungsstärke

$$C_{\mathbf{q}} = E_{\mathbf{q}} \sqrt{\frac{2\pi \mathrm{e}^2}{4\pi\varepsilon_0\varepsilon_r V \hbar\omega_{\mathbf{q}}}}\, \langle \Psi_{\mathbf{q}}^B|\, \mathbf{e}_{\mathbf{q}\lambda} \cdot \sum_j \mathbf{r}_j \mathrm{e}^{\mathrm{i}\mathbf{q}\cdot\mathbf{r}_j} \,|0\rangle \;, \tag{1.135}$$

und $D_{\mathbf{q}} = |C_{\mathbf{q}}|^2 / E_{\mathbf{q}}$. In Dipolnäherung $\exp(\mathrm{i}\mathbf{q}\cdot\mathbf{r}_j) \approx 1$ und unter Nutzung der Defini-

tion der Oszillatorstärke [18]

$$f = \frac{2m_0 E_{\mathbf{q}}}{\hbar^2} |\left\langle \Psi^B_{\mathbf{q}} \right| \mathbf{e}_{\mathbf{q}\lambda} \cdot \sum_j \mathbf{r}_j \left| 0 \right\rangle|^2 \,, \tag{1.136}$$

folgt schließlich für die Kopplungsstärke [And14]

$$C_{\mathbf{q}} = \sqrt{\frac{\hbar^2 e^2 f}{4\varepsilon_0 \varepsilon_r m_0 V}} \sqrt{\frac{E_{\mathbf{q}}}{\hbar\omega_{\mathbf{q}}}} \,. \tag{1.137}$$

Damit erhält man für die Bewegungsgleichung (1.130)

$$\mathrm{i}\hbar\, \dot{\hat{a}}_{\mathbf{q}}(t) = \hbar\omega_{\mathbf{q}} \hat{a}_{\mathbf{q}}(t) + \mathrm{i}C_{\mathbf{q}} \left(\hat{b}_{\mathbf{q}}(t) - \hat{b}^\dagger_{-\mathbf{q}}(t) \right) + 2D_{\mathbf{q}} \left(\hat{a}_{\mathbf{q}}(t) + \hat{a}^\dagger_{-\mathbf{q}}(t) \right) \,. \tag{1.138}$$

Analog folgt eine Bewegungsgleichung für die Bogolonoperatoren,

$$\mathrm{i}\hbar\, \dot{\hat{b}}_{\mathbf{q}}(t) \;\; = \;\; E_{\mathbf{q}} \hat{b}_{\mathbf{q}}(t) - \mathrm{i}C_{\mathbf{q}} \left(\hat{a}_{\mathbf{q}}(t) + \hat{a}^\dagger_{-\mathbf{q}}(t) \right) \,. \tag{1.139}$$

Mit Hilfe von Gl. (1.138) und der dazu adjungierten sind wir nun in der Lage, den Erwartungswert $\left\langle \dot{\hat{a}}^\dagger_{\mathbf{q}'}(t_2) \dot{\hat{a}}_{\mathbf{q}}(t_1) \right\rangle$, der die Feld–Feld–Korrelationsfunktion (1.128) bestimmt, zu bilden. Offensichtlich treten in dieser Größe alle möglichen Erwartungswerte der Formen $\left\langle X^\dagger_{\mathbf{q}'}(t_2) Y_{\mathbf{q}}(t_1) \right\rangle$, $\left\langle X_{\mathbf{q}'}(t_2) Y^\dagger_{\mathbf{q}}(t_1) \right\rangle$, $\left\langle X^\dagger_{\mathbf{q}'}(t_2) Y^\dagger_{\mathbf{q}}(t_1) \right\rangle$ und $\langle X_{\mathbf{q}'}(t_2) Y_{\mathbf{q}}(t_1) \rangle$ auf, wobei X und Y jeweils für die Operatoren $\hat{a}$ oder $\hat{b}$ stehen. Alle 16 derartigen Erwartungswerte können als Korrelationsfunktionen betrachtet werden, wie sie aus der Theorie der reellzeitigen Greenfunktionen bekannt sind [FW71, KSK05]. Um diese Korrelationsfunktionen zu bestimmen, sollen zunächst Greenfunktionen auf der Keldysh–Kontur definiert werden:

$$\mathrm{i}\hbar G^{\alpha\beta}_{XY}(\mathbf{q}, \mathbf{q}', t_1, t_2) = \begin{pmatrix} \langle T_{\mathcal{C}}\, X_{\mathbf{q}}(t_1) Y^\dagger_{\mathbf{q}'}(t_2) \rangle & \langle T_{\mathcal{C}}\, X_{\mathbf{q}}(t_1) Y_{\mathbf{q}'}(t_2) \rangle \\ \langle T_{\mathcal{C}}\, X^\dagger_{\mathbf{q}}(t_1) Y^\dagger_{\mathbf{q}'}(t_2) \rangle & \langle T_{\mathcal{C}}\, X^\dagger_{\mathbf{q}}(t_1) Y_{\mathbf{q}'}(t_2) \rangle \end{pmatrix} \,. \tag{1.140}$$

Zu beachten ist, daß die Matrixelemente dieser Greenfunktionen wiederum Matrizen sind, deren Elemente jeweils durch Positionierung der beiden Zeiten auf den Ufern der Keldysh–Kontur bestimmt sind.

[18] Man beachte, daß diese Definition im Prinzip den *Exziton*zustand $\langle \Psi^X_{\mathbf{q}} |$ beinhaltet, in (1.135) aber der *Bogolon*zustand auftritt. Hier soll jedoch f nicht aus einer mikroskopischen Theorie hergeleitet, sondern ein experimentell bestimmter Wert verwendet werden. Im Experiment ist aber ein Exzitonzustand natürlicherweise durch Wechselwirkung renormiert, also ein Bogolonzustand.

Um diese Korrelationsfunktionen zu bestimmen, müssen nun Bewegungsgleichungen für die verschiedenen Greenfunktionen abgeleitet werden. Dies wird im folgenden am Beispiel von G^{11}_{aa} skizziert.

Die freien Greenfunktionen genügen offensichtlich den Gleichungen

$$\left(\mathrm{i}\hbar\frac{\partial}{\partial t_1} - \hbar\omega_q\right) G^{(0)}_{aa}(\mathbf{q},\mathbf{q}';t_1,t_2) = \delta_{\mathbf{q}\mathbf{q}'}\delta(t_1-t_2)\,, \tag{1.141}$$

$$\left(\mathrm{i}\hbar\frac{\partial}{\partial t_1} - E_q\right) G^{(0)}_{bb}(\mathbf{q},\mathbf{q}';t_1,t_2) = \delta_{\mathbf{q}\mathbf{q}'}\delta(t_1-t_2)\,. \tag{1.142}$$

Für G^{11}_{aa} erhält man unter Nutzung der Bewegungsgleichung (1.138) (in Integralform, Integration über quergestrichene Variablen wird implizit vorausgesetzt)

$$\begin{aligned} G^{11}_{aa}(\mathbf{q},\mathbf{q}';t_1,t_2) &= G^{(0)}_{aa}(\mathbf{q},\mathbf{q}';t_1,t_2) \\ &\quad +\mathrm{i}G^{(0)}_{aa}(\mathbf{q},\bar{\mathbf{q}};t_1,\bar{t})C_{\bar{q}}\left[G^{11}_{ba}(\bar{\mathbf{q}},\mathbf{q}';\bar{t},t_2) - G^{21}_{ba}(-\bar{\mathbf{q}},\mathbf{q}';\bar{t},t_2)\right] \\ &\quad +2G^{(0)}_{aa}(\mathbf{q},\bar{\mathbf{q}};t_1,\bar{t})D_{\bar{q}}\left[G^{21}_{aa}(-\bar{\mathbf{q}},\mathbf{q}';\bar{t},t_2) + G^{11}_{aa}(\bar{\mathbf{q}},\mathbf{q}';\bar{t},t_2)\right]\,. \end{aligned} \tag{1.143}$$

Entsprechend erhält man für G^{11}_{ba} und G^{21}_{ba}

$$G^{11}_{ba}(\mathbf{q},\mathbf{q}';t_1,t_2) = -\mathrm{i}G^{(0)}_{bb}(\mathbf{q},\bar{\mathbf{q}};t_1,\bar{t})C_{\bar{q}}\left[G^{11}_{aa}(\bar{\mathbf{q}},\mathbf{q}';\bar{t},t_2) + G^{21}_{aa}(-\bar{\mathbf{q}},\mathbf{q}';\bar{t},t_2)\right], \tag{1.144}$$

$$G^{21}_{ba}(\mathbf{q},\mathbf{q}';t_1,t_2) = \mathrm{i}G^{(0)}_{bb}(\mathbf{q},\bar{\mathbf{q}};-t_1,-\bar{t})C_{\bar{q}}\left[G^{21}_{aa}(\bar{\mathbf{q}},\mathbf{q}';\bar{t},t_2) + G^{11}_{aa}(-\bar{\mathbf{q}},\mathbf{q}';\bar{t},t_2)\right]. \tag{1.145}$$

Wir setzen letztere beiden Größen in Gl. (1.143) ein und nutzen aus, daß die freien Greenfunktionen diagonal in der Wellenzahl sind, $G^{(0)}_{aa(bb)}(\mathbf{q},\mathbf{q}';t_1,t_2) \propto \delta_{\mathbf{q}\mathbf{q}'}$. Dann folgt für G^{11}_{aa} insgesamt

$$\begin{aligned} &G^{11}_{aa}(\mathbf{q},\mathbf{q}';t_1,t_2) = G^{(0)}_{aa}(\mathbf{q};t_1,t_2)\delta_{\mathbf{q}\mathbf{q}'} \\ &+C_q^2 G^{(0)}_{aa}(\mathbf{q};t_1,\bar{t})G^{(0)}_{bb}(\mathbf{q};\bar{t},\bar{\bar{t}})\left[G^{11}_{aa}(\mathbf{q},\mathbf{q}';\bar{\bar{t}},t_2) + G^{21}_{aa}(-\mathbf{q},\mathbf{q}';\bar{\bar{t}},t_2)\right] \\ &+C_q^2 G^{(0)}_{aa}(\mathbf{q};t_1,\bar{t})G^{(0)}_{bb}(-\mathbf{q};-\bar{t},-\bar{\bar{t}})\left[G^{21}_{aa}(-\mathbf{q},\mathbf{q}';\bar{\bar{t}},t_2) + G^{11}_{aa}(\mathbf{q},\mathbf{q}';\bar{\bar{t}},t_2)\right] \\ &+2D_q G^{(0)}_{aa}(\mathbf{q};t_1,\bar{t})\left[G^{21}_{aa}(-\mathbf{q},\mathbf{q}';\bar{t},t_2) + G^{11}_{aa}(\mathbf{q},\mathbf{q}';\bar{t},t_2)\right]\,. \end{aligned} \tag{1.146}$$

In die Gleichung für G^{11}_{aa} geht G^{21}_{aa} ein. Für letztere Größe findet man zunächst

$$\begin{aligned} &G^{21}_{aa}(\mathbf{q},\mathbf{q}';t_1,t_2) = -\mathrm{i}G^{(0)}_{aa}(\mathbf{q},\bar{\mathbf{q}};-t_1,-\bar{t})C_{\bar{q}}\left[G^{21}_{ba}(\bar{\mathbf{q}},\mathbf{q}';\bar{t},t_2) - G^{11}_{ba}(-\bar{\mathbf{q}},\mathbf{q}';\bar{t},t_2)\right] \\ &+2G^{(0)}_{aa}(\mathbf{q},\bar{\mathbf{q}};-t_1,-\bar{t})D_{\bar{q}}\left[G^{21}_{aa}(\bar{\mathbf{q}},\mathbf{q}';\bar{t},t_2) + G^{11}_{aa}(-\bar{\mathbf{q}},\mathbf{q}';\bar{t},t_2)\right] \end{aligned} \tag{1.147}$$

bzw. nach Einsetzen von G^{21}_{ba} und G^{11}_{ba}

$$\begin{aligned}
& G^{21}_{aa}(\mathbf{q},\mathbf{q}';t_1,t_2) = \\
= \; & C_q^2 G^{(0)}_{aa}(\mathbf{q};-t_1,-\bar{t}) G^{(0)}_{bb}(\mathbf{q};-\bar{t},-\bar{\bar{t}}) \left[G^{21}_{aa}(\mathbf{q},\mathbf{q}';\bar{\bar{t}},t_2) + G^{11}_{aa}(-\mathbf{q},\mathbf{q}';\bar{\bar{t}},t_2) \right] \\
& + C_q^2 G^{(0)}_{aa}(\mathbf{q};-t_1,-\bar{t}) G^{(0)}_{bb}(-\mathbf{q};\bar{t},\bar{\bar{t}}) \left[G^{11}_{aa}(-\mathbf{q},\mathbf{q}';\bar{\bar{t}},t_2) + G^{21}_{aa}(\mathbf{q},\mathbf{q}';\bar{\bar{t}},t_2) \right] \\
& + 2D_q G^{(0)}_{aa}(\mathbf{q};-t_1,-\bar{t}) \left[G^{21}_{aa}(\mathbf{q},\mathbf{q}';\bar{t},t_2) + G^{11}_{aa}(-\mathbf{q},\mathbf{q}';\bar{t},t_2) \right] . \qquad (1.148)
\end{aligned}$$

Analog entstehen die Gleichungen für die restlichen zwölf Greenfunktionen.

1.5.2 Anregungsspektrum der Bogolaritonen

Wir betrachten nun die Lösungsstrategie der bisher abgeleiteten vier Gleichungen (1.146), (1.148), (1.144) und (1.145). Offensichtlich sind zunächst Gln. (1.146) und (1.148) gekoppelt zu lösen. Hierzu gehen wir in beiden Gleichungen von der Kontur zur physikalischen Zeitachse über und bilden jeweils $g^<$ und $g^{\mathrm{r/a}}$. Nach Fouriertransformation bzgl. $t_1 - t_2$ (im stationären Fall) erhält man zunächst für die retardierten bzw. avancierten Funktionen

$$\begin{aligned}
& g^{11\mathrm{r/a}}_{aa}(\mathbf{q},\mathbf{q}';\omega) = g^{(0)\mathrm{r/a}}_{aa}(\mathbf{q};\omega)\delta_{\mathbf{q}\mathbf{q}'} \\
& + C_q^2 g^{(0)\mathrm{r/a}}_{aa}(\mathbf{q};\omega) g^{(0)\mathrm{r/a}}_{bb}(\mathbf{q};\omega) \left[g^{11\mathrm{r/a}}_{aa}(\mathbf{q},\mathbf{q}';\omega) + g^{21\mathrm{r/a}}_{aa}(-\mathbf{q},\mathbf{q}';\omega) \right] \\
& + C_q^2 g^{(0)\mathrm{r/a}}_{aa}(\mathbf{q};\omega) g^{(0)\mathrm{a/r}}_{bb}(-\mathbf{q};-\omega) \left[g^{21\mathrm{r/a}}_{aa}(-\mathbf{q},\mathbf{q}';\omega) + g^{11\mathrm{r/a}}_{aa}(\mathbf{q},\mathbf{q}';\omega) \right] \\
& + 2D_q g^{(0)\mathrm{r/a}}_{aa}(\mathbf{q};\omega) \left[g^{21\mathrm{r/a}}_{aa}(-\mathbf{q},\mathbf{q}';\omega) + g^{11\mathrm{r/a}}_{aa}(\mathbf{q},\mathbf{q}';\omega) \right] , \qquad (1.149)
\end{aligned}$$

$$\begin{aligned}
& g^{21\mathrm{r/a}}_{aa}(\mathbf{q},\mathbf{q}';\omega) = \\
= \; & C_q^2 g^{(0)\mathrm{a/r}}_{aa}(\mathbf{q};-\omega) g^{(0)\mathrm{a/r}}_{bb}(\mathbf{q};-\omega) \left[g^{21\mathrm{r/a}}_{aa}(\mathbf{q},\mathbf{q}';\omega) + g^{11\mathrm{r/a}}_{aa}(-\mathbf{q},\mathbf{q}';\omega) \right] \\
& + C_q^2 g^{(0)\mathrm{a/r}}_{aa}(\mathbf{q};-\omega) g^{(0)\mathrm{r/a}}_{bb}(-\mathbf{q};\omega) \left[g^{11\mathrm{r/a}}_{aa}(-\mathbf{q},\mathbf{q}';\omega) + g^{21\mathrm{r/a}}_{aa}(\mathbf{q},\mathbf{q}';\omega) \right] \\
& + 2D_q g^{(0)\mathrm{a/r}}_{aa}(\mathbf{q};-\omega) \left[g^{21\mathrm{r/a}}_{aa}(\mathbf{q},\mathbf{q}';\omega) + g^{11\mathrm{r/a}}_{aa}(-\mathbf{q},\mathbf{q}';\omega) \right] . \qquad (1.150)
\end{aligned}$$

Die Lösung dieser beiden Gleichungen ist gegeben durch

$$\begin{aligned}
& g^{11\mathrm{r/a}}_{aa}(\mathbf{q},\mathbf{q}';\omega) \qquad (1.151) \\
& = \frac{g^{(0)\mathrm{r/a}}_{aa,+} \left(1 - 2D_q g^{(0)\mathrm{a/r}}_{aa,-} - C_q^2 g^{(0)\mathrm{a/r}}_{aa,-} \left(g^{(0)\mathrm{r/a}}_{bb,+} + g^{(0)\mathrm{a/r}}_{bb,-} \right) \right)}{1 - 2D_q \left(g^{(0)\mathrm{r/a}}_{aa,+} + g^{(0)\mathrm{a/r}}_{aa,-} \right) - C_q^2 \left(g^{(0)\mathrm{r/a}}_{aa,+} + g^{(0)\mathrm{a/r}}_{aa,-} \right) \left(g^{(0)\mathrm{r/a}}_{bb,+} + g^{(0)\mathrm{a/r}}_{bb,-} \right)} \delta_{\mathbf{q},\mathbf{q}'}
\end{aligned}$$

sowie

$$g_{aa}^{21\mathrm{r/a}}(\mathbf{q},\mathbf{q}';\omega) \tag{1.152}$$
$$= \frac{g_{aa,+}^{(0)\mathrm{r/a}} g_{aa,-}^{(0)\mathrm{a/r}} \left(2D_q + C_q^2 \left(g_{bb,+}^{(0)\mathrm{r/a}} + g_{bb,-}^{(0)\mathrm{a/r}}\right)\right)}{1 - 2D_q \left(g_{aa,+}^{(0)\mathrm{r/a}} + g_{aa,-}^{(0)\mathrm{a/r}}\right) - C_q^2 \left(g_{aa,+}^{(0)\mathrm{r/a}} + g_{aa,-}^{(0)\mathrm{a/r}}\right)\left(g_{bb,+}^{(0)\mathrm{r/a}} + g_{bb,-}^{(0)\mathrm{a/r}}\right)} \delta_{\mathbf{q},\mathbf{q}'} ,$$

wobei $g_{xx}^{(0)\mathrm{r/a}}(\mathbf{q},\mathbf{q}';\omega) = g_{xx}^{(0)\mathrm{r/a}}(q;\omega)\delta_{\mathbf{q},\mathbf{q}'}$ mit $q = |\mathbf{q}|$ ausgenutzt und zur Abkürzung $g_{xx,\pm}^{(0)\mathrm{r/a}} = g_{xx}^{(0)\mathrm{r/a}}(q;\pm\omega)$ $(x = a, b)$ eingeführt wurde.

Die freien retardierten bzw. avancierten Funktionen folgen aus den Gln. (1.141) und (1.142), $g_{aa}^{(0)\mathrm{r/a}^{-1}}(\mathbf{q};\omega) = \hbar\omega - \hbar\omega_{\mathbf{q}} \pm \mathrm{i}\epsilon$ und $g_{bb}^{(0)\mathrm{r/a}^{-1}}(\mathbf{q};\omega) = \hbar\omega - E_{\mathbf{q}} \pm \mathrm{i}\epsilon$. Damit folgt für $g_{aa}^{11\mathrm{r/a}}$

$$g_{aa}^{11\mathrm{r/a}}(\mathbf{q},\mathbf{q}',\omega) = \frac{1}{\hbar} \frac{((\omega \pm \mathrm{i}\epsilon) + \omega_{\mathbf{q}} + 2d_{\mathbf{q}})((\omega \pm \mathrm{i}\epsilon)^2 - e_{\mathbf{q}}^2) + 2c_{\mathbf{q}}^2 e_{\mathbf{q}}}{((\omega \pm \mathrm{i}\epsilon)^2 - \omega_{\mathbf{q}}^2 - 4d_{\mathbf{q}}\omega_{\mathbf{q}})((\omega \pm \mathrm{i}\epsilon)^2 - e_{\mathbf{q}}^2) - 4c_{\mathbf{q}}^2 e_{\mathbf{q}}\omega_{\mathbf{q}}} \delta_{\mathbf{q},\mathbf{q}'} \tag{1.153}$$

mit $E_{\mathbf{q}} = \hbar e_{\mathbf{q}}$, $C_{\mathbf{q}} = \hbar c_{\mathbf{q}}$ und $D_{\mathbf{q}} = \hbar d_{\mathbf{q}}$. Die Pole dieser Funktionen bestimmen das Anregungsspektrum der neuen Quasiteilchen. Man findet vier Lösungen $(\omega \pm \mathrm{i}\epsilon) = \pm\Omega_{\mathbf{q}}^{\pm}$ mit

$$\Omega_{\mathbf{q}}^{\pm 2} = \frac{1}{2}(e_{\mathbf{q}}^2 + \omega_{\mathbf{q}}^2 + 4d_{\mathbf{q}}\omega_{\mathbf{q}}) \pm \frac{1}{2}\sqrt{(e_{\mathbf{q}}^2 - \omega_{\mathbf{q}}^2 - 4d_{\mathbf{q}}\omega_{\mathbf{q}})^2 + 16c_{\mathbf{q}}^2 e_{\mathbf{q}}\omega_{\mathbf{q}}}\,. \tag{1.154}$$

Die beiden positiven Zweige entsprechen gerade dem Polaritonspektrum, siehe Abb. 1.12. Am Schnittpunkt der „freien“ Bogolonendispersion und der der freien Photonen erkennt man das bekannte Verhalten des vermiedenen Überschneidens (*avoided crossing*) der beiden Polaritonzweige. Die beiden zusätzlichen Zweige liegen bei negativen Frequenzen. Die neuen Quasiteilchen, die im Unterschied zum Polariton aus wechselwirkenden Exzitonen (Bogolonen) und Photonen entstehen, sollen im folgenden als „Bogolaritonen“ bezeichnet werden.

Aus den retardierten bzw. avancierten Greenfunktionen (1.153) folgt die photonische Spektralfunktion $A_{aa}(\omega)$,

$$\begin{aligned} A_{aa}(\mathbf{q},\mathbf{q}',\omega) &= \mathrm{i}\hbar\left[g_{aa}^{11\mathrm{r}}(\mathbf{q},\mathbf{q}',\omega) - g_{aa}^{11\mathrm{a}}(\mathbf{q},\mathbf{q}',\omega)\right] \\ &= 2\pi\delta(\mathbf{q}-\mathbf{q}') \\ &\times \left[U_{\mathbf{q}}^{+2}\delta(\omega-\Omega_{\mathbf{q}}^{+}) + V_{\mathbf{q}}^{+2}\delta(\omega+\Omega_{\mathbf{q}}^{+}) + U_{\mathbf{q}}^{-2}\delta(\omega-\Omega_{\mathbf{q}}^{-}) + V_{\mathbf{q}}^{-2}\delta(\omega+\Omega_{\mathbf{q}}^{-})\right]. \end{aligned} \tag{1.155}$$

Die Gewichte der positiven und negativen oberen bzw. unteren Bogolaritonzweige

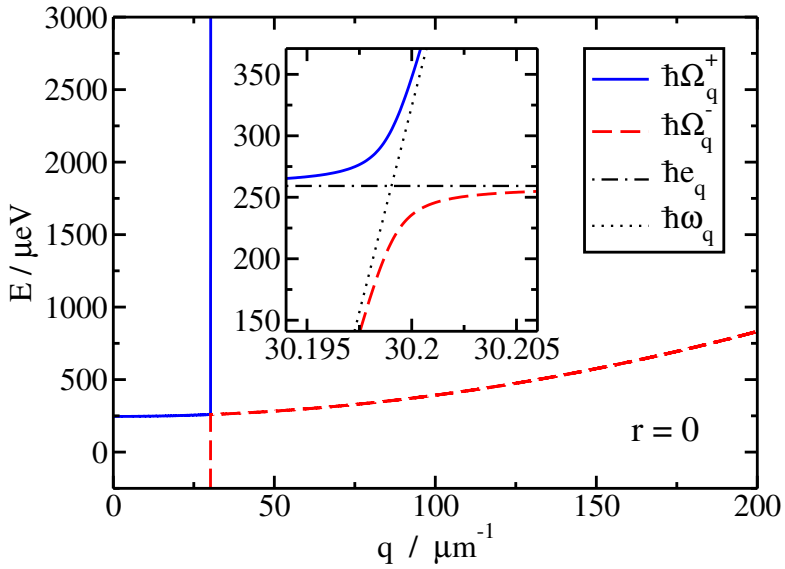

Abbildung 1.12: Bogolaritonspektrum $E = \hbar\Omega_q^{\pm} - E_g - V_0 + \mu$ als Funktion der Wellenzahl q für $r = 0$ und $T = 2$ K. Der vergrößerte Ausschnitt zeigt das Verhalten am Kreuzungspunkt der freien Photon- und Bogolondispersionen. Abbildung entnommen aus A.12.

folgen durch Partialbruchzerlegung. Man erhält

$$U_{\mathbf{q}}^{+2} = \frac{(\Omega_{\mathbf{q}}^{+} + \omega_{\mathbf{q}} + 2d_{\mathbf{q}})(\Omega_{\mathbf{q}}^{+2} - e_{\mathbf{q}}^2) + 2c_{\mathbf{q}}^2 e_{\mathbf{q}}}{2\Omega_{\mathbf{q}}^{+}(\Omega_{\mathbf{q}}^{+2} - \Omega_{\mathbf{q}}^{-2})}, \tag{1.156}$$

$$V_{\mathbf{q}}^{+2} = \frac{(\Omega_{\mathbf{q}}^{+} - \omega_{\mathbf{q}} - 2d_{\mathbf{q}})(\Omega_{\mathbf{q}}^{+2} - e_{\mathbf{q}}^2) - 2c_{\mathbf{q}}^2 e_{\mathbf{q}}}{2\Omega_{\mathbf{q}}^{+}(\Omega_{\mathbf{q}}^{+2} - \Omega_{\mathbf{q}}^{-2})}, \tag{1.157}$$

$$U_{\mathbf{q}}^{-2} = \frac{(\Omega_{\mathbf{q}}^{-} + \omega_{\mathbf{q}} + 2d_{\mathbf{q}})(\Omega_{\mathbf{q}}^{-2} - e_{\mathbf{q}}^2) + 2c_{\mathbf{q}}^2 e_{\mathbf{q}}}{2\Omega_{\mathbf{q}}^{-}(\Omega_{\mathbf{q}}^{-2} - \Omega_{\mathbf{q}}^{+2})}, \tag{1.158}$$

$$V_{\mathbf{q}}^{-2} = \frac{(\Omega_{\mathbf{q}}^{-} - \omega_{\mathbf{q}} - 2d_{\mathbf{q}})(\Omega_{\mathbf{q}}^{-2} - e_{\mathbf{q}}^2) - 2c_{\mathbf{q}}^2 e_{\mathbf{q}}}{2\Omega_{\mathbf{q}}^{-}(\Omega_{\mathbf{q}}^{-2} - \Omega_{\mathbf{q}}^{+2})}. \tag{1.159}$$

Offensichtlich zerfällt die Bogolaritondispersion für verschwindende Exziton–Photon–Kopplung $c_{\mathbf{q}} = d_{\mathbf{q}} = 0$ in die beiden freien Dispersionen, d.h. $\Omega_{\mathbf{q}}^{+} = \max\{e_{\mathbf{q}}, \omega_{\mathbf{q}}\}$ und $\Omega_{\mathbf{q}}^{-} = \min\{e_{\mathbf{q}}, \omega_{\mathbf{q}}\}$. Entsprechend findet man $U_{\mathbf{q}}^{\pm 2} = 1$ für $e_{\mathbf{q}} \lessgtr \omega_{\mathbf{q}}$ und $U_{\mathbf{q}}^{\pm 2} = 0$ für $e_{\mathbf{q}} \gtrless \omega_{\mathbf{q}}$, so daß die Spektralfunktion in Gl. (1.155) in dem Fall in die Spektralfunktion freier Photonen übergeht: $A_{aa}(\mathbf{q}, \mathbf{q}', \omega) = 2\pi\delta(\mathbf{q} - \mathbf{q}')\delta(\omega - \omega_{\mathbf{q}})$.

Die Gewichte der einzelnen Zweige sind in der Abb. 1.13 dargestellt. Das spektrale Gewicht in den negativen Zweigen ist im betrachteten – unkondensierten – Fall offensichtlich vernachlässigbar klein.

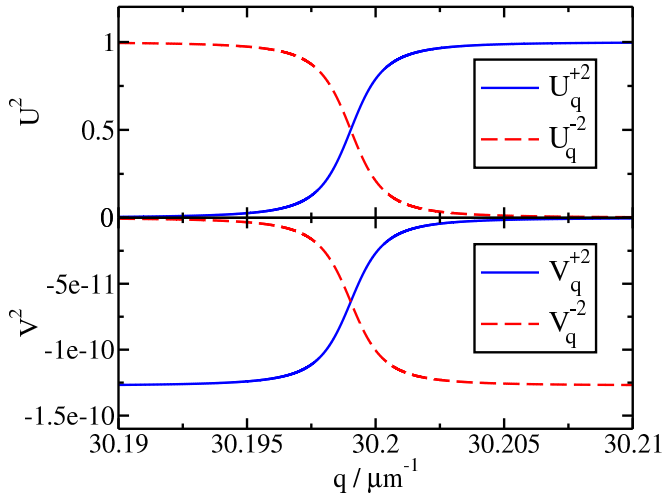

Abbildung 1.13: Spektrale Gewichte der vier Bogolaritonzweige als Funktion der Wellenzahl q für $r = 0$ und $T = 2$ K. Abbildung entnommen aus A.12.

Mit Hilfe der spektralen Gewichte kann nun die photonische Spektralfunktion als Funktion der Wellenzahl q und der Energie $\hbar\omega$ dargestellt werden, siehe Abb. 1.14 (zur besseren Darstellbarkeit leicht numerisch verbreitert). Gezeigt ist die Umgebung des Kreuzungspunktes der freien Photon- und Bogolondispersionen, so daß die Renormierung der photonischen Dispersion deutlich wird.

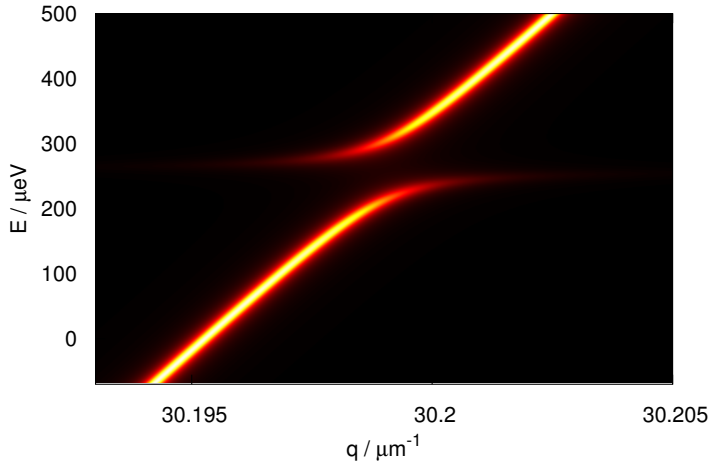

Abbildung 1.14: Photonische Spektralfunktion in Abhängigkeit von q und $E = \hbar\omega - E_g - V_0 + \mu$ in der Umgebung der Kreuzung der freien Photon- und Bogolondispersionen für $r = 0$ und $T = 2$ K. Abbildung entnommen aus A.12.

Die Argumente der Deltafunktionen in Gl. (1.155) bestimmen die kritischen Wellenzahlen $q_0^{\pm}$, d.h. $E = \hbar\omega = \hbar\Omega_q^{\pm}(q_0^{\pm})$ (für festes r), dargestellt in Abb. 1.15. Die Lumineszenz an der gegebenen Energie E hängt also von der Zustandsdichte der Bogolaritonen an diesen zwei kritischen Wellenzahlen ab. Frühere Arbeiten hierzu [HK83, SVG94] nahmen dagegen den (intuitiven) festen Wert $q_0 \approx 30.2\ \mu\mathrm{m}^{-1}$ am Kreuzungspunkt der freien Photon- und Bogolondispersionen an. Dieser Wert wird in der Tat für (fast) alle Energien (mit Ausnahme der Umgebung des Kreuzungspunktes) angenommen, wobei es nun für $E \geq \hbar\Omega_q^{+}$ eine zweite Lösung gibt.

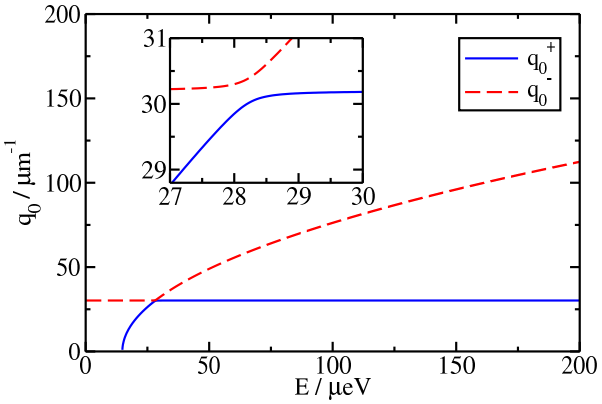

Abbildung 1.15: Kritische Wellenzahlen $q_0^{\pm}$ in Abhängigkeit von $E = \hbar\omega - E_g - V_0 + \mu$ für $r = 0$ und $T = 2$ K. Abbildung entnommen aus A.12.

Der nächste Schritt wäre nun die Berechnung der photonischen Korrelationsfunktion aus den Gln. (1.146) und (1.148). Formal geht man genauso vor wie oben im Fall der retardierten Funktion. Der fundamentale Unterschied besteht darin, daß in die Lösungen der erhaltenen Gleichungen die Korrelationsfunktionen der „freien“ (also nicht mit dem jeweils anderen Subsystem wechselwirkenden) Bogolonen und Photonen eingehen. Die in diesen enthaltenen Verteilungsfunktionen entsprechen dem jeweiligen Gleichgewicht der Untersysteme. Das chemische Potential der „freien“ Bogolonen aber, das z.B. im unkondensierten Fall unterhalb des niedrigsten (renormierten) bogolonischen Energiewertes liegt, schneidet nun das neue Quasiteilchenspektrum. Die Bogolaritonen können nur im stationären Zustand („Nachfüttern“ von Exzitonen durch Dauerstrichanregung) existieren, der Gleichgewichtszustand des gekoppelten Systems ist offenbar nur durch das chemische Potential der „freien“ Photonen bestimmt. Eine (Quasi-)Gleichgewichtstheorie der bogolaritonischen Besetzung ist also nicht sinnvoll.

Ähnliche Situationen findet man in der Literatur meist in Arbeiten, in denen Exziton–Polaritonen betrachtet werden. Als Beispiel herausgegriffen sei die Arbeit [YNK+15],

die den Anspruch stellt, Kohärenzphänomene im Gleichgewicht und Nichtgleichgewicht, wie BEK, BCS–Phase, Laser, Superfluoreszenz und Superradianz, in einer einheitlichen Theorie darzustellen. Hier wird im allgemeinen Fall des Nichtgleichgewichts μ als Parameter (Frequenz des rotierenden Bezugssystems) eingeführt, der beim Übergang zum Gleichgewicht Bedingungen zu erfüllen hat, um als chemisches Potential des Elektron–Loch–Systems im Quasigleichgewicht interpretierbar zu sein.

1.6 Zusammenfassung und Ausblick

Um die in den vorgestellten Arbeiten erzielten Resultate zusammenfassend werten zu können, sollte man sie in Hinblick auf zwei Fragestellungen betrachten: (i) Haben die theoretischen Untersuchungen unsere Kenntnisse über die Physik des Elektron–Loch–Plasmas (ELP) bzw. des Exzitonengases auf der einen Seite und der Quantenkondensation in diesen Systemen auf der anderen Seite vertieft? (ii) Konnten in der theoretischen Analyse der experimentellen Befunde eindeutige Signaturen eines Bose–Einstein–Kondensats (BEK) von Exzitonen nachgewiesen werden?

Die erste Frage kann ohne weiteres positiv beantwortet werden. Hervorzuheben sind hier auf dem Gebiet der Thermodynamik des ELP insbesondere zum einen die Ableitung des implizit formulierten Massenwirkungsgesetzes unter Berücksichtigung der Vielteilcheneffekte auf hohem theoretischen Niveau und zum anderen die spektrale Fundierung des Mott–Effektes. Während ersteres unter anderem die Grenzen des Existenzbereichs der Exzitonen zu ermitteln erlaubt, werfen die Untersuchungen optischer Eigenschaften in Form der Suszeptibilität ein neues Licht auf die Interpretation des Mott–Effektes. Desweiteren konnte das Konzept der zeitlich langreichweitigen Ordnung (*time long-range order*) in den Zweiteilchenkorrelationen als grundlegendes Prinzip der Quantenkondensation in Elektron–Loch–Systemen herausgearbeitet und auf dieser Grundlage die gemeinsame Phasengrenze von BEK und BCS–Kondensat untersucht werden. Zum anderen konnten wir auf dem Gebiet ultrakalter atomarer Gase wohletablierte theoretische Zugänge zur Beschreibung sowohl der Thermodynamik als auch der Kinetik von Bosegasen auf das Exzitonensystem übertragen. Das entwickelte Modell mit seinen notwendigen Ergänzungen und Erweiterungen, die den halbleiterspezifischen Aspekten Rechnung tragen, geht über bisherige Arbeiten auf dem Gebiet hinaus. Von den Resultaten der Modellierung des Experiments soll die Untersuchung der Evolution der Exzitonentemperatur hervorgehoben werden, insbesondere der (für

das Erreichen der Kondensationsbedingungen negative) Nachweis der Unmöglichkeit des Erreichens der Badtemperatur bei sehr tiefen Temperaturen.

Die Beurteilung der zweiten Frage fällt dagegen eher zwiespältig aus. Zum einen konnten in der theoretischen Analyse der experimentellen Resultate *deutliche Indizien* gefunden werden, die für den Nachweis eines exzitonischen Kondensats sprechen – der „Knick“ im Verlauf der integrierten Intensität über der Anregungsleistung, der für den Übergang von Exzitonen ins (nicht oder nur schwach) leuchtende Kondensat spricht, sowie die bimodale räumliche Exzitonenverteilung in der Falle mit einem zentralen nichtgaußartigen Anteil, der vom Kondensat herrühren kann. Zum anderen fehlt für einen eindeutigen Nachweis (vgl. die Snokeschen Kriterien [Sno03]) insbesondere die Untersuchung der Kohärenzeigenschaften der Lumineszenz. Der überzeugende Beweis, die vielzitierte „*smoking gun*“ steht also noch aus.

Was bleibt also für die Theorie zu tun? Beginnen wir zunächst mit der Thermodynamik des ELP. Hier wäre es für die genauere Analyse des Mott–Übergangs wichtig, die Wechselwirkung zwischen den Exzitonen bzw. Ladungsträgern und Exzitonen zu berücksichtigen und damit zum einen eine geschlossene Behandlung von Ein- und Zweiteilchenebene zu erhalten, zum anderen aber insbesondere die Beschreibung des Systems kurz unterhalb der Mott–Dichte, wo es praktisch als reines Exzitonengas vorliegt, realistischer zu gestalten. Hier sollte auch der Einfluß der Exzitonen auf die Abschirmung der Coulomb–Wechselwirkung zwischen den Ladungsträgern einbezogen werden. Im Elektron–Loch–Bild erforderte die Beschreibung dieser Wechselwirkungen allerdings die Einbeziehung von Drei- und Vierteilchen–Selbstenergien, was eher unrealistisch erscheint. Im chemischen Bild (Elektronen, Löcher, Exzitonen) dagegen ist es hinreichend, eine Zweiteilchen–(Zwei–Exzitonen–)Selbstenergie zu betrachten. Zu beachten ist hier aber zum einen, daß es sich dabei um eine bosonische Selbstenergie handelt. Zudem ist hierfür die Beschreibung der Wechselwirkung zweier Exzitonen nötig. Diese Wechselwirkung, die sich nicht als (lokales) Wechselwirkungspotential schreiben läßt und dessen Bestimmung die (approximative) Lösung eines Vierteilchenproblems erfordert, stände im Interesse einer Weiterentwicklung der Thermodynamik des ELP weit oben auf der Prioritätenliste.

Eine hochinteressante aktuelle Entwicklungsrichtung ist die Untersuchung sogenannter Rydberg–Exzitonen in Kupferoxydul [KFS$^+$14] (also Exzitonen hoher Hauptquantenzahl in Analogie zu den Rydberg–Atomen). Mit Blick auf die bei gegebener Temperatur und Dichte maximal erreichbare Hauptquantenzahl wäre eine Analyse des Mott–Übergangs von Exzitonen in (hoch)angeregten Zuständen von großem Interesse.

Hinsichtlich der Thermodynamik des Exzitonengases erscheint eine Verbesserung der Theorie im homogenen Fall kaum realistisch, da dies bedeutete, über die Hartree–Fock–Bogoljubow–Popow–Theorie hinauszugehen und Dämpfungseffekte zu berücksichtigen. Das ist im Prinzip im Rahmen der Beljajew–Approximation möglich [SG98, GNZ09], aber extrem aufwendig und insbesondere im Mehrkomponentenfall kaum praktikabel [Koc11]. Dagegen sollte eine Berücksichtigung der Ortsabhängigkeit über die Lokaldichtenäherung hinaus im Prinzip möglich sein. Hierzu wären zumindest die tiefliegenden Energiezustände der Exzitonen in der Falle numerisch zu berechnen [BFBS00]. Eine Weiterentwicklung der Thermodynamik wäre zum einen sicher von theoretischem Interesse, trüge aber andererseits sehr wahrscheinlich kaum zum besseren Verständnis der experimentellen Resultate bei, da sich hier die Nichtgleichgewichtsbeschreibung als unverzichtbar herausgestellt hat.

Ungeachtet der Erfolge letzteren Zuganges bei der Beschreibung der experimentellen Befunde sind noch eine Reihe von Problemen offen geblieben. Hier wäre zunächst ein tieferes Verständnis des augerartigen Zweikörperzerfalls zu nennen, das zur Aufhebung der Diskrepanz zwischen den theoretischen und den experimentell ermittelten Raten beitragen sollte. Zu diesem Punkt laufen derzeit Untersuchungen [SS17]. Eine weitere Aufgabe wäre die Berücksichtigung der Wellenzahlabhängigkeit der strahlenden Zerfallsrate in der exzitonischen Lebensdauer.

Auf dem Weg zum Verständnis der Lumineszenz der Exzitonen konnten Fortschritte erzielt werden; so ist der vorgestellte Zugang vielversprechend (Bogolaritonenspektrum). Zu klären ist das Problem der Besetzung der neuen Quasiteilchen. Da das Lichtfeld primär an die Ladungsträger (Elektronen und Löcher) koppelt, stellt sich die Frage, ob eine Theorie der Lumineszenz bereits vom Niveau der Ladungsträger ausgehen sollte. Diese Frage muß eingehend geprüft werden.

Literaturverzeichnis

[AEM+95] ANDERSON, M. H. ; ENSHER, J. R. ; MATTHEWS, M. R. ; WIEMAN, C. E. ; CORNELL, E. A.: Observation of Bose–Einstein Condensation in a Dilute Atomic Vapor. In: *Science* 269 (1995), S. 198

[AGD65] ABRIKOSOV, A. A. ; GORKOV, L. P. ; DZYALOZHINSKI, N. N.: *Quantum Field Theoretical Methods in Statistical Physics*. 2. Aufl. Oxford : Pergamon Press, 1965

[And14] ANDREANI, L. C.: Exciton Polaritons in Bulk Semiconductors and in Confined Electron and Photon Systems. In: AUFFÈVES, A. *et al.* (Hrsg.): *Strong Light–Matter Coupling. From Atoms to Solid-State Systems*. Singapore : World Scientific, 2014, S. 37

[BBB62] BLATT, J. M. ; BÖER, K. W. ; BRANDT, W.: Bose–Einstein Condensation of Excitons. In: *Phys. Rev.* 126 (1962), S. 1691

[BBH04] BÁNYAI, L. A. ; BUNDARU, A. M. ; HAUG, H.: Quasiclassical approach to Bose condensation in a finite potential well. In: *Phys. Rev. B* 70 (2004), S. 045201

[BF06] BRONOLD, F. X. ; FEHSKE, H.: Possibility of an excitonic insulator at the semiconductor-semimetal transition. In: *Phys. Rev. B* 74 (2006), S. 165107

[BFBS00] BERGEMAN, T. ; FEDER, D. L. ; BALAZS, N. L. ; SCHNEIDER, B. I.: Bose condensates in a harmonic trap near the critical temperature. In: *Phys. Rev. A* 61 (2000), S. 063605

[BGC02] BUTOV, L. V. ; GOSSARD, A. C. ; CHEMLA, D. S.: Macroscopically ordered state in an exciton system. In: *Nature* 418 (2002), S. 751

[BKS99] BORNATH, Th. ; KREMP, D. ; SCHLANGES, M.: Two-particle problem in a nonequilibrium many-particle system. In: *Phys. Rev. E* 60 (1999), S. 6382

[Bog46] BOGOLJUBOW, N. N.: *Probleme der dynamischen Theorie in der statistischen Physik (in russ.)*. Moskau : Gostechisdat, 1946

[Bon98] BONITZ, M.: *Quantum Kinetic Theory*. Stuttgart. Leipzig : B. G. Teubner, 1998 (Teubner–Texte zur Physik Bd. 33)

[Bra10] BRANDT, J. C.: *Interactions of $1S$ excitons in Cu_2O: A high resolution spectroscopy study*, Technische Universität Dortmund, Diss., 2010

[CBMD08] COMBESCOT, M. ; BETBEDER-MATIBET, O. ; DUBIN, F.: The many-body physics of composite bosons. In: *Phys. Rep.* 463 (2008), S. 215

[Clo65] CLOIZEAUX, J. des: Exciton instability and crystallographic anomalies in semiconductors. In: *J. Phys. Chem. Solids* 26 (1965), S. 259

[DDM66] DAUNOIS, A. ; DEISS, J. L. ; MEYER, B.: Étude spectrophotométrique de l'absorption bleue et violette de Cu_2O. In: *J. Phys. France* 27 (1966), S. 142

[DGPS99] DALFOVO, F. ; GIORGINI, S. ; PITAEVSKII, L. P. ; STRINGARI, S.: Theory of Bose–Einstein condensation in trapped gases. In: *Rev. Mod. Phys.* 71 (1999), S. 463

[DMA+95] DAVIS, K. B. ; MEWES, M.-O. ; ANDREWS, M. R. ; DRUTEN, N. J. ; DURFEE, D. S. ; KURN, D. M. ; KETTERLE, W.: Bose–Einstein Condensation in a Gas of Sodium Atoms. In: *Phys. Rev. Lett.* 75 (1995), S. 3969

[Eag69] EAGLES, D. M.: Possible Pairing without Superconductivity at Low Carrier Concentrations in Bulk and Thin-Film Superconducting Semiconductors. In: *Phys. Rev.* 186 (1969), S. 456

[Ein25] EINSTEIN, A.: Quantentheorie des einatomigen idealen Gases, 2. Abhandlung. In: *Sitzungsberichte Preuß. Akademie, Phys.-math.* (1925), S. 3

[EKK76] EBELING, W. ; KRAEFT, W. D. ; KREMP, D.: *Theory of Bound States and Ionization Equilibrium in Plasmas and Solids*. Berlin : Akademie–Verlag, 1976. – russ.: Mir, Moskau (1979)

[Fre31] FRENKEL, J.: On the Transformation of Light into Heat in Solids. I; II. In: *Phys. Rev.* 37 (1931), S. 17;1276

[FRTM98] FERNÁNDEZ-ROSSIER, J. ; TEJEDOR, C. ; MERLIN, R.: Coherent light emission from exciton condensates in semiconductor quantum wells. In: *Solid State Commun.* 108 (1998), S. 473

[FSTU82] FEHRENBACH, G. W. ; SCHÄFER, W. ; TREUSCH, J. ; ULBRICH, R. G.: Transient Optical Spectra of a Dense Exciton Gas in a Direct-Gap Semiconductor. In: *Phys. Rev. Lett.* 49 (1982), S. 1281

[FW71] FETTER, A. L. ; WALECKA, J. D.: *Quantum Theory of Many-Particle Systems*. New York : McGraw–Hill, 1971

[GA07] GERACE, D. ; ANDREANI, L. C.: Quantum theory of exciton-photon coupling in photonic crystal slabs with embedded quantum wells. In: *Phys. Rev. B* 75 (2007), S. 235325

[GK52] GROSS, E. F. ; KARRYEV, N. A.: Opticheskii Spektr Eksitona. In: *Dokl. Akad. Nauk SSSR* 84 (1952), S. 471

[Gla63] GLAUBER, R. J.: The Quantum Theory of Optical Coherence. In: *Phys. Rev.* 130 (1963), S. 2529

[GNZ09] GRIFFIN, A. ; NIKUNI, T. ; ZAREMBA, E.: *Bose-Condensed Gases at Finite Temperatures*. Cambridge : Cambridge University Press, 2009

[Gri96] GRIFFIN, A.: Conserving and gapless approximations for an inhomogeneous Bose gas at finite temperatures. In: *Phys. Rev. B* 53 (1996), S. 9341

[GSN61] GRUN, J. B. ; SIESKIND, M. ; NIKITINE, S.: Détermination de l'intensité d'oscillateur des raies de la série verte de Cu_2O aux basses températures. In: *J. Phys. Radium* 22 (1961), S. 176

[HJ96] HAUG, H. ; JAUHO, A.-P.: *Quantum Kinetics in Transport and Optics of Semiconductors*. Berlin, Heidelberg : Springer–Verlag, 1996 (Springer Series in Solid-State Sciences 123)

[HK52] HAYASHI, M. ; KATSUKI, K.: Hydrogen-like Absorption Spectrum of Cuprous Oxide. In: *J. Phys. Soc. Jpn.* 7 (1952), S. 599

[HK83] HAUG, H. ; KRANZ, H. H.: Bose-Einstein condensation in nonequilibrium systems. In: *Z. Phys. B: Condens. Matter* 53 (1983), S. 151

[HK04] HAUG, H. ; KOCH, S. W.: *Quantum Theory of the Optical and Electronic Properties of Semiconductors*. 4. Aufl. Singapore : World Scientific, 2004

[HLR+12] HIGH, A. A. ; LEONARD, J. R. ; REMEIKA, M. ; BUTOV, L. V. ; HANSON, M. ; GOSSARD, A. C.: Condensation of Excitons in a Trap. In: *Nano Lett.* 12 (2012), S. 2605

[HR68] HALPERIN, B. I. ; RICE, T. M.: The Excitonic State at the Semiconductor-Semimetal Transition. New York : Academic Press, 1968, S. 115

[HT78] HAUG, H. ; THOAI, D. B. T.: Dynamical Screening of Excitons by Free Carriers. In: *Phys. Status Solidi B* 85 (1978), S. 561

[JW06] JANG, J. I. ; WOLFE, J. P.: Exciton decay in Cu_2O at high density and low temperature: Auger recombination, spin-flip scattering, and molecule formation. In: *Solid State Commun.* 137 (2006), S. 91

[KB96] KAVOULAKIS, G. M. ; BAYM, G.: Auger decay of degenerate and Bose-condensed excitons in Cu_2O. In: *Phys. Rev. B* 54 (1996), S. 16625

[KBW96] KAVOULAKIS, G. M. ; BAYM, G. ; WOLFE, J. P.: Quantum saturation and condensation of excitons in Cu_2O: A theoretical study. In: *Phys. Rev. B* 53 (1996), S. 7227

[Kel64] KELDYSH, L. V.: In: *Zh. Eksp. Teor. Fiz.* 47 (1964), 1515 S. – Diagram Technique for Nonequilibrium Processes, Sov. Phys. JETP **20**, 1018 (1965)

[KFS+14] KAZIMIERCZUK, T. ; FRÖHLICH, D. ; SCHEEL, S. ; STOLZ, H. ; BAYER, M.: Giant Rydberg excitons in the copper oxide Cu_2O. In: *Nature* 514 (2014), S. 343

[KJHK99] KIRA, M. ; JAHNKE, F. ; HOYER, W. ; KOCH, S. W.: Quantum theory of spontaneous emission and coherent effects in semiconductor microstructures. In: *Prog. Quant. Electron.* 23 (1999), S. 189

[KK64] KELDYSH, L. V. ; KOPAEV, Yu. V.: In: *Fiz. Tverd. Tela* 6 (1964), 2791 S. – Possible instability of the semimetallic state toward Coulomb interaction, Sov. Phys. Solid State **6**, 2219 (1965)]

[KK68] KELDYSH, L. V. ; KOZLOV, A. N.: In: *Zh. Eksp. Teor. Fiz.* 54 (1968), 978 S. – Collective Properties of Excitons in Semiconductors, Sov. Phys. JETP **27**, 521 (1968)]

[KKER86] KRAEFT, W. D. ; KREMP, D. ; EBELING, W. ; RÖPKE, G.: *Quantum Statistics of Charged Particle Systems*. Berlin : Akademie–Verlag, 1986

[KKK77] KILIMANN, K. ; KRAEFT, W. D. ; KREMP, D.: Lifetime and level shift of bound states in plasmas. In: *Phys. Lett.* 61A (1977), S. 393

[KKK+84] KREMP, D. ; KILIMANN, M. K. ; KRAEFT, W. D. ; STOLZ, H. ; ZIMMERMANN, R.: Ladder approximation of the equation of state for degenerate Fermi systems. In: *Physica A* 127 (1984), S. 646

[KKL84] KREMP, D. ; KRAEFT, W. D. ; LAMBERT, A. J. D.: Equation of state and ionization equilibrium for nonideal plasmas. In: *Physica A* 127 (1984), S. 72

[KKS93] KREMP, D. ; KRAEFT, W. D. ; SCHLANGES, M.: Quantum Statistical Equation of State for Nonideal Dense Plasmas. In: *Contrib. Plasma Phys.* 33 (1993), S. 567

[Kli05] KLINGSHIRN, C.: *Semiconductor Optics*. Berlin, Heidelberg : Springer–Verlag, 2005

[KM75] KREINGOLD, F. I. ; MAKAROV, V. L.: Investigation of Mechanism of Deformation Stimulation of a Paraexciton Level in Luminescence of Cuprous-Oxide Crystals. In: *Sov. Phys. Semicond.* 8 (1975), S. 962

[Koc11] KOCH, Th.: *pers. Mitteilung*. 2011

[KRK+06] KASPRZAK, J. ; RICHARD, M. ; KUNDERMANN, S. ; BAAS, A. ; JEAMBRUN, P. ; KEELING, J. M. J. ; MARCHETTI, F. M. ; SZYMANSKA, M. H. ; ANDRE, R. ; STAEHLI, J. L. ; SAVONA, V. ; LITTLEWOOD, P. B. ; DEVEAUD, B. ; DANG, Le S.: Bose–Einstein condensation of exciton polaritons. In: *Nature* 443 (2006), S. 409

[KS69] KWOK, P. C. ; SCHULTZ, T. D.: Correlation functions and Green functions: zero-frequency anomalies. In: *J. Phys. C: Solid State Phys.* 2 (1969), S. 1196

[KSH10] KREMP, D. ; SEMKAT, D. ; HENNEBERGER, K.: BEC–BCS transition in excitonic systems. In: *J. Phys.: Conf. Ser.* 220 (2010), S. 012004

[KSK05] KREMP, D. ; SCHLANGES, M. ; KRAEFT, W.-D.: *Quantum Statistics of Nonideal Plasmas*. Berlin, Heidelberg : Springer–Verlag, 2005 (Springer Series on Atomic, Optical, and Plasma Physics 25)

[Lai98] LAIKHTMAN, B.: Coherence of the exciton condensate luminescence. In: *Europhys. Lett.* 43 (1998), S. 53

[Lai07] LAIKHTMAN, B.: Are excitons really bosons? In: *J. Phys.: Condens. Matter* 19 (2007), S. 295214

[Leg80] LEGGETT, A. J.: Diatomic molecules and cooper pairs. In: PEKALSKI, A. (Hrsg.) ; PRZYSTAWA, J. (Hrsg.): *Modern Trends in the Theory of Condensed Matter*. Berlin, Heidelberg : Springer–Verlag, 1980, S. 13

[LO02] LOZOVIK, Yu. E. ; OVCHINNIKOV, I. V.: Many-photon coherence of Bose-condensed excitons: Luminescence and related nonlinear optical phenomena. In: *Phys. Rev. B* 66 (2002), S. 075124

[LZ12] LEGGETT, A. J. ; ZHANG, S.: The BEC–BCS Crossover: Some History and Some General Observations. In: ZWERGER, W. (Hrsg.): *The BCS–BEC Crossover and the Unitary Fermi Gas*. Berlin, Heidelberg : Springer–Verlag, 2012, S. 33

[Mos62] MOSKALENKO, S. A.: In: *Fiz. Tverd. Tela* 4 (1962), 276 S. – Reversible Optico-Hydrodynamic Phenomena in a Nonideal Exciton Gas, Sov. Phys. – Solid State 4, 199 (1962)

[MRS+11] MANZKE, G. ; RICHTER, F. ; SEMKAT, D. ; BURAU, G. K. G. ; KIESELING, F. ; STOLZ, H.: Transition from excitonic to plasma emission from localized electron-hole pair states in GaAs-AlGaAs quantum wells. In: *Phys. Status Solidi C* 8 (2011), S. 1161

[NGS61] NIKITINE, S. ; GRUN, J. B. ; SIESKIND, M.: Etude spectrophotométrique de la série jaune de Cu_2O aux basses températures. In: *J. Phys. Chem. Sol.* 17 (1961), S. 292

[NSR85] NOZIÉRES, P. ; SCHMITT-RINK, S.: Bose condensation in an attractive fermion gas: From weak to strong coupling superconductivity. In: *J. Low Temp. Phys.* 59 (1985), S. 195

[OGW99] O'HARA, K. E. ; GULLINGSRUD, J. R. ; WOLFE, J. P.: Auger decay of excitons in Cu_2O. In: *Phys. Rev. B* 60 (1999), S. 10872

[OO01] OKUMURA, S. ; OGAWA, T.: Boson representation of two-exciton correlations: An exact treatment of composite-particle effects. In: *Phys. Rev. B* 65 (2001), S. 035105

[PJ08] PROUKAKIS, N. P. ; JACKSON, B.: Finite-temperature models of Bose–Einstein condensation. In: *J. Phys. B: At. Mol. Opt. Phys.* 41 (2008), S. 203002

[PO56] PENROSE, O. ; ONSAGER, L.: Bose–Einstein Condensation and Liquid Helium. In: *Phys. Rev.* 104 (1956), S. 576

[PSMH00] PENG, Q. Y. ; SCHMIELAU, T. ; MANZKE, G. ; HENNEBERGER, K.: Excitonic absorption and gain in ZnSe. In: *J. Cryst. Growth* 214-215 (2000), S. 810

[RG71] RAMOS, J. G. ; GOMES, A. A.: Remarks on the retarded, advanced and thermodynamic Green's functions. In: *Nuovo Cimento A* 3 (1971), S. 441

[Ric07] RICHTER, F.: *Mott–Übergänge und Existenzgebiete exzitonischer Bose–Einstein–Kondensation*, Universität Rostock, Diplomarbeit, 2007

[RZR84] RÖSLER, M. ; ZIMMERMANN, R. ; RICHERT, W.: The Electron–Hole Plasma at Finite Temperatures. Calculation of Exchange-Correlation Energies and Padé Approximants. In: *Phys. Status Solidi B* 121 (1984), S. 609

[San10] SANDFORT, Ch.: *Acoustic and optical phonon scattering of the yellow $1S$ excitons in Cu_2O: A high resolution spectroscopy study*, Technische Universität Dortmund, Diss., 2010

[SB06] SEMKAT, D. ; BONITZ, M.: Generalized quantum kinetic equations. In: BONITZ, M. (Hrsg.) ; SEMKAT, D. (Hrsg.): *Introduction to Computational Methods in Many-Body Physics*. Paramus, New Jersey : Rinton Press, 2006, S. 171

[SBF+11] SANDFORT, C. ; BRANDT, J. ; FINKE, C. ; FRÖHLICH, D. ; BAYER, M. ; STOLZ, H. ; NAKA, N.: Paraexcitons of Cu_2O confined by a strain trap and high magnetic fields. In: *Phys. Rev. B* 84 (2011), S. 165215

[SC95] SNOKE, D. W. ; CRAWFORD, J. D.: Hysteresis in the Mott transition between plasma and insulating gas. In: *Phys. Rev. E* 52 (1995), S. 5796

[SC01] SHUMWAY, J. ; CEPERLEY, D. M.: Quantum Monte Carlo treatment of elastic exciton-exciton scattering. In: *Phys. Rev. B* 63 (2001), S. 165209

[Sch03] SCHMIELAU, T.: Phase Space Filling in the Electron–Hole Pair Green's Function. In: BONITZ, M. (Hrsg.) ; SEMKAT, D. (Hrsg.): *Progress in Non-equilibrium Green's Functions II*. Singapore : World Scientific, 2003, S. 265

[Sch17] SCHÖNE, F.: *pers. Mitteilung*. 2017

[Sem01] SEMKAT, D.: *Kurzzeitkinetik und Anfangskorrelationen in nichtidealen Vielteilchensystemen*, Universität Rostock, Diss., 2001

[SG98] SHI, H. ; GRIFFIN, A.: Finite-temperature excitations in a dilute Bose-condensed gas. In: *Phys. Rep.* 304 (1998), S. 1

[SK82] SCHLANGES, M. ; KREMP, D.: The equation of state for the hydrogen plasma on account of atom-atom interaction. In: *Ann. Phys. (Leipzig)* 39 (1982), S. 69

[SK14] SNOKE, D. W. ; KAVOULAKIS, G. M.: Bose–Einstein condensation of excitons in Cu_2O: progress over 30 years. In: *Rep. Prog. Phys.* 77 (2014), S. 116501

[SKG+16] SCHÖNE, F. ; KRÜGER, S.-O. ; GRÜNWALD, P. ; STOLZ, H. ; SCHEEL, S. ; ASSMANN, M. ; HECKÖTTER, J. ; THEWES, J. ; FRÖHLICH, D. ; BAYER, M.: Deviations of the exciton level spectrum in Cu_2O from the hydrogen series. In: *Phys. Rev. B* 93 (2016), S. 075203

[SKH09] SEMKAT, D. ; KREMP, D. ; HENNEBERGER, K.: Quantum condensation in electron–hole plasmas. In: *Phys. Status Solidi C* 6 (2009), S. 546

[SMTH00] SCHMIELAU, T. ; MANZKE, G. ; TAMME, D. ; HENNEBERGER, K.: T-Matrix Approach to the Linear Optical Response of Highly Excited Semiconductors. In: *Phys. Status Solidi B* 221 (2000), S. 215

[SNKS12] SCHWARTZ, R. ; NAKA, N. ; KIESELING, F. ; STOLZ, H.: Dynamics of excitons in a potential trap at ultra-low temperatures: paraexcitons in Cu_2O. In: *New J. Phys.* 14 (2012), S. 023054

[Sno03] SNOKE, D. W.: When should we say we have observed Bose condensation of excitons? In: *Phys. Status Solidi B* 238 (2003), S. 389

[Sob10] SOBKOWIAK, S.: *Optische Signaturen der Bose–Einstein–Kondensation in der Theorie wechselwirkender mehrkomponentiger Exzitonengase in Fallen*, Universität Rostock, Diplomarbeit, 2010

[Sob14] SOBKOWIAK, S.: *Theoretische Beschreibung von Exzitonen in druckinduzierten Potentialfallen bei ultratiefen Temperaturen in Kupferoxydul*, Universität Rostock, Diss., 2014

[SRK+10] SEMKAT, D. ; RICHTER, F. ; KREMP, D. ; MANZKE, G. ; KRAEFT, W.-D. ; HENNEBERGER, K.: Mott transition in electron–hole plasmas. In: *J. Phys.: Conf. Ser.* 220 (2010), S. 012005

[SS17] SCHÖNE, F. ; STOLZ, H.: *in Vorbereitung*. 2017

[SSS+11] SOBKOWIAK, S. ; SEMKAT, D. ; STOLZ, H. ; KOCH, Th. ; FEHSKE, H.: Phase separation of multicomponent excitonic Bose–Einstein condensates. In: *Phys. Status Solidi C* 8 (2011), S. 1178

[Sto75] STOLZ, H.: *Die Bedeutung der Bose–Einstein–Kondensation für das Verständnis makroskopischer Quantenphänomene*. Berlin : Akademie der Wissenschaften der DDR, Zentralinstitut für Elektronenphysik, 1975 (ZIE Preprint 75-6)

[SVG94] SHI, H. ; VERECHAKA, G. ; GRIFFIN, A.: Theory of the decay luminescence spectrum of a Bose-condensed interacting exciton gas. In: *Phys. Rev. B* 50 (1994), S. 1119

[SW02] SCHÄFER, W. ; WEGENER, M.: *Semiconductor Optics and Transport Phenomena*. Berlin, Heidelberg : Springer–Verlag, 2002

[Wan37] WANNIER, G.: The Structure of Electronic Excitation Levels in Insulating Crystals. In: *Phys. Rev.* 52 (1937), S. 191

[WOW00] WARREN, J. T. ; O'HARA, K. E. ; WOLFE, J. P.: Two-body decay of thermalized excitons in Cu_2O. In: *Phys. Rev. B* 61 (2000), S. 8215

[Yan62] YANG, G. N.: Concept of Off-Diagonal Long-Range Order and the Quantum Phases of Liquid He and of Superconductors. In: *Rev. Mod. Phys.* 34 (1962), S. 694

[YCKG11] YOSHIOKA, K. ; CHAE, E. ; KUWATA-GONOKAMI, M.: Transition to a Bose–Einstein condensate and relaxation explosion of excitons at sub-Kelvin temperatures. In: *Nat. Commun.* 2 (2011), S. 328

[YIMKG10] YOSHIOKA, K. ; IDEGUCHI, T. ; MYSYROWICZ, A. ; KUWATA-GONOKAMI, M.: Quantum inelastic collisions between paraexcitons in Cu_2O. In: *Phys. Rev. B* 82 (2010), S. 041201(R)

[YMFKG13] YOSHIOKA, K. ; MORITA, Y. ; FUKUOKA, K. ; KUWATA-GONOKAMI, M.: Generation of ultracold paraexcitons in cuprous oxide: A path toward a stable Bose–Einstein condensate. In: *Phys. Rev. B* 88 (2013), S. 041201(R)

[YNK+15] YAMAGUCHI, M. ; NII, R. ; KAMIDE, K. ; OGAWA, T. ; YAMAMOTO, Y.: Generating functional approach for spontaneous coherence in semiconductor electron–hole–photon systems. In: *Phys. Rev. B* 91 (2015), S. 115129

[Zim76] ZIMMERMANN, R.: Excitons and Electron–Hole Plasma. A Ground State Calculation. In: *Phys. Status Solidi B* 76 (1976), S. 191

[Zim88] ZIMMERMANN, R.: *Many-Particle Theory of Highly Excited Semiconductors*. Leipzig : BSB B. G. Teubner Verlagsgesellschaft, 1988 (Teubner–Texte zur Physik Bd. 18)

[ZKK+78] ZIMMERMANN, R. ; KILIMANN, K. ; KRAEFT, W. D. ; KREMP, D. ; RÖPKE, G.: Dynamical screening and self-energy of excitons in the electron–hole plasma. In: *Phys. Status Solidi B* 90 (1978), S. 175

[ZNG99] ZAREMBA, E. ; NIKUNI, T. ; GRIFFIN, A.: Dynamics of Trapped Bose Gases at Finite Temperatures. In: *J. Low Temp. Phys.* 116 (1999), S. 277

[ZS85] ZIMMERMANN, R. ; STOLZ, H.: The Mass Action Law in Two-Component Fermi Systems Revisited. Excitons and Electron–Hole Pairs. In: *Phys. Status Solidi B* 131 (1985), S. 151

Anhang A

Publikationen

Im folgenden schließen sich die publizierten Artikel in chronologischer Reihenfolge an.

A.1

Artikel 1

D. Kremp, D. Semkat, and K. Henneberger:

Quantum condensation in electron-hole plasmas

Phys. Rev. B **78**, 125315 (2008)

Quantum condensation in electron-hole plasmas

D. Kremp, D. Semkat, and K. Henneberger
Universität Rostock, Institut für Physik, D-18051 Rostock, Germany
(Received 30 January 2008; revised manuscript received 22 May 2008; published 12 September 2008)

We consider quantum condensation in the electron-hole plasma of highly excited semiconductors. A theoretical approach applying the concept of time long-range order in the framework of real time Green's functions is presented and generalizations of the basic equations of quantum condensation are derived. For the quasiequilibrium case, we solve the coupled system of number and gap equations in ladder approximation for a statically screened Coulomb potential. The resulting phase boundary shows a smooth crossover from the Bose-Einstein condensation (BEC) of excitons to a BCS state of electron-hole pairs.

DOI: 10.1103/PhysRevB.78.125315 PACS number(s): 71.35.Ee, 03.75.Hh, 71.35.Lk, 74.20.Fg

I. INTRODUCTION

In this paper, an electron-hole (e-h) plasma, excited in a model semiconductor with parabolic nondegenerate conduction and valence bands is considered. Both electrons (e) and holes (h) are mobile Fermi particles with the effective masses m_e and m_h. Due to the attractive Coulomb interaction between electrons and holes, bound electron-hole pairs, the excitons, and the formation of an ionization equilibrium $e+h \rightleftarrows X$ are observed.

The properties of the e-h plasma are well investigated, see, e.g., Refs. 1–5. Of particular interest for our consideration are the thermodynamic functions and the ionization equilibrium.[3,6,7] A special feature of the e-h plasma is the lowering of the coupling with increasing density by many-particle effects such as screening of the Coulomb interaction and, therefore, a breakup of the excitons usually referred to as Mott effect (density ionization).[8–11]

Because of the Mott transition, roughly at $r_{sc} \simeq a_X$ (where r_{sc} denotes the screening length and a_X denotes the excitonic Bohr radius) the density-temperature ($n-T$) plane is divided into an area where bound states are possible $r_{sc} > a_X$ and an area without bound states $r_{sc} < a_X$, i.e., a high-density e-h liquid.

In the excitonic area, the formation of an ionization equilibrium turns up with a strong dominance of excitons at lower temperatures. Since the excitons behave approximately like composite Bose particles, Bose condensation in the region $n\lambda^3 > 2.61$ [where λ is the thermal deBroglie wavelength with $\lambda^2 = 2\pi\hbar^2/(mk_BT)$] may be expected if the chemical potential reaches the exciton $1s$ ground-state energy.[5,12–14] At higher densities the region of Bose condensation of excitons is, of course, limited by the Mott transition. However, we underline that the vanishing of the excitons does not imply a disappearance of the condensed phase. As proposed by Keldysh and Kopaev[15] and others,[16–18] in the high-density highly degenerate e-h liquid the formation of weakly bound cooperative Cooper pairs of electrons and holes and their Bose condensation to a BCS state may be expected, known as excitonic insulator.

It was shown by Leggett[19] and generalized and extended to finite temperatures by Noziéres and Schmitt-Rink[20] that the crossover from the BEC to the BCS regime is smooth, despite the fact that the limits of BCS state and BEC of excitons are physically quite different. This is a general behavior of Fermi systems with Bose-like bound states and has been the subject of many papers mostly for Fermi atoms interacting via a contact potential[21–23] and nuclear matter.[24] However, for e-h plasmas there exist only a few papers. In spite of the fundamental importance of Ref. 20, the special features of Coulomb systems mentioned above are not taken into account. Moreover, a separable potential was assumed. Further investigations to the crossover problem in e-h plasmas have been carried out in Refs. 25 and 26. The first paper is restricted to the optical behavior at the crossover and the second one considers the crossover for Coulomb systems more in detail but a simultaneous consideration of the density is missing.

The outline of this paper is as follows: In Sec. II we derive the basic equations of quantum condensation within the formalism of real time Green's functions on the Keldysh contour in order to describe both equilibrium and nonequilibrium systems. A convenient but rarely investigated approach to quantum condensation in the framework of Green's functions is the *time long-range order* (TLRO), i.e., the specific asymptotic behavior of the two-particle correlation function in the condensate. Beside TLRO the well-known *off-diagonal long-range order* (ODLRO) (Refs. 27 and 28) is a general property of quantum condensates. ODLRO proves to be a direct consequence of TLRO. The concept of TLRO opens the possibility to formulate the theory without explicit use of "anomalous" propagators. Starting with the Bethe-Salpeter equation for the two-particle (e-h) Green's function, generalized Gorkov equations on the Keldysh contour are derived from which equations for the correlation functions and the retarded ones follow.

In Sec. III e-h plasmas in thermodynamic quasiequilibrium are considered. Then we get the well-known BCS scheme[29] in real time Green's function formulation generalized by the self-energy of the normal phase. Furthermore, in an e-h plasma all relations are generalized for a two-component system.

The BEC-BCS crossover is driven by the breakup of the Bose-like bound states. In e-h plasmas this effect is due to many-particle effects such as weakening of the screened Coulomb potential with increasing density, self-energy, and Pauli blocking. Section IV is, on that account, devoted to these problems. We consider here the lowering of the ionization energy of the excitons, their density ionization, and the

disappearance of bound states carefully on the basis of the screened ladder Bethe-Salpeter equation.[8–10,30] For the complete grand canonical description of the plasma we need of course the density as a function of the chemical potential. This function determines all thermodynamical properties of the system. Especially we remark that the density is, in spite of the disappearance of the bound-state contribution, a smooth function of the coupling parameter.

Finally we consider in Sec. V the phase boundary of the quantum condensate defined by vanishing gap function, i.e., we determine for a model semiconductor from the linearized gap equation with the screened Coulomb potential the critical temperature as a function of the chemical potential.[26] Using the density equation in ladder approximation, we find finally the critical temperature as a function of the density.

Similar to the Fermi atom systems with contact potential or to nuclear matter, we find for the *e-h* plasma with screened Coulomb interaction a smooth crossover from BEC to the excitonic insulator, too.

II. TWO-PARTICLE CORRELATION FUNCTION: TIME LONG-RANGE ORDER

It is a widely used concept to consider the highly excited semiconductor as an *e-h* plasma with the Hamiltonian in Coulomb gauge given by

$$\mathrm{H} = \sum_{a=e,h} \int d\mathbf{r}_1 \Psi_a(\mathbf{r}_1,t)\left\{\frac{1}{2m_a}[-i\hbar\nabla_1 - e_a\mathbf{A}(\mathbf{r}_1,t)]^2 + \epsilon_a\right\} \times \Psi_a^\dagger(\mathbf{r}_1,t) + \frac{1}{2}\sum_{a,b}\int d\mathbf{r}_1 d\mathbf{r}_2 \Psi_a^\dagger(\mathbf{r}_1,t)\Psi_b^\dagger(\mathbf{r}_2,t)V_{ab}(\mathbf{r}_1-\mathbf{r}_2) \times \Psi_b(\mathbf{r}_2,t)\Psi_a(\mathbf{r}_1,t). \quad (1)$$

Here, $\epsilon_e - \epsilon_h = \epsilon_g$ is the energy gap, $V_{ab}(\mathbf{r}_1-\mathbf{r}_2) = e_a e_b V(|\mathbf{r}_1-\mathbf{r}_2|)$ is the long-range Coulomb interaction, and $\Psi_a, \Psi_a^\dagger (a=e,h)$ are fermionic field operators for electrons (holes) obeying the usual commutation relations. $\mathbf{A}(\mathbf{r}_1,t)$ is the transverse electromagnetic field.

A unified description of quantum condensation in Fermi systems with bound states both in equilibrium and nonequilibrium can be found within the formalism of real time Green's functions.

Since we are concerned with the behavior of electron-hole pairs, the starting point is the two-particle Green's function,

$$G_{ab}(12,1'2') = \frac{1}{(i\hbar)^2}\langle \mathrm{T}_\mathcal{C}\{\Psi_a(1)\Psi_b(2)\Psi_b^\dagger(2')\Psi_a^\dagger(1')\}\rangle, \quad (2)$$

with $1=\{\mathbf{r}_1,t_1,s_1^{(3)}\}$, and the time ordering $T_\mathcal{C}$ on the double-time Keldysh contour $\mathcal{C}$.[31,32] By positioning the time variables t_1,t_2,t_1',t_2' at the contour, we get the various two-particle functions. Here, e.g., the two-particle correlation function $g_{ab}^<$ is of interest,

$$g_{ab}^<(12,1'2') \equiv g_{ab}^{++--}(12,1'2') = \frac{1}{(i\hbar)^2}\langle \Psi_a^\dagger(1')\Psi_b^\dagger(2')\Psi_b(2)\Psi_a(1)\rangle. \quad (3)$$

This function follows from Eq. (2) by positioning t_1,t_2 on the upper branch and t_1',t_2' on the lower branch of the Keldysh contour. For equal times, $g_{ab}^<$ is just the two-particle density matrix.

Let us first consider the time behavior of G_{ab}. Usually one would expect $G_{ab}(12,1'2')$ to vanish if the difference of all primed and all unprimed times tends to infinity, i.e., $|\{t_1,t_2\} - \{t_1',t_2'\}| \to \infty$. Otherwise, TLRO occurs; that means the structure of the two-particle function is

$$G_{ab}(12,1'2') = \hat{G}_{ab}(12,1'2') + C_{ab}(12,1'2'), \quad (4)$$

with the properties

$$\lim_{|\{t_1,t_2\}-\{t_1',t_2'\}|\to\infty} \hat{G}_{ab}(12,1'2') = 0;$$

$$\lim_{|\{t_1,t_2\}-\{t_1',t_2'\}|\to\infty} C_{ab}(12,1'2') \neq 0. \quad (5)$$

The concept of TLRO was introduced and elaborated in Refs. 33 and 34 for the one-particle correlation function. In connection with bound states and the two-particle correlation function we mention Ref. 35.

From the consideration above the question arises under which conditions one gets a nonvanishing C_{ab}.

The dynamics of pairs of particles is determined by the Bethe-Salpeter equation (BSE) for $G_{ab}(12,1'2')$ in the "particle-particle channel." The BSE can be written in the form,

$$\int_\mathcal{C} d\bar{1} G_a^{-1}(1,\bar{1}) G_{ab}(\bar{1}2,1'2') - i\hbar\int_\mathcal{C} d3 d\bar{1} d\bar{2} G_b(2,3) W_{ab}(13,\bar{1}\bar{2}) G_{ab}(\bar{1}\bar{2},1'2') = G_b(2,2')\delta(1-1'). \quad (6)$$

Here, W_{ab} is an effective two-particle interaction. In terms of Feynman diagrams, W_{ab} is the sum of all amputated irreducible two-particle diagrams in the particle-particle channel. Equation (6) has to be completed by an equation for the one-particle Green's function, the Dyson equation;

$$\int_\mathcal{C} d\bar{1}[G_a^{0^{-1}}(1,\bar{1}) - \Sigma_a(1,\bar{1})]G_a(\bar{1},1') = \delta(1-1'), \quad (7)$$

with the free inverse one-particle Green's function,

$$G_a^{0^{-1}}(1,\bar{1}) = \left\{i\hbar\frac{\partial}{\partial t_1} + \frac{1}{2m_a}[-i\hbar\nabla_1 - e_a\mathbf{A}(1)]^2 + \epsilon_a\right\}\delta(1-\bar{1}).$$

The general solution of the BSE is

$$G_{ab}(12,1'2') = \hat{G}_{ab}(12,1'2') + F_{ab}(12)F^*_{ab}(1'2'), \quad (8)$$

where $\hat{G}_{ab}(12,1'2')$ is a special solution of Eq. (6), which obeys the asymptotic condition,

$$\lim_{|\{t_1,t_2\}-\{t_1',t_2'\}|\to\infty} \hat{G}_{ab}(12,1'2') = 0. \quad (9)$$

Comparing the solution structure [Eq. (8)] with Eq. (4), the TLRO term can be identified by $C_{ab}(12,1'2') = F_{ab}(12)F^*_{ab}(1'2')$. The function F_{ab} is a solution of the homogeneous equation to Eq. (6),

$$\int_{\mathcal{C}} d\bar{1} G_a^{-1}(1,\bar{1})F_{ab}(\bar{1}2) - \int_{\mathcal{C}} d\bar{2} G_b(2,\bar{2})D_{ab}(1\bar{2}) = 0, \quad (10)$$

with the abbreviation

$$D_{ab}(12) = i\hbar \int_{\mathcal{C}} d\bar{1}d\bar{2} W_{ab}(12,\bar{1}\bar{2})F_{ab}(\bar{1}\bar{2}). \quad (11)$$

For the function D_{ab}, from Eqs. (6) and (10) follows immediately the integral equation,

$$D_{ab}(12) = i\hbar \int_{\mathcal{C}} d\bar{1}d\bar{2}d\bar{\bar{1}}d\bar{\bar{2}} W_{ab}(12,\bar{1}\bar{2})G_a(\bar{1},\bar{\bar{1}})G_b(\bar{2},\bar{\bar{2}}) \times D_{ab}(\bar{\bar{1}}\bar{\bar{2}}). \quad (12)$$

In the Dyson Eq. (7), the self-energy Σ_a is defined by

$$\int_{\mathcal{C}} d\bar{1}\Sigma_a(1,\bar{1})G_a(\bar{1},1') = \sum_b \int_{\mathcal{C}} d2 V_{ab}(1-2)G_{ab}(12,1'2^+), \quad (13)$$

with $V_{ab}(1-2)=V_{ab}(\mathbf{r}_1-\mathbf{r}_2)\delta(t_1-t_2)$ and $t_2^+=t_2+\epsilon$, $\epsilon\to 0$. Inserting Eq. (8), we find that $\Sigma_a(1,\bar{1})$ has the structure $\Sigma_a(1,\bar{1})=\hat{\Sigma}_a(1,\bar{1})+\Sigma_a^{\mathrm{LRO}}(1,\bar{1})$, with $\hat{\Sigma}_a(1,\bar{1})$ being the self-energy of the normal phase, and a TLRO term $\Sigma_a^{\mathrm{LRO}}(1,\bar{1})$ given by

$$\int_{\mathcal{C}} d\bar{1}\Sigma_a^{\mathrm{LRO}}(1,\bar{1})G_a(\bar{1},1') = \int_{\mathcal{C}} d2\Delta_{ab}(12)F^*_{ab}(1'2^+). \quad (14)$$

Here, the gap function $\Delta_{ab}(12)=i\hbar V_{ab}(1-2)F_{ab}(12)$ is introduced, which is fundamental for the description of the quantum condensate. Note that $\Delta_{ab}\neq 0$ only for $a\neq b$. Using Eq. (10), Σ_a^{LRO} is explicitly given by

$$\Sigma_a^{\mathrm{LRO}}(1,1') = \int_{\mathcal{C}} d2d\bar{2}\Delta_{ab}(12)D^*_{ab}(1'\bar{2})G_b(\bar{2},2^+). \quad (15)$$

Above the critical temperature T_{crit} for quantum condensation, $\hat{\Sigma}_a$ is the only contribution, while for vanishing temperatures Σ_a^{LRO} dominates. At finite temperatures lower than the critical one, however, the number of particles excited out of the condensate will be significant and both terms have to be taken into account.

Therefore, the Dyson equation on the Keldysh contour $\mathcal{C}$ takes the form,

$$\int_{\mathcal{C}} d\bar{1}[G_a^{0^{-1}}(1,\bar{1}) - \hat{\Sigma}_a(1,\bar{1}) - \Sigma_a^{\mathrm{LRO}}(1,\bar{1})]G_a(\bar{1},1') = \delta(1-1'). \quad (16)$$

Although Eqs. (15) and (16) determine the single-particle properties of the system completely, often a transformation is advantageous. Using Eq. (14), from Eqs. (10) and (16) we obtain the following equivalent system of equations for the two functions G_a and F_{ab}:

$$\int_{\mathcal{C}} d\bar{1}[G_a^{0^{-1}}(1,\bar{1}) - \hat{\Sigma}_a(1,\bar{1})]G_a(\bar{1},1') - \int_{\mathcal{C}} d2\Delta_{ab}(12)F^*_{ab}(1'2^+) = \delta(1-1'), \quad (17)$$

$$\int_{\mathcal{C}} d\bar{1}[G_b^{0^{-1}}(2,\bar{2}) - \hat{\Sigma}_b(2,\bar{2})]F_{ab}(1\bar{2}) + \int_{\mathcal{C}} d\bar{2}G_a(1,\bar{1})D_{ab}(\bar{1}2) = 0. \quad (18)$$

Obviously, Eqs. (17) and (18) generalize the well-known Gorkov equations in various aspects: (i) They are nonequilibrium equations on the Keldysh contour and, therefore, a compact representation of equations for the various Keldysh components. (ii) By approximations for W_{ab}, the approximation level of the theory is determined. (iii) The influence of the normal phase is taken into account by $\hat{\Sigma}$. Let us finally remember, that the first Gorkov equation is the Dyson equation, while the second one is a consequence of the Bethe-Salpeter equation for the two-particle Green's function.

The concept of time long-range order applied successfully above is closely connected with the principle of ODLRO as an expression of a macroscopic order state in a quantum condensate introduced by Onsager and Penrose[27] and Yang.[28] ODLRO is a property of the reduced density matrices written in the two-particle case as

$$\varrho_{ab}(\mathbf{r}_1\mathbf{r}_2,\mathbf{r}_1'\mathbf{r}_2';t) = \hat{\varrho}_{ab}(\mathbf{r}_1\mathbf{r}_2,\mathbf{r}_1'\mathbf{r}_2';t) + \Phi_{ab}(\mathbf{r}_1\mathbf{r}_2,t)\Phi^*_{ab}(\mathbf{r}_1'\mathbf{r}_2',t), \quad (19)$$

where $\hat{\varrho}_{ab}$ vanishes if the difference of all primed and all unprimed times tends to infinity. Since the two-particle density matrix is given by $g_{ab}^<$ for $t_1=t_2=t_1'=t_2'=t$, from Eq. (8) follows ODLRO and, therefore, quantum condensation if Eq. (10) has a solution.

In the following, our considerations are specified to the *e-h* plasma. Here, the interaction is the long-range Coulomb interaction and the typical features of Coulomb systems, i.e., collective behavior and Coulomb divergences have to be taken into account.[3,32,36,37] An appropriate approximation follows if the effective interaction is restricted to

$$W_{ab}(12,\bar{1}\bar{2}) = V^s_{ab}(1,2)\delta(1-\bar{1})\delta(2-\bar{2}). \quad (20)$$

Here, V^s is the screened Coulomb potential,

$$V^s_{ab}(1,2) = V_{ab}(1-2) + \sum_{cd} \int_{\mathcal{C}} d3d4 V_{ac}(1-3) \times \Pi_{cd}(34) V^s_{db}(4,2), \tag{21}$$

with Π_{ab} being the polarization function connected with the two-particle Green's function by

$$\Pi_{ab}(12,1'2') = L_{ab}(12,1'2') - \int_{\mathcal{C}} d3d4 \Pi_{ab}(13,1'3^+) V^s_{ab}(3,4) \Pi_{ab}(42,4^+2') \tag{22}$$

and $L_{ab}(12,1'2') = G_{ab}(12,1'2') - G_a(1,1')G_b(2,2')$. The function $\Pi_{ab}(12)$ follows from $\Pi_{ab}(12) = \Pi_{ab}(12,1^+2^+)$. The approximation (20) defines the dynamically screened ladder approximation for the two-particle Green's function. It represents the simplest scheme to account for bound and scattering states in systems with Coulomb interaction. It removes the Coulomb divergences from the ladder sum and describes the influence of the dynamical screening on the bound and scattering states.

The screened ladder approximation, however, does not include three-particle and four-particle processes and, thus, cannot describe carrier-exciton and exciton-exciton interactions.

The self-energy in terms of the screened potential is written according to

$$\Sigma_a(1,1') = \Sigma^{\mathrm{H}}_a(1,1') + \Sigma^s_a(1,1'), \tag{23}$$

$$\int_{\mathcal{C}} d\bar{1} \Sigma^s_a(1,\bar{1}) G_a(\bar{1},1') = \sum_b \int_{\mathcal{C}} d2 V^s_{ab}(1,2) \Pi_{ab}(12,1'2^+), \tag{24}$$

where Σ^s_a denotes the "screened" self-energy and Σ^{H}_a is the Hartree (mean field) contribution. In screened ladder approximation, Π_{ab} reduces to

$$\Pi_{ab}(12,1'2') = L_{ab}(12,1'2') - \int_{\mathcal{C}} d3d4 G_a(1,3^+) G_b(3,1') \times V^s_{ab}(3,4) G_a(2,4^+) G_b(4,2'). \tag{25}$$

Obviously, the TLRO contribution to Π_{ab} agrees with that of the screened ladder sum L_{ab}. The structure of the screened self-energy is, therefore, $\Sigma^s_a = \hat{\Sigma}^s_a + \Sigma^{\mathrm{LRO}}_a$, with Σ^{LRO}_a given again by Eq. (14) but now Δ_{ab} is

$$\Delta_{ab}(12) = i\hbar V^s_{ab}(1,2) F_{ab}(12). \tag{26}$$

F_{ab} is a solution of Eqs. (10) and (11) with W_{ab} now given by Eq. (20). Furthermore, Eq. (11) shows that $D_{ab} = \Delta_{ab}$. Then Eq. (12) yields an integral equation for the gap function,

$$\Delta_{ab}(12) = i\hbar \int_{\mathcal{C}} d\bar{1} d\bar{2} V^s_{ab}(1,2) G_a(1,\bar{1}) G_b(2,\bar{2}) \Delta_{ab}(\bar{1}\bar{2}). \tag{27}$$

In this way, the theory may be considered in terms of the screened potential and the usual problems connected with the Coulomb interaction are overcome.

For the dynamics of a pair of particles, it is often sufficient to consider the special two-time function (particle-particle channel),

$$G_{ab}(12,1'2')\big|^{t_1=t_2=t}_{t'_1=t'_2=t'} = G_{ab}(t,t'). \tag{28}$$

For it the TLRO condition reads

$$G_{ab}(t,t') = \hat{G}_{ab}(t,t') + \frac{1}{(i\hbar)^2} \Phi_{ab}(t) \Phi^*_{ab}(t'). \tag{29}$$

Here, Φ_{ab} is the macro-wave-function given by $\Phi_{ab}(\mathbf{r}_1\mathbf{r}_2,t_1) = i\hbar F_{ab}(12)|_{t_1=t_2}$.

In the steady state, the two-time correlation function depends only on the microscopic time $\tau = t - t'$ and we can consider the Fourier transform. Furthermore, in order to find the equilibrium solution of the BSE corresponding to the grand canonical density operator, the Kubo-Martin-Schwinger (KMS) condition $g^<_{ab}(\omega) = e^{-\beta(\hbar\omega-\mu_a-\mu_b)} g^>_{ab}(\omega)$ has to be fulfilled. That requires $\Phi_{ab}(\mathbf{r}_1,\mathbf{r}_2,t) = e^{\frac{i}{\hbar}(\mu_a+\mu_b)t} \Phi_{ab}(\mathbf{r}_1,\mathbf{r}_2)$. Then TLRO produces an additional term in the spectral representation of $g^<_{ab}$,

$$g^<_{ab}(\omega) = a_{ab}(\omega) \frac{\mathcal{P}}{e^{\beta(\hbar\omega-\mu_b-\mu_a)} - 1} + 2\pi\delta(\hbar\omega - \mu_b - \mu_a) \Phi_{ab} \Phi^*_{ab}. \tag{30}$$

In screened ladder approximation [Eq. (20)] it is useful to consider the T-matrix connected with G_{ab} by the relation $T_{ab} = V^s_{ab} + V^s_{ab} G_{ab} V^s_{ab}$. TLRO in the Green's function then induces TLRO in the corresponding T-matrix;

$$T_{ab}(12,1'2') = \hat{T}_{ab}(12,1'2') + \frac{1}{i\hbar} \Delta_{ab}(12) \Delta^*_{ab}(1'2'). \tag{31}$$

Corresponding to Eq. (30), in the steady state we obtain also an additional TLRO term in the spectral representation of $T^<_{ab}$;

$$T^<_{ab}(\omega) = 2\,\mathrm{Im}\, T^{\mathrm{R}}_{ab}(\omega) \frac{\mathcal{P}}{e^{\beta(\hbar\omega-\mu_b-\mu_a)} - 1} + 2\pi\delta(\hbar\omega - \mu_b - \mu_a) \Delta_{ab} \Delta^*_{ab}. \tag{32}$$

The screened ladder T-matrix obeys the many-particle form of the Lippmann-Schwinger equation, which follows from the Bethe-Salpeter equation. On the Keldysh contour it reads

$$T_{ab}(12,1'2') = V^s_{ab}(1,2)\delta(1-1')\delta(2-2') + i\hbar\int_{\mathcal{C}} d\bar{1}d\bar{2} \times V^s_{ab}(1,2)G_a(1,\bar{1})G_b(2,\bar{2})T_{ab}(\bar{1}\bar{2},1'2'). \tag{33}$$

The self-energy in screened ladder approximation is now explicitly given by

$$\hat{\Sigma}_a(1,1') = \pm i\hbar\sum_b \int_{\mathcal{C}} d2d\bar{2}[\hat{T}_{ab}(12,1'\bar{2}) \pm \delta_{ab}\hat{T}_{ab}(12,\bar{2}1') - V^s_{ab}(1,2)G_a(1,1')G_b(2,\bar{2})V^s_{ab}(1',\bar{2})]G_b(\bar{2},2), \tag{34}$$

$$\Sigma^{\mathrm{LRO}}_a(1,1') = \int_{\mathcal{C}} d2d\bar{2}\Delta_{ab}(12)\Delta^*_{ab}(1'\bar{2})G_b(\bar{2},2). \tag{35}$$

Since the polarization function Π_{ab} determines also the optical properties of the excited semiconductor, its TLRO contribution shall be given explicitly, too. As discussed above, it is, in screened ladder approximation, just equivalent to the TLRO part of G_{ab}, cf. Eqs. (4) and (8), i.e., one gets for the two-time polarization function,

$$\Pi^{\mathrm{LRO}}_{ab}(12) = \Pi^{\mathrm{LRO}}_{ab}(12,1^+2^+) = F_{ab}(12)F^*_{ab}(12). \tag{36}$$

Again, the TLRO contribution is the same in all Keldysh components. Taking into account,

$$\Phi_{ab}(\mathbf{r}_1\mathbf{r}_2) = \int d\bar{\mathbf{r}}_1 d\bar{\mathbf{r}}_2 \mathcal{G}^{\mathrm{R}}_{ab}(\mathbf{r}_1\mathbf{r}_2,\bar{\mathbf{r}}_1\bar{\mathbf{r}}_2;\omega)|_{\hbar\omega=\mu_a+\mu_b}\Delta_{ab}(\bar{\mathbf{r}}_1\bar{\mathbf{r}}_2) \tag{37}$$

[cf. Eqs. (26) and (27)], in quasiequilibrium one obtains

$$\Pi^{\mathrm{LRO}}_{ab}(\mathbf{r}_1\mathbf{r}_2,\omega) = |\Phi_{ab}(\mathbf{r}_1\mathbf{r}_2)|^2 \cdot 2\pi\delta(\hbar\omega-\mu_a-\mu_b). \tag{38}$$

The nonequilibrium generalizations of the Gorkov equations obtain, in screened ladder approximation, finally the following form:

$$\left[i\hbar\frac{\partial}{\partial t_1} + \frac{1}{2m_a}(-i\hbar\nabla_1 - e_a\mathbf{A}(1))^2 + \epsilon_a\right]G_a(1,1') - \int_{\mathcal{C}} d\bar{1}\hat{\Sigma}_a(1,\bar{1})G_a(\bar{1},1') - \int_{\mathcal{C}} d\bar{1}\Delta_{ab}(1\bar{1})F^*_{ab}(1'\bar{1}) = \delta(1-1'), \tag{39}$$

$$\left[i\hbar\frac{\partial}{\partial t'_1} - \frac{1}{2m_b}(-i\hbar\nabla_{1'} - e_b\mathbf{A}(1'))^2 - \epsilon_b\right]F^*_{ab}(11') + \int_{\mathcal{C}} d\bar{1}\hat{\Sigma}^*_b(1',\bar{1})F^*_{ab}(1\bar{1}) - \int_{\mathcal{C}} d\bar{1}\Delta^*_{ab}(\bar{1}1')G_a(\bar{1},1) = 0. \tag{40}$$

Equations (39) and (40) are the basic equations for the description of the nonequilibrium behavior of the *e-h* plasma as a quantum many-particle system including the quantum condensate. From Eqs. (39) and (40), by time specialization on the Keldysh contour, there follow equations for the correlation functions, the retarded and advanced functions, and the macro-wave–function, which are given in Appendix.

III. SOLUTION IN EQUILIBRIUM

We consider now a spatially homogeneous *e-h* plasma in thermodynamic quasiequilibrium. Then all two-point functions depend only on $t-t'$ and $\mathbf{r}-\mathbf{r}'$, and the Fourier transformation $t-t'\to\omega$, $\mathbf{r}-\mathbf{r}'\to\mathbf{p}/\hbar$ is meaningful. Furthermore, $\Delta_{ab}(\mathbf{p},t)$ has the structure $\Delta_{ab}(\mathbf{p},t) = e^{(i/\hbar)(\mu_a+\mu_b)t}\Delta_{ab}(\mathbf{p})$. Therefore, it is convenient to replace $F^{\mathrm{R}}_{ab}(\mathbf{p};t,t') \to e^{-(i/\hbar)(\mu_a+\mu_b)t}F^{\mathrm{R}}_{ab}(\mathbf{p};t-t')$. Then, in Fourier space, the equations for the retarded and advanced functions [see Eqs. (A3) and (A4) in the Appendix] read

$$[\hbar\omega - E_a(\mathbf{p}) - \hat{\Sigma}^{\mathrm{R/A}}_a(\mathbf{p},\omega)]g^{\mathrm{R/A}}_a(\mathbf{p},\omega) - \Delta_{ab}(\mathbf{p})F^{*\mathrm{A/R}}_{ab}(-\mathbf{p},-\omega) = 1, \tag{41}$$

$$[\hbar\omega - E_b(\mathbf{p}) + \mu_a + \mu_b - \hat{\Sigma}^{*\mathrm{A/R}}_b(-\mathbf{p},-\omega)]F^{*\mathrm{R/A}}_{ab}(\mathbf{p},\omega) + \Delta^*_{ab}(\mathbf{p})g^{\mathrm{A/R}}_a(-\mathbf{p},-\omega) = 0, \tag{42}$$

with $E_{a/b}(\mathbf{p}) = p^2/(2m_{a/b})$. These equations can be solved in a straightforward way. Identifying the self-energy of the condensed phase with

$$\Sigma^{\mathrm{LRO}}_a(\mathbf{p},\omega) = \frac{|\Delta_{ab}(\mathbf{p})|^2}{\hbar\omega + E_b(\mathbf{p}) - \mu_a - \mu_b + \hat{\Sigma}^{*\mathrm{R}}_b(\mathbf{p},\omega)}, \tag{43}$$

for g^{R}_a follows

$$g^{\mathrm{R}}_a(\mathbf{p},\omega) = \frac{1}{\hbar\omega - E_a(\mathbf{p}) - \hat{\Sigma}^{\mathrm{R}}_a(\mathbf{p},\omega) - \Sigma^{\mathrm{LRO}}_a(\mathbf{p},\omega)}. \tag{44}$$

With the solution [Eqs. (43) and (44)] the well-known BCS scheme[29,38] generalized to a two-component system and including the influence of the normal phase is obtained. The spectral function, which determines, in the thermodynamic equilibrium, the properties of the many-particle system, completely follows immediately from Eq. (44),

$$a_a(\mathbf{p},\omega) = \frac{\Gamma_a(\mathbf{p},\omega)}{[\hbar\omega - E_a(\mathbf{p}) - \mathrm{Re}\,\hat{\Sigma}^{\mathrm{R}}_a(\mathbf{p},\omega) - \mathrm{Re}\,\Sigma^{\mathrm{LRO}}_a(\mathbf{p},\omega)]^2 + \left[\frac{1}{2}\Gamma_a(\mathbf{p},\omega)\right]^2},$$

$$\Gamma_a(\mathbf{p},\omega) = 2[\mathrm{Im}\,\hat{\Sigma}_a^{\mathrm{R}}(\mathbf{p},\omega) + \mathrm{Im}\,\Sigma_a^{\mathrm{LRO}}(\mathbf{p},\omega)]. \tag{45}$$

Here, $\hat{\Sigma}_a^{\mathrm{R}}$ follows from Eq. (34). This approximation comprises both the random-phase approximation (RPA) self-energy and higher-order ladder terms and, thus, describes collective effects such as screening, as well as strong collisions, and bound states.

An essential simplification can be obtained if we can assume that $\Gamma_a(\mathbf{p},\omega) < \mathrm{Re}\,\hat{\Sigma}_a^{\mathrm{R}}(\mathbf{p},\omega)$. Then the spectral function may be expanded into a Taylor series with respect to Γ_a (*extended quasiparticle approximation*),

$$a_a(\mathbf{p},\omega) = 2\pi\delta[\hbar\omega - E_a(\mathbf{p}) - \mathrm{Re}\,\Sigma_a^{\mathrm{LRO}}(\mathbf{p},\omega) - \mathrm{Re}\,\hat{\Sigma}_a^{\mathrm{R}}(\mathbf{p},\omega)] + \Gamma_a(\mathbf{p},\omega)\frac{d}{d\Gamma_a}a(\mathbf{p},\omega)|_{\Gamma_a\to 0}. \tag{46}$$

Following now the ideas of the extended quasiparticle approximation,[3,32,39,40] we get finally,

$$a_a(\mathbf{p},\omega) = |u_p|^2\left\{\left[1 + |u_p|^2\frac{\partial}{\partial\omega}\mathrm{Re}\,\hat{\Sigma}_a^{\mathrm{R}}(\mathbf{p},\omega)|_{\hbar\omega=E_a^+(\mathbf{p})}\right] \times 2\pi\delta[\hbar\omega - E_a^+(\mathbf{p})] - \Gamma_a(\mathbf{p},\omega)\frac{\partial}{\partial\omega}\frac{\mathcal{P}}{\hbar\omega - E_a^+(\mathbf{p})}\right\} + |v_p|^2\left\{\left[1 + |v_p|^2\frac{\partial}{\partial\omega}\mathrm{Re}\,\hat{\Sigma}_a^{\mathrm{R}}(\mathbf{p},\omega)|_{\hbar\omega=E_a^-(\mathbf{p})}\right] \times 2\pi\delta[\hbar\omega - E_a^-(\mathbf{p})] - \Gamma_a(\mathbf{p},\omega)\frac{\partial}{\partial\omega}\frac{\mathcal{P}}{\hbar\omega - E_a^-(\mathbf{p})}\right\}, \tag{47}$$

where $E_a^{\pm}$ are the renormalized dispersion relations,

$$E_a^{\pm}(\mathbf{p}) = \left[\frac{1}{2}\{\varepsilon_a(\mathbf{p},\omega) - \varepsilon_b(\mathbf{p},\omega)\} \pm \sqrt{\varepsilon_{ab}^2(\mathbf{p},\omega) + |\Delta_{ab}(\mathbf{p})|^2}\right]_{\hbar\omega=E_a^{\pm}(\mathbf{p})}, \tag{48}$$

with $\varepsilon_a(\mathbf{p},\omega) = E_a(\mathbf{p}) - \mu_a + \mathrm{Re}\,\hat{\Sigma}_a^{\mathrm{R}}(\mathbf{p},\omega)$ and $\varepsilon_{ab}(\mathbf{p},\omega) = \frac{1}{2}[\varepsilon_a(\mathbf{p},\omega) + \varepsilon_b(\mathbf{p},\omega)]$.

The spectral weights u_p and v_p are given by

$$\left.\begin{matrix}|u_p|^2\\ |v_p|^2\end{matrix}\right\} = \frac{1}{1 - \frac{\partial}{\partial\omega}\mathrm{Re}\,\Sigma_a^{\mathrm{LRO}}(\mathbf{p},\omega)|_{\hbar\omega=E_a^{\pm}(\mathbf{p})}} = \frac{1}{2}\left[1 \pm \frac{\varepsilon_{ab}(\mathbf{p},\omega)}{\sqrt{\varepsilon_{ab}^2(\mathbf{p},\omega) + |\Delta_{ab}(\mathbf{p})|^2}}\right]_{\hbar\omega=E_a^{\pm}(\mathbf{p})}, \tag{49}$$

with $|u_p|^2 + |v_p|^2 = 1$. Particularly, if $\Delta_{ab} = 0$, also $v_p = 0$ and, therefore, $u_p = 1$ in this limit.

Equation (47) is an extension of the usual quasiparticle picture, which follows from Eq. (47) by restriction to the δ-function terms. The additional terms describe bound and scattering contributions between quasiparticles if Γ_a is taken in screened ladder approximation.

If the number of particles excited out of the condensate is negligible there holds $\hat{\Sigma}_a^{\mathrm{R}} \to 0$. Then the dispersion relation has explicit solutions given by

$$E_a^{\pm}(\mathbf{p}) = \frac{1}{2}[e_a(\mathbf{p}) - e_b(\mathbf{p})] \pm \sqrt{e_{ab}^2(\mathbf{p}) + |\Delta_{ab}(\mathbf{p})|^2}, \tag{50}$$

with $e_{a/b}(\mathbf{p}) = E_{a/b}(\mathbf{p}) - \mu_{a/b}$ and $e_{ab}(\mathbf{p}) = \frac{1}{2}[e_a(\mathbf{p}) + e_b(\mathbf{p})]$, which are the poles of the Green's function [Eq. (44)] with $\hat{\Sigma}_a^{\mathrm{R}} \to 0$, and can be interpreted as quasiparticle energies.[18,35] The functions u_p, v_p follow as residuals of the poles. Obviously, the one-particle energy cannot be less than $\Delta_{ab}(0)$. Thus, the excited states of the system are separated from the ground state by a gap, which is just given by the gap function. Then the spectral function has the simple form,

$$a_a(\mathbf{p},\omega) = 2\pi\{|u_p|^2\delta[\hbar\omega - E_a^+(\mathbf{p})] + |v_p|^2\delta[\hbar\omega - E_a^-(\mathbf{p})]\}. \tag{51}$$

IV. DENSITY, DEGREE OF IONIZATION, AND MOTT EFFECT

For a complete description of the system in the grand canonical ensemble it is necessary to determine the density as a function of the chemical potential and the temperature. A useful starting point is the general quantum statistical relation,

$$n_a(\mu,T) = \int \frac{d\mathbf{p}}{(2\pi\hbar)^3}\frac{d\omega}{2\pi}a_a(\mathbf{p},\omega)f_a(\omega), \tag{52}$$

with the Fermi function $f_a(\omega) = [\mathrm{e}^{(1/k_BT)(\hbar\omega-\mu_a)} + 1]^{-1}$. The inversion of Eq. (52) gives the chemical potential as a function of n and T, and, therefore, all thermodynamic properties of

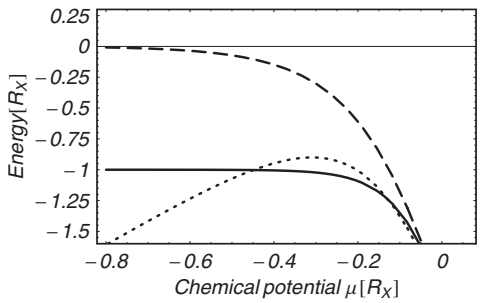

FIG. 1. Two-particle spectrum vs μ: continuum edge (dashed line), ground-state energy E_b (solid line), and effective chemical potential 2ζ [dotted line; for explanation see after Eq. (64)]; phase boundary of BEC defined by $2\zeta = E_b$. Temperature $T = 0.07R_X$, where R_X denotes the excitonic Rydberg.

the electron-hole plasma. In order to investigate the critical temperature of quantum condensation as a function of the density, it is sufficient to consider relation (52) for the normal phase, i.e., to use spectral function (47) with $v_p \to 0$ and $u_p \to 1$, which yields, following Refs. 3, 40, and 41,

$$n_a(\mu_a,T) = \int \frac{d\mathbf{p}}{(2\pi\hbar)^3} f(\varepsilon_a^{\mathrm{RPA}}) + \sum_{nl} (2l+1) \times \int \frac{d\mathbf{P}}{(2\pi\hbar)^3} n_{ab}^B\left(\frac{P^2}{2M} + E_{nl}\right) + \int_0^\infty \frac{d\omega}{2\pi} n_{ab}^B(\omega) \mathrm{Im}\, F(\omega), \tag{53}$$

$$F(\omega) = \mathrm{Tr}_{12}\left[\frac{d}{d\omega} \mathcal{G}_{ab}^{\mathrm{R}}(\omega) T_{ab}^{\mathrm{R}}(\omega)\right], \tag{54}$$

with[3,32]

$$\varepsilon_a^{\mathrm{RPA}}(\mathbf{p}) = E_a(\mathbf{p}) + \mathrm{Re}\, \Sigma_a^{\mathrm{RPA}}(\mathbf{p},\omega)|_{\hbar\omega=\varepsilon_a^{\mathrm{RPA}}} = E_a(\mathbf{p}) + \Sigma_a^{\mathrm{HF}}(\mathbf{p}) + \mathrm{Re}\, \Sigma_a^{\mathrm{MW}}(\mathbf{p},\omega)|_{\hbar\omega=\varepsilon_a^{\mathrm{RPA}}},$$

$$n_{ab}^B(\omega) = \frac{1}{e^{(1/k_BT)(\hbar\omega-\mu_a-\mu_b)} - 1}.$$

Equation (53) contains, besides the quasiparticle contribution (first term on the right-hand side), also contributions from two-particle bound (second term) and scattering states (third term). The latter terms correspond to the Gaussian fluctuations about the saddle point within the functional-integral formulation of the problem for Fermi atom systems.[21] Note that in the first term on the right-hand side of Eq. (53) $f(\varepsilon_a^{\mathrm{RPA}})$ occurs because we have expanded the full quasiparticle distribution $f(\varepsilon_a)$ with respect to the higher-order ladder terms, which have been transferred into the scattering contribution [last term on the right-hand side of Eq. (53)].

A further evaluation is possible if we carry out a partial-wave expansion and introduce scattering phases. Then a generalized Beth-Uhlenbeck expression for the scattering part may be derived,[3,41]

$$\int_0^\infty \frac{d\omega}{2\pi} n_{ab}^B(\omega) \mathrm{Im}\, F(\omega) = \int \frac{d\mathbf{P}}{(2\pi\hbar)^3} \sum_l (2l+1) \times \int_0^\infty \frac{d\omega}{2\pi} n_{ab}^B(\omega) \frac{d}{d\omega} \delta_l(\omega). \tag{55}$$

Obviously, for the application of this relation we need the solution of the two-particle bound and scattering problem. Quantum mechanics determines the properties of a two-particle system from the stationary Schrödinger equation. In a dense plasma the influence of the surrounding medium has to be taken into account, i.e., (i) influence of the Pauli blocking or phase space occupation effect, (ii) self-energy corrections to the kinetic energy, and (iii) screening of the interaction between the two particles.

A solution of this problem needs a careful analysis of the Bethe-Salpeter equation for the two-time two-particle Green's function [Eq. (28)] in dynamically screened ladder approximation, following from Eq. (6) for $t_1=t_2$, $t_1'=t_2'$. As differential equation, this equation is given by

$$\left\{i\hbar\frac{\partial}{\partial t} - \mathrm{H}_{ab}^0\right\} G_{ab}(t,t') - \int dt_1 dt_2 [\Sigma_a(t,t_1)\delta(t-t_2) + \Sigma_b(t,t_2)\delta(t-t_1)] G_{ab}(t_1t_2,t't') - \int dt_1 dt_2 dt_3 dt_4 [G_a(t,t_1)\delta(t-t_2) + G_b(t,t_2)\delta(t-t_1)] W_{ab}(t_1t_2,t_3t_4) G_{ab}(t_3t_4,t't') = -i\hbar N_{ab}(t)\delta(t-t'), \tag{56}$$

with $\mathrm{H}_{ab}^0 = \mathrm{H}_a + \mathrm{H}_b$. Because of the dynamical self-energy and the dynamical character of the effective interaction, this equation also contains the two-particle Green's function with three time arguments. Therefore, Eq. (56) is not a closed equation for $G_{ab}(t,t')$. Approximate solutions of this problem resulting in complicated Bethe-Salpeter equations are given for the Matsubara Green's functions in Refs. 8 and 9 and for the real time functions in Refs. 11 and 30. The result of such investigations is an effective Schrödinger equation for the determination of the two-particle properties of the electron-hole plasma following from the homogeneous BSE,[8,30]

$$[\mathrm{H}_{ab}^0 + \mathrm{V}_{ab} - E_{\alpha\mathbf{P}}(\omega,t) + \mathrm{H}_{ab}^{pl}(\omega,t)]|\psi_{\alpha\mathbf{P}}(\omega,t)\rangle = 0. \tag{57}$$

The influence of the surrounding plasma on the two-particle properties is described by the in-medium part $\mathrm{H}_{ab}^{pl}(\omega,t)$, explicitly given in Ref. 32. As numerical solutions of the full dynamical Schrödinger equation (57) and its static limit show[32] that it is, in many cases, sufficient to use the static limit because that limit describes all the essential features of the two-particle spectrum. It is given by

$$[\mathrm{H}_{ab}^{\mathrm{eff}} - \mathrm{N}_{ab}\mathrm{V}_{ab}^s]|\psi_E\rangle = E|\psi_E\rangle, \tag{58}$$

$$\mathrm{H}_{ab}^{\mathrm{eff}} = \mathrm{H}_{ab}^0 + \Sigma_a + \Sigma_b; \quad \Sigma_a = \Sigma_a^{\mathrm{HF}} + \Delta, \tag{59}$$

where Δ is the rigid shift approximation of the Montroll-Ward part of the self-energy[3] and V_{ab}^s is the statically screened Coulomb potential,

$$\Delta = -\frac{\kappa e^2}{2}, \quad V_{ab}^s(r) = -\frac{e_a e_b}{4\pi\epsilon_0\epsilon_r}\frac{e^{-\kappa r}}{r},$$

$$\kappa^2 = \frac{e^2}{\epsilon_0\epsilon_r k_B T}\left(\frac{\partial n_e}{\partial\mu} + \frac{\partial n_h}{\partial\mu}\right). \tag{60}$$

The resulting two-particle spectrum with static screening is shown in Fig. 1. Here and in all subsequent figures, results are shown for a model semiconductor with equal masses of electrons and holes and a background dielectric constant of $\epsilon_r=7$, corresponding approximately to the parameters of Cu_2O. It turns out that the plasma modifies the electron-hole pair in the following way:[8]

(1) There is a lowering of the continuum edge (Fig. 1) given by

$$\Delta E_{ab} = \Sigma_a^{\mathrm{HF}} + \Sigma_b^{\mathrm{HF}} + \Delta. \tag{61}$$

(2) The exciton ground-state energy can be written as

$$E_b = E_b^0 + \delta, \tag{62}$$

where δ is determined by the solution of Eq. (58). The energy E_b is lowered but it shows a weaker density dependence as compared to the continuum edge (Fig. 1). This follows from an approximative compensation of the many-particle effects.[8]

(3) The influence of the plasma leads to a lowering of the ionization energy, i.e., we have an effective ionization energy (Fig. 1). In our approximation it is given by

$$I^{\mathrm{eff}} = |E_b| + \Delta E_{\mathrm{eh}} = |E_b^0| - \delta + \Delta E_{\mathrm{eh}}. \tag{63}$$

In contrast to the isolated exciton, we have only a finite number of bound states.

(4) For $I^{\mathrm{eff}}=0$, the bound state vanishes and merges into the scattering continuum (Fig. 1). This is usually referred to as the *Mott effect*.

Due to the lowering of the ionization energy it may be expected that the bound-state part of the density has discontinuities at the critical values of the coupling parameter connected with drastic changes in the thermodynamic functions. However, one can show that the total density is a smooth function of the coupling parameter[6,32] because there is a compensation of the discontinuities by contributions of the scattering part. By application of the higher-order Levinson theorems,[32] these parts may be transferred into the bound-state contribution. At lower temperatures, the remainder of the scattering part can be neglected. Using the self-energy in rigid shift approximation and taking into account only the lowest bound state, we get for the electron density,

$$\begin{aligned} n_e(\zeta_e,\zeta_h,T) &= (2s+1)\int \frac{d\mathbf{p}}{(2\pi\hbar)^3}\frac{1}{\mathrm{e}^{1/k_BT[E(\mathbf{p})-\zeta_e]}+1} \\ &\quad + (2s+1)^2\int \frac{d\mathbf{P}}{(2\pi\hbar)^3} \\ &\quad \times\left\{\frac{1}{\mathrm{e}^{1/k_BT[P^2/2M+I^{\mathrm{eff}}(\zeta_e,\zeta_h,T)-\zeta_e-\zeta_h]}-1}\right. \\ &\quad - \frac{1}{\mathrm{e}^{1/k_BT(P^2/2M-\zeta_e-\zeta_h)}-1} \\ &\quad \left. - \frac{M}{P^2}I^{\mathrm{eff}}(\zeta_e,\zeta_h,T)\frac{1}{\mathrm{e}^{1/k_BT(P^2/2M-\zeta_e-\zeta_h)}-1}\right\} \\ &= n_{\mathrm{QP}}(\zeta_e,\zeta_h,T) + n_{\mathrm{bound}}(\zeta_e,\zeta_h,T), \end{aligned} \tag{64}$$

with the effective chemical potential $\zeta=\mu+\kappa e^2/2$, the quasiparticle energy $E(\mathbf{p})=p^2/(2m_e)+\Sigma^{\mathrm{HF}}(p=0)/2$, and $M=m_e+m_h$.

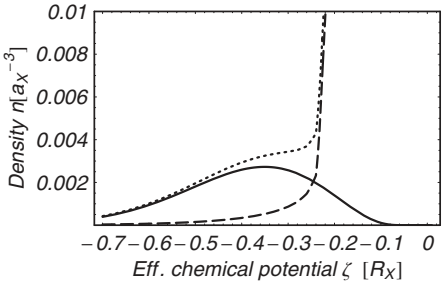

FIG. 2. Electron density as a function of the effective chemical potential: total density n_e (dotted line), quasiparticle contribution n_{QP} (dashed line), and bound-state contribution n_{bound} (solid line), see Eq. (64). Temperature $k_BT=0.133R_X$.

The first term in Eq. (64) is the contribution of the free quasiparticles. The second term is a generalization of the Planck-Larkin bound-state contribution to Bose particles.[6,40] The densities as a function of the effective chemical potential ζ are plotted in Fig. 2.

With the subdivision of the density [Eq. (64)], the bound and quasiparticle fractions are given and the degree of ionization as a function of μ,

$$\alpha(\mu,T) = \frac{n_{\mathrm{QP}}(\mu,T)}{n_{\mathrm{tot}}(\mu,T)}, \tag{65}$$

may be determined. With $n(\mu,T)$ from Eq. (64) we obtain $\alpha(n,T)$. Isotherms of the degree of ionization as a function of the density are shown in Fig. 3. We observe a very strong increase in the degree of ionization up to $\alpha=1$ due to the lowering of the ionization energy.[6,7] This behavior is usually referred to as *Mott transition* as a consequence of the Mott effect.

V. GAP AND PHASE BOUNDARY OF QUANTUM CONDENSATION

The crucial quantity in the theory is the gap function Δ_{ab}. It determines all relevant quantities of the quantum condensate, e.g., the quasiparticle energy, the spectral weights, the macro-wave–function, etc. For its determination we start from Eq. (27). In the Fourier representation follows

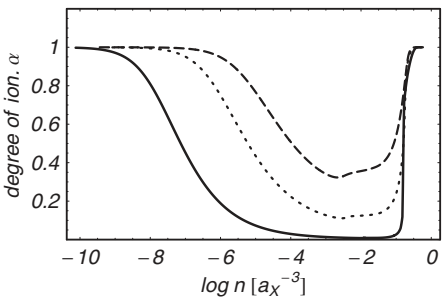

FIG. 3. Degree of ionization for temperatures of $0.1R_X$ (solid line), $0.15R_X$ (dotted line), and $0.2R_X$ (dashed line).

$$\Delta_{ab}(\mathbf{p}) = i\hbar \int \frac{d\bar{\mathbf{p}}}{(2\pi\hbar)^3} V^s_{ab}(\mathbf{p}-\bar{\mathbf{p}}) \times \mathcal{G}^{\mathrm{R}}_{ab}(\bar{\mathbf{p}}, -\bar{\mathbf{p}}; \omega)\Big|_{\hbar\omega=\mu_a+\mu_b} \Delta_{ab}(\bar{\mathbf{p}}), \tag{66}$$

where V^s_{ab} is the statically screened Coulomb potential. The free pair propagator,

$$\mathcal{G}^{\mathrm{R}}_{ab}(\omega) = \int \frac{d\bar{\omega}}{2\pi} \int \frac{d\bar{\bar{\omega}}}{2\pi} \frac{g^{>}_a(\bar{\omega}) g^{>}_b(\bar{\bar{\omega}}) - g^{<}_a(\bar{\omega}) g^{<}_b(\bar{\bar{\omega}})}{\omega - \bar{\omega} - \bar{\bar{\omega}} + i\epsilon}, \tag{67}$$

entering the gap equation will be calculated with the spectral representation for $g^{<}_a$ and spectral function (51). However, in order to get the usual form of the gap equation one has to replace one of the correlation functions in each product in Eq. (67) by the quasiparticle one.[3] By this procedure, we get the nonlinear gap equation,

$$\Delta_{ab}(\mathbf{p}) = \frac{e^2}{\epsilon_0\epsilon_r} \int \frac{d\bar{\mathbf{p}}}{(2\pi\hbar)^3} \frac{\hbar^2}{(\mathbf{p}-\bar{\mathbf{p}})^2 + \hbar^2\kappa^2} \times \frac{\Delta_{ab}(\bar{\mathbf{p}})}{2\sqrt{[e_{ab}(\bar{\mathbf{p}})]^2 + |\Delta_{ab}(\bar{\mathbf{p}})|^2}} \{f[E^+_a(\bar{\mathbf{p}})] - f[E^-_a(\bar{\mathbf{p}})]\}. \tag{68}$$

Comparing the gap equation with Eq. (26) the macro-wave-function may be expressed in terms of the gap function. It follows immediately

$$\Phi_{ab}(\mathbf{p}) = \frac{\Delta_{ab}(\mathbf{p})}{2\sqrt{[e_{ab}(\mathbf{p})]^2 + |\Delta_{ab}(\mathbf{p})|^2}} \{f[E^+_a(\mathbf{p})] - f[E^-_a(\mathbf{p})]\}. \tag{69}$$

With Δ_{ab} from Eq. (69), a nonlinear Schrödinger-like equation for the macro-wave-function follows,

$$[e_a(\mathbf{p}) + e_b(\mathbf{p})]\Phi_{ab}(\mathbf{p}) - \sqrt{\{f[E^+_a(\mathbf{p})] - f[E^-_a(\mathbf{p})]\}^2 - 4|\Phi_{ab}(\mathbf{p})|^2} \times \int \frac{d\bar{\mathbf{p}}}{(2\pi\hbar)^3} V_{ab}(\mathbf{p}-\bar{\mathbf{p}})\Phi_{ab}(\bar{\mathbf{p}}) = 0. \tag{70}$$

We shall remark here that Eq. (70) follows directly from Eq. (A9) (see Appendix) in the homogeneous stationary case using spectral function (51).

A central problem in the theory of quantum condensation is the calculation of the critical temperature T_{crit} as a function of the chemical potential or the density, i.e., the phase boundary of the condensate. This boundary is determined by the vanishing of the gap. Under this condition Eq. (68) reduces to the linearized form,

$$\Delta_{ab}(\mathbf{p}) = -\frac{e^2}{\epsilon_0\epsilon_r} \int \frac{d\bar{\mathbf{p}}}{(2\pi\hbar)^3} \frac{\hbar^2}{(\mathbf{p}-\bar{\mathbf{p}})^2 + \hbar^2\kappa^2} \frac{\Delta_{ab}(\bar{\mathbf{p}})}{e_{ab}(\bar{\mathbf{p}})} \times \{1 - f[e_a(\bar{\mathbf{p}})] - f[e_b(\bar{\mathbf{p}})]\}. \tag{71}$$

Discretizing the momentum on a lattice transforms the homogeneous integral Eq. (71) into a homogeneous linear system of equations, which has nontrivial solutions, only if the coefficient determinant vanishes. This condition yields a connection $T_{\mathrm{crit}}(\mu)$, i.e., the phase boundary of the quantum condensate. It is plotted in Fig. 4.

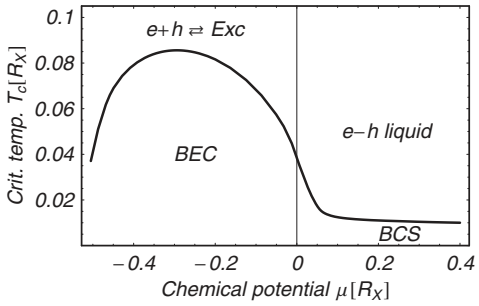

FIG. 4. Critical temperature as a function of the chemical potential.

We find the inset of the Bose condensation of excitons at $\mu_e+\mu_h=-1$ and $T=0$. With increasing chemical potential, the critical temperature increases and reaches maximum. The region of Bose condensation of excitons is limited by the Mott transition and we observe a smooth crossover to the phase boundary of a BCS state. A similar result has been obtained in Ref. 26. The critical temperatures of BEC agree approximately, however, we find a lower BCS critical temperature.

With the density relation (64), the critical temperature may be determined as a function of the density. The result is shown in Fig. 5. At lower densities, the critical temperature agrees with the condition for Bose condensation of ideal excitons, $n\lambda^3=2.61$, as a consequence of the neglection of the exciton-exciton interaction in our model. With increasing density, a strong deviation from the ideal behavior occurs due to the lowering of the ionization energy and the Mott effect. Furthermore, a smooth crossover to the BCS regime can be observed.

This behavior is confirmed in Fig. 6 where the critical temperature is given in units of the Fermi energy vs the inverse Fermi momentum. This curve shows a monotonic run in contrast to calculations for short-range interacting Fermi atoms.[42] We are here, however, in agreement with results from Haussmann.[23]

VI. CONCLUSION AND OUTLOOK

Summarizing our investigations, we have presented a description of quantum condensation in the electron-hole plasma of highly excited semiconductors.

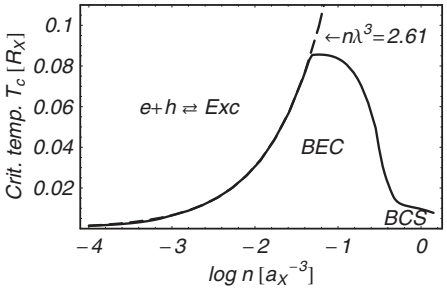

FIG. 5. Phase boundary of the quantum condensate vs density.

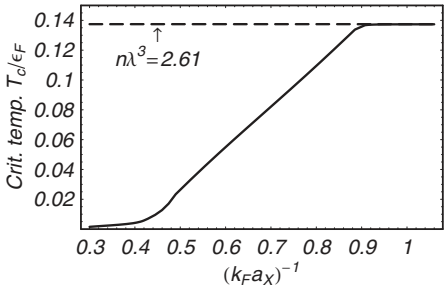

FIG. 6. Critical temperature of quantum condensation vs inverse Fermi momentum.

In the framework of real time Green's functions applying the concept of time long-range order for the two-particle Green's function, we have derived nonequilibrium Gorkov equations on the Keldysh time contour. In order to consider electron-hole plasmas, the theory has been specified to systems with Coulomb interaction using the screened ladder approximation.

In thermodynamic quasiequilibrium, we have obtained the usual BCS scheme of equations in terms of the screened potential for the two-component case including the influence of the normal phase.

The analysis of the density in screened ladder approximation and the associated two-particle problem in a plasma environment shows a lowering of the ionization energy and finally a breakup of bound states with increasing density, the Mott effect. Therefore, we observe a transition from a partially ionized *e-h* plasma to a high-density *e-h* liquid connected with a change in the physical nature of the quantum condensate (BEC-BCS crossover). At this transition, the density remains a smooth function of the coupling. The phase boundary of the quantum condensate arises from the condition of vanishing gap function. Therefore, we have determined the critical temperature as a function of the chemical potential by solution of the linearized gap equation with a statically screened Coulomb potential. The result shows a smooth crossover from the Bose-Einstein condensate of excitons to BCS states at high densities as expected for Fermi systems with bound states. Using the density equation in screened ladder approximation obtained before, we have eliminated the chemical potential in favor of the density and confirmed the smooth crossover in the critical temperature vs n.

The presented theoretical scheme has been elaborated in detail approximating the general effective interaction W_{ab} in the Bethe-Salpeter equation by the dynamically screened potential. The approach is, however, not restricted to that approximation. The freedom in choosing an appropriate W_{ab} opens the possibility to account for three-particle and four-particle processes, i.e., carrier-exciton and exciton-exciton interactions.

ACKNOWLEDGMENTS

We would like to thank T. Schmielau (Sheffield), G. Manzke, Th. Bornath, W.-D. Kraeft, F. Richter, K. Kilimann (Rostock), H. Fehske, and F. X. Bronold (Greifswald) for many fruitful discussions. This work was supported by the Deutsche Forschungsgemeinschaft (Collaborative Research Center SFB 652).

APPENDIX

In Sec. III, generalized Gorkov equations on the Keldysh time contour have been derived, see Eqs. (39) and (40). By time specialization on the contour, there follow Kadanoff-Baym-like equations[43] for the correlation functions $g_a^{\gtrless}$ and $F_{ab}^{\gtrless}$,

$$\left\{ i\hbar\frac{\partial}{\partial t_1} + \frac{1}{2m_a}[-i\hbar\nabla_1 - e_a\mathbf{A}(1)]^2 + \epsilon_a \right\} g_a^{\gtrless}(1,1') - \int d\bar{1}[\hat{\Sigma}_a^{\mathrm{R}}(1,\bar{1})g_a^{\gtrless}(\bar{1},1') + \hat{\Sigma}_a^{\gtrless}(1,\bar{1})g_a^{\mathrm{A}}(\bar{1},1')] - \int d\bar{1}\Delta_{ab}(1\bar{1})F_{ab}^{*\gtrless}(1'\bar{1}) = 0, \tag{A1}$$

$$\left\{ i\hbar\frac{\partial}{\partial t_1'} - \frac{1}{2m_b}[-i\hbar\nabla_{1'} - e_b\mathbf{A}(1')]^2 - \epsilon_b \right\} F_{ab}^{*\gtrless}(11') - \int d\bar{1}[\hat{\Sigma}_b^{*\mathrm{R}}(1',\bar{1})F_{ab}^{*\gtrless}(1\bar{1}) + \hat{\Sigma}_b^{*\lessgtr}(1',\bar{1})F_{ab}^{*\mathrm{R}}(1\bar{1})] - \int d\bar{1}\Delta_{ab}^*(\bar{1}1')g_a^{\lessgtr}(\bar{1},1) = 0. \tag{A2}$$

The equations for the retarded and advanced Green's functions follow easily from the definition and Eqs. (A1) and (A2) as

$$\left\{ i\hbar\frac{\partial}{\partial t_1} + \frac{1}{2m_a}[-i\hbar\nabla_1 - e_a\mathbf{A}(1)]^2 + \epsilon_a \right\} g_a^{\mathrm{R/A}}(1,1') - \int d\bar{1}\hat{\Sigma}_a^{\mathrm{R/A}}(1,\bar{1})g_a^{\mathrm{R/A}}(\bar{1},1') - \int d\bar{1}\Delta_{ab}(1\bar{1})F_{ab}^{*\mathrm{A/R}}(1'\bar{1}) = \delta(1-1'), \tag{A3}$$

$$\left\{ i\hbar\frac{\partial}{\partial t_1'} - \frac{1}{2m_b}[-i\hbar\nabla_{1'} - e_b\mathbf{A}(1')]^2 - \epsilon_b \right\} F_{ab}^{*\mathrm{R/A}}(11') - \int d\bar{1}\hat{\Sigma}_b^{*\mathrm{A/R}}(1',\bar{1})F_{ab}^{*\mathrm{R/A}}(1\bar{1}) - \int d\bar{1}\Delta_{ab}^*(\bar{1}1')g_a^{\mathrm{A/R}}(\bar{1},1) = 0. \tag{A4}$$

From Eqs. (A1)–(A4), kinetic equations for the Wigner function (Boltzmann equation) and the macro-wave-function may be derived. The latter one follows from adding Eq. (A2) and the corresponding one differentiating after the dashed variables;

$$\left\{ i\hbar\frac{\partial}{\partial t} + \frac{1}{2m_a}[-i\hbar\nabla_1 - e_a\mathbf{A}(\mathbf{r}_1,t)]^2 + \frac{1}{2m_b}[-i\hbar\nabla_{1'} - e_b\mathbf{A}(\mathbf{r}_1',t)]^2 + \epsilon_a + \epsilon_b \right\}\Phi_{ab}(\mathbf{r}_1\mathbf{r}_1',t) - V_{ab}(\mathbf{r}_1 - \mathbf{r}_1')\Phi_{ab}(\mathbf{r}_1\mathbf{r}_1',t)$$
$$+ \int d\bar{\mathbf{r}}_1[V_{ab}(\mathbf{r}_1 - \bar{\mathbf{r}}_1)\Phi_{ab}(\mathbf{r}_1\bar{\mathbf{r}}_1,t)\varrho_b(\mathbf{r}_1'\bar{\mathbf{r}}_1,t) + V_{ab}(\bar{\mathbf{r}}_1 - \mathbf{r}_1')\Phi_{ab}(\bar{\mathbf{r}}_1\mathbf{r}_1',t)\varrho_a(\mathbf{r}_1\bar{\mathbf{r}}_1,t)] + i\hbar\int d\bar{\mathbf{r}}_1\int d\bar{t}[\hat{\Sigma}_b^<(\mathbf{r}_1't,\bar{\mathbf{r}}_1\bar{t})F_{ab}^<(\mathbf{r}_1t,\bar{\mathbf{r}}_1\bar{t})$$
$$- \hat{\Sigma}_b^>(\mathbf{r}_1't,\bar{\mathbf{r}}_1\bar{t})F_{ab}^>(\mathbf{r}_1t,\bar{\mathbf{r}}_1\bar{t}) + F_{ab}^>(\bar{\mathbf{r}}_1\bar{t},\mathbf{r}_1't)\hat{\Sigma}_a^<(\mathbf{r}_1t,\bar{\mathbf{r}}_1\bar{t}) - F_{ab}^<(\bar{\mathbf{r}}_1\bar{t},\mathbf{r}_1't)\hat{\Sigma}_a^>(\mathbf{r}_1t,\bar{\mathbf{r}}_1\bar{t})] = 0. \tag{A5}$$

Besides the coupling of Φ_{ab} to the one-particle density matrix ϱ (equivalent to the coupling of F_{ab} and g_a), Eq. (A5) is not closed. As in the usual kinetic theory, a reconstruction problem has to be solved, that is here, expressing F_{ab} by Φ_{ab}. This can be done approximately applying the semigroup property of the retarded Green's function,

$$g_a^{\mathrm{R}}(1,1') = i\hbar\int d\bar{\mathbf{r}}_1 g_a^{\mathrm{R}}(\mathbf{r}_1t_1,\bar{\mathbf{r}}_1\bar{t}_1)g_a^{\mathrm{R}}(\bar{\mathbf{r}}_1\bar{t}_1,\mathbf{r}_1't_1') \tag{A6}$$

(note that this relation is exact only in the free or quasiparticle case), which implies for $g_a^{\gtrless}$,

$$g_a^{\gtrless}(1,1') = i\hbar\int d\bar{\mathbf{r}}_1 g_a^{\mathrm{R}}(\mathbf{r}_1t_1,\bar{\mathbf{r}}_1\bar{t}_1)g_a^{\gtrless}(\bar{\mathbf{r}}_1\bar{t}_1,\mathbf{r}_1't_1'). \tag{A7}$$

Then one finds

$$F_{ab}^{\gtrless}(11') = \int d\bar{\mathbf{r}}_1\{\Theta(t_1 - t_1')g_a^{\mathrm{R}}(\mathbf{r}_1t_1,\bar{\mathbf{r}}_1t_1')\Phi_{ab}(\bar{\mathbf{r}}_1\mathbf{r}_1',t_1') + \Theta(t_1' - t_1)g_b^{\mathrm{R}}(\mathbf{r}_1't_1',\bar{\mathbf{r}}_1t_1)\Phi_{ab}(\mathbf{r}_1\bar{\mathbf{r}}_1,t_1)\}. \tag{A8}$$

Inserting these relations into Eq. (A5), one finally obtains

$$\left\{ i\hbar\frac{\partial}{\partial t} + \frac{1}{2m_a}[-i\hbar\nabla_1 - e_a\mathbf{A}(\mathbf{r}_1,t)]^2 + \frac{1}{2m_b}[-i\hbar\nabla_{1'} - e_b\mathbf{A}(\mathbf{r}_1',t)]^2 + \epsilon_a + \epsilon_b \right\}\Phi_{ab}(\mathbf{r}_1\mathbf{r}_1',t) - V_{ab}(\mathbf{r}_1 - \mathbf{r}_1')\Phi_{ab}(\mathbf{r}_1\mathbf{r}_1',t)$$
$$+ \int d\bar{\mathbf{r}}_1[V_{ab}(\mathbf{r}_1 - \bar{\mathbf{r}}_1)\Phi_{ab}(\mathbf{r}_1\bar{\mathbf{r}}_1,t)\varrho_b(\bar{\mathbf{r}}_1\mathbf{r}_1',t) + V_{ab}(\bar{\mathbf{r}}_1 - \mathbf{r}_1')\Phi_{ab}(\bar{\mathbf{r}}_1\mathbf{r}_1',t)\varrho_a(\bar{\mathbf{r}}_1\mathbf{r}_1,t)]$$
$$- i\hbar\int d\bar{\mathbf{r}}_1 d\bar{\bar{\mathbf{r}}}_1\int d\bar{t}[\hat{\Sigma}_b^{\mathrm{R}}(\mathbf{r}_1't,\bar{\mathbf{r}}_1\bar{t})g_a^{\mathrm{R}}(\mathbf{r}_1t,\bar{\bar{\mathbf{r}}}_1\bar{t})\Phi_{ab}(\bar{\bar{\mathbf{r}}}_1\bar{\mathbf{r}}_1,\bar{t}) + \hat{\Sigma}_a^{\mathrm{R}}(\mathbf{r}_1t,\bar{\mathbf{r}}_1\bar{t})g_b^{\mathrm{R}}(\mathbf{r}_1't,\bar{\bar{\mathbf{r}}}_1\bar{t})\Phi_{ab}(\bar{\mathbf{r}}_1\bar{\bar{\mathbf{r}}}_1,\bar{t})] = 0. \tag{A9}$$

This equation describes the dynamics of Φ_{ab} as the order parameter of quantum condensation. Due to the coupling to the one-particle density matrix, Eq. (A9) has to be solved simultaneously with the corresponding kinetic equation, which follows from Eq. (A1) in the equal-time limit.

[1] *Electron Hole Droplets in Semiconductors*, edited by C. D. Jeffries and L. V. Keldysh (North-Holland, Amsterdam, 1983).

[2] H. Haug and S. Schmitt-Rink, Prog. Quantum Electron. **9**, 3 (1984).

[3] R. Zimmermann, *Many-Particle Theory of Highly Excited Semiconductors* (Teubner, Leipzig, 1988).

[4] H. Haug and S. W. Koch, *Quantum Theory of the Optical and Electronic Properties of Semiconductors*, 4th ed. (World Scientific, Singapore, 1993).

[5] L. V. Keldysh, in *Bose–Einstein Condensation*, edited by A. Griffin, D. W. Snoke, and S. Stringari (Cambridge University Press, Cambridge, 1995).

[6] W. Ebeling, W. D. Kraeft, and D. Kremp, *Theory of Bound States and Ionization Equilibrium in Plasmas and Solids* (Akademie-Verlag, Berlin, 1976); *Theory of Bound States and Ionization Equilibrium in Plasmas and Solids* (Mir, Moscow, 1977).

[7] W. D. Kraeft, K. Kilimann, and D. Kremp, Phys. Status Solidi B **72**, 461 (1975).

[8] K. Kilimann, W. D. Kraeft, and D. Kremp, Phys. Lett. **61**, 393 (1977); R. Zimmermann, K. Kilimann, W. D. Kraeft, D. Kremp and G. Röpke, Phys. Status Solidi B **90**, 175 (1978).

[9] H. Haug and D. B. Tran Thoai, Phys. Status Solidi B **85**, 561 (1978).

[10] T. Schmielau, G. Manzke, D. Tamme, and K. Henneberger, Phys. Status Solidi B **221**, 215 (2000).

[11] T. Schmielau, Ph.D. thesis, Universität Rostock, 2001.

[12] S. A. Moskalenko, Fiz. Tverd. Tela (Leningrad) **4**, 246 (1962).
[13] J. P. Wolfe, J. L. Lin, and D. W. Snoke, in *Bose–Einstein Condensation*, edited by A. Griffin, D. W. Snoke, and S. Stringari (Cambridge University Press, Cambridge, 1995).
[14] E. Hanamura and H. Haug, Phys. Rep. **33**, 209 (1977).
[15] L. V. Keldysh and Yu. V. Kopaev, Sov. Phys. Solid State **6**, 2219 (1965).
[16] J. des Cloizeaux, J. Phys. Chem. Solids **26**, 259 (1965).
[17] B. I. Halperin and T. M. Rice, in *Solid State Physics*, edited by F. Seitz, D. Turnbull, and H. Ehrenreich (Academic, New York, 1968).
[18] R. Zimmermann, Phys. Status Solidi B **76**, 191 (1976).
[19] A. J. Leggett, in *Modern Trends in the Theory of Condensed Matter*, edited by A. Pekalski and R. Przystawa (Springer-Verlag, Berlin, 1980).
[20] P. Noziéres and S. Schmitt-Rink, J. Low Temp. Phys. **59**, 195 (1985).
[21] C. A. R. Sá de Melo, M. Randeria, and J. R. Engelbrecht, Phys. Rev. Lett. **71**, 3202 (1993).
[22] Y. Ohashi and A. Griffin, Phys. Rev. Lett. **89**, 130402 (2002); P. Pieri, L. Pisani, and G. C. Strinati, Phys. Rev. B **70**, 094508 (2004).
[23] R. Haussmann, Phys. Rev. B **49**, 12975 (1994).
[24] G. Röpke, in *Bose–Einstein Condensation*, edited by A. Griffin, D. W. Snoke, and S. Stringari (Cambridge University Press, Cambridge, 1995).
[25] T. J. Inagaki and M. Aihara, Phys. Rev. B **66**, 075204 (2002).
[26] F. X. Bronold and H. Fehske, Phys. Rev. B **74**, 165107 (2006).
[27] G. Penrose and L. Onsager, Phys. Rev. **104**, 576 (1956).
[28] G. N. Yang, Rev. Mod. Phys. **34**, 694 (1962).
[29] A. A. Abrikosov, L. P. Gorkov, and N. N. Dzyalozhinski, *Methods of Quantum Field Theory in Statistical Physics* (Fizmatgiz, Moscow, 1962) (Russian) *Methods of Quantum Field Theory in Statistical Physics* (Prentice-Hall, Englewood Cliffs, NJ, 1963).
[30] Th. Bornath, D. Kremp, and M. Schlanges, Phys. Rev. E **60**, 6382 (1999).
[31] L. V. Keldysh, Zh. Eksp. Teor. Fiz. **47**, 1515 (1964) [Sov. Phys. JETP **20**, 235 (1965)].
[32] D. Kremp, M. Schlanges, and W.-D. Kraeft, *Quantum Statistics of Nonideal Plasmas* (Springer, Berlin, 2005).
[33] P. C. Kwok and T. D. Schultz, J. Phys. C **2**, 1196 (1969).
[34] J. G. Ramos and A. A. Gomes, Nuovo Cimento Soc. Ital. Fis., A **3**, 441 (1971).
[35] H. Stolz, *Die Bedeutung der Bose–Einstein–Kondensation für das Verständnis makroskopischer Quantenphänomene*, ZIE-Preprint 75-6 (Akademie der Wissenschaften der DDR, Zentralinstitut für Elektronenphysik, Berlin, 1975).
[36] H. Stolz, *Einführung in die Vielelektronentheorie der Kristalle* (Akademie-Verlag, Berlin, 1974).
[37] W. Schäfer and M. Wegener, *Semiconductor Optics and Transport Phenomena* (Springer–Verlag, Berlin, 2002).
[38] A. L. Fetter and J. D. Walecka, *Quantum Theory of Many Particle Systems* (McGraw-Hill, New York, 1971).
[39] R. Zimmermann and H. Stolz, Phys. Status Solidi B **131**, 151 (1985).
[40] D. Kremp, W. D. Kraeft, and A. J. D. Lambert, Physica A **127**, 72 (1984).
[41] D. Kremp, W. D. Kraeft, and M. Schlanges, Contrib. Plasma Phys. **33**, 567 (1993).
[42] M. Randeria, in *Bose–Einstein Condensation*, edited by A. Griffin, D. W. Snoke, and S. Stringari (Cambridge University Press Cambridge, 1995).
[43] L. P. Kadanoff and G. Baym, *Quantum Statistical Mechanics* (Benjamin, New York, 1962).

A.2

Artikel 2

F. Richter, D. Semkat, D. Kremp, and K. Henneberger:

Ionization equilibrium and Mott transition in an excited semiconductor, phase diagram

Phys. Status Solidi C **6**, 532 (2009)

Phys. Status Solidi C **6**, No. 2, 532–536 (2009) / **DOI** 10.1002/pssc.200880314

physica status solidi c
www.pss-c.com
current topics in solid state physics

Ionization equilibrium and Mott transition in an excited semiconductor, phase diagram

F. Richter*, D. Semkat, D. Kremp, and K. Henneberger

Universität Rostock, Institut für Physik, 18051 Rostock, Germany

Received 23 May 2008, revised 13 June 2008, accepted 17 June 2008
Published online 21 October 2008

PACS 71.35.Ee, 71.35.Lk

* Corresponding author: e-mail felix.richter2@uni-rostock.de, Phone: +49-381-4986926, Fax: +49-381-4986922

The thermodynamic properties of an electron–hole plasma in a highly excited semiconductor are investigated. Special attention is directed to the influence of many-particle effects like screening, lowering of the ionization energy, and Mott effect on the ionization equilibrium. In particular, the Mott effect limits the region of existence of excitons and, therefore, of a possible Bose–Einstein condensate at low temperatures. Results for the chemical potential and the degree of ionization are presented for cuprous oxide. A possible window for the occurrence of a BEC of excitons taking into account the Mott effect is shown.

1 Introduction Dense electron–hole plasmas (EHP) in excited semiconductors are interesting physical systems both from the experimental and the theoretical point of view. The aim of this paper is to discuss the ionization equilibrium, the Mott transition and the phase diagram of an EHP excited in a semiconductor with parabolic valence and conduction bands. The electrons and the holes are Fermi particles with the effective masses m_e and m_h. Due to the attractive Coulomb interaction between electrons and holes, bound electron–hole pairs, the excitons, and the formation of an ionization equilibrium $e + h \rightleftarrows X$ are observed.

The behavior of an EHP in an excited semiconductor in principle is well understood [1,3]. A special feature is the lowering of the coupling with increasing density by many-particle effects like screening of the Coulomb interaction and, therefore, a breakup of the excitons usually referred to as Mott effect (density ionization) [5–7].

A qualitative overview about the different states of the EHP which could guide in particular experimentalists in the choice of parameters for experiments is given by the density–temperature ($n - T$) plane.

Because of the Mott transition which occurs roughly at $r_{sc} \simeq a_X$ (r_{sc} denotes the screening length, a_X the excitonic Bohr radius), the $n - T$ plane is divided into an area where bound states are possible ($r_{sc} > a_X$) and an area without bound states ($r_{sc} < a_X$), i.e., a high-density e–h liquid.

In the excitonic area, the formation of an ionization equilibrium turns up, with a strong dominance of excitons at lower temperatures. Since the excitons behave approximately like composite Bose particles, Bose condensation in the region $n\lambda^3 > 2.61$ [λ is the thermal deBroglie wavelength, $\lambda^2 = 2\pi\hbar^2/(mk_BT)$] may be expected if the chemical potential reaches the exciton 1s ground state energy [2, 8,9]. At higher densities, the region of Bose condensation of excitons is, of course, limited by the Mott transition. However, we underline that the vanishing of the excitons does not imply a disappearance of the condensed phase. As proposed, e.g., by Keldysh and Kopaev [10], in the high-density highly degenerate e–h liquid the formation of weakly bound cooperative Cooper pairs of electrons and holes and their Bose condensation to a BCS state may be expected, known as excitonic insulator.

Details of BEC of excitons and e–h pairs, however, are not in the main focus of the present work. For an overview and recent investigations see, e.g., [11–13].

2 Theory There are several possibilities for the quantum statistical approach to the equilibrium properties of the

EHP, outlined, e.g., in [14, 1]. A useful starting point is the general quantum statistical relation

$$n_a(\mu,T) = \int \frac{d\mathbf{p}}{(2\pi\hbar)^3}\frac{d\omega}{2\pi}\, a(\mathbf{p},\omega)\, f_a(\omega), \qquad (1)$$

expressing the particle density n_a as a function of the chemical potential μ and the temperature T. $f(\omega)$ is a Bose- or Fermi-like distribution, $a(\mathbf{p},\omega) = -2\mathrm{Im}\, g_a^r(\mathbf{p},\omega)$ the spectral function.

In the case of small damping, i.e., $\Gamma \ll \mathrm{Re}\Sigma^R$, we can expand the spectral function into a series with respect to Γ. The first order approximation reads (*extended quasiparticle approximation*) [17, 15]

$$\begin{aligned} a(\mathbf{p}\omega,\mathbf{R}t) &= 2\pi\,\delta\left(\omega - E(\mathbf{p},\mathbf{R}t)\right) \\ &\times\left\{1 + \frac{\partial}{\partial\omega}\mathcal{P}\int\frac{d\bar\omega}{2\pi}\,\frac{\Gamma_a(\mathbf{p}\bar\omega,\mathbf{R}t)}{\omega-\bar\omega}\Big|_{\omega=E}\right\} \\ &-\Gamma_a(\mathbf{p}\omega,\mathbf{R}t)\,\frac{\partial}{\partial\omega}\,\frac{\mathcal{P}}{\omega - E(\mathbf{p},\mathbf{R}t)}\,. \end{aligned} \qquad (2)$$

We proceed with the following steps:

1. In order to take into account bound states we assume for the self-energy Σ_a and, therefore, for Γ_a, the screened ladder approximation [1, 3].
2. According to the Γ_a expansion of the spectral function we expand the distribution function to e.g. [18]

$$f(E' + \mathrm{Re}\,\Sigma'') \approx f(E') + \mathrm{Re}\,\Sigma''\,\frac{df}{dE'},$$

where $E' = p^2/(2m) + \mathrm{Re}\,\Sigma^{\mathrm{RPA}}$ is the quasiparticle energy in *random phase approximation* (RPA), and Σ'' means higher order ladder terms convergent also for vanishing screening.

3. Using the bilinear expansion of the T-matrix, the density may be separated into bound and scattering parts.

In this way, we finally get for the electron density

$$\begin{aligned} n_e(\mu_e,\mu_h,T) &= \int\frac{d\mathbf{p}}{(2\pi\hbar)^3} f(E_e') \\ &+ \sum_{nl}(2l+1)\int\frac{d\mathbf{P}}{(2\pi\hbar)^3}\,\frac{1}{e^{\beta\left(\frac{P^2}{2M}+E_{nl}-\mu_e-\mu_h\right)}-1} \\ &+ \int_\Delta^\infty \frac{d\omega}{2\pi}\, n_{eh}^B(\omega)\,\mathrm{Im}\,F(\omega) \end{aligned} \qquad (3)$$

with $F(\omega) = \mathrm{Tr}_{12}\left[\frac{d}{d\omega}\mathcal{G}_{ab}^{\mathrm{R}}(\omega)T_{ab}^{\mathrm{R}}(\omega)\right]$, T_{ab}^{R} being the retarded T-matrix, $\beta = \frac{1}{k_BT}$, and $M = m_e + m_h$. The first term in (3) is the density of the free quasiparticles. The second term is the contribution of bound states [1, 3, 18] and the third one that of scattering states.

Obviously, for the application of this relation we need the solution of the two-particle bound and scattering problem under the influence of the surrounding dense e–h plasma. This problem was intensely discussed in [5]. We find a weak dependence of the bound state energy on the density and a strong decrease of the continuum edge due to the self-energy connected with a lowering of the effective ionisation energy $I^{\mathrm{eff}}(n,T)$. In particular, for vanishing ionisation energy, $I^{\mathrm{eff}}(n,T) = 0$, the bound state disappears at the Mott density.

The bound state contribution in Eq. (3) has a discontinuity if the difference of the bound state energy and the interaction parts of the chemical potentials μ_e, μ_h vanishes. However, the scattering part has the same discontinuity with opposite sign so that the total density is an analytical function. By application of the higher order Levinson theorems [16, 17] the corresponding parts may be transferred into the bound state contribution. At lower temperatures, the remainder of the scattering part can usually be neglected. Taking into account only the ground state we get for the electron density

$$\begin{aligned} n_e(\mu_e,\mu_h,T) &= \int\frac{d\mathbf{p}}{(2\pi\hbar)^3} f(E_e') + \int\frac{d\mathbf{P}}{(2\pi\hbar)^3} \\ &\times\left\{\frac{1}{e^{\beta\left(\frac{P^2}{2M}+E_{nl}-\mu_e-\mu_h\right)}-1} - \frac{1}{\mathrm{e}^{\beta\left(\frac{P^2}{2M}-\mu_e^{\mathrm{id}}-\mu_h^{\mathrm{id}}\right)}-1}\right. \\ &\left.-\frac{M}{P^2}(E_0-\Delta\mu_{eh})\frac{1}{\mathrm{e}^{\beta\left(\frac{P^2}{2M}-\mu_e^{\mathrm{id}}-\mu_h^{\mathrm{id}}\right)}-1}\right\}. \end{aligned} \qquad (4)$$

Here, we introduced the subdivision $\mu_e + \mu_h = \mu_e^{\mathrm{id}} + \mu_h^{\mathrm{id}} + \Delta\mu_{eh}$ separating the interaction contribution from the ideal parts of the chemical potential.

3 Chemical picture. BEC of the bound states

Up to now we considered the e–h plasma in grand canonical description as a two-component system with electrons and holes in scattering and bound states. We will call this description the physical picture. Then, Eq. (3) provides appropriate thermodynamics of the plasma. In contrast, the density expansion of the chemical potential following by approximate inversion of (3) leads to inconsistencies due to exponential divergencies at low temperatures.

In the following we will develop an alternative view on the bound states. Looking at their distribution function

$$n_{eh}^B\left(\frac{P^2}{2M}+E_{nl}\right) = \frac{1}{z_e^{-1}z_h^{-1}e^{\beta\left(E_{nl}+\frac{P^2}{2M}\right)}-1}, \qquad (5)$$

with $z_a = e^{\beta\mu_a}$ it is, obviously, convenient to consider *bound states as a new particle species (excitons)* which are characterized by the fugacity z_X, and the ideal distribution function

$$z_X = z_e z_h e^{-\beta E_{nl}}; \qquad n_X^B\left(\frac{P^2}{2M}\right) = \frac{1}{z_X^{-1}e^{\beta\frac{P^2}{2M}}-1}. \qquad (6)$$

Performing the latter step, we have made a fundamental change from the physical picture – the basic constituents

are only electrons and holes which can be in scattering or bound states – to a chemical picture where we have electrons, holes, and excitons as basic constituents of the system.

The density reads in the chemical picture

$$n_e(\mu,T) = \int \frac{d\mathbf{p}}{(2\pi\hbar)^3} f(E_e') + \int_{\Delta}^{\infty} \frac{d\omega}{2\pi} n_{eh}^B(\omega) \mathrm{Im}\, F(\omega) + \sum_{nl} (2l+1) \int \frac{d\mathbf{P}}{(2\pi\hbar)^3} n_X^B \left(\frac{P^2}{2M} \right) . \quad (7)$$

The excitons (bound Fermi particles) behave approximately like bosons. The singularities of the bound state contribution $E_{nl} + P^2/(2M) = \mu_e + \mu_h$ are well known to be connected with the Bose condensation of the bound states.

In the chemical picture, the EHP is characterized by the densities of free electrons n_e^*, free holes n_h^*, and the density of excitons n_X. We have a partially ionized plasma in the ionization equilibrium $e + h \rightleftarrows X$ which is controlled by the definition of the fugacities of the new particles (6). The latter relation determines the composition of the system and plays the role of a mass-action-law (MAL). It is equivalent to the well-known thermodynamic condition for the chemical (ionization) equilibrium

$$\mu_X = \mu_e + \mu_h - E_{nl} . \quad (8)$$

In the grand canonical description, the condition (8) is only a consequence of the definition of excitons.

From the previous consideration the chemical potential is in principle known. It is obtained by inversion of $n_e = n_e(\mu^{id} + \Delta\mu)$ [3,18]. Here, μ^{id} is the ideal contribution, and $\Delta\mu$ is the correlation part. The inversion with respect to the first order in $\Delta\mu$ is usually referred to as *incomplete inversion*. Then the ideal contribution for arbitrary degeneracy follows in well-known manner from

$$n_a(\mu_a^{id},T) = \int \frac{d\mathbf{p}}{(2\pi\hbar)^3} \frac{1}{e^{\beta\left(\frac{p^2}{2m_a} - \mu_a^{id}\right)} + 1} \quad (9)$$

and the chemical potential of the excitons is given by

$$n_X(\mu_X,T) = \int \frac{d\mathbf{P}}{(2\pi\hbar)^3} \frac{1}{e^{\beta\left(\frac{P^2}{2M} - \mu_X\right)} - 1} . \quad (10)$$

An analytical evaluation of the chemical potential from (3), in particular the correlation part in RPA, is possible only in limiting cases ($n\lambda^3 \ll 1$, $n\lambda^3 \gg 1$). In the general case numerical evaluations are necessary, carried out, e.g., for the EHP in [20]. For practical purposes it is useful to construct Padé formulae for the chemical potential and other thermodynamical functions from the limiting cases and the numerical results. Such formulae were given for the first time for hydrogen plasmas by Ebeling *et al.* [19].

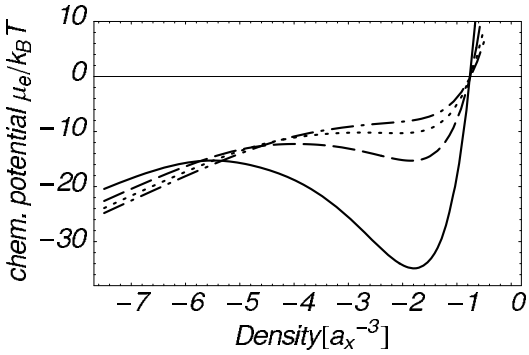

Figure 1 Chemical potential μ_e/k_BT vs. density for several temperatures k_BT: $0.03R_X$ (solid line), $0.07R_X$ (dashed line), $0.11R_X$ (dotted line), $0.15R_X$ (dash-dotted line).

For the EHP, Zimmermann [1] proposed a simple formula given by

$$\Delta\mu_Z(n,T) = \frac{C\, r_s^{-\frac{3}{4}}}{(1 + B\, r_s^3 \tau^2)^{\frac{1}{4}}} \quad (11)$$

with $(r_s a_X)^3 = 3/(4\pi n)$, $\tau = k_BT/R_X$, $C = 3.24$, $B = (C/2\sqrt{12})^4$, R_X being the excitonic Rydberg. A more general Padé formula was given by Rösler *et al.* [20].

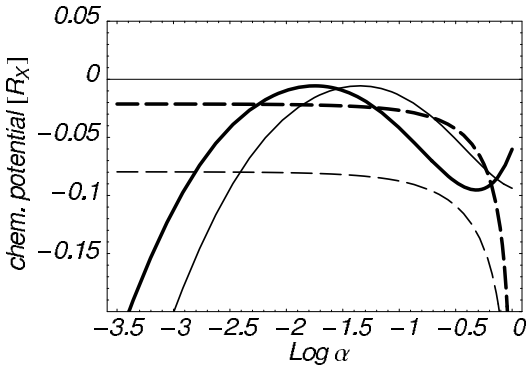

Figure 2 Chemical potential of the excitons μ_X [l.h.s. of Eq. (13); dashed lines] and sum of the chemical potentials of electrons and holes minus binding energy $\mu - E_{nl}$ [r.h.s. of Eq. (13); solid lines] vs. α for $k_BT = 0.09R_X$ and two densities: $n_e = 0.01a_X^{-3}$ (thin lines) and $n_e = 0.025a_X^{-3}$ (thick lines).

Isotherms of the chemical potential of the electrons are shown in Fig. 1. This and all subsequent results have been obtained for the EHP in cuprous oxide (Cu_2O) which is of special interest, amongst other things, due to the high exciton binding energy. Due to the interaction part $\Delta\mu$, below a critical temperature a van der Waals loop appears, i.e., a region with an instability $\frac{\partial\mu}{\partial n} \geq 0$, which may be a signal of a phase transition [3,1].

In order to describe the plasma composition we introduce the degree of ionization by

$$\alpha = \frac{n_e^*}{n_e}, \qquad n_e = n_e^* + n_X \,. \tag{12}$$

In terms of α and n_e, Eq. (8) is now

$$\mu_X[(1-\alpha)n_e, T] = \mu[\alpha n_e, T] - E_{nl} \tag{13}$$

with $\mu = \mu_e + \mu_h$ and the degree of ionization α as a function of density and temperature is obtained as the root of this equation. Figure 2 illustrates the solution of Eq. (13).

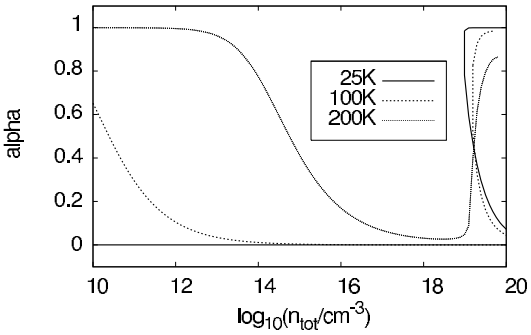

Figure 3 Degree of ionization α vs. density for several temperatures.

Isotherms of the degree of ionization as a function of the density are shown in Fig. 3. We observe a very strong increase of α up to $\alpha = 1$ due to the lowering of the ionization energy [4, 3]. This behavior is usually referred to as *Mott transition* as a consequence of the Mott effect. At low enough temperatures, the curves exhibit a region where α is multivalued, i.e., a bistability occurs. The reason of this behavior is obvious from Fig. 2: the van der Waals loop in the chemical potential. While for lower densities there is nevertheless only a single intersection of the curves, for higher densities three intersections are possible leading to three solutions for α for a given temperature and density. Thus, we find a bistability (the intermediate solution is unstable) and, therefore, a phase transition from an exciton gas to a fully ionized EHP. This effect is, however, possibly a theoretical artefact. Whether inclusion of the exciton–exciton interaction would remove the bistability (as known from the atom–atom interaction in the hydrogen plasma) is still an open question.

For an overview of the ionization state of the EHP, in Fig. 4 isolines $\alpha(n, T) = \text{const.}$ are shown. At lower temperatures we find a strong dominance of excitons and Bose–Einstein condensation (BEC) of excitons may be expected under the condition

$$(1-\alpha)n_e\Lambda^3 \geq 2.61 \,. \tag{14}$$

This condition is given in Fig. 4 by the shaded grey area. Note that the breakup at the Mott density does not mean a disappearance of the condensate. Instead, a closer investigation shows a smooth crossover to a BCS-type condensate at high densities [21, 13].

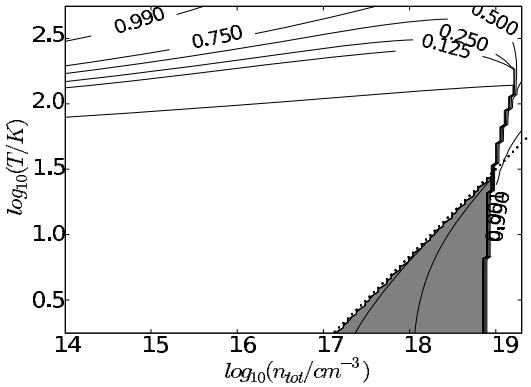

Figure 4 Isolines of the degree of ionization in the density–temperature plane. The shaded grey area denotes the region where BEC of excitons is possible, cf. Eq. (14).

Acknowledgements We would like to thank G. Manzke (Rostock) and T. Schmielau (Sheffield) for many fruitful discussions. This work was supported by the Deutsche Forschungsgemeinschaft (Collaborative Research Center SFB 652).

References

[1] R. Zimmermann, Many-Particle Theory of Highly Excited Semiconductors (Teubner, Leipzig, 1988).
[2] L. V. Keldysh, in: Bose–Einstein Condensation, edited by A. Griffin, D.W. Snoke, and S. Stringari (Cambridge University Press, 1995).
[3] W. Ebeling, W. D. Kraeft, and D. Kremp, Theory of Bound States and Ionization Equilibrium in Plasmas and Solids (Akademie-Verlag, Berlin, 1976; Mir, Moscow, 1977).
[4] W. D. Kraeft, K. Kilimann, and D. Kremp, Phys. Status Solidi B **72**, 461 (1975).
[5] K. Kilimann, W. D. Kraeft, and D. Kremp, Phys. Lett. A **61**, 393 (1977); R. Zimmermann, K. Kilimann, W. D. Kraeft, D. Kremp, and G. Röpke, Phys. Status Solidi B **90**, 175 (1978).
[6] H. Haug and D. B. Tran Thoai, Phys. Status Solidi B **85**, 561 (1978).
[7] T. Schmielau, G. Manzke, D. Tamme, and K. Henneberger, Phys. Status Solidi B **221**, 215 (2000).
[8] S. A. Moskalenko, Fiz. Tverd. Tela **4**, 246 (1962).
[9] E. Hanamura and H. Haug, Phys. Rep. C **33**, 209 (1979).
[10] L. V. Keldysh and Yu. V. Kopaev, Sov. Phys. Solid State **6**, 2219 (1965).
[11] S. A. Moskalenko and D. W. Snoke, Bose-Einstein Condensation of Excitons and Biexcitons and Coherent Nonlinear Optics with Excitons (Cambridge University Press, 2000).
[12] J. Kasprzak et al., Nature **443**, 409 (2006).
[13] D. Kremp, D. Semkat, and K. Henneberger, submitted to Phys. Rev. B.
[14] D. Kremp, M. Schlanges, and W.-D. Kraeft,Quantum Statistics of Nonideal Plasmas (Springer, Berlin, 2005).

[15] R. Zimmermann and H. Stolz, Phys. Status Solidi B **131**, 151 (1985).
[16] D. Bollé, Ann. Phys. (N.Y.) **121**, 131 (1979).
[17] D. Kremp, W. D. Kraeft, and A. J. D. Lambert, Physica A **127**, 72 (1984).
[18] D. Kremp, W. D. Kraeft, and M. Schlanges, Contrib. Plasma Phys. **33**, 567 (1993).
[19] W. Ebeling and W. Richert, Phys. Lett. A **108**, 80 (1985).
[20] M. Rösler, R. Zimmermann, and W. Richert, Phys. Status Solidi B **121**, 609 (1984).
[21] P. Noziéres and S. Schmitt-Rink, J. Low Temp. Phys. **59**, 195 (1985).

A.3

Artikel 3

D. Semkat, F. Richter, D. Kremp, G. Manzke, W.-D. Kraeft, and K. Henneberger:

Ionization equilibrium in an excited semiconductor: Mott transition vs. Bose-Einstein condensation

Phys. Rev. B **80**, 155201 (2009)

Ionization equilibrium in an excited semiconductor: Mott transition versus Bose-Einstein condensation

D. Semkat, F. Richter, D. Kremp, G. Manzke, W.-D. Kraeft, and K. Henneberger
Institut für Physik, Universität Rostock, 18051 Rostock, Germany
(Received 15 June 2009; revised manuscript received 4 September 2009; published 2 October 2009)

The ionization equilibrium of an electron-hole plasma in a highly excited semiconductor is investigated. Special attention is directed to the influence of many-particle effects such as screening and lowering of the ionization energy causing, in particular, the Mott effect (density ionization). This effect limits the region of existence of excitons and, therefore, of a possible Bose-Einstein condensate at low temperatures. Results for the chemical potential and the degree of ionization are presented for zinc selenide (ZnSe). A possible window for the occurrence of a Bose-Einstein condensate of excitons is shown, taking into account the Mott effect.

DOI: 10.1103/PhysRevB.80.155201 PACS number(s): 71.35.Ee, 71.35.Lk, 03.75.Hh, 03.75.Kk

I. INTRODUCTION

Dense electron-hole plasmas (EHPs) in excited semiconductors have attracted unwaning attention for decades both by experiment and theory. The understanding of the equilibrium properties of such a plasma, expressed by its phase diagram, is of fundamental importance for any investigation in this field. The aim of this paper is, therefore, to discuss certain aspects of the phase diagram of an EHP: the ionization equilibrium and, closely connected with the latter, the Mott transition.

Electrons and holes are Fermi particles with the effective masses m_e and m_h (parabolic valence and conduction bands). Due to the attractive Coulomb interaction between them, bound electron-hole pairs, the excitons, and the formation of an ionization equilibrium $e+h \rightleftarrows X$ are observed.

The behavior of an EHP in an excited semiconductor is, in principle, well understood.[1,2] A special feature is the weakening of the coupling with increasing density caused by many-particle effects such as screening of the Coulomb interaction and, therefore, a breakup of the excitons usually referred to as Mott effect (density ionization).[3–6]

The Mott effect is, in principle, understood as caused by lowering of the band edge, while the exciton energy only weakly changes with increasing density. This behavior is caused by an interplay of several many-particle effects. There are various approaches which can be found in the literature to describe the Mott effect, e.g., simple limiting cases known from quantum statistics such as Debye shift or Coulomb-hole shift for the band edge as well as statistically founded or empirical formulas for the Mott density in semiconductors (see, e.g., Refs. 7–9). Such formulas, however, are far away from the capabilities of modern many-particle theory and usually do not give more than a rough estimate. On the other hand, previous investigations of the ionization equilibrium[10] neglected degeneracy effects, e.g., by using the Saha equation. For this, a central aim of this work is to present a consistent quantum statistical theory of the ionization equilibrium and provide reliable data for the temperature dependence of the Mott density. A first step into that direction has been done in Ref. 11, where a general mass-action law (MAL) has been derived and applied to the ionization equilibrium in cuprous oxide (Cu_2O). A self-contained presentation of the theory together with a consistent treatment of the many-particle effects will be given in the present work.

A qualitative overview of the different states of the EHP which could guide in particular experimentalists in the choice of parameters for experiments can be given in the density-temperature (n-T) plane. Because of the Mott effect, which occurs roughly at $r_{sc} \simeq a_X$ (r_{sc} denotes the screening length, a_X the excitonic Bohr radius), the n-T plane is divided into an area where bound states are possible ($r_{sc} > a_X$) and an area without bound states ($r_{sc} < a_X$), i.e., a high-density electron-hole liquid. This subdivision, however, can only give a qualitative picture.

The behavior in the excitonic area is essentially governed by the formation of an ionization equilibrium, with a strong dominance of excitons at lower temperatures. Since the excitons behave approximately like composite Bose particles, Bose-Einstein condensation (BEC) in the region $n\Lambda_X^3 \geq 2.61$ [Λ_X is the thermal de Broglie wavelength, $\Lambda_X^2 = 2\pi\hbar^2/(Mk_BT)$, $M=m_e+m_h$] may be expected if the chemical potential reaches the exciton $1s$ ground-state energy.[12–14] At higher densities, the region of BEC of excitons is, of course, limited by the Mott transition. However, we underline that the vanishing of the excitons does not imply a disappearance of the condensed phase. As proposed, e.g., by Keldysh and Kopaev,[15] in the high-density highly degenerate electron-hole liquid, the formation of weakly bound cooperative Cooper pairs of electrons and holes and their Bose condensation to a BCS state may be expected, known as excitonic insulator. Details of BEC of excitons and electron-hole pairs, however, are not in the main focus of the present work. For an overview and recent investigations see, e.g., Refs. 16–19.

The ionization equilibrium is a topic which is extensively discussed in plasma physics, too.[2,20,21]

This paper is organized as follows. In Sec. II we derive briefly the basic quantum statistical theory of thermodynamics of the EHP. In Sec. III we introduce the chemical picture by redefining the bound states and discuss the resulting mass-action law. Since the latter needs the solution of the two-particle bound and scattering problem as an input, we discuss, in Sec. IV, the two-particle spectrum on the basis of the semiconductor Bloch equations. Finally, in Sec. V we present results of the solution of the general mass-action law valid for arbitrary degeneracy.

II. GENERAL THEORY

There are several possibilities for the quantum statistical approach to the equilibrium properties of the EHP, outlined, e.g., in Refs. 1, 21, and 22. For a better understanding, we will give a short review of the approach used here to describe the ionization equilibrium. A useful starting point is the general quantum statistical relation

$$n_a(\{\mu_c\},T) = g_a \int \frac{d\mathbf{k}}{(2\pi)^3} \int \frac{d\omega}{2\pi} A_a(\mathbf{k},\omega) f_a(\omega), \tag{1}$$

expressing the carrier density n_a of the species a as a function of the chemical potentials $\{\mu_c\}$ and the temperature T. $f_a(\omega)$ is a Fermi-like distribution, and g_a denotes the band multiplicity (including spin degeneracy) of species a. The spectral function $A_a(\mathbf{k},\omega) = -2\ \mathrm{Im}\ g_a^r(\mathbf{k},\omega)$ is related to the imaginary part of the retarded Green's function of carriers $g_a^r(\mathbf{k},\omega)$ and is explicitly given by[21]

$$A_a(\mathbf{k},\omega) = \frac{\hbar\Gamma_a(\mathbf{k},\omega)}{\left[\hbar\omega - \frac{\hbar^2k^2}{2m_a} - \mathrm{Re}\ \Sigma_a^r(\mathbf{k},\omega)\right]^2 + \left[\frac{1}{2}\Gamma_a(\mathbf{k},\omega)\right]^2}, \tag{2}$$

with the single-particle damping Γ_a defined by the self-energies $\Sigma_a^{\gtrless}$,

$$\Gamma_a(\mathbf{k},\omega) = -2\ \mathrm{Im}\ \Sigma_a^r(\mathbf{k},\omega) = i[\Sigma_a^>(\mathbf{k},\omega) - \Sigma_a^<(\mathbf{k},\omega)]. \tag{3}$$

The spectral function accounts for many-particle effects compactly in the retarded self-energy $\Sigma_a^r(\mathbf{k},\omega)$. With an appropriate approximation for the self-energy, the inversion of Eq. (1) gives $\mu_a = \mu_a(n_a,T)$ and, therefore, any thermodynamic property of the EHP in the grand canonical description.

In the case of small damping, i.e., $\Gamma_a \ll \mathrm{Re}\ \Sigma_a^r$, we can expand the spectral function into a series with respect to Γ_a. The first-order approximation reads[23,24]

$$A_a(\mathbf{k},\omega) = 2\pi\hbar\,\delta[\hbar\omega - E_a(\mathbf{k})] \times \left[1 + \frac{1}{\hbar}\frac{\partial}{\partial\omega}\mathcal{P}\int \frac{d\bar{\omega}}{2\pi}\ \frac{\Gamma_a(\mathbf{k},\bar{\omega})}{\omega - \bar{\omega}}\bigg|_{\hbar\omega = E_a(\mathbf{k})}\right] - \Gamma_a(\mathbf{k},\omega)\frac{\partial}{\partial\omega}\frac{\mathcal{P}}{\hbar\omega - E_a(\mathbf{k})}, \tag{4}$$

where $\mathcal{P}$ denotes the Cauchy principal value. The quasiparticle energy $E_a(\mathbf{k})$ is the solution of the dispersion relation

$$E_a(\mathbf{k}) = \frac{\hbar^2k^2}{2m_a} + \mathrm{Re}\ \Sigma_a^r(\mathbf{k},\omega)|_{\hbar\omega = E_a(\mathbf{k})}. \tag{5}$$

The approximation (4) is referred to as *extended quasiparticle approximation*.[24] Its physical interpretation is clear: The first (pole) contribution describes the free quasiparticles, including renormalization, the second (off-pole) term represents the interaction between the quasiparticles. Using the expansion (4), the carrier density is given by[23,24]

$$\begin{aligned} n_a(\{\mu_c\},T) &= g_a \int \frac{d\mathbf{k}}{(2\pi)^3} f_a(E_a(\mathbf{k})) - g_a \int \frac{d\mathbf{k}}{(2\pi)^3} \int \frac{d\omega}{2\pi} \\ &\times \left\{\Gamma_a(\mathbf{k},\omega)[f_a(\omega) - f_a(E_a(\mathbf{k}))]\frac{\partial}{\partial\omega}\frac{\mathcal{P}}{\hbar\omega - E_a(\mathbf{k})}\right\} \\ &= n_a^0 + n_a^{\mathrm{corr}}. \end{aligned} \tag{6}$$

The total density n_a is, therefore, subdivided into a contribution of the free quasiparticles n_a^0 and the correlated ones n_a^{corr} (second virial coefficient for quasiparticles).

We proceed with the following steps:

(i) Obviously, the function Γ_a is a key quantity of the theoretical approach. For its determination, there exist well-known standard approximation schemes.[21,22] In order to address the problems of screening and forming of bound states we consider the self-energy and, therefore, the damping Γ_a in screened ladder approximation[1,2]

$$\Gamma_a(\mathbf{k}_1,\omega) = -2\sum_b \int \frac{d\mathbf{k}_2}{(2\pi)^3} \mathrm{Im}\langle\mathbf{k}_1\mathbf{k}_2|T_{ab}^r(\omega + E_b(\mathbf{k}_2))|\mathbf{k}_1\mathbf{k}_2\rangle \times [f_b(E_b(\mathbf{k}_2)) \mp n_{ab}^B(\omega + E_b(\mathbf{k}_2))]. \tag{7}$$

The retarded off-shell T matrix obeys a Bethe-Salpeter (or Lippmann-Schwinger) equation, $T_{ab}^r = V_{ab}^s + i\hbar V_{ab}^s \mathcal{G}_{ab}^r T_{ab}^r$, where V_{ab}^s is the screened Coulomb potential, and $\mathcal{G}_{ab}^r$ is the free two-particle retarded Green's function given by the single-particle correlation functions $g_a^{\gtrless}$ via

$$\mathcal{G}_{ab}^r(\omega) = \int \frac{d\bar{\omega}}{2\pi} \int \frac{d\bar{\bar{\omega}}}{2\pi} \frac{g_a^>(\bar{\omega})g_b^>(\bar{\bar{\omega}}) - g_a^<(\bar{\omega})g_b^<(\bar{\bar{\omega}})}{\omega - \bar{\omega} - \bar{\bar{\omega}} + i\epsilon}. \tag{8}$$

(ii) To be consistent with the Γ_a expansion of the spectral function, we expand the distribution function according to[25]

$$f_a(\epsilon_a + \mathrm{Re}\ \Sigma_a'') \approx f_a(\epsilon_a) + \mathrm{Re}\ \Sigma_a'' \frac{df}{d\epsilon_a}, \tag{9}$$

where

$$\epsilon_a(\mathbf{k}) = \frac{\hbar^2k^2}{2m_a} + \mathrm{Re}\ \Sigma_a^{\mathrm{RPA}}(\mathbf{k},\omega)|_{\hbar\omega = \epsilon_a(\mathbf{k})} \tag{10}$$

is the quasiparticle energy in *random phase approximation* (RPA) including the Hartree-Fock (HF) self-energy Σ_a^{HF}, and Σ_a'' means higher-order ladder terms convergent also for vanishing screening.

(iii) Inserting Eqs. (7) and (9) into Eq. (6), we get for the density

$$n_a(\{\mu_c\},T) = g_a \int \frac{d\mathbf{k}}{(2\pi)^3} f_a(\epsilon_a(\mathbf{k})) + g_a \sum_b \int_{-\infty}^{\infty} \frac{d\omega}{2\pi} n_{ab}^B(\omega)\mathrm{Im}\ F(\omega) \tag{11}$$

with

$$F(\omega) = \mathrm{Tr}_{12}\left[\frac{d}{d\omega}\mathcal{G}_{ab}^r(\omega)T_{ab}^r(\omega)\right].$$

The main concern of our approach is to describe the influence of bound states on the properties of an EHP. Bound and scattering state contributions arise from the off-pole terms in Eq. (6) determined in screened ladder approximation by the off-shell T matrix, see Eq. (7). The bound states appear in the off-shell T matrix as poles at the real frequency axis. From the bilinear expansion of the T matrix, we obtain for the bound state part[1,21,26]

$$F^{\text{bound}}(\omega) = \sum_{n,l} \pi(2l+1)\,\delta(\hbar\omega - E_{nl}),$$

with E_{nl} being the bound state energy of the level given by the set of quantum numbers $\{n,l\}$. Using this relation, the bound and scattering state parts for the electron density may be separated,

$$n_e(\mu_e,\mu_h,T) = g_e \int \frac{d\mathbf{k}}{(2\pi)^3} f_e(\epsilon_e(\mathbf{k})) + g_e g_h \sum_{nl} (2l+1) \int \frac{d\mathbf{K}}{(2\pi)^3} \times \frac{1}{\exp\left[\beta\left(\frac{\hbar^2K^2}{2M} + E_{nl} - \mu_e - \mu_h\right)\right] - 1} + g_e \int_\Delta^\infty \frac{d\omega}{2\pi} n_{eh}^B(\omega) \text{Im}\, F(\omega) \tag{12}$$

with Δ representing the lowering of the band (continuum) edge and $\beta=(k_BT)^{-1}$. The first term in Eq. (12) is the density of the free quasiparticles. The second term is the contribution of bound states,[1,2,25] and the third one that of scattering states.

III. CHEMICAL PICTURE

Up to now we considered the EHP in grand canonical description as a two-component system with electrons and holes in scattering and bound states. This description is usually referred to as the physical picture. Then, Eq. (12) provides appropriate thermodynamics of the plasma. In contrast, the density expansion of the chemical potential following by approximate inversion of Eq. (12) leads to inconsistencies at low temperatures due to exponential divergences of the bound state part.[2,21]

In the following we briefly recall an alternative view on the bound states.[2] Looking at the corresponding distribution function

$$n_{eh}^B\left(\frac{\hbar^2K^2}{2M} + E_{nl}\right) = \frac{1}{z_e^{-1}z_h^{-1}\exp\left[\beta\left(E_{nl} + \frac{\hbar^2K^2}{2M}\right)\right] - 1} \tag{13}$$

with the fugacities $z_a=e^{\beta\mu_a}$, it is, obviously, convenient to consider *bound states as a new particle species (excitons)*, which are characterized by the fugacity z_X,

$$z_X = z_e z_h e^{-\beta E_{nl}} = e^{\beta\mu_X} \tag{14}$$

and by the ideal distribution function

$$n_X^B\left(\frac{\hbar^2K^2}{2M}\right) = \frac{1}{z_X^{-1}\exp\left[\beta\frac{\hbar^2K^2}{2M}\right] - 1}. \tag{15}$$

With the latter step we have made a fundamental change from the physical picture where the basic constituents are only electrons and holes, being in scattering or bound states, to a chemical picture where we have electrons, holes, and excitons as basic constituents of the system.

We should emphasize here, however, the limitations of this picture or, more precisely, of the underlying extended quasiparticle approximation for the spectral function $A_a(\mathbf{k},\omega)$, Eq. (4): While $A_a(\mathbf{k},\omega)$ exhibits, at lower densities, distinct bound state peaks and the pair continuum, the peaks broaden for higher densities due to the damping. Thus, a well-defined distinction between bound and scattering states becomes problematic around the Mott density.[5,6,27] A quantitative demonstration of the effect for zinc oxide (ZnO) has been given by Klingshirn, see Fig. 24b in Ref. 28. However, in ZnSe the excitonic linewidth is much smaller,[38] as will be discussed in Sec. IV.

The electron density in the chemical picture consists of "free" (quasiparticle n_e^{QP} and scattering n_e^{scatt}) and the bound (exciton) n_X contributions, cf. Eq. (12),

$$\begin{aligned} n_e(\mu_e,\mu_h,\mu_X,T) &= g_e \int \frac{d\mathbf{k}}{(2\pi)^3} f_e(\epsilon_e(\mathbf{k})) \\ &\quad + g_e \int_\Delta^\infty \frac{d\omega}{2\pi} n_{eh}^B(\omega) \text{Im}\, F(\omega) \\ &\quad + g_e g_h \sum_{nl} (2l+1) \int \frac{d\mathbf{K}}{(2\pi)^3} n_X^B\left(\frac{\hbar^2K^2}{2M}\right) \\ &= n_e^{\text{QP}} + n_e^{\text{scatt}} + n_X. \end{aligned} \tag{16}$$

The excitons consisting of two bound Fermi particles are described approximately as bosons [cf. Eqs. (13) and (15)]. The singularities of the bound state contribution $E_{nl}+\hbar^2K^2/(2M)=\mu_e+\mu_h$ are well known to be connected to the Bose condensation of the excitons.

In the chemical picture, the EHP is characterized by the densities of free electrons $n_e^*=n_e^{\text{QP}}+n_e^{\text{scatt}}$, free holes n_h^* (with $n_h^*=n_e^*$), and the density of excitons n_X (total electron density $n_e=n_e^*+n_X$). We have a partially ionized plasma in the ionization equilibrium

$$e + h \rightleftarrows X, \tag{17}$$

which is controlled by the definition of the fugacities of the new particles (14). The latter relation determines the composition of the system described by the degree of ionization

$$\alpha = \frac{n_e^*}{n_e} \tag{18}$$

and plays the role of a MAL. It is equivalent to the well-known thermodynamic condition for the chemical (ionization) equilibrium

$$\mu_X = \mu_e + \mu_h - E_{nl}. \tag{19}$$

In the grand canonical description, the condition (19) is just a consequence of the definition of excitons, Eqs. (14) and (15). The chemical potential of the excitons μ_X is given by the inversion of

$$n_X(\mu_X,T) = g_e g_h \int \frac{d\mathbf{K}}{(2\pi)^3} \frac{1}{\exp\left[\beta\left(\frac{\hbar^2 K^2}{2M} - \mu_X\right)\right] - 1}. \tag{20}$$

We should again stress the fact that the degree of ionization is, due to the damping of the two-particle states, not really a well-defined quantity around the Mott density. It gives, however, a good qualitative measure for the state of the EHP.

From the previous consideration, in principle, the chemical potential of free carriers (neglecting scattering states) is known, too. It is defined by

$$n_a^*(\mu_a,T) = g_a \int \frac{d\mathbf{k}}{(2\pi)^3} \frac{1}{e^{\beta[\epsilon_a(\mathbf{k})-\mu_a]} + 1}. \tag{21}$$

An analytical determination of the chemical potential from Eq. (21) is possible at most in limiting cases (nondegenerate or highly degenerate, respectively). In the general case, knowing the RPA quasiparticle energy $\epsilon_a(\mathbf{k})$, μ_a can be obtained by numerical inversion of Eq. (21). The determination of $\epsilon_a(\mathbf{k})$ according to Eq. (10) is, however, a numerically expensive task. As an alternative to the *complete inversion* of Eq. (21), one can split the chemical potential according to[2,25]

$$\mu_a = \mu_a^{\mathrm{id}} + \Delta\mu_a. \tag{22}$$

Here, μ_a^{id} is the ideal contribution and $\Delta\mu_a$ is the correlation part. The inversion of Eq. (21) with respect to the first order in $\Delta\mu_a$ is usually referred to as *incomplete inversion*.[29] Then the ideal contribution, for arbitrary degeneracy, follows in well-known manner from

$$n_a^*(\mu_a^{\mathrm{id}},T) = g_a \int \frac{d\mathbf{k}}{(2\pi)^3} \frac{1}{\exp\left[\beta\left(\frac{\hbar^2 k^2}{2m_a} - \mu_a^{\mathrm{id}}\right)\right] + 1}. \tag{23}$$

Numerical calculations for the correlation part $\Delta\mu_a$ have been performed, e.g., for a hydrogen plasma in Ref. 29 and for the EHP in Ref. 30. From the numerical results and the limiting cases, Padé formulas have been constructed in Refs. 30 and 31. A formula very similar to that in Ref. 30 has been proposed in Ref. 1.

With the subdivision (22) for the chemical potential of the species a introduced above, and $\Delta\mu_{eh}=\Delta\mu_e+\Delta\mu_h$, a generalized MAL follows from Eq. (14),

$$z_X = e^{\beta\mu_e^{\mathrm{id}}} e^{\beta\mu_h^{\mathrm{id}}} e^{-\beta(E_{nl}-\Delta\mu_{eh})}, \tag{24}$$

which determines the plasma composition implicitly.

The procedure is simpler for a nondegenerate EHP. Then it holds

$$z_a = \frac{n_a \Lambda_a^3}{g_a} e^{\beta\Delta\mu_a}, \quad z_X = \frac{n_X \Lambda_X^3}{g_e g_h} \tag{25}$$

with $\Lambda_a^2 = 2\pi\hbar^2/(m_a k_B T)$, and we immediately arrive at the Saha equation for nonideal plasmas,[2,10]

$$\frac{1-\alpha}{\alpha^2} = n_e \Lambda_{eh} e^{-\beta(E_{nl}-\Delta\mu_{eh})} \tag{26}$$

with $\Lambda_{eh}^2 = 2\pi\hbar^2/(m_{eh}k_B T)$, $m_{eh}^{-1} = m_e^{-1} + m_h^{-1}$. For arbitrary degeneracy, the degree of ionization α has to be determined by Eq. (19) and (24) instead of the Saha Eq. (26). In terms of α and n_e, Eq. (19) gets the form

$$\mu_X[(1-\alpha)n_e,T] = \mu_e[\alpha n_e,T] + \mu_h[\alpha n_e,T] - E_{nl}. \tag{27}$$

Equation (27) represents a form of the MAL defined by Eq. (14), which allows for the determination of the degree of ionization α as a function of density and temperature and, therefore, can be regarded as a generalized Saha equation. The degree of ionization is given implicitly by Eq. (27) and has to be obtained numerically.[11]

IV. ELECTRON-HOLE PAIR SPECTRUM

The influence of many-body effects on the composition of the partially ionized EHP according to Eqs. (27) together with Eqs. (21) and (20) is contained in two quantities, namely, (i) the quasiparticle energies $\epsilon_a(\mathbf{k})$ and (ii) the two-particle bound state (exciton) energy E_{nl}. It is well known from both optical experiments[32] and from the theoretical point of view[3] that the exciton energy only weakly changes with increasing excitation, while the ionization is mainly generated by the lowering of the band edge, described in our approach by the quasiparticle energies of carriers. According to Ref. 3, this behavior can be described by an effective wave equation considering the influence of screening both by self-energies and by a renormalization of the Coulomb interaction.

Experimentally the influence of many-body effects in an excited semiconductor can be determined by measuring the optical spectrum detected with a weak probe pulse. A corresponding theoretical description is given by the semiconductor Bloch equations (SBEs).[33] If one considers the carriers to be in quasiequilibrium, the carrier distributions are Fermi functions with given chemical potential and temperature, which are not affected by the weak probe pulse, and only the kinetic equation for the polarization has to be solved. In this case, the equation for the polarization $p(\mathbf{k},\omega)$, generated by the probe pulse $E(\omega)$ and coupled via the dipole matrix element d to the semiconductor, can be written in excitonic units as[34–38]

$$\{\omega - \mathbf{k}^2 - \Delta^{\mathrm{HF}}(\mathbf{k}) - \Sigma^r(\mathbf{k},\omega)\}p(\mathbf{k},\omega) + \int \frac{d\mathbf{q}}{(2\pi)^3}\{N(\mathbf{k})V_{eh}(\mathbf{k}-\mathbf{q}) + \Theta(\mathbf{k},\mathbf{q},\omega)\}p(\mathbf{q},\omega) = N(\mathbf{k})dE(\omega). \tag{28}$$

Many-body effects are contained (i) as HF renormalized carrier energies $\Delta^{\mathrm{HF}}(\mathbf{k})$ and Pauli blocking $N(\mathbf{k})=1-f_e(\mathbf{k})$

$-f_h(\mathbf{k})$, and (ii) as screening effects in the renormalized interaction matrix $\Theta(\mathbf{k},\mathbf{q},\omega)$,

$$\Theta(\mathbf{k},\mathbf{q},\omega) = \Delta V^{\mathrm{eff}}(\mathbf{k},\mathbf{q},\omega) - i\Gamma(\mathbf{k},\mathbf{q},\omega)$$
$$= \sum_{a\neq b} \int \frac{d\bar{\omega}}{2\pi} \times \frac{[1-f_a(\mathbf{k})]V_{ab}^{>}(\mathbf{k}-\mathbf{q},\bar{\omega}) + f_a(\mathbf{k})V_{ab}^{<}(\mathbf{k}-\mathbf{q},\bar{\omega})}{\hbar\omega - \epsilon_a(\mathbf{k}) - \epsilon_b(\mathbf{q}) - \hbar\bar{\omega} + i[\Gamma_a(\mathbf{k}) + \Gamma_b(\mathbf{q})]/2}, \tag{29}$$

whose real and imaginary parts, $\Delta V^{\mathrm{eff}}(\mathbf{k},\mathbf{q},\omega)$ and $\Gamma(\mathbf{k},\mathbf{q},\omega)$, are the effective interaction and the so-called off-diagonal dephasing, respectively, and in the interband self-energy $\Sigma^r(\mathbf{k},\omega)$,

$$\Sigma^r(\mathbf{k},\omega) = \Delta e^{sc}(\mathbf{k},\omega) - i\Gamma(\mathbf{k},\omega) = \int \frac{d\mathbf{q}}{(2\pi)^3}\Theta(\mathbf{q},\mathbf{k},\omega)$$
$$= \Sigma_e^r(\mathbf{k},\omega-\epsilon_h) + \Sigma_h^r(\mathbf{k},\omega-\epsilon_e), \tag{30}$$

with its real and imaginary parts $\Delta e^{sc}(\mathbf{k},\omega)$ and $\Gamma(\mathbf{k},\omega)$ being the renormalized interband self-energy and the diagonal dephasing, respectively.

It is important to notice that the various many-body quantities widely compensate each other pairwise in the case of bound states. This concerns on one hand the HF energies and the Pauli blocking, and the renormalized interband self-energy $\Delta e^{sc}(\mathbf{k},\omega)$ and the effective interaction $\Delta V^{\mathrm{eff}}(\mathbf{k},\mathbf{q},\omega)$ on the other hand as well as the so-called diagonal and off-diagonal dephasing $\Gamma(\mathbf{k},\omega)$, $\Gamma(\mathbf{k},\mathbf{q},\omega)$, respectively. Moreover, there is an exact relation of the (two-particle) interband self-energy Σ^r for an energy $\hbar\omega$ to the (single-particle) carrier self-energies Σ_a^r at shifted energies $\hbar\omega-\varepsilon_b$ given in Eq. (30). The appearance of this energy shift becomes physically clear if one looks at the energies in the denominator of the effective interaction matrix $\Theta(\mathbf{k},\mathbf{q},\omega)$. It becomes resonant if the incident photon with the energy $\hbar\omega$ generates an interband transition, described by the renormalized quasiparticle energies $\varepsilon_a(\mathbf{k})+\varepsilon_b(\mathbf{q})$, accompanied by absorption or emission of a plasmon with the energy $\hbar\bar{\omega}$. The quasiparticle energies $\varepsilon_a(\mathbf{k})$ and the quasiparticle damping $\Gamma(\mathbf{k},\omega)$ here are determined from Eqs. (10) and (3) using the RPA self-energy

$$\Sigma_a^{\gtrless}(\mathbf{k},\omega) = \int \frac{d\mathbf{q}}{(2\pi)^3} \int \frac{d\omega'}{2\pi} g_a^{\gtrless}(\mathbf{k}-\mathbf{q},\omega-\omega')V_{aa}^{\gtrless}(\mathbf{q},\omega'). \tag{31}$$

The correlation functions of the screened potential $V_{ab}^{\gtrless}(\mathbf{q},\omega)$ appearing in the Eqs. (29)–(31) are related to the inverse retarded dielectric function $\varepsilon^{r^{-1}}(\mathbf{q},\omega)$ via

$$V_{ab}^{<}(\mathbf{q},\omega) = 2iV_{ab}(\mathbf{q})\mathrm{Im}\ \varepsilon^{r^{-1}}(\mathbf{q},\omega)n^B(\omega),$$
$$V_{ab}^{>}(\mathbf{q},\omega) = 2iV_{ab}(\mathbf{q})\mathrm{Im}\ \varepsilon^{r^{-1}}(\mathbf{q},\omega)[1+n^B(\omega)]. \tag{32}$$

The function $n^B(\omega)$ represents the Bose distribution of the elementary excitations in the plasma (plasmons), and, in our calculations, we use the Lindhard dielectric function. Contributions of bound electron-hole pairs to the dielectric screening function in the sense of atomic (excitonic) polarizabilities[39] are small as compared to that of the free carriers and are neglected. This is justified if the description of the Mott transition is addressed; however, excitonic contributions to screening should be incorporated if the properties of the pure excitonic gas phase are investigated.

For weak probe pulses the macroscopic polarization $P(\omega)$ depends linearly on the electric field

$$P(\omega) = \int \frac{d\mathbf{k}}{(2\pi)^3} p(\mathbf{k},\omega) = \chi(\omega)E(\omega), \tag{33}$$

where the susceptibility $\chi(\omega)$ characterizes the dielectric properties of the semiconductor. The experimental verification of this approach was given in several optical experiments, measuring the transmission/reflection of semiconductor heterostructures. In previous papers[35–38] we have demonstrated how the influence of many-body effects on the exciton line, e.g., carrier-induced line broadening, shift of the exciton resonance and band gap shrinkage show up in the phase and amplitude of transmitted/reflected light.

The semiconductor Bloch equation approach sketched above describes systems with a band structure in an electromagnetic field. In general, the two-particle problem in a surrounding medium needs a careful analysis of the Bethe-Salpeter equation for the two-particle Green's function.

A first approach in this direction was given in Refs. 3 and 4 using the dynamically screened ladder approximation. However, this result has some serious shortcomings, especially in the degenerate plasma. There, a static contribution in addition to the Hartree-Fock term, and, moreover, a division by the Pauli blocking factors $1-f_a(\mathbf{k}_1)-f_b(\mathbf{k}_2)$ occur. In a subsequent paper[27] it was shown that these shortcomings are produced by using an inappropriate retarded Green's function and by the treatment of the retardation of the screened potential by the Shindo approximation. The corrected effective Schrödinger equation was derived in Refs. 27 and 40 and for the EHP in Refs. 37 and 38. For an electron-hole pair system, both approaches are in full agreement for zero center-of-mass momentum.

Numerical solutions for the pair spectrum have been given in Refs. 35–38 using the SBE and in Refs. 3, 41, and 42 using the effective Schrödinger equation in the nondegenerate case.

Our numerical calculations were performed for zinc selenide (ZnSe) with an excitonic $1s$ ground state energy of 22.4 meV and effective electron and hole masses of $m_e = 0.15m_e^0$ and $m_h = 0.86m_e^0$, m_e^0 being the free electron mass. In Fig. 1 the imaginary part of the susceptibility χ is presented for a temperature of 30 K and different carrier densities. In order to present a better resolution of the different exciton states, we have used a logarithmic scale. The Mott transition is obviously generated by the decreasing band edge and takes place first for the higher exciton states. The position of the exciton nearly stays unchanged; there is only a weak shift to lower energies. The shift turns to higher energies if the temperature is decreased. This can be seen in

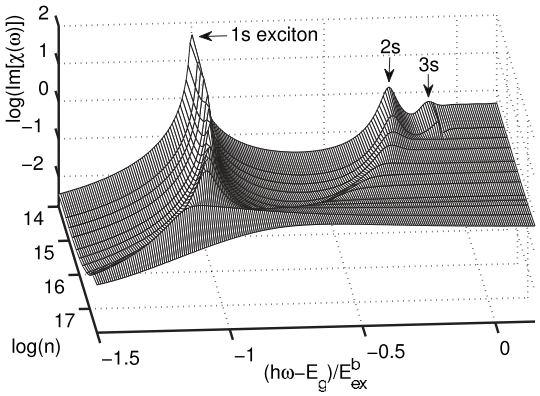

FIG. 1. Imaginary part of the susceptibility on a logarithmic scale for different carrier densities $n[\mathrm{cm}^{-3}]$ from the solution of the SBE (28). E_g is the band gap and E_{ex}^b is the $1s$-exciton energy.

Fig. 2, where the positions of the $1s$-exciton peak and of the band edge are shown for different temperatures.

The two-particle spectrum shown in Fig. 2 exhibits the following peculiarities: (i) There is a lowering of the band (continuum) edge due to the many-body effects contained in the self-energy. (ii) The exciton ground-state energy remains nearly constant up to higher densities. This follows from the approximative compensation of the many-particle effects for the bound states.[3] Moreover, at low temperatures, $\Theta(\mathbf{k},\mathbf{q},\omega)$ and, therefore, $\Sigma^r(\mathbf{k},\omega)$ are small, and Coulomb Hartree-Fock self-energy and Pauli blocking dominate. However, they nearly compensate each other at low densities, too, but lead to a weak shift for higher densities. (iii) The difference between band edge and exciton energy defines the effective ionization energy I^{eff}, which is lowered with increasing density. (iv) For $I^{\mathrm{eff}}=0$, the bound state vanishes and merges into the scattering continuum. This process is referred to as *Mott effect*, and the corresponding density is called Mott density.

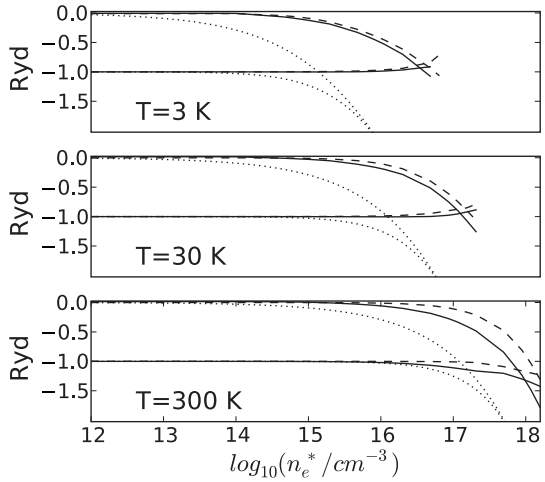

FIG. 2. Two-particle spectrum vs density in ZnSe: band edge (upper curves) and exciton ground state energy (lower curves). Solid lines: solution of the full SBE, dashed lines: solution with $\Theta(\mathbf{k},\mathbf{q},\omega)=0$ and $\Sigma^r(\mathbf{k},\omega)=0$ (Hartree-Fock approximation), dotted lines: static limit of $\Theta(\mathbf{k},\mathbf{q},\omega)$ and classical limit for $\Delta e^{sc}(\mathbf{k},\omega)$ (Debye approximation). Ryd denotes the excitonic Rydberg.

Above that point, the bound state does not exist, and the bound state energy is no longer a meaningful quantity. (v) Finally, the results for the exciton energy show a different behavior for high and low temperatures, i.e., we observe a blue (low T) or a red shift (high T), respectively.[35]

While the exciton energy appears in Fig. 2 as a well-defined line, in fact, the exciton is broadened due to a finite damping.[28] At low temperatures, however, this broadening is small: the excitonic full width at half maximum is $\gamma=0.012$ Ryd for 3 K and $\gamma=0.07$ Ryd for 30 K just below the Mott density, respectively.

In addition to our results from the solution of the full SBE (28), in Fig. 2 we show a comparison to two approximations: That is (i) a solution with screening effects being neglected in the SBE and only the HF energies and the Pauli blocking considered, i.e., $\Theta(\mathbf{k},\mathbf{q},\omega)=0$ and $\Sigma^r(\mathbf{k},\omega)=0$ (Hartree-Fock approximation). (ii) A further frequently used approximation is the static limit of $\Theta(\mathbf{k},\mathbf{q},\omega)$. It follows from Eq. (29) if $\bar{\omega}$ exceeds all other terms in the denominator. If furthermore, for $\Delta e^{sc}(\mathbf{k},\omega)$ [cf. Eq. (30)] the classical limit is applied, it leads to the Debye shift κe^2 (κ is the inverse screening length defined by $\kappa^2=(e^2/\epsilon_0\epsilon_r k_B T)(\frac{\partial n_e}{\partial \mu_e}+\frac{\partial n_h}{\partial \mu_h})$, ϵ_r is the background dielectric constant). Figure 2 shows that this approximation provides an inadequate description of both bound state energy and band edge even at room temperature. In particular, the Mott effect occurs at far too low densities. Static screening becomes a convenient approximation far above room temperature but completely fails at low temperatures.

V. CHEMICAL POTENTIAL AND DEGREE OF IONIZATION

The MAL given by Eq. (27) represents a relation between the chemical potentials of the EHP constituents (μ_e,μ_h,μ_X). While we assume μ_X to be the chemical potential of ideal bosons, Eq. (20), μ_e and μ_h [Eq. (21)] contain correlation contributions in the RPA quasiparticle energy $\epsilon_a(\mathbf{k})$, Eq. (10). The quasiparticle retarded self-energy of carriers is given in RPA by Eq. (31) or, in an alternative representation, by

$$\Sigma_a^{\mathrm{RPA}}(\mathbf{k},\omega)\big|_{\hbar\omega=\varepsilon_a(\mathbf{k})}=\Sigma_a^{\mathrm{HF}}(\mathbf{k})+\int\frac{d\mathbf{q}}{(2\pi)^3}\int\frac{d\omega'}{2\pi}\times\frac{[1-f^a(\varepsilon_a(\mathbf{q}))+n^B(\omega')]\hat{V}(\mathbf{k}-\mathbf{q},\omega')}{\varepsilon_a(\mathbf{k})-\varepsilon_a(\mathbf{q})-\hbar\omega'+i\Gamma_a(\mathbf{q})/2},\tag{34}$$

where $\hat{V}(\mathbf{q},\omega)$ is related to the correlation functions of the screened potential, Eq. (32) by $\hat{V}(\mathbf{q},\omega)=i[V^{>}(\mathbf{q},\omega)-V^{<}(\mathbf{q},\omega)]$. The quasiparticle energy $\varepsilon_a(\mathbf{k})$ is, in turn, given by Eq. (10).

In comparison to earlier calculations,[30] where quasiparticle energies $\varepsilon_a(\mathbf{k})$ on the right-hand side (r.h.s.) of Eq. (34) were replaced by kinetic energies and the damping $\Gamma_a(\mathbf{q})$ was neglected, we solve Eqs. (34) and (10) self-consistently by iteration. Our iteration procedure shows that both real and imaginary parts of the self-energy are reduced. These

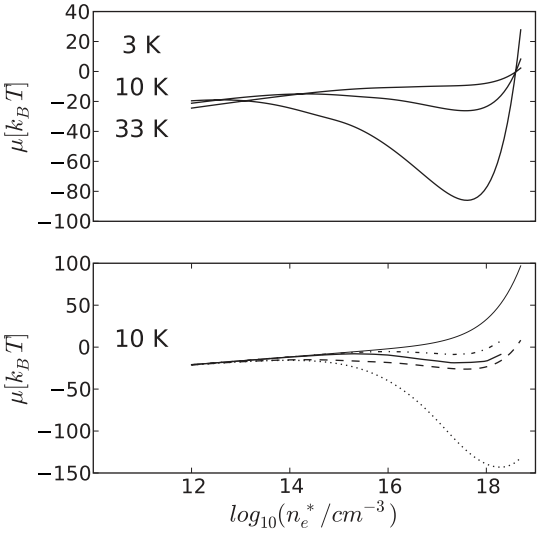

FIG. 3. Sum of the chemical potentials of electrons and holes $\mu=\mu_e+\mu_h$ vs density in ZnSe. Upper panel: μ^{RZR} for several temperatures T: 3 K (upper curve), 10 K (middle), 33 K (lower). Lower panel: μ^{iter} according to the self-consistent solution of Eqs. (34) and (10) (bold solid line), μ^{RZR} (dashed), μ^{id} (thin solid), μ^{HF} (dash-dotted), Debye approximation $\mu^{\mathrm{D}}=\mu_e^{\mathrm{id}}+\mu_h^{\mathrm{id}}-\kappa e^2$ (dotted), for $T=10$ K.

changes of the quasiparticle energies influence the chemical potentials, calculated from Eq. (21).

Figure 3 shows isotherms of the sum $\mu=\mu_e+\mu_h$ vs density. In order to illustrate the general behavior of the chemical potential, at first, we apply the idea of incomplete inversion of the density according to Eq. (22) with the correlation part given by the Padé formula from Ref. 30 and denote the resulting chemical potential by $\mu^{\mathrm{RZR}}=\mu_e^{\mathrm{id}}+\mu_h^{\mathrm{id}}+\Delta\mu_{eh}$.

The upper panel compares μ for several temperatures. At lower temperatures, a van der Waals loop occurs, i.e., a region with an instability $\partial\mu/\partial n\leq 0$, which may be a signal of a phase transition.[1,2,43] The lower panel shows a comparison of several approximations for μ: self-consistent iterative solution of Eqs. (34) and (10) (later on referred to as μ^{iter}), μ^{RZR}, Hartree-Fock and Debye approximations, and ideal chemical potential. What can be seen immediately is that the van der Waals loop is caused by many-particle effects. The latter ones are strongly overestimated by the Debye approximation. The other approximations deviate from the self-consistent result considerably, too. These quantitative differences will show up again in the ionization equilibrium, which is very sensitive to the actual form of the chemical potential.

Figure 4 represents a graphical solution of Eq. (27). For illustrative purposes we use again μ^{RZR} like in the upper panel of Fig. 3. Solid and dashed lines represent the r.h.s. and left-hand side (l.h.s.) terms of Eq. (27), respectively, for given temperatures T and total densities n_e. Their intersections indicate the possible values of the degree of ionization $\alpha(n_e,T)$. Here and in the following we consider only the ground state, i.e., $n=1$, $l=0$, $E_{nl}\equiv E_1$.

Isotherms of the degree of ionization as a function of the density obtained by numerical solution of the MAL (27) are

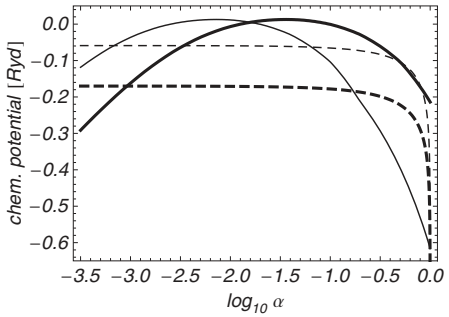

FIG. 4. Graphical solution of Eq. (27): chemical potential of the excitons μ_X [l.h.s. of Eq. (27); dashed lines] and sum of the chemical potentials of electrons and holes minus binding energy $\mu_e+\mu_h-E_1$ [r.h.s. of Eq. (27); solid lines] vs α for $T=20$ K and two densities: $n_e=10^{17}$ cm^{-3} (bold lines; single solution for α) and $n_e=5\times10^{17}$ cm^{-3} (thin lines; three solutions for α).

shown in Fig. 5 (chemical potentials of carriers: μ^{iter}). We observe a very strong increase in α up to $\alpha=1$ at high densities due to the lowering of the ionization energy.[2,10] This behavior is usually referred to as *Mott transition* as a consequence of the Mott effect.

The comparison given in Fig. 6 shows the influence of the approximations applied for the chemical potential, cf. Fig. 3, on the degree of ionization. Obviously, the absolute position (and, as detailed investigations show, also the temperature dependence) of the Mott density vary for different approximations for the chemical potential.

At low enough temperatures, the curves exhibit a region where α is multivalued around the Mott density, i.e., a bistability occurs. The reason of this behavior is obvious from Figs. 3 and 4: the van der Waals loop in the chemical potential. Nevertheless, for lower densities there is only a single intersection of the curves, but for higher densities, three intersections are possible leading to three solutions for α for a given combination of temperature and density. Thus, we find a bistability (the intermediate solution is unstable), which may give rise to a first-order phase transition from an exciton gas to a fully ionized EHP (*Mott phase transition*). This effect has been addressed as a possible scenario for finding an excitonic condensate still at rather high densities (and, thus, at rather high temperatures).[44] It is, however, probably a theoretical artifact. Already the step from using μ^{RZR} to μ^{iter},

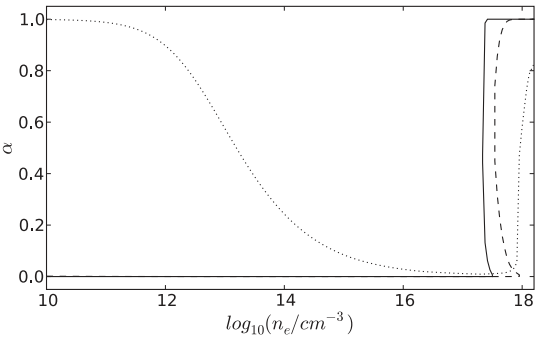

FIG. 5. Degree of ionization α vs density for several temperatures T, Eq. (27): 2 K (solid line), 10 K (dashed), and 30 K (dotted).

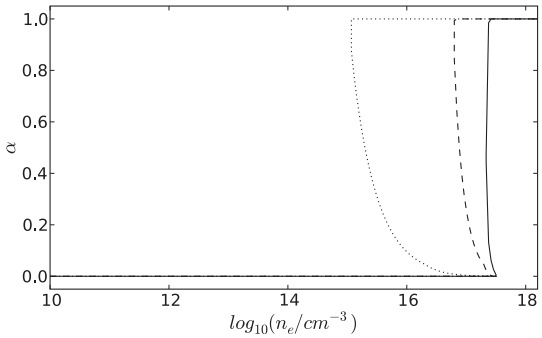

FIG. 6. Degree of ionization α vs density, Eq. (27), for $T=2$ K. Comparison of several approximations for the chemical potential: μ^{iter} (solid line), μ^{RZR} (dashed), and Debye approximation μ^{D} (dotted).

i.e., in particular, the inclusion of the single-particle damping and the complete inversion of the density instead of the incomplete one, reduces the density range of bistability significantly, cf. Fig. 6. The question whether the inclusion of the exciton-exciton interaction (which should be very important just below the Mott density since there are only excitons) would remove the bistability completely is still to be resolved. It is, however, very likely as similar experiences from the atom-atom interaction in the hydrogen plasma[21] show.

For an overview of the ionization state of the EHP, in Fig. 7, isolines $\alpha(n_e,T)=$const. in the density-temperature plane are shown. With increasing temperature at fixed density, thermal ionization takes place quite smoothly, while at fixed temperature with increasing density, the Mott transition appears as an abrupt jump from $\alpha=0$ to $\alpha=1$.

At lower temperatures we find a strong dominance of the excitons ($\alpha\approx 0$). Regarding them as noninteracting bosons, Bose-Einstein condensation (BEC) may be expected under the condition

$$(1-\alpha)n_e\Lambda_X^3 \geq 2.61. \tag{35}$$

This condition is given in Fig. 7 by the triangle bordered by the dashed line at the bottom. Note that the breakup of excitons at the Mott density does not mean a disappearance of the condensate. Instead, a closer investigation shows a smooth crossover to a BCS-type condensate at high densities.[18,19,45] Thus, the physical nature of the condensed particles changes, i.e., we find excitons below the Mott density, and Cooper-like electron-hole pairs far above it. To which extent the survival of the excitons as resonances just above the Mott density plays a role has still to be investigated.

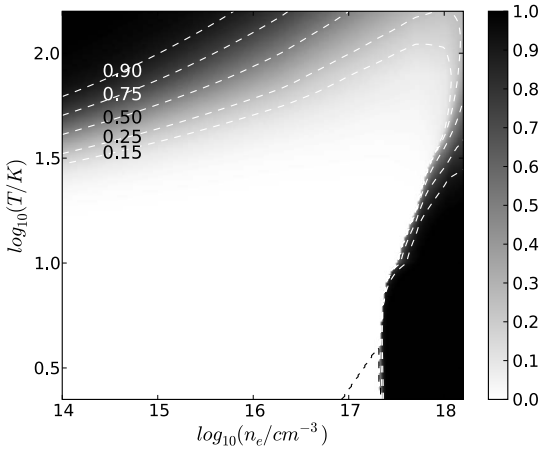

FIG. 7. Isolines of the degree of ionization in the density-temperature plane for ZnSe. The dashed triangle at the bottom borders the region where BEC of excitons is possible, cf. Eq. (35).

VI. SUMMARY AND OUTLOOK

The ionization equilibrium of an EHP has been investigated on a quantum statistical footing. Using the spectral function of carriers in extended quasiparticle approximation and transforming into a chemical picture, a very general mass-action law (MAL) has been considered which, in contrast to earlier papers, accounts for the Fermi/Bose character of carriers/excitons. This is indispensable for discussing the Mott transition at low temperatures and its interplay with a possible BEC of excitons. Many-body effects are included in the calculation of chemical potentials of carriers by their self-energies within quasiparticle approximation. The dynamical screened self-energies in RPA, depending itself on the chemical potentials again, have been computed self-consistently. In contrast to earlier papers not only the renormalization of the energy, but the damping (finite life time) of carriers have been incorporated, too. We have demonstrated that the changes of the chemical potentials due to many-body effects within our approach are strongly reduced in comparison to earlier approximations. In particular, an approximation based on static screening overestimates the influence of many-body effects at low temperatures by orders of magnitude (see Fig. 3).

The influence of many-body effects on the exciton energies has been obtained by using the semiconductor Bloch equations (SBE) considering the quasiparticle self-energies of carriers. We found that the Mott transition of excitons is shifted to higher carrier densities as compared to earlier approximations. For lower temperatures, the effects of dynamical screening in the SBE widely cancel and a simple model including the Coulomb Hartree-Fock renormalization (HF carrier energies and Pauli blocking) is applicable. Again, the approximation with static screening fails completely at low temperatures and is only valid far above room temperature (see Fig. 2).

This behavior is reflected in the degree of ionization, calculated with the generalized MAL for ZnSe and compared to the different approximations, too (see Figs. 5 and 6). The Mott transition, expressed by an abrupt increase in the degree of ionization, is shifted to higher carrier densities. For a temperature of 10 K, the Mott density is increased by more than one order of magnitude in comparison to those following by static screening approximation. In particular, the multivaluedness occurring around the Mott density is strongly suppressed within our approach. We assume that it will very likely vanish completely after inclusion of the exciton-exciton interaction. This assumption is based on calculations for the ionization equilibrium in hydrogen.[21]

Given the drastic deviations in chemical potentials, Mott density and extension of the ionization hysteresis that result from the mentioned earlier approximations for the many-particle effects, our previous calculations for Cu_2O as presented in Ref. 11 are to be taken with a grain of salt. They will be re-assessed on the present theoretical level in a forthcoming publication.

Finally, we have presented an overview of the ionization state in ZnSe as a function of temperature and density of carriers (see Fig. 7). Due to the increase in the Mott density, the possible window for the occurrence of BEC of noninteracting excitons is extended to higher temperatures.

ACKNOWLEDGMENTS

We would like to thank T. Schmielau (Sheffield), Th. Bornath, and H. Stolz (Rostock) for many fruitful discussions. This work was supported by the Deutsche Forschungsgemeinschaft (Collaborative Research Center SFB 652).

[1] R. Zimmermann, *Many-Particle Theory of Highly Excited Semiconductors* (Teubner, Leipzig, 1988).
[2] W. Ebeling, W. D. Kraeft, and D. Kremp, *Theory of Bound States and Ionization Equilibrium in Plasmas and Solids* (Akademie-Verlag, Berlin, 1976).
[3] K. Kilimann, W. D. Kraeft, and D. Kremp, Phys. Lett. **61A**, 393 (1977); R. Zimmermann, K. Kilimann, W. D. Kraeft, D. Kremp, and G. Röpke, Phys. Status Solidi B **90**, 175 (1978).
[4] H. Haug and D. B. Tran Thoai, Phys. Status Solidi B **85**, 561 (1978).
[5] Q. Y. Peng, T. Schmielau, G. Manzke, and K. Henneberger, J. Cryst. Growth **214-215**, 810 (2000).
[6] T. Schmielau, G. Manzke, D. Tamme, and K. Henneberger, Phys. Status Solidi B **221**, 215 (2000).
[7] C. F. Klingshirn, *Semiconductor Optics*, 3rd ed. (Springer, Berlin, 1995).
[8] C. Klingshirn, R. Hauschild, J. Fallert, and H. Kalt, Phys. Rev. B **75**, 115203 (2007).
[9] D. Snoke, Solid State Commun. **146**, 73 (2008).
[10] W. D. Kraeft, K. Kilimann, and D. Kremp, Phys. Status Solidi B **72**, 461 (1975).
[11] F. Richter, D. Semkat, D. Kremp, and K. Henneberger, Phys. Status Solidi C **6**, 532 (2009).
[12] L. V. Keldysh, in *Bose-Einstein Condensation*, edited by A. Griffin, D. W. Snoke, and S. Stringari (Cambridge University Press, Cambridge, 1995).
[13] S. A. Moskalenko, Fiz. Tverd. Tela (Leningrad) **4**, 276 (1962).
[14] E. Hanamura and H. Haug, Phys. Rep. **33**, 209 (1977).
[15] L. V. Keldysh and Yu. V. Kopaev, Sov. Phys. Solid State **6**, 2219 (1965).
[16] S. A. Moskalenko and D. W. Snoke, *Bose-Einstein Condensation of Excitons and Biexcitons and Coherent Nonlinear Optics with Excitons* (Cambridge University Press, Cambridge, 2000).
[17] J. Kasprzak *et al.*, Nature (London) **443**, 409 (2006).
[18] F. X. Bronold and H. Fehske, Phys. Rev. B **74**, 165107 (2006).
[19] D. Kremp, D. Semkat, and K. Henneberger, Phys. Rev. B **78**, 125315 (2008); D. Semkat, D. Kremp, and K. Henneberger, Phys. Status Solidi C **6**, 546 (2009).
[20] R. Redmer, Phys. Rep. **282**, 35 (1997).
[21] D. Kremp, M. Schlanges, and W.-D. Kraeft, *Quantum Statistics of Nonideal Plasmas* (Springer, Berlin, 2005).
[22] L. P. Kadanoff and G. Baym, *Quantum Statistical Mechanics* (Benjamin, New York, 1962).
[23] R. Zimmermann and H. Stolz, Phys. Status Solidi B **131**, 151 (1985).
[24] D. Kremp, W. D. Kraeft, and A. J. D. Lambert, Physica A **127**, 72 (1984).
[25] D. Kremp, W. D. Kraeft, and M. Schlanges, Contrib. Plasma Phys. **33**, 567 (1993).
[26] D. Kremp, M. K. Kilimann, W. D. Kraeft, H. Stolz, and R. Zimmermann, Physica A **127**, 646 (1984).
[27] Th. Bornath, D. Kremp, and M. Schlanges, Phys. Rev. E **60**, 6382 (1999).
[28] C. Klingshirn, Phys. Status Solidi B **244**, 3027 (2007).
[29] W. Stolzmann and W.-D. Kraeft, Ann. Phys. (Leipzig) **491**, 388 (1979).
[30] M. Rösler, R. Zimmermann, and W. Richert, Phys. Status Solidi B **121**, 609 (1984).
[31] W. Ebeling and W. Richert, Phys. Lett. **108A**, 80 (1985).
[32] G. W. Fehrenbach, W. Schäfer, J. Treusch, and R. G. Ulbrich, Phys. Rev. Lett. **49**, 1281 (1982).
[33] H. Haug and S. W. Koch, *Quantum Theory of the Optical and Electronic Properties of Semiconductors*, 4th ed. (World Scientific, Singapore, 1993).
[34] A. Girndt, F. Jahnke, A. Knorr, S. W. Koch, and W. W. Chow, Phys. Status Solidi B **202**, 725 (1997).
[35] G. Manzke, Q. Y. Peng, K. Henneberger, U. Neukirch, K. Hauke, K. Wundke, J. Gutowski, and D. Hommel, Phys. Rev. Lett. **80**, 4943 (1998).
[36] J. S. Nägerl, B. Stabenau, G. Böhne, S. Dreher, R. G. Ulbrich, G. Manzke, and K. Henneberger, Phys. Rev. B **63**, 235202 (2001).
[37] G. Manzke and K. Henneberger, Phys. Status Solidi B **234**, 233 (2002).
[38] M. Seemann, F. Kieseling, H. Stolz, R. Franz, G. Manzke, K. Henneberger, T. Passow, and D. Hommel, Phys. Rev. B **72**, 075204 (2005).
[39] G. Röpke and R. Der, Phys. Status Solidi B **92**, 501 (1979).
[40] T. Schmielau, Ph.D. thesis, Universität Rostock, 2001.
[41] S. Arndt, W. D. Kraeft, and J. Seidel, Phys. Status Solidi B **194**, 601 (1996).
[42] J. Seidel, S. Arndt, and W. D. Kraeft, Phys. Rev. E **52**, 5387 (1995).
[43] W. Ebeling, W. D. Kraeft, D. Kremp, and K. Kilimann, Phys. Status Solidi B **78**, 241 (1976).
[44] D. W. Snoke and J. D. Crawford, Phys. Rev. E **52**, 5796 (1995).
[45] P. Nozières and S. Schmitt-Rink, J. Low Temp. Phys. **59**, 195 (1985).

A.4

Artikel 4

H. Stolz and D. Semkat:

Unique signatures for Bose-Einstein condensation in the decay luminescence lineshape of weakly interacting excitons in a potential trap

Phys. Rev. B **81**, 081302(R) (2010)

PHYSICAL REVIEW B **81**, 081302(R) (2010)

Unique signatures for Bose-Einstein condensation in the decay luminescence lineshape of weakly interacting excitons in a potential trap

Heinrich Stolz and Dirk Semkat
Institut für Physik, Universität Rostock, D-18501 Rostock, Germany
(Received 11 December 2009; published 8 February 2010)

We calculate the spatially resolved optical emission spectrum of a weakly interacting Bose gas of excitons confined in a three dimensional potential trap due to interband transitions involving weak direct and phonon mediated exciton-photon interactions. Applying the local-density approximation, we show that for a noncondensed system the spatiospectral lineshape of the direct process reflects directly the shape of the potential. The existence of a Bose-Einstein condensate changes the spectrum in a characteristic way so that it directly reflects the constant chemical potential of the excitons and the renormalization of the quasiparticle excitation spectrum. Typical examples are given for parameters of the lowest yellow excitons in Cu_2O.

DOI: 10.1103/PhysRevB.81.081302 PACS number(s): 78.20.−e, 78.30.−j, 71.35.Lk

The condensation of bosons into the system ground state at sufficiently low temperature in thermal equilibrium is one of the manifestations of quantum nature of matter.[1] To reach a sufficient density, the concept of trapping the particles in a potential well has allowed the realization of atomic Bose-Einstein condensates.[2,3] Also for bosonic quasiparticles, such as microcavity polaritons, this concept has been fruitful.[4] For excitons, bound electron-hole-pair excitations in semiconductors, which have been the first type of quasiparticles where Bose-Einstein condensation (BEC) has been predicted (for an overview, see Ref. 5), the use of potential traps has a long history. Especially promising have been the exciton states in the semiconductor cuprous oxide (Cu_2O). Due to their optically forbidden nature, long lifetime are expected and one should be able to trap a very large number of particles in quasi thermal equilibrium (see, e.g., Refs. 6 and 7). However, despite several experimental studies of dense exciton states in this material,[5,6,8–10] none of these resulted in a clear demonstration of the existence of a Bose condensed state of excitons. We will show in this Rapid Communication that a reason for these failures might be a wrong assignment of the decay luminescence spectrum of an exciton condensate, since all earlier papers used only qualitative arguments where the condensate has been put by hand into the spectrum, but a rigorous calculation of the decay luminescence spectrum of excitons in a trap under weak exciton-photon interaction has not been performed. In this Rapid Communication we will give a calculation based on a mean-field description of the exciton system, which not only clarifies these issues but predicts significant changes in the luminescence spectrum in the presence of a condensate. This will provide unique criteria for the onset of BEC in an excitonic system.

In the theory of interacting Bose gases, several approximations have been developed;[11,12] for a review see Ref. 13. The critical temperature for BEC can be roughly approximated by that of a noninteracting system. Taking the confining potential to be that of a $3d$ harmonic oscillator $V_{\mathrm{ext}}=\alpha r^2$, it is given by

$$k_B T_{c0} = \hbar\Omega_0 \left(\frac{N}{\zeta(3)} \right)^{1/3} \tag{1}$$

with $\Omega_0=\sqrt{2\alpha/M}$ being the oscillator frequency, N the total number of particles in the trap, M the mass of the particles, and ζ the Riemann zeta function. For an exciton mass of $M=2.6m_e$ that represents the mass of the paraexcitons in Cu_2O (Ref. 14) and typical α parameters of exciton traps ($\alpha \simeq 0.05\ \mu\mathrm{eV}/\mu\mathrm{m}^2$, see, e.g., Ref. 6), this results in $\hbar\Omega_0=72$ neV and for $N=10^{10}$ excitons in the trap a critical temperature of 1.27 K is expected. For the noninteracting system, in the condensate all particles are in the ground state of the oscillator the size of which is $a_{osc}=\sqrt{\hbar/M\Omega_0}=0.74\ \mu$m. From this it was concluded in previous investigations that the spatial shrinking of the luminescence line is an indication of the onset of BEC.[5,6] However, for an interacting system this is not the case. Here the condensate will form a cloud with radius $R_0=\sqrt{15}(Na_S/a_{osc})^{1/5}$ where a_S is the s-wave scattering length,[13] which for large N can be much larger than a_{osc}. Assuming again $N=10^{10}$ particles, a temperature of $T=0.5$ K, and a scattering length of $2.8a_B$,[15] the size of the cloud is $R_0=39\ \mu$m, much larger than the size of the oscillator ground state and also the de Broglie wavelength $\lambda_B=\sqrt{2\pi\hbar^2/(Mk_BT)}$ which at $T=0.5$ K is 65 nm.

Since $R_0 \gg a_{osc} \gg \lambda_B$, we can apply the local-density approximation (LDA) or semiclassical approximation.[13] Here all thermodynamic quantities are function of the spatial coordinate. Furthermore, for temperatures not too close to T_c, the Thomas-Fermi approximation[13] where the kinetic energy of the particles in the condensate is neglected, represents a rather good description of the condensate because the thickness of the layer where it breaks down $\delta=(a_{osc}^4/R_0)^{1/3}$ (Ref. 13) is only $\delta=0.15\ \mu$m. Therefore, the luminescence spectrum will be derived under these two approximations in the following.

It is by now well established that, at densities far below the Mott density, excitons can be described as a weakly interacting Bose gas.[16–18] The interaction can be parametrized by a scattering length a_S of the order of the Bohr radius, its magnitude depending on the details of the spin structure of the exciton states.

We confine the excitons with an external potential $V_{\mathrm{ext}}(\mathbf{r})$, which for simplicity will be assumed to be that of a $3d$ harmonic oscillator $V_{\mathrm{ext}}=\alpha r^2$. The statistical theory of such a weakly interacting system with interaction energy $U_0=4\pi a_S\hbar^2/M$ in a potential trap is well established for the

atomic case[11–13] and we will shortly review these results, only. In the standard mean-field theory, one has to solve the Gross-Pitaevski (GP) equation which reads for $T=0$ as

$$-\frac{\hbar^2}{2M}\Delta\Psi(\mathbf{r})+V(\mathbf{r})\Psi(\mathbf{r})+U_0|\Psi(\mathbf{r})|^2\Psi(\mathbf{r})=\mu\Psi(\mathbf{r}) \quad (2)$$

to obtain the wave function of the condensate $\Psi(\mathbf{r})$ and the condensate density $n_c(\mathbf{r})=|\Psi(\mathbf{r})|^2$ for a given chemical potential μ.

The linear response and thus the luminescence spectrum is represented by the Hartree-Fock-Bogoliubov equations which we use in the Popov approximation (HFBP), which is valid also at temperatures around T_c.

As discussed earlier, we can apply the LDA or semiclassical approximation. Here the densities of the condensate $n_c(\mathbf{r})$ and of the thermal excitons in excited states $n_T(\mathbf{r})$ and the Bogoliubov amplitudes are local functions $u(\mathbf{p},\mathbf{r})$, $v(\mathbf{p},\mathbf{r})$ that solve the coupled equations

$$\begin{pmatrix} \mathcal{L}(\mathbf{p},\mathbf{r}) & U_0 n_c(\mathbf{r}) \\ -U_0 n_c(\mathbf{r}) & -\mathcal{L}(\mathbf{p},\mathbf{r}) \end{pmatrix}\begin{pmatrix} u(\mathbf{p},\mathbf{r}) \\ v(\mathbf{p},\mathbf{r}) \end{pmatrix}=\epsilon(\mathbf{p},\mathbf{r})\begin{pmatrix} u(\mathbf{p},\mathbf{r}) \\ v(\mathbf{p},\mathbf{r}) \end{pmatrix} \quad (3)$$

with

$$\mathcal{L}(\mathbf{p},\mathbf{r})=p^2/2M+V_{\text{ext}}(\mathbf{r})-\mu+2U_0 n(\mathbf{r}) \quad (4)$$

and the renormalized energies of the excited states

$$\epsilon(\mathbf{p},\mathbf{r})=[(\mathcal{L}(\mathbf{p},\mathbf{r}))^2-(U_0 n_c(\mathbf{r}))^2]^{1/2}. \quad (5)$$

$n=n_c+n_T$ is the total density. The Bogoliubov amplitudes u and v are given by the usual relations

$$u(\mathbf{p},\mathbf{r})^2=\frac{1}{2}\{\mathcal{L}(\mathbf{p},\mathbf{r})/\epsilon(\mathbf{p},\mathbf{r})+1\}, \quad (6a)$$

$$v(\mathbf{p},\mathbf{r})^2=\frac{1}{2}\{\mathcal{L}(\mathbf{p},\mathbf{r})/\epsilon(\mathbf{p},\mathbf{r})-1\}. \quad (6b)$$

The density of the excitons in thermally excited states can be found by integrating over the excited states

$$n_T(\mathbf{r})=\int\frac{d^3\mathbf{p}}{8\pi^3}\left[\frac{\mathcal{L}(\mathbf{p},\mathbf{r})}{\epsilon(\mathbf{p},\mathbf{r})}\left(n_B(\mathbf{p},\mathbf{r})+\frac{1}{2}\right)-\frac{1}{2}\right]\Theta(\epsilon(\mathbf{p},\mathbf{r})^2) \quad (7)$$

where the Bose function is given by

$$n_B(\mathbf{p},\mathbf{r})=\frac{1}{\exp[\epsilon(\mathbf{p},\mathbf{r})/k_BT]-1} \quad (8)$$

and Θ is the Heaviside function which is equal to one when the argument is positive and zero otherwise. For temperatures not too close to T_c, the thickness of the surface of the BEC cloud is much smaller than the radius $\delta\ll R_0$. Then one can neglect the kinetic-energy term in Eq. (2) and the system can by be described quite accurately in the Thomas-Fermi approximation. Then the density of the condensate is given by[12]

$$n_c(\mathbf{r})=\frac{\mu-V_{\text{ext}}(\mathbf{r})-2U_0 n_T}{U_0}\Theta(\mu-V_{\text{ext}}(\mathbf{r})-2U_0 n_T). \quad (9)$$

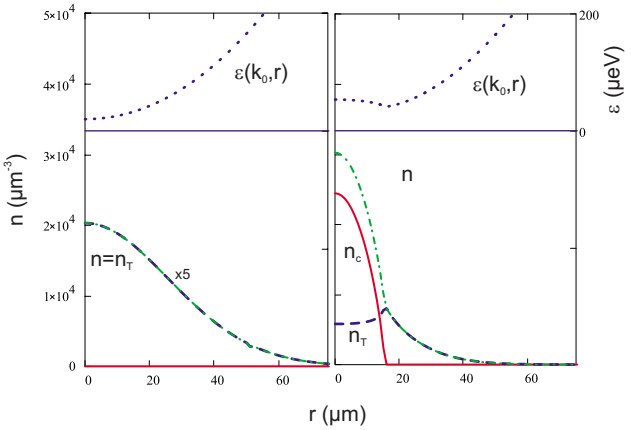

FIG. 1. (Color online) Density (full and dashed lines) and renormalized quasiparticle energy (dotted line) for $N=1\times10^9$ excitons in the trap. $T=1$ K (left) and $T=0.5$ K (right). Parameters are: $\alpha=0.06$ μeV/μm^2, $U_0=0.75$ neV/μm^3.

For a given chemical potential, Eqs. (7) and (9) allow a self-consistent solution for all the relevant quantities. The total number of particles N is then found by integrating the total density over the volume of the trap.

Finally, it should be noted that if the temperature is too high to allow for a condensate, the HFBP approximation goes over smoothly into the description of a weakly interacting Bose gas with a chemical potential $\mu=\mu_{\text{ideal}}+2U_0 n_T$.[12] In Fig. 1 typical results for the density profiles obtained by this procedure are shown for the case of a normal system above T_c (left) and with a condensate present (right). The calculation shows that the diameter of the cloud is somewhat smaller than predicted by the simple approximation given above (18 vs 24.5 μm).

Excitonic systems have one distinct property compared to other Bose gases in that they decay by emitting photons under energy and momentum conservation. This can proceed either directly, whereby momentum conservation requires that only excitons with the same momentum as the emitted photons are involved, or with assistance of momentum supplying phonons such that all exciton states can participate in the optical emission.[21] The latter process has been considered already for a homogeneous Bose gas of interacting excitons by several authors.[19,20] Here it was shown, that the luminescence spectrum is determined by the excitonic spectral function $A(\mathbf{k},\omega)$,

$$I(\omega')\propto 2\pi|S(\mathbf{k}=0)|^2\delta(\hbar\omega'-\mu)n_c + \sum_{\mathbf{k}\neq0}|S(\mathbf{k})|^2 n_B(\hbar\omega'-\mu)A(\mathbf{k},\hbar\omega'-\mu) \quad (10)$$

with $S(\mathbf{k})$ representing the exciton-photon coupling and n_B being usual Bose function (8). In the case of phonon-assisted transitions, we have $\omega'=\omega-\omega_{gX}-\omega_{\text{phonon}}$ with $\hbar\omega_{gX}$ being the excitonic band gap of the semiconductor. $S(\mathbf{k})$ can be assumed to be $\mathbf{k}$ independent. The first term in Eq. (10) gives rise to a δ shaped luminescence line at the position of the chemical potential of the system, the strength of which is

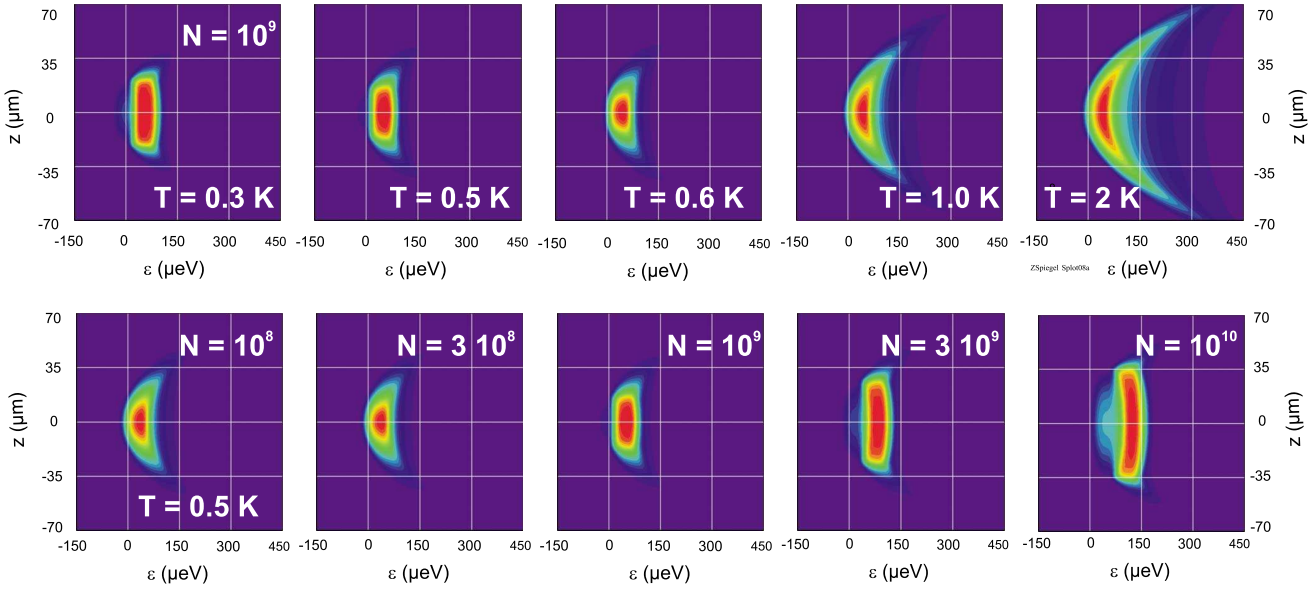

FIG. 2. (Color online) Luminescence spectra of the direct luminescence process. Upper row with constant particle number $N=1\times10^9$ and at constant temperature ($T=0.5$ K) with increasing particle numbers in the trap (lower row). The critical temperature T_c is approximately 0.6 K (upper row, middle).

determined by the coupling function at $k=0$ and the condensate density.

The case of the $3d$ bulk state with direct exciton-photon coupling can be treated in the same way with $\omega'=\omega-\omega_{gX}$ and $S(\mathbf{k})=S_0\delta(\mathbf{k}-\mathbf{k}_0)$. $\mathbf{k}_0$ is the wavevector of the intersection of photon and exciton dispersion. Its modulus is given by $k_0=\omega_{gX}n/c$, where n is the refraction index and c is the vacuum velocity of light. Here we see already a remarkable difference between direct and phonon-assisted luminescence processes: due to the form of $S(\mathbf{k})$, the condensate itself does not contribute in the direct luminescence process. However, we will show that, in case of a potential trap, there will be indirect signatures of the condensate.

A first-principles calculation of the decay luminescence spectrum in a trap is a challenging task (see, e.g., Ref. 17 for the case of a $2d$ potential trap). Here we proceed in a much simpler way by noting that the optical wavelength of the emission (in case of Cu_2O about 200 nm) is much smaller than the size of the exciton cloud with diameter $2R_0$. Therefore, one can apply a local approximation also for the spectral function, which then becomes that of the homogeneous case[19] but now in addition a function of $\mathbf{r}$,

$$A(\mathbf{r},\mathbf{k},\omega)=2\pi[u(\mathbf{k},\mathbf{r})^2\delta(\hbar\omega-\epsilon(\mathbf{k},\mathbf{r})) - v(\mathbf{k},\mathbf{r})^2\delta(\hbar\omega+\epsilon(\mathbf{k},\mathbf{r}))]. \quad (11)$$

Here $\epsilon(\mathbf{k},\mathbf{r})$ are the renormalized energies [Eq. (5)]. This means that in Eq. (10) the frequency ω' is determined by the local exciton energy $\hbar\omega'_{loc}=\hbar\omega-\hbar\omega_{gX}-V_{\text{ext}}(\mathbf{r})$ while μ is the local chemical potential $\mu_{loc}=\mu-V_{\text{ext}}(\mathbf{r})$. Obviously, the external potential cancels in the argument of $I(\omega')$, which depends only on the global chemical potential of the system, as it should. The lineshape of the luminescence spectrum is determined by the renormalized energies of the excited states of the system, but now evaluated at each point in the trap.

While for the phonon-assisted process, Eq. (11) gives rise to a smooth spectrum,[19] the direct process behaves differently. Emission will come only from the states with wave vector k_0. The intensity, therefore, reflects only the occupation of this state, but the spectral position of the line at $\mu+\epsilon(\mathbf{k}_0,\mathbf{r})$ directly gives the renormalization of the quasiparticle energy dispersion due to the condensate. Furthermore, due to the pole of the δ-function at $\hbar\omega'=\mu-\epsilon(\mathbf{k},\mathbf{r})$ in the condensate ($v\neq0$) emission occurs also at the low energy side of the chemical potential. Both effects provide unique and sensitive footprints of the onset of BEC.

We now apply the foregoing results to study the behavior of the luminescence line in the case of a weak direct exciton-photon interaction with parameters adjusted to the case of the lowest exciton state in Cu_2O. Made up from both positive parity and doubly degenerate valence and conduction bands, the four exciton states split in a triply degenerate orthoexciton and in a single paraexciton, which is the energetically lowest exciton state, split off by 12 meV from the ortho states due to electron-hole exchange.[5] While the latter are optically weakly allowed [quadrupole transition, oscillator strength 3×10^{-9} (Ref. 22)], the paraexciton as a pure spin triplet state is forbidden in all orders. Its intrinsic decay is only possible via an odd-parity optical phonon with Γ_5^- symmetry, from which we expect a very long lifetime of these exciton states[14] and thus an almost true equilibrium BEC of $3d$ excitons.

In a strain trap, the paraexciton becomes weakly allowed due to mixing with higher lying exciton states, the oscillator strength remains quite small so that the theory given above is applicable. The weak variation in the transition probability with strain across the trap will be neglected. In the typical experimental situation, one images a small stripe of width Δx elongated along the z direction centered in the center of the trap onto the entrance slit of a spectrograph. Integrating over

the y direction perpendicular to z we obtain a spatially resolved spectrum $I(z,\omega)$. In order to compare with any real experimental situation, one has to convolute the spectra with the finite resolution of the spectrograph. For this we take a slit function of supergaussian shape $s(x) \propto \exp(-(x/\Delta)^4)$ with full width at half maximum $1.825\Delta = 75$ μeV.

There are three parameters that influence the behavior of the excitons: trap potential constant α, interaction strength U_0 and mass M. For the model calculations we assumed the following parameters $M = 2.6m_e$, $\alpha = 0.06$ $\mu\text{eV}/\mu\text{m}^2$ and $U_0 = 0.75$ neV μm^3. In Fig. 2 we have plotted a series of spatially resolved spectra for a range of exciton numbers and temperatures. While the upper row shows the variation in temperature at constant $N = 10^9$, the lower series demonstrates the influence of N at a temperature of $T = 0.5$ K. While at $T > T_c$ or equivalently $N < N_c$, the lineshape follows strictly the parabolic shape of the potential well, as one expects for a normal gas, below T_c the spectrum changes drastically. The low energy side becomes almost flat. The crossover, however, is smooth since the flattening starts at a single point in the trap center. For very high particle number a weak shoulder develops at the low energy side, which represents the anomalous luminescence via the negative pole due to the condensate. In contrast to the case of a noninteracting system, the spatial width of the spectrum may become even larger than the thermal width (compare, e.g., spectra for $N = 3 \times 10^9$ and $N = 10^{10}$). The quantitative behavior, of course, will depend on the fine details of the shape of the potential trap, but the qualitative features will be the same. Thus, these drastic changes in the luminescence spectrum can be considered as a unique footprint of the Bose-Einstein condensation of excitons in a potential trap.

Finally, we ask whether an experimental realization seems to be possible with the present knowledge of the exciton properties in Cu_2O. Previous experiments with excitons in Cu_2O (Refs. 6, 7, and 10) have shown that, under quasi-cw excitation with an absorbed laser power of 50 mW, 2×10^9 excitons can be put into a trap but with an excitonic temperature of about 2.5 K which certainly is not enough for a BEC. Extrapolating the data, one should either increase the pump power to a value of 10 W or reduce the temperature of the exciton system below 0.75 K. Both strategies seem to be possible by present day technology.

We have shown that the luminescence spectrum of the direct recombination luminescence of excitons in a potential trap changes in a unique way if a condensate of excitons is present. This change is independent of the details of the excitonic systems and reflects directly the renormalization of the quasiparticle energies due to the interaction of the excitons.

We acknowledge the support by the Deutsche Forschungsgemeinschaft (Collaborative Research Center SFB 652 "Starke Korrelationen im Strahlungsfeld").

[1] A. Einstein, Sitzungsber. Preuss. Akad. Wiss., Phys. Math. Kl. **1925**, 3.
[2] M. H. Anderson, J. R. Ensher, M. R. Matthews, C. E. Wieman, and E. A. Cornell, Science **269**, 198 (1995).
[3] K. B. Davis, M.-O. Mewes, M. R. Andrews, N. J. van Druten, D. S. Durfee, D. M. Kurn, and W. Ketterle, Phys. Rev. Lett. **75**, 3969 (1995).
[4] R. Balili, V. Hartwell, D. Snoke, L. Pfeiffer, and K. West, Science **316**, 1007 (2007).
[5] S. A. Moskalenko and D. W. Snoke, *Bose-Einstein Condensation of Excitons and Biexcitons* (Cambridge University Press, Cambridge, 2000).
[6] D. P. Trauernicht, J. P. Wolfe, and A. Mysyrowicz, Phys. Rev. B **34**, 2561 (1986).
[7] D. W. Snoke and V. Negoita, Phys. Rev. B **61**, 2904 (2000).
[8] N. Naka and N. Nagasawa, Phys. Rev. B **65**, 075209 (2002).
[9] D. W. Snoke, J. P. Wolfe, and A. Mysyrowicz, Phys. Rev. Lett. **64**, 2543 (1990).
[10] J.-L. Lin and J. P. Wolfe, Phys. Rev. Lett. **71**, 1222 (1993).
[11] A. Griffin, Phys. Rev. B **53**, 9341 (1996).
[12] J. Reidl, A. Csordàs, R. Graham, and P. Szèpfalusy, Phys. Rev. A **59**, 3816 (1999); T. Bergeman, D. L. Feder, N. L. Balazs, and B. I. Schneider, *ibid.* **61**, 063605 (2000); N. P. Proukakis and B. Jackson, J. Phys. B **41**, 203002 (2008).
[13] C. J. Pethick and H. Smith, *Bose-Einstein Condensation in Dilute Gases* (Cambridge University Press, Cambridge, 2002).
[14] J. Brandt, D. Fröhlich, Ch. Sandfort, M. Bayer, H. Stolz, and N. Naka, Phys. Rev. Lett. **99**, 217403 (2007).
[15] K. E. O'Hara and J. P. Wolfe, Phys. Rev. B **62**, 12909 (2000).
[16] S. Okumura and T. Ogawa, Phys. Rev. B **65**, 035105 (2001).
[17] R. Zimmermann, in *Problems of Condensed Matter Physics—Quantum Coherence Phenomena in Electron-Hole and Coupled Light-Matter Systems*, edited by A. L. Ivanov and S. G. Tikhodeev (Oxford University Press, Oxford, 2007), p. 281.
[18] D. Semkat, F. Richter, D. Kremp, G. Manzke, W.-D. Kraeft, and K. Henneberger, Phys. Rev. B **80**, 155201 (2009).
[19] H. Shi, G. Verechaka, and A. Griffin, Phys. Rev. B **50**, 1119 (1994).
[20] H. Haug and H. Kranz, Z. Phys. B **53**, 151 (1983).
[21] See any textbook on optical properties of semiconductors, e.g., C. Klingshirn, *Semiconductor Optics* (Springer Verlag, Berlin, Heidelberg, 2005).
[22] D. Fröhlich, A. Kulik, B. Uebbing, A. Mysyrowicz, V. Langer, H. Stolz, and W. von der Osten, Phys. Rev. Lett. **67**, 2343 (1991).

A.5

Artikel 5

S. Sobkowiak, D. Semkat, H. Stolz, Th. Koch, and H. Fehske:

Interacting multi-component exciton gases in a potential trap: Phase separation and Bose-Einstein condensation

Phys. Rev. B **82**, 064505 (2010)

Interacting multicomponent exciton gases in a potential trap: Phase separation and Bose-Einstein condensation

S. Sobkowiak, D. Semkat, and H. Stolz
Institut für Physik, Universität Rostock, 18051 Rostock, Germany

Th. Koch and H. Fehske
Institut für Physik, Ernst-Moritz-Arndt-Universität Greifswald, 17489 Greifswald, Germany

(Received 3 May 2010; published 5 August 2010)

The system under consideration is a multicomponent gas of interacting paraexcitons and orthoexcitons confined in a three-dimensional potential trap. We calculate the spatially resolved optical emission spectrum due to interband transitions involving weak direct and phonon-mediated exciton-photon interactions. For each component, the occurrence of a Bose-Einstein condensate changes the spectrum in a characteristic way so that it directly reflects the constant chemical potential of the excitons and the renormalization of the quasiparticle excitation spectrum. Moreover, the interaction between the components leads, in dependence on temperature and particle number, to modifications of the spectra indicating phase separation of the subsystems. Typical examples of density profiles and luminescence spectra of ground-state paraexcitons and orthoexcitons in Cu_2O are given.

DOI: 10.1103/PhysRevB.82.064505 PACS number(s): 78.20.−e, 78.30.−j, 71.35.Lk

I. INTRODUCTION

Excitons in semiconductors have been promising candidates for the observation of Bose-Einstein condensation for several decades. At present, cuprous oxide (Cu_2O) is in the focus of experimental efforts due to the large binding energy and long lifetime of the exciton states. In order to obtain sufficiently high densities, entrapment by an external potential is an approved method.

The theoretical description of excitons in potential traps has been carried out so far mostly in the frame of a model of ideal bosons. Concepts for the inclusion of the interaction are well known from the theory of atomic condensates[1–4] and first applications to excitons exist, too.[5] Recent investigations in the framework of a mean-field formalism in local-density approximation (LDA) have shown distinct signatures of a condensate in the decay luminescence spectrum of the noncondensed excitons.[6] It is the aim of the present paper to introduce a generalization of this theory to a multicomponent gas of interacting paraexcitons and orthoexcitons, where the consequences of the interaction on the condensation process are of particular interest. We show results for the densities of the individual components and their spatially resolved luminescence spectra for several parameter regimes and highlight experimentally relevant cases.

II. THERMODYNAMICS OF EXCITONS IN A POTENTIAL TRAP

The thermodynamics of a one-component Bose gas has been investigated in detail, see, e.g., Refs. 1–4. First applications of these concepts to excitons have been presented in Ref. 5 and, looking at spectral signatures of a condensate, in Ref. 6. In analogy to generalizations for multicomponent atomic gases, e.g., Refs. 7–12 and spinor polaritons, e.g., Refs. 13 and 14, in the following, we generalize this approach to the case of multiple species of excitons, i.e., paraexcitons and orthoexcitons, adopting a mean-field coupling scheme between the components.[15]

The multicomponent exciton gas is considered in second quantization. We start from the Hamiltonian for a K-component system in the grand-canonical ensemble,

$$\mathcal{H} = \sum_{i=1}^{K} \int d\mathbf{r} \psi_i^\dagger(\mathbf{r},t) \left[-\frac{\hbar^2 \nabla^2}{2M_i} + V_i(\mathbf{r}) - \mu_i \right] \psi_i(\mathbf{r},t) + \frac{1}{2} \sum_{i,j=1}^{K} \int d\mathbf{r} h_{ij} \psi_i^\dagger(\mathbf{r},t) \psi_j^\dagger(\mathbf{r},t) \psi_j(\mathbf{r},t) \psi_i(\mathbf{r},t) \tag{1}$$

with respective external potentials V_i and chemical potentials μ_i for each species. We assume a contact potential for the exciton-exciton interaction with the matrix h_{ij} containing the intraspecies and interspecies interaction strengths. Its components are given by the s-wave scattering lengths a_{ij}^s,

$$h_{ij} = 2\pi\hbar^2 \left(\frac{1}{M_i} + \frac{1}{M_j} \right) a_{ij}^s. \tag{2}$$

The Bose field operator ψ_i obeys the Heisenberg equation of motion

$$i\hbar \frac{\partial \psi_i(\mathbf{r},t)}{\partial t} = \left[-\frac{\hbar^2 \nabla^2}{2M_i} + V_i(\mathbf{r}) - \mu_i \right] \psi_i(\mathbf{r},t) + \sum_{j=1}^{K} h_{ij} \psi_j^\dagger(\mathbf{r},t) \psi_j(\mathbf{r},t) \psi_i(\mathbf{r},t). \tag{3}$$

We decompose the field operators ψ_i in the usual fashion,

$$\psi_i(\mathbf{r},t) = \Phi_i(\mathbf{r}) + \tilde{\psi}_i(\mathbf{r},t), \tag{4}$$

where Φ_i is the (scalar) condensate wave function with $\Phi_i(\mathbf{r}) = \langle \psi_i(\mathbf{r},t) \rangle = \langle \psi_i(\mathbf{r}) \rangle$ and $\tilde{\psi}_i$ is the operator of the thermal excitons. Inserting the decomposition Eq. (4) into Eq. (3) and

following the steps of Ref. 1, we obtain (arguments dropped for the sake of brevity)

$$0 = \left[-\frac{\hbar^2\nabla^2}{2M_i} + V_i - \mu_i + h_{ii}(n_{ii} + \tilde{n}_{ii}) + \sum_{j\neq i} h_{ij} n_{jj} \right] \Phi_i + h_{ii}\tilde{m}_{ii}\Phi_i^* + \sum_{j\neq i} h_{ij}(\tilde{n}_{ji}\Phi_j + \tilde{m}_{ji}\Phi_j^*) \quad (5)$$

and

$$i\hbar\frac{\partial\tilde{\psi}_i}{\partial t} = \left(-\frac{\hbar^2\nabla^2}{2M_i} + V_i - \mu_i + 2h_{ii}n_{ii} + \sum_{j\neq i} h_{ij} n_{jj} \right) \tilde{\psi}_i + h_{ii} m_{ii} \tilde{\psi}_i^\dagger + \sum_{j\neq i} h_{ij}(n_{ij}\tilde{\psi}_j + m_{ij}\tilde{\psi}_j^\dagger) \quad (6)$$

with $n_{ij} \equiv \Phi_j^*\Phi_i + \tilde{n}_{ij}$, $m_{ij} \equiv \Phi_j\Phi_i + \tilde{m}_{ij}$, and the normal and anomalous averages $\tilde{n}_{ij} = \langle \tilde{\psi}_i^\dagger \tilde{\psi}_j \rangle$ and $\tilde{m}_{ij} = \langle \tilde{\psi}_i \tilde{\psi}_j \rangle$, respectively. Equation (5) generalizes the familiar Gross-Pitaevskii equation by including (i) the coupling to the thermal excitons and (ii) the coupling of multiple components.

In a first approximation, we neglect all nondiagonal averages, i.e., $\tilde{m}_{ij} = \tilde{n}_{ij} = m_{ij} = n_{ij} = 0 \quad \forall\, i \neq j$, reducing Eqs. (5) and (6) to effective one-species equations with an additional mean-field contribution from the other species,

$$0 = \left[-\frac{\hbar^2\nabla^2}{2M_i} + V_i - \mu_i + h_{ii}(n_{ii} + \tilde{n}_{ii}) + \sum_{j\neq i} h_{ij} n_{jj} \right] \Phi_i + h_{ii}\tilde{m}_{ii}\Phi_i^*, \quad (7)$$

$$i\hbar\frac{\partial\tilde{\psi}_i}{\partial t} = \left(-\frac{\hbar^2\nabla^2}{2M_i} + V_i - \mu_i + 2h_{ii}n_{ii} + \sum_{j\neq i} h_{ij} n_{jj} \right) \tilde{\psi}_i + h_{ii} m_{ii} \tilde{\psi}_i^\dagger . \quad (8)$$

Thanks to this simplification, Eq. (8) can be formally solved by a Bogoliubov transformation,

$$\tilde{\psi}_i = \sum_\sigma [u_i(\sigma) a_i(\sigma) e^{-iE_i(\sigma)t/\hbar} + v_i^*(\sigma) a_i^\dagger(\sigma) e^{iE_i(\sigma)t/\hbar}], \quad (9)$$

where σ enumerates the quasiparticle states. Thereby the Bogoliubov amplitudes u_i and v_i satisfy the relation $\Sigma_\sigma[u_i(\sigma)^2 - v_i(\sigma)^2] = 1$. The excitation spectrum $E_i(\sigma)$ is given by the solution of the eigenvalue problem,

$$\begin{pmatrix} \mathcal{L}_i & h_{ii}m_{ii} \\ -h_{ii}m_{ii}^* & -\mathcal{L}_i \end{pmatrix} \begin{pmatrix} u_i(\sigma) \\ v_i(\sigma) \end{pmatrix} = E_i(\sigma) \begin{pmatrix} u_i(\sigma) \\ v_i(\sigma) \end{pmatrix} \quad (10)$$

with

$$\mathcal{L}_i = -\frac{\hbar^2\nabla^2}{2M_i} + V_i - \mu_i + 2h_{ii}n_{ii} + \sum_{j\neq i} h_{ij} n_{jj}. \quad (11)$$

Equations (7) and (10) are the multicomponent generalizations of the Hartree-Fock-Bogoliubov equations. They represent a system of $3K$ equations which are coupled via the interaction matrix elements h_{ij}.

To guarantee gapless spectra, we next apply the Popov approximation, i.e., we neglect the anomalous averages $\tilde{m}_{ii}$ in Eqs. (7) and (10) and find

$$0 = \left[-\frac{\hbar^2\nabla^2}{2M_i} + V_i - \mu_i + h_{ii}(n_{ii} + \tilde{n}_{ii}) + \sum_{j\neq i} h_{ij} n_{jj} \right] \Phi_i \quad (12)$$

and

$$\begin{pmatrix} \mathcal{L}_i & h_{ii}\Phi_i^2 \\ -h_{ii}\Phi_i^{*2} & -\mathcal{L}_i \end{pmatrix} \begin{pmatrix} u_i(\sigma) \\ v_i(\sigma) \end{pmatrix} = E_i(\sigma) \begin{pmatrix} u_i(\sigma) \\ v_i(\sigma) \end{pmatrix}. \quad (13)$$

Since the extension of the potential trap is large compared to the typical length scale of the system (e.g., the thermal de Broglie wavelength of the excitons), we can use the LDA. Then the excitons are treated as a locally homogeneous system and the spatial dependence enters only via the trap potential. In that case, the Bogoliubov equations are readily solved, yielding the density $n_i^T \equiv \tilde{n}_{ii}$ of thermally excited excitons as

$$n_i^T(\mathbf{r}) = \int \frac{d^3\mathbf{k}}{8\pi^3} \left[\frac{L_i(\mathbf{k},\mathbf{r})}{E_i(\mathbf{k},\mathbf{r})} \left\{ n_B[E_i(\mathbf{k},\mathbf{r})] + \frac{1}{2} \right\} - \frac{1}{2} \right] \times \Theta[E_i(\mathbf{k},\mathbf{r})^2] \quad (14)$$

with $n_B(E) = [\exp(E/k_BT) - 1]^{-1}$ being the usual Bose function. The excitation spectrum E_i is explicitly given by

$$E_i(\mathbf{k},\mathbf{r}) = \sqrt{L_i(\mathbf{k},\mathbf{r})^2 - [h_{ii}n_i^c(\mathbf{r})]^2}, \quad (15)$$

$$L_i(\mathbf{k},\mathbf{r}) = \frac{\hbar^2k^2}{2M_i} + V_i(\mathbf{r}) - \mu_i + 2h_{ii}n_i(\mathbf{r}) + \sum_{j\neq i} h_{ij} n_j(\mathbf{r}) \quad (16)$$

with $n_i^c \equiv |\Phi_i|^2$ and $n_i \equiv n_{ii} = n_i^T + n_i^c$. In consistence with the LDA, we apply the Thomas-Fermi approximation to the Gross-Pitaevskii equation, neglecting the kinetic-energy term in Eq. (12). Then we obtain finally for the densities of the condensates

$$n_i^c(\mathbf{r}) = \frac{1}{h_{ii}} \left[\mu_i - V_i(\mathbf{r}) - 2h_{ii}n_i^T(\mathbf{r}) - \sum_{j\neq i} h_{ij} n_j(\mathbf{r}) \right] \times \Theta \left[\mu_i - V_i(\mathbf{r}) - 2h_{ii}n_i^T(\mathbf{r}) - \sum_{j\neq i} h_{ij} n_j(\mathbf{r}) \right]. \quad (17)$$

Expressions (14)–(17) have to be solved self-consistently. Although they look very similar to the one-component case, a coupling between the components appears via L_i and n_i^c.

In what follows we calculate the densities of excitons in Cu_2O in a strain induced potential trap.[16] In addition to the paraexcitons (labeled "p"), two spin projections of orthoexcitons are captured by the trap, denoted by "+" and "–," while the zero component is expelled and plays no role. Thus, the number of components $K = 3$. In addition to the usual symmetry of the interaction matrix, $h_{ij} = h_{ji}$ with $i,j = p,+,-$, in our case it holds that $h_{++} = h_{--}$ and $h_{p+} = h_{p-}$, leaving four independent parameters h_{pp}, h_{++}, h_{p+}, and h_{+-}. As extensive works on two-component systems[7–9,12] have shown, one of the most interesting aspects of multicomponent systems—the occurrence of phase separation—is closely tied to the proportions of interspecies and intraspecies interaction strengths.

According to Eq. (2), the interaction strengths are given by the s-wave scattering lengths of the corresponding channels, which can be obtained by the solution of the four-particle scattering problem. The case of positronium-positronium scattering some time ago received much attention[17–19] and quite reliable values of the scattering length for both the singlet and the triplet channel have been obtained. In contrast, the description of exciton-exciton interaction is a long-standing problem and so far no satisfying solution for the general case has been obtained. Especially for Cu_2O, we expect a strong effect of the nonparabolicity of the valence band[20] and of the rather large electron-hole exchange interaction[21] on the scattering lengths. Therefore, the values we deduced from the scattering lengths of the positronium problem given in Ref. 17 ($h_{++}=0.71\ h_{pp}$, $h_{p+}=0.33\ h_{pp}$, and $h_{+-}=1.77\ h_{pp}$ with $h_{pp}=7.5\times10^{-4}\ \mu\text{eV}\ \mu\text{m}^3$), should be considered as representative, only. Nevertheless, they allow to show the general behavior of the multicomponent exciton system. In the calculation we also neglect the difference in the paraexciton and orthoexciton mass due to the k-dependent exchange interaction.[22]

III. LUMINESCENCE SPECTRUM

Excitons decay by emitting photons. This takes place either directly, whereby momentum conservation requires that only excitons with the same momentum as the emitted photons are involved, or with assistance of momentum supplying phonons such that all exciton states can participate in the optical emission. Because the optical wavelength of the emission is much smaller than the trapped exciton cloud, we apply a local approximation to the emission spectrum, which, for the homogeneous case, is determined by the excitonic spectral function $A(\mathbf{k},\omega)$,[23,24]

$$I_i(\mathbf{r},\omega) \propto 2\pi|S_i(\mathbf{k}=0)|^2\delta(\hbar\omega'-\mu_i)n_i^c(\mathbf{r}) + \sum_{\mathbf{k}\neq0}|S_i(\mathbf{k})|^2 n_B(\hbar\omega'-\mu_i)A_i(\mathbf{r},\mathbf{k},\hbar\omega'-\mu_i) \tag{18}$$

with $S_i(\mathbf{k})$ representing the exciton-photon coupling. The spectral function is given by the Bogoliubov amplitudes u_i and v_i and the quasiparticle spectrum in Eq. (15),

$$A_i(\mathbf{r},\mathbf{k},\omega) = 2\pi\hbar\{u_i^2(\mathbf{k},\mathbf{r})\delta[\hbar\omega - E_i(\mathbf{k},\mathbf{r})] - v_i^2(\mathbf{k},\mathbf{r})\delta[\hbar\omega + E_i(\mathbf{k},\mathbf{r})]\}. \tag{19}$$

In order to account for a finite spectral resolution being important for comparison with measured spectra, we convolute the spectral intensity, Eq. (18), with a slit function of the shape $\exp[-(\omega/\Delta)^4]$. Here, Δ is a measure for the spectral resolution. Furthermore, in a typical experimental situation, one images a small stripe of width $2\Delta x$ elongated along the z direction onto the entrance slit of a spectrograph. Integrating over the y direction perpendicular to z we obtain the spatially resolved spectrum of the thermal excitons (in the following, the direct condensate contribution is not considered),

$$I_i(\omega,z) \propto \int_{-\Delta x}^{\Delta x} dx \int_{-\infty}^{\infty} dy \int d\mathbf{k}|S_i(\mathbf{k})|^2 u_i^2(\mathbf{k},\mathbf{r}) \times n_B[E_i(\mathbf{k},\mathbf{r})]\exp[-\varepsilon_-^4(\omega',\mathbf{k},\mathbf{r})] - \int_{-\Delta x}^{\Delta x} dx \int_{-\infty}^{\infty} dy \int d\mathbf{k}|S_i(\mathbf{k})|^2 v_i^2(\mathbf{k},\mathbf{r}) \times n_B[-E_i(\mathbf{k},\mathbf{r})]\exp[-\varepsilon_+^4(\omega',\mathbf{k},\mathbf{r})] \tag{20}$$

with $\varepsilon_\pm(\omega',\mathbf{k},\mathbf{r}) \equiv [\hbar\omega' - \mu \pm E(\mathbf{k},\mathbf{r})]/\Delta$.

In the case of phonon-assisted transitions (being relevant for the orthoexcitons), we have $\omega' = \omega - E_{gX}/\hbar - \omega_{\text{phonon}}$ with E_{gX} being the excitonic band gap of the semiconductor. We assume $S(\mathbf{k})$ to be a constant. Then the first term in Eq. (18) gives rise to a δ-shaped luminescence line at the position of the chemical potential with a strength determined by the condensate density.

For trapped paraexcitons, the zero-phonon decay is relevant and can be treated by setting $\omega' = \omega - E_{gX}/\hbar$ and $S(\mathbf{k}) = S_0\delta(\mathbf{k}-\mathbf{k}_0)$. Here $\mathbf{k}_0$ is the wave vector of the intersection of photon and exciton dispersion. Its modulus is given by $k_0 = E_{gX}n/\hbar c$, where n is the refraction index and c is the vacuum velocity of light. Due to the form of $S(\mathbf{k})$, the condensate itself does not contribute to the direct luminescence process.

However, as discussed for the one-component exciton gas in Ref. 6, in case of a potential trap there will be indirect signatures of the condensate in the spatially resolved luminescence spectrum. The spectral line shape follows the density distribution in the trap, which in turn is bordered by the minimal excitation energy $E(\mathbf{k}=0,\mathbf{r})$. For a noncondensed gas the latter quantity is roughly parabolic due to the trapping potential while it is zero in the presence of a condensate. Thus with increasing particle number (or decreasing temperature) the flat bottom of the spectrum of thermal excitons may be a footprint of Bose-Einstein condensation.

IV. RESULTS

We evaluate the density distributions of the trapped excitons in an iterative way. In each step, we keep the distributions of two of the components fixed. Under the constraint of fixed particle number, we iterate the subset of Eqs. (14)–(17) belonging to the third component to self-consistency. We cycle through the components until self-consistency of the whole system, Eqs. (14)–(17), is achieved.

Depending on the temperature and particle numbers in the trap, there may occur six distinct situations, featuring a condensate of (i) none of the species, (ii) only the paraexcitons, (iii) only one species of orthoexcitons, (iv) both species of orthoexcitons, (v) paraexcitons and one species of orthoexcitons, and (vi) all species. To analyze these cases, we set the particle numbers of each component to one of two values: $N_i = 5\times10^9$ or $N_i = 5\times10^8$ for $i = p,+,-$, respectively. We get a rough estimate of the corresponding critical temperatures by applying a harmonic approximation to the Hertzian potentials. Then, a simple Thomas-Fermi calculation for the single-component case[25] yields $T_c^0 \approx 2$ K for $N = 5\times10^9$ and $T_c^0 \approx 1$ K for $N = 5\times10^8$.

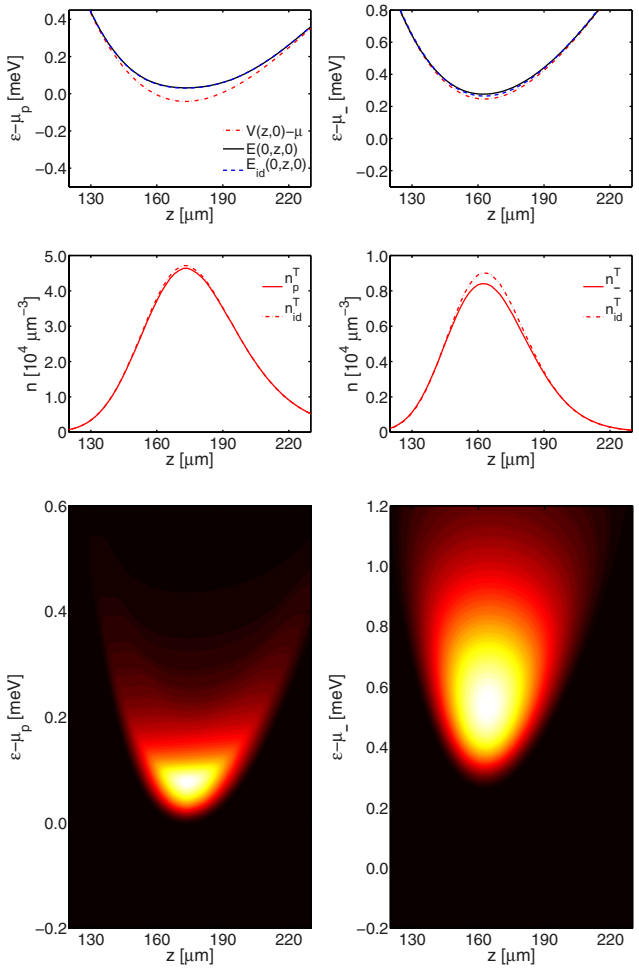

FIG. 1. (Color online) Potentials and density profiles in z direction at $(x,y)=(0,0)$, and luminescence spectra for paraexcitons (left column) and ortho(−)excitons (right column) for a temperature of $T=2.2$ K and particle numbers of $N_p=5\times10^9$ and $N_-=N_+=5\times10^8$ in the trap. The corresponding chemical potentials are $\mu_p=-2260$ μeV and $\mu_-=\mu_+=-5920$ μeV. Upper row: external trap potential V_i, quasiparticle energy at $\mathbf{k}=0$ shifted by μ (i.e., renormalized potential) $E(0,z,0)$, and the same quantity without interspecies interaction $E_{id}(0,z,0)$. Middle row: densities of thermal excitons with (n^T) and without interspecies interaction (n_{id}^T). Lower row: luminescence spectra.

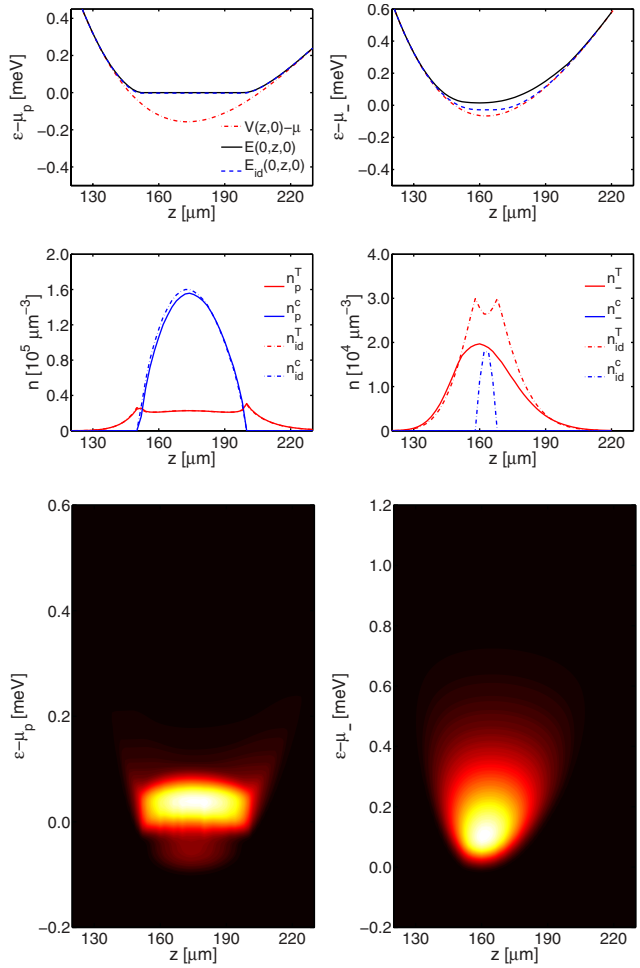

FIG. 2. (Color online) Same presentation as in Fig. 1 but for a temperature of $T=1.2$ K and particle numbers of $N_p=5\times10^9$ and $N_-=N_+=5\times10^8$ in the trap. The chemical potentials are $\mu_p=-2140$ μeV and $\mu_-=\mu_+=-5610$ μeV. In the middle row, additionally the densities of condensed excitons with (n^c) and without interspecies interaction (n_{id}^c) appear.

For our calculations, we use values of $\Delta=41$ μeV for the spectral resolution and $\Delta x=25$ μm for the entrance slit of the spectrograph being typical for a triple high-resolution spectrograph used in the current experiments which are underway.[26] In the following figures we show the respective trap potentials V_i, minimal excitation energies $E_i(\mathbf{k}=0,z,\varrho=0)$, and density distributions of paraexcitons and orthoexcitons versus the z coordinate. We compare the results to the case without intercomponent interaction (labeled "id").

We first investigate case (i) by setting $N_p=5\times10^9$, $N_\pm=5\times10^8$, and a temperature $T=2.2$ K well above both of the estimated critical values. As Fig. 1 shows, in the absence of any condensate, the line shapes $E_i(\mathbf{k}=0,z,\varrho=0)$ roughly follow the external potentials and the presence of multiple components causes only a weak additional renormalization. Both paraexciton and orthoexciton densities—the latter being equal for + and − species—concentrate in the centers of their traps. A noticeable redistribution of the orthoexcitons with respect to the one-component case results from the large number of paraexcitons as well as from the ortho-ortho interaction. The corresponding luminescence spectra of thermal excitons are shown in Fig. 1, lower row. Because the modulus of the photon vector $|\mathbf{k}_0|\approx30$ μm^{-1} is rather small, the integrated zero-phonon spectrum of the paraexcitons almost directly resembles the minimal excitation energy $E_p(\mathbf{k}=0,z,\varrho=0)$. In the case of orthoexcitons, every $\mathbf{k}$ vector contributes and we find a broad energy distribution above $E_\pm(\mathbf{k}=0,z,\varrho=0)$.

Keeping the particle numbers constant, we lower the temperature to $T=1.2$ K and show case (ii) in Fig. 2. Now the renormalized potential of the paraexcitons (Fig. 2, upper left panel) is cut at the chemical potential causing an almost flat bottom of the luminescence spectrum (Fig. 2, lower left panel). Again the densities of thermal and condensed paraex-

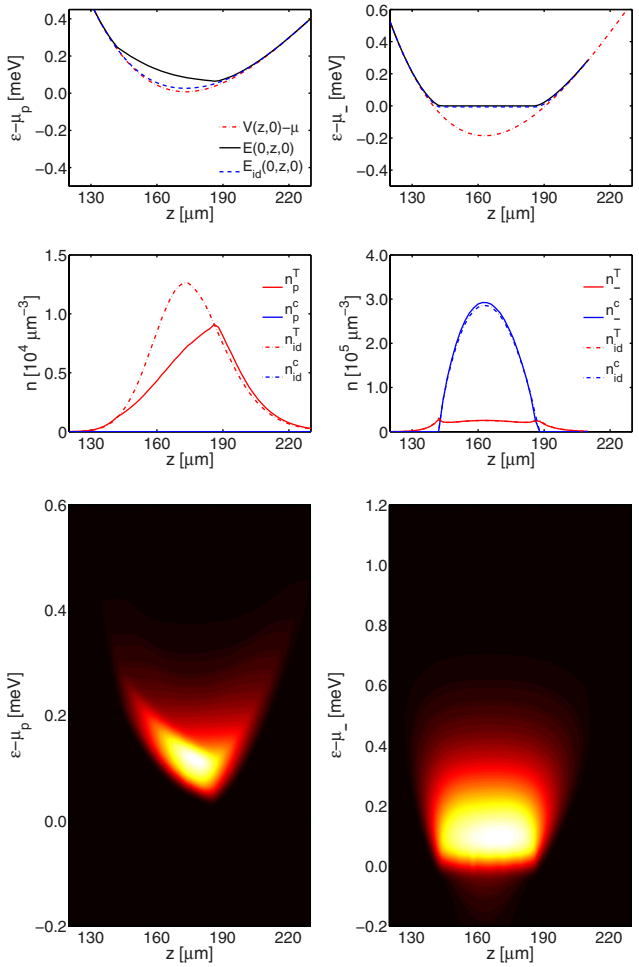

FIG. 3. (Color online) Same presentation as in Fig. 1 but for a temperature of $T=1.2$ K and particle numbers of $N_p=N_+=5\times10^8$ and $N_-=5\times10^9$ in the trap. The chemical potentials are $\mu_p=-2310$ μeV, $\mu_+=-5550$ μeV, and $\mu_-=-5490$ μeV.

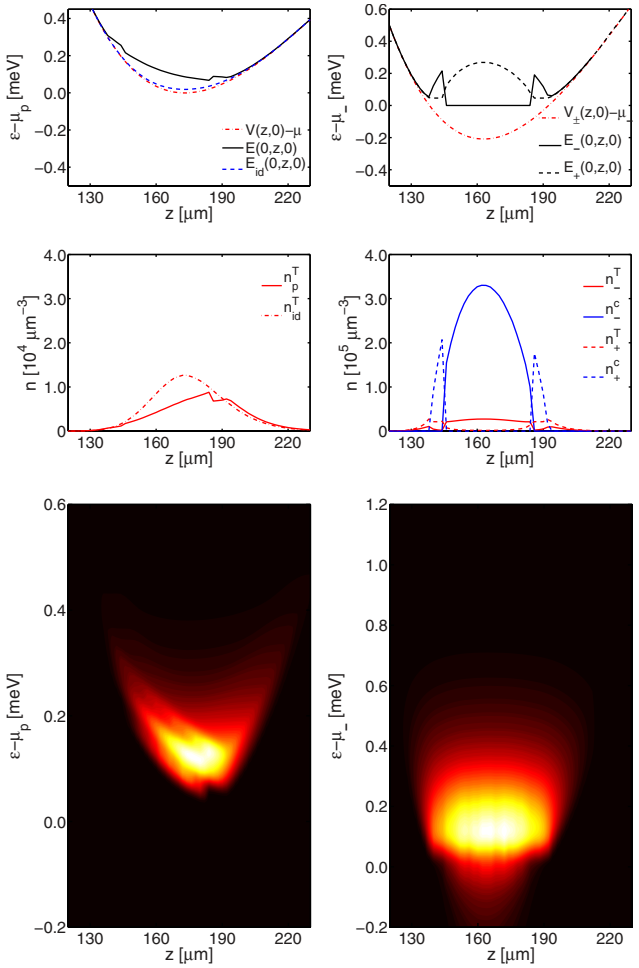

FIG. 4. (Color online) Same presentation as in Fig. 1 but for a temperature of $T=1.2$ K and particle numbers of $N_p=5\times10^8$ and $N_-=N_+=5\times10^9$ in the trap. The chemical potentials are $\mu_p=-2300$ μeV, $\mu_-=-5420$ μeV, and $\mu_+=-5470$ μeV.

citons show no significant deviation from the single component case (Fig. 2, middle left panel). In contrast, while isolated orthoexcitons would have been condensed, there is no orthocondensate in the fully interacting case, which shows that the presence of multiple repulsive components lowers the critical temperature. Due to the even higher concentration of paraexcitons and the different minimum positions of the external potentials ($z_p=174$ μm and $z_\pm=164$ μm), the thermal orthoexcitons are slightly pushed aside (Fig. 2, middle right panel). Their spectrum (Fig. 2, lower right panel) is qualitatively nearly unchanged with respect to case (i). However, due to the lower temperature, the spectrum is less widespread. Furthermore, the chemical potential nearly touches the renormalized potential causing already a smoother curvature of the spectral shape.

If we exchange the particle numbers of paraexcitons and one species of orthoexcitons, i.e., $N_+=5\times10^9$, $N_p=N_-=5\times10^8$, we realize case (iii), which is presented in Fig. 3. While in this case the density distributions of thermal and condensed ortho(+)excitons deviate only weakly from the one-component case, the displacement of the thermal paraexcitons is expressed in a heavily distorted zero-phonon spectrum.

Increasing also the particle number of the remaining orthospecies by an order of magnitude, we generate case (iv), depicted in Fig. 4. As Shi *et al.*[9] showed, even for finite temperature the condition for phase separation of mutually interacting trapped condensates coincides with the $T=0$ result of Ho and Shenoy:[7] $h_{+-}^2>h_{++}h_{--}$. Due to their strong repulsion, the two orthocondensates fulfill this condition and separate into a ball-and-shell structure with finite overlap, as seen in Refs. 7 and 8. Yet, as found in Ref. 12, at $T>0$ no pure + or − phases exist and the respective thermal particles are not entirely expelled. References 8 and 27 pointed out that in general the component with the weaker self-interaction forms the outer shell. In the case of orthoexcitons, this criterion does not apply and the labels + and − can be interchanged in all the results presented here. In principle, there should exist an unstable solution with equal distributions of the orthocondensates. The breaking of this symmetry is a consequence of our iterative numerical method. Because of the symmetry of the interaction, the paraexcitons react to the combined density of the orthoexciton species. That is

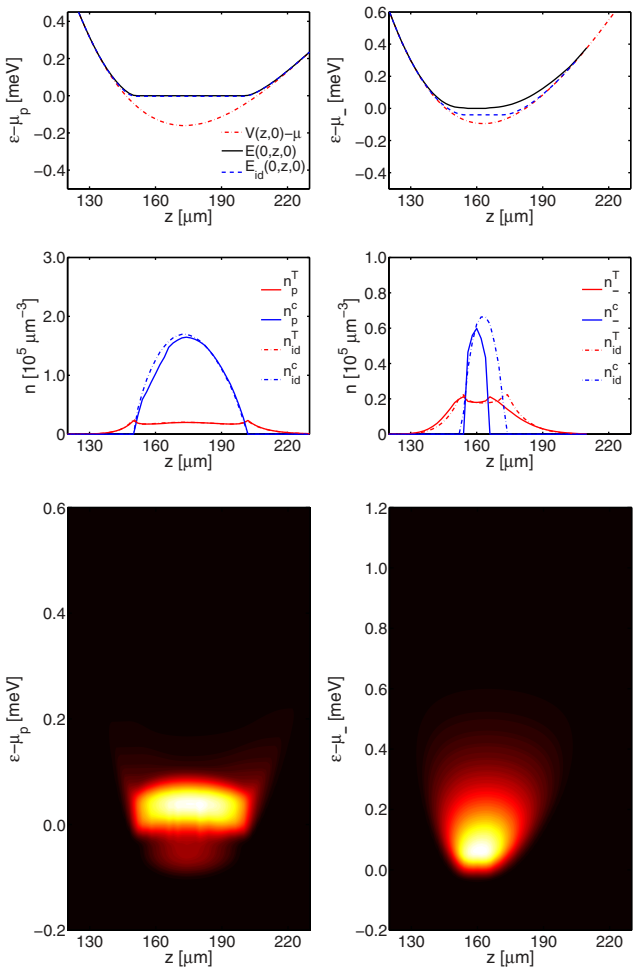

FIG. 5. (Color online) Same presentation as in Fig. 1 but for a temperature of $T=1.05$ K and particle numbers of $N_p=5\times10^9$ and $N_-=N_+=5\times10^8$ in the trap. The chemical potentials are $\mu_p=-2140$ μeV, $\mu_-=-5585$ μeV, and $\mu_+=-5580$ μeV.

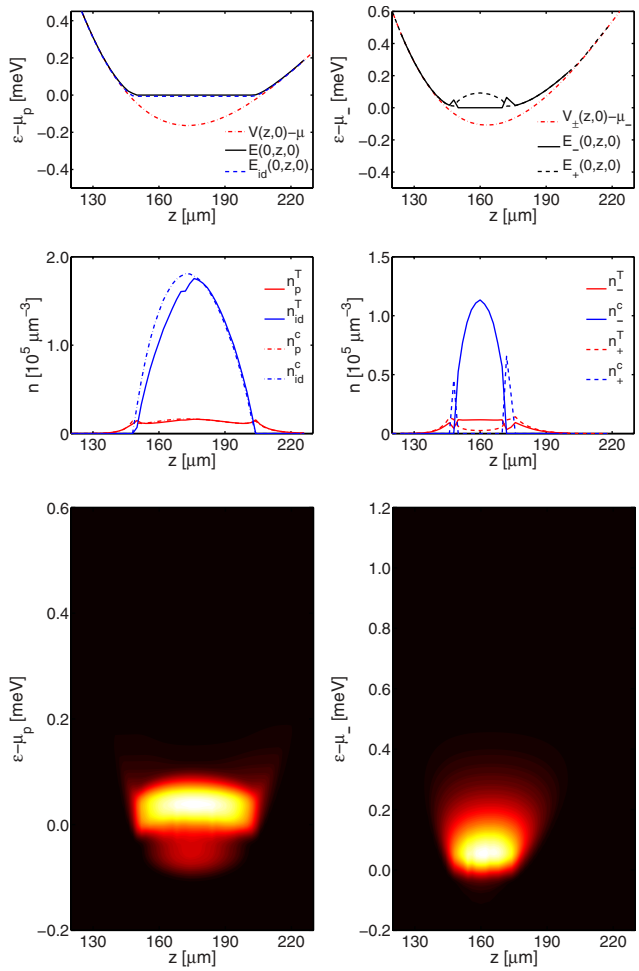

FIG. 6. (Color online) Upper and lower row: same presentation as in Fig. 1, middle row: density profiles and potentials for paraexcitons (left column) and both orthospecies (right column) for a temperature of $T=0.8$ K and particle numbers of $N_p=5\times10^9$ and $N_-=N_+=5\times10^8$ in the trap. The chemical potentials are $\mu_p=-2140$ μeV, $\mu_-=-5560$ μeV, and $\mu_+=-5570$ μeV.

why the distortion of the paraspectrum is strongest in the area of overlapping orthocondensates.

Let us switch back to the parameters of case (ii), i.e., $N_p=5\times10^9$ and $N_+=N_-=5\times10^8$, and lower the temperature to $T=1.05$ K. As Fig. 5 shows, besides condensed paraexcitons we now find a small condensate of only one species of orthoexcitons [case (v)]. While in the single-component case, for $N_+=N_-$, both orthospecies have the same critical temperature, now the mutual repulsion prevents the simultaneous condensation of the second species. We have to lower the temperature to $T=0.8$ K, to get condensates of all the components [case (vi), Fig. 6]. While the orthospecies again form a ball-and-shell structure, orthocondensate and paracondensate do not separate because of their weak interaction ($h_{p+}^2<h_{pp}h_{++}$).

V. CONCLUSION AND OUTLOOK

We have presented a theoretical approach for the description of multicomponent interacting excitonic gases in potential traps. The resulting system of equations has been subject to a number of approximations to make it numerically feasible. Finally, coupled multicomponent equations for the densities of thermal excitons in Hartree-Fock-Bogoliubov-Popov approximation and the condensate densities following from the Gross-Pitaevskii equation in Thomas-Fermi approximation have been obtained and numerically solved. Compared to previous calculations,[6] an experimentally realistic, anharmonic trap potential has been used. Six "typical" (but not necessarily experimentally realizable) situations leading to Bose-Einstein condensate in one or more of the species have been compared. The spatially resolved decay luminescence spectra of thermal paraexcitons and orthoexcitons exhibit clear signatures of a condensate. On the one hand, there is a flat bottom at the chemical potential known from the single-component case.[6] On the other hand, the interspecies interaction causes additional modifications of the spectra: if there is a condensate in one of the species, the spectrum of the respective other component is clearly distorted.

TABLE I. Summary of cases (i)–(vi): occurrence of a condensate in one or more species, of spatial separation between ortho(+) (o_+) and ortho(−) (o_-) excitons and of a deformation of the thermal paraexciton spectrum in dependence on temperature and particle numbers.

Case No.	Temperature (K)	$N_p/5\times10^9$	$N_+/5\times10^9$	$N_-/5\times10^9$	Condensate?	Orthoexciton separation?	Paraspectrum deformation?
(i)	2.2	1	0.1	0.1			
(ii)	1.2	1	0.1	0.1	p		
(iii)	1.2	0.1	0.1	1	o_-		√
(iv)	1.2	0.1	1	1	o_+,o_-	√	√
(v)	1.05	1	0.1	0.1	p,o_-		
(vi)	0.8	1	0.1	0.1	p,o_+,o_-	√	

In a typical experiment in the bulk or involving rather shallow potential traps, orthoexcitons are produced by laser excitation, but are converted fast into paraexcitons at a rate of 0.3 ns^{-1}.[28,29] Therefore, under quasiequilibrium conditions, the particle number ratio orthoexciton/paraexciton is small which corresponds to the cases (i), (ii), (v), and (vi). By increasing the stress, however, the conversion rate decreases by more than an order of magnitude.[29] By continuous excitation of orthoexcitons, therefore, it should be possible to obtain higher orthoexciton/paraexciton ratios like in cases (iii) and (iv). For an exciton number of 5×10^9, the density in the center of the trap is about 10^{17} cm^{-3} which is experimentally achievable. The same holds for the considered temperatures of $T=0.8\ldots2.2$ K.[26]

Table I summarizes the essential information obtained from the cases (i)–(vi) discussed above. Obviously, three conclusions can be drawn: first, if the temperature is low enough (below the respective critical temperature), every species can form a condensate. Its primary signature is a flat bottom of the respective spectrum. Second, a spatial separation occurs only between the condensates of the two orthospecies, because of their strong repulsion. It shows up only in the densities, not in the combined spectrum. Therefore, it is important for future experiments to measure also the spectrally integrated density profile. Third, at occurrence of any orthocondensate but no paracondensate, the paraspectrum is distorted in a characteristic way indicating a condensate in at least one of the *other* species.

The presented theory is obviously only a first step toward a deeper understanding of the physics of trapped excitons. To go beyond that includes the solution of the Gross-Pitaevskii equation (without the Thomas-Fermi approximation) and the inclusion of anomalous densities already on the single-component level. Moreover, a general multicomponent theory requires the consideration of mixed averages which overcomes the effective single-component picture but complicates the Bogoliubov transformation remarkably.

ACKNOWLEDGMENTS

We would like to thank G. Manzke and F. Richter (Rostock), and A. Alvermann (Greifswald) for many fruitful discussions. This work was supported by the Deutsche Forschungsgemeinschaft via Collaborative Research Center SFB 652, projects B1 and B5.

[1] A. Griffin, Phys. Rev. B **53**, 9341 (1996).
[2] F. Dalfovo, S. Giorgini, L. P. Pitaevskii, and S. Stringari, Rev. Mod. Phys. **71**, 463 (1999).
[3] T. Bergeman, D. L. Feder, N. L. Balazs, and B. I. Schneider, Phys. Rev. A **61**, 063605 (2000).
[4] N. P. Proukakis and B. Jackson, J. Phys. B **41**, 203002 (2008).
[5] L. A. Bányai, A. M. Bundaru, and H. Haug, Phys. Rev. B **70**, 045201 (2004).
[6] H. Stolz and D. Semkat, Phys. Rev. B **81** 081302(R) (2010).
[7] T. L. Ho and V. B. Shenoy, Phys. Rev. Lett. **77**, 3276 (1996).
[8] E. P. Bashkin and A. V. Vagov, Phys. Rev. B **56**, 6207 (1997).
[9] H. Shi, W. M. Zheng, and S. T. Chui, Phys. Rev. A **61**, 063613 (2000).
[10] W. Zhang, S. Yi, and L. You, Phys. Rev. A **70**, 043611 (2004).
[11] M.-S. Chang, Q. Qin, W. Zhang, L. You, and M. S. Chapman, Nat. Phys. **1**, 111 (2005).
[12] B. Van Schaeybroeck, arXiv:0901.3048 (unpublished).
[13] I. A. Shelykh, G. Malpuech, and A. V. Kavokin, Phys. Status Solidi A **202**, 2614 (2005).
[14] J. Kasprzak, R. André, L. S. Dang, I. A. Shelykh, A. V. Kavokin, Yu. G. Rubo, K. V. Kavokin, and G. Malpuech, Phys. Rev. B **75**, 045326 (2007).
[15] S. Sobkowiak, Diploma thesis, Universität Rostock, 2010.
[16] D. W. Snoke and V. Negoita, Phys. Rev. B **61**, 2904 (2000).
[17] J. Shumway and D. M. Ceperley, Phys. Rev. B **63**, 165209 (2001).
[18] K. Oda, T. Miyakawa, H. Yabu, and T. Suzuki, J. Phys. Soc. Jpn. **70**, 1549 (2001).
[19] I. A. Ivanov, J. Mitroy, and K. Varga, Phys. Rev. A **65**, 022704 (2002).
[20] M. French, R. Schwartz, H. Stolz, and R. Redmer, J. Phys.: Condens. Matter **21**, 015502 (2009).
[21] G. Kuwabara, M. Tanaka, and H. Fukutani, Solid State Commun. **21**, 599 (1977).
[22] G. Dasbach, D. Fröhlich, R. Klieber, D. Suter, M. Bayer, and H. Stolz, Phys. Rev. B **70**, 045206 (2004).

[23] H. Shi, G. Verechaka, and A. Griffin, Phys. Rev. B **50**, 1119 (1994).
[24] H. Haug and H. Kranz, Z. Phys. B: Condens. Matter **53**, 151 (1983).
[25] L. Pitaevskii and S. Stringari, *Bose-Einstein Condensation* (Oxford University Press, New York, 2003).
[26] R. Schwartz, N. Naka, and H. Stolz (unpublished).
[27] P. Öhberg and S. Stenholm, Phys. Rev. A **57**, 1272 (1998).
[28] S. Denev and D. W. Snoke, Phys. Rev. B **65**, 085211 (2002).
[29] J. P. Wolfe and J. I. Jang, Solid State Commun. **134**, 143 (2005).

A.6

Artikel 6

G. Manzke, D. Semkat, F. Richter, D. Kremp, and K. Henneberger:

Mott transition versus Bose-Einstein condensation of excitons

J. Phys.: Conf. Ser. **210**, 012020 (2010)

Journal of Physics: Conference Series **210** (2010) 012020 doi:10.1088/1742-6596/210/1/012020

Mott transition versus Bose-Einstein condensation of excitons

G Manzke, D Semkat, F Richter, D Kremp, and K Henneberger
Institute of Physics, University of Rostock, D-18051 Rostock, GERMANY

E-mail: guenter.manzke@uni-rostock.de

Abstract. We investigate the influence of many-body effects on both the chemical potentials of carriers, and the Mott transition of para-excitons in Cu_2O over a wide range of temperatures and carrier densities, in order to determine the region where an excitonic fraction can exist. In contrast to simplified approximations used in the literature we consider full dynamical screening between carriers and find out that (i) the chemical potentials are much less decreased by the many-body effects, and (ii) for low temperatures the density, where the Mott transition appears, is one order of magnitude higher. This leads to an extension of the region of existence of excitons and, therefore, of a possible BEC, to higher temperatures.

1. Introduction

Collective quantum phenomena have been of great interest in semiconductor physics for many years. Following the theory of the ideal Bose gas, the Bose-Einstein condensation (BEC) of excitons should occur, when their chemical potential reaches the exciton resonance by reduction of the temperature or increase of their density (for an overview see [1, 2, 3]). On the other hand, the existence of an excitonic fraction in a semiconductor is limited due to the Mott transition of excitons, induced by many-body effects between excitons and their constituents (electrons and holes). In particular, the weakening of the Coulomb interaction due to screening leads to a breakup of the excitonic binding with increasing carrier density (density ionization). Considering the chemical equilibrium of unbound and bound electron-hole pairs (excitons), the degree of ionization can be used to describe the composition of the partially ionized electron-hole plasma (EHP) in an excited semiconductor [4, 5].

The aim of our paper is the investigation of the influence of many-body effects on the chemical potentials of electrons, holes, and para-excitons in Cu_2O, which have a long life time [6]. We determine the composition of the partially ionized electron-hole plasma in dependence on the temperature and the density of carriers. In comparison to recent treatments [7, 8] we go beyond simple approximations for the many-body effects (static screening) or interpolation formulas for the chemical potentials valid for a wide range of temperatures and densities (for a review see [4, 5]). Our approach is based on a self-consistent calculation of one-particle carrier selfenergies in quasi-particle approximation including the dynamical screening of the Coulomb interaction. In a series of papers we have demonstrated that this approach is convenient to describe the details of the excitonic absorption at lower excitation, showing up in phase-resolved interferometric measurements [10, 11]. In this paper we extend our treatment to higher densities and lower

temperatures in order to describe the Mott transition and to reach the region where BEC can be expected.

2. Quasi-particle approximation and chemical potentials of carriers

The influence of many-body effects between carriers in the EHP of an excited semiconductor can be described by their retarded selfenergies Σ^r_a, with $a = e, h$ denoting electrons, holes. Within quasi-particle approximation their real part describes the renormalization of the energy dispersion ε and the imaginary part the damping Γ (inverse life time) of carrier states

$$\varepsilon^a_k = \hbar^2 k^2/2m_a - \Sigma^{\rm HF}_{a,k} - {\rm Re}\,\Sigma^{sc}_{a,k}(\varepsilon^a_k), \quad \Gamma^a_k = -2\,{\rm Im}\,\Sigma^{sc}_{a,k}(\varepsilon^a_k). \tag{1}$$

We use the selfenergy in *random phase approximation* (RPA), which can be split into a Hartree-Fock contribution $\Sigma^{\rm HF}_{a,k}$ and a second term $\Sigma^{sc}_{a,k}$ which considers the dynamical screening between carriers

$$\Sigma^{\rm HF}_{a,k} = \sum_q f^a(\varepsilon^a_q) v_{k-q}, \quad \Sigma^{sc}_{a,k}(\omega) = \sum_q \int \frac{d\omega'}{2\pi} \frac{\left[1 - f^a(\varepsilon^a_q) + n^B(\omega')\right]\, \hat{V}_{k-q}(\omega')}{\omega - \varepsilon^a_q - \omega' + i\Gamma^a_q/2}. \tag{2}$$

The Fermi distribution $f^a(\varepsilon^a_q)$ contains the renormalized dispersion and the chemical potential μ_a of carriers being related to the carrier density n^*_a by

$$n^*_a = \sum_q f^a(\varepsilon^a_q), \quad f^a(\varepsilon^a_q) = \left[e^{(\varepsilon^a_q - \mu_a)/kT} + 1\right]^{-1}. \tag{3}$$

$n^B(\omega')$ is a Bose distribution of the elementary excitations in the EHP (plasmons), which are determined by the dynamical screened potential $\hat{V}$. For further details we refer to [10, 11]. In order to determine the quasi-particle energy and damping for a given carrier density and temperature, the Eqns. (1)-(3) have to be solved self-consistently, including the chemical potential. We start our numerical procedure with the calculation of the chemical potential μ_0

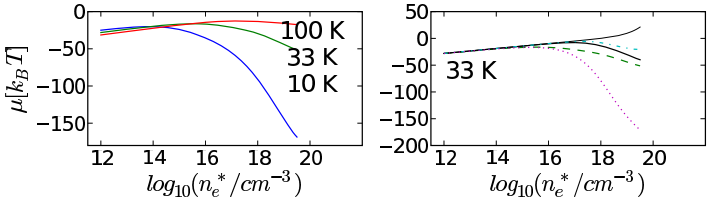

Figure 1. Sum of the chemical potentials of electrons and holes in dependence of the density of carriers within QPA as solution of Eqns. (1)-(3), left: comparison of QPA for different temperatures, right: comparison of the QPA (solid,bold) with that of free carriers (solid,thin), and with different approximations for the selfenergy: only Hartree-Fock selfenergy (dash-dotted), Debye shift (dotted), and with the Padé formula of [13] (dashed).

of free (non-correlated) carriers, considering only the kinetic energy part in (1) for the iteration of (3). This is used to iterate the Eqns. (1),(2) self-consistently. As a result we get the quasi-particle energy and damping which than are employed in the calculation of the carrier density of the correlated EHP with (3). In earlier papers the quasi-particle energy was approximated by the so-called Debye shift [4] or Coulomb-hole selfenergy [12], given in excitonic units by $\Sigma^{CH} = -\kappa a_{ex} E^b_{ex}$ (κ - inverse screening length). We use the following parameters for Cu_2O [6]:

binding energy $E_{ex}^b = 150$meV, Bohr radius $a_{ex} = 0.65$nm. In [13] a Padé formula for the sum of the chemical potentials was presented for a wide range of temperatures and densities. The formula was constructed with some data points (n, T) of the numerical iteration of Eqns. (1)-(3) and known analytical formulas for limiting cases. However, the damping was neglected ($\Gamma \to 0$) in the numerical iteration. Our calculations show that this leads to exaggerated quasi-particle energies. In [10] we have shown, that the consideration of the quasi-particle damping is necessary for a correct description of the excitonic lineshape, too.

Results of our numerical iteration, as described above, for different temperatures and a comparison of our results with simplified earlier treatments are given in Fig. 1 for the sum $\mu = \mu_e + \mu_h$ of the chemical potentials of electrons and holes in units of the thermal energy kT. The strong influence of many-body effects becomes obvious. Comparing the behavior of the chemical potential in QPA (left part), the largest deviation from that for ideal particles is found for low temperatures. A comparison of our approach with different approximations is presented in the right part for a temperature of $T = 33$K. As one can see, the CH shift (dashed line) overestimates the influence of screening considerably. The deviation becomes larger for lower temperatures. Only for temperatures where the thermal energy kT is of the order of the excitonic binding energy ($kT = E_{ex}^b = 150$meV for $T = 1740$K) the Debye approximation (static screening) comes closer to the QPA (dynamic screening) presented above. The deviation of the Padé formula from [13], which has been used in a previous paper [8] is still remarkable. As we have pointed out, this is due to the neglected quasi-particle damping in (2). In contrast we find that the Hartree-Fock approximation ($\Sigma^{sc} = 0$) comes closer to the full calculations at higher carrier densities, even for higher temperatures.

3. Composition of the partially ionized electron-hole plasma

Depending on the carrier density and temperature, electrons and holes in an excited semiconductor can bind to excitons, and the total density of carriers n_a at quasi-equilibrium is split into a part of free (correlated, but non-bound) carriers n_a^* and a part bound to excitons n_X, where due to charge neutrality $n_e = n_h$ is valid. The EHP can be considered to be in a

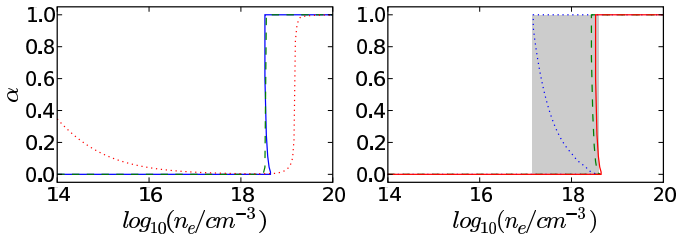

Figure 2. Degree of ionization α vs. density, Eq. (4). Left: for different temperatures $T = 10K$ (solid), $T = 33K$ (dashed), and $T = 100K$ (dotted), Right: comparing different approximations for the chemical potential: our treatment (solid), CH shift (dotted), Padé formula [13] (dashed).

chemical (ionization) equilibrium $e + h \rightleftarrows X$, and the composition can be characterized by the degree of ionization

$$\alpha = \frac{n_a*}{n_a}, \quad n_a = n_a^* + n_X. \tag{4}$$

The chemical potential of excitons follows from the well-known thermodynamic condition for the chemical equilibrium [4]

$$\mu_X = \mu_e + \mu_h - E_{ex}^b, \; n_X(\mu_X, T) = \sum_K \left[\mathrm{e}^{\left(\frac{\hbar^2 K^2}{2M} - \mu_X\right)/kT} - 1 \right]^{-1} \tag{5}$$

Here the excitons are considered as ideal bosons with the density-dependent binding energy E_{ex}^b and the scattering states in the excitonic spectrum are neglected. For further details we refer to [8, 9].

The degree of ionization, calculated with our chemical potentials (last section) is presented in the left part of Fig. 2. At lower densities most e-h pairs are bound to excitons ($\alpha \ll 1$), while a breaking of the excitonic binding appears very abruptly at the Mott density. A comparison with the CH shift (static screening) in the right part of the figure shows, that (i) the Mott density is increased by nearly one order of magnitude, and (ii) the region of multivaluedness (shaded area) where a phase transition may be expected [4], is reduced considerably. An overview for

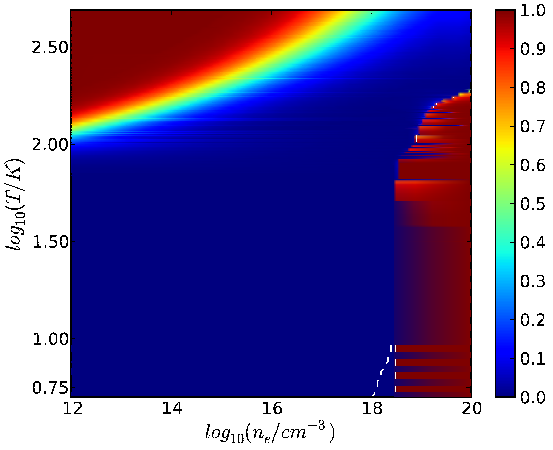

Figure 3. Contour plot of the degree of ionization in the density–temperature plane for Cu_2O. Excitons are dominant in the low density and low temperature region, where $\alpha \ll 1$. The dashed triangle at the bottom borders the region where BEC of ideal excitons is possible: $(1-\alpha)n_e\Lambda_X^3 \geq 2.612$ [3].

the degree of ionization in a wide range of temperatures and densities is presented in Fig. 3. Due to the increased Mott density at low temperatures ($n^{Mott} = 3 * 10^{18} cm^{-3}$) the region where BEC of ideal bosons can be expected is shifted to higher temperatures (see peak of the dashed triangle in Fig. 3).

Acknowledgments

Authors wishing to thank W.-D. Kraeft and H. Stolz for many discussions and the Deutsche Forschungsgemeinschaft (Collaborative Research Center SFB 652) for financial support.

References

[1] Moskalenko S A 1962 *Fiz. Tverd. Tela* **4** 246
[2] Hanamura E and Haug H 1977 *Phys. Rep.* **33** 209
[3] Moskalenko S A and Snoke D W 2000 *Bose-Einstein Condensation of Excitons and Biexcitons and Coherent Nonlinear Optics with Excitons* (Cambridge: University Press)
[4] Ebeling W, Kraeft W D and Kremp D 1976 *Theory of Bound States and Ionization Equilibrium in Plasmas and Solids* (Berlin: Akademie-Verlag)
[5] Zimmermann R 1988 *Many-Particle Theory of Highly Excited Semiconductors* (Leipzig: Teubner)
[6] Fröhlich D, Brandt J, Sandfort C, Bayer M and Stolz H 2008 *Phys. Status Solidi* B **243** 2367
[7] Snoke D 2008 *Solid State Communications* **146** 73
[8] Richter F, Semkat D, Kremp D and Henneberger K 2009 *Phys. Status Solidi* C **6** 532
[9] Semkat D, Richter F, Kremp D, Manzke G, Kraeft W D and Henneberger K 2009 *Phys. Rev.* B **80** 155201
[10] Nägerl J S, Stabenau B, Böhne G, Dreher S, Ulbrich R G, Manzke G and Henneberger K 2001 *Phys. Rev.* B **63** 235202
[11] Seemann M, Kieseling F, Stolz H, Franz R, Manzke G, Henneberger K, Passow T and Hommel D 2005 *Phys. Rev.* B **72** 075204
[12] Haug H and Koch S W 1990 *Quantum Theory of the Optical and Electronic Properties of Semiconductors* (Singapore: World Scientific Publ.)
[13] Rösler M, Zimmermann R and Richert W 1984 *Phys. Status Solidi* B **121** 609

A.7

Artikel 7

G. Manzke, D. Semkat, and H. Stolz:

Mott transition of excitons in GaAs-GaAlAs quantum wells

New J. Phys. **14**, 095002 (2012)

New Journal of Physics
The open-access journal for physics

Mott transition of excitons in GaAs-GaAlAs quantum wells

G Manzke[1], **D Semkat and H Stolz**
University of Rostock, Institute of Physics, 18051 Rostock, Germany
E-mail: guenter.manzke@uni-rostock.de

New Journal of Physics **14** (2012) 095002 (17pp)
Received 18 May 2012
Published 5 September 2012
Online at http://www.njp.org/
doi:10.1088/1367-2630/14/9/095002

Abstract. We investigate the breakup of bound electron–hole pairs, known as Mott transition of excitons, in GaAs-GaAlAs quantum wells with increasing excitation, comparing two different theoretical approaches. Firstly, a *thermodynamic approach* is used to investigate the ionization equilibrium between electrons, holes and excitons, where the abrupt jump of the degree of ionization from 0 to 1 indicates the Mott density. It is extended to a self-consistent quasi-particle approximation (QPA) for the carrier properties, including dynamical screening of the Coulomb interaction between carriers. Secondly, a *spectral approach* based on the semiconductor Bloch equations within linear optical response is used, considering the quasi-particle (QP) properties of carriers and the dynamical screening between electron–hole pairs. While the first is effectively a one-particle approach, in the second the whole two-particle spectrum is analyzed. Within the *thermodynamic approach*, a simple criterion for the Mott transition can be given: namely, if the sum of chemical potentials of carriers, reflecting the effective shrinkage of the band edge, crosses the exciton energy with increasing excitation. We demonstrate that this simple picture cannot be maintained in the two-particle approach. Here, a compact quantity, which describes the behavior of the band edge, does not exist. In fact, the behavior of the single states in the spectrum is generated by the interplay of dynamical screening in the interband self-energy and the effective interaction of the electron–hole pairs. Moreover, the band edge cannot be clearly resolved,

[1] Author to whom any correspondence should be addressed.

since it is merged with excited exciton states (e.g. 2s state), which show up only for densities far below the Mott density. Instead of a Mott density, only a density range can be given, where the Mott transition appears. We demonstrate that a small damping as a prerequisite for the validation of the extended QPA in the *thermodynamic approach* breaks down, analyzing (i) the dephasing processes with increasing excitation, (ii) the strong increase of the excitonic linewidth and (iii) comparing with the lifetime of carriers in the QP description.

Contents

1. Introduction

Description of the composition of a partially ionized electron–hole plasma (EHP), consisting of electrons, holes and excitons, in terms of the density of particles and the temperature, is an old problem in semiconductor physics. The breaking of the excitonic binding can be caused by either thermal ionization or, with increasing density, the screening of the Coulomb interaction between carriers. The latter phenomenon is usually referred to as the Mott transition.

Many experiments have shown that the exciton energy stays nearly unchanged with increasing excitation (for early experiments, see [1–4]), while the exciton is broadened and vanishes from the spectra due to the decreasing band edge. In [5], this behavior was founded theoretically, including the dynamic screening between excited carriers in a Bethe–Salpeter equation. It was shown that the nearly unchanged exciton energy with increasing excitation is caused by a wide cancelation of the dynamically screened two-particle self-energy with the dynamically screened effective two-particle interaction. The important point here is that both screening effects have to be taken into account on the same footing. Only in this case their cancelation is given.

Simplifying the dynamically screened self-energy in a quasi-static approximation by the Coulomb hole (CH) self-energy, as applied in [6, 7] for the calculation of gain spectra, the cancelation with the effective static screened interaction is strongly reduced and the exciton undergoes a strong shift to lower energies. In [5], the Lindhard dielectric function in the dynamically screened potential was reduced to a plasmon-pole approximation. The complete Lindhard dielectric function in the dynamically screened potential is included in [8–10].

Besides these more or less numerical extensive investigations, it is of interest to find simple analytical formulae for the Mott density n^{M}, which can be easily applied in comparison with experiments. A rough estimation of the Mott density is $n^{\mathrm{M}}a_{\mathrm{X}}^3 = 1$ [12], where a_{X} is the Bohr radius of the exciton. A more physically founded condition $\kappa a_{\mathrm{X}} = 0.84$ (κ is the inverse screening length) was found by the authors of [13], investigating the behavior of bound states

of a statically screened Coulomb potential by the solution of Schrödinger's equation. Other approaches, based on the renormalization of the energy of carriers due to static screening, were directed toward the investigation of the chemical equilibrium between electrons, holes and excitons in an excited semiconductor as a function of the temperature and the density of particles [14, 15]. This thermodynamic point of view allows the determination of the degree of ionization of the EHP via a mass-action law. This concept is also well known in plasma physics (see, e.g., [15, 16]); applications to the EHP are given in [17–23].

However, the question is whether these approaches applying static screening correspond to those with dynamical screening in the Bethe–Salpeter equation. In [24, 25], it was shown how the concept of dynamical screening with the Bethe–Salpeter equation can be extended to the semiconductor Bloch equations [7, 26]. In contrast to the approaches based on the Bethe–Salpeter equation [5, 8–10], problems arising due to the use of the Shindo approximation are omitted. These problems restrict the validation of these approaches at low temperatures to lower densities, well below the Mott transition. The results of our theoretical concept were confirmed in [11], where it was shown how to circumvent the Shindo approximation in the derivation of the Bethe–Salpeter equation. The theoretical approach was successfully applied to the description of subtleties of polariton propagation in bulk semiconductors [25, 27] and quantum wells [28]. However, the excitation in the experiments was rather low with densities of excited carriers well below the Mott transition. In [29, 30], we extended our theoretical concept to higher excitations and to the description of the Mott transition in bulk ZnSe. The main point here was to include the renormalization of the dynamically screened carrier self-energies and the chemical potentials within quasi-particle approximation (QPA) in a self-consistent way into the semiconductor Bloch equations, e.g. one-particle and two-particle properties are considered on the same footing.

The unbroken interest in the experimental verification of the Mott transition manifests itself in a series of papers, where the buildup of excitons was investigated in the time-resolved photoluminescence (PL) [32–38]. Here, the question of how the optically induced coherent polarization is transferred into an incoherent exciton population was considered. Furthermore, the conditions where the PL is dominated by plasma or by an incoherent exciton population were investigated. Otherwise, terahertz spectroscopy allows us to study the interplay of optically generated excitons and unbound electron–hole pairs (see [39]). In [40], a model for the dielectric function considering both the excitonic and EHP contributions was applied to describe the experimental data.

Recent experiments [41] have shown the transition from excitonic to plasma emission in the resonance fluorescence from localized excitons in quantum wells. Working with a tunable continuous wave laser with a spectral width much smaller than the exciton binding energy, one is able to detect the dielectric response over the whole spectral range between the 1s exciton and the band edge and open a direct comparison with results of the semiconductor Bloch equations. In a subsequent paper [42], we have extended the concept of self-consistent determination of the self-energies and chemical potentials for the carriers and its inclusion into the semiconductor Bloch equations presented for bulk ZnSe in [30] to quantum wells. There we could give a theoretical explanation of the weak exciton shift observed in the experiments, which changes from higher to lower energies when the temperatures increase from $T = 5\,\mathrm{K}$ to $T = 15\,\mathrm{K}$. This corresponds to the results reported in [24] for bulk semiconductors. Moreover, our results agree with terahertz studies [40], where a lowering of the shift of the 1s–2p transition was found for $T = 6\,\mathrm{K}$.

One aim of this paper is to extend our theoretical investigations in [41, 42] to higher densities to describe the Mott transition as an interplay of the broadening and decreasing of the exciton peak and of band edge shrinkage. The second aim is a comparison with a more thermodynamic treatment of the Mott transition, consisting of the description of the chemical equilibrium between electrons, holes and excitons, and of the degree of ionization in a partially ionized EHP. An actual overview of this approach for bulk semiconductors can be found in [30], where the Mott transition was discussed with the possibility of Bose–Einstein condensation of excitons. In particular, results were presented for the carrier self-energies including dynamical screening and compared with the Hartree–Fock (HF) approximation and the results of the CH approximation [6, 7] based on static screening. In this paper, we apply this *thermodynamic view* of the Mott transition to quantum wells, including the dynamical screening and carrier self-energies within QPA, and discuss the validity of simple approximations based on static screening. Finally, we compare the results of the *spectral approach* with the semiconductor Bloch equations.

Our paper is organized as follows. In section 2, we extend the description of the Mott transition from the *thermodynamic point of view* presented in [30] to quantum wells. Investigating the one-particle properties of carriers (self-energies and chemical potentials) and the degree of ionization, one can obtain a simple criterion for the Mott transition. Section 3 starts with a description of the *spectral approach* based on the semiconductor Bloch equations. We analyze the linear susceptibility as a fingerprint of the composition of the EHP and show that the Mott transition has to be understood within an interplay of the decrease and broadening of the exciton peak and band gap shrinkage. Finally, in section 4 we discuss the connections between both approaches and analyze the limitations of the chemical picture the investigation of the ionization equilibrium is based on.

2. Ionization equilibrium and Mott transition—the thermodynamic approach

From a thermodynamic viewpoint, the partially ionized plasma in semiconductors can be described within a chemical picture as an ionization equilibrium between electrons (e), holes (h) and excitons (X) [43],

$$\mathbf{e}+\mathbf{h} \rightleftarrows \mathbf{X}. \tag{1}$$

Applying the concept of extended quasi-particle (QP) approximation [30, 43, 44], the density of free carriers is split into a QP contribution, considering many-body effects between carriers of one species, and a scattering part $n_a^* = n_a^{\mathrm{QP}} + n_a^{\mathrm{scatt}}$ ($a = \mathrm{e}, \mathrm{h}$, $n_{\mathrm{h}}^* = n_{\mathrm{e}}^*$), which describes the scattering states of interacting electrons and holes. With the density of electron–hole bound states (excitons) n_{X}, the total carrier density is given by $n_a = n_a^* + n_{\mathrm{X}}$, where due to electric neutrality $n_{\mathrm{e}} = n_{\mathrm{h}} = n$. In the following, we will neglect the influence of scattering states [44]. Our QP picture is based on the QPA for the retarded one-particle Green's function [45],

$$\begin{aligned} G^{\mathrm{r}}_{a,k}(\omega) &= 1/[\omega - \varepsilon^a_k + \mathrm{i}\Gamma^a_k/2], \\ \varepsilon^a_k &= e^a_k + \Delta^{a,\mathrm{HF}}_k + \mathrm{Re}\,\Sigma^{\mathrm{r}}_{a,k}(\varepsilon^a_k), \\ \Gamma^a_k &= -2\,\mathrm{Im}\,\Sigma^{\mathrm{r}}_{a,k}(\varepsilon^a_k), \end{aligned} \tag{2}$$

with the kinetic energies $e^a_k = \hbar^2 k^2/2m_a$, the Coulomb HF self-energy $\Delta^{a,\mathrm{HF}}_k$ and $a = \mathrm{e}, \mathrm{h}$ standing for electrons and holes. Effects of screening the Coulomb interaction are contained

in the renormalized energies ε_k^a and the damping (inverse lifetime) Γ_k^a, which are related to the retarded QP self-energy

$$\Sigma_{a,k}^{\mathrm{r}}(\varepsilon_k^a) = \sum_q \int \frac{\mathrm{d}\omega}{2\pi} \frac{[1-f_q^a]\, V_{k-q}^{aa,>}(\omega) + f_q^a\, V_{k-q}^{aa,<}(\omega)}{\varepsilon_k^a - \varepsilon_q^a - \omega + \mathrm{i}\Gamma_q^a/2}. \tag{3}$$

For the consideration of the confinement of carriers quantum wells by an expansion of Green's functions with respect to their eigenfunctions in the growth direction, see [46–49]. It leads to an effective two-dimensional (2D) description of carrier motion in the layers. The distance of the lowest eigenenergy to higher sub-bands is, for the considered quantum wells, sufficiently large to restrict the analysis to the consideration of the lowest eigenstate. This simplifies the whole notation, since indices and sums over sub-band levels can be omitted. Moreover, one arrives at a quasi-2D description, where the confinement is contained in the quasi-2D Coulomb interaction

$$v_q^{\mathrm{eh}} = \frac{4\pi}{q} \int \mathrm{d}z_{\mathrm{e}}\, \mathrm{d}z_{\mathrm{h}}\, |\Phi_{\mathrm{e}}(z_{\mathrm{e}})|^2\, |\Phi_{\mathrm{h}}(z_{\mathrm{h}})|^2 \mathrm{e}^{-q(z_{\mathrm{e}}-z_{\mathrm{h}})}, \tag{4}$$

containing the eigenfunctions $\Phi_a(z_a)$ of carriers in the wells.

A detailed description of the dynamically screened potentials $V_{k-q}^{aa,\gtrless}(\omega)$ is given in [50]. In that paper, the QP energies and damping have been determined with Fermi distributions $f_q^{a,0}$ of ideal (non-interacting) carriers only including their kinetic energy e_k^a

$$f_k^{a,0} = f^{a,0}(e_k^a) = \left[\mathrm{e}^{(e_k^a-\mu_a^0)/kT}+1\right]^{-1} \tag{5}$$

and the chemical potentials μ_a^0. This approximate treatment is valid for low excitations, where the influence of many-body effects on the chemical potentials is small. In [30], we have demonstrated for a bulk semiconductor (ZnSe) that there is a pronounced influence of many-body effects on the chemical potentials even at higher excitation around the Mott transition. In this paper, we extend the earlier treatments for quantum wells [28, 50] and include the renormalized carrier energies in the distributions $f^{a,0}(e_k^a) \to f^a(\varepsilon_k^a)$. The change of chemical potentials μ_a has to be determined for a given density n_a^* and temperature T of carriers from

$$n_a^* = \sum_k f^a(\varepsilon_k^a), \qquad f^a(\varepsilon_k^a) = \left[\mathrm{e}^{(\varepsilon_k^a-\mu_a)/kT}+1\right]^{-1}. \tag{6}$$

Now equation (6) has to be included in the self-consistent solution of equations (2)–(4). For a fixed density and temperature, we obtain both the QP quantities ε_k^a, Γ_k^a and the chemical potential μ_a.

A simple approximation for the QP energy is the so-called Debye shift [15] or CH self-energy [7] Δ_a^{CH}, which represents the renormalization of the kinetic energy of carriers by static screening of the Coulomb interaction with each other,

$$\varepsilon_k^{a,\mathrm{CH}} = e_k^a - \Delta_a^{\mathrm{CH}}, \qquad \Delta_a^{\mathrm{CH}} = \frac{2}{\alpha_a}\left[1-\mathrm{e}^{-2\pi\alpha_a n_a^*/kT}\right]. \tag{7}$$

The mass ratio $\alpha_{\mathrm{e/h}} = m_{h/e}/(m_{\mathrm{e}}+m_{\mathrm{h}})$ results from the transition to bulk excitonic units (exciton binding energy $E_{\mathrm{X}}^{\mathrm{b}} = 4.2\,\mathrm{meV}$; excitonic Bohr radius $a_{\mathrm{X}} = 12.4\,\mathrm{nm}$). All the results presented in this paper are performed for a 19.8 nm quantum well with an exciton binding energy of $E_{\mathrm{qw}}^{\mathrm{b}} = 7.21\,\mathrm{meV} = 1.716 E_{\mathrm{X}}^{\mathrm{b}}$. The mass ratios are $\alpha_{\mathrm{e}} = 0.87$, $\alpha_{\mathrm{h}} = 0.13$. Within excitonic units, the CH self-energy corresponds to the inverse static screening length $\Delta_a^{\mathrm{CH}} = \kappa_a$. Replacing (7)

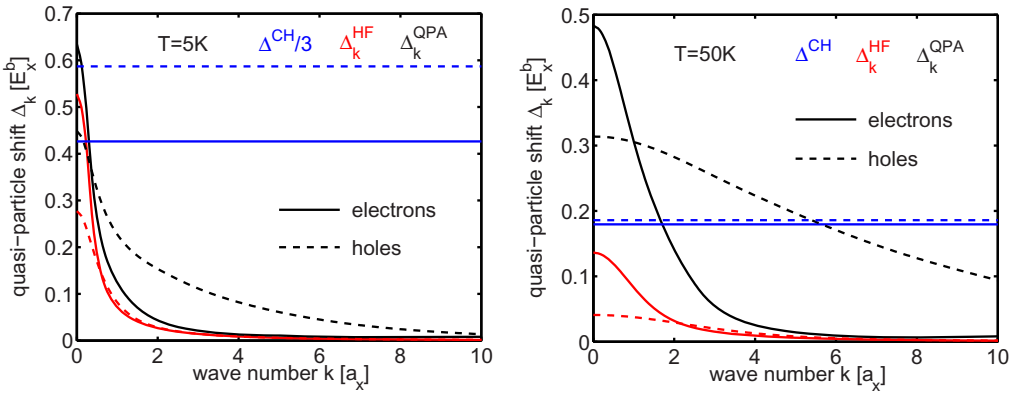

Figure 1. QP shifts $\Delta_k^a = (\varepsilon_k^a - e_k^a)$ of electrons (solid lines) and holes (dashed lines) for $n = 5 \times 10^{15}\,\mathrm{cm}^{-3}$ at $T = 5\,\mathrm{K}$ (left) and for $T = 50\,\mathrm{K}$ (right) within CH, HF and QPA.

in (6), the corresponding chemical potential is shifted by $\mu_a^{\mathrm{CH}} = \mu_a^0 - \Delta_a^{\mathrm{CH}}$. A comparison of the CH self-energy with the HF energies $\Delta_k^{a,\mathrm{HF}}$ (2) and with the QPA shift, determined by the self-consistent solution of equations (2)–(6), is presented in figure 1. Throughout this paper densities are given in units of cm^{-3}. For that the 2D densities following from (6) are divided by the well width. Comparing first the QPA with the HF approximation, the role of dynamical screening is clearly visible, where the differences become weaker for lower temperatures. For higher temperatures, the CH shift (7) only weakly depends of the mass ratio α_a and is of the order of the HF and QP shifts. For $T = 5\,\mathrm{K}$, the CH shift overestimates the screening by a factor of 3 (note that for $T = 5\,\mathrm{K}$, $\Delta^{\mathrm{CH}}/3$ is presented in order to make it comparable with the other approximations).

The question now is: how do the chemical potentials change within the different approximations for the QP energies? In bulk semiconductors (3D case), the sum over the wave vector in (6) for ideal particles (5) cannot be performed analytically, and the chemical potentials as a function of carrier density and temperature have to be determined by numerical inversion. In contrast to that, for the quasi-2D description in quantum wells, this inversion can be performed analytically [6, 7]:

$$n_a^{*,0} = \frac{kT}{2\pi\alpha_a} \ln\left|\mathrm{e}^{\mu_a^0/kT} + 1\right|. \tag{8}$$

In the left part of figure 2, we present the sum of chemical potentials of both carrier species $\mu = \mu_\mathrm{e} + \mu_\mathrm{h}$ following from the inversion of equation (6). A comparison is given for different approximations as considered in figure 1. In the right part, the deviations from the chemical potentials μ_0 of ideal carriers are shown. For all temperatures, the many-body effects give rise to a decrease of the chemical potentials. Effects of dynamical screening considered in QPA dominate for higher temperatures in comparison to the HF approximation, while the HF approximation gives the dominant contribution at low temperatures. The opposite holds for the CH approximation. For carrier densities up to $n = 10^{16}\,\mathrm{cm}^{-3}$ which are relevant for the description of the Mott transition (see the next section), a strong decrease is found, in particular, for low temperatures. Additionally, in the right figure, the dashed horizontal line

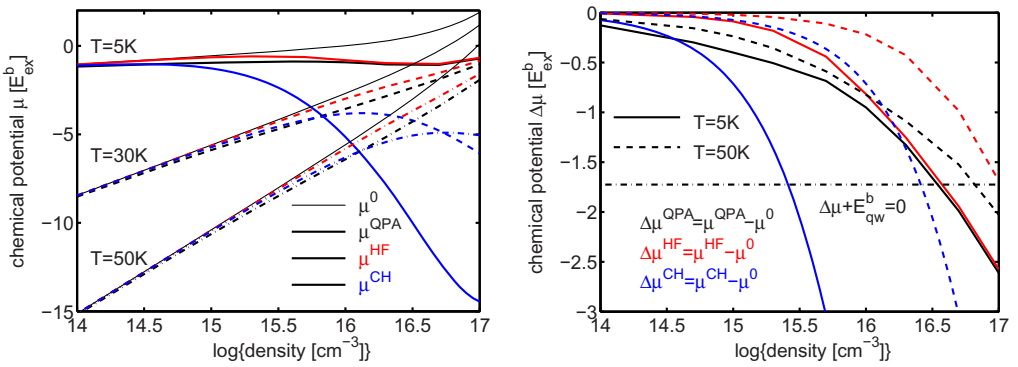

Figure 2. Sum of the chemical potentials of electrons and holes for different temperatures and different approximations in dependence of the carrier density (left). Deviation of the chemical potentials from those of non-interacting particles (right).

marks the exciton energy in the non-excited quantum well. As we have seen above, within the CH approximation, $\Delta\mu^{\mathrm{CH}}$ is equal to the CH self-energy. Such a simple picture is not valid for the HF approximation and for the QPA, since the QP energies are not rigid shifts but still depend on the wave vector. Nevertheless, $\Delta\mu$ can be considered for these approximations as an effective shift, too. Having in mind the simple picture, in which the Mott transition is generated by the decrease of the band edge with increasing excitation, while the exciton energy stays nearly unchanged, the cross point of $\Delta\mu$ with the exciton energy can be considered as Mott density. This will be supported by the following investigations of the degree of ionization in the partially ionized plasma, consisting of non-bound carriers and excitons. The excitons are considered as ideal bosons in thermal equilibrium with the distribution

$$f^{\mathrm{X}}(E_K) = \left[\mathrm{e}^{(E_K-\mu_{\mathrm{X}})/kT}+1\right]^{-1} \tag{9}$$

containing the kinetic energy of the center-of-mass motion $E_K = \alpha_{\mathrm{e}}\alpha_{\mathrm{h}}K^2$ (in excitonic units) and the chemical potential μ_{X} of the excitons. As for the ideal carriers (6) and (8), the density n_{X} of excitons can be calculated analytically:

$$n_{\mathrm{X}} = \sum_K f^X(E_K) = \frac{kT}{\pi\alpha_{\mathrm{e}}\alpha_{\mathrm{h}}} \ln\left|1-\mathrm{e}^{\mu_{\mathrm{X}}/kT}\right|. \tag{10}$$

The chemical potentials of carriers and excitons are connected via the binding energy of excitons in the quantum wells $E_{\mathrm{X}}^{\mathrm{qw}}$ by the well-known thermodynamic condition for the chemical (ionization) equilibrium,

$$\mu_{\mathrm{X}} = \mu_{\mathrm{e}} + \mu_{\mathrm{h}} - E_{\mathrm{X}}^{\mathrm{qw}}. \tag{11}$$

Applying the relations (7) and (8), a Saha equation for the degree of ionization α [15],

$$n_a^* = \alpha\, n, \quad n_{\mathrm{X}} = (1-\alpha)\, n, \tag{12}$$

can be derived, characterizing the composition of the partially ionized plasma:

$$\mathrm{e}^{\pi\alpha_{\mathrm{e}}\alpha_{\mathrm{h}}n(1-\alpha)} = \left|1 - z_{\mathrm{e}}^0 z_{\mathrm{h}}^0\, \mathrm{e}^{(E_{\mathrm{X}}^{\mathrm{qw}}-\Delta^{\mathrm{CH}})}\right|. \tag{13}$$

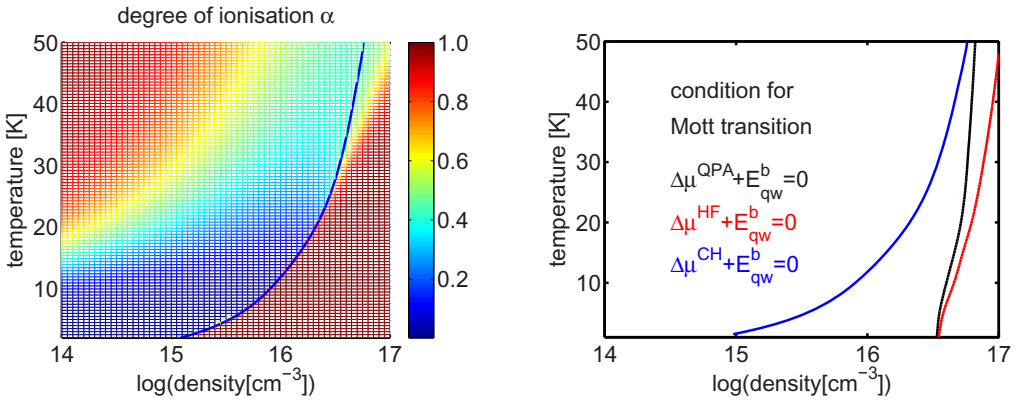

Figure 3. Degree of ionization for the CH approximation according to equation (13) as a function of density and temperature, where the blue line corresponds to $\Delta\mu^{\mathrm{CH}} = E^{\mathrm{b}}_{\mathrm{qw}}$ (left). Conditions for the Mott transition with QPA, CH and HF approximation (right).

It is advantageous to introduce here the fugacities z^0_a

$$z^0_a = \mathrm{e}^{\mu^0_a/kT} = \mathrm{e}^{2\pi\alpha_a n\alpha/kT} - 1, \tag{14}$$

and the total CH self-energy $\Delta^{\mathrm{CH}} = \Delta^{\mathrm{CH}}_{\mathrm{e}} + \Delta^{\mathrm{CH}}_{\mathrm{h}}$. Equation (13) can be used to determine the degree of ionization in terms of density and temperature of carriers. For the bulk case, the sums over the wave vectors in (6)–(10) can be performed only numerically. However, an analytical form of the Saha equation can be given if Fermi/Bose distributions of carriers/excitons are replaced by Boltzmann distributions [44]. Doing this for the quasi-2D description in quantum wells, Saha's equation (13) has the form

$$\frac{1-\alpha_{\mathrm{B}}}{(\alpha_{\mathrm{B}})^2} = n\lambda^2\,\mathrm{e}^{(E^{\mathrm{qw}}_{\mathrm{X}} - 2n\lambda^2\alpha_{\mathrm{B}})/kT}, \quad \lambda^2 = \frac{4\pi}{kT}, \tag{15}$$

where λ is the thermal wavelength in units of the bulk excitonic Bohr radius. The CH self-energy in the case of Boltzmann distributions is simply $E^{\mathrm{B}}_{\mathrm{CH}} = 2n\lambda^2\alpha_{\mathrm{B}}$.

For simplicity, first results for the degree of ionization by the solution of the Saha equation (13) with the CH self-energy are presented in the left part of figure 3. Regions where most carriers are bound in excitons ($\alpha \to 0$) are given in blue and regions with high degree of ionization ($\alpha \to 1$) in red. With increasing temperature, thermal ionization occurs. As a Mott transition the strong increase of α with increasing carrier density is understood. Additionally, with a blue line the condition $\Delta\mu^{\mathrm{CH}} = \mu^{\mathrm{CH}} - \mu^0 = -\Delta^{\mathrm{CH}} = E^{\mathrm{b}}_{\mathrm{qw}}$ is plotted which describes those values of temperature and density where the total CH self-energy (corresponding to the sum of the changes of chemical potentials with respect to the chemical potentials of ideal carriers) crosses the exciton binding energy. In particular, at low temperatures, the condition exactly corresponds to those densities where the excitons are ionized and can be used as a criterion for the Mott transition. Within excitonic units, the criterion can be rewritten as $\kappa\, a_{\mathrm{X}} = 1$, and corresponds to the condition $\kappa a_{\mathrm{X}} = 0.84$ found in [13] for the vanishing of the bound states in a statically screened potential.

The abrupt increase of α in the left part of figure 3 for low temperatures can be explained as follows. For low temperatures, the Saha equation (13) has three solutions for α as a function of n, corresponding to a classical hysteresis curve with two stable (upper and lower) and one unstable solution [20]. The question arises as to whether this may give rise to a first-order phase transition from an exciton gas to a fully ionized EHP (Mott phase transition) or to the possible existence of an excitonic condensate still at rather high densities. In [30] we have shown that for the bulk case the hysteresis is strongly reduced if the chemical potentials are used within QPA instead of CH approximation. Moreover, it is known for hydrogen plasmas that the atom–atom interaction completely destroys the bistability [31]. The same can be expected by inclusion of the exciton–exciton interaction. This also holds for quantum wells. The reduction of the hysteresis can be seen in the right part of figure 3, where we have used the upper values for α to compare the condition for the Mott transition following from the CH self-energy (blue line, as shown in the left part) with the corresponding conditions for the QPA (black) and for the HF approximation (red). Here $\Delta\mu$ describes the deviations of the respective chemical potentials from those of ideal carriers.

The CH self-energy (static screening) strongly overestimates the screening effects for low temperatures; here the HF approximation is very close to the full QPA. However, for higher temperatures we find better agreement of the CH approximation with the QPA than in the bulk case (see [30]). Actually, the comparison of the CH approximation representing only a rigid shift with both the other approximations is questionable, because the latter ones describe QP energies depending on the wave vector. However, $\Delta\mu$ represents a kind of effective rigid energy shift due to the many-body effects. Finally, the condition $\Delta\mu = -E_{\mathrm{X}}^{\mathrm{qw}}$ is a convenient Mott criterion from the thermodynamic point of view. Applying the simple criterion $n^{\mathrm{M}} a_{\mathrm{X}}^2 L = 1$ [12], the Mott density would be at $n^{\mathrm{M}} = 3.3 \times 10^{17}\,\mathrm{cm}^{-3}$. The thermal ionization corresponding to $kT = E_{\mathrm{qw}}^{\mathrm{b}}$ would appear above $T = 20\,\mathrm{K}$. Both conditions are only rough estimations.

3. Semiconductor Bloch equations—the spectral approach

Another approach to the description of the Mott transition of excitons in semiconductors more related to experiments is the investigation of the optical response. The dielectric response of a semiconductor to an external light field can be described with the semiconductor Bloch equations. In the linear case, the following equation for the susceptibility in semiconductor quantum wells can be derived [25, 50]:

$$\left\{\omega - \varepsilon_k^{\mathrm{HF}} - \Sigma_k^{\mathrm{r}}(\omega) + \mathrm{i}\,\gamma_0\right\}\,\chi_k(\omega) + \sum_q \left\{N_k\, v_{k-q}^{\mathrm{eh}} + \Theta_{k,q}(\omega)\right\}\chi_q(\omega) \;=\; N_k. \tag{16}$$

Equation (16) represents a generalization of an effective two-particle Schrödinger equation of the electron–hole motion derived first in [5]. It corresponds to the treatment in [47, 51], where the equation was solved in the time domain. We have considered an additional broadening γ_0 of the excitons which is caused by the roughness of the quantum wells. It was determined by the fit of the excitonic spectrum at low excitation $\gamma_0 = 0.16\,\mathrm{meV} = 0.038 E_{\mathrm{X}}^{\mathrm{b}}$. The terms with the carrier distributions in $N_k = 1 - f_k^{\mathrm{e}} - f_k^{\mathrm{h}}$ (Pauli blocking) partially compensate with the sum over the HF contribution of carriers $\varepsilon_k^{\mathrm{HF}} = \sum_a (\mathrm{e}_k^a + \Delta_k^{a,\mathrm{HF}})$. Screening effects are contained in the effective interaction $\Theta_{k,q}(\omega)$ and in the retarded interband self-energy $\Sigma_k^{\mathrm{r}}(\omega)$. Both are

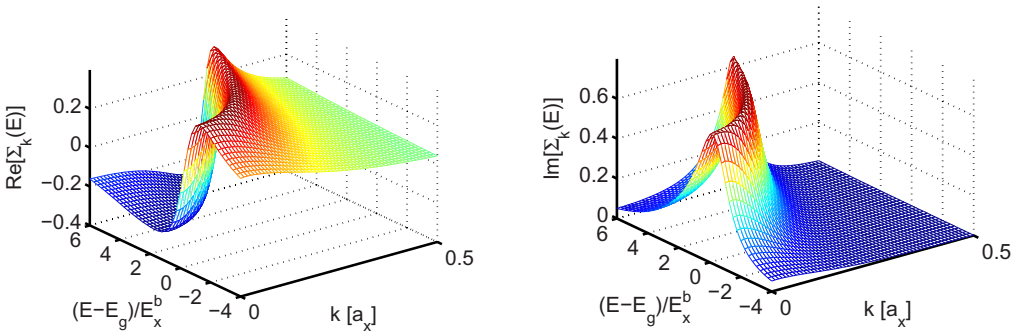

Figure 4. Real (left) and imaginary parts of the interband self-energy in excitonic units (17) as a function of the energy E relatively to the band edge E_g for $T = 30\,\mathrm{K}$ and $n = 10^{15}\,\mathrm{cm}^{-3}$.

connected to each other,

$$\Sigma^{\mathrm{r}}_k(\omega) = \sum_q \Theta_{q,k}(\omega), \qquad \Theta_{k,q}(\omega) = \sum_{a\neq b} \int \frac{\mathrm{d}\bar{\omega}}{2\pi} \frac{[1-f^a_k]V^{ab,>}_{k-q}(\bar{\omega}) + f^a_k V^{ab,<}_{k-q}(\bar{\omega})}{\omega - \varepsilon^a_k - \varepsilon^{\mathrm{b}}_q - \bar{\omega} + \mathrm{i}[\Gamma^a_k + \Gamma^b_q]/2} \tag{17}$$

and compensate likewise. In contrast to the one-particle self-energy (2), the interband self-energy (17) does not describe transitions within the bands, but an interband transition which is initiated by a photon with the energy ω of the external probe field. The photon generates an electron–hole pair with the energies $\varepsilon^a_k + \varepsilon^b_q$ accompanied by the absorption/emission of a quantum $\bar{\omega}$ of the elementary excitations in the EHP [25]. Moreover, in contrast to the one-particle description, where we have applied the QPA (2), the interband self-energy is a dynamical quantity, depending on the energy ω. Neglecting the QP damping in the denominator of $\Sigma^{\mathrm{r}}_k(\omega)$ (17) and replacing in the sense of a QP description $\omega \to \varepsilon^a_k + \varepsilon^b_k$, the interband self-energy corresponds to the sum of the carrier self-energies $\Sigma^{\mathrm{r}}_{\mathrm{e},k}(\varepsilon^{\mathrm{e}}_k) + \Sigma^{\mathrm{r}}_{\mathrm{h},k}(\varepsilon^{\mathrm{h}}_k)$ in QPA. Earlier, this treatment was used as dephasing rate approximation for the imaginary part of the self-energy. In [25, 27], we have demonstrated that only the dynamical treatment of the interband quantities provides the correct description of polariton propagation in bulk semiconductors for excitations well below the Mott transition. This will be examined in the following for higher excitations up to the Mott transition for quantum wells. The results of the previous section for the QPA are incorporated here in to the QP energy and damping and also into the chemical potentials of the carrier distributions.

In figure 4, we show the real and the imaginary part of the interband self-energy according to (17). The imaginary part, representing the so-called diagonal dephasing $\Gamma_k(\omega) = \mathrm{Im}\,\Sigma^{\mathrm{r}}_k(\omega)$, is peaked at the two-particle dispersion and decreases to lower and higher energies. For $k = 0$, the maximum is at the band edge which is renormalized by the many-body effects (interband self-energy and HF energy). Within the dephasing rate approximation, the imaginary part would be constant over the whole energy range and correspond roughly to the peak value. The energy range of interest for the description of the Mott transition is between the exciton energy and the band edge.

In figure 5, the diagonal dephasing is presented within this energy region for two temperatures and different carrier densities. The vertical dashed lines mark the exciton position $-E^{\mathrm{b}}_{\mathrm{qw}}$, and the horizontal line the inhomogeneous (background) damping γ_0. While the diagonal dephasing is more or less localized around the non-renormalized band edge $E - E_g = 0$ for

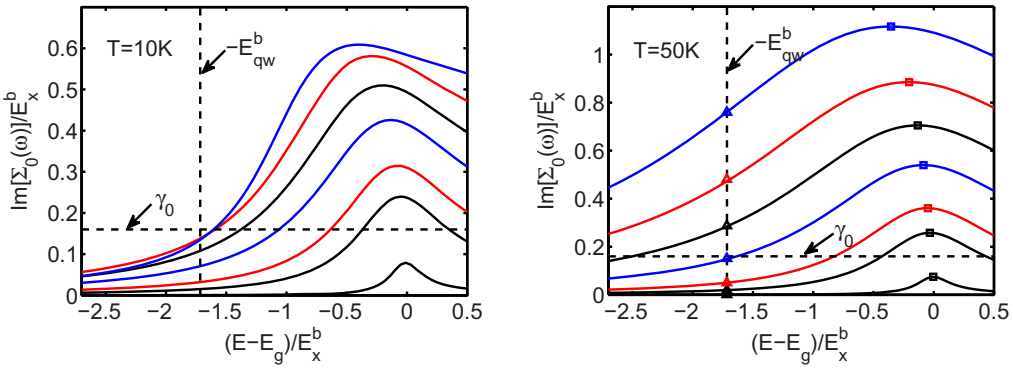

Figure 5. Diagonal dephasing at $k = 0$ at $T = 10\,\mathrm{K}$ (left) and $T = 50\,\mathrm{K}$ (right) with increasing carrier densities (in cm^{-3}) from bottom to top: $n = 10^{13},\ 10^{14},\ 2\times10^{14},\ 5\times10^{14},\ 10^{15},\ 2\times10^{15}$ and $5\times10^{15}\,\mathrm{cm}^{-3}$. Markers highlight the dephasing at the exciton (▲) and the maximum dephasing (□).

low excitation, it grows upward with increasing excitation due to the many-body effects. This becomes clear considering the increase at the exciton energy $E^{\mathrm{b}}_{\mathrm{qw}}$ of the non-excited quantum well (triangles in the right part of figure 5 and at the maximum (squares)). For low excitation the maximum is direct at the non-renormalized band edge, while it is shifted to lower energies with increasing excitation. The behavior of the diagonal dephasing and of the renormalization of the interband energy will be compared later with the QP properties (2) and the shift of the exciton which is generated by an interplay of the retarded interband self-energy and the effective interaction (17). For lower temperatures, there is a stronger decrease of the diagonal dephasing towards the exciton. Whereas, at $T = 50\,\mathrm{K}$, the carrier-induced diagonal dephasing for $n = 5\times10^{14}\,\mathrm{cm}^{-3}$ grows up to the inhomogeneous broadening γ_0, it becomes a multiple of γ_0 for higher densities. This is in contrast to lower temperatures. For $T = 5\,\mathrm{K}$, the carrier-induced diagonal dephasing stays below the inhomogeneous broadening at the exciton. However, we see here the limitation of validity of the QP treatment within the one-particle description for low temperatures and high densities (close to the Mott transition). As shown in figure 2, the total chemical potential of electrons and holes strongly increases for lower temperatures and comes into the order of the exciton binding energy. The imaginary part of the susceptibility should have a transition from gain to absorption at the chemical potentials according to the Kubo–Martin–Schwinger (KMS) relation [52]. This property is not fulfilled within the QP description for the carriers (2) in the interband self-energy and the effective interaction (17). On the other hand, we want to omit a more intuitive manipulation to solve this problem as shown in [7] for the free carrier absorption. The complete dynamical treatment of the one-particle retarded Green's function and its inclusion into interband self-energy in the semiconductor Bloch equations is a very extensive numerical problem. A principal way to solve the problem was demonstrated in [53] for static screening with a Bethe–Salpeter equation, completely neglecting the dynamical screening. A dynamical treatment for the one-particle properties was presented in [54, 55] and included in the calculation of the retarded interband self-energy $\Sigma^{\mathrm{r}}_k(\omega)$. However, it is an open question of how to include it in the effective interaction $\Theta_{q,k}(\omega)$ on the same level in order to get the correct description of the excitonic features below the Mott transition. These features arise with strong compensation of both terms in the two-particle equation (16). For this reason, we have to restrict ourselves to the description

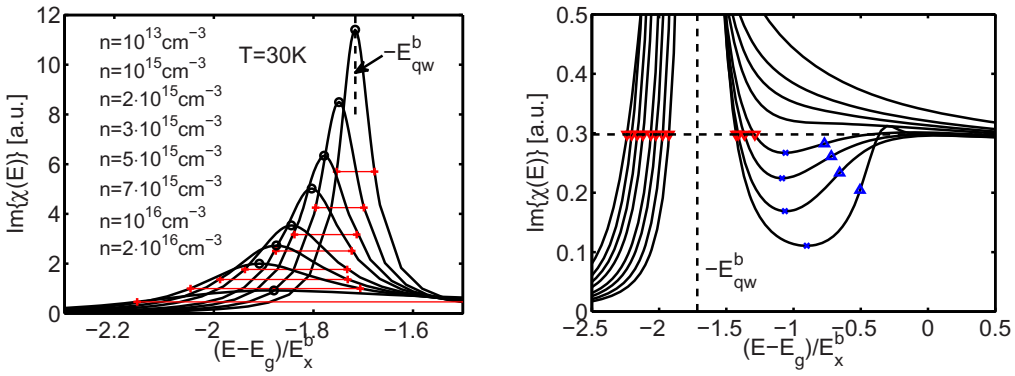

Figure 6. Imaginary part of the susceptibility according to (16) in the excitonic (left) and the band edge region (right) at $T = 30\,\mathrm{K}$ and with increasing carrier densities given in the left figure from top to bottom. Markers and additional dashed lines: peak absorption (left, ○), half maximum absorption (left, +), full width at half maximum (left, thin red horizontal lines), minimum (right, ×) and half minimum absorption (right, ▲), exciton energy at low excitation (vertical dashed line), level of the band edge absorption (horizontal black dashed line) and crossing with the excitonic absorption (▼).

of the Mott transition for temperatures above $T = 20\,\mathrm{K}$, where the transition from gain to absorption in our treatment within the QPA is well below the exciton. Nevertheless, we are able to describe the broadening and the subtleties of the exciton shift at lower temperatures below $T = 20\,\mathrm{K}$ (see [42]), but for carrier densities below the Mott transition.

Results for the susceptibility calculated by the solution of the semiconductor Bloch equation (16) including the many-body effects within QPA are given in figure 6 for the imaginary part of the susceptibility $\chi(E) = \sum_k \chi_k(E)$, describing the absorption in the quantum well. With increasing excitation, (i) a decrease of the excitonic absorption peak, (ii) an increase of the linewidth and (iii) a weak shift of the exciton peak to lower energies appear. In [42], we have reported that this shift turns to higher energies, if the temperature is decreased down to $T = 5\,\mathrm{K}$. It is an advantage of our spectral investigation of the Mott transition in comparison with investigations of the dynamics of the PL in [32–38] that we are able to address single electron–hole pair states in the optical response over the whole spectrum. In order to analyze the spectra in more detail, we have marked the maximum and the half-maximum absorption at the exciton left part, which are considered in figure 7. In the right part of figure 6, the whole spectral range between exciton and the band edge is shown on the level of the band edge absorption. For the lowest density $n = 10^{13}\,\mathrm{cm}^{-3}$, the 2s state of the exciton is still resolved, which disappears with increasing excitation. In any case the band edge is merged with the higher excited exciton states up to the 2s state and cannot be identified separately. For a quantitative description of the behavior of these states near the band edge, additional markers are set in figure 6. The blue crosses in the left part mark the minimum absorption between the exciton and the band edge, and the blue triangles those points where the band edge absorption is decreased to one half of the absorption minimum. Already for densities above $n = 4 \times 10^{15}\,\mathrm{cm}^{-3}$, the band edge and the higher excited exciton states merge with the exciton, giving rise to an increasingly asymmetric look of the exciton line at the bottom. The single markers are summarized in figure 7. In the left part, the normalized peak (left scale) and the FWHM (right) of the excitonic absorption are

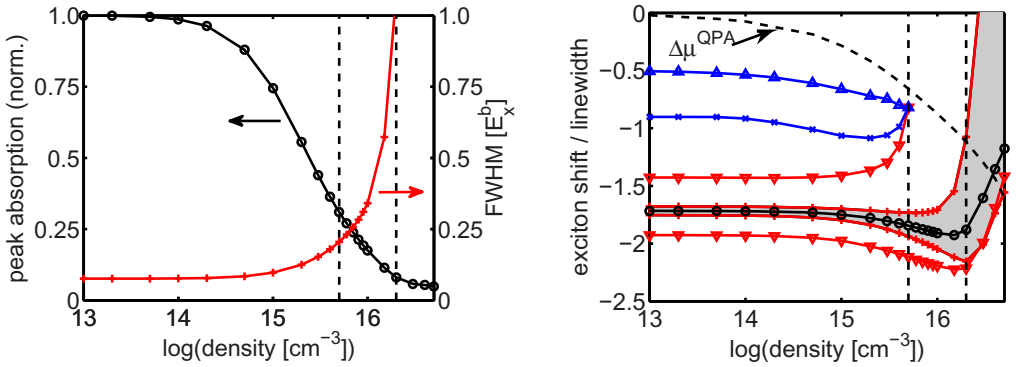

Figure 7. Left: normalized peak absorption and full-width at half-maximum (FWHM) for $T = 30\,\mathrm{K}$ as a function of the density, markers corresponding to figure 6. Right: exciton energy (○), FWHM (+ and gray shaded area), level, where the excitonic absorption corresponds to the band edge absorption (▼), minimum (×) and half minimum absorption (▲). For a better understanding of the single markers, compare with figure 6.

given. With increasing carrier density, the maximum absorption strongly decreases, while the excitonic broadening (FWHM) is increased due to the many-body effects. For low densities, the influence of screening vanishes and the broadening changes into the inhomogeneous broadening ($2\gamma_0 = 0.076 E_\mathrm{X}^\mathrm{b}$). The vertical dashed lines mark the region where the Mott transition occurs. This is explained in more detail in the discussion of the right part of the figure. The position and the increase of the linewidth of the exciton resonance are marked by the shaded area in the right part. The strong increase of the upper half value of the maximum absorption above $n = 2 \times 10^{16}\,\mathrm{cm}^{-3}$ indicates that the band edge absorption is higher than one half of the peak absorption. The question is now whether this density corresponds to the Mott density where the exciton line is bleached out. To answer this question, one should first have a look at the other curves in the right figure, which compare the band edge with excitonic absorption. The red triangles mark those energies where the level of band edge absorption (including the absorption of the excited exciton states) crosses the excitonic absorption (see the horizontal dashed line in figure 6). Additionally, the curves with blue markers according to figure 6 are given, representing the minimum and one half of minimum and band edge absorption. The latter three curves end in one point at a density of about $n = 5 \times 10^{15}\,\mathrm{cm}^{-3}$, which means that band edge and 1s-exciton merge into each other. Should this density be considered as the Mott density? As seen in the left part of the figure, the peak absorption is reduced nearly to 1/4 of the peak absorption at low excitation, and the HWHM is increased to more than sixfold of the inhomogeneous broadening. Finally, from the spectral point of view, the Mott density cannot clearly be determined, but it is for the considered temperature of $T = 30\,\mathrm{K}$ in a density region between $n = 6 \times 10^{15}$ and $2 \times 10^{16}\,\mathrm{cm}^{-3}$, marked by both dashed lines in figure 7, the Mott range.

4. Comparison between the two approaches

Finally, we want to compare our results above for the *spectral description* of the Mott transition with the change of the chemical potentials within QPA (see section 2 and the results in figure 2),

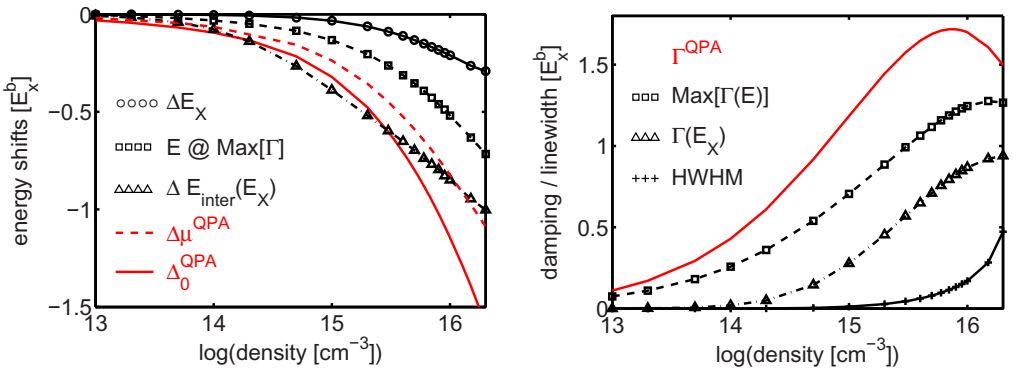

Figure 8. Comparison of energy shifts $\Delta\mu^{\mathrm{QPA}}$ and damping Γ^{QPA} within QPA (red curves) with corresponding spectral properties (black curves) for $T = 50\,\mathrm{K}$. Left: shift of the exciton energy ΔE_{X}, energy E@Max[Γ], where the diagonal dephasing becomes a maximum (compare with figure 5), and shift of interband energy at the exciton $\Delta E_{\mathrm{inter}}(E_{\mathrm{X}})$. Right: carrier-induced broadening (HWHM) of the exciton, maximum diagonal dephasing Max[$\Gamma(E)$] (see figure 5) and diagonal dephasing at the exciton $\Gamma(E_{\mathrm{X}})$.

representing a comparison of a two-particle with a one-particle description. In the right part of figure 7, we have added the shift of the chemical potentials in QPA by a dashed line. From the *thermodynamic point of view*, the Mott transition appears when this line crosses the exciton energy. This is the case for $T = 30\,\mathrm{K}$ above the highest considered density $n = 5 \times 10^{16}\,\mathrm{cm}^{-3}$ in figures 6 and 7 and that at a much higher density than the density range found by the investigation of spectral properties. This is to be expected, since the QPA (2) and the *thermodynamic concept* of the description of the chemical equilibrium (1) described in section 2 are valid for small damping Γ_k^a or longlife times of the carrier states, which is not valid in the Mott region. This is demonstrated in figure 8.

In our *thermodynamic approach* presented in the last section, the shift of the chemical potential $\Delta\mu^{\mathrm{QPA}}$ corresponds to an effective shift of the sum of one-particle energies of electrons and holes in QPA (see (2) and figure 2). Within the two-particle (*spectral*) *approach* based on the semiconductor Bloch equations (16), the shift of the interband energy $\Delta E_{\mathrm{inter}}(E) = \mathrm{Re}[\Sigma_0(E)] + \Delta_0^{\mathrm{HF}}$ is a comparable quantity. Since the retarded interband self-energy $\Sigma_k^{\mathrm{r}}(\omega)$ depends on the energy ω (see the discussion after figure 5), we compare $\Delta E_{\mathrm{inter}}(E)$ at the energy where the diagonal dephasing (see right part of figure 5) becomes a maximum and that at the exciton energy. While the QP-shift Δ_0^{QPA} corresponds in a wide density range to the interband shift at maximum dephasing, the shift at the exciton is much lower. However, the interband shift at the exciton is still much larger than the shift of the exciton. This is due to the compensation of the interband energy with the effective interaction and the Pauli blocking in the semiconductor Bloch equations. The problem here is to find a convenient quantity for an effective description of the band edge shrinkage which can explain the vanishing of the exciton line at lower densities than those expected by the discussed interband and QP shifts (see figure 7). Finally, the shrinking gap is described by an interplay of the interband self-energy with the effective interaction and of the HF renormalization with the Pauli blocking which cannot be expressed by one compact quantity.

A similar behavior is found for the broadening (HWHM) of the exciton presented in the right part of figure 8. Due to the compensation of the diagonal dephasing with the imaginary part of the effective interaction, the half-width of the exciton (HWHM) is much smaller than the dephasing at the exciton ($\Gamma(E_X)$). Only for higher densities, this compensation is weakened and the excitonic linewidth strongly increases as we have already discussed in the description of the Mott transition. Furthermore, we find that the QP damping $\Gamma^{QPA} = \Gamma_0^e + \Gamma_0^h$ (see (2)) is much larger than the maximum diagonal dephasing $\mathrm{Max}[\Gamma_0(E)]$ at the two-particle dispersion. Considering that the QP damping corresponds to the inverse life time of carrier states T_1^a and the inverse diagonal dephasing to the dephasing time T_2, this contradicts the simple relation $1/T_1^e + 1/T_1^h = 1/T_2$ used in the description of two-level systems (see [7]).

5. Summary

We have studied the Mott transition of excitons in GaAs–GaAlAs quantum wells. Many-body effects were taken into account including the dynamical screening of the Coulomb interaction both in the one-particle properties of the carriers and in the two-particle properties of electron–hole pairs. The Mott transition is described within two approaches. The first one is a *thermodynamic approach*, based on the self-consistent calculation of self-energies and chemical potentials of carriers in the framework of the chemical equilibrium between unbound carriers and excitons. The second one is a *spectral approach* focused on the electron–hole pair properties which can be seen experimentally in the dielectric response and which is calculated here with the semiconductor Bloch equations. A comparison of the dynamically screened self-energy in QPA with simple approximations shows that the HF approximation is convenient for low temperatures ($T < 10\,\mathrm{K}$), where the CH approximation (static screening) drastically overestimates the effect of screening. This is contrary to the case of higher temperatures ($T > 50\,\mathrm{K}$), where the HF approximation fails and static screening becomes a more convenient approximation. Studying the degree of ionization, we find that the Mott density n^{Mott} is reached when the change of the chemical potential due to many-body effects crosses the exciton binding energy $\Delta\mu = -E_{qw}^b$. This corresponds to the general view of the Mott transition, to be generated by the decreasing band edge with increasing density, while the exciton energy stays nearly unchanged. The changes of the chemical potential play here the role of an effective rigid shift of the band edge.

In contrast, it is difficult to identify the band edge in the region of the Mott transition within the *spectral approach*. For low excitation, the 1s-exciton can be clearly resolved. However, the band edge absorption cannot be separated from the absorption of the higher excited excitonic bound states. With increasing excitation, the band edge first bleaches the 2s-state and then immerses into the upper exciton tail. Further increase of the excitation leads to an increasing broadening and a decreasing peak of the 1s-exciton absorption, while the band edge cannot by identified any more. Thus, the Mott transition does not occur as an abrupt jump at a certain density, but is rather a smooth transition in a broader density region. This density region lies considerably below the predicted Mott density in the *thermodynamic approach*.

Our analysis shows that the band edge shift cannot be adequately described within the QPA for the one-particle self-energies. Rather the interband self-energy and the diagonal dephasing (i) strongly change over the spectral range between the exciton and the band edge and (ii) cannot be described as the sum of the one-particle self-energies calculated with QPA.

Moreover, the electron–hole pair spectrum is generated by the interplay of the interband self-energy and the effective interaction which widely cancel each other. The cancelation of the real part of both effects results in a nearly unchanged exciton position which undergoes only a weak shift depending on the temperature. For the imaginary parts it is reflected by the much lower excitonic broadening in comparison to the diagonal dephasing (imaginary part of the interband self-energy).

Finally, the large increase of the one-particle damping in the vicinity of the Mott transition shows the limit of validity of the QP picture both in the calculation of the chemical potentials and in its use for the derivation of the mass-action law within the *thermodynamic approach*. Therefore, for the considered system of quantum wells the *spectral approach* should be preferred for a consistent picture of the Mott transition.

Acknowledgments

The authors thank the Deutsche Forschungsgemeinschaft (Collaborative Research Center SFB 652) for financial support.

References

[1] Asnin V M 1973 *Fiz. Tverd. Tela* **15** 3298
[2] Egorov V D, Müller G O, Weber H H, Zimmermann R, Diete A F, Lysenko V G, Revenko V I and Timofeev V B 1977 *Nuovo Cimento* B **39** 628
[3] Shah J, Combescot M and Dayem A H 1977 *Phys. Rev. Lett.* **38** 1497
[4] Fehrenbach G W, Schäfer W, Treusch J and Ulbrich R G 1982 *Phys. Rev. Lett.* **49** 1281
[5] Kilimann K, Kraeft W D and Kremp D 1977 *Phys. Lett.* A **61** 393
Zimmermann R, Kilimann K, Kraeft W D, Kremp D and Röpke G 1978 *Phys. Status Solidi* b **90** 175
[6] Ell C, Blank R, Benner S and Haug H 1989 *J. Opt. Soc. Am.* B **6** 2006
[7] Haug H and Koch S W 1990 *Quantum Theory of the Optical and Electronic Properties of Semiconductors* (Singapore: World Scientific)
[8] Schäfer W, Binder R and Schuldt K H 1988 *Z. Phys.* B **70** 145
[9] Böhne G, Sure T, Ulbrich R G and Schäfer W 1990 *Phys. Rev.* B **41** 7549
[10] Arndt S, Kraeft W D and Seidel J 1996 *Phys. Status Solidi* b **194** 601
[11] Bornath Th, Kremp D and Schlanges M 1999 *Phys. Rev.* E **60** 6382
[12] Klingshirn C F 1995 *Semiconductor Optics* (Berlin: Springer) (3rd edn 2007)
[13] Rogers F J, Graboske H C Jr and Harwood D J 1970 *Phys. Rev.* A **1** 1577
[14] Zimmermann R 1988 *Many-Particle Theory of Highly Excited Semiconductors* (Leipzig: Teubner)
[15] Ebeling W, Kraeft W D and Kremp D 1976 *Theory of Bound States and Ionization Equilibrium in Plasmas and Solids* (Berlin: Akademie-Verlag)
Ebeling W, Kraeft W D and Kremp D 1979 *Theory of Bound States and Ionization Equilibrium in Plasmas and Solids* (Moscow: Mir)
[16] Redmer R 1997 *Phys. Rep.* **282** 35
[17] Pavesi L, Staehli J L and Capozzi V 1988 *Solid State Commun.* **61** 321
[18] Pavesi L, Staehli J L and Capozzi V 1988 *J. Phys. C: Solid State Phys.* **21** 1485
[19] Pavesi L, Staehli J L and Capozzi V 1989 *Phys. Rev.* B **39** 10982
[20] Snoke D W and Crawford J D 1995 *Phys. Rev.* E **52** 5796
[21] Portnoi M E and Galbraith I 1999 *Phys. Rev.* B **60** 5570
[22] Reinholz H 2002 *Solid State Commun.* **123** 489
[23] Snoke D 2008 *Solid State Commun.* **146** 73

[24] Manzke G, Peng Q Y, Henneberger K, Neukirch U, Hauke K, Wundke K, Gutowski J and Hommel D 1998 *Phys. Rev. Lett.* **80** 4943
[25] Nägerl J S, Stabenau B, Böhne G, Dreher S, Ulbrich R G, Manzke G and Henneberger K 2001 *Phys. Rev.* B **63** 235202
[26] Lindberg M and Koch S W 1988 *Phys. Rev.* B **38** 3342
[27] Seemann M, Kieseling F, Stolz H, Franz R, Manzke G, Henneberger K, Passow T and Hommel D 2005 *Phys. Rev.* B **72** 075204
[28] Nacke Ch, Stolz H, Manzke G and Henneberger K 2002 *Eur. Phys. J.* B **30** 303
[29] Manzke G, Henneberger K, Seemann M and Stolz H 2009 *Phys. Status Solidi* c **6** 520
[30] Semkat D, Richter F, Kremp D, Manzke G, Kraeft W-D and Henneberger K 2009 *Phys. Rev.* B **80** 155201
[31] Kremp D, Schlanges M and Kraeft W-D 2005 *Quantum Statistics of Nonideal Plasmas* (Berlin: Springer)
[32] Kira M, Jahnke F and Koch S W 1998 *Phys. Rev. Lett.* **81** 3263
[33] Chatterjee C, Ell C, Moser S, Khitrova G, Gibbs H M, Hoyer W, Kira M, Koch S W, Prineas J P and Stolz H 2004 *Phys. Rev. Lett.* **92** 067402
[34] Kappei L, Szczytko J, Morier-Genoud F and Devaud B 2005 *Phys. Rev. Lett.* **94** 147403
[35] Koch S W, Kira M, Khitrova G and Gibbs H M 2006 *Nature Mater.* **5** 523
[36] Amo A, Martin M D, Vina L, Toropov A I and Zhuravlev K S 2006 *Phys. Rev.* B **73** 035205
[37] Amo A, Martin M D, Vina L, Toropov A I and Zhuravlev K S 2007 *J. Appl. Phys.* **101** 081717
[38] Stern M, Garmider V, Umansky V and Bar-Joseph I 2008 *Phys. Rev. Lett.* **100** 256402
[39] Kaindl R A, Carnahan M A, Hägele D, Lövenich R and Chemla D S 2003 *Nature* **423** 734
[40] Huber R, Kaindl R A, Schmid B A and Chemla D S 2005 *Phys. Rev.* B **72** 161314
[41] Burau G K G, Manzke G, Kieseling F, Stolz H, Reuter D and Wieck A 2010 *J. Phys.: Conf. Ser.* **210** 012017
[42] Manzke G, Richter F, Semkat D, Burau G K G, Kieseling F and Stolz H 2011 *Phys. Status Solidi* c **8** 1161
[43] Kremp D, Schlanges M and Kraeft W-D 2005 *Quantum Statistics of Nonideal Plasmas* (Berlin: Springer)
[44] Kremp D, Kraeft W D and Schlanges M 1993 *Contrib. Plasma Phys.* **33** 567
[45] Kadanoff L P and Baym G 1962 *Quantum Statistical Mechanics* (New York: Benjamin)
[46] Pereira M F Jr, Koch S W and Chow W W 1993 *J. Opt. Soc. Am.* B **10** 765
[47] Girndt A, Jahnke F, Knorr A, Koch S W and Chow W W 1997 *Phys. Status Solidi* b **202** 725
[48] Jahnke F, Kira M and Koch S W 1997 *Z. Phys.* B **104** 559
[49] Pereira M F Jr and Henneberger K 1998 *Phys. Rev.* B **58** 2064
[50] Manzke G and Henneberger K 2002 *Phys. Status Solidi* b **234** 233
[51] Lorke M, Nielsen N T, Seebeck J, Gartner P and Jahnke F 2005 *Phys. Rev.* B **73** 085324
[52] Kubo R 1957 *J. Phys. Soc. Japan* **12** 570
Martin P C and Schwinger J 1959 *Phys. Rev.* **115** 1342
[53] Hannewald K, Glutsch S and Bechstedt F 2000 *Phys. Rev.* B **62** 4519
[54] Peng Q Y, Schmielau T, Manzke G and Henneberger K 2000 *J. Cryst. Growth* **214–215** 810
[55] Schmielau T, Manzke G, Tamme D and Henneberger K 2000 *Phys. Status Solidi* b **221** 215

A.8

Artikel 8

H. Stolz, R. Schwartz, F. Kieseling, S. Som, M. Kaupsch, S. Sobkowiak, D. Semkat, N. Naka, Th. Koch, and H. Fehske:

Condensation of excitons in Cu_2O at ultracold temperatures: experiment and theory

New J. Phys. **14**, 105007 (2012)

New Journal of Physics
The open-access journal for physics

Condensation of excitons in Cu_2O at ultracold temperatures: experiment and theory

Heinrich Stolz[1,5], Rico Schwartz[1], Frank Kieseling[1], Sunipa Som[1], Maria Kaupsch[1], Siegfried Sobkowiak[1], Dirk Semkat[1], Nobuko Naka[2,3], Thomas Koch[4] and Holger Fehske[4]

[1] Institut für Physik, Universität Rostock, D-18051 Rostock, Germany
[2] Department of Physics, Kyoto University, Kyoto 606-8502, Japan
[3] PRESTO, JST, 4-1-8 Honcho Kawaguchi, Saitama 332-0012, Japan
[4] Institut für Physik, Ernst-Moritz-Arndt-Universität Greifswald, D-17487 Greifswald, Germany
E-mail: heinrich.stolz@uni-rostock.de

New Journal of Physics **14** (2012) 105007 (37pp)
Received 18 May 2012
Published 10 October 2012
Online at http://www.njp.org/
doi:10.1088/1367-2630/14/10/105007

Abstract. We present experiments on the luminescence of excitons confined in a potential trap at milli-Kelvin bath temperatures under continuous-wave (cw) excitation. They reveal several distinct features like a kink in the dependence of the total integrated luminescence intensity on excitation laser power and a bimodal distribution of the spatially resolved luminescence. Furthermore, we discuss the present state of the theoretical description of Bose–Einstein condensation of excitons with respect to signatures of a condensate in the luminescence. The comparison of the experimental data with theoretical results with respect to the spatially resolved as well as the integrated luminescence intensity shows the necessity of taking into account a Bose–Einstein condensed excitonic phase in order to understand the behaviour of the trapped excitons.

[5] Author to whom any correspondence should be addressed.

Contents

1. Introduction

Almost 50 years ago, excitons [1, 2] were identified as particularly interesting candidates for Bose–Einstein condensation (BEC), as they consist of an electron and a hole in a semiconductor, both fermions bound to form a bosonic excitation and thus resembling most closely neutral atoms of usual matter. Due to their rather small mass comparable to the free electron mass, it was speculated that for exciton densities of the order of $10^{18}\,\mathrm{cm}^{-3}$—easily achievable by absorption of photons—critical temperatures of some 10 K may be reached.

Due to their unique properties, the excitons of the so-called yellow series in the semiconductor cuprous oxide (Cu_2O) are still considered the most promising candidates for excitonic BEC [3–5]. This is related to the large binding energy of 150 meV, which shifts the Mott density to $3 \times 10^{18}\,\mathrm{cm}^{-3}$ at cryogenic temperatures [6, 7]. Made up from doubly degenerate valence and conduction bands, the ground state of this series splits into the triply degenerate orthoexciton and the non-degenerate paraexciton, which is the energetically lowest exciton state, lying $\Delta = 12.1$ meV below the orthoexciton states. Due to the positive parity of the bands, the orthoexciton is only weakly optically allowed (quadrupole transition with oscillator strength 3×10^{-9} [8]), while the paraexciton as a pure triplet state with respect to the electron and hole spins [9] is optically forbidden in all orders. Its decay is only possible via an odd parity optical phonon resulting in a long lifetime in the microsecond range during which thermodynamic quasi-equilibrium may be reached.

As in all physical systems for which BEC has been demonstrated up to now, excitons should be confined in a potential trap. This has the advantage that (i) the diffusion process, which reduces the exciton density, is suppressed and (ii) the critical number of particles required

for the phase transition decreases much faster with temperature than in free space. The critical particle number is given by

$$N_{\mathrm{crit}} = \zeta(3)\left(\frac{k_{\mathrm{B}}T}{\hbar\Omega_0}\right)^3, \tag{1}$$

where Ω_0 is the average oscillator frequency of the trapping potential and ζ denotes the Riemann Zeta function [10].

Despite the promising properties mentioned above, all previous studies to create a dense gas of excitons in Cu_2O either in a bulk crystal or in a potential trap did not demonstrate conclusively excitonic BEC [4, 11–15]. The main reason for this failure turned out to be the existence of a very efficient exciton–exciton annihilation process that sets in at high exciton densities and whose rate scales with the square of the exciton density n

$$\frac{\mathrm{d}n}{\mathrm{d}t} = -an^2. \tag{2}$$

Due to the rather large value of a of the order of $10^{-16}\,\mathrm{cm}^3\,\mathrm{ns}^{-1}$, this process was believed to prevent the formation of a BEC of paraexcitons.

However, in recent experiments using pulsed excitation, we have found in agreement with earlier studies [16] that this process can be damped in shallow potential traps by almost two orders of magnitude [17]. While this allowed the accumulation of large exciton numbers, the temperatures in these experiments were still too high to undercut the critical temperature for BEC, which was predicted to require a bath temperature as low as 100 mK at experimental conditions. Furthermore, the high pulse energies needed to create sufficient exciton numbers resulted in a substantial heating of the exciton gas during the laser pulse. Our strategy to overcome these problems was twofold: firstly, we reduced the temperature of the He bath as much as possible by preventing thermal radiation from the surroundings to reach the sample. In this way we reached a minimum temperature of 35 mK for zero incident laser power, which increases at laser powers of about 1 mW to 250 mK within 1 h. Secondly, we switched over to cw-excitation, for which the possibility of creating large paraexciton numbers has been demonstrated recently [18]. By reducing the thermal load, we were able to get to effective exciton temperatures as low as 200 mK at low excitation power. The main advantage of cw-excitation, however, is the possibility of achieving a quasi-equilibrium situation in which the decay rate of excitons is cancelled by the formation and relaxation rate of the species in the trap. This allows us to drive the system through the various possibly existing phases by simply changing the excitation power of the driving laser, as was exemplified by the condensation experiments of exciton polaritons in semiconductor microcavities (for a review, see [19]). In contrast to polariton systems, the lifetime broadening for paraexcitons is extremely small due to their long lifetime of the order of μs. Therefore, we can neglect any damping effects due to the excitonic decay in the spectra [20, 21].

The paper is organized as follows. In section 2, we briefly sketch the experimental setup and present a typical set of experimental results which reflect a variety of experimental conditions obtained by changing the bath temperature and the excitation conditions. We concentrate in particular on the spatial profiles of the luminescence intensity and on the totally integrated intensity dependent on the excitation power. These results are analysed theoretically in section 3 by calculating the excitonic luminescence of an interacting Bose gas on a mean field level. Thereby, we start with the usual assumption of global equilibrium and then extend the theory to the case of excitons in local thermodynamic equilibrium. Finally, we compare the theoretical

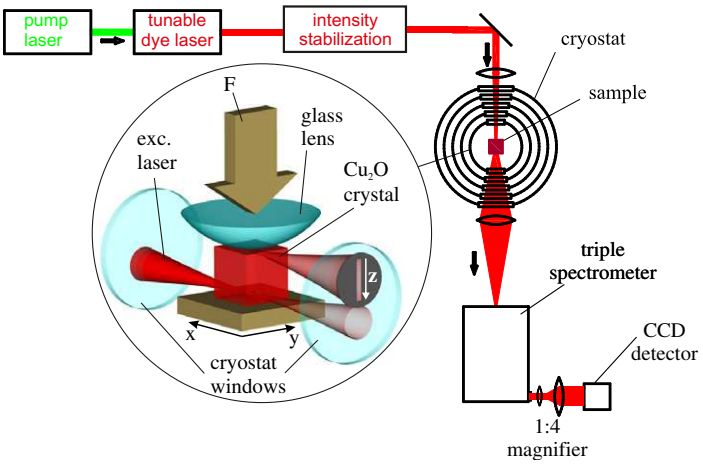

Figure 1. Main features of the experimental setup. Excitons are created by a dye laser propagating along the x-direction normal to the strain axis (z-direction). The laser was focused either directly into the trap or onto a spot close to the trap. In the latter case the excitons diffuse towards the trap due to the gradient force initiated by the potential trap. The emission out of the trap is monitored by spatially resolving along the y- and z-directions, while integrating along the x-direction.

results with the measurements and show that there is excellent qualitative agreement if we take into account the occurrence of a Bose–Einstein condensate of excitons. Section 4 gives our conclusions and an outlook to further experiments.

2. Experiment

2.1. Experimental setup

For the studies at subkelvin temperatures, we used the same experimental setup as reported previously [17], but implemented a narrow-band tunable dye laser (Coherent CR599, laser dye Rhodamin 6G) pumped by a 5 W green solid state laser (Verdi 5), see figure 1. The laser power was stabilized by a closed feedback loop to within 1%, the laser frequency and line width (<0.5 GHz) were measured with a wavemeter (High Finesse WS7, resolution 60 MHz). In order to enhance both the spectral and spatial resolutions, we employed a fourfold magnification optical imaging system between the spectrometer exit slit and the detector.

For the experiments we used natural cuprous oxide crystals originally found in Namibia in the form of millimetre sized cubic specimens with well defined facets (see [18] for details). The quality of these samples was checked according to a low defect density, leading to long paraexciton lifetimes up to 1 μs. For such samples, previous high resolution absorption measurements in a magnetic field revealed a paraexciton line width as narrow as 80 neV, demonstrating their extreme high quality [22].

The potential trap for the confinement of the exciton gas was made by the well-known Hertzian stress technique [11, 14, 23, 24], where a spherical stressor made of glass (radius 7.75 mm) is pressed with a force F against a flat surface of the crystal along a direction which we denote as the z-direction (figure 1). As a result, a confining potential is generated in

Table 1. Parameters for the trapping potential and rate model.

Parameter	Value
Potential curvature $\alpha_{\parallel}$	$0.1334\,\mu\text{eV}\,\mu\text{m}^{-2}$
Potential curvature $\alpha_{\perp}$	$0.0733\,\mu\text{eV}\,\mu\text{m}^{-2}$
Lifetime of paraexcitons	650 ns
Ortho–para conversion rate	$0.2\,\text{ns}^{-1}$ [a]
Two-body decay rate A_{PP}	$2 \times 10^{-18}\,\text{cm}^3\,\text{ns}^{-1}$ [b]
Two-body decay rate A_{OO}	$4.9 \times 10^{-17}\,\text{cm}^3\,\text{ns}^{-1}$
Relaxation rate Γ_{rel}	$6 \times 10^{7}\,\text{s}^{-1}$
Potential trap minimum V_0	1.35 meV

[a] Taken from [16].
[b] Due to the lower strain, the two-body decay rate A_{PP} is reduced by a factor of two compared to [17].

which the energies of ortho- and paraexcitons are lowered compared to the bulk. This potential $V_{\text{ext}}(x, y, z)$ can be calculated from the known strain parameters of the yellow exciton states (for a recent calculation with refined parameters see [18]). To achieve agreement between the calculated potential profiles and the experimentally measured low energy border lines of the spatio-spectral images, we had to use a stressor radius 50% larger than the nominal one [17]. For a simple description, we decompose the potential trap and give in table 1 the parameters of the harmonic oscillator potential along z, $V(z) = \alpha_{\parallel}(z - z_0)^2 - V_0$, and of the two-dimensional harmonic oscillator normal to z in the xy plane, $V(x, y) = \alpha_{\perp}(x^2 + y^2)$.

As the resonant creation process of the excitons we used the indirect absorption process involving an odd parity optical Γ_3^--phonon into the orthoexcitons in the trap (see inset in figure 2). These orthoexcitons quickly transformed into paraexcitons. The laser beam was positioned about 100 μm away from the trap centre in the positive z-direction, i.e. away from the stressor lens. In order to confine the primarily created orthoexcitons in the trap and to avoid any excitation outside the trap, which may lead to losses of the excitons, we tuned the energy of the laser photons to slightly ($\approx$0.5 meV) below the onset of the phonon sideband in the bulk (at 2048.56 meV). Through this process, about half of the incoming photons are transformed into excitons.

To detect the primarily excited orthoexcitons for the calibration of the number of excited excitons, we have chosen the **k**-vector of the excitation beam along the direction of observation.

In the experimental setup (figure 1), the emitted light was imaged onto the entrance slit of a high resolution triple spectrograph (T64000, Jobin Yvon) usable either in subtractive or additive mode with a diffraction-limited spatial resolution of the order of 10 μm. The astigmatism of the spectrograph was corrected by a cylindrical lens (focal length $F = -1000\,\text{mm}/F = 1000\,\text{mm}$ for subtractive and additive dispersions, respectively) in front of the entrance slit [18]. To obtain a z-resolved spectrum $I(z, \omega)$, along the direction of the applied strain, the luminescence from a small strip of width $2\Delta y$ centred in the trap was integrated along the x-direction perpendicular to z (see figure 1). Detection was done either by an intensified charge-coupled device (CCD) camera (Andor iStar) which could be gated with a minimum temporal resolution of 5 ns or with a nitrogen cooled CCD camera with high quantum efficiency (Andor Newton), which allowed long integration times.

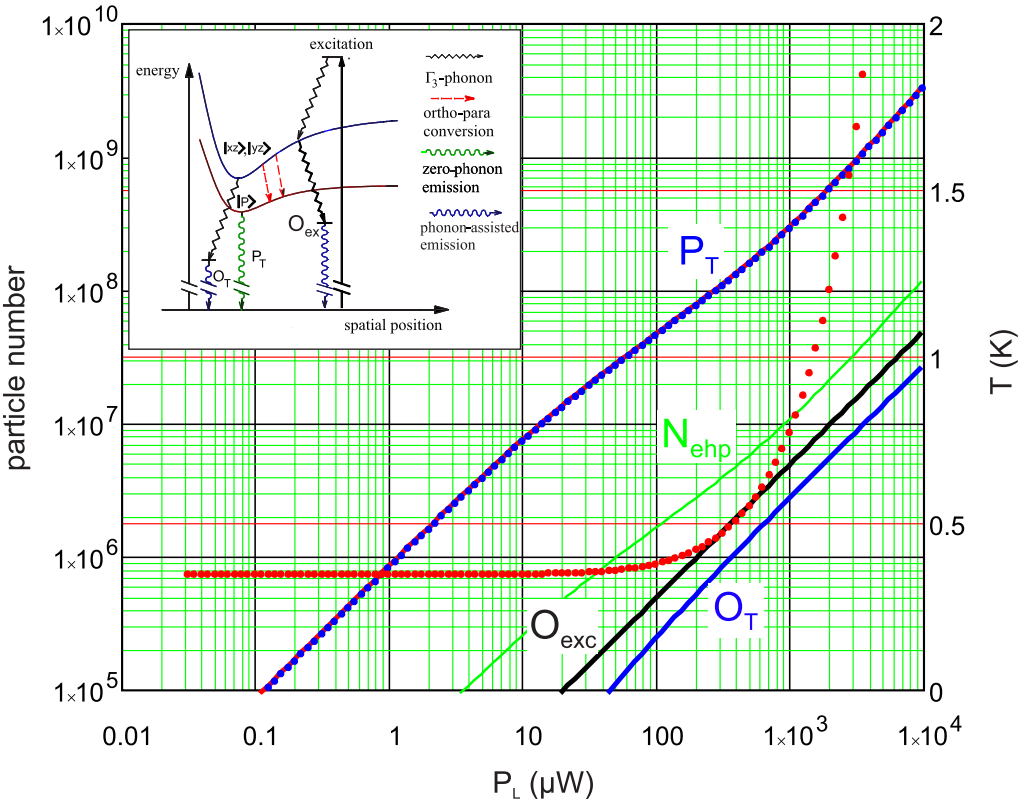

Figure 2. Numbers of para- and orthoexcitons and unbound electron–hole pairs and effective exciton temperature (dotted red line) as a function of excitation laser power as expected from the rate model. The inset schematically shows the laser excitation process to create the orthoexcitons, their conversion into paraexcitons and the luminescence processes to detect the excitons.

2.2. Application of the rate model to cw-excitation

With some adaptions, the rate model developed in [17] can also be applied to describe the cw experiments. These concern the following:

- Even under resonant excitation of excitons, a considerable density of unbound electron–hole pairs is generated [25]. This implies that the formation of an exciton from the hot electron–hole pair generated in the two-body decay (Auger-like process) takes a finite time comparable with other exciton relaxation times, e.g. the ones related to phonon scattering. In a fast initial relaxation stage with a duration of several picoseconds [26], the carriers thermalize by longitudinal optical (LO) and longitudinal acoustic (LA) phonon scattering. For a strained crystal with an exciton potential trap, these electron–hole pairs will then undergo different relaxation scenarios depending on whether the strain also causes a trapping potential for the unbound electron–hole pairs or not. In the latter case, the electrons and holes will diffuse from the place of generation (the potential trap) into the whole crystal and form excitons which themselves will drift again into the trap. In the former case, the electron–hole pairs will stay inside their trap and form a stable electron–hole plasma cloud with a density which is three orders of magnitude smaller than

the exciton concentration according to the results in [25]. As derived in appendix A, strain leads to a trapping potential for unbound electron–hole pairs which is similar to that for the paraexcitons. To take this effect into account, we included in the rate model the unbound electron–hole pairs with a total number of N_{ehp}. They are generated via the two-body decay of the ortho- and paraexcitons and recombine with a rate $\Gamma_{\mathrm{rc}} N_{\mathrm{ehp}}^2$. The recombination rate should depend on temperature in the same way as the two-body decay of the excitons ($\propto T^{-3/2}$).

Due to heating and incomplete relaxation, the excitons may not cool down to bath temperature. We can describe this effect by assuming an effective exciton temperature T_{eff}, a cooling time of 200 ns [17] and heating processes due to the energy release by ortho–para conversion $C_{\mathrm{O}} = 10\,\mathrm{meV}$ per exciton, Auger-like two-body decay with $C_{\mathrm{XX}} = 2\,\mathrm{eV}$ per exciton pair, and a non-radiative decay of paraexcitons (guessed release $C_{\mathrm{P}} = 0.25\,\mathrm{eV}$ per exciton). The temperature rise due to this heating is characterized by a constant C_{heat} which was adjusted to $C_{\mathrm{heat}} = 7 \times 10^9\,\mathrm{K\,J^{-1}}$.

We thus obtain the following set of rate equations for the numbers of primarily excited orthoexcitons (O_{exc}), trapped ortho- and paraexcitons (O_{T} and P_{T}, respectively), and unbound electron–hole pairs N_{ehp}, and the effective exciton temperature T_{eff}:

$$\frac{\mathrm{d}O_{\mathrm{exc}}}{\mathrm{d}t} = N_0 G(t) - \Gamma_{\mathrm{rel}} O_{\mathrm{exc}} - \Gamma_{\mathrm{OP}} O_{\mathrm{exc}} - \Gamma_{\mathrm{O}} O_{\mathrm{exc}}, \tag{3}$$

$$\frac{\mathrm{d}O_{\mathrm{T}}}{\mathrm{d}t} = \Gamma_{\mathrm{rel}} O_{\mathrm{exc}} - \Gamma_{\mathrm{OP}} O_{\mathrm{T}} - 2A_{\mathrm{OO}} O_{\mathrm{T}}^2 - A_{\mathrm{OP}} O_{\mathrm{T}} P_{\mathrm{T}} - \Gamma_{\mathrm{O}} O_{\mathrm{T}} + \frac{1}{2}\Gamma_{\mathrm{rc}} N_{\mathrm{ehp}}^2, \tag{4}$$

$$\frac{\mathrm{d}P_{\mathrm{T}}}{\mathrm{d}t} = \Gamma_{\mathrm{OP}} O_{\mathrm{T}} + \Gamma_{\mathrm{OP}} O_{\mathrm{exc}} - 2A_{\mathrm{PP}} P_{\mathrm{T}}^2 - \Gamma_{\mathrm{P}} P_{\mathrm{T}} - A_{\mathrm{OP}} O_{\mathrm{T}} P_{\mathrm{T}} + \frac{1}{4}\Gamma_{\mathrm{rc}} N_{\mathrm{ehp}}^2, \tag{5}$$

$$\frac{\mathrm{d}N_{\mathrm{ehp}}}{\mathrm{d}t} = A_{\mathrm{PP}} P_{\mathrm{T}}^2 + A_{\mathrm{OO}} O_{\mathrm{T}}^2 + A_{\mathrm{OP}} O_{\mathrm{T}} P_{\mathrm{T}} - \Gamma_{\mathrm{rc}} N_{\mathrm{ehp}}^2 - \Gamma_{\mathrm{ehp}} N_{\mathrm{ehp}}, \tag{6}$$

$$\begin{aligned}\frac{\mathrm{d}T_{\mathrm{eff}}}{\mathrm{d}t} = {} & C_{\mathrm{heat}}[C_{\mathrm{XX}}(A_{\mathrm{PP}} P_{\mathrm{T}}^2 + A_{\mathrm{OO}} O_{\mathrm{T}}^2 + A_{\mathrm{OP}} O_{\mathrm{T}} P_{\mathrm{T}}) \\ & + C_{\mathrm{O}}\Gamma_{\mathrm{OP}}(O_{\mathrm{T}} + O_{\mathrm{exc}}) + C_{\mathrm{P}}\Gamma_{\mathrm{P}} P_{\mathrm{T}}] - \Gamma_{\mathrm{cool}}(T_{\mathrm{eff}} - T_{\mathrm{fin}})\,.\end{aligned} \tag{7}$$

Here, T_{fin} denotes the final temperature to which the exciton gas would relax without additional heating. In an equilibrium situation, this would correspond to the bath temperature.

To simulate the cw-excitation, we solved the system of rate equations by assuming for $G(t)$ a rectangular shaped excitation pulse of width $\Delta T_{\mathrm{L}} = 25\,\mu\mathrm{s}$ and a unit pulse area. The number of initially excited excitons N_0 is given by

$$N_0 = \frac{A P_{\mathrm{L}}}{\hbar\omega_{\mathrm{L}}} \Delta T_{\mathrm{L}}, \tag{8}$$

with the conversion factor from incident laser photons into primarily excited excitons $A = 0.45$. All other parameters are taken from [17]. Since we used the same sample under similar conditions, the calculation allows us to obtain the number of para- and orthoexcitons in the trap dependent on laser power, whereby we approximate the accuracy to ±50%. In figure 2 we

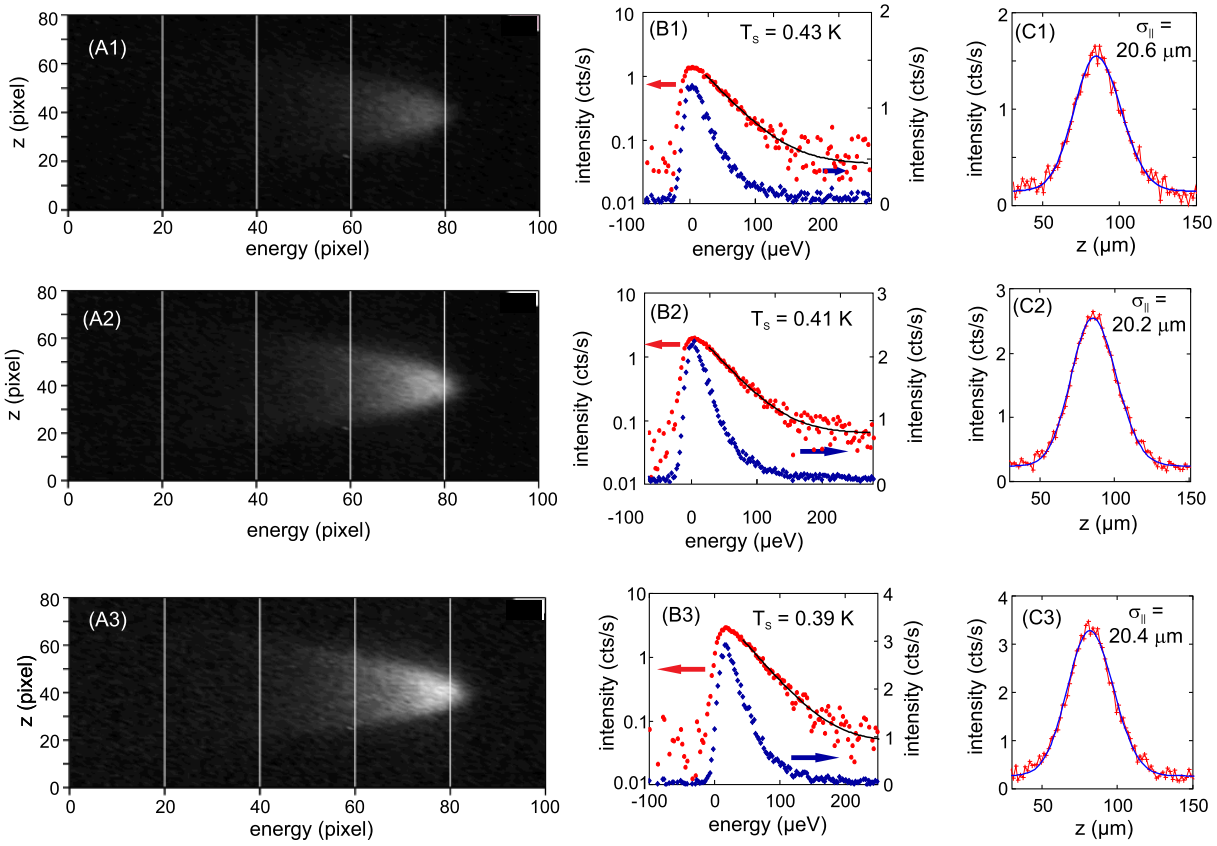

Figure 3. Spectra and spatial luminescence profiles at low excitation power P_L with $P_L = 1.5\,\mu$W (upper row), $P_L = 3\,\mu$W (middle row) and $P_L = 5\,\mu$W (lower row). T_s denotes the temperature extracted from the high-energy tail of the spectra.

show a set of typical results. The final temperature $T_{fin} = 0.35$ K was chosen to reproduce the experimentally observed temperature dependence in figure 5B. The results at high power levels do change somewhat due to the temperature dependence of the Auger process, but not by more than 20% by varying T_{fin} from 0.2 to 0.5 K.

The number of paraexcitons in the trap at low laser powers turns out to be determined by two parameters, the paraexciton lifetime $1/\Gamma_P$ and the fraction of absorbed photons A. From figure 2 one can estimate the number of paraexcitons in the trap to be about 8×10^6 for a laser power of $10\,\mu$W. The number of unbound electron–hole pairs would be around 3×10^5. At power levels of 1 mW, which was the maximum laser power used in the mK experiments, paraexciton numbers of 2×10^8 can be realized and the number of electron–hole pairs increases to 10^7. Assuming thermal equilibrium, this would correspond to densities of about $n_P = 2 \times 10^{16}\,\text{cm}^{-3}$ and $n_{ehp} = 10^{14}\,\text{cm}^{-3}$.

2.3. Experimental results

2.3.1. Low excitation power. The first experimental results we want to show were obtained at rather low laser excitation powers between 1 and 5 μW with high spectral resolution (figure 3).

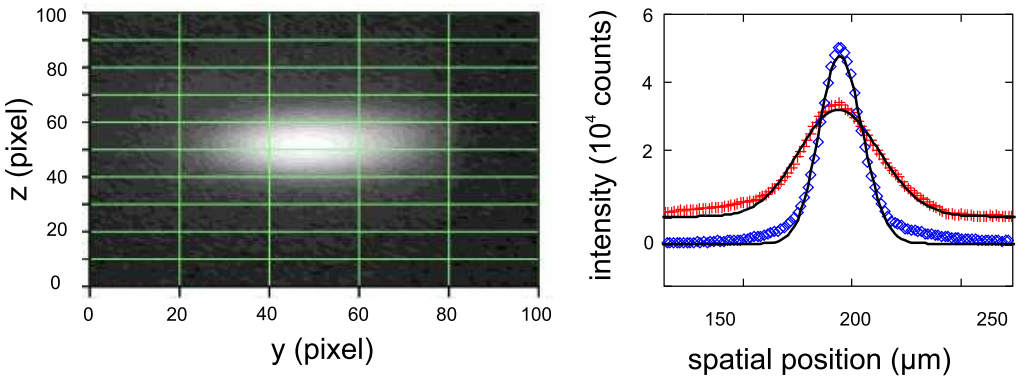

Figure 4. Left panel: spatial image of the exciton cloud at a low excitation power of $P_L = 30\,\mu$W. Right panel: marginal intensity distributions along z (blue circles) and y (red circles) with fits to Gaussians according to equation (9).

Excitation was performed via the phonon-assisted absorption of the orthoexcitons with an energy slightly below the bulk exciton gap as described in section 2.1. Orthoexcitons were converted rapidly into paraexcitons and relaxed down to the bottom of the trap.

From the z-resolved spectra (A panels) we obtained the z-integrated spectra (B panels) and the z-profiles (C panels). As already can be seen in the z-resolved spectra, there is no change in both the spectral and spatial distributions, only an increase in the overall intensity which is almost proportional to the laser power. This demonstrates that we are in the linear excitation regime and that bimolecular decay processes are not important. The high-energy tail of the spectra can be fitted quite well by a Boltzmann distribution with an effective exciton temperature of about 0.4 K. A two-dimensional spatial image of the exciton cloud was obtained by using the spectrometer in the subtractive mode, the output stage at zero wavelength and by setting the intermediate slit of the subtractive stage to just let past the emission from the paraexcitons in the trap. A typical example is shown in figure 4. The spatial profiles are described by simple Gaussian distributions

$$I(y,z) = n_0 \exp\left(-y^2/\sigma_\perp^2\right) \exp\left(-z^2/\sigma_\parallel^2\right) \tag{9}$$

with width parameters $\sigma_\perp$ and $\sigma_\parallel$ of about 20 μm.

According to the theoretical predictions in thermal equilibrium (see section 3), the width parameters are related to the curvature of the trap α and temperature T by

$$\sigma_{\perp,\parallel} = \sqrt{\frac{k_B T}{\alpha_{\perp,\parallel}}}\,. \tag{10}$$

However, the ratio of the resulting width parameters does not fit the ratio of the potential curvatures as obtained from the strain calculation. It comes out about 30% larger. As the origin of this broadening we identified a small vibrational motion of the sample in the y-direction of the order of 10 μm which could be directly observed by imaging a submicron sized needle. For a quantitative theoretical model of the light emission of the excitons, this effect has to be taken into account.

Using the curvature parallel to the z-direction from table 1, and subtracting the spatial blurring due to the diffraction of our optical imaging setup (7 μm), we obtain from the spatial

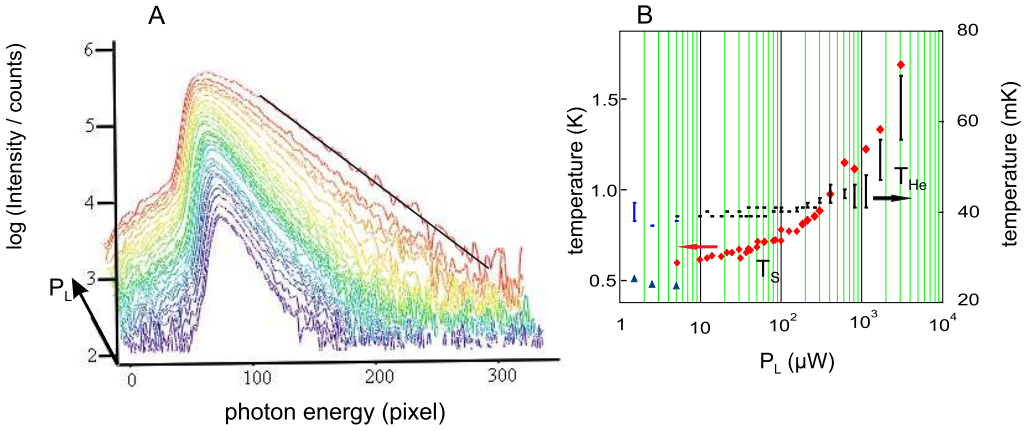

Figure 5. Panel A: series of spectra taken at increasing laser powers P_L from 5 μW to 3 mW in a logarithmic intensity scale. The spectral position is given in CCD-pixels, 1 pixel corresponds to 2.5 μeV. Panel B: spectral temperature T_s as obtained from a Boltzmann fit of the high-energy tail of the spectra shown in panel A (left ordinate) and the temperature of the mixing chamber T_{He} (right ordinate).

profiles temperatures of about 0.45 K, in good agreement with those from the spectra. At first sight, we would conclude that the excitons are in a state of quasi-thermal equilibrium, albeit with a temperature which is more than an order of magnitude larger than the bath temperature, which in these experiments was around 38 mK. There are two possible explanations for this difference:

(i) The heating of the exciton cloud due to the excess kinetic energy of about 8 meV in the ortho–para conversion process or due to the exciton–exciton annihilation process. The excess electronic energy is in both cases converted into phonons and finally increases the temperature of the lattice which, however, is unknown in the present experiment. This heat has to be transferred into the surrounding He bath, where it would lead to an increase in the temperature of the mixing chamber, which could be measured during the experiment.

Indeed we observe this heating effect at higher laser powers. As shown in figure 5, the effective exciton temperature and the temperature of the mixing chamber rise from their initial values very steeply to above $P_L = 1000\,\mu$W. Presuming a well-defined relation between the lattice temperature of the crystal and that of the mixing chamber, we have to conclude from these data that, at low laser powers, the heating effect is not present and the lattice temperature should be close to that of the He bath at very low laser powers. This conclusion is also in agreement with the results of the rate model presented in the foregoing section. There the heating of the exciton cloud starts at laser powers well above 100 μW and is not present at low powers.

(ii) The discrepancy of the lattice temperature T_{latt} and that of the exciton cloud may result because the excitons do not reach global thermodynamic equilibrium during their finite lifetime. This standard point of view means that, due to elastic exciton–exciton scattering, a quasi-thermal equilibrium state is established very fast with a temperature above that of the lattice. Hereafter, the exciton gas cools down to the lattice temperature by the emission of acoustic phonons. The time-scale of this process increases with decreasing lattice

temperature. In an external potential provided by the trap, the excitons are additionally driven by force and drift terms into the potential minimum, as described by the Boltzmann equation [27]. The detailed balance of these processes is determined by the interplay between the various exciton relaxation mechanisms.

In a recent paper, we published a detailed numerical simulation by solving the Boltzmann transport equation for excitons in a potential trap under pulsed optical excitation considering phonon relaxation and exciton–exciton annihilation [28]. The simulation indeed showed a strong non-equilibrium situation. While the local exciton energy distribution was reached within the exciton lifetime of several 100 ns and with an equilibrium with the lattice down to temperatures above 300 mK, the spatial distribution, which is governed by the force and drift terms, remained much broader than when in thermal equilibrium. For the case of still lower lattice temperatures, which was not considered in [28], we obtain local thermodynamic quasi-equilibrium also at temperatures down to 50 mK by including elastic exciton–exciton scattering as is shown in detail in appendix B. Albeit in this range the exciton temperature does not come down to the lattice temperature within the exciton lifetime, it is much lower than the observed values of T_s. According to these results, in our experiments we should expect a non-equilibrium situation in which the excitons are in a local quasi-thermal equilibrium with a temperature T_X, which we assume to be the same at all points in the trap. Globally, the exciton distribution will be quite different, but still can be described approximately by a Gaussian dependence on position.

Considering the effect of such a situation on the experimentally measured luminescence spectra, we recall that only excitons near k_0 participate in light emission, where $\mathbf{k}_0$ is the wave vector of the intersection of the photon and exciton dispersions. Its modulus is given by $k_0 = E_{gX} n/\hbar c$, with E_{gX} being the excitonic band gap, n the refraction index and c the vacuum velocity of light. This means, we observe the exciton distribution function $f_{eq}(\mathbf{k}, \mathbf{r})$ only at one point in local k-space. Furthermore, due to energy conservation, at a certain spectral position $\hbar\omega$ we only observe those excitons which are at that spatial position in the trap where the trap potential $V_{ext}(\mathbf{r}) = \hbar\omega - E_0 - \varepsilon_0$. Here, E_0 is the energy of the trap bottom and ε_0 is the kinetic energy of the excitons at k_0. If we have a spatial distribution

$$n(r) \propto \exp(-r^2/\sigma^2), \tag{11}$$

this yields a spectral distribution of the form

$$I(\hbar\omega) \propto \exp(-(\hbar\omega - E_0 - \varepsilon_0)/(\alpha\sigma^2)), \tag{12}$$

which suggests a Boltzmann distribution with an effective temperature $T_s = \alpha\sigma^2/k_B$. Then the spectral distribution of luminescence intensity in reality describes the spatial distribution and vice versa. Therefore, it has to result in the same effective exciton temperature, which is also a consistency check for the trap potential. Consequently, we will designate this temperature as the *spatial temperature* T_s of the exciton cloud. Obviously, T_s corresponds to T_{eff} of the rate model, cf equation (7). On the other hand, it is not possible to extract the local effective exciton temperature T_X from the intensity of the zero-phonon transition. This would require a spectroscopic technique which is sensitive to the local exciton distribution like the transitions between 1S and 2P exciton states (see [29, 30]). Hence, at the present stage of measurements, all we can state is that T_X may differ considerably from both the lattice temperature, which will set a minimum value, and the spatial temperature, which will set a maximum value, as in the latter case we would have global equilibrium.

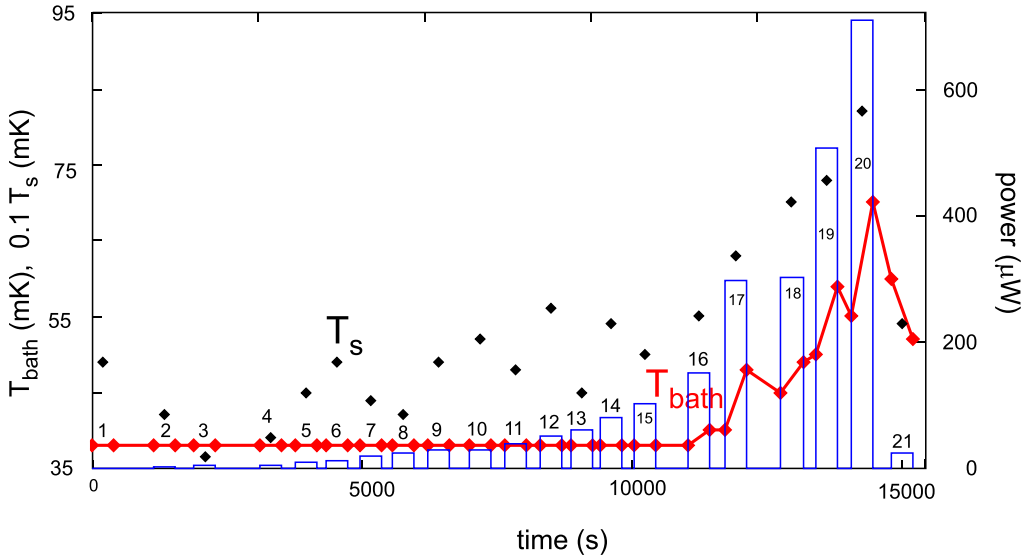

Figure 6. Time profiles of laser power (blue bars), the temperature of the mixing chamber (red diamonds) and the spatial temperature (black diamonds) for the measurements shown in figure 7. The red line is a guide for the eye.

2.3.2. Power-dependent experiments. In the following section we will present a series of measurements under controlled conditions of excitation and cooling times such that we are able to influence the thermodynamic state of the system in order to optimize any possible phase transition. The laser power ranged from below 1 μW to about 700 μW. For each measurement we noted the temperature of the mixing chamber (He bath temperature T_{bath}) at the beginning and at the end. Between the measurements, the laser beam was blocked, so that the crystal could cool down (see figure 6).

In order to obtain the best signal-to-noise ratio, the ICCD camera was operated in the photon counting mode. Here, the CCD-chip is read out after a short exposure time (T_1) and the positions of the single photon peaks are determined and stored. A single photon is identified if the signal falls between a lower and an upper discriminator level (which was adjusted so that only single photon signals fall in this range). For a number N_{acc} of accumulations, the data are summed in the memory. Advantages of this method are that signals due to cosmic rays are easily detected and eliminated and that one can estimate the error of the intensity signal due to the Poissonian statistics as the square root of the number of photons collected at each pixel. Due to the Poissonian statistics, the probability of detecting n photons is given by

$$P_n = \frac{\lambda^n}{n!}\exp(-\lambda), \tag{13}$$

where λ is the average photon number for each exposure. As we detect only single photons and throw away all higher photon number events, λ should be much smaller than one. However, for moderate values, we can obtain the true number of detected photons, λN_{acc} from the measured number N_{det} by applying the correction formula

$$\lambda N_{\mathrm{acc}} = -\ln\left(1 - \frac{N_{\mathrm{det}}}{N_{\mathrm{acc}}}\right). \tag{14}$$

For the measurements of the z-resolved luminescence spectra shown in figure 7 we have $T_1 = 0.5\,\mathrm{s}$ and $N_{\mathrm{acc}} = 400$. In order to keep the maximum number of detected photons well below N_{acc}, we inserted neutral density filters before the entrance slit of the monochromator. Their transmission factors have been determined by direct intensity calibration as $D1 = 0.314$ and $D2 = 0.0333$.

In figure 7, each measurement is numbered according to its position in time given in figure 6. For each image we specify the laser power, the maximum number of counted photons (which allows us to judge the signal-to-noise ratio) and the totally integrated intensity. At first sight, all the images look very much the same, despite the three orders of magnitude increase in laser power. In particular, we observe neither the sharp spatial and spectral peak at the bottom of the trap, which is expected as a signature for BEC in case of an ideal Bose gas, nor the predicted flattening of the emission along the z-direction in case of an interacting Bose gas [31]. In this respect, the measurements shown are similar to those reported in all earlier work [11, 15]. A closer look, however, reveals subtle changes of the shape of the spectra depending on the laser power. For power levels below $30\,\mu\mathrm{W}$, the z-resolved spectrum of the exciton cloud shows no significant changes—here note especially measurements 9 and 21, which were taken under very different He bath temperatures (see figure 6). For power levels above $30\,\mu\mathrm{W}$, the images change gradually by showing a spectral narrowing and a slight blue shift. These changes suddenly come to a stop between measurements 17 and 18, with the images from now on both spatially and spectrally much broader and resembling those taken at low powers. The latter data have been taken at almost the same laser power of $300\,\mu\mathrm{W}$, but the He bath temperature was significantly different. Measurement 17 started at $T_{\mathrm{bath}} = 42\,\mathrm{mK}$. During the measurement, the laser power resulted in a heating up to $T_{\mathrm{bath}} = 49\,\mathrm{mK}$. In contrast, measurement 18 already started at $T_{\mathrm{bath}} = 45\,\mathrm{mK}$ and stopped at $T_{\mathrm{bath}} = 50\,\mathrm{mK}$. This temperature variation of the mixing chamber should directly reflect the actual lattice temperature T_{latt} of the Cu_2O crystal. At the beginning of measurement 17, T_{latt} must have been quite close to that of the bath while at the start of measurement 18, T_{latt} has only cooled down to midway between start and end of measurement 17. This difference in lattice temperature is reflected in a concomitant difference in the spectral temperature which is $T_{\mathrm{s}} = 0.62\,\mathrm{K}$ for measurement 17 and $T_{\mathrm{s}} = 0.72\,\mathrm{K}$ for measurement 18. The totally integrated intensities of both measurements are expected to be similar due to the same laser power, however, that of measurement 18 is about 30% larger.

We can resolve this puzzle by assuming that the difference between both measurements comes from the existence of a Bose–Einstein condensate of excitons in measurement 17, while measurement 18 describes a normal exciton cloud at temperatures above the critical temperatures for BEC for the actual number of excitons in the trap, which is the same in both measurements. Then the lower intensity in 17 would be the result of the decreased number of thermalized excitons, since according to [31] and anticipating the discussion in section 3, excitons in the condensate are in the ground state ($k = 0$), and, therefore, could not emit light with wave vector k_0 at all (as in a homogeneous system), or is strongly suppressed (as would be the case in the trap).

Thus, we propose the following scenario for measurement 17: in the beginning, we have a system with a large fraction of the excitons in a condensate, with a reduced luminescence intensity. As time increases, the crystal heats up and the condensate fraction is reduced. When the lattice temperature reaches the critical temperature, we have a situation just like in measurement 18. Therefore, after being integrated over the exposure time T_1, the z-resolved spectra should look the same. In a first approximation, the image of 17 is a superposition of

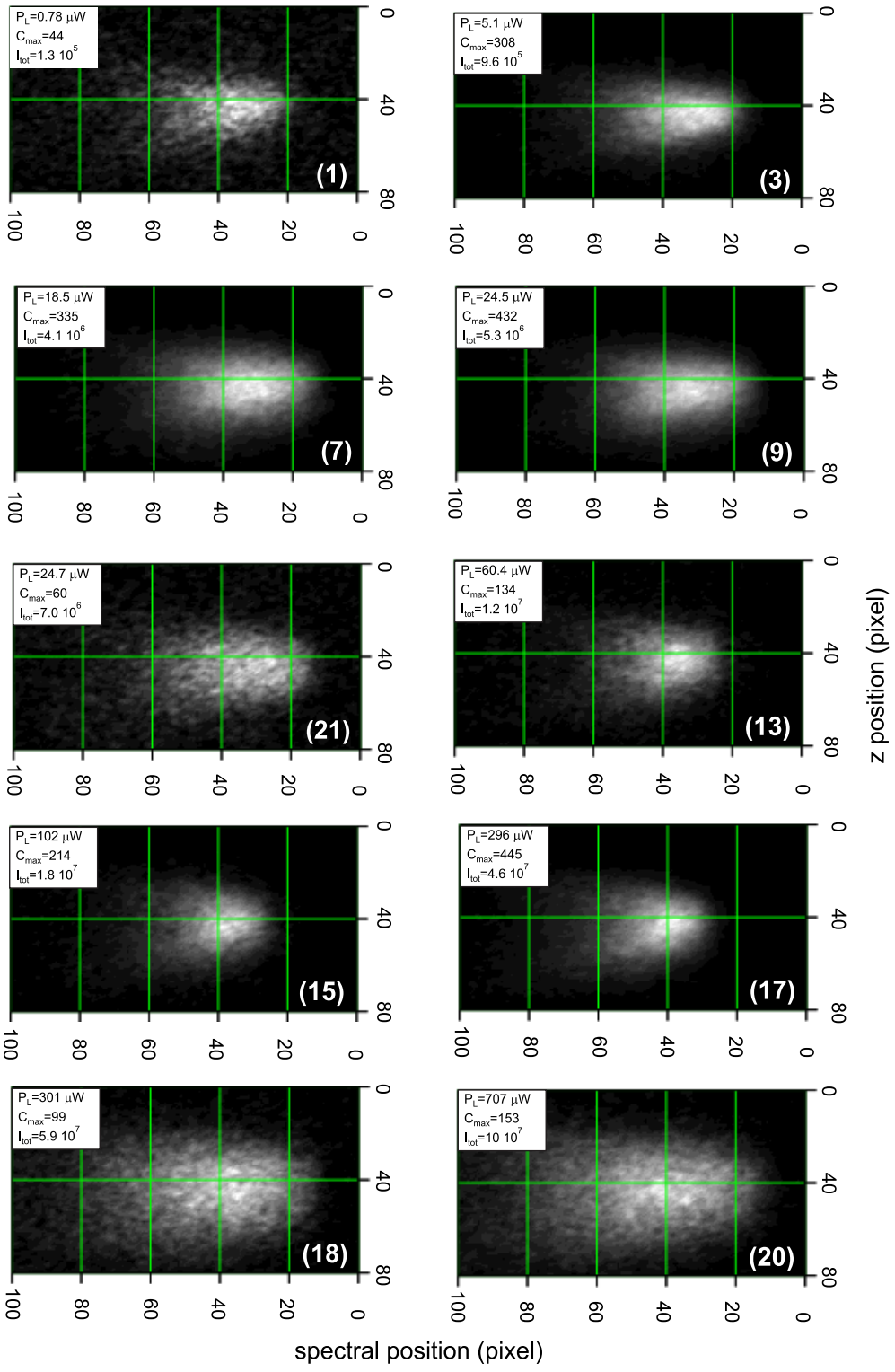

Figure 7. Series of z-resolved luminescence spectra for different excitation powers P_{L} and bath temperatures (see figure 6). $C_{\max}$ denotes the peak value and I_{tot} the totally integrated intensity. The numbers in parentheses denote the measurement numbers, cf figure 6.

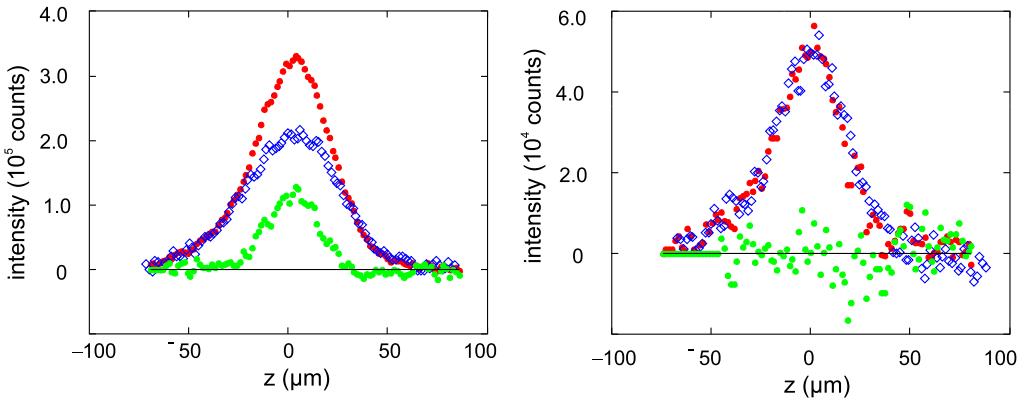

Figure 8. Comparison of the z-profiles of measurements 17 and 18 (left panel) and 9 and 21 (right panel). Each pair was taken at the same laser power, but at different bath temperatures. For details see text.

that of measurement 18 reduced by a factor γ and that of a system with a condensate. To demonstrate that this is indeed the case, we compare in figure 8 in the left panel the z-profiles for both measurements. By assuming $\gamma = 0.6$, the wings of both profiles do coincide exactly, which is clearly visible in the difference profile. The difference around the trap centre, however, has a characteristic, non-Gaussian line shape resembling that of a condensate (compare figure 9). A similar comparison of measurements 9 and 21, both taken at a laser power of 25 μW (right panel of figure 8) shows no difference in the z-profiles within the statistical errors.

While such a comparison of different measurements seems to be intuitively correct, there are several objections against this procedure. First, the measurements we compare have quite different values for the spatial temperature and thus different spatial extensions in the trap. Second, we cannot exclude *a priori* that, e.g. measurement 18 also has a condensate. To overcome these difficulties, we have to look for a way to analyse each measurement for itself. Theoretical studies of the thermodynamics of an interacting Bose gas of excitons [31] have shown that even in the case of a BEC both the density of excitons and the spectrally integrated luminescence intensity outside the condensate region closely follow a Gaussian distribution reflecting the temperature of the exciton gas. Therefore, by fitting a Gaussian only to the wings at larger z of the intensity profile, we should have access to the distribution of thermal excitons only. If there is no condensate present, this Gaussian should also describe the intensity profile in the centre of the trap. On the other hand, any deviation of the measured profile from this curve is a clear indication of an additional luminescing component in the trap. If the line shape of this component is non-Gaussian, this would clearly indicate the existence of a condensate.

For the measurements shown in figure 7, the results of such a fitting procedure are shown in figure 9. The red and blue diamonds are the experimental points, whereby the blue diamonds mark those intensity points that have been used in the fitting. The blue line gives the shape of the Gaussian. In order to reproduce the obviously different line shapes for positive and negative z values due to the Morse-type potential of the trap in the z-direction, we used for the fit an asymmetric Gaussian function of the form

$$S(z) \propto \exp\left(-\frac{(z-z_0)^2}{(\Theta(z_0-z)\sigma_- + \Theta(z-z_0)\sigma_+)^2}\right). \tag{15}$$

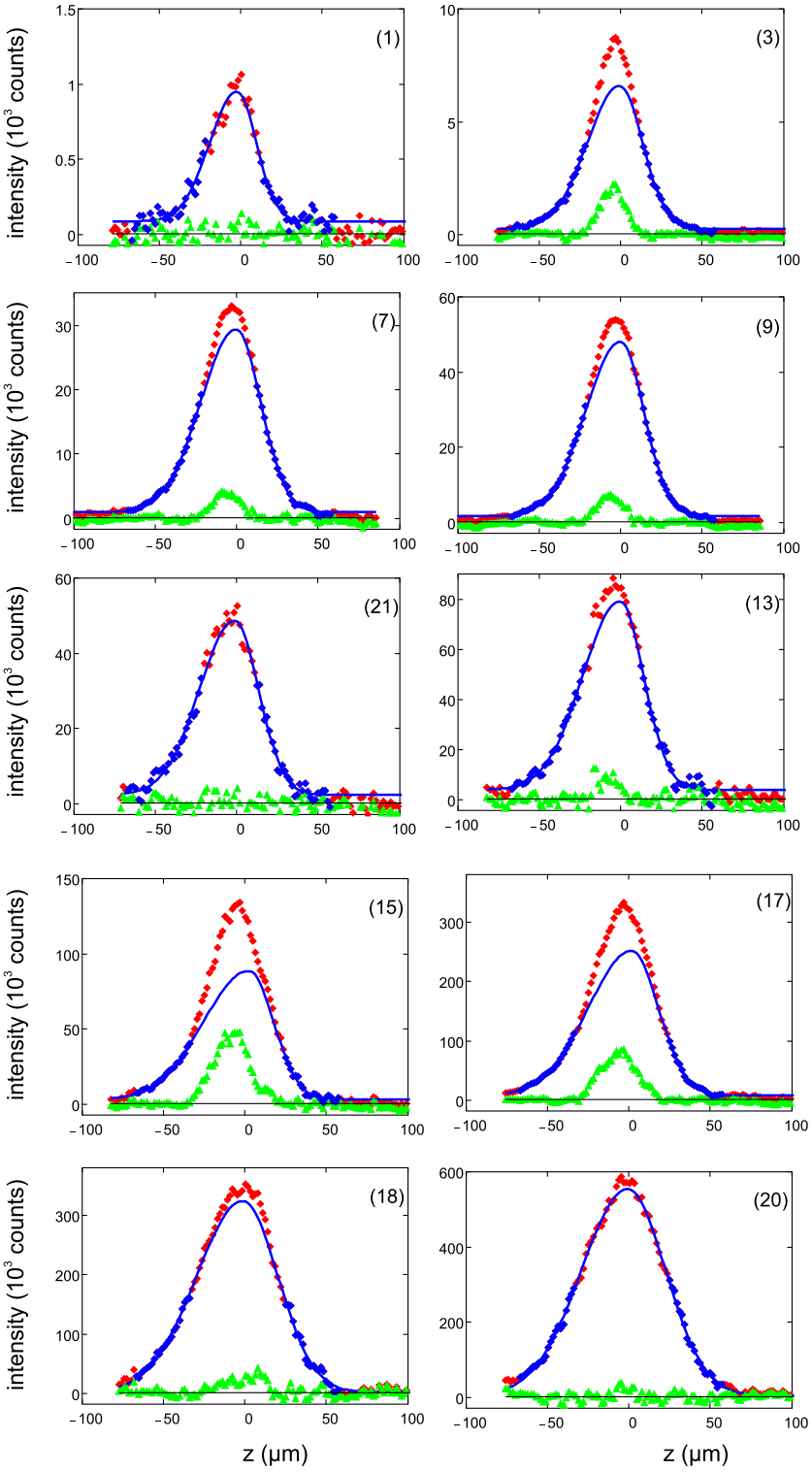

Figure 9. Comparison of z-profiles with fits by a Gaussian. Red and blue diamonds: total measured profiles, solid blue lines: Gaussian fit of the total profiles, blue diamonds: data points used for the fit, green triangles: the difference between total profile and fit. The numbers in parentheses denote the measurement numbers, cf figure 6.

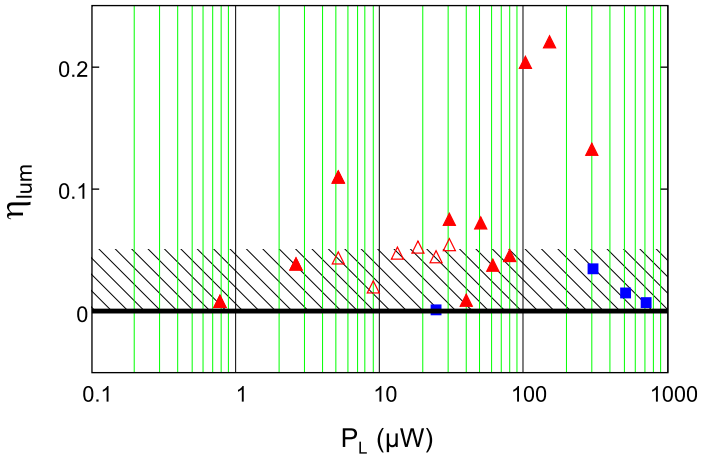

Figure 10. Power dependence of the ratio between integrated intensities of the condensate and of the total band. Filled red triangles: measurements 1–3 and 10–17, open red triangles: measurements 4–9, blue squares: measurements 18–21. Between measurements 3 and 4, and between measurements 9 and 10, there was a change of the neutral density filter, cf figure 6. The shaded band denotes an area where the contribution is too small for a significant proof of a condensate.

For all measurements, the ratio of σ_+/σ_- is obtained as 1.5, in consistence with the shape of the potential. The number of data points for the fitting was chosen for each set of data such that the average error per point becomes minimal. If we choose less points, the statistical error due to noise will increase; if we choose more points, the systematic error increases if the profiles contain an additional contribution. The green triangles show the difference between the experimental points and the Gaussian fits. In total, the results of the procedure substantiate our previous analysis. The measurements at very low power (1) and at high bath temperature (20, 21), where we expect no condensate, indeed can be fitted completely by a single Gaussian. Measurements 15 and 17 show clearly a bimodal distribution and thus a strong condensate component. However, in measurement 18 a small additional contribution remains. To show systematically the results of the fit, we have plotted in figure 10 the ratio of the green component to that of the overall intensity. Looking more closely at the results shown in figure 10, we can identify at least four sets of data with a strong condensate contribution, while most of the other measurements show a contribution below 0.05, which we will consider as not significant. The occurrence of a condensate in the power range between 60 and 300 μW is understandable in view of the rather high number of paraexcitons in the trap which, according to the rate model (figure 2) is about 4×10^7 at 100 μW. The appearance of a condensate at the low power of 5 μW is rather surprising and requires further consideration. Indeed, the theory presented in the next section will show that, under the conditions of our experiments (a bath temperature of 38 mK and no heating of the sample), condensation will take place at exciton numbers as low as 4×10^6 (see figure 19).

Here we stress that the luminescence fraction η_{lum} shown in figure 10 is different from the fraction of particles in the condensate $\eta_c = N_c/N_{\mathrm{tot}}$. If f_{lum} denotes the ratio of the luminescence efficiency of excitons in the condensate to that of excitons in the thermal cloud (see section 3.2),

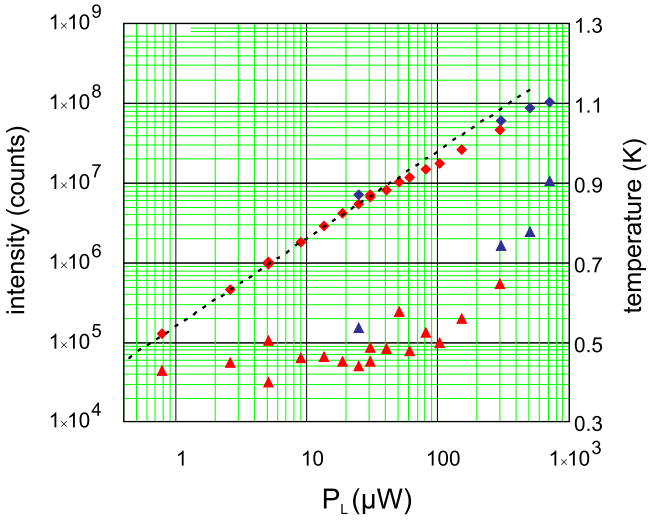

Figure 11. Dependence of the totally integrated intensity (squares) and spatial temperature (triangles) on the laser power. The blue points mark measurements 18–21. The dashed line gives a power dependence according to P_{L}^{b} with $b = 1.1$ which describes the low power regime quite accurately.

the relation is given by

$$\eta_{\mathrm{lum}} = \frac{f_{\mathrm{lum}}\eta_{\mathrm{c}}}{1 - \eta_{\mathrm{c}} + f_{\mathrm{lum}}\eta_{\mathrm{c}}}. \tag{16}$$

At present, f_{lum} is neither known experimentally nor theoretically (see section 3.2), however, it must be smaller than one because otherwise we would not observe a kink in the luminescence dependence on laser power (see figures 11 and 12) so that $\eta_{\mathrm{c}} > \eta_{\mathrm{lum}}$.

Our interpretation is further substantiated by the dependence of the totally integrated intensity on the excitation laser power which is shown in figure 11.

At low power, the dependence is almost linear, indicating that decay processes by exciton–exciton collisions are not important. Actually, the dependence is even slightly superlinear which might be due to the effect of increasing homogeneous broadening at higher exciton numbers. At power levels of about 60 μW, we clearly observe a kink resulting in a weaker slope at higher power levels. This is just the behaviour predicted by the theory in section 3.3.3. The critical power at the kink is in full agreement with the conclusion drawn from figure 10, where we observed the onset of condensation at powers above 60 μW. This dependence is abruptly changed for the measurements 18–21 in agreement with the vanishing of the condensate. At high exciton numbers (under these conditions, we expect $N \simeq 1 \times 10^8$ according to figure 2) we have a substantial effect of the two-body decay resulting in sublinear behaviour, see the data marked by blue symbols.

We note that the theory presented in the next section attributes such a kink in the power dependence of the total intensity of an exciton gas in a trap to the occurrence of condensation. Actually, in all of our measurements using different potential traps and under different excitation conditions such a kink shows up, provided that the He bath temperature is below 400 mK. Exemplarily this is shown in figures 12 and 13 for three different sets of data. In figure 12 we compare two measurements which have the same dependence of the He bath temperature

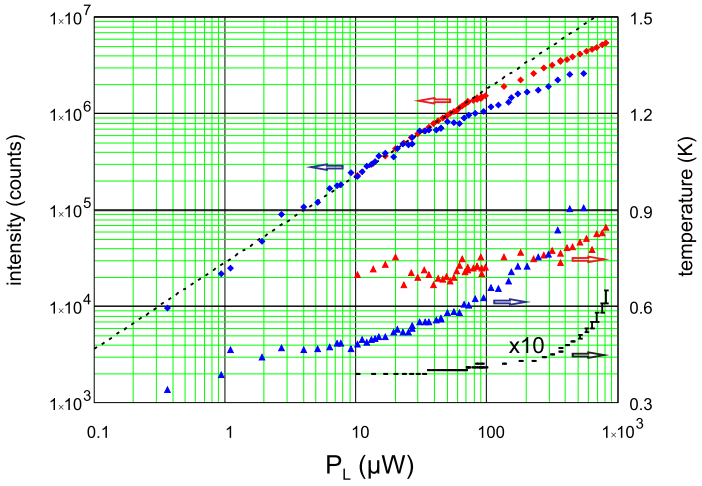

Figure 12. Dependence of the totally integrated intensity (squares), spatial temperature (triangles) and start and final bath temperature during the measurement (black bars) on the laser power for two different sets of data.

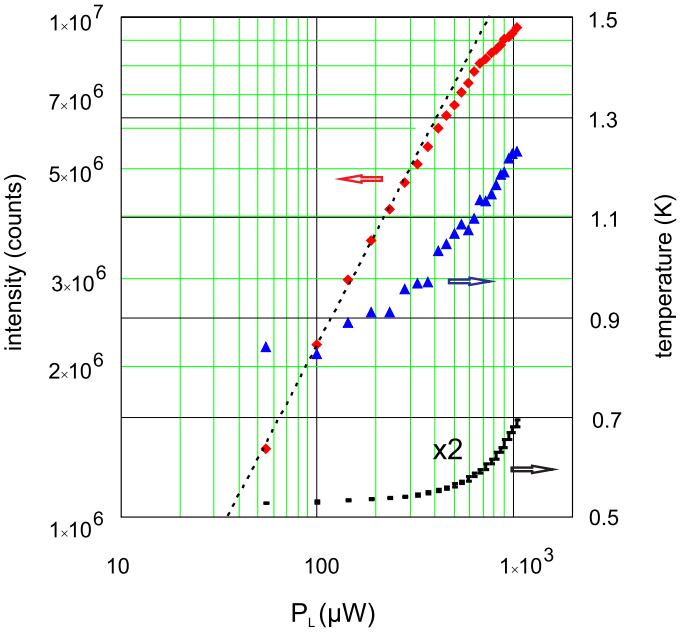

Figure 13. Dependence of the totally integrated intensity (squares), spatial temperature (triangles), and start and final bath temperature during the measurement (black bars) on the laser power.

but differ in their spatial temperatures. While at low powers both curves coincide, the curve corresponding to lower spatial temperature shows the kink at lower powers. In figure 13 we display the power dependence for the case where both the He bath temperature and the spatial temperature are much higher and the kink occurs at powers one order of magnitude larger than in the measurements of figure 12. This dependence of the onset of BEC on both the bath temperature and the spatial temperature will be explained by the theory presented in the next

section. The data in figure 13 furthermore demonstrate that the origin of the kink cannot be the Auger like decay of excitons at high densities, as one might suspect. This deviation from linearity in the power dependence already shows up below the kink.

3. Theory

After presenting the experimental results, in this section we will provide the theoretical description, attempting to explain the main effects found in the luminescence spectra.

So far, excitons in potential traps have been described mostly by theoretical models of non-interacting bosons. Concepts, to include e.g. interaction effects, have been worked out for atomic condensates. Along this line, the thermodynamics of a one-component Bose gas has been investigated extensively, see, e.g., [32–35]. First applications of excitons exist too [36]. Recently, distinct signatures of a condensate in the decay luminescence spectrum of the non-condensed excitons have been predicted using a mean-field formalism in local density approximation [31]. In analogy to generalizations for multi-component atomic gases [37–41] and spinor polaritons [42, 43], a generalization to a multi-component gas of interacting paraexcitons and orthoexcitons has been given in [44].

Here, we focus on the thermodynamics of weakly interacting excitons in a trap and assume the whole exciton gas to be in thermodynamic equilibrium. This allows us to apply the theory developed in [31, 44].

3.1. Thermodynamics of trapped excitons

In order to write down the Hamiltonian of the exciton system, the interaction potential between excitons has to be modelled. The description of exciton–exciton interaction is a long-standing problem (see, e.g., [45–50]), and so far no satisfying solution for the general case has been obtained. For our calculations, we assume a contact potential interaction $V(\mathbf{r}-\mathbf{r}') = U_0\delta(\mathbf{r}-\mathbf{r}')$, where the interaction strength U_0 is given by the s-wave scattering length a_s via $U_0 = 4\pi a_s/M$. M is the exciton mass $M = 2.6m_e$ in units of the free electron mass m_e [22]. This leads to the Hamiltonian in second quantization for the grand canonical ensemble:

$$\mathcal{H} = \int \mathrm{d}^3\mathbf{r}\, \psi^\dagger(\mathbf{r},t)\left(-\frac{\hbar^2\nabla^2}{2M} + V_{\mathrm{ext}}(\mathbf{r}) - \mu\right)\psi(\mathbf{r},t) + \frac{1}{2}\int \mathrm{d}^3\mathbf{r}\, U_0\psi^\dagger(\mathbf{r},t)\psi^\dagger(\mathbf{r},t)\psi(\mathbf{r},t)\psi(\mathbf{r},t), \tag{17}$$

with the trap potential $V_{\mathrm{ext}}(\mathbf{r})$ and the chemical potential μ. Decomposing the field operators in the usual fashion $\psi(\mathbf{r},t) = \Phi(\mathbf{r}) + \tilde{\psi}(\mathbf{r},t)$, with the condensate wave function $\Phi(\mathbf{r}) = \langle\psi(\mathbf{r},t)\rangle = \langle\psi(\mathbf{r})\rangle$ and the operator of the thermal excitons $\tilde{\psi}(\mathbf{r},t)$, one arrives at the Gross–Pitaevskii equation (GPE)

$$0 = \left(-\frac{\hbar^2\nabla^2}{2M} + V_{\mathrm{ext}}(\mathbf{r}) - \mu + U_0\left[n(\mathbf{r}) + n^{\mathrm{T}}(\mathbf{r})\right]\right)\Phi(\mathbf{r}) + U_0\tilde{m}(\mathbf{r})\Phi^*(\mathbf{r}), \tag{18}$$

and the equations of motion for the thermal excitons

$$\mathrm{i}\hbar\frac{\partial\tilde{\psi}(\mathbf{r},t)}{\partial t} = \left(-\frac{\hbar^2\nabla^2}{2M} + V_{\mathrm{ext}}(\mathbf{r}) - \mu + 2U_0 n(\mathbf{r})\right)\tilde{\psi}(\mathbf{r},t) + U_0\left[\Phi^2(\mathbf{r}) + \tilde{m}(\mathbf{r})\right]\tilde{\psi}^\dagger(\mathbf{r},t), \tag{19}$$

with the normal and anormal averages $n^{\mathrm{T}} = \langle\widetilde{\psi}^{\dagger}\widetilde{\psi}\rangle$ and $\widetilde{m} = \langle\widetilde{\psi}\widetilde{\psi}\rangle$, the condensate density $n^{\mathrm{c}} = |\Phi|^2$ and the total density $n = n^{\mathrm{c}} + n^{\mathrm{T}}$.

Since the spatial extension of the potential trap is large compared to the typical length scales of the interacting exciton gas (in particular with respect to the thermal deBroglie wavelength of the excitons), we can use the local density approximation, thus treating the excitons as a locally homogeneous system. The equation of motion (19) is solved by a Bogoliubov transformation. In the so-called Hartree–Fock–Bogoliubov–Popov limit ($\widetilde{m} \to 0$), the quasiparticle energy reads

$$E(\mathbf{k}, \mathbf{r}) = \sqrt{\mathcal{L}(\mathbf{k}, \mathbf{r})^2 - (U_0 n^{\mathrm{c}}(\mathbf{r}))^2}, \tag{20}$$

with

$$\mathcal{L}(\mathbf{k}, \mathbf{r}) = \hbar^2 k^2/2M + V_{\mathrm{ext}}(\mathbf{r}) - \mu + 2U_0 n(\mathbf{r}). \tag{21}$$

Within these approximations, the non-condensate density n^{T} is given by

$$n^{\mathrm{T}}(\mathbf{r}) = \int \frac{\mathrm{d}^3\mathbf{k}}{(2\pi)^3} \left[\frac{\mathcal{L}(\mathbf{k}, \mathbf{r})}{E(\mathbf{k}, \mathbf{r})} \left(n_{\mathrm{B}}(E(\mathbf{k}, \mathbf{r})) + \frac{1}{2}\right) - \frac{1}{2}\right] \Theta\Big(E^2(\mathbf{k}, \mathbf{r})\Big). \tag{22}$$

Applying the Thomas–Fermi approximation to the GPE (18), i.e. neglecting the kinetic energy term, yields the condensate density as

$$n^{\mathrm{c}}(\mathbf{r}) = \frac{1}{U_0}\Big[\mu - V_{\mathrm{ext}}(\mathbf{r}) - 2U_0 n^{\mathrm{T}}(\mathbf{r})\Big] \Theta\Big(\mu - V_{\mathrm{ext}}(\mathbf{r}) - 2U_0 n^{\mathrm{T}}(\mathbf{r})\Big). \tag{23}$$

Evaluating equations (22) and (23), n^{T} and n^{c} have to be determined self-consistently.

3.2. Theory of decay luminescence

Since the optical wavelength of the emission is much smaller than the trapped exciton cloud, we apply a local approximation to the emission spectrum [51, 52] as well, which is determined by the excitonic spectral function $A(\mathbf{r}, \mathbf{k}, \omega)$,

$$I(\mathbf{r}, \omega) \propto 2\pi\hbar |S(\mathbf{k} = 0)|^2 \delta(\hbar\omega' - \mu) n^{\mathrm{c}}(\mathbf{r}) + \sum_{\mathbf{k}\neq 0} |S(\mathbf{k})|^2 n_{\mathrm{B}}(\hbar\omega' - \mu) A(\mathbf{r}, \mathbf{k}, \hbar\omega' - \mu), \tag{24}$$

with $S(\mathbf{k})$ representing the exciton–photon coupling. The spectral function is given by the quasiparticle spectrum in (20):

$$A(\mathbf{r}, \mathbf{k}, \omega) = 2\pi\hbar \left[u^2(\mathbf{k}, \mathbf{r})\delta(\hbar\omega - E(\mathbf{k}, \mathbf{r})) - v^2(\mathbf{k}, \mathbf{r})\delta(\hbar\omega + E(\mathbf{k}, \mathbf{r}))\right], \tag{25}$$

where $u(\mathbf{k}, \mathbf{r})$ and $v(\mathbf{k}, \mathbf{r})$ are the Bogoliubov amplitudes,

$$\begin{aligned} u(\mathbf{k}, \mathbf{r})^2 &= \frac{1}{2}(\mathcal{L}(\mathbf{k}, \mathbf{r})/E(\mathbf{k}, \mathbf{r}) + 1), \\ v(\mathbf{k}, \mathbf{r})^2 &= \frac{1}{2}(\mathcal{L}(\mathbf{k}, \mathbf{r})/E(\mathbf{k}, \mathbf{r}) - 1). \end{aligned} \tag{26}$$

In Cu_2O, the decay of ground-state paraexcitons in the yellow series is optically forbidden. However, due to the applied strain, a mixing with the green series takes place and the decay becomes weakly allowed [53]. The paraexcitons decay directly, whereby momentum conservation requires that only excitons with the same momentum as the emitted photons are involved. This zero-phonon decay can be treated by setting $\omega' = \omega - E_{\mathrm{gX}}/\hbar$ with the excitonic band gap E_{gX} and $|S(\mathbf{k})|^2 = S_0^2\delta(\mathbf{k} - \mathbf{k}_0)$ with $\mathbf{k}_0$ being the wave vector of the intersection of the photon and exciton dispersions.

Due to the form of $S(\mathbf{k})$, a condensate of paraexcitons in Cu_2O (energetically in the ground state, i.e. $k = 0$) should not contribute to the luminescence spectrum. However, this statement holds rigorous only for homogeneous, infinitely extended systems. Due to the finite size of the condensate, it is spread out in $\mathbf{k}$-space, and a weak contribution to the luminescence should be expected. Taking the condensate as a classical coherent emitter, the radiation follows from classical Maxwell equations as the Fourier transform of the polarization [54] at the wave vector of the emitted photon $\mathbf{k}_0$. Since the polarization is proportional to the condensate wave function, the (dimensionless) strength of the contribution S_c ($|S(\mathbf{k} = 0)|^2 = S_c S_0^2$) should be proportional to the components of the Fourier transform of the ground-state wave function at $\mathbf{k} = \mathbf{k}_0$. Our calculations show that S_c is of the order of 10^{-6} to 10^{-7}. Therefore, we will discuss possible effects of a BEC in the spectrum considering a weakly luminescing as well as a completely dark condensate.

Furthermore, to account for the finite spectral resolution in experiments, we convolve the spectral intensity (24) with a spectral response function of the shape $\exp[-(\omega/\Delta)^2]$. Here, Δ is a measure for the spectral resolution. Using these assumptions, the spectrum reads:

$$I(\mathbf{r}, \omega) \propto S_c (2\pi)^3 \exp\left[-\left(\frac{\hbar\omega' - \mu}{\Delta}\right)^2\right] n^c(\mathbf{r}) + u^2(\mathbf{k}_0, \mathbf{r}) n_B(E(\mathbf{k}_0, \mathbf{r})) \exp\left[-\varepsilon_-^2(\omega', \mathbf{k}_0, \mathbf{r})\right]$$
$$- v^2(\mathbf{k}_0, \mathbf{r}) n_B(-E(\mathbf{k}_0, \mathbf{r})) \exp\left[-\varepsilon_+^2(\omega', \mathbf{k}_0, \mathbf{r})\right], \tag{27}$$

with $\varepsilon_\pm(\omega', \mathbf{k}, \mathbf{r}) \equiv (\hbar\omega' - \mu \pm E(\mathbf{k}, \mathbf{r}))/\Delta$. As explained in section 2, in the experiment, a spectrograph is used to obtain different spectra by integrating over either one or more spatial coordinates and/or ω. Here, we consider the z-resolved luminescence spectrum $I(z, \omega)$, the z-profiles of the luminescence $I(z)$, the spatially integrated luminescence $I(\omega)$, and the totally integrated luminescence I_{tot}. The z-resolved luminescence spectrum is obtained by imaging a small strip of width $2\Delta y$ elongated along the z-direction onto the entrance slit of the spectrograph, hence integrating over the x- and y-direction. The z-profiles are generated by integrating $I(z, \omega)$ over the energy (ω). Integrating over all spatial dimensions yields the spatially integrated luminescence $I(\omega)$. As a fourth option, one can also integrate over $\mathbf{r}$ and ω, arriving at the totally integrated luminescence I_{tot}, which only depends on the exciton number N and the temperature T.

3.3. Results

3.3.1. Luminescence spectrum. For the calculations, we used an anharmonic potential trap fitted to the experimental of section 2 but with a trap minimum of $V_0 = 1.04$ meV. The s-wave scattering length was chosen to be $a_s = 2.18 a_B$ (taken from [55], see also [56–58]) with the excitonic Bohr radius $a_B = 0.7$ nm.

First, we revisit the flat bottomed shape of the spectrum discussed in [31]. In figure 14, we plot the luminescence spectrum for a constant temperature $T = 0.6$ K and three different exciton numbers (left column: $N = 2.5 \times 10^7$, middle column: $N = 2.5 \times 10^8$, right column: $N = 8.0 \times 10^8$). The condensate is expected to remain completely dark. The left image of figure 14 shows a thermal spectrum exhibiting the typical nearly parabolic shape that was also found in the experimental results presented in figures 3 and 7. Increasing the exciton number by a factor of 10 while keeping the temperature constant results in the onset of a BEC with a condensate fraction of $N_c/N = 0.05$. The shape of the spectrum is altered and develops a flat bottom at the chemical potential as reported in [31]. Further increasing the exciton number

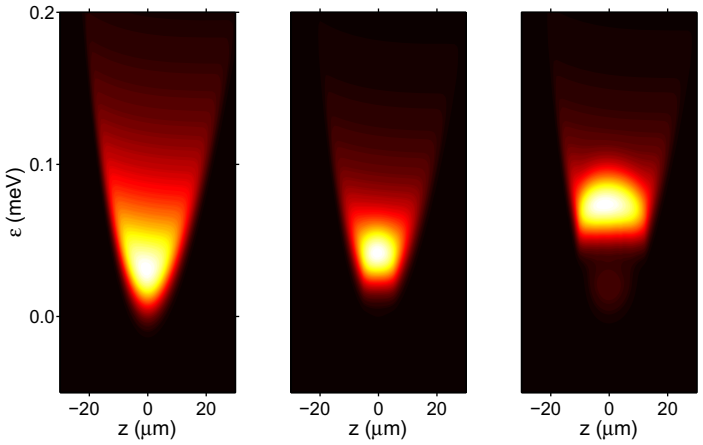

Figure 14. z-resolved luminescence spectra $I(z, \omega)$ at $T = 0.6\,\mathrm{K}$ with dark condensate. The exciton numbers are $N = 2.5 \times 10^7$ (left), $N = 2.5 \times 10^8$ (middle) and $N = 8.0 \times 10^8$ (right). Condensate fractions are $N_\mathrm{c}/N = 0$ (left), $N_\mathrm{c}/N = 0.05$ (middle) and $N_\mathrm{c}/N = 0.50$ (right). Trap minimum is at $V_0 = 1.04\,\mathrm{meV}$ and $\varepsilon = \hbar\omega - E_\mathrm{gX} - V_0$.

leads to a more pronounced flat bottom and an energetic shift of the spectrum with the chemical potential. Additionally, a new contribution to the thermal spectrum below the chemical potential, arising from the v^2-term in equation (25), becomes faintly visible. These effects are linked to the occurrence of a BEC and would indicate its existence even without direct emission from the condensate.

Comparing these predictions with the experimental findings, e.g. figures 3 and 7, one has to conclude that the signatures were not observed in the experiment. However, if the condensate exhibits a very weak luminescence, the changes in the spectrum predicted from theory are much more subtle. This can be seen in the left column of figure 15 ($S_\mathrm{c} = 10^{-6}/3$), cf again figures 3 and 7. In contrast to the case of a dark condensate, there is no drastic qualitative change in the spectra from top to bottom. Also, the shift on the energy axis appears to be smaller and could well be an interaction effect of thermal excitons. Therefore, the contribution from the condensate hides the flat bottom as well as the shift on the energy axis, without being a clearly visible delta-shaped peak, as expected for a fully contributing condensate. This explains why a conclusive detection of a condensate via spectral signatures requires a very careful analysis of the experiments.

The spectra in the left column of figure 15 consist of different contributions. To illustrate this, we plot the results for the spatially integrated luminescence $I(\omega)$ in the middle column of figure 15, cf the measurements shown in figures 3 and 5. The upper panel shows a spectrum in the non-condensed case at low densities. Its shape is given by a Bose distribution convolved with the spectral resolution of the spectrometer. The middle panel shows a spectrum at higher densities, where interaction effects are already important and a very small condensate contribution already occurs, nearly invisible in the total curve. Compared to the previous case, the peak becomes narrower and shifts to higher energies, while the tail remains qualitatively the same. The bottom graph shows the case with a condensate fraction of 0.5 including a distinct condensate contribution (dashed-dotted blue) which has a Gaussian shape and is centred at

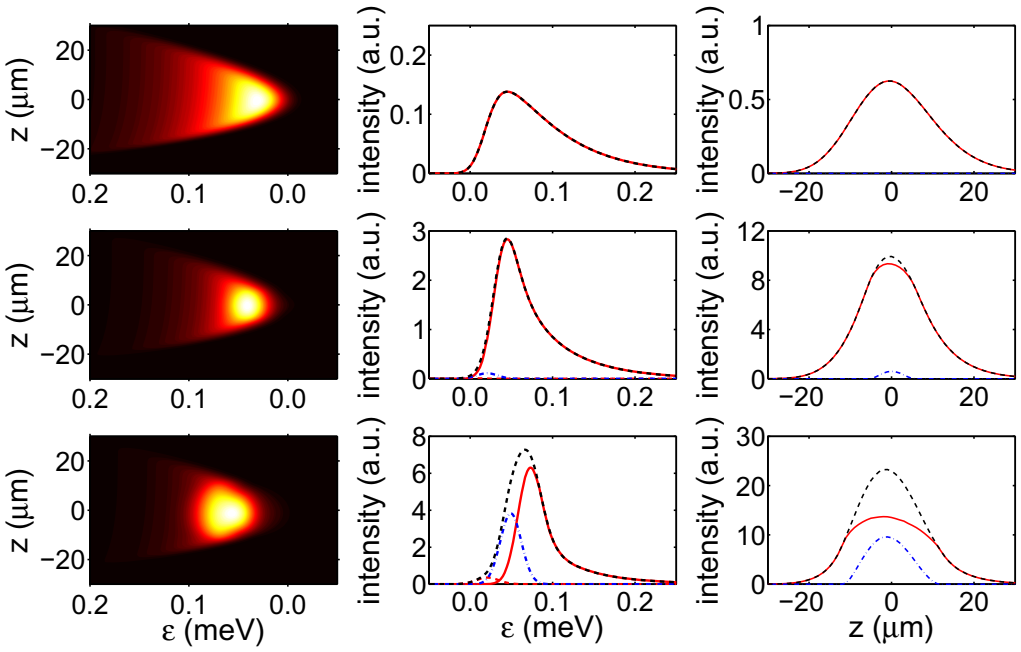

Figure 15. z-resolved luminescence spectra, z-integrated luminescence and z-profiles of the luminescence with weakly luminescing condensate ($S_c = 10^{-6}/3$) for the same parameters as in figure 14. Left column: luminescence spectra $I(z, \omega)$. Middle column: z-integrated luminescence $I(\omega)$. Right column: z-profiles $I(z)$. Red curves (full and dashed) denote the contributions from thermal excitons, the blue dash-dotted curve gives the condensate contribution, and the total emission is shown as a dashed black line.

the chemical potential. The contribution from the thermal excitons consists of the u^2 part of the spectral function (solid red) and the v^2 part of the spectral function (dashed red), compare with equation (27). The black line represents the sum over all contributions. In contrast to the very weakly condensed case (middle), the contribution related to the v^2 term appears below the chemical potential (dashed red). Except for this additional contribution, the total emission is only slightly shifted towards higher energies and has a higher maximum compared to the middle graph in figure 15. The width of all the Gaussian-like peaks in figure 15 is directly given by the spectral resolution $\Delta = 18\,\mu$eV.

3.3.2. Spatially resolved luminescence. The results for the spatially resolved luminescence $I(z)$ are presented in the right column of figure 15 and should be compared to the experimental results shown in figures 3, 4, 8 and 9.

Without any contribution from the condensate, one would expect the solid red line. The non-condensed case follows a Gaussian shape (top graph), while the onset of the BEC leads to a deformation in the form of a plateau (middle and bottom graphs). However, taking a weakly luminescing condensate (dashed blue) into account, the total emission (black dashed) looks Gaussian-like again, masking the signature of the condensate (middle and bottom graphs).

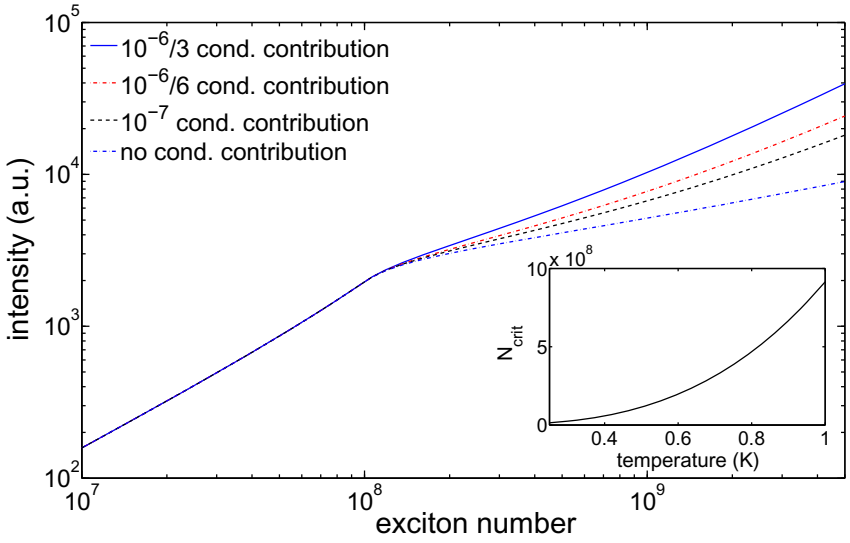

Figure 16. Totally integrated luminescence I_{tot} for $T = 0.5\,\mathrm{K}$ and different fractions of condensate contribution. Change of N_{crit} (position of kink) with temperature is shown in the inset.

3.3.3. Totally integrated luminescence. Integrating over all variables ($\mathbf{r}$ and ω) yields the totally integrated luminescence I_{tot}, which had been considered in the experiments in figures 11–13. In figure 16, we show the numerical results for I_{tot} as a function of the exciton number N for a fixed temperature of $T = 0.5\,\mathrm{K}$. Remember that N is connected to the excitation laser power P_{L}, cf the results of the rate model, figure 2. For small N, the totally integrated luminescence increases linearly with the exciton number until a critical value is reached. At the critical exciton number, the curve has a kink and continues with a weaker slope afterwards. The additional contribution from a weakly luminescing condensate does not alter the behaviour qualitatively in this case, as can be seen from the other curves in figure 16. As shown in the inset of figure 16, the critical exciton number shifts with the temperature approximately as expected with T^3, equation (1). Obviously, here the interaction has no drastic effect on the behaviour known for an ideal gas.

However, in the experimental situation, it is merely impossible to measure over orders of magnitude of particle number without changing the exciton temperature. The temperature will rise as a result of the energy introduced into the system by the laser. Therefore, experimental points may lie anywhere in the N–T plane. The theoretical results for the totally integrated luminescence as a function of exciton number and temperature are shown in figure 17. Depending on how fast the temperature increases with exciton number, it is very well possible to never cross the phase boundary and observe the kink in the totally integrated luminescence.

3.4. Discussion

In the previous section, we presented the different spectral signatures of a non-emitting condensate in the thermal emission of excitons in global thermal equilibrium. The five main signatures are: (i) the formation of a flat bottom in the luminescence spectrum $I(z, \omega)$, (ii) the

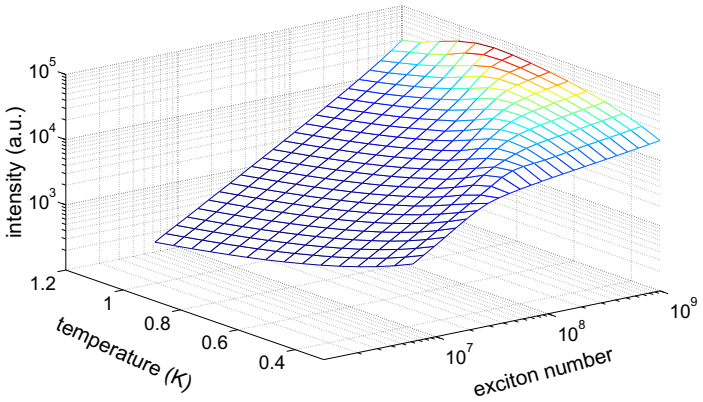

Figure 17. Totally integrated luminescence I for a range of different temperatures and exciton numbers in the same potential trap as in figure 14.

shift on the energy axis of the spectrum $I(z, \omega)$, (iii) a deviation of the z-profiles $I(z)$ from the Gaussian shape, (iv) the appearance of the v^2 term in the spatially integrated luminescence $I(\omega)$ and (v) the kink in the totally integrated luminescence I_{tot} at N_{crit}.

If the contribution from the condensate is much weaker than that which we estimated (i.e. S_{c} of the order of 10^{-6}–10^{-7}), signature (i) should be experimentally visible. This is neither the case in the current experiment nor any others previously. If the contribution is much stronger though, one should expect the delta-shaped peak as predicted by the standard theory [1, 51, 52]. This substantiates our estimation for S_{c}.

However, if the condensate contribution is comparable to that of the thermal excitons, the flat bottom in (i) can be masked as shown in figure 15. The changes in the shape are very subtle and probably not detectable in an actual experiment. The shift on the energy axis (ii) is also altered by the condensate contribution. Additionally, there are numerous other effects that can change the energetic position of the spectrum, e.g. a background plasma of electrons and holes [6, 7]. Therefore, this shift might not be a good indicator for the onset of the BEC. The deformation of the z-profiles (iii) would also be masked by the condensate contribution. Here, the latter one complements the thermal luminescence, again resulting in a Gaussian profile. Contrarily, in the measured profiles (figure 9), the condensate adds a contribution to the thermal Gaussian profile. We will revisit this point later.

Without a condensate, the spectra can be fitted with a renormalized Bose distribution convolved with the spectral resolution of the spectrometer. With a condensate, the v^2 peak (iv) causes a characteristic deformation of the low energy flank of the spatially integrated luminescence. For a dark condensate, however, it would be a free standing peak separated from the rest of the spectrum. Both cases should be detectable in an experiment though. However, this signature (iv) as well as the energetic shift (ii) are very subtle and are probably masked by noise, compare figures 3 and 7.

The most promising signature of condensation would be the kink in the totally integrated luminescence (v), as it is not altered qualitatively by the condensate contribution. In this case it only changes the slope after the kink, but does not hide the kink itself. Although in figures 11–13 no isotherms are plotted—the exciton temperature rises with excitation power—there is obviously a kink in the measured integrated intensity. Looking at figure 17, a path on the surface will exhibit a kink even with increasing temperature, if the ridge is

crossed. Therefore, we can relate the kink in the experimental figures, at least qualitatively, to the occurrence of a condensate.

3.5. Excitons in local equilibrium

As stated above, the theory derived in section 3 assumes that the exciton gas in the trap is in global thermodynamic equilibrium. The experimental results presented in the previous section show, however, that this is obviously not the case and that the exciton temperature is the key quantity to detect deviations from global equilibrium. The conclusions are that (i) the *spectral* (or *spatial*) temperature is not equal to the exciton temperature and (ii) the assumption of global equilibrium, therefore, must be wrong, cf the discussion in section 2.3.1.

In contrast to the latter statement, the luminescence spectra calculated by the equilibrium theory reproduce the measured spectra qualitatively quite well, cf figures 3 and 15. Thus it seems to be reasonable to abandon the global equilibrium assumption, but to keep the local equilibrium assumption. In this case, the thermally excited excitons still have an equilibrium (Bose) distribution, but with spatially varying temperature and chemical potential. The space dependence of the latter quantities is in principle unknown, but from the experiment we can conclude that the temperature should not vary over the dimension of the trap, see section 2.3.1. The only criterion for the spatial dependence $\mu(\mathbf{r})$ is that the spectra must be reproduced. Therefore, we demand that the spatially integrated spectrum $I(\omega)$ (at least its high-energy tail) follows a Bose distribution with the spatial temperature and some formal constant chemical potential $\tilde{\mu}$ which is used to fix the particle number. This leads to

$$\mu(\mathbf{r}) = \left(1 - \frac{T_X}{T_s}\right)\left(V_{ext}(\mathbf{r}) + E_0 + 2U_0 n^T(\mathbf{r})\right) + \frac{T_X}{T_s}\tilde{\mu}, \tag{28}$$

which allows direct use of the theory of section 3.1 in this non-equilibrium situation also.

In what follows, we apply the local equilibrium theory to two typical experimental situations. Thereby we fix the total particle number $N = 10^8$ and the spatial temperature $T_s = 0.6\,\mathrm{K}$ and vary the exciton temperature. The condensate contributes to the luminescence with $S_c = 4 \times 10^{-7}$. The spatially resolved spectra for both cases are displayed in figure 18, left column. As expected, in the uncondensed case ($T_X = 0.25\,\mathrm{K}$, upper row), the spectrum just follows the external potential. The condensed case ($T_X = 0.15\,\mathrm{K}$, lower row) with a condensate fraction $\eta_c = 0.2$ looks qualitatively not very different. In particular, due to the spatial variation of the chemical potential according to equation (28), the flat bottom of the spectrum (cf figure 14) disappears.

In the condensed case ($T_X = 0.15\,\mathrm{K}$), the z-profile of the luminescence exhibits a clearly non-Gaussian shape (figure 18, right column, lower panel, red line). For the slightly higher temperature of $T_X = 0.25\,\mathrm{K}$ (upper panel), the shape is approximately Gaussian. Therefore, we fit the thermal component of the z-profile for the condensed case by an asymmetric (due to the potential asymmetry) Gaussian. In order to exclude the condensate contribution, we omit in the fitting procedure the data points in the centre of the trap where the condensate is situated. The size of the excluded area is determined by minimizing the error of the fit. The fitting result is given by the dash-dotted blue line in the lower right figure. It basically follows the thermal profile component. The small deviations from the Gaussian shape are caused by the potential anharmonicity and by the renormalization of the potential due to the interparticle interaction. Thus, the procedure to extract the thermal component from the experimental z-profiles shown in figure 9, where a Gaussian fit has been applied, too, seems to be justified.

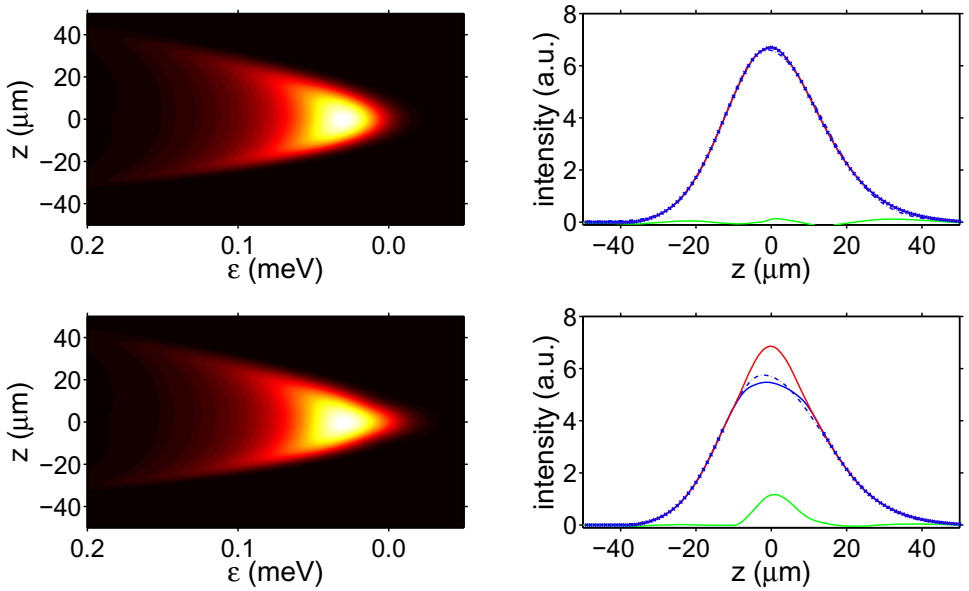

Figure 18. Spatially resolved luminescence spectra (left) and z-profiles of the intensity (right) for $N = 10^8$ and $T_s = 0.6$ K. Upper row: exciton temperature $T_X = 0.25$ K (uncondensed case), lower row: $T_X = 0.15$ K (condensed case, $\eta_c = 0.2$). Solid red lines: total profiles (thermal + condensate), solid blue: only thermal contribution, dash-dotted blue: Gaussian fit of the total profiles, blue crosses: data points used for the fit, solid green: the difference between the total profile and the fit. The ratio between the integrated intensities of the condensate and of the total band is $\eta_{lum} = 0.07$.

The difference between the total z-profiles and the Gaussian fits is given by the green lines. It basically reflects the condensate contribution. For the condensed case we obtain a luminescence fraction $\eta_{lum} = 0.07$ which would set $f_{lum} = 0.25$.

The two cases depicted in figure 18 can be compared to the measured z-profiles shown in figure 9. The 'uncondensed case' (upper row in figure 18) obviously corresponds, e.g. to measurements 1 and 21, where the difference between data and fit is just noise. On the other hand, the 'condensed case' (lower row in figure 18) finds its counterparts, e.g. in measurements 3 and 17. In each case, a striking qualitative agreement is found. This substantially corroborates our explanation of the experimental findings with the occurrence of an excitonic BEC.

Figure 19 shows the critical particle number for BEC dependent on exciton temperature T_X and spatial temperature T_s. The global equilibrium case is represented by the diagonal $T_X = T_s$. If the excitons are excited outside the trap, their spatial profile will be at first always broader than when in equilibrium. Therefore, $T_s < T_X$ can be ruled out in the current experiment. Obviously, for a given exciton temperature, the critical number is smallest for global thermal equilibrium and increases with increasing spectral temperature. Even at low powers, i.e. for quite low exciton numbers, a condensate is possible if the exciton temperature is close to the He bath temperature, cf the situation shown in figure 9, measurement 3, where the spatial temperature is 0.35 K and the exciton number is 4×10^6 which just corresponds to the critical number at $T_X = 0.04$ K.

With the help of this figure, we can systemize the experimentally observed power dependence of the totally integrated intensity shown in figures 11–13. This is done by examining

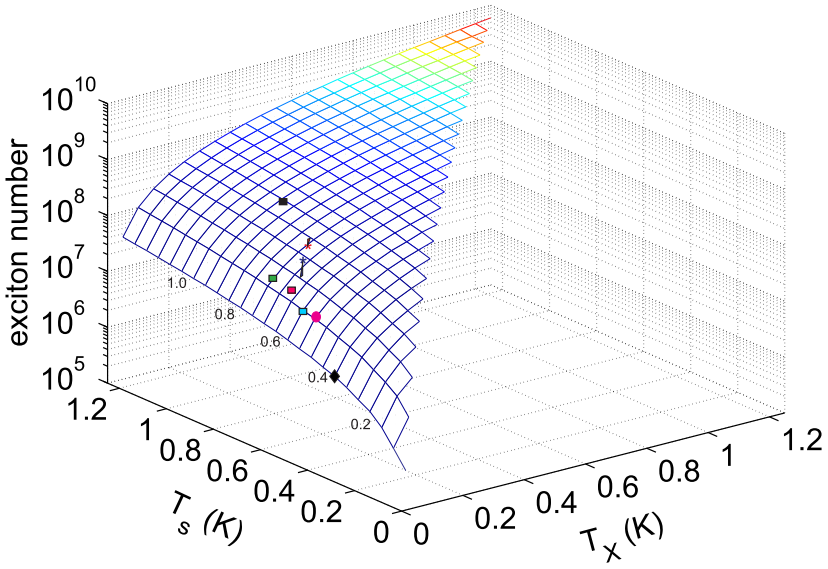

Figure 19. Critical particle number N_{crit} for BEC versus exciton temperature T_{X} and spatial temperature T_{s}. The diagonal $T_{\mathrm{X}} = T_{\mathrm{s}}$ corresponds to global equilibrium; $T_{\mathrm{X}} > T_{\mathrm{s}}$ is, for excitation outside the trap, physically meaningless. The blue coloured rectangle corresponds to the critical power of 30 μW for the data shown in figure 12 (blue symbols), the red coloured rectangle corresponds to the critical power of 60 μW for the data shown in figure 12 (red symbols), the black coloured rectangle corresponds to the critical power of 600 μW for the data shown in figure 13, and the green coloured rectangle corresponds to the critical power of 78 μW (data not shown). The magenta coloured dot corresponds to the critical power of 40 μW from the measurements shown in figure 11. The stars denote the conditions of measurements 17 (blue) and 18 (red), and the black diamond denotes the critical number for measurement 3, all from figure 7.

the exciton temperature T_{X} as the critical number (corresponding to the critical power and the respective spatial temperature) crosses the critical surface. These points are plotted as coloured rectangles in figure 19. The values for T_{X} give a very systematic picture. With increasing critical power, both the spatial and the exciton temperature rise. Thereby, T_{X} is always larger than the bath temperature, which is consistent with the expected crystal heating, compare appendix C.

Figure 19 also compares the data for the measurements 17 (blue star) and 18 (red star) of figures 7 and 9 showing that the conditions in measurement 17 are such that we are well above N_{crate}, while for measurement 18 we are just touching the critical surface.

4. Conclusions and outlook

We have presented a series of experiments that investigate the luminescence from paraexcitons in cuprous oxide after cw-excitation. The excitons have been confined in a potential trap with the host crystal immersed in liquid helium at temperatures down to 38 mK. The spatially resolved luminescence spectra do not show notable variations when varying the laser excitation power from below 1 μW to above 1 mW. However, we observed a number of characteristic changes

in the spatial profiles of the luminescence and in the totally integrated intensity: In the spatial profiles, a new component in the centre of the trap occurs at intermediate laser powers which cannot be fitted by a thermal Gaussian distribution. This component vanishes at very low power and at very high power levels. At the mentioned intermediate power levels, we see deviations from the linear dependence of the totally integrated intensity on the laser power: most notably a well defined kink appears in the slope of the curves. From the linear dependence of the total intensity on laser power, we conclude that two-body decay processes of the excitons do not play any significant role. This is in agreement with previous measurements under pulsed excitation in the same samples [17].

With increasing laser power, we observe a slight increase in the effective temperature that is inferred from the high-energy tail of the luminescence spectra from 0.35 K up to a maximum of 1 K. This spectral temperature does only reflect the spatial distribution of excitons in the trap and is not identical to the local temperature which determines the energy distribution of the excitons at each point in the trap. The local temperature will be determined by exciton relaxation processes and is expected to go down almost to the bath temperature at low excitation power.

Recently, [15] reported a strong heating of the exciton gas at high pump powers and claimed that this effect originates from a relaxation explosion of excitons when a transition into a Bose–Einstein condensate takes place. We observe a similar heating under high excitation powers but can definitely rule out the existence of a BEC in this high power range.

In order to understand the observed features of the luminescence spectra, we theoretically analysed the thermodynamics and the luminescence properties of excitons in a potential trap. Thereby the excitons are described as an interacting Bose gas in the framework of a Hartree–Fock–Bogoliubov–Popov approach. Already under the assumption of global thermal equilibrium, this theoretical approach suggests that the observed kink in the totally integrated intensity signals the transition into a Bose–Einstein condensate of trapped paraexcitons. Taking into account the specific non-equilibrium situation in the trap, the theory also consistently describes the characteristic changes in the spatial profiles of the luminescence: while the theory predicts almost no changes in the spatially resolved spectra, it allows us to identify the additional component in the spatial profiles as due to a weakly luminescing condensate.

To conclude, we have presented strong evidence, both from experiment and theory, that at ultracold temperatures in the range of 100 mK, paraexcitons in Cu_2O undergo a transition into a Bose–Einstein condensate.

Nevertheless, further experimental investigations are necessary to prove the existence of a BEC of excitons in cuprous oxide beyond any doubt. For example, direct measurements of the lattice temperature and of the local exciton temperature will provide a better understanding of the thermodynamics. Thereby, it might be intriguing to apply spatially resolved Brillouin scattering since the energies of the phonons involved are comparable to the thermal energy. The local exciton temperature would be detectable via infrared absorption of the 1S–2P transition [29, 30]. The most important aspect, however, must be the direct proof of the macroscopic coherence of the condensate by interferometric methods or by means of intensity correlation measurements, both currently under way.

Theoretically, one can try to improve the exciton density calculations by using more advanced approximations, e.g. by solving the Gross–Pitaevskii equation exactly instead of using the Thomas–Fermi approximation. It also seems to be necessary to improve the luminescence theory in order to account, more rigorously, for the inhomogeneity of the system,

e.g. following the ideas of [59]. Moreover, one should also include the spectral broadening due to exciton–exciton interaction. This would require the inclusion of higher order correlations beyond the Hartree–Fock–Bogoliubov–Popov approximation by calculating the densities and the spectral function on the level of the Beliaev approximation [60]. Recently, we have shown that, already for the thermal excitons, a more realistic description requires us to take the lifetime broadening of the exciton states into account [17], which relaxes the strict wave vector conservation in (24).

Quite recent results by Naka *et al* [25] show that the Auger-decay produces a significant number of free electrons and holes which are also captured by the trap (see figure 2). This should lead to a shift and a broadening of the exciton states by the surrounding electron–hole plasma [6, 7, 61, 62]. An inclusion of this 'plasma damping' in the theory requires taking into account collisions of the excitons with charged fermions. This is clearly beyond the scope of the theory of weakly interacting bosons.

Acknowledgments

We thank Dietmar Fröhlich (Dortmund) for supplying the sample. Furthermore, we thank him, Günter Manzke and Wolf-Dietrich Kraeft (Rostock), Manfred Bayer, Jan Brandt, and Christian Sandfort (Dortmund), and Andreas Alvermann (Greifswald) for many helpful discussions and critical comments. Our special thanks go to Herwig Ott (Kaiserslautern) for lending us the CR599 laser system. We acknowledge the support by the Deutsche Forschungsgemeinschaft (Collaborative Research Center SFB 652 'Starke Korrelationen im Strahlungsfeld') and by JSPS KAKENHI (grant no. 21740227).

Appendix A. Strain Hamiltonian for electron–hole states

For the derivation of the energy shifts of electron–hole pairs we consider that the top Γ_7^+ valence band states can be written as [9]

$$\Psi^7_{+1/2} = -\frac{1}{\sqrt{6}}\left[(Y_2^{-2} - Y_2^2)\alpha_\mathrm{v} + 2Y_2^{-1}\beta_\mathrm{v}\right], \tag{A.1}$$

$$\Psi^7_{-1/2} = +\frac{1}{\sqrt{6}}\left[(Y_2^{-2} - Y_2^2)\beta_\mathrm{v} - 2Y_2^{1}\alpha_\mathrm{v}\right]. \tag{A.2}$$

Here Y_2^m denotes the spherical harmonics and $\alpha_{\mathrm{c,v}}$, $\beta_{\mathrm{c,v}}$ the electron spin functions of the valence and conduction bands. By inspection of table VI of [9] we immediately see the paraexciton state

$$\Phi_{12} = \Phi_\mathrm{YS}\frac{1}{\sqrt{2}}\left(\Psi^7_{-1/2}\alpha_\mathrm{c} + \Psi^7_{+1/2}\beta_\mathrm{c}\right) \tag{A.3}$$

with Φ_YS being the envelope function of the yellow 1S state. We immediately see that the paraexciton state has the same behaviour as the Γ_7^+ band states. In all matrix elements of the strain Hamiltonian, all terms containing the electron–hole exchange are missing. Since the interaction with the Γ_8^+ states does not change, the electron–hole pairs show the same behaviour under strain, i.e. they experience an effective trapping potential similar to the paraexcitons.

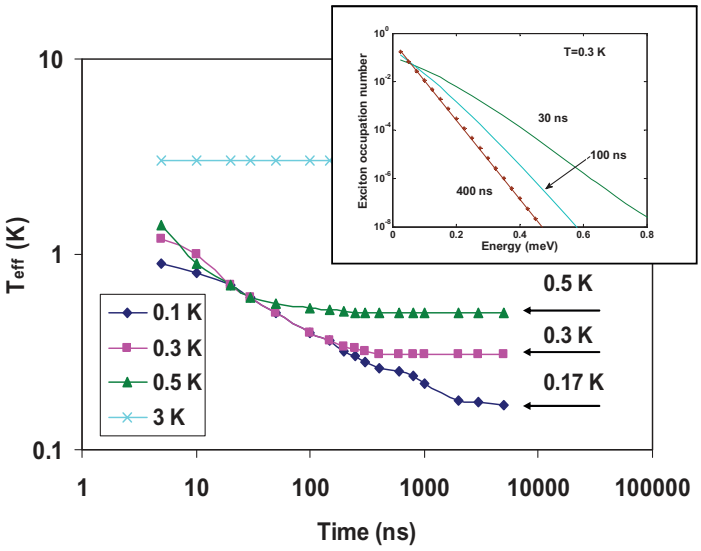

Figure B.1. Cooling behaviour of laser excited paraexcitons for different bath temperatures. Plotted are the effective temperatures of the distribution function obtained by fitting with a Bose distribution. The cooling curve for a lattice temperature of 0.05 K is identical to that of 0.1 K. The inset shows as an example the distribution for a lattice temperature of 0.3 K, an exciton density of $n = 1 \times 10^{15}\,\mathrm{cm}^{-3}$ at $t = 100\,\mathrm{ns}$ from which a temperature of $T_{\mathrm{eff}} = 0.33\,\mathrm{K}$ is derived.

Appendix B. Exciton relaxation

A central problem in the dynamics of excitons at milli-Kelvin temperatures is the relaxation and thermalization by contact to a bath of thermal phonons, as the acoustical modes will freeze out [63]. Therefore, we have simulated the relaxation of hot, laser excited excitons by assuming interactions with longitudinal acoustic phonons and Auger-like two-particle decay in a potential trap by integrating the Boltzmann equation [28]. Here we present additional results for the homogeneous situation including elastic exciton–exciton scattering, where the model follows closely that described in [64–66]. The resulting system of differential equations was integrated using as an initial distribution a Gaussian of width 0.1 meV centred at $e_{\mathrm{L}} = 5\,\mathrm{meV}$. The initial exciton density was assumed to be $n_0 = 1 \times 10^{15}\,\mathrm{cm}^{-3}$. For the elastic exciton–exciton scattering cross section $\sigma = 50\,\mathrm{nm}^2$ [66] was taken. The main results are shown in figure B.1, where the effective temperature of the exciton gas obtained by fitting the distribution function by a Bose distribution (see inset) is plotted for different lattice temperatures as a function of time.

Appendix C. Thermal behaviour of the dilution refrigerator and the sample

The ^{3}He/^{4}He dilution cryostat uses a mixture of ^{3}He and ^{4}He for the cooling process. The coldest region is inside the mixing chamber, consisting of a ^{3}He-rich (100% ^{3}He) and a ^{3}He-poor (6.4% ^{3}He) phase separated by a phase boundary, the basic thermodynamics of which is well known [67]. In the following analysis, we assume that the sample is immersed inside

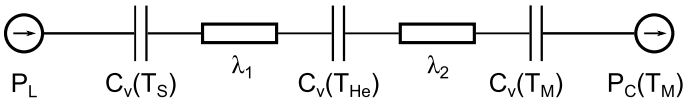

Figure C.1. A thermal network describing the sample and mixing chamber in the ^{3}He/^{4}He dilution cryostat. For an explanation, see text.

the dilute ^{3}He/^{4}He mixture and that the resistor measuring the bath temperature is placed in between the sample and the phase boundary in the mixing chamber.

To derive a connection between the sample temperature and the measured bath temperature we have to consider the whole system as a thermal network as shown in figure C.1. The incoming laser beam with power P_L hits the sample which is at a temperature T_S and has a heat capacity $C_\mathrm{v}(T_\mathrm{S})$. It is surrounded by the dilute ^{3}He/^{4}He mixture (temperature T_He), which itself is connected to the mixing chamber at a temperature T_M with heat capacities $C_\mathrm{v}(T_\mathrm{He})$ and $C_\mathrm{v}(T_\mathrm{M})$, respectively. The mixing chamber is cooled with a power $P_\mathrm{C}(T_\mathrm{M})$ depending on its temperature. The heat conduction between the different compartments is represented by the heat conductivities λ_1 and λ_2. Applying the continuity equation for the energy flow, the network is described by the following system of equations:

$$C_\mathrm{v}(T_\mathrm{S})\frac{\mathrm{d}T_\mathrm{S}}{\mathrm{d}t} = F_\mathrm{heat}(P_\mathrm{L}) - \lambda_1(T_\mathrm{S} - T_\mathrm{He}), \tag{C.1}$$

$$C_\mathrm{v}(T_\mathrm{He})\frac{\mathrm{d}T_\mathrm{He}}{\mathrm{d}t} = \lambda_1(T_\mathrm{S} - T_\mathrm{He}) - \lambda_2(T_\mathrm{He} - T_\mathrm{M}), \tag{C.2}$$

$$C_\mathrm{v}(T_\mathrm{M})\frac{\mathrm{d}T_\mathrm{M}}{\mathrm{d}t} = \lambda_2(T_\mathrm{He} - T_\mathrm{M}) - P_\mathrm{C}(T_\mathrm{M}). \tag{C.3}$$

Here F_heat gives the connection between the laser input power and the heat generated in the sample due to the excitonic relaxation and decay processes (compare section 2.2). For the parameters given in table 1, the results are shown in figure C.2. We can approximate the dependence with a function of the form

$$F_\mathrm{heat} = \alpha P_\mathrm{L} + \beta\left[P_\mathrm{XX}\left(\sqrt{1 + P_\mathrm{L}/P_\mathrm{XX}} - 1\right)\right]^2 \tag{C.4}$$

with the fit parameters $\alpha = 0.045$, $\beta = 0.014\,\mu\mathrm{m}^{-1}$ and $P_\mathrm{XX} = 16.67\,\mu\mathrm{W}$.

C.1. Heat capacities

Regarding the heat capacity of the *sample*, it is necessary to take into consideration that not only the crystal is heated by the laser, but, due to the good thermal contact supplied by the pressure on the sample, also the sample holder, which consisted of pure titanium. Therefore, we assumed the temperatures of sample and sample holder to be the same. The variation of the heat capacity of the sample Cu_2O with temperature is well approximated by the Debye model as a T^3 temperature dependence. A fit of measured data [68] by

$$C_{\mathrm{v}_{Cu_2O}} = AT^B, \tag{C.5}$$

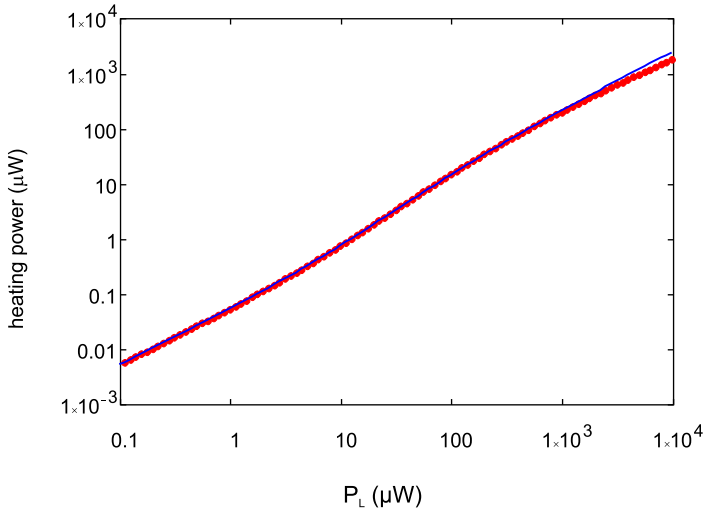

Figure C.2. Comparison of the amount of heating as a function of laser power. The full red dots are obtained from the rate model of section 2.2, the full line is the fit according to equation (C.4).

results in the parameters $A = 8.06 \pm 0.05\,\mathrm{J\,mol^{-1}\,K^{-4}}$ and $B = 3.0 \pm 0.05$. For the specimen holder, we consider only the superconducting state below the critical temperature ($T_{c_{Ti}} = 0.4\,\mathrm{K}$ [69]), restricting the following analysis to the interesting case of $T_S < 0.4\,\mathrm{K}$. Here, the heat capacity is composed of an electron and a phonon part, $C_{v_{Ti}} = C_{v_e} + C_{v_{ph}}$. While the phonon part is negligible, the electron part is given by

$$C_{v_{Ti}} = C_{v_e} = C_{Ti}\,\gamma_{Ti}\,T_c\,\exp\left(\frac{-1.5T_c}{T}\right), \tag{C.6}$$

with $C_{Ti} = 9.17$ and the Sommerfeld constant $\gamma_{Ti} = 3.3\,\mathrm{mJ\,mol^{-1}K^{-2}}$ [69].

Experimental data for the *heat capacity of the helium mixture* [70] for different concentrations of ^{3}He in ^{4}He were interpolated to a concentration of $x_{^3He} = 6.4\%$ and fitted resulting in a dependence

$$C_v(T_{He,M}) = D\left(\frac{T_{He,M}}{\mathrm{K}}\right)^E + F, \tag{C.7}$$

with $D = 0.417\,\mathrm{J\,mol^{-1}\,K^{-1}}$, $E = 6.117$ and $F = 0.7\,\mathrm{J\,mol^{-1}K^{-1}}$.

C.2. Cooling power

For the description of the cooling power P_C of the dilution process, where the ^{3}He-atoms flow from the ^{3}He-rich (concentrated) to the -poor (dilute) phase, we consider the enthalpy of the system. By assuming that pure ^{3}He flows through the heat exchangers into the mixing chamber with the dilute phase, the cooling power is given in accordance with [67] by

$$P_C = \dot{n}_3[H_d(T) - H_c(T)] \tag{C.8}$$

$$= \dot{n}_3[95T_M^2 - 11T_W^2], \tag{C.9}$$

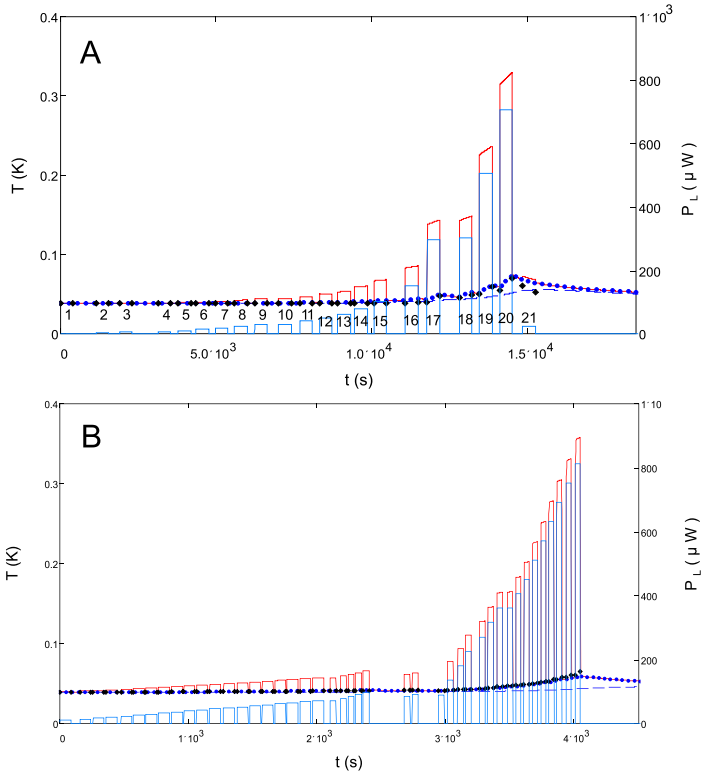

Figure C.3. The numerical solution of the system of differential equations expressed as the variation of temperature (cf equations (C.2) and (C.3)) with measurement time for $\lambda_1 = 6 \times 10^{-4}$ and $\lambda_2 = 27 \times 10^{-4}\,\mathrm{W\,K^{-1}}$. The solid red framed bars represent the temperature of the sample T_S, the blue dotted curve shows the temperature of the surrounding helium bath T_{He} and the blue dashed line describes the temperature in the mixing chamber T_M. The solid blue framed bars are the representation of the measured incoming laser power P_L. The measured helium temperatures are shown as black diamonds.

with the molar flow rate $\dot{n}_3$, the temperature in the mixing chamber T_M and the temperature behind the heat exchanger T_W. To obtain the unknown parameters of equation (C.9), we take as calibration points the lowest temperature reached without any heat load $T_M = 20\,\mathrm{mK}$ and $P_C = 100\,\mu\mathrm{W}$ at $T_M = 100\,\mathrm{mK}$. From these data we obtain $\dot{n}_3 = 1.25 \times 10^{-4}\,\mathrm{mol\,s^{-1}}$ and $T_W = 0.115\,\mathrm{K}$. From this cooling power we have to subtract the heat load P_0 due to the cryostat windows, which leads to a minimum temperature of $T_M = 38\,\mathrm{mK}$ corresponding to a power of $P_0 = 13.4\,\mu\mathrm{W}$.

C.3. Determination of the temperatures in the cryostat system

To obtain the temperatures of the different parts of the thermal network from the system of coupled differential equations, it is necessary to specify the amount of substance in the system.

The Cu_2O specimen is a cube with an edge length of 3 mm, a molar mass of $M = 143.09\,\mathrm{g\,mol^{-1}}$ and a density of $\rho = 6.48\,\mathrm{g\,cm^{-3}}$. Hence, the amount of substance inside the cube is $n_{Cu_2O} = 1.398 \times 10^{-3}\,\mathrm{mol}$. From the measured weight of the titanium sample holder

of $m = 26\,\mathrm{g}$ and a molar mass of $M = 47.9\,\mathrm{g\,mol^{-1}}$, we obtain $n_{\mathrm{Ti}} = 0.5\,\mathrm{mol}$. The amount of substance in the helium mixture can only be estimated. In our system, a 15% helium ^{3}He/^{4}He mixture of approximately $V = 400\,\mathrm{l}$ circulates under a pressure of $p = 0.8\,\mathrm{bar}$. That leads to an amount of $n_{^3\mathrm{He}/^4\mathrm{He}}$ mixture $= 14.3\,\mathrm{mol}$ from which only about two thirds are in the mixing chamber. For our calculations, we assume that 1 mol is in the bath and 2.75 mol is in the mixing chamber. Then the only quantities which have still to be specified are the heat conductivities $\lambda_{1,2}$. This was done by adjusting the solutions of the coupled differential equations to different measurements until all the data could be described by the same set of parameters. As examples we show in figure C.3 the results for the series of measurements from figures 5 and 6.

The calculations were done with $\lambda_1 = 6 \times 10^{-4}$ and $\lambda_2 = 27 \times 10^{-4}\,\mathrm{W\,K^{-1}}$ and show an almost quantitative agreement with the experimental data, despite very large changes in laser power (solid blue framed bars) during the measurements, which indicates the correctness of our model.

References

[1] Blatt J M, Böer K W and Brandt W 1962 *Phys. Rev.* **126** 1691
[2] Moskalenko S A 1962 *Fiz. Tverd. Tela* **4** 276
Moskalenko S A 1962 *Sov. Phys. Solid State* **4** 276 (Engl. transl.)
[3] Fröhlich D, Kenklies R, Uihlein C and Schwab C 1979 *Phys. Rev. Lett.* **43** 1260
[4] Snoke D W 2002 *Science* **298** 1368
[5] Alvermann A, Littlewood P B and Fehske H 2011 *Phys. Rev.* B **84** 035126
[6] Semkat D, Richter F, Kremp D, Manzke G, Kraeft W-D and Henneberger K 2009 *Phys. Rev.* B **80** 155201
[7] Manzke G, Semkat D, Richter F, Kremp D and Henneberger K 2010 *J. Phys.: Conf. Ser.* **210** 012020
[8] Fröhlich D, Kulik A, Uebbing B, Mysyrowicz A, Langer V, Stolz H and von der Osten W 1991 *Phys. Rev. Lett.* **67** 2343
[9] Waters R G, Pollak F H, Bruce R H and Cummins H Z 1980 *Phys. Rev.* B **21** 1665
[10] Pethick C J and Smith H 2002 *Bose–Einstein Condensation in Dilute Gases* (Cambridge: Cambridge University Press)
[11] Trauernicht D P, Wolfe J P and Mysyrowicz A 1986 *Phys. Rev.* B **34** 2561
[12] Snoke D W, Wolfe J P and Mysyrowicz A 1990 *Phys. Rev. Lett.* **64** 2543
[13] Lin J-L and Wolfe J P 1993 *Phys. Rev. Lett.* **71** 1222
[14] Snoke D W and Negoita V 2000 *Phys. Rev.* B **61** 2904
[15] Yoshioka K, Chae E and Kuwata-Gonokami M 2011 *Nature Commun.* **2** 328
[16] Denev S and Snoke D W 2002 *Phys. Rev.* B **65** 085211
[17] Schwartz R, Naka N, Kieseling F and Stolz H 2012 *New J. Phys.* **14** 023054
[18] Sandfort Ch, Brandt J, Finke Ch, Fröhlich D, Bayer M, Stolz H and Naka N 2011 *Phys. Rev.* B **84** 165215
[19] Deng H, Haug H and Yamamoto Y 2010 *Rev. Mod. Phys.* **82** 1489
[20] Szymańska M H, Keeling J and Littlewood P B 2007 *Phys. Rev.* B **75** 195331
[21] Aßmann M, Tempel J-S, Veita F, Bayer M, Rahimi-Iman A, Löffler A, Höfling S, Reitzenstein S, Worschech L and Forchel A 2011 *Proc. Natl Acad. Sci. USA* **108** 1804
[22] Brandt J, Fröhlich D, Sandfort Ch, Bayer M, Stolz H and Naka N 2007 *Phys. Rev. Lett.* **99** 217403
[23] Wolfe J P, Markiewicz R S, Kittel C and Jeffries C D 1977 *Phys. Rev.* B **15** 1988
[24] Naka N and Nagasawa N 2002 *Phys. Rev.* B **65** 075209
[25] Naka N, Akimoto I, Shirai M and Kan'no K 2012 *Phys. Rev.* B **85** 035209
[26] Kavoulakis G M, Baym G and Wolfe J P 1996 *Phys. Rev.* B **53** 7227
[27] Ashcroft N W and Mermin N D 1976 *Solid State Physics* (Fort Worth, TX: Harcourt Brace College Publishers)
[28] Som S, Kieseling F and Stolz H 2012 *J. Phys.: Condens. Matter* **24** 335803

[29] Jörger M, Fleck T, Klingshirn C and von Baltz R 2005 *Phys. Rev.* B **71** 235210
[30] Kubouchi M, Yoshioka K, Shimano R, Mysyrowicz A and Kuwata-Gonokami M 2005 *Phys. Rev. Lett.* **94** 016403
[31] Stolz H and Semkat D 2010 *Phys. Rev.* B **81** 081302
[32] Griffin A 1996 *Phys. Rev.* B **53** 9341
[33] Dalfovo F, Giorgini S, Pitaevskii L P and Stringari S 1999 *Rev. Mod. Phys.* **71** 463
[34] Bergeman T, Feder D L, Balazs N L and Schneider B I 2000 *Phys. Rev.* A **61** 063605
[35] Proukakis N P and Jackson B 2008 *J. Phys. B: At. Mol. Opt. Phys.* **41** 203002
[36] Bányai L A, Bundaru A M and Haug H 2004 *Phys. Rev.* B **70** 045201
[37] Ho T L and Shenoy V B 1996 *Phys. Rev. Lett.* **77** 3276
[38] Bashkin E P and Vagov A V 1997 *Phys. Rev.* B **56** 6207
[39] Shi H, Zheng W M and Chui S T 2000 *Phys. Rev.* A **61** 063613
[40] Zhang W, Yi S and You L 2004 *Phys. Rev.* A **70** 043611
[41] Chang M-S, Qin Q, Zhang W, You L and Chapman M S 2005 *Nature Phys.* **1** 111
[42] Shelykh I A, Malpuech G and Kavokin A V 2005 *Phys. Status Solidi* a **202** 2614
[43] Kasprzak J, André R, Dang L S, Shelykh I A, Kavokin A V, Rubo Yu G, Kavokin K V and Malpuech G 2007 *Phys. Rev.* B **75** 045326
[44] Sobkowiak S, Semkat D, Stolz H, Koch Th and Fehske H 2010 *Phys. Rev.* B **82** 064505
[45] Sheboul M I and Ekardt W 1976 *Phys. Status Solidi* b **73** 165
[46] Ciuti C, Savona V, Piermarocchi C, Quattropani A and Schwendimann P 1998 *Phys. Rev.* B **58** 7926
[47] Okumura S and Ogawa T 2001 *Phys. Rev.* B **65** 035105
[48] Zimmermann R and Schindler Ch 2007 *Solid State Commun.* **144** 395
[49] Schindler Ch and Zimmermann R 2008 *Phys. Rev.* B **78** 045313
[50] Combescot M, Betbeder-Matibet O and Dubin F 2008 *Phys. Rep.* **463** 215
[51] Shi H, Verechaka G and Griffin A 1994 *Phys. Rev.* B **50** 1119
[52] Haug H and Kranz H 1983 *Z. Phys.* B **53** 151
[53] Kreingold F I and Makarov V L 1975 *Sov. Phys. Semicond.* **8** 962
[54] Born M and Wolf E 1999 *Principles of Optics* 7th edn (Cambridge: Cambridge University Press)
[55] Shumway J and Ceperley D M 2001 *Phys. Rev.* B **63** 165209
[56] Ivanov I A, Mitroy J and Varga K 2002 *Phys. Rev.* A **65** 022704
[57] Shumway J and Ceperley D M 2005 *Solid State Commun.* **134** 19
[58] Sharma H, Kumari K and Chakraborty S 2009 *Eur. Phys. J.* D **53** 189
[59] Richter F, Florian M and Henneberger K 2008 *Phys. Rev.* B **78** 205114
[60] Hohenberg P C and Martin P C 1965 *Ann. Phys., NY* **34** 291
[61] Nägerl J S, Stabenau B, Böhne G, Dreher S, Ulbrich R G, Manzke G and Henneberger K 2001 *Phys. Rev.* B **63** 235202
[62] Semkat D, Richter F, Kremp D, Manzke G, Kraeft W-D and Henneberger K 2010 *J. Phys.: Conf. Ser.* **220** 012005
[63] Brandt J, Felbier P, Fröhlich D, Sandfort Ch, Bayer M and Stolz H 2010 *Phys. Rev.* B **81** 155214
[64] Ell C, Ivanov A L and Haug H 1998 *Phys. Rev.* B **57** 9663
[65] Snoke D W, Braun D and Cardona M 1991 *Phys. Rev.* B **44** 2991
[66] O'Hara K E and Wolfe J P 2000 *Phys. Rev.* B **62** 12909
[67] Enss Ch and Hunklinger S 2000 *Tieftemperaturphysik* (Berlin: Springer)
[68] Gregor L V 1962 *J. Phys. Chem.* **66** 1645
[69] Martienssen W and Warlimont H 2005 *Springer Handbook of Condensed Matter and Materials Data* (Berlin: Springer)
[70] De Bruyn Ouboter R, Taconis K W, Le Pair C and Beenakker J J M 1960 *Physica* **26** 853

A.9

Artikel 9

D. Semkat, S. Sobkowiak, G. Manzke, and H. Stolz:

Comment on "Condensation of Excitons in a Trap"

Nano Lett. **12**, 5055 (2012)

NANO LETTERS

Letter

pubs.acs.org/NanoLett

Comment on "Condensation of Excitons in a Trap"

Dirk Semkat,* Siegfried Sobkowiak, Günter Manzke, and Heinrich Stolz

Institut für Physik, Universität Rostock, D-18051 Rostock, Germany

Condensation of excitons is still a fascinating topic of solid state physics. In a recent Letter "Condensation of Excitons in a Trap",[1] High et al. claim to have observed a condensed state in a system of indirect excitons in double quantum well structures within an electrostatic potential trap. As in every Bose−Einstein condensate, spontaneous coherence of matter waves should emerge in the exciton system. This coherence is transferred to the decay luminescence and thus should be observable in the light emission from the exciton cloud. Indeed, the authors have observed in a series of experiments a pronounced increase of the coherence of the light emitted from the excitons either by lowering the temperature or by increasing the power of the laser exciting the excitons (compare Figures 3d,e, 4, and 5 of ref 1).

The coherence properties of the emitted light were measured with the well-known technique of shift interferometry.[2] Here two images of the same object, shifted by a small amount of δ, are superimposed, and by varying the phase delay between the two light paths, interference fringes are generated (see Figure 2 of ref 1). To determine the interference contrast, the authors use the simple formula $C = (I_{12} - I_1 - I_2)/2(I_1I_2)^{1/2}$. Further support for the interpretation of the occurrence of a "condensate" is derived by the authors from a simple ideal Boson model for the excitons captured in a harmonic trap from the critical temperature $T_c = (6^{1/2})/(\pi)\hbar\omega_{2d}$ with $\omega_{2d} = (\omega_x\omega_y)^{1/2}$ being the $2d$ oscillator frequency. With the assumptions for the trap oscillator frequencies the authors give, this indeed would lead to a critical temperature for BEC for $N \simeq 3 \times 10^3$ excitons in the trap of 2 K.

As will be shown in this comment, there are several objections against the statements in ref 1 based on a rigorous theory of shift interferometry as well as on the thermodynamic properties of a dense interacting exciton gas in a potential trap.

Theory of Shift Interferometry. We start with a single point emitter at position x_o,y_o in the object plane at $-d_1$, which is imaged by a lens. The amplitude of the light field at a point (x_i,y_i) in the image plane at d_2 is then given by[3]

$$E_I(x_i, y_i) = \frac{M}{d_1\lambda^2}\exp[-ikd_1(1 + 1/M)] \times \exp\left[-\frac{ikM}{2d_1}(x_i^2 + y_i^2)\right]E_O(x_o, y_o) \times \exp\left[-\frac{ik}{2d_1}(x_o^2 + y_o^2)\right]\cdot P_{2d}(x_o + Mx_i, y_o + My_i) \quad (1)$$

with $E_O(x,y)$ denoting the field amplitude of the emitter and $P_{2d}(x,y)$ the amplitude point spread function (PSF) of the lens. $M = d_1/d_2$ is the system magnification.

In shift interferometry we superimpose on this image that of an identical object shifted by δ in, for example, the x direction and with an additional phase Φ. Its field is given by

$$E_I'(x_i, y_i, \delta) = \frac{M}{d_1\lambda^2}\exp[-ikd_1(1 + 1/M) + i\Phi] \times \exp\left[-\frac{ikM}{2d_1}(x_i^2 + y_i^2)\right]E_O(x_o, y_o) \times \exp\left[-\frac{ik}{2d_1}((x_o - \delta)^2 + y_o^2)\right] \times P_{2d}(x_o - \delta + Mx_i, y_o + My_i) \quad (2)$$

Using the notation of ref 1, the interference pattern of a single point emitter is given by

$$I_{12}(x_i, y_i, \delta) = |E_I(x_i, y_i) + E_I'(x_i, y_i, \delta)|^2 = I_1 + I_2 + I_{inter} \quad (3)$$

While I_1 and I_2 are the images of the two shifted objects, the interference term is given by

$$I_{inter} = 2\mathrm{Re}[E_I(x_i, y_i)E_I'^*(x_i, y_i, \delta)] \propto 2|E_O(x_o, y_o)|^2\mathrm{Re}\left\{\exp\left[-\frac{ik}{d_1}x_o\delta - i\Phi\right] \times P_{2d}(x_o + Mx_i, y_o + My_i) \times P_{2d}^*(x_o - \delta + Mx_i, y_o + My_i)\right\} \quad (4)$$

In the following, we are interested only in the case of an incoherently emitting cloud of thermal excitons. Then we can approximate the first-order field correlation function $G_O(x, y, x', y') = E_O(x, y)E^*_O(x', y')$, which represents the mutual coherence function of the emitter[4] by

$$G_O(x, y, x', y') = I_O(x, y, x', y')\delta(x - x')\delta(y - y') \quad (5)$$

with $I_O = |E_O(x_o, y_o)|^2$ representing the intensity distribution of the emitter. Therefore, we obtain the interference pattern of the total emission by integrating eq 4 over the whole emitter. This gives the following expression

$$I_{inter}(x_i, y_i) \propto 2\int\int I_O(x_o, y_o)\mathrm{Re}\left\{\exp\left[-\frac{ik}{d_1}x_o\delta - i\Phi\right] \times P_{2d}(x_o + Mx_i, y_o + My_i) \times P_{2d}^*(x_o - \delta + Mx_i, y_o + My_i)\right\}dx_o dy_o \quad (6)$$

Received: July 6, 2012
Published: July 23, 2012

dx.doi.org/10.1021/nl302504h | Nano Lett. 2012, 12, 5055−5057

Equation 6 is the central relation for shift interferometry. It shows that the interference pattern depends not only on the PSF but also on the intensity distribution of the emitting source!

To obtain quantitative results, we need the PSF of the actual imaging setup, which fortunately can be obtained from Figure 2S of the supporting material of ref 1. For our purposes, the point spread function can be approximated quite well by a simple Gaussian,[5]

$$P_{2d}(x, y) = P_0 \exp\left(-\frac{x^2 + y^2}{\sigma_p^2}\right) \tag{7}$$

Noting that the intensity distribution shown in Figure 2S of ref 1 is given by the square of the PSF, eq 7, we obtain $\sigma_p = 2.0\ \mu$m.

Representing the intensity distribution of the exciton cloud also by a Gaussian with different halfwidths in x- and y-directions as

$$I_O(x, y) = I_0 \exp\left[-\left(\frac{x}{\sigma_x}\right)^2 - \left(\frac{y}{\sigma_y}\right)^2\right] \tag{8}$$

the interference pattern can be calculated analytically. Fortunately, due to the choice of the PSF, the final result factorizes into a product of x- and y-dependent functions, so that for a shift in x-direction, the result for the interference contrast $C(\sigma_x, \delta) = (I_{12} - I_1 - I_2)/2(I_1 I_2)^{1/2}$ depends only on δ and σ_x.

As a first result we demonstrate in Figure 1 that, contrary to the statement in ref 1, the image of a point source (full red line)

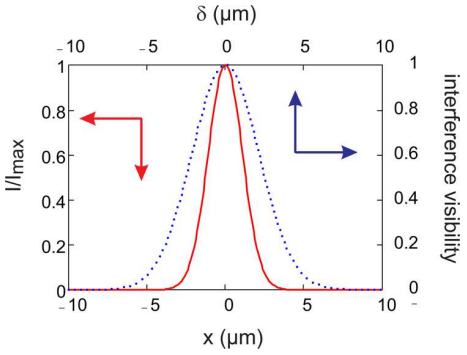

Figure 1. Comparison of the relative intensity of a point source (full red line) with the interference visibility function (blue dashed line) for a PSF given by eq 7 with $\sigma_P = 2.0\ \mu$m and a source size $\sigma_x = 6\ \mu$m (see eq 8).

is different from the interference visibility function; that is, the contrast as a function of shift δ of an incoherent source is much larger than the optical resolution. Therefore, Figure 1S of ref 1 seems to be incorrect, and the scale of upper and lower abscissa must differ by a factor of 1.4. By comparing Figures 1b and 2c of ref 1, one can deduce that it must be the shifts given in ref 1 (in the following: δ_B) that have to be scaled by $V = 1.4$ to get consistency ($\delta = V{\cdot}\delta_B$).

The interference contrast at $x = 0$ is shown in Figure 2 as a function of the source size for different shifts. Looking more closely at the curve for $\delta_B = \delta/V = 4\ \mu$m, our theory predicts a contrast of 0.07 at source sizes above 6 μm HWHM in agreement with the experiment. Reducing the source size, the

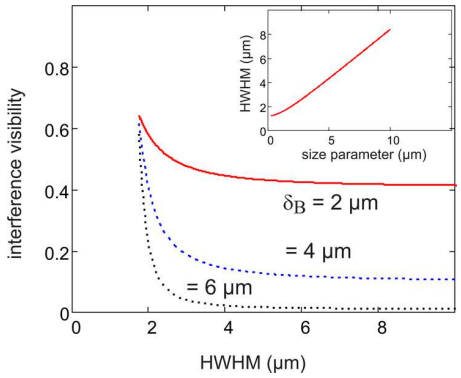

Figure 2. Contrast at $x = 0$ for different effective shifts $\delta_B = \delta/V$ as a function of the HWHM of the exciton cloud, which is given in the inset as a function of the size parameter σ_x (see eq 8). To allow a direct comparison with the results of ref 1. the contrast was scaled by 0.65, which is the maximum contrast in the experiments.

contrast increases reaching values of about 0.2−0.3 for sizes of 2 μm similar to those measured experimentally (Figure 3e of ref 1). This shows that our theory is able to reproduce the experimental results of ref 1 almost quantitatively without the necessity of a coherent condensate.

Thermodynamics. To analyze the thermodynamics of the exciton gas in the trap, we use a Hartree−Fock−Bogoliubov−Popov (HFBP) theory (for an overview, see ref 6) which we have recently applied to excitons in bulk Cu_2O.[7] We use a local density approximation well-justified by the extension of the trap (Figure 1 in ref 1) which is, even in the narrower y-direction, still large compared to typical length scales, for example, the 2d excitonic Bohr radius.

Applying the HFBP theory in local density approximation to the 2d case, the densities of thermally excited n^T and of condensed excitons n^c (in Thomas−Fermi approximation) in an external potential V_{ext} form a coupled system of equations,

$$n^T(r) = \int \frac{d^2k}{(2\pi)^2}\left[\frac{\mathcal{L}(k, r)}{E(k, r)}\left(n_B(E(k, r)) + \frac{1}{2}\right) - \frac{1}{2}\right] \times \Theta(E^2(k, r)) \tag{9}$$

$$n^c(r) = \frac{1}{U_0}[\mu - V_{ext}(r) - 2U_0 n^T(r)] \times \Theta(\mu - V_{ext}(r) - 2U_0 n^T(r)) \tag{10}$$

Here n_B is the Bose distribution, and the quasiparticle energy E is given by (compare[7])

$$E(k, r) = \sqrt{\mathcal{L}(k, r)^2 - (U_0 n^c(r))^2} \tag{11}$$

with

$$\mathcal{L}(k, r) = \hbar^2 k^2/2M + V_{ext}(r) - \mu + 2U_0 n(r) \tag{12}$$

The total density is given by $n = n^T + n^c$, μ is the global chemical potential, and U_0 is the strength of the interexcitonic interaction. We extract the latter parameter from the experimentally given energy shift of $\delta E = 1.3$ meV at $n = 3 \times 10^{10}$ cm^{-2} by $\delta E = 2U_0 n$ leading to $U_0 = 2.2\ \mu$eV·μm^2. The trap potential was taken directly from Figure 1c and d of ref 1.

In Figure 3, the critical particle number N_{crit} for Bose−Einstein condensation according to eqs 9−12 is presented in dependence on the temperature by the black curve. The dotted

dx.doi.org/10.1021/nl302504h | Nano Lett. 2012, 12, 5055−5057

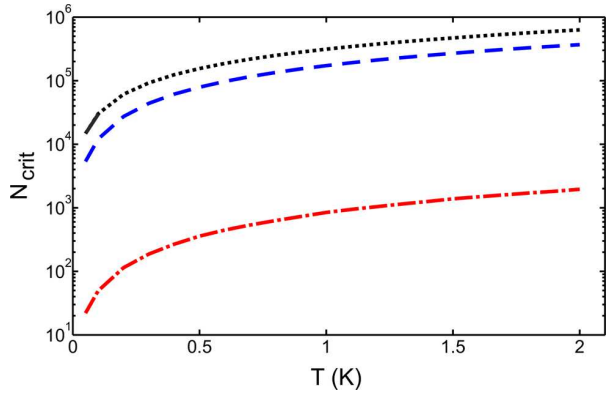

Figure 3. Critical particle number for BEC vs temperature in the trap. Black line: interacting case (solid: particle number captured by the trap, dotted: particle number too large to be captured). Dashed blue line: weakly interacting case ($U_0/100$). Dash−dotted red line: noninteracting case.

part of the line denotes the region, where the particle number exceeds the capacity of the trap. Additionally, corresponding curves are shown for the weakly interacting case ($U_0/100$; dashed blue line) and the noninteracting case (dash−dotted red line).

For a temperature of 2 K, we obtain a critical particle number of about $N_{crit} \simeq 6.3 \times 10^5$ corresponding to a (homogeneous) density of about 6.3×10^{12} cm^{-2}, much higher than the estimate given in ref 1. This discrepancy is obviously due to the rather strong exciton−exciton interaction which has been neglected there. Even with the much weaker interaction of $U_0/100$, N_{crit} is still about 3.7×10^5. Neglecting the interaction, our theory yields $N_{crit} \simeq 2 \times 10^3$ consistent with the noninteracting estimate.

Due to the finite trap depth, there is a temperature-dependent maximum exciton number N_{max} in the trap determined by the condition that the chemical potential reaches the excitonic band gap just outside the trap. The critical curve is only meaningful if $N_{crit} \leq N_{max}$. For the interacting case (black line in Figure 3) this holds only at the lowest temperatures of about 50 mK; that is, the maximum exciton number for $T \gtrsim 50$ mK is always undercritical in the given trap.

Conclusions. As has been shown in this comment, there are several objections against the statements in ref 1 which together make the claims of the Letter highly questionable. First, based on the theory of imaging of partially coherent light, we have derived a rigorous expression for the contrast of a shift interferometer with an arbitrary source. This equation allows us to explain the experimental observations simply by the also observed reduction in spot size (see Figure 3e), without any necessity to assume the occurrence of a condensate. Second, we derived from a 2d Hartree−Fock−Bogoliubov−Popov theory the thermodynamic properties of a dense interacting exciton gas in a potential trap. Using the trap parameters as given in ref 1 we find at $T = 100$ mK the critical particle number of $N_{crit} \simeq 3 \times 10^4$, which is too high to be captured in the trap.

AUTHOR INFORMATION

Notes

The authors declare no competing financial interest.

ACKNOWLEDGMENTS

This work was supported by the Deutsche Forschungsgemeinschaft (Collaborative Research Center SFB 652).

REFERENCES

(1) High, A. A.; Leonard, J. R.; Remeika, M.; Butov, L. V.; Hanson, M.; Gossard, A. C. *Nano Lett.* **2012**, *12*, 2605.
(2) Barrett, H. H.; Myers, K. J. *Foundations of Image Science*; John Wiley & Sons: New York, 2004.
(3) Gu, M. *Advanced Optical Imaging Theory*; Springer-Verlag: Berlin, 2000.
(4) Born, M.; Wolf, E. *Principles of Optics*, 7th ed.; Cambridge University Press: Cambridge, 1999.
(5) Zhang, B.; Zerubia, J.; Olivo-Marin, J.-C. *Appl. Opt.* **2007**, *46*, 1819.
(6) Proukakis, N. P.; Jackson, B. *J. Phys. B* **2008**, *41*, 203002.
(7) Sobkowiak, S.; Semkat, D.; Stolz, H.; Koch, T.; Fehske, H. *Phys. Rev. B* **2010**, *82*, 064505.

A.10

Artikel 10

S. Sobkowiak, D. Semkat, and H. Stolz:

Modeling of the thermalization of trapped paraexcitons in Cu_2O at ultra-low temperatures

Phys. Rev. B **90**, 075206 (2014)

Modeling of the thermalization of trapped paraexcitons in Cu_2O at ultralow temperatures

S. Sobkowiak,* D. Semkat, and H. Stolz
Institut für Physik, Universität Rostock, 18051 Rostock, Germany

(Received 24 June 2014; revised manuscript received 11 August 2014; published 26 August 2014; corrected 12 September 2014)

We theoretically analyze the relaxation of paraexcitons in cuprous oxide due to exciton-phonon and exciton-exciton scattering. Particular attention is paid to the evolution of the distribution function as well as to the cooling process of the exciton gas. The results underline the importance of interexcitonic collisions at moderate and higher densities which prevent the formation of the typical bottleneck and accelerate the thermalization at ultralow temperatures significantly. Furthermore, we discuss the impact of strain on the exciton-phonon coupling and show that the overall cooling process of the excitons benefits from strain induced effects. However, for very low lattice temperatures ($T \ll 1.0$ K), the process of thermalization is slow, and the excitons might not reach the lattice temperature within their finite lifetime.

DOI: 10.1103/PhysRevB.90.075206 PACS number(s): 71.35.Lk, 63.20.kk, 67.85.Jk

I. INTRODUCTION

Cuprous oxide (Cu_2O) has been in the focus of experimental studies for decades and continues to be of interest today [1–7]. Due to the long lifetime and the high binding energy, paraexcitons in Cu_2O are a good candidate for the experimental realization of an excitonic Bose-Einstein condensate (BEC) in a three-dimensional system. In typical experiments, excitons created by a pump laser are collected in stress induced potential traps in order to create sufficiently high densities. To cool the excitons to ultralow temperatures, the Cu_2O specimen is placed inside a ^{3}He/^{4}He dilution cryostate. The crystal itself is cooled by the surrounding helium bath, and the excitons in turn are cooled via interaction with the crystal lattice (phonons). Obviously, the creation of the lowest possible bath temperature and, therefore, the lowest possible exciton temperature is favorable in the pursuit of creating an excitonic BEC [8]. Recently, two groups [6,7] reported helium bath temperatures of the order of 100 mK with the lowest value being [6] 35 mK. It is natural to wonder how these extremely low temperatures affect the thermalization of the excitons, which only exist for a finite lifetime. Even though this question is important to address, a thorough theoretical investigation of the thermalization processes in these types of experiments has to our knowledge not yet been carried out. Such an analysis is especially important since it has long been known that a bottleneck effect can prevent effective cooling via acoustic phonons at very low temperatures [9].

Additionally, to determine the exciton temperature from experimental data, the luminescence spectrum is fitted by a Bose distribution. However, even the lowest reported values of these "spectral temperatures" ($T_S = 0.35$ K in Ref. [6] and $T_S = 0.097$ K in Ref. [7]) are still well above the corresponding helium bath temperatures, indicating a nonequilibrium state of the system. Therefore, a theoretical analysis of the different heating and cooling mechanisms is needed to improve the understanding of the recent experimental results and stimulate further progress.

As a first step, in this paper we theoretically examine the relaxation process of the $1s$ paraexcitons of the so-called yellow series in Cu_2O. These excitons consist of a hole in the Γ_7^+ valence band and an electron in the Γ_6^+ conduction band, and they have a Γ_2^+ symmetry. The experimentally determined lifetimes for these excitons are [7] $\tau = 300$ ns and [5] $\tau = 650$ ns and hence remarkably long. The main question we want to address is: Do the excitons reach the crystal lattice temperature of the order of 100 mK within their finite lifetime? For this purpose, the excitons will be modeled as a homogeneous gas (neglecting the trap potential) coupled to a bath of acoustic phonons without considering the Auger-like two-body decay. Furthermore, we will assume that the crystal lattice and the helium bath have the same temperature at all times. The results can be considered as a lower boundary for the achievable temperatures in actual experiments, since the Auger-like decay and a possible heating of the specimen by the pump laser will only hinder the cooling process.

The typical exciton densities created by pulsed excitation experiments vary from 10^{12} cm^{-3} to 10^{16} cm^{-3}. At high densities, exciton-exciton (X-X) collisions will play an important role. However, as we will show in this paper, at ultralow temperatures, the contribution from X-X scattering cannot be neglected even for low densities due to the bottleneck effect. Therefore, our model will include exciton-phonon (X-Ph) as well as X-X scattering.

II. THEORY

Taking into account collisions with phonons as well as X-X scattering, the Boltzmann equation for the homogeneous system under consideration reads

$$\frac{\partial f_{\mathbf{k}}(t)}{\partial t} = C_{\text{X-X}} + C_{\text{X-Ph}}. \tag{1}$$

A. Exciton-exciton scattering

Assuming hard sphere scattering, the X-X collision term $C_{\text{X-X}}$ is given by [10]

$$C_{\text{X-X}} = \frac{g^2}{\hbar(2\pi)^5} \int d\mathbf{k}_2 d\mathbf{k}_3 d\mathbf{k}_4 [(1+f_{\mathbf{k}})(1+f_{\mathbf{k}_2}) f_{\mathbf{k}_3} f_{\mathbf{k}_4} - f_{\mathbf{k}} f_{\mathbf{k}_2}(1+f_{\mathbf{k}_3})(1+f_{\mathbf{k}_4})] \delta(\mathbf{k}+\mathbf{k}_2-\mathbf{k}_3-\mathbf{k}_4) \times \delta(E_{\mathbf{k}}+E_{\mathbf{k}_2}-E_{\mathbf{k}_3}-E_{\mathbf{k}_4}) \tag{2}$$

*siegfried.sobkowiak@uni-rostock.de

with the interaction strength g, the excitonic distribution functions $f_{\mathbf{k}}$, and the excitonic energies $E_{\mathbf{k}}$. Using the s-wave scattering length [11] $a_s = 2.1\ \mathrm{a_B}$, a Bohr radius of $a_B = 0.7$ nm and an exciton mass of [12] $m = 2.6\ \mathrm{m_0}$ (m_0: free electron mass) yields an interaction strength of $g = 4\pi\hbar^2 a_s/m = 0.54$ eV nm^3. For the dispersion relation we take $E_{\mathbf{k}} = \hbar^2\mathbf{k}^2/2m$.

B. Exciton-phonon scattering

For yellow paraexcitons in unstrained crystals, it follows from symmetry that only scattering by longitudinal acoustic (LA) phonons is possible. However, due to stress, the exciton states of the yellow series mix with the higher lying states of the so-called green series (hole in the Γ_8^+ valence band and electron in the Γ_6^+ conduction band) and scattering with transversal acoustic (TA) phonons becomes allowed (for details see Appendix). Both processes can be described by the X-Ph scattering term [9]

$$\begin{aligned} C_{\text{X-Ph}} = -\frac{\pi D^2}{\varrho v_s}\int \frac{d\mathbf{k}'}{(2\pi)^3}|\mathbf{k}'-\mathbf{k}|\Big\{\Big[f_{\mathbf{k}}\big(1+f^{\text{Ph}}_{\mathbf{k}-\mathbf{k}'}\big)(1+f_{\mathbf{k}'}) \\ -(1+f_{\mathbf{k}})f^{\text{Ph}}_{\mathbf{k}-\mathbf{k}'}f_{\mathbf{k}'}\Big]\delta(E_{\mathbf{k}}-E_{\mathbf{k}'}-\hbar\omega_{\mathbf{k}-\mathbf{k}'}) \\ +\Big[f_{\mathbf{k}}f^{\text{Ph}}_{\mathbf{k}'-\mathbf{k}}(1+f_{\mathbf{k}'})-(1+f_{\mathbf{k}})\big(1+f^{\text{Ph}}_{\mathbf{k}'-\mathbf{k}}\big)f_{\mathbf{k}'}\Big] \\ \times\delta(E_{\mathbf{k}}-E_{\mathbf{k}'}+\hbar\omega_{\mathbf{k}'-\mathbf{k}})\Big\}, \end{aligned} \tag{3}$$

with the deformation potential D, the crystal density [9] $\varrho = 6.11\times10^3$ kg/m^3, and the speed of sound v_s. The phonons are assumed to be in equilibrium at the helium bath temperature T_{Bath} at all times. Hence, their distribution function is given by $f^{\text{Ph}}_{\mathbf{k}'-\mathbf{k}} = [\exp(\hbar\omega_{\mathbf{k}'-\mathbf{k}}/k_B T_{\text{Bath}})-1]^{-1}$ with the phonon energy $\hbar\omega_{\mathbf{k}'-\mathbf{k}} = \hbar v_s|\mathbf{k}'-\mathbf{k}|$.

The LA- and TA-phonon scattering terms only differ by the values of v_s and D. The speeds of sound are well known and given by [13] $v_s^{\text{LA}} = 4.5\times10^3$ m/s and $v_s^{\text{TA}} = 1.3\times10^3$ m/s. The stress has almost no effect on the LA-phonon deformation potential, and the value given by [14] $D^{\text{LA}} = 1.68$ eV can be used. The deformation potential for the TA phonons, however, has to be calculated from the applied stress (see Appendix for details). For our calculations we used $D^{\text{TA}} = 0.064$ eV which corresponds to a very flat trap, hence simulating an almost homogeneous system with finite coupling to TA phonons.

III. RESULTS

Since the system is generally in nonequilibrium, it is not possible to define a temperature. Nevertheless, a measure is needed to describe the progression of the cooling process. For this purpose we will use the kinetic energy per particle and identify it with an "effective temperature" T_{eff} via

$$\frac{E}{N} = \frac{1}{N}\int\frac{d\mathbf{k}}{(2\pi\hbar)^3}\frac{\hbar^2k^2}{2m}f_{\mathbf{k}} = \frac{3}{2}k_B T_{\text{eff}}\,. \tag{4}$$

For our simulations we consider the following experimental situation. Orthoexcitons are primarily created via pulsed laser excitation and rapidly convert via phonon assisted processes to paraexcitons. The conversion process is on the order of a few ps and hence faster than the timescale we want to follow. The resulting paraexcitons have an energy of about 8 meV,

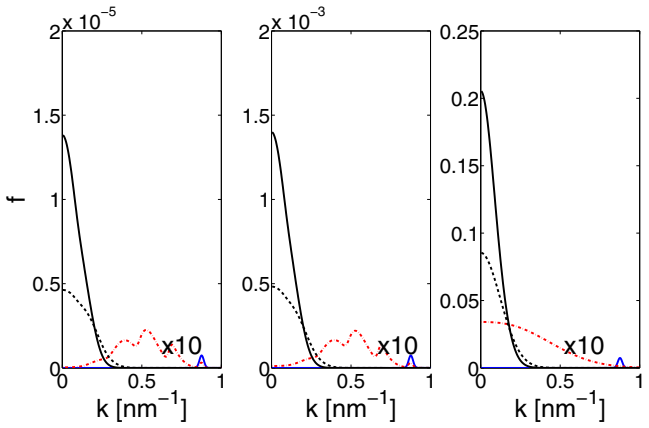

FIG. 1. (Color online) Distribution function at $t = 0$ ns (solid blue line), 0.05 ns (dash dotted red line), 0.5 ns (dashed black line), and 1.0 ns (solid black line) with $n = 10^{12}$ cm^{-3} (left panel), $n = 10^{14}$ cm^{-3} (middle panel), and $n = 10^{16}$ cm^{-3} (right panel). Excitons undergo X-X, X-Ph$^{\text{LA}}$, and X-Ph$^{\text{TA}}$ scattering at a lattice temperature of $T_{\text{Bath}} = 0.1$ K.

which corresponds to an initial "effective temperature" of approximately 87 K.

Starting from the initial distribution, we directly solved Eq. (1) using standard MATLAB routines. The X-X scattering term [Eq. (2)] was calculated using the method explained in Ref. [10], and the X-Ph scattering term [Eq. (3)] was computed directly.

Figure 1 shows the evolution of the distribution function in the first nanosecond for different exciton densities. In all cases, the distribution function relaxes quickly into a Bose-like shape. During this first nanosecond, the excitons undergo rapid cooling from an initial "effective temperature" of roughly 87 K down to about 4 K. This first phase of very effective cooling lasts approximately until 5 ns after the creation of the excitons. During this time, the X-Ph scattering terms are dominant and the influence of the X-X scattering is only important for very high densities (right panel in Fig. 1). Therefore, the excitons might be considered to be in the collisionless regime for densities of $n \leqslant 10^{15}$ cm^{-3} during this time. However, this is not the case for longer time scales, due to the bottleneck effect.

The second phase shown in Fig. 2 is characterized by a significant drop in the cooling efficiency. This is due to the fact that energy states lower than $E \leqslant E_0 = mv_s^2/2 = \hbar^2k_0^2/2m$ couple only via anti-Stokes scattering to the phonon bath and, therefore, effective cooling is no longer possible for these states [9]. This freezing out of phonons divides the excitons into two subsystems: excitons with energies lower than E_0 which can interact with phonons only by anti-Stokes scattering and excitons with energies higher than E_0 which can undergo Stokes- and anti-Stokes scattering. The corresponding k value for LA phonons is around $k_0^{\text{LA}} = 0.1$ nm^{-1} and for TA phonons around $k_0^{\text{TA}} = 0.03$ nm^{-1}. When the excitons only couple via LA phonons the resulting distribution functions are for all densities qualitatively the same (see Fig. 2). After the initial phase, the distribution function starts forming a plateau at low k values followed by a high energy tail (left column). For later

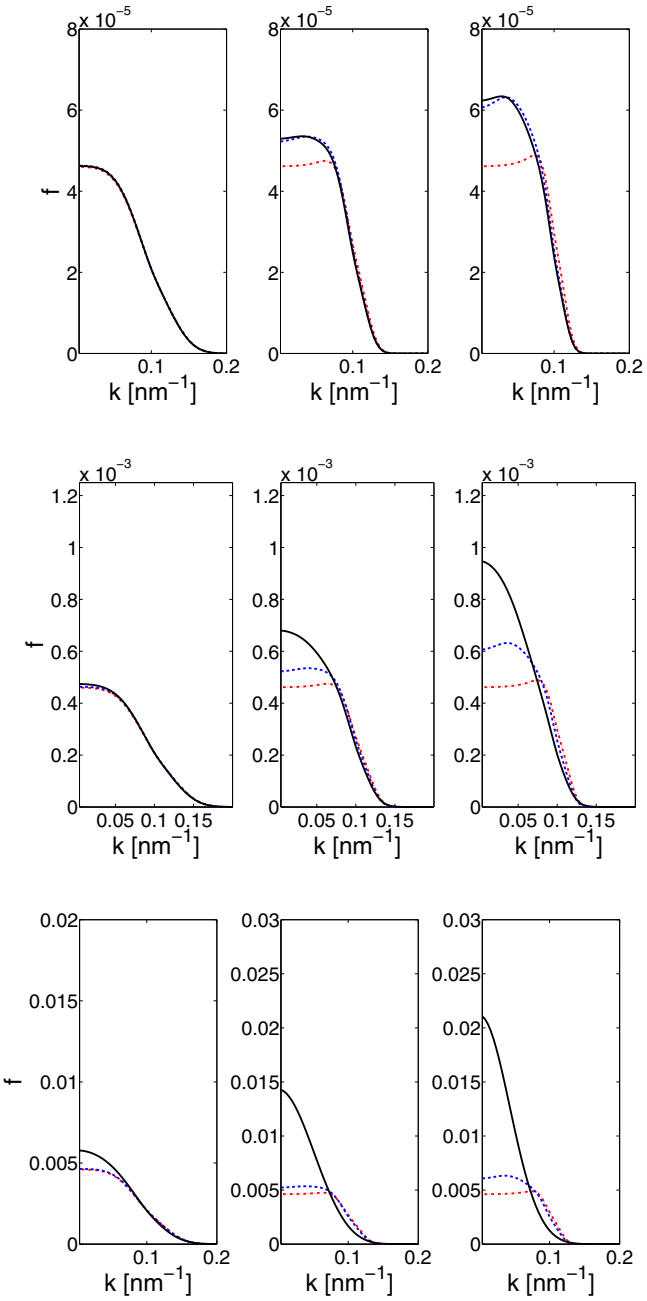

FIG. 2. (Color online) Distribution function after $t = 10$ ns (left column), 50 ns (middle column), and 100 ns (right column) at a bath temperature of $T_{\text{Bath}} = 0.1$ K and an exciton density of $n = 10^{12}$ cm^{-3} (top row), $n = 10^{13}$ cm^{-3} (middle row), and $n = 10^{14}$ cm^{-3} (bottom row). The different curves include the following scattering processes: X-Ph$^{\text{LA}}$ (dash-dotted red curve); X-Ph$^{\text{LA}}$ and X-Ph$^{\text{TA}}$ (dashed blue curve); X-X, X-Ph$^{\text{LA}}$, and X-Ph$^{\text{TA}}$ (solid black curve).

times, the plateau widens and the distribution function forms a peak below the k_0^{LA} value. At the same time the Maxwellian tail becomes increasingly steep. The result is a distribution function far away from equilibrium with very slow cooling. The additional inclusion of the TA phonons does not change this behavior qualitatively. Due to the lower k_0 value the peak and the plateau only shift towards lower k states. However, the

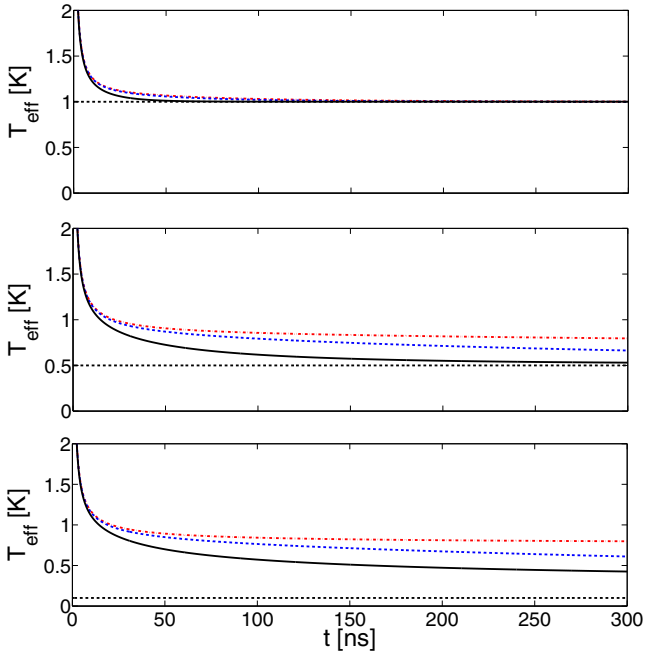

FIG. 3. (Color online) Development of the exciton's "effective temperature" T_{eff} for $n = 10^{14}$ cm^{-3} at a lattice temperature of 1 K (top panel), 0.5 K (middle panel), and 0.1 K. The different curves include the following scattering processes: X-Ph$^{\text{LA}}$ (dash-dotted red curve); X-Ph$^{\text{LA}}$ and X-Ph$^{\text{TA}}$ (dashed blue curve); X-X, X-Ph$^{\text{LA}}$, and X-Ph$^{\text{TA}}$ (solid black curve). The dashed black curve shows the respective bath temperatures.

additional inclusion of X-X scattering can dramatically alter the shape of the distribution function. Only for the extremely low density of $n = 10^{12}$ cm^{-3}, the X-X scattering is too weak to qualitatively change the results at this time scale. Therefore, only in this case the excitons can be truly considered to be in the collisionless regime. However, for densities $n \geqslant 10^{13}$ cm^{-3}, the X-X scattering prevents the formation of the plateau and brings the distribution into a Bose-like shape, resulting in an improved overall cooling of the excitons. This can be easily understood by considering the following scenario. Assume two excitons, both having the wave vector k_0 before a collision. After the scattering, one has $k_1 > k_0$ and the other $k_2 < k_0$, with $k_1 + k_2 = 2k_0$ since $C_{\text{X-X}}$ is momentum conserving. The exciton with k_1 can be cooled effectively by phonons again and the exciton with k_2 has been scattered into a lower energy state. Hence, the X-X scattering (in conjunction with the X-Ph scattering) effectively contributes to the cooling process of the excitons, even though the collision itself is energy conserving.

This can be seen in Fig. 3 where the development of the "effective temperature" for different bath temperatures is shown. In the first phase, up to around 5 ns, the excitons are rapidly cooled down to an "effective temperature" of around 1.5 K. This process is almost independent of the used bath temperature and exciton density. Since the bottleneck effect only plays a role for very low temperatures, the elevated value of $T_{\text{Bath}} = 1$ K can be easily reached after about 100 ns well within the lifetime of the excitons. For lower bath temperatures, however, the mechanisms discussed above play

a major role and lead to a very slow cooling of the excitons. As can be seen from Fig. 3, the inclusion of the X-X scattering improves the overall cooling which might be counterintuitive since the process itself is energy conserving. For very low bath temperatures the exciton lifetime of $\tau = 300$ ns is not long enough to reach thermal equilibrium with the lattice even under these optimal cooling conditions considered here. Even the longer lifetime of $\tau = 650$ ns reported in Ref. [5] is probably not long enough to reach full equilibration with the lattice.

IV. CONCLUSION AND OUTLOOK

We have shown that, due to the freezing out of phonons at ultralow temperatures ($T_{\mathrm{Bath}} \ll 1$ K), the thermalization process of the excitons can take longer than their lifetime, even under optimal conditions for cooling (no Auger-like decay and constant lattice temperature). As energy loss mechanisms, scattering with longitudinal and transversal acoustic phonons has been considered. For the latter we presented a quantitative way to calculate the deformation potential from the elements of the strain tensor. Taking into account only exciton-phonon scattering, the distribution function relaxes into a Bose-like shape within the first nanosecond for all considered densities. However, on longer timescales, the bottleneck effect leads to a nonequilibrium distribution function and a very inefficient cooling of the excitons. The inclusion of exciton-exciton scattering leads to an overall improved cooling efficiency and keeps the distribution function for most densities in a Bose-like shape even on long timescales. Therefore, for almost all experimentally relevant densities, exciton-exciton scattering cannot be neglected at ultralow temperatures.

The theory used in this paper can not fully describe the experimental situation. In order to extend the model the Auger effect, the inhomogeneity of the system, e.g., a potential trap, and a possible condensate have to be taken into account. Corresponding nonequilibrium theories exist already for atomic systems and for microcavity polaritons [15], in particular the theory of ultracold atoms has been extensively covered in the literature [16]. Typically the system is separated into a condensed and a noncondensed phase. One possible way of describing both phases self-consistently is to use a nonequilibrium Gross-Pitaevskii equation for the condensate wave function coupled to a quantum Boltzmann equation for the noncondensed particles [17]. Using such an approach and taking into account all relevant effects (phonons, Auger effect, etc.) should result in a model capable of fully describing typical experiments. This is work in progress and will be the subject of a forthcoming publication.

ACKNOWLEDGMENTS

We would like to thank G. Manzke, W.-D. Kraeft, Th. Bornath, Th. Koch, and H. Fehske for many fruitful discussions. This work was supported by the Deutsche Forschungsgemeinschaft via Collaborative Research Center SFB 652.

APPENDIX A: EXCITON STATES AND STRAIN

Under strain the four 1s states of the yellow series mix with the eight 1s states of the green series. In total 12 exciton states can be constructed (see Ref. [18]) which are designated by $\Phi_1,\ldots,\Phi_{12}$. The influence of the strain on the effective exciton Hamiltonian is given by the deformation Hamiltonian

$$H_D = a(\varepsilon_{xx}+\varepsilon_{yy}+\varepsilon_{zz}) - 3b\left(\left[L_x^2 - L^2/3\right]\varepsilon_{xx} + c.p.\right) - \frac{6}{\sqrt{3}}d([L_xL_y + L_yL_x]\varepsilon_{xy} + c.p.) \quad \text{(A1)}$$

with the strain tensor ε_{ij}, the angular momentum operator L_i, the cyclic permutations $c.p.$, and the deformation potentials a and b. Extending the analysis in Ref. [18] to arbitrary strain, we can derive the following coupling matrix between the yellow paraexciton (Φ_{12}, symmetry Γ_2^+) and the green paraexciton states with symmetry Γ_3^+ (Φ_2, Φ_{11}):

$$H_{23} = \begin{pmatrix} \Delta_1 - e + h & \sqrt{3}f & \sqrt{6}f \\ \sqrt{3}f & \Delta_1 + h + e & -\sqrt{2}e \\ \sqrt{6}f & -\sqrt{2}e & J_Y/2 + h \end{pmatrix}, \quad \text{(A2)}$$

with $\Delta_1 = \Delta + J_G/2$, $h = a(\varepsilon_{xx}+\varepsilon_{yy}+\varepsilon_{zz})$, $e = -3b/2(\varepsilon_{xx}+\varepsilon_{yy}-2\varepsilon_{zz})$, and $f = b/2(\varepsilon_{xx}-\varepsilon_{yy})$. Here J_G (J_Y) is the electron-hole exchange interaction for the green (yellow) series and Δ is the spin orbit energy. The binding energies of the yellow and green paraexcitons are approximately equal [19] and hence do not appear in Eq. (A2) explicitly. For the same reason, we assume J_Y and J_G to be equal as well. All other coupling matrix elements to the yellow paraexciton state are zero. Near the trap center, the relation $\varepsilon_{xx} = \varepsilon_{yy}$ holds and Φ_{12} couples only to the Φ_{11} state. The strain shifted yellow paraexciton, therefore, is given by

$$\Phi_{\mathrm{para}} = \alpha_1\Phi_{11} + \alpha_2\Phi_{12}\,. \quad \text{(A3)}$$

The expressions for α_1 and α_2 follow from the diagonalization of the 2×2 submatrix in H_{23} for $f = 0$.

APPENDIX B: PHONON SCATTERING

In an unstrained crystal, it follows from symmetry that yellow paraexcitons may only scatter with LA phonons, while the green paraexcitons may also scatter with TA

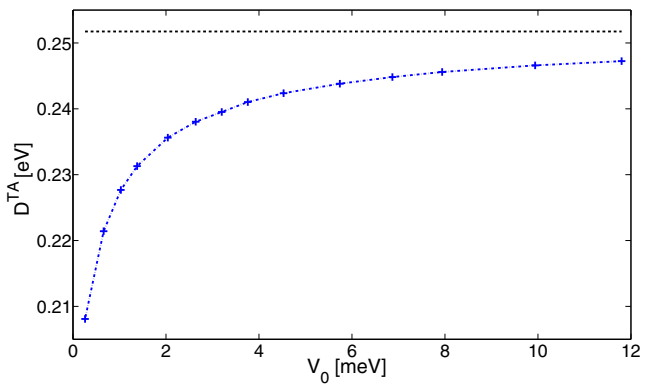

FIG. 4. (Color online) Deformation potential D^{TA} for the interaction between the strain shifted 1s yellow paraexcitons and TA phonons (dashed blue line) as a function of the trap depths V_0. The dashed black line indicates the maximum value for D^{TA}.

phonons. Due to the strain induced mixing of the yellow and green exciton states (A3), the coupling of the strain shifted yellow $1s$ paraexciton with TA phonons is possible. It follows from the strain Hamiltonian (A2) that intra state scattering for Φ_{11} is possible. The matrix element of the process scales as $b/4\sin(2\Theta)[1+2\sin^2(\phi)]$ for TA_1 mode (assuming the standard form of the strain tensor for the TA phonons [20]) and is zero for the TA_2 mode. This results in an effective angular averaged scattering matrix element between the strained paraexciton states and the TA phonons,

$$D^{\mathrm{TA}} = \sqrt{\frac{3}{5}}\left(\sqrt{2}\alpha_1\alpha_2 - \frac{|\alpha_1|^2}{2}\right) b\,. \tag{B1}$$

The elements of the strain tensor ε_{ij} and the trap depths V_0 can be calculated from the applied stress as discussed in Ref. [6]. In order to evaluate Eq. (B1) we used the values $\Delta = 128$ meV, $a = -2.1$ eV, and $b = 0.65$ eV taken from Ref. [21]. The results are shown in Fig. 4. The maximum value for D^{TA} is given by $D^{\mathrm{TA}}_{\mathrm{max}} = 0.5b\sqrt{3/5} \approx 0.252$ eV.

[1] D. W. Snoke, J. P. Wolfe, and A. Mysyrowicz, Phys. Rev. Lett. **64**, 2543 (1990).
[2] J. L. Lin and J. P. Wolfe, Phys. Rev. Lett. **71**, 1222 (1993).
[3] D. Snoke, Science **298**, 1368 (2002).
[4] K. Yoshioka, E. Chae, and M. Kuwata-Gonokami, Nat. Commun. **2**, 328 (2011).
[5] R. Schwartz, N. Naka, F. Kieseling, and H. Stolz, New J. Phys. **14**, 023054 (2012).
[6] H. Stolz, R. Schwartz, F. Kieseling, S. Som, M. Kaupsch, S. Sobkowiak, D. Semkat, N. Naka, Th. Koch, and H. Fehske, New J. Phys. **14**, 105007 (2012).
[7] K. Yoshioka, Y. Morita, K. Fukuoka, and M. Kuwata-Gonokami, Phys. Rev. B **88**, 041201 (2013).
[8] D. W. Snoke, Phys. Status Solidi B **238**, 389 (2003).
[9] A. L. Ivanov, C. Ell, and H. Haug, Phys. Rev. E **55**, 6363 (1997).
[10] D. W. Snoke and J. P. Wolfe, Phys. Rev. B **39**, 4030 (1989).
[11] J. Shumway and D. M. Ceperley, Phys. Rev. B **63**, 165209 (2001).
[12] J. Brandt, D. Fröhlich, C. Sandfort, M. Bayer, H. Stolz, and N. Naka, Phys. Rev. Lett. **99**, 217403 (2007).
[13] D. P. Trauernicht and J. P. Wolfe, Phys. Rev. B **33**, 8506 (1986).
[14] K. Reimann and K. Syassen, Phys. Rev. B **39**, 11113 (1989).
[15] H. Haug, T. D. Doan, and D. B. Tran Thoai, Phys. Rev. B **89**, 155302 (2014).
[16] N. P. Proukakis and B. Jackson, J. Phys. B: At. Mol. Opt. Phys. **41**, 203002 (2008).
[17] A. Griffin, T. Nikuni, and E. Zaremba, *Bose-Condensed Gases at Finite Temperatures* (Cambridge University Press, Cambridge, 2009).
[18] R. G. Waters, F. H. Pollak, R. H. Bruce, and H. Z. Cummins, Phys. Rev. B **21**, 1665 (1980).
[19] A. Alvermann, P. B. Littlewood, and H. Fehske, Phys. Rev. B **84**, 035126 (2011).
[20] P. Y. Yu and M. Cardona, *Fundamentals of Semiconductors* (Springer, Berlin, 2005).
[21] H.-R. Trebin, H. Z. Cummins, and J. L. Birman, Phys. Rev. B **23**, 597 (1981).

A.11

Artikel 11

S. Sobkowiak, D. Semkat, and H. Stolz:

Hydrodynamic description of trapped ultracold paraexcitons in Cu_2O

Phys. Rev. B **91**, 075209 (2015)

PHYSICAL REVIEW B **91**, 075209 (2015)

Hydrodynamic description of trapped ultracold paraexcitons in Cu_2O

S. Sobkowiak,* D. Semkat, and H. Stolz
Institut für Physik, Universität Rostock, 18051 Rostock, Germany
(Received 20 October 2014; revised manuscript received 23 January 2015; published 26 February 2015)

In this paper we present a theoretical model to describe the dynamics of paraexcitons in cuprous oxide at ultralow temperatures inside potential traps. A possible condensate is described by a generalized Gross-Pitaevskii equation. The noncondensed excitons evolve under a set of hydrodynamic equations, which were derived from a quantum Boltzmann equation. The model takes into account the finite lifetime of the excitons, the pump laser, the Auger-like two-body decay, as well as exciton-exciton and exciton-phonon scattering. The numerical results show the strong influence of the Auger effect on exciton temperatures and densities not only at high pump powers but also at ultralow temperatures. Furthermore, the excitons do not cool down to very low bath temperatures ($T_B \ll 0.5$ K) under continuous wave excitation. We also compare the results of the theoretical model with experimental data.

DOI: 10.1103/PhysRevB.91.075209 PACS number(s): 71.35.Lk, 63.20.kk, 67.85.Jk

I. INTRODUCTION

The experimental realization of an excitonic Bose-Einstein condensate (BEC) in a bulk material is a long standing problem. Initially put forward by Moskalenko [1] and Blatt *et al.* [2], the first experiments in excitonic systems were already carried out over 40 years ago [3]. Signatures of an excitonic BEC were first found using exciton-polaritons in microcavities [4–6]. Over the last decade experiments in these system have generated many interesting results and received a lot of attention (for an overview see [7]). Another intensively investigated system are indirect excitons in quantum wells [8–10], however, claims for an observation of an excitonic BEC are still under debate [11]. In bulk materials, despite many efforts from numerous research groups [12–16], no experiment so far has shown Bose-Einstein condensation of excitons demonstrating all the required criteria [17]. However, recent experimental results showed strong evidence for an excitonic condensate in cuprous oxide (Cu_2O) [18]. The long lifetime and the high binding energy of the excitons make this material a promising candidate for the realization of a BEC in a bulk material.

In typical experiments, excitons created by a pump laser are collected in stress induced potential traps. Using a ^{3}He/^{4}He dilution cryostate, the crystal specimen can be cooled to temperatures of the order of 100 mK [18,19]. The excitons in turn are cooled via interaction with the crystal lattice (phonons). Since excitons only have a finite lifetime and can undergo an Auger-like two-body decay, they might not reach the lattice temperature. Experimentally the exciton temperature is usually determined by fitting the decay luminescence spectrum with a Bose distribution. This spectral temperature T_S typically does not agree with the temperature of the helium bath T_B [16,18], hinting to a nonequilibrium state of the system. To understand this and other aspects of the recent experimental results, a theoretical model is needed. In order to identify a possible condensate in the experimental results, it is especially important to be able to differentiate between the features of a quasiequilibrium, a nonequilibrium, and a condensed case. Additionally, it would be beneficial to know the parameters for which the onset of condensation can be expected. In this paper we aim to develop such a theoretical model and thereby stimulating further progress in the field.

The situation in the experiments under consideration is quite complex. The theoretical model has to take into account the inhomogeneity of the system, the finite lifetime, a possible condensate, the Auger effect, exciton-exciton (X-X), and exciton-phonon (X-Ph) collisions. The semiconductor specific aspects (Auger effect, X-X, and X-Ph collisions) have already been investigated by different authors [20–22]. However, these papers only dealt with homogeneous systems. On the other hand, there is extensive literature on ultracold condensed atoms in potential traps. Excitons at the densities and temperatures present in typical experiments can be regarded as a gas of ultracold bosons. Therefore, extending the theory of ultracold atoms by taking into account semiconductor specific effects, should result in a model suitable for the description of trapped excitons in Cu_2O.

The paper is organized as follows: In the next section we discuss important features of the experiments under consideration. In the following two sections the theoretical model is developed and the implementation of the different processes is explained. In the last section typical numerical results are shown and first comparisons to experimental data are made.

II. EXPERIMENTAL BACKGROUND

The experiments in Refs. [16,18] investigate excitons consisting of a hole in the Γ_7^+ valence band and an electron in the Γ_6^+ conduction band (so-called yellow series). Since the valence and the conduction band both are doubly degenerate, the ground state of this series splits into the nondegenerate paraexciton and the triply degenerate orthoexciton. The different orthoexcitons are labeled according to their spin projection by (+), (0), and (−). Due to electron-hole exchange interaction, the paraexcitons are the energetically lowest state lying 12.12 meV below the orthoexcitons. The paraexcitons also have a long lifetime of $\tau = 650$ ns [16], making them the main focus of the experimental efforts. In the experiments presented in Refs. [16,18], the pump laser initially creates

*siegfried.sobkowiak@uni-rostock.de

orthoexcitons under involvement of a Γ_3^- phonon, outside of the trap center. These rapidly convert to paraexcitons via a phonon assisted process (reported rates are $\Gamma_{\text{O-P}} = 0.2\ \text{ns}^{-1}$ [23] and $\Gamma_{\text{O-P}} = 0.29\ \text{ns}^{-1}$ [22]). The potential trap created by the stress applied on the specimen is attractive for ortho(+), ortho(−), and paraexcitons, while being repulsive for ortho(0)excitons. The shape of the trap can be approximated by an isotropic harmonic oscillator potential with its minimum usually lying 1 to 3 meV below the band gap. The treatment of such an inhomogeneous three-component Bose gas is numerically quite cumbersome. As a first approximation we assume the ortho-para conversion to be almost instantaneous, taking only the paraexcitons directly into account in our model.

The excitation laser can be run in pulsed or continuous wave (cw) mode. Under cw excitation, new excitons are constantly created while others decay. After some time, both processes will balance out and the system will form a stationary, nonequilibrium state. However, under pulsed excitation, no new excitons will be created after the laser pulse. Therefore, after an initial nonequilibrium phase, the excitons will reach some kind of quasiequilibrium state. Their temperature, however, may still be different from the temperature of the crystal lattice.

III. MODEL

There are various approaches to theoretically describe ultracold atomic gases in nonequilibrium (for an overview see, e.g., Ref. [24]). The one most suitable for our purpose are the Zaremba-Nikuni-Griffin (ZNG) equations. Since these equations are well established in the literature, we will only briefly review the most important definitions and assumptions. A more detailed overview can be found in Ref. [25].

A. ZNG equations

In the ZNG equations, the system is split into a condensed and a noncondensed part by dividing the Bose-field operator $\hat{\psi}(\mathbf{r},t)$ into $\hat{\psi}(\mathbf{r},t) = \Phi(\mathbf{r},t) + \tilde{\psi}(\mathbf{r},t)$. The condensed phase is described by the condensate wave function $\Phi(\mathbf{r},t)$ and the noncondensed (thermal) phase by the fluctuation operator $\tilde{\psi}(\mathbf{r},t)$. The interaction of particles with each other is assumed to be well described by s-wave scattering with the interaction strength g.

The dynamics of the condensate is governed by a generalized Gross-Pitaevskii equation (GGPE)

$$i\hbar\frac{\partial\Phi(\mathbf{r},t)}{\partial t} = \Big[-\frac{\hbar^2\nabla^2}{2m} + V_{\text{ext}}(\mathbf{r}) + gn_c(\mathbf{r},t) + 2g\tilde{n}(\mathbf{r},t) - iR(\mathbf{r},t)\Big]\Phi(\mathbf{r},t), \tag{1}$$

with the condensate density $n_c(\mathbf{r},t) = |\Phi(\mathbf{r},t)|^2$, the density of the thermal particles $\tilde{n}(\mathbf{r},t) = \langle\tilde{\psi}^\dagger(\mathbf{r},t)\tilde{\psi}(\mathbf{r},t)\rangle$, and the coupling term $R(\mathbf{r},t)$. The latter is responsible for transferring particles between the condensed and the noncondensed phase and will be discussed later. In order to derive Eq. (1), the anomalous densities $\tilde{m}(\mathbf{r},t) = \langle\tilde{\psi}(\mathbf{r},t)\tilde{\psi}(\mathbf{r},t)\rangle$ were neglected.

Using an amplitude and phase representation for the wave function given by $\Phi(\mathbf{r},t) = \sqrt{n_c(\mathbf{r},t)}e^{i\theta(\mathbf{r},t)}$, the condensate velocity $\mathbf{v}_c(\mathbf{r},t)$ and the local time-dependent condensate chemical potential $\mu_c(\mathbf{r},t)$ can be introduced via

$$\begin{aligned}\mathbf{v}_c(\mathbf{r},t) &= \frac{\hbar}{m}\nabla\theta(\mathbf{r},t)\,,\\ \mu_c(\mathbf{r},t) &= -\frac{\hbar^2\nabla^2\sqrt{n_c(\mathbf{r},t)}}{2m\sqrt{n_c(\mathbf{r},t)}} + V_{\text{ext}}(\mathbf{r})\\ &\quad + gn_c(\mathbf{r},t) + 2g\tilde{n}(\mathbf{r},t).\end{aligned} \tag{2}$$

Using the above expressions, the energy of a particle in the condensate can be written as

$$\varepsilon_c(\mathbf{r},t) = -\hbar\frac{\partial\theta(\mathbf{r},t)}{\partial t} = \frac{1}{2}m\mathbf{v}_c^2(\mathbf{r},t) + \mu_c(\mathbf{r},t). \tag{3}$$

It should be noted that, to describe the condensate, Griffin *et al.* [25] used two coupled equations for $n_c(\mathbf{r},t)$ and $\mathbf{v}_c(\mathbf{r},t)$, which are equivalent to the GGPE (1).

The evolution of the thermal particles is described by the equation of motion for the fluctuation operator $\tilde{\psi}(\mathbf{r},t)$. Under the assumption of a slowly varying mean-field potential $U(\mathbf{r},t) = V_{\text{ext}}(\mathbf{r}) + 2g[n_c(\mathbf{r},t) + \tilde{n}(\mathbf{r},t)]$, it is possible to transform the equation of motion for $\tilde{\psi}(\mathbf{r},t)$ into a quantum Boltzmann equation for the Wigner distribution function $f(\mathbf{p},\mathbf{r},t)$. The result is given by

$$\frac{\partial f(\mathbf{p},\mathbf{r},t)}{\partial t} + \frac{\mathbf{p}}{m}\cdot\nabla_{\mathbf{r}}f(\mathbf{p},\mathbf{r},t) - \nabla_{\mathbf{r}}U(\mathbf{r},t)\cdot\nabla_{\mathbf{p}}f(\mathbf{p},\mathbf{r},t) = \left.\frac{\partial f(\mathbf{p},\mathbf{r},t)}{\partial t}\right|_{\text{coll.}}. \tag{4}$$

Using the first three moments of this equation, Griffin *et al.* [26] also derived a set of hydrodynamic equations describing the noncondensed particles. In the original ZNG formalism, the collision term on the right-hand side of Eq. (4) contains particle-particle collisions only. Collisions involving just thermal states are described by $C_{\text{X-X}}$, while $C_{\text{X}_c\text{-X}}$ contains collisions involving condensed and noncondensed states. The latter term transfers particles into or out of the condensate and is, therefore, related to the term $R(\mathbf{r},t)$ in the GGPE (1).

In the ZNG equations, the energy dispersion for the noncondensed particles is Hartree-Fock-like and, therefore, given by $\varepsilon_{\mathbf{p}}(\mathbf{r},t) = p^2/2m + U(\mathbf{r},t)$. The corresponding results using a Bogoliubov quasiparticle spectrum can be found in [27]. Since for typical experimental parameters only small or no condensates are expected, the Hartree-Fock-like dispersion is a good approximation.

B. Extensions

In order to include semiconductor specific effects, the collision term is extended to

$$\left.\frac{\partial f(\mathbf{p},\mathbf{r},t)}{\partial t}\right|_{\text{coll.}} = C_{\text{X-X}} + C_{\text{X}_c\text{-X}} + C_{\text{Ph}} + C_{\text{C-D}}, \tag{5}$$

where C_{Ph} describes X-Ph collisions and $C_{\text{C-D}}$ stands for processes that can create or destroy excitons. The latter namely includes the influence of the finite lifetime C_τ, the pump laser C_{laser}, and the Auger effect C_{Auger}. The X-Ph collision term has two contributions given by $C_{\text{Ph}} = C_{\text{X-Ph}} + C_{\text{X}_c\text{-Ph}}$. The term $C_{\text{X-Ph}}$ stands for X-Ph scattering within the thermal phase, while $C_{\text{X}_c\text{-Ph}}$ represents scattering of excitons into or out of the

condensate by phonons. In order to stay consistent with the GGPE (1) the coupling term $R(\mathbf{r},t)$ also needs to be extended with corresponding terms. This and the explicit form of the collision terms will be discussed in the next section.

The full numerical solution of the quantum Boltzmann equation (4) with the collision terms given by Eq. (5) is a challenging task. As we will discuss in the following, for the experiments under consideration it is beneficial to rewrite the Boltzmann equation (4) into a set of hydrodynamic equations. These are derived by multiplying Eq. (4) with ($\varphi_0 = 1, \varphi_1 = \mathbf{p}$, $\varphi_2 = p^2/2m$) and integrating over the whole momentum space [25]. This results in a set of three coupled equations for the density, momentum density, and kinetic energy density of the thermal excitons. The quantities are given by

$$\begin{aligned}\tilde{n}(\mathbf{r},t) &= \int \frac{d\mathbf{p}}{(2\pi\hbar)^3} f(\mathbf{p},\mathbf{r},t),\\ m\tilde{n}(\mathbf{r},t)\mathbf{v}_n(\mathbf{r},t) &= \int \frac{d\mathbf{p}}{(2\pi\hbar)^3}\mathbf{p} f(\mathbf{p},\mathbf{r},t),\\ E(\mathbf{r},t) &= \int \frac{d\mathbf{p}}{(2\pi\hbar)^3}\frac{p^2}{2m} f(\mathbf{p},\mathbf{r},t),\end{aligned} \tag{6}$$

where we have introduced the (normal) velocity $\mathbf{v}_n(\mathbf{r},t)$ of the noncondensed excitons.

Collision processes that conserve one or several of these quantities will not appear in the corresponding hydrodynamic equation. Since the X-X collision term $C_{\text{X-X}}$ conserves particle number, momentum, and kinetic energy, it will not appear at all. Therefore, the numerically demanding calculation of $C_{\text{X-X}}$ will not be necessary for evaluating the hydrodynamic equations.

Besides being coupled to each other, the resulting hydrodynamic equations will also be connected to the GGPE (1) by the moments of different collision terms. Additionally, they are in general not closed since the next higher moment will appear in the equation for the energy. One possible way of closing the equations is to assume a partial local equilibrium for the distribution function $f(\mathbf{p},\mathbf{r},t) = \tilde{f}_{\mathbf{p}}(\mathbf{r},t)$ given by

$$\begin{aligned}\tilde{f}_{\mathbf{p}}(\mathbf{r},t) &= [e^{[(\mathbf{p}-m\mathbf{v}_n)^2/2m+U-\tilde{\mu}(\mathbf{r},t)]/k_{\text{B}}T(\mathbf{r},t)} - 1]^{-1}\\ &= [e^{[\tilde{p}^2/2m-\tilde{\mu}_{\text{eff}}(\mathbf{r},t)]/k_{\text{B}}T(\mathbf{r},t)} - 1]^{-1}.\end{aligned} \tag{7}$$

Here k_{B} is Boltzmann's constant and $T(\mathbf{r},t)$ and $\tilde{\mu}(\mathbf{r},t)$ are the space- and time-dependent temperature and chemical potential. Rewriting the distribution function using the shifted momentum $\tilde{\mathbf{p}} = \mathbf{p} - m\mathbf{v}_n$ and the effective chemical potential $\tilde{\mu}_{\text{eff}}(\mathbf{r},t) = \tilde{\mu}(\mathbf{r},t) - U(\mathbf{r},t)$ recovers the simple form of a Bose distribution. The vanishing of the effective chemical potential [$\tilde{\mu}_{\text{eff}}(\mathbf{r},t) \to 0$] marks the onset of a possible condensate.

As we have shown in Ref. [28], the X-X and X-Ph collisions force the momentum distribution function into partial local equilibrium in less than 1 ns for the experimentally relevant parameters. On the other hand, the lifetime of the excitons and the time scales relevant for the drift into the trap center and the thermalization are usually of the order of several 100 ns. Due to this separation of time scales, the assumption of partial local equilibrium is justified after the initial stage of relaxation. The relaxation into partial local equilibrium, however, has to be treated separately.

The trap potential is well approximated by an isotropic harmonic oscillator potential [$V_{\text{ext}}(r) = \alpha r^2$]. Therefore, for our calculations we use spherical symmetry. Even though this does not match the excitation geometry exactly, the impact on the physical quantities in the trap center should be limited since the excitation region is far away from it. The result for the hydrodynamic equations in quasi-one-dimension is

$$\begin{aligned}&\frac{\partial\tilde{n}}{\partial t} + \frac{\partial}{\partial r}[\tilde{n}v_n]\\ &\quad= \Gamma^{(0)}_{\text{X}_\text{c}\text{-X}} + \Gamma^{(0)}_{\text{X}_\text{c}\text{-Ph}} + \Gamma^{(0)}_{\text{C-D}} - \frac{2}{r}\tilde{n}v_n,\\ &\frac{\partial}{\partial t}[m\tilde{n}v_n] + \frac{\partial}{\partial r}[m\tilde{n}v_n^2 + \tilde{P}]\\ &\quad= -\tilde{n}\frac{\partial U}{\partial r} - \frac{2}{r}m\tilde{n}v_n^2 + mv_c\Gamma^{(0)}_{\text{X}_\text{c}\text{-X}} + \Gamma^{(1)}_{\text{X-Ph}} + \Gamma^{(1)}_{\text{X}_\text{c}\text{-Ph}} + \Gamma^{(1)}_{\text{C-D}},\\ &\frac{\partial E}{\partial t} + \frac{\partial}{\partial r}[(E+\tilde{P})v_n]\\ &\quad= -\tilde{n}v_n\frac{\partial U}{\partial r} + (\varepsilon_c - U)\Gamma^{(0)}_{\text{X}_\text{c}\text{-X}} - \frac{2}{r}(E+\tilde{P})v_n + \Gamma^{(2)}_{\text{X-Ph}}\\ &\qquad+ \Gamma^{(2)}_{\text{X}_\text{c}\text{-Ph}} + \Gamma^{(2)}_{\text{C-D}},\end{aligned} \tag{8}$$

where $\Gamma^{(n)}$ stands for the nth moment of the collision term C given by

$$\Gamma^{(n)} = \int \frac{d\mathbf{p}}{(2\pi\hbar)^3}\varphi_n(\mathbf{p})\, C. \tag{9}$$

The local kinetic pressure $\tilde{P}(\mathbf{r},t)$ is given by

$$\tilde{P}(\mathbf{r},t) = \frac{2}{3}\int \frac{d\mathbf{p}}{(2\pi\hbar)^3}\frac{(\mathbf{p}-m\mathbf{v}_n)^2}{2m}\tilde{f}_{\mathbf{p}}(\mathbf{r},t). \tag{10}$$

In order to solve this system of equations, the moments of the collision terms are needed. These are discussed in the following section.

IV. COLLISION TERMS

A. Exciton-exciton collisions ($C_{\text{X}_\text{c}\text{-X}}$)

The collision term $C_{\text{X}_\text{c}\text{-X}}$ describes collisions between two excitons which scatter an exciton into or out of the condensate. Therefore, it is responsible for exchanging excitons between the condensed and the noncondensed phase. In the hydrodynamic equations (8) only the zeroth moment of $C_{\text{X}_\text{c}\text{-X}}$ appears. Under the assumption of partial local equilibrium it is given by [25]

$$\begin{aligned}\Gamma^{(0)}_{\text{X}_\text{c}\text{-X}} = &-\frac{2g^2 n_c}{(2\pi)^5\hbar}(1 - e^{-[\tilde{\mu}-\mu_c-\frac{m}{2}(\mathbf{v}_n-\mathbf{v}_c)^2]/k_{\text{B}}T})\\ &\times\int d\mathbf{k}_1 d\mathbf{k}_2 d\mathbf{k}_3\,\delta(\mathbf{k}_c+\mathbf{k}_1-\mathbf{k}_2-\mathbf{k}_3)\\ &\times\delta\big(\varepsilon_c+\varepsilon_{\mathbf{k}_1}-\varepsilon_{\mathbf{k}_2}-\varepsilon_{\mathbf{k}_3}\big)\big(1+\tilde{f}_{\mathbf{k}_1}\big)\tilde{f}_{\mathbf{k}_2}\tilde{f}_{\mathbf{k}_3},\end{aligned} \tag{11}$$

with $\mathbf{k}_c = m\mathbf{v}_c/\hbar$. The corresponding term for the GGPE (1) reads

$$R_{\text{X}_\text{c}\text{-X}}(\mathbf{r},t) = \frac{\hbar\Gamma^{(0)}_{\text{X}_\text{c}\text{-X}}}{2n_c(\mathbf{r},t)}. \tag{12}$$

B. Exciton-phonon collisions (C_{Ph})

In an unstrained crystal of Cu_2O, the yellow $1s$ paraexcitons can interact with longitudinal acoustic (LA), but not with transversal acoustic (TA) phonons. However, when stress is applied, as in the experiments under consideration, interaction with either type of phonons is possible. The collision term $C_{\text{X-Ph}}$ for both processes is given by [20]

$$\begin{aligned} C_{\text{X-Ph}} = -\frac{\pi D^2}{\varrho v_s}\int \frac{d\mathbf{k}'}{(2\pi)^3}|\mathbf{k}'-\mathbf{k}|\{\big[f_{\mathbf{k}}\big(1+f^{\text{Ph}}_{\mathbf{k}-\mathbf{k}'}\big)(1+f_{\mathbf{k}'}) \\ -(1+f_{\mathbf{k}})f^{\text{Ph}}_{\mathbf{k}-\mathbf{k}'}f_{\mathbf{k}'}\big]\delta(\varepsilon_{\mathbf{k}}-\varepsilon_{\mathbf{k}'}-\hbar\omega_{\mathbf{k}-\mathbf{k}'}) \\ +\big[f_{\mathbf{k}}f^{\text{Ph}}_{\mathbf{k}'-\mathbf{k}}(1+f_{\mathbf{k}'})-(1+f_{\mathbf{k}})\big(1+f^{\text{Ph}}_{\mathbf{k}'-\mathbf{k}}\big)f_{\mathbf{k}'}\big] \\ \times\,\delta(\varepsilon_{\mathbf{k}}-\varepsilon_{\mathbf{k}'}+\hbar\omega_{\mathbf{k}'-\mathbf{k}})\}, \end{aligned} \tag{13}$$

with the deformation potential D, the crystal density $\varrho = 6.11\times10^3\ \text{kg/m}^3$ [20], and the speed of sound v_s. The first (second) term on the right-hand side represent Stokes (anti-Stokes) scattering, respectively. The phonons are assumed to be in equilibrium at the lattice temperature T_{Ph}, therefore, their distribution function is given by $f^{\text{Ph}}_{\mathbf{k}'-\mathbf{k}} = [\exp(\hbar\omega_{\mathbf{k}'-\mathbf{k}}/k_BT_{\text{Ph}})-1]^{-1}$ with the phonon energy $\hbar\omega_{\mathbf{k}'-\mathbf{k}} = \hbar v_s|\mathbf{k}'-\mathbf{k}|$.

Applying the integration over all $\mathbf{k}$ on $C_{\text{X-Ph}}$ to calculate the moments, allows the exchange of $\mathbf{k}$ and $\mathbf{k}'$ in the Stokes scattering term. This results in a very compact form for all moments

$$\begin{aligned} \Gamma^{(n)}_{\text{X-Ph}} = -\frac{\pi D^2}{\varrho v_s}\int \frac{d\mathbf{k}d\mathbf{k}'}{(2\pi)^6}|\mathbf{k}'-\mathbf{k}|[\varphi_n(\mathbf{k})-\varphi_n(\mathbf{k}')] \\ \times\big[f_{\mathbf{k}}f^{\text{Ph}}_{\mathbf{k}'-\mathbf{k}}(1+f_{\mathbf{k}'})-(1+f_{\mathbf{k}})\big(1+f^{\text{Ph}}_{\mathbf{k}'-\mathbf{k}}\big)f_{\mathbf{k}'}\big] \\ \times\,\delta(\varepsilon_{\mathbf{k}}-\varepsilon_{\mathbf{k}'}+\hbar\omega_{\mathbf{k}'-\mathbf{k}}). \end{aligned} \tag{14}$$

From Eq. (14) it follows directly that $\Gamma^{(0)}_{\text{X-Ph}}$ vanishes ($\varphi_0 = 1$).

The second X-Ph collision term $C_{\text{X}_c\text{-Ph}}$ can also be extracted from Ref. [20] and has already been given in Ref. [29]. Within our model its moments read

$$\begin{aligned} \Gamma^{(n)}_{\text{X}_c\text{-Ph}} = -\frac{\pi D^2 n_c}{\rho v_s}\int \frac{d\mathbf{k}}{(2\pi)^3}\varphi_n(\mathbf{k})|\mathbf{k}_c-\mathbf{k}|\{\big[f_{\mathbf{k}}\big(1+f^{\text{Ph}}_{\mathbf{k}-\mathbf{k}_c}\big) \\ -(1+f_{\mathbf{k}})f^{\text{Ph}}_{\mathbf{k}-\mathbf{k}_c}\big]\delta(\varepsilon_{\mathbf{k}}-\varepsilon_c-\hbar\omega_{\mathbf{k}-\mathbf{k}_c}) \\ +\big[f_{\mathbf{k}}f^{\text{Ph}}_{\mathbf{k}_c-\mathbf{k}}-(1+f_{\mathbf{k}})\big(1+f^{\text{Ph}}_{\mathbf{k}_c-\mathbf{k}}\big)\big] \\ \times\,\delta(\varepsilon_{\mathbf{k}}-\varepsilon_c+\hbar\omega_{\mathbf{k}_c-\mathbf{k}})\}. \end{aligned} \tag{15}$$

In the system under consideration the corresponding imaginary part of (15) is typically very small compared to the other dispersive shift terms in (1) and has been neglected. Therefore, the term for the GGPE (1) reads

$$R_{\text{X}_c\text{-Ph}}(\mathbf{r},t) = \frac{\hbar\Gamma^{(0)}_{\text{X}_c\text{-Ph}}}{2n_c(\mathbf{r},t)}. \tag{16}$$

The speeds of sound are given by $v_s^{\text{LA}} = 4.5\times10^3$ m/s and $v_s^{\text{TA}} = 1.3\times10^3$ m/s [30]. The deformation potential for the TA phonons depends on the applied stress and can be calculated using the method explained in Ref. [28]. In this paper we use the value $D^{\text{TA}} = 0.235$ eV, which corresponds to a trap depth of around 2 meV. For the LA phonons we use the value $D^{\text{LA}} = 1.68$ eV given by Ref. [31].

C. Lifetime (C_τ)

Since the decay of the excitons mainly originates from nonradiative transitions, the lifetime can be described by a constant τ. Its collision term is given by $C_\tau = -\tilde{f}_{\mathbf{p}}(\mathbf{r},t)/\tau$. Therefore, the calculation of the moments is straightforward and yields

$$\begin{aligned} \Gamma^{(0)}_\tau &= -\tilde{n}(\mathbf{r},t)/\tau, \\ \Gamma^{(1)}_\tau &= -m\tilde{n}(\mathbf{r},t)\mathbf{v}_n(\mathbf{r},t)/\tau, \\ \Gamma^{(2)}_\tau &= -E(\mathbf{r},t)/\tau. \end{aligned} \tag{17}$$

For our computations we used the value $\tau = 650$ ns [18]. We assume the same lifetime for the condensed excitons.

D. Pump laser (C_{laser})

In order to incorporate new excitons into the system of Eqs. (8), their relaxation into partial local equilibrium has to be treated first. We assume that the excitons created by the laser are at rest and do not gain any velocity during this initial relaxation. Therefore, we simulate the relaxation into partial local equilibrium by solving a homogeneous Boltzmann equation for an initial momentum distribution function at all relevant points in space. For this we take into account X-X and X-Ph scattering (see Ref. [28] for details). The initial energy of the excitons depends on the wavelength of the laser, the exchange splitting between ortho- and paraexcitons, and the energy of the phonon emitted during the conversion process. For the excitation scheme considered here the initial energy is about 8 meV. Therefore, the initial momentum distribution function is peaked at the corresponding $\mathbf{k}$ value and normalized to the density of the newly created excitons $n_{\text{laser}}(\mathbf{r},t)$. Its value can be estimated from the pulse shape and the fraction of absorbed photons [16]. For our calculations we assume $n_{\text{laser}}(\mathbf{r},t)$ to be a Gaussian distribution along r with its maximum at r_{max} outside the trap center and a width of σ. The normalization is chosen to reproduce the same rate of exciton generation as a laser with a given pump power P_{L} would create in actual experiments.

The relaxation into partial local equilibrium takes no more than 1 ns. The remaining exciton energy after this initial relaxation $E_{\text{laser}}(\mathbf{r},t)$ typically corresponds to temperatures around 4 K. Since we assumed the excitons to be at rest during this time, the new excitons enter the hydrodynamic equations with density $n_{\text{laser}}(\mathbf{r},t)$ and energy $E_{\text{laser}}(\mathbf{r},t)$ but with $\Gamma^{(1)}_{\text{laser}} = \mathbf{0}$. The moments of C_{laser} are (symbolically) given by

$$\begin{aligned} \Gamma^{(0)}_{\text{laser}} &= n_{\text{laser}}(\mathbf{r},t), \\ \Gamma^{(1)}_{\text{laser}} &= \mathbf{0}, \\ \Gamma^{(2)}_{\text{laser}} &= E_{\text{laser}}(\mathbf{r},t). \end{aligned} \tag{18}$$

E. Auger effect (C_{Auger})

The Auger-like two-body decay destroys two excitons, recombining one and ionizing the other. The resulting electron-hole pair can rebind to form a high energy exciton. The transition matrix elements of the dominant terms for the Auger effect are linear in $\mathbf{k}$ [32]. Note that this means that the condensed excitons should not undergo an Auger-like decay.

For the thermal excitons we use a **k**-averaged Auger rate A as found in experiments [16,33,34]. The destruction of excitons due to the Auger effect can then be described by the collision term $C^{\mathrm{D}}_{\mathrm{Auger}} = -2A\tilde{n}(\mathbf{r},t)\tilde{f}_{\mathbf{p}}(\mathbf{r},t)$ [22]. The calculation of the moments for this term is straightforward.

For our model we assume that all electron-hole pairs rebind and that the newly formed excitons are equally distributed over the four possible exciton states (one para- and three orthoexcitons). Since ortho(0) excitons are expelled from the trap, they will not be refed into Eqs. (8). The newly formed excitons are assumed to be at rest. Their energy is equivalent to the binding energy of 150 meV. Therefore, they can emit different optical phonons. Taking this into account, we calculate their energy after the relaxation into partial local equilibrium (E_{Auger}) the same way we did for the excitons created by the pump laser (by solving a homogeneous Boltzmann equation). The moments are given by

$$\begin{aligned}\Gamma^{(0)}_{\mathrm{Auger}} &= -2A\tilde{n}^2(\mathbf{r},t) + \frac{3}{4}A\tilde{n}^2(\mathbf{r},t),\\ \Gamma^{(1)}_{\mathrm{Auger}} &= -2Am\tilde{n}^2(\mathbf{r},t)\mathbf{v}_n(\mathbf{r},t),\\ \Gamma^{(2)}_{\mathrm{Auger}} &= -2A\tilde{n}(\mathbf{r},t)E(\mathbf{r},t) + \frac{3}{4}A\tilde{n}(\mathbf{r},t)E_{\mathrm{Auger}}.\end{aligned} \tag{19}$$

The value of the Auger rate A has been determined theoretically and experimentally. However, the results vary over several orders of magnitude. The theoretical calculations predict $A = 2\times10^{-21}$ cm^3 ns^{-1} [35] and $A = 3\times10^{-22}$ cm^3 ns^{-1} [32] while the values $A = 2\times10^{-18}$ cm^3 ns^{-1} [18], $A = 7\times10^{-17}$ cm^3 ns^{-1} [33], and $A = 4\times10^{-16}$ cm^3 ns^{-1} [34] were found experimentally. Therefore, the Auger rate A is a source of uncertainty.

F. Summary of the model

The model consists of a GGPE (1) describing the condensed excitons coupled to a set of hydrodynamic equations (8) for the noncondensed excitons. The coupling term $R(\mathbf{r},t)$ in (1) reads

$$R(\mathbf{r},t) = R_{\mathrm{X_c\text{-}X}}(\mathbf{r},t) + R_{\mathrm{X_c\text{-}Ph}}(\mathbf{r},t) + \hbar/\tau. \tag{20}$$

The distribution function for the thermal excitons is given by (7). The initial relaxation into this partial local equilibrium is treated separately. For our numerical calculations we usually start with thermal excitons only. Monitoring the effective chemical potential the condensate is seeded into the system if necessary.

Comparable approaches using a GGPE coupled to a quantum Boltzmann or hydrodynamic equations are also used to describe exciton-polaritons in microcavities [29,36].

V. RESULTS

For the calculations we choose parameters comparable to the values found in Refs. [16,18]. The laser is placed 100 μm outside of the trap center ($r_{\max} = 100\ \mu$m) with a width of $\sigma = 3\ \mu$m. For the interaction strength g we use $g = 4\pi\hbar^2 a_s/m = 0.54$ eV nm^3, which corresponds to a s-wave scattering length of $a_s = 2.1\,a_B$ [37], a Bohr radius of $a_B = 0.7$ nm, and an exciton mass of [38] $m = 2.6\,m_0$ (m_0: free electron mass). For the discussion it is useful to review the different temperatures present in our theoretical model. There is the temperature of the helium bath T_{B} and the temperature of the phonons (of the crystal lattice) T_{Ph}. For our calculations we assume $T_{\mathrm{Ph}} = T_{\mathrm{B}}$. Additionally, there is the temperature of the excitons, which will be depending on space and time $T(r,t)$. We will further introduce the exciton temperature in the trap center $T_0 = T(r=0,t)$ and the mean exciton temperature

$$\langle T\rangle = \frac{1}{N}\int d\mathbf{r}T(r,t)\tilde{n}(r,t) \tag{21}$$

which both depend on time only. The temperature extracted from fitting the experimental spectra will be called the spectral temperature T_{S}. In the following we will present some general results for cw excitation and discuss different features before comparing theoretical results with experimental data.

A. General results

For the calculations in this section, the trap parameter α was set to $\alpha = 0.11\ \mu$eV μm^{-2}. Figure 1 shows results for a moderate pumping power of $P_{\mathrm{L}} = 26.4\ \mu$W and a phonon temperature of $T_{\mathrm{Ph}} = 0.5$ K. As can be seen very well, the stationary state of the system shows strong deviations from the corresponding equilibrium situation. The density profile is similar to a Gaussian shape, with an increased value at the trap center. The shape of the other quantities is due to the constant creation of excitons by the pump laser at $r = 100\ \mu$m. The newly created "hot" excitons drift towards the center of the trap. At first their velocity increases strongly, slows down afterwards, and is zero in the central region of the trap. During the drift process, the excitons are cooled via phonon interaction. The temperature drops progressively, reaching a minimum of $T_{\min} = 0.54$ K around $r = 20\ \mu$m. As of this point, the temperature rises slightly reaching a local maximum of $T_0 = 0.55$ K at $r = 0$ due to the Auger effect. The effective chemical potential behaves inversely. However, it increases

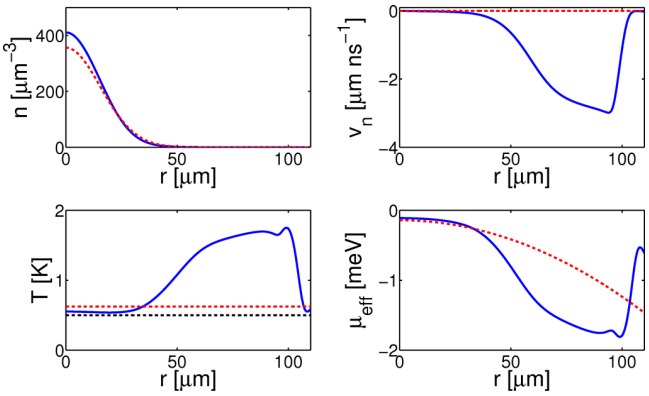

FIG. 1. (Color online) Density $\tilde{n}(r)$, velocity $v_n(r)$, temperature $T(r)$, and effective chemical potential $\tilde{\mu}_{\mathrm{eff}}(r)$ for the stationary state (blue solid line) at a phonon temperature of $T_{\mathrm{Ph}} = 0.5$ K and a laser power of $P_{\mathrm{L}} = 26.4\ \mu$W. The dashed red curves represent the corresponding values of a distribution function in equilibrium with the same mean temperature $\langle T\rangle = 0.62$ K and the same exciton number $N = 2.13\times10^7$. The dashed black curve shows the phonon temperature T_{Ph}. The Auger rate is set to $A = 2.0\times10^{-18}$ cm^3/ns.

steadily towards the trap center. The results shown in Fig. 1 are typical for cw excitation. The curves for the outer region of the trap ($r > 60\ \mu$m) do not differ qualitatively for other parameters. Therefore, we will concentrate on the inner region of the trap for the following results.

For the experimental realization of an excitonic condensate, one has to create high densities at low temperatures. Since the Auger effect scales quadratically with the density, it seems favorable to use low pump powers at ultralow temperatures in order to minimize its influence. The results for $P_L = 2.8\ \mu$W and different phonon temperatures are shown in Fig. 2. The total number of excitons varies only weakly between $N = 2.74 \times 10^6$ ($T_{Ph} = 1.0$ K) and $N = 2.57 \times 10^6$ ($T_{Ph} = 0.037$ K). Since the extension of the thermal cloud shrinks with decreasing temperatures, the density in the trap center has to increase accordingly. Therefore, lowering the phonon temperature at a constant pump power actually increases the influence of the Auger effect. The temperature curves illustrate this well. For the cases $T_{Ph} = 1.0$ K and $T_{Ph} = 0.5$ K, the exciton temperatures in the trap center are very close to the respective phonon temperatures. The monotonous course of the curves clearly indicates a very weak influence of the Auger effect. In case of the ultralow phonon temperature of $T_{Ph} = 0.037$ K, the temperature forms the typical shape for a strong influence of the Auger effect (minimum outside the trap center and a local maximum at $r = 0$). The temperature in the trap center is $T_0 = 0.25$ K and hence well above the phonon temperature. The mean temperature $\langle T \rangle = 0.38$ K is even one order of magnitude higher than the phonon temperature. This clearly illustrates the crucial role of the Auger effect, which becomes increasingly important not only at high pump powers but also at ultralow temperatures. However, there is another important effect at ultralow temperatures, the finite thermalization time. Due to the "freezing out" of phonons [20], the thermalization time becomes increasingly longer at lower and lower bath temperatures. Setting $A = 0$ results in the dashed-dotted black temperature curve in Fig. 2. The exciton

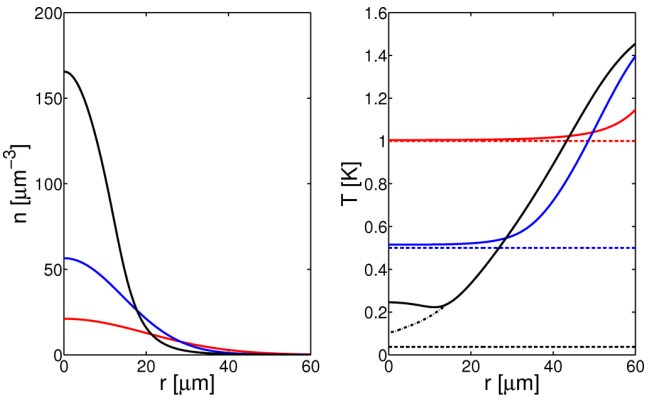

FIG. 2. (Color online) Density $\tilde{n}(r)$ and temperature $T(r)$ for the stationary state at a laser power of $P_L = 2.8\ \mu$W, a phonon temperature of $T_{Ph} = 1.0$ K (solid red curve), $T_{Ph} = 0.5$ K (solid blue curve), and $T_{Ph} = 0.037$ K (solid black curve), and an Auger rate of $A = 2.0 \times 10^{-18}$ cm^3/ns. The dashed lines of the same color show the respective phonon temperatures. The dash-dotted black line in the right panel shows the temperature for $T_B = 0.037$ K and $A = 0$.

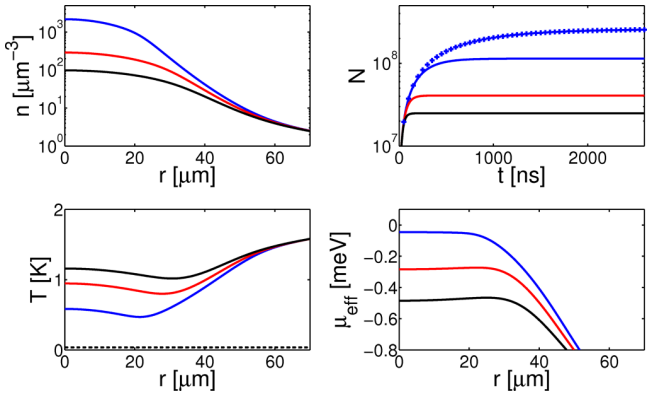

FIG. 3. (Color online) Density $\tilde{n}(r)$, temperature $T(r)$, and effective chemical potential $\tilde{\mu}_{eff}(r)$ for the stationary state at a phonon temperature of $T_{Ph} = 0.037$ K and a laser power of $P_L = 262\ \mu$W as well as the evolution of the total exciton number $N(t)$. The Auger rates are $A = 2.0 \times 10^{-18}$ cm^3/ns [18] (blue curves), $A = 7.0 \times 10^{-17}$ cm^3/ns [33] (red curves), and $A = 4.0 \times 10^{-16}$ cm^3/ns [34] (black curves). The blue crosses mark the development of the exciton number without the Auger effect. The black dashed line represents the phonon temperature.

temperature is monotonously dropping towards the trap center, however, it never reaches the actual bath temperature. This is due to the finite lifetime of the excitons which in this case is too short for a complete thermalization. Hence, even if the Auger effect could be "turned off" in the actual experiments, one can still not expect the excitons to be fully thermalized with the lattice at ultralow bath temperatures. However, in most experimentally relevant cases, the influence of the Auger effect will be dominant compared to the finite thermalization time. Therefore, the uncertainty associated with the Auger rate A is problematic for any predictions of the onset of a BEC of excitons.

How the Auger rate affects the different quantities is shown in Fig. 3. The results were obtained by using three different Auger rates from the literature and keeping all other parameters (phonon temperature, pump power, ...) constant. Important values for the different curves in Fig. 3 are listed in Table I. While the shape of the density profiles stay qualitatively the same, the quantitative value in the trap center changes by more than one order of magnitude between the smallest and the largest Auger rate. Accordingly, the exciton number in the stationary state changes by more than a factor of four between these cases. The temperature curves all display the typical form indicating a strong influence of the Auger effect. The temperature in the trap center and the mean temperature for $A = 2.0 \times 10^{-18}$ cm^3/ns and $A = 4.0 \times 10^{-16}$ cm^3/ns

TABLE I. Key values in the stationary state for the results shown in Fig. 3.

A (cm^3/ns)	$N/10^8$	$\langle T \rangle$ (K)	T_0 (K)	T_{min} (K)	$\tilde{n}_0$ (μm^{-3})
2×10^{-18}	1.14	0.65	0.58	0.47	2175.6
7×10^{-17}	0.41	1.03	0.95	0.80	288.9
4×10^{-16}	0.25	1.24	1.16	1.02	98.2

differ by approximately a factor of two. Due to the strong heating introduced by the Auger effect, the maximum of the effective chemical potential for $A = 4.0 \times 10^{-16}$ cm^3/ns and $A = 7.0 \times 10^{-17}$ cm^3/ns does not even lie in the center of the trap. For these high Auger rates, there will probably be no onset of a BEC within our model.

B. Comparison with experiments

In the following we compare theoretical results with the corresponding experimental data for two different situations.

The first set of examples is taken from Ref. [18]. In the experiment, cw excitation was used over a wide range of pumping powers for a helium bath temperature of $T_B = 0.037$ K. The experimentally determined Auger rate is $A = 2.0 \times 10^{-18}$ cm^3/ns and the trap parameter is $\alpha = 0.09\ \mu$eV μm^{-2}.

The result for the temperature using a pump power of $P_L = 3\ \mu$W is shown in the left panel of Fig. 4. It first falls to a minimum of $T_{min} = 0.23$ K at $r = 10\ \mu$m and reaches a local maximum in the trap center with $T_0 = 0.25$ K. The mean temperature is $\langle T \rangle = 0.40$ K and hence very close to the experimentally determined spectral temperature of $T_S = 0.41$ K (compare Fig. 3 of Ref. [18]). The experimentally determined exciton number was $N_{Expt} = 2.6 \times 10^6$ which agrees well with the value of $N = 2.78 \times 10^6$ predicted by our model. In the right panel of Fig. 4 we compare the experimentally determined exciton numbers and spectral temperatures T_S with the corresponding theoretical results for exciton number and mean temperature $\langle T \rangle$ over a wide range of pumping powers. As before, the quantities agree well with the experimental values. This suggests to identify the spectral temperature T_S from the experiments with the mean temperature of the excitons $\langle T \rangle$, which seems intuitively plausible. If this is correct, the spectral temperature is actually considerably higher than the temperature of the excitons in the trap center (see Fig. 4). This was already proposed in Ref. [18] to explain some of the experimental features and is consistent with the typical results discussed in the previous section. To further substantiate the identification $T_S = \langle T \rangle$ one would need to calculate the spectrum and apply the same fitting procedure as in the experiments. For this a theory of luminescence for interacting excitons in an inhomogeneous system in a nonequilibrium state is needed. To our knowledge, there is no fully developed theory for this purpose at the moment. This is an open problem that needs to be solved in the future.

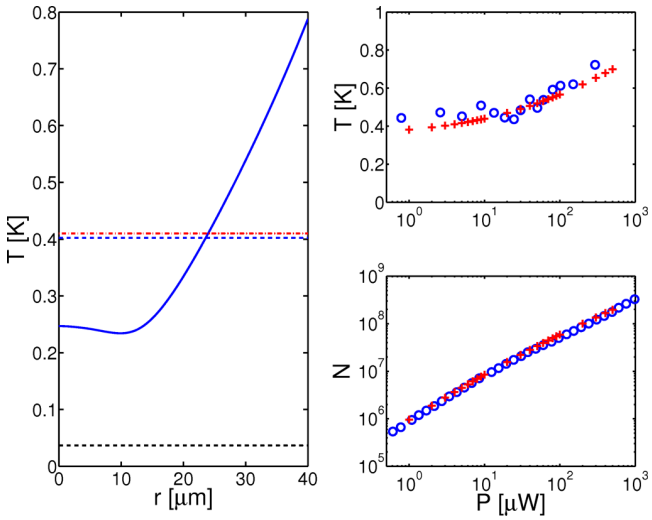

FIG. 4. (Color online) Left panel: Exciton temperature $T(r)$ (solid blue curve) and the mean exciton temperature $\langle T \rangle = 0.40$ K (dashed blue curve) under cw excitation with a pump power of $P_L = 3\ \mu$W and a phonon temperature of $T_{Ph} = 0.037$ K (dashed black curve) in the stationary state. The dashed red curve shows the experimentally determined spectral temperature $T_S = 0.41$ K (compare Fig. 3 in Ref. [18]). Right panel: Experimentally determined exciton numbers and spectral temperatures T_S (blue circles) for different pump powers (compare Fig. 11 in Ref. [18]) in comparison with the exciton numbers and the mean temperatures $\langle T \rangle$ (red crosses) as predicted by our theory.

The second set of experimental data is taken from Ref. [16], Figs. 8 and 9. Using pulsed excitation, the exciton number and the spectral temperature T_S were experimentally determined for a bath temperature of $T_B = 0.82$ K. For the calculations we used $\alpha = 0.11\ \mu$eV μm^{-2} and $A = 2.0 \times 10^{-18}$ cm^3/ns. The theoretical results for the mean temperature and the exciton number as well as their experimental counterparts are shown in Fig. 5. The calculated exciton numbers agree well with the experimental results. Only the second and third value show stronger discrepancies. The reason for this is probably the neglection of the orthoexcitons in our calculations. In the experiments, the orthoexcitons create new paraexcitons by conversion even when the laser is switched off. In the present form of the theoretical model this effect is not included.

The calculated mean temperature $\langle T \rangle$ and the experimentally determined spectral temperature T_S do not agree. The

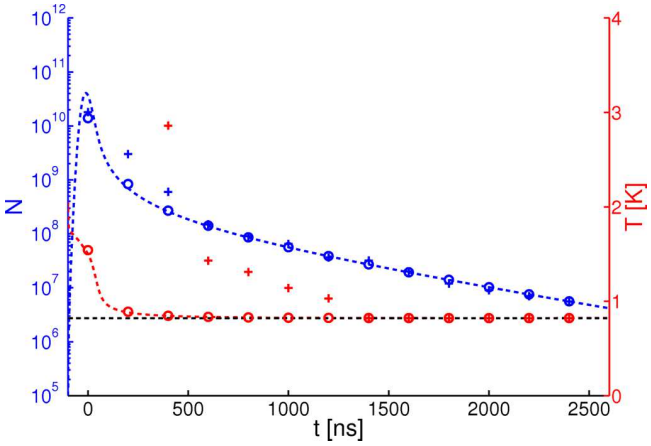

FIG. 5. (Color online) Calculated exciton number $N(t)$ (dashed blue line) and mean temperature $\langle T \rangle$ (dashed red line) under pulsed excitation for a phonon temperature of $T_{Ph} = 0.82$ K. The laser pulse has been modeled according to the data provided in Ref. [16]. The blue and red circles represent the theoretical values averaged over a gate width of 200 ns. The blue and red crosses represent the experimentally determined values with the same gate width [16]. The Auger rate is set to $A = 2.0 \times 10^{-18}$ cm^3/ns.

first two points of the spectral temperature are even off the scale (the values are 12.5 and 6.0 K). According to the theory presented here and in Ref. [28], temperatures around 4 K should be reached in less than 1 ns. However, in this case, the experimentally determined spectral temperature T_S is 6.0 K after 400 ns. Since the parameters and the collision term for the X-Ph interaction are well known, we exclude both as origin of the discrepancy. An increased Auger rate can also not explain the differences since the newly formed excitons cool rapidly to temperatures around 4 K. The most probable explanation for the differences is a heating of the specimen by the pump laser and, therefore, $T_{Ph} > T_B$. As a result, the excitons cool only to the respective lattice temperature, which is higher than the temperature of the surrounding helium bath. Once the laser is turned off, the crystal slowly cools down to the bath temperature and the excitons with it. Therefore, it is very likely that the temperature curves in Ref. [16] actually show the cooling process of the crystal rather than that of the excitons.

VI. CONCLUSION AND OUTLOOK

In this paper we developed a theoretical model to describe trapped ultracold paraexcitons in Cu_2O out of equilibrium. It uses a generalized Gross-Pitaevskii equation for describing a possible condensate and a set of hydrodynamic equations for the thermal excitons. The finite lifetime, the Auger-like two-body decay, the pump laser, exciton-exciton, and exciton-phonon interaction have been taken into account.

The numerical results obtained using continuous wave excitation revealed some important features of the stationary states of the excitonic system. First of all, the stationary states are true nonequilibrium situations which cannot be approximated using a global equilibrium distribution. Second, the excitons do not fully thermalize with the crystal lattice at ultralow temperatures ($T_{Ph} \ll 1.0$ K). There is a distinct gap between the actual exciton and the respective phonon temperature which continuously increases for sinking phonon temperatures. This is due to the long thermalization time and the Auger effect. The latter strongly influences the exciton densities and temperatures for high pumping powers and at ultralow temperatures.

Comparing the exciton numbers predicted by our model with experimental results for pulsed and continuous wave excitation yields reasonable agreement. Furthermore, comparing the mean temperature $\langle T \rangle$ from the calculations with the experimentally determined spectral temperatures T_S under continuous wave excitation suggests the identification $\langle T \rangle = T_S$. As a result, the excitons in the trap center are actually cooler than the spectral temperature suggests. This preposition was already made in a previous paper [18] to explain some of the experimental features. However, comparing the experimentally determined and theoretically predicted temperatures under pulsed excitation showed strong discrepancies between the two. The most probable explanation for this is a heating of the crystal. If that is the case then the experimentally determined evolution of the spectral temperature is closely related to the cooling process of the crystal lattice rather than that of the excitons. It is well known that high pump powers can lead to heating of the specimen and even of the surrounding helium bath. In principle, the temperature of the crystal lattice can be determined using Brillouin scattering. However, this is very difficult experimentally and, to our knowledge, has not been done yet. If our interpretation of the experimental data is correct, experiments under pulsed excitation with varying pump powers might be an opportunity to study the cooling process of the crystal lattice indirectly in a simple fashion.

In conclusion, the theoretical results obtained by our model are intuitively plausible and yield reasonable agreement with the exciton numbers and spectral temperatures obtained experimentally. The results presented in this paper are, therefore, an important step to improve the understanding of the experiments. Unfortunately, there are still some crucial problems that need to be addressed. Most importantly, the theoretical model must be able to reliably predict parameters for the onset of Bose-Einstein condensation (i.e., the vanishing of the effective chemical potential). However, within the present model, a quantitative discussion of the condensation parameters would not yield reliable results mainly due to the uncertainties associated with the Auger decay. Since the Auger effect reduces the density while increasing the temperature, its modeling and the parameters associated with it are of paramount importance for predicting the condensation threshold. However, the Auger rates A reported in the literature by different authors vary over 6 orders of magnitude. Additionally, to our knowledge, there are no theoretical results that agree with any of the experimentally determined Auger rates. Furthermore, using a $\mathbf{k}$-averaged constant A as Auger rate is itself already a simplification. According to the theoretical works on the Auger decay [32], the rate A should be proportional to some power of k. Using such a k-dependent rate would primarily destroy high energy excitons, while affecting low energy excitons much less. An inclusion of such a k-dependent Auger rate will have strong effects on the parameters for condensation. Moreover, in a strain free crystal of Cu_2O, the Auger decay of the paraexcitons under consideration is negligible [32]. The experimentally observed Auger decay of these excitons is due to the ortho-para Auger decay and the effects the applied stress has on the exciton states. The former can only be included by modeling a multicomponent system of para- and orthoexcitons. Therefore, considering these uncertainties, we refrain from a discussion of the condensation threshold at this point. In order to make reliable predictions for the onset of Bose-Einstein condensation, the problems discussed above have to be addressed first.

Another important extension to the theoretical model is using a symmetry which fits the experimental geometry better, i.e., cylindrical (quasi-two-dimensional) instead of spherical (quasi-one-dimensional). This should yield more realistic theoretical results. More importantly though, in order to directly compare the theoretical and experimental results, we need to be able to calculate the luminescence spectrum of the excitons. Being able to differentiate between the spectra of excitons in quasiequilibrium, a stationary state, or a condensed case is crucial. It is especially important to identify unique spectral features of a condensate like it was already done for excitons in equilibrium [39,40]. This requires us to develop a

theory of excitonic luminescence for inhomogeneous systems in nonequilibrium. One possible approach is to start from the first order correlation function [41] treating the photons by an equation of motion method [42,43]. This is work in progress and will be the subject of a future publication.

ACKNOWLEDGMENTS

We would like to thank G. Manzke, W.-D. Kraeft, Th. Bornath, Th. Koch, and H. Fehske for many fruitful discussions. This work was supported by the Deutsche Forschungsgemeinschaft via Collaborative Research Center SFB 652.

[1] S. A. Moskalenko, Fiz. Tverd. Tela **4**, 276 (1962) [Sov. Phys.-Solid State **4**, 199 (1962)].
[2] I. M. Blatt, K. W. Boer, and W. Brandt, Phys. Rev. **126**, 1691 (1962).
[3] H. Kuroda, S. Shionoya, H. Saito, and E. Hanamura, Solid State Commun. **12**, 533 (1973).
[4] H. Deng, G. Weihs, C. Santori, J. Bloch, and Y. Yamamoto, Science **298**, 199 (2002).
[5] J. Kasprzak, M. Richard, S. Kundermann, A. Baas, P. Jeambrun, J. M. J. Keeling, F. M. Marchetti, M. H. Szymańska, R. André, J. L. Staehli, V. Savona, P. B. Littlewood, B. Deveaud, and L. S. Dang, Nature (London) **443**, 409 (2006).
[6] R. B. Balili, V. Hartwell, D. Snoke, L. Pfeiffer, and K. West, Science **316**, 1007 (2007).
[7] H. Deng, H. Haug, and Y. Yamamoto, Rev. Mod. Phys. **82**, 1489 (2010).
[8] Z. Vörös, D. W. Snoke, L. Pfeiffer, and K. West, Phys. Rev. Lett. **97**, 016803 (2006).
[9] A. A. High, J. R. Leonard, M. Remeika, L. V. Butov, M. Hanson, and A. C. Gossard, Nano Lett. **12**, 2605 (2012).
[10] G. J. Schinner, J. Repp, E. Schubert, A. K. Rai, D. Reuter, A. D. Wieck, A. O. Govorov, A. W. Holleitner, and J. P. Kotthaus, Phys. Rev. B **87**, 205302 (2013).
[11] D. Semkat, S. Sobkowiak, G. Manzke, and H. Stolz, Nano Lett. **12**, 5055 (2012).
[12] D. W. Snoke, J. P. Wolfe, and A. Mysyrowicz, Phys. Rev. Lett. **64**, 2543 (1990).
[13] J. L. Lin and J. P. Wolfe, Phys. Rev. Lett. **71**, 1222 (1993).
[14] D. Snoke, Science **298**, 1368 (2002).
[15] K. Yoshioka, E. Chae, and M. Kuwata-Gonokami, Nat. Commun. **2**, 328 (2011).
[16] R. Schwartz, N. Naka, F. Kieseling, and H. Stolz, New J. Phys. **14**, 023054 (2012).
[17] D. W. Snoke, Phys. Status Solidi B **238**, 389 (2003).
[18] H. Stolz, R. Schwartz, F. Kieseling, S. Som, M. Kaupsch, S. Sobkowiak, D. Semkat, N. Naka, Th. Koch, and H. Fehske, New J. Phys. **14**, 105007 (2012).
[19] K. Yoshioka, Y. Morita, K. Fukuoka, and M. Kuwata-Gonokami, Phys. Rev. B **88**, 041201 (2013).
[20] A. L. Ivanov, C. Ell, and H. Haug, Phys. Rev. E **55**, 6363 (1997).
[21] D. W. Snoke and J. P. Wolfe, Phys. Rev. B **39**, 4030 (1989).
[22] K. E. O'Hara and J. P. Wolfe, Phys. Rev. B **62**, 12909 (2000).
[23] S. Denev and D. W. Snoke, Phys. Rev. B **65**, 085211 (2002).
[24] N. P. Proukakis and B. Jackson, J. Phys. B **41**, 203002 (2008).
[25] A. Griffin, T. Nikuni, and E. Zaremba, *Bose-Condensed Gases at Finite Temperatures* (Cambridge University Press, Cambridge, 2009).
[26] E. Zaremba, T. Nikuni, and A. Griffin, J. Low Temp. Phys. **116**, 277 (1999).
[27] M. Imamovic-Tomasovic and A. Griffin, J. Low Temp. Phys. **122**, 617 (2001).
[28] S. Sobkowiak, D. Semkat, and H. Stolz, Phys. Rev. B **90**, 075206 (2014).
[29] H. Haug, T. D. Doan, and D. B. Tran Thoai, Phys. Rev. B **89**, 155302 (2014).
[30] D. P. Trauernicht and J. P. Wolfe, Phys. Rev. B **33**, 8506 (1986).
[31] K. Reimann and K. Syassen, Phys. Rev. B **39**, 11113 (1989).
[32] G. M. Kavoulakis and G. Baym, Phys. Rev. B **54**, 16625 (1996).
[33] K. E. O'Hara, J. R. Gullingsrud, and J. P. Wolfe, Phys. Rev. B **60**, 10872 (1999).
[34] K. Yoshioka, T. Ideguchi, A. Mysyrowicz, and M. Kuwata-Gonokami, Phys. Rev. B **82**, 041201 (2010).
[35] J. I. Jang and J. P. Wolfe, Solid State Commun. **137**, 91 (2006).
[36] M. Wouters and V. Savona, Phys. Rev. B **79**, 165302 (2009).
[37] J. Shumway and D. M. Ceperley, Phys. Rev. B **63**, 165209 (2001).
[38] J. Brandt, D. Fröhlich, C. Sandfort, M. Bayer, H. Stolz, and N. Naka, Phys. Rev. Lett. **99**, 217403 (2007).
[39] S. Sobkowiak, D. Semkat, H. Stolz, Th. Koch, and H. Fehske, Phys. Rev. B **82**, 064505 (2010).
[40] S. Sobkowiak, D. Semkat, H. Stolz, Th. Koch, and H. Fehske, Phys. Status Solidi C **8**, 1178 (2011).
[41] R. J. Glauber, Phys. Rev. **130**, 2529 (1963).
[42] H. Stolz, *Time-Resolved Light Scattering from Excitons*, Springer Tracts in Modern Physics, Vol. 130 (Springer, Berlin, 1994).
[43] B. Laikhtman, Europhys. Lett. **43**, 53 (1998).

A.12

Artikel 12

Th. Koch, D. Semkat, H. Stolz, and H. Fehske:

Theory of zero-phonon decay luminescence of semiconductor excitons

Fortschr. Phys. **65**, 1600068 (2017)

Fortschr. Phys. 65, No. 6–8, 1600068 (2017) / DOI 10.1002/prop.201600068

Fortschritte der Physik
Progress of Physics

Original Paper

Theory of zero-phonon decay luminescence of semiconductor excitons

Thomas Koch[1,*], *Dirk Semkat*[2], *Heinrich Stolz*[2], *and Holger Fehske*[1]

Received 6 June 2016, revised 11 August 2016, accepted 12 August 2016
Published online 26 September 2016

We present a theoretical approach to the zero-phonon decay luminescence of excitons. In a two-step approach, the weakly interacting condensed exciton gas is Bogolyubov transformed before the resulting quasiparticles are coupled to the photon field. The field–field correlation function, which gives the luminescence intensity and first-order coherence, is calculated in the framework of real-time Green's functions of the photons. The resulting spectrum of the new, so-called bogolariton, quasiparticles is discussed.

1 Introduction

Excitons in excited semiconductors have been suggested as promising candidates for the observation of Bose–Einstein condensation (BEC) more than five decades ago [1, 2]. Due to their rather small mass comparable to the free electron mass, the conditions for densities and temperatures should be easily achievable in the experiment. However, despite many efforts creating a dense gas of excitons either in a bulk crystal or in a potential trap, a conclusive demonstration of excitonic BEC is still missing.

At present, cuprous oxide (Cu_2O) is in the focus of both experimental and theoretical efforts (for a recent overview see Ref. [3]), namely because of the large binding energy and the long lifetime of the exciton states in this material [4, 5]. In current experiments, entrapment of the excitons in a strain induced external potential is used to obtain sufficiently high particle densities. Due to the strain, the usually forbidden direct (zero-phonon) decay of lowest paraexciton state becomes weakly allowed. As a consequence, the excitonic system is accessible by the exciton decay luminescence, which should feature signatures of exciton condensation. The most obvious evidence, of course, would be the detection of coherence. On the other hand, an exciton condensate is also reflected in the luminescence and photon spectra [6, 7]. Theory must provide, therefore, an approach both to coherence as well as spectral properties of the luminescence signal.

Previous theoretical approaches to the excitonic decay luminescence [8, 9] were based on an exciton-photon coupling Hamiltonian containing only "normal" terms, i.e., the creation of a photon and simultaneous destruction of an exciton. However, since the Bogolyubov picture of exciton condensation accounts for anomalous exciton-exciton interaction terms, anomalous exciton-photon coupling terms should also be included when deriving the luminescence. This allows to account for the polariton effect in a very general manner. In contrast to microcavity systems, the trapped excitons couple to free photon modes. Then the exciton–photon interaction is inherently a quasi-equilibrium problem, where the luminescence should take place via transient polariton-like states.

In the following, we start with a brief summary of the thermodynamics of excitons in a potential trap, where the exciton Hamiltonian is diagonalised by a Bogolyubov transformation. Then we elaborate in detail the coupling of the Bogolyubov quasiparticles to the photon field. Within a Green's functions framework, we analyse the resulting new quasiparticle dispersion and discuss its consequences for the field–field correlation function and the decay luminescence intensity.

2 Trapped exciton gas

Since in Cu_2O the paraexciton lifetime far exceeds the time to reach thermal (quasi-)equilibrium [10, 11], for the moment we do not consider recombination and

[1] Institut für Physik, Ernst–Moritz–Arndt–Universität Greifswald, 17489 Greifswald, Germany
[2] Institut für Physik, Universität Rostock, 18051 Rostock, Germany
* Corresponding author E-mail: thomas.koch@physik.uni-greifswald.de

neglect the coupling to the light field. Consequently, we model the trapped excitons as a gas of structureless, interacting bosons in an external potential. Furthermore, the extension of the potential trap is considered to be large compared to the thermal de Broglie wavelength of the excitons. That is why we apply the local density approximation, i.e., we treat the excitons as a locally homogeneous system where the spatial dependence enters only via $V_{\text{ext}}(\mathbf{r})$. With the $\mathbf{r}$ argument omitted for brevity, the corresponding Hamiltonian in the grand canonical ensemble reads

$$\hat{H}_{\text{x}} = \sum_{\mathbf{q}} \left(\frac{\hbar^2 q^2}{2m} + E_g + V_{\text{ext}} - \mu \right) \hat{B}^\dagger_{\mathbf{q}} \hat{B}_{\mathbf{q}} + \frac{U}{2V} \sum_{\mathbf{qpk}} \hat{B}^\dagger_{\mathbf{p+q}} \hat{B}^\dagger_{\mathbf{k-q}} \hat{B}_{\mathbf{p}} \hat{B}_{\mathbf{k}}, \tag{1}$$

with the creation (annihilation) operators $\hat{B}^\dagger_{\mathbf{q}}$ ($\hat{B}_{\mathbf{q}}$) of excitons with wave vector $\mathbf{q}$, the effective exciton mass m, the excitonic gap energy E_g (i.e., the band gap minus the exciton binding energy), the trapping potential V_{ext} and the equilibrium chemical potential μ. We assume solely contact interaction whose strength is given by the s-wave scattering length a_{s}:

$$U = \frac{4\pi\hbar^2 a_{\text{s}}}{m}. \tag{2}$$

To account for a possible exciton condensate, we apply to Eq. (1) the Bogolyubov prescription, i.e., we replace the operators $\hat{B}^{(\dagger)}_0$ by $\sqrt{N_c}$, where N_c is the number of condensed particles. Accordingly, from now on the operators $\hat{B}_{\mathbf{q}}$ refer to the non-condensed particles with $\mathbf{q} \neq 0$. Retaining only those parts of the Hamiltonian that are quadratic in $\hat{B}_{\mathbf{q}}$, we have

$$\hat{H}_{\text{x}} \approx E_c + \sum_{\mathbf{q}} \left(\frac{\hbar^2 q^2}{2m} + E_g + V_{\text{ext}} - \mu \right) \hat{B}^\dagger_{\mathbf{q}} \hat{B}_{\mathbf{q}} + \frac{U n_c}{2} \sum_{\mathbf{q}\neq 0} \left(2\hat{B}^\dagger_{\mathbf{q}} \hat{B}_{\mathbf{q}} + \hat{B}^\dagger_{\mathbf{q}} \hat{B}^\dagger_{-\mathbf{q}} + \hat{B}_{\mathbf{q}} \hat{B}_{-\mathbf{q}} \right), \tag{3}$$

with the energy E_c of the condensate.

The quadratic Hamiltonian in Eq. (3) may be diagonalised by the Bogolyubov transformation

$$\hat{B}_{\mathbf{q}} = u_{\mathbf{q}} \hat{b}_{\mathbf{q}} - v^*_{-\mathbf{q}} \hat{b}^\dagger_{-\mathbf{q}}. \tag{4}$$

The new operators $\hat{b}^{(\dagger)}_{\mathbf{q}}$ obey the bosonic commutation relations $[\hat{b}_{\mathbf{q}}, \hat{b}^\dagger_{\mathbf{q}'}] = \delta_{\mathbf{q},\mathbf{q}'}$, provided the Bogolyubov amplitudes $u_{\mathbf{q}}$ and $v_{\mathbf{q}}$ satisfy the relation $|u_{\mathbf{q}}|^2 - |v_{-\mathbf{q}}|^2 = 1$. Under this condition, the anomalous terms in the Hamiltonian vanish for

$$u^2_{\mathbf{q}}(\mathbf{r}) = \frac{1}{2} \left(\frac{L_{\mathbf{q}}(\mathbf{r})}{E_{\mathbf{q}}(\mathbf{r})} + 1 \right), \tag{5}$$

$$v^2_{\mathbf{q}}(\mathbf{r}) = \frac{1}{2} \left(\frac{L_{\mathbf{q}}(\mathbf{r})}{E_{\mathbf{q}}(\mathbf{r})} - 1 \right). \tag{6}$$

Here, $E_{\mathbf{q}}$ is the Bogolyubov dispersion

$$E_{\mathbf{q}}(\mathbf{r}) = \sqrt{L^2_{\mathbf{q}}(\mathbf{r}) - U^2 n^2_c(\mathbf{r})}, \tag{7}$$

$$L_{\mathbf{q}}(\mathbf{r}) = \frac{\hbar^2 q^2}{2m} - \mu + E_g + V_{\text{ext}}(\mathbf{r}) + 2Un(\mathbf{r}), \tag{8}$$

and $n = n_c + n_T$ is the total particle density. The density of thermal excitations follows as

$$n_T(\mathbf{r}) = \int \frac{\mathrm{d}^3 q}{8\pi^3} \left[\frac{L_{\mathbf{q}}(\mathbf{r})}{E_{\mathbf{q}}(\mathbf{r})} \left(n_B(E_{\mathbf{q}}(\mathbf{r})) + \frac{1}{2} \right) - \frac{1}{2} \right] \Theta\left(E_{\mathbf{q}}(\mathbf{r})^2 \right), \tag{9}$$

with $n_B(E) = [\exp(E/k_B T) - 1]^{-1}$, while the Thomas–Fermi result for the density of trapped condensate particles reads [12]

$$n_c(\mathbf{r}) = \max\{0, \frac{1}{U} \left(\mu - V_{\text{ext}}(\mathbf{r}) - E_g - 2Un_T(\mathbf{r}) \right)\}. \tag{10}$$

As is well known, the Bogolyubov quasiparticles, the so-called bogolons, represent phonon like excitations in the long wavelength limit and free excitons in the limit of large $\mathbf{q}$. The excitonic spectral function $A_{BB}(\mathbf{q}, \omega, \mathbf{r})$ features two branches at $\hbar\omega = \pm E_{\mathbf{q}}$, weighted by the Bogolyubov amplitudes:

$$A_{BB}(\mathbf{q}, \omega, \mathbf{r}) = 2\pi\hbar \big[u^2_{\mathbf{q}}(\mathbf{r}) \delta(\hbar\omega - E_{\mathbf{q}}(\mathbf{r})) - v^2_{\mathbf{q}}(\mathbf{r}) \delta(\hbar\omega + E_{\mathbf{q}}(\mathbf{r})) \big]. \tag{11}$$

In the non-condensed situation, i.e, for $n_c = 0$ and $E_{\mathbf{q}} = L_{\mathbf{q}}$, we have $v_{\mathbf{q}} = 0$ and $u_{\mathbf{q}} = 1$, so that only one spectral branch remains and the Bogolyubov quasiparticles become free excitons in a Hartree–Fock mean field.

3 Bogolon-photon coupling

Excitons decay by emitting photons. In cuprous oxide, direct (i.e. zero-phonon) paraexciton decay becomes weakly allowed when strain is applied. In the following, we aim on describing this zero-phonon decay process.

Thanks to the Bogolyubov transformation outlined above, the system of interacting excitons is transformed to a system of non-interacting quasiparticles with the

Hamiltonian

$$\hat{H}_{\rm x} = \sum_{\mathbf{q}} E_{\mathbf{q}} \hat{b}^{\dagger}_{\mathbf{q}} \hat{b}_{\mathbf{q}}. \tag{12}$$

Accordingly, we write the Hamiltonian of the free photon field as a sum of oscillator modes,

$$\hat{H}_p = \sum_{\mathbf{q}} \hbar\omega_{\mathbf{q}} \hat{a}^{\dagger}_{\mathbf{q}} \hat{a}_{\mathbf{q}}, \tag{13}$$

with the photonic operators $a^{(\dagger)}_{\mathbf{q}}$ and the dispersion $\omega_{\mathbf{q}} = cq$. Here, $c = c_0/\sqrt{\varepsilon_b}$ is the velocity of light in the medium, where c_0 is the vacuum velocity of light and ε_b is the background dielectric constant.

To model the bogolon-photon interaction, we start from the minimal coupling Hamiltonian [13],

$$\hat{H}_{\rm xp} = -\frac{e}{m_0} \sum_j \hat{\mathbf{A}}(\hat{\mathbf{r}}_j) \cdot \hat{\mathbf{p}}_j + \frac{e^2}{2m_0} \sum_j |\hat{\mathbf{A}}(\hat{\mathbf{r}}_j)|^2, \tag{14}$$

where m_0 is the free electron mass and $\hat{\mathbf{r}}_j$ and $\hat{\mathbf{p}}_j$ are the position and momentum of the j-th electron. We now insert into Eq. (14) the Heisenberg equation of motion $\mathrm{i}\hbar\hat{\mathbf{p}}_j = m_0[\hat{\mathbf{r}}_j, \hat{H}_{\rm x}]$. Thereby we expand the position operator in terms of the many-body wave functions of the bogolons, $\Psi^B_{\mathbf{q}}$, as follows [13]:

$$\begin{aligned}\hat{\mathbf{r}}_j = &\sum_{\mathbf{q}} \langle 0|\,\hat{\mathbf{r}}_j\,|\Psi^B_{\mathbf{q}}\rangle\, \hat{b}_{\mathbf{q}} + \sum_{\mathbf{q}} \langle \Psi^B_{\mathbf{q}}|\,\hat{\mathbf{r}}_j\,|0\rangle\, \hat{b}^{\dagger}_{\mathbf{q}} \\ &+ \sum_{\substack{\mathbf{q},\mathbf{q}'\\ \mathbf{q}\neq\mathbf{q}'}} \sum \langle \Psi^B_{\mathbf{q}}|\,\hat{\mathbf{r}}_j\,|\Psi^B_{\mathbf{q}'}\rangle\, \hat{b}^{\dagger}_{\mathbf{q}} \hat{b}_{\mathbf{q}'}.\end{aligned} \tag{15}$$

In the following, we neglect the last term on the r.h.s of Eq. (15), i.e., we take into account only transitions from the Bogolyubov ground state, i.e., the condensate, to the excited states and vice versa. After evaluating the commutator $[\hat{\mathbf{r}}_j, \hat{H}_{\rm x}]$ and expanding the vector potential operator $\hat{\mathbf{A}}$ into the set of normal modes,

$$\hat{\mathbf{A}}(\mathbf{r}) = \sum_{\mathbf{q}\lambda} \sqrt{\frac{\hbar}{2\varepsilon_0 V \omega_{\mathbf{q}}}}\, \mathbf{e}_{\mathbf{q}\lambda} \left(\hat{a}_{\mathbf{q}} + \hat{a}^{\dagger}_{-\mathbf{q}}\right) \mathrm{e}^{\mathrm{i}\mathbf{q}\cdot\mathbf{r}}, \tag{16}$$

the total Hamiltonian $\hat{H} = \hat{H}_{\rm x} + \hat{H}_{\rm p} + \hat{H}_{\rm xp}$ takes the form:

$$\begin{aligned}\hat{H} = &\sum_{\mathbf{q}} E_{\mathbf{q}} \hat{b}^{\dagger}_{\mathbf{q}} \hat{b}_{\mathbf{q}} + \sum_{\mathbf{q}} \hbar\omega_{\mathbf{q}} \hat{a}^{\dagger}_{\mathbf{q}} \hat{a}_{\mathbf{q}} \\ &+ \mathrm{i} \sum_{\mathbf{q}} C_{\mathbf{q}} (\hat{a}_{\mathbf{q}} + \hat{a}^{\dagger}_{-\mathbf{q}})(\hat{b}_{-\mathbf{q}} - \hat{b}^{\dagger}_{\mathbf{q}}) \\ &+ \sum_{\mathbf{q}} D_{\mathbf{q}} (\hat{a}_{-\mathbf{q}} + \hat{a}^{\dagger}_{\mathbf{q}})(\hat{a}_{\mathbf{q}} + \hat{a}^{\dagger}_{-\mathbf{q}}),\end{aligned} \tag{17}$$

with the coupling strength parameters

$$C_{\mathbf{q}} = E_{\mathbf{q}} \sqrt{\frac{2\pi \mathrm{e}^2}{4\pi\varepsilon_0\varepsilon_r V \hbar\omega_{\mathbf{q}}}} \left\langle \Psi^B_{\mathbf{q}} \middle| \mathbf{e}_{\mathbf{q}\lambda} \cdot \sum_j \mathbf{r}_j \mathrm{e}^{\mathrm{i}\mathbf{q}\cdot\mathbf{r}_j} \middle| 0 \right\rangle, \tag{18}$$

and $D_{\mathbf{q}} = |C_{\mathbf{q}}|^2/E_{\mathbf{q}}$. Using the dipole approximation $\exp(\mathrm{i}\mathbf{q}\cdot\mathbf{r}_j) \approx 1$ and the definition of the oscillator strength

$$f = \frac{2m_0 E_{\mathbf{q}}}{\hbar^2} \left| \left\langle \Psi^B_{\mathbf{q}} \middle| \mathbf{e}_{\mathbf{q}\lambda} \cdot \sum_j \mathbf{r}_j \middle| 0 \right\rangle \right|^2, \tag{19}$$

we obtain the coupling strength as [14]

$$C_{\mathbf{q}} = \sqrt{\frac{\hbar^2 e^2 f}{4\varepsilon_0\varepsilon_r m_0 V}} \sqrt{\frac{E_{\mathbf{q}}}{\hbar\omega_{\mathbf{q}}}}. \tag{20}$$

Note that definition (19) originally involves the *exciton* state $\langle\Psi^X_{\mathbf{q}}|$. However, we will not derive f microscopically, but use an experimentally obtained value for our calculations. Exciton states in the experiment are by nature "dressed", i.e. bogolon, states.

For later use, we note the Heisenberg equations of motions of the photon and bogolon operators, which follow from Eq. (17) as

$$\begin{aligned}\mathrm{i}\hbar\dot{\hat{a}}_{\mathbf{q}}(t) = &\hbar\omega_{\mathbf{q}} \hat{a}_{\mathbf{q}}(t) + \mathrm{i}C_{\mathbf{q}} \left(\hat{b}_{\mathbf{q}}(t) - \hat{b}^{\dagger}_{-\mathbf{q}}(t)\right) \\ &+ 2D_{\mathbf{q}} \left(\hat{a}_{\mathbf{q}}(t) + \hat{a}^{\dagger}_{-\mathbf{q}}(t)\right),\end{aligned} \tag{21}$$

$$\mathrm{i}\hbar\dot{\hat{b}}_{\mathbf{q}}(t) = E_{\mathbf{q}} \hat{b}_{\mathbf{q}}(t) - \mathrm{i}C_{\mathbf{q}} \left(\hat{a}_{\mathbf{q}}(t) + \hat{a}^{\dagger}_{-\mathbf{q}}(t)\right). \tag{22}$$

4 Luminescence spectrum

In experiments, the photoelectric effect is used for luminescence measurements. That is why only normal-ordered components of the field–field correlation functions are considered, e.g.,

$$g^{(1)}_{EE}(\mathbf{r}_1, t_1; \mathbf{r}_2, t_2) = \left\langle \hat{\mathbf{E}}^{(-)}(\mathbf{r}_2, t_2) \hat{\mathbf{E}}^{(+)}(\mathbf{r}_1, t_1) \right\rangle. \tag{23}$$

The field components of positive and negative frequencies are [15]:

$$\hat{\mathbf{E}}^{(-)}(\mathbf{r}, t) = \sum_{\mathbf{q}\lambda} \sqrt{\frac{\hbar\omega_{\mathbf{q}}}{2\epsilon_0 V}}\, \mathbf{e}_{\mathbf{q}\lambda} \mathrm{e}^{-\mathrm{i}\mathbf{q}\cdot\mathbf{r}}\, \hat{a}^{\dagger}_{\mathbf{q}}(t), \tag{24}$$

$$\hat{\mathbf{E}}^{(+)}(\mathbf{r}, t) = \sum_{\mathbf{q}\lambda} \sqrt{\frac{\hbar\omega_{\mathbf{q}}}{2\epsilon_0 V}}\, \mathbf{e}_{\mathbf{q}\lambda} \mathrm{e}^{\mathrm{i}\mathbf{q}\cdot\mathbf{r}}\, \hat{a}_{\mathbf{q}}(t). \tag{25}$$

Inserting these into Eq. (23) and evaluating the sum over polarisation vectors, the field–field correlation function reads

$$g^{(1)}_{EE}(\mathbf{r}_1,\mathbf{r}_2,t_1,t_2) = \frac{\hbar}{2V\epsilon_0}\sum_{\mathbf{q}\mathbf{q}'}(1+\cos\Theta)\sqrt{\omega_{\mathbf{q}}\omega_{\mathbf{q}'}} \times \mathrm{i}\hbar g^{<}_{aa}(\mathbf{q},\mathbf{q}',t_1,t_2)\,\mathrm{e}^{\mathrm{i}(\mathbf{q}\cdot\mathbf{r}_1-\mathbf{q}'\cdot\mathbf{r}_2)}, \quad (26)$$

where Θ is the angle between the wave vectors $\mathbf{q}$ and $\mathbf{q}'$ and we have defined the photonic correlation function

$$\mathrm{i}\hbar g^{<}_{aa}(\mathbf{q},\mathbf{q}',t_1,t_2) \equiv \left\langle \hat{a}^{\dagger}_{\mathbf{q}'}(t_2)\hat{a}_{\mathbf{q}}(t_1)\right\rangle. \quad (27)$$

To calculate $g^{<}_{aa}$ we have to evaluate a number of similar real-time correlation functions of (mixed) photon and bogolon operators, which may be represented by the matrix

$$\mathrm{i}\hbar g^{\alpha\beta<}_{XY}(\mathbf{q},\mathbf{q}',t_1,t_2) = \begin{pmatrix} \langle Y^{\dagger}_{\mathbf{q}'}(t_2)X_{\mathbf{q}}(t_1)\rangle & \langle Y_{\mathbf{q}'}(t_2)X_{\mathbf{q}}(t_1)\rangle \\ \langle Y^{\dagger}_{\mathbf{q}'}(t_2)X^{\dagger}_{\mathbf{q}}(t_1)\rangle & \langle Y_{\mathbf{q}'}(t_2)X^{\dagger}_{\mathbf{q}}(t_1)\rangle \end{pmatrix}, \quad (28)$$

where X and Y represent the operators $\hat{a}$ and/or $\hat{b}$, while α and β are the matrix indizes. Specifically, we have $g^{<}_{aa} = g^{11<}_{aa}$. The correlation functions in Eq. (28) can be determined from the more general Keldysh Green functions defined as [16–18]

$$\mathrm{i}\hbar G^{\alpha\beta}_{XY}(\mathbf{q},\mathbf{q}',t_1,t_2) = \begin{pmatrix} \langle T_{\mathscr{C}}\, X_{\mathbf{q}}(t_1)Y^{\dagger}_{\mathbf{q}'}(t_2)\rangle & \langle T_{\mathscr{C}}\, X_{\mathbf{q}}(t_1)Y_{\mathbf{q}'}(t_2)\rangle \\ \langle T_{\mathscr{C}}\, X^{\dagger}_{\mathbf{q}}(t_1)Y^{\dagger}_{\mathbf{q}'}(t_2)\rangle & \langle T_{\mathscr{C}}\, X^{\dagger}_{\mathbf{q}}(t_1)Y_{\mathbf{q}'}(t_2)\rangle \end{pmatrix}, \quad (29)$$

with the time ordering operator $T_{\mathscr{C}}$ defined on the two-branch time contour (chronological/antichronological ordering when both times are on the upper/lower branch; otherwise ordering of operators with times on the upper branch right from those on the lower one). The functions G may be calculated by using Eqs. (21) and (22). Then, using the free Green functions of photons and bogolons,

$$\left(\mathrm{i}\hbar\frac{\partial}{\partial t_1} - \hbar\omega_{\mathbf{q}}\right) G^{(0)}_{aa}(\mathbf{q},\mathbf{q}',t_1,t_2) = \delta(\mathbf{q}-\mathbf{q}')\delta(t_1-t_2), \quad (30)$$

$$\left(\mathrm{i}\hbar\frac{\partial}{\partial t_1} - E_{\mathbf{q}}\right) G^{(0)}_{bb}(\mathbf{q},\mathbf{q}',t_1,t_2) = \delta(\mathbf{q}-\mathbf{q}')\delta(t_1-t_2), \quad (31)$$

and defining the matrix multiplication $f_1(\mathbf{q},t)\bullet f_2(\mathbf{q},t) \equiv \sum_{\mathbf{q}}\int_{\mathscr{C}} \mathrm{d}t\, f_1(\mathbf{q},t)f_2(\mathbf{q},t)$, the coupled selfconsistent Dyson equations can be written as:

$$\begin{aligned} G^{11}_{aa}(\mathbf{q},\mathbf{q}',t_1,t_2) &= G^{(0)}_{aa}(\mathbf{q},\mathbf{q}',t_1,t_2) + G^{(0)}_{aa}(\mathbf{q},\bar{\mathbf{q}},t_1,\bar{t})\bullet \\ &\bullet\widetilde{C}_{\bar{\mathbf{q}}}\left[G^{(0)}_{bb}(\bar{\mathbf{q}},\bar{\bar{\mathbf{q}}},\bar{t},\bar{\bar{t}}) + G^{(0)}_{bb}(-\bar{\mathbf{q}},-\bar{\bar{\mathbf{q}}},-\bar{t},-\bar{\bar{t}})\right]\bullet \\ &\bullet\widetilde{C}\;\bar{\bar{\mathbf{q}}}\left[G^{11}_{aa}(\bar{\bar{\mathbf{q}}},\mathbf{q}',\bar{\bar{t}},t_2) + G^{21}_{aa}(-\bar{\bar{\mathbf{q}}},\mathbf{q}',\bar{\bar{t}},t_2)\right] \\ &\qquad + 2G^{(0)}_{aa}(\mathbf{q},\bar{\mathbf{q}},t_1,\bar{t})\bullet \\ &\bullet D_{\bar{\mathbf{q}}}\left[G^{11}_{aa}(\bar{\bar{\mathbf{q}}},\mathbf{q}',\bar{\bar{t}},t_2) + G^{21}_{aa}(-\bar{\bar{\mathbf{q}}},\mathbf{q}',\bar{\bar{t}},t_2)\right], \end{aligned} \quad (32)$$

$$\begin{aligned} G^{21}_{aa}(\mathbf{q},\mathbf{q}',t_1,t_2) &= G^{(0)}_{aa}(\mathbf{q},\bar{\mathbf{q}},-t_1,-\bar{t})\bullet \\ &\bullet\widetilde{C}_{\bar{\mathbf{q}}}\left[G^{(0)}_{bb}(\bar{\mathbf{q}},\bar{\bar{\mathbf{q}}},-\bar{t},-\bar{\bar{t}}) + G^{(0)}_{bb}(-\bar{\mathbf{q}},-\bar{\bar{\mathbf{q}}},\bar{t},\bar{\bar{t}})\right] \\ &\bullet\widetilde{C}_{\bar{\bar{\mathbf{q}}}}\left[G^{21}_{aa}(\bar{\bar{\mathbf{q}}},\mathbf{q}',\bar{\bar{t}},t_2) + G^{11}_{aa}(-\bar{\bar{\mathbf{q}}},\mathbf{q}',\bar{\bar{t}},t_2)\right] \\ &\qquad - 2G^{(0)}_{aa}(\mathbf{q},\bar{\mathbf{q}},-t_1,-\bar{t})\bullet \\ &\bullet D_{\bar{\mathbf{q}}}\left[G^{21}_{aa}(\bar{\bar{\mathbf{q}}},\mathbf{q}',\bar{\bar{t}},t_2) + G^{11}_{aa}(-\bar{\bar{\mathbf{q}}},\mathbf{q}',\bar{\bar{t}},t_2)\right]. \end{aligned} \quad (33)$$

To get the frequency-dependent intensity signal $I(\mathbf{r},\omega)$ we consider the Fourier transform of the correlation function in Eq. (26) for $\mathbf{r}_1 = \mathbf{r}_2 = \mathbf{r}$, i.e.,

$$\begin{aligned} I(\mathbf{r},\omega) &\propto g^{(1)}_{EE}(\mathbf{r},\mathbf{r},\omega) \\ &= \frac{\hbar}{2V\epsilon_0}\sum_{\mathbf{q}\mathbf{q}'}(1+\cos\Theta)\sqrt{\omega_{\mathbf{q}}\omega_{\mathbf{q}'}} \\ &\quad\times \mathrm{i}\hbar g^{11<}_{aa}(\mathbf{q},\mathbf{q}',\omega)\,\mathrm{e}^{\mathrm{i}(\mathbf{q}-\mathbf{q}')\cdot\mathbf{r}}. \end{aligned} \quad (34)$$

In order to obtain the correlation function $g^{11<}_{aa}$, we use $G^{(0)} \propto \delta(\mathbf{q}-\mathbf{q}')$ and apply the usual Langreth rules [19]. That results in a system of four coupled equations for $g^{11<}_{aa}$, $g^{21<}_{aa}$, and the two respective retarded or advanced functions, a closed solution of which is still pending. However, the solution of the subsystem of retarded and advanced functions can be given straightforwardly,

$$g^{11\mathrm{r/a}}_{aa}(\mathbf{q},\mathbf{q}',\omega) = \delta(\mathbf{q}-\mathbf{q}') \times\frac{1}{\hbar}\,\frac{((\omega\pm\mathrm{i}\epsilon)+\omega_{\mathbf{q}}+2d_{\mathbf{q}})((\omega\pm\mathrm{i}\epsilon)^2-e^2_{\mathbf{q}})+2c^2_{\mathbf{q}}e_{\mathbf{q}}}{((\omega\pm\mathrm{i}\epsilon)^2-\omega^2_{\mathbf{q}}-4d_{\mathbf{q}}\omega_{\mathbf{q}})((\omega\pm\mathrm{i}\epsilon)^2-e^2_{\mathbf{q}})-4c^2_{\mathbf{q}}e_{\mathbf{q}}\omega_{\mathbf{q}}}. \quad (35)$$

with $E_{\mathbf{q}} = \hbar e_{\mathbf{q}}$, $C_{\mathbf{q}} = \hbar c_{\mathbf{q}}$, and $D_{\mathbf{q}} = \hbar d_{\mathbf{q}}$. The poles of these functions give the excitation spectrum. We find four

solutions $(\omega \pm i\epsilon) = \pm\Omega_{\mathbf{q}}^{\pm}$, with

$$\Omega_{\mathbf{q}}^{\pm 2} = \frac{1}{2}\left(e_{\mathbf{q}}^2 + \omega_{\mathbf{q}}^2 + 4d_{\mathbf{q}}\omega_{\mathbf{q}}\right) \pm \frac{1}{2}\sqrt{\left(e_{\mathbf{q}}^2 - \omega_{\mathbf{q}}^2 - 4d_{\mathbf{q}}\omega_{\mathbf{q}}\right)^2 + 16c_{\mathbf{q}}^2 e_{\mathbf{q}}\omega_{\mathbf{q}}}. \quad (36)$$

This result is analogous to the Hopfield polariton spectrum [20] with its non-crossing upper and lower polariton branches. Note however, that the energy $E_{\mathbf{q}}$ is now the Bogolyubov dispersion of the interacting, condensed exciton system. Therefore, the new quasiparticles will be called "bogolaritons" in the following.

The retarded and advanced Green functions give the photonic spectral function $A_{aa}(\omega)$, which follows from Eq. (35) as

$$\begin{aligned} A_{aa}(\mathbf{q},\mathbf{q}',\omega) &= i\hbar\left[g_{aa}^{11r}(\mathbf{q},\mathbf{q}',\omega) - g_{aa}^{11a}(\mathbf{q},\mathbf{q}',\omega)\right] \\ &= 2\pi\delta(\mathbf{q}-\mathbf{q}') \\ &\quad \times \left[U_{\mathbf{q}}^{+2}\delta(\omega-\Omega_{\mathbf{q}}^{+}) + V_{\mathbf{q}}^{+2}\delta(\omega+\Omega_{\mathbf{q}}^{+})\right. \\ &\quad \left. + U_{\mathbf{q}}^{-2}\delta(\omega-\Omega_{\mathbf{q}}^{-}) + V_{\mathbf{q}}^{-2}\delta(\omega+\Omega_{\mathbf{q}}^{-})\right]. \end{aligned} \quad (37)$$

The weights of the positive and negative upper and lower bogolariton branches in the photon spectral function are

$$U_{\mathbf{q}}^{+2} = \frac{(\Omega_{\mathbf{q}}^{+} + \omega_{\mathbf{q}} + 2d_{\mathbf{q}})(\Omega_{\mathbf{q}}^{+2} - e_{\mathbf{q}}^2) + 2c_{\mathbf{q}}^2 e_{\mathbf{q}}}{2\Omega_{\mathbf{q}}^{+}(\Omega_{\mathbf{q}}^{+2} - \Omega_{\mathbf{q}}^{-2})}, \quad (38)$$

$$V_{\mathbf{q}}^{+2} = \frac{(\Omega_{\mathbf{q}}^{+} - \omega_{\mathbf{q}} - 2d_{\mathbf{q}})(\Omega_{\mathbf{q}}^{+2} - e_{\mathbf{q}}^2) - 2c_{\mathbf{q}}^2 e_{\mathbf{q}}}{2\Omega_{\mathbf{q}}^{+}(\Omega_{\mathbf{q}}^{+2} - \Omega_{\mathbf{q}}^{-2})}, \quad (39)$$

$$U_{\mathbf{q}}^{-2} = \frac{(\Omega_{\mathbf{q}}^{-} + \omega_{\mathbf{q}} + 2d_{\mathbf{q}})(\Omega_{\mathbf{q}}^{-2} - e_{\mathbf{q}}^2) + 2c_{\mathbf{q}}^2 e_{\mathbf{q}}}{2\Omega_{\mathbf{q}}^{-}(\Omega_{\mathbf{q}}^{-2} - \Omega_{\mathbf{q}}^{+2})}, \quad (40)$$

$$V_{\mathbf{q}}^{-2} = \frac{(\Omega_{\mathbf{q}}^{-} - \omega_{\mathbf{q}} - 2d_{\mathbf{q}})(\Omega_{\mathbf{q}}^{-2} - e_{\mathbf{q}}^2) - 2c_{\mathbf{q}}^2 e_{\mathbf{q}}}{2\Omega_{\mathbf{q}}^{-}(\Omega_{\mathbf{q}}^{-2} - \Omega_{\mathbf{q}}^{+2})}. \quad (41)$$

We note that for vanishing exciton-photon coupling, i.e. for $c_{\mathbf{q}} = d_{\mathbf{q}} = 0$, we have $\Omega_{\mathbf{q}}^{+} = \max\{e_{\mathbf{q}}, \omega_{\mathbf{q}}\}$ and $\Omega_{\mathbf{q}}^{-} = \min\{e_{\mathbf{q}}, \omega_{\mathbf{q}}\}$. Accordingly we find $U_{\mathbf{q}}^{\pm 2} = 1$ for $e_{\mathbf{q}} \lessgtr \omega_{\mathbf{q}}$ and $U_{\mathbf{q}}^{\pm 2} = 0$ for $e_{\mathbf{q}} \gtrless \omega_{\mathbf{q}}$, so that the spectral function in Eq. (37) reduces to that of the free photons: $A_{aa}(\mathbf{q},\mathbf{q}',\omega) = 2\pi\delta(\mathbf{q}-\mathbf{q}')\delta(\omega-\omega_{\mathbf{q}})$.

5 Results

As with the theoretical description, our numerical evaluation takes two steps: First, we calculate self-consistently the paraexciton density distribution in the trap and the corresponding bogolon spectrum. Second, we keep the exciton distribution fixed and insert $E_{\mathbf{q}}$, as well as the free photon dispersion $\omega_{\mathbf{q}}$ into the combined "bogolariton" spectrum $\Omega_{\mathbf{q}}^{\pm}$.

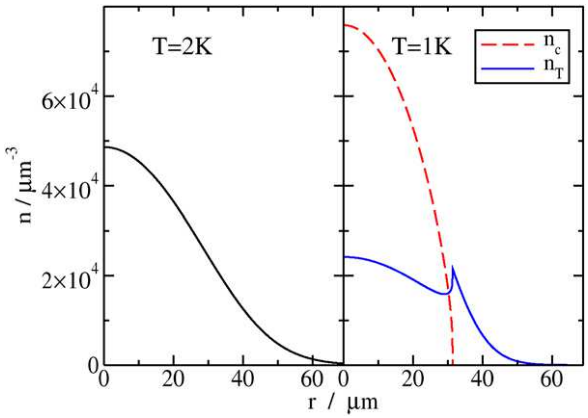

Figure 1 Exciton density (n) as a function of the trap radius (r) for a total number of excitons $N = 10^{10}$. Left panel: non-condensed situation with $T = 2$ K and $\mu - E_g = 231$ μeV. Right panel: condensed situation with $T = 1$ K, $\mu - E_g = 314$ μeV, and $N_c = N_T = 5 \times 10^9$.

Although the typical experimental situation features a trap with cylindrical symmetry [4, 5], for simplicity we will consider a spherical harmonic trap, $V_{\text{ext}}(r) = V_0 + \alpha r^2$, with $V_0 = -2$ meV and $\alpha = 0.21$ μeV/μm^2 fitted to the bottom of the experimentally observed strain trap potentials. The paraexciton interaction strength is given by the corresponding s-wave scattering length (cf. Eq. 2). The latter follows, in principle, from a four-particle scattering problem (two electrons and two holes), which has no satisfying solution for excitons, so far. That is why in our calculations we use a representative value of $a_s = 2.18$ a_B (with the excitonic Bohr radius $a_B = 0.7$ nm) deduced from the scattering lengths of the positronium problem given in Ref. [21]. With the effective exciton mass $m = 2.6m_e$, we then have $U = 2.53 \times 10^{-3}$ μeVμm^3. The exciton-bogolon interaction is determined by the oscillator strength per unit cell, f/V, where we use the experimental value $f = 4.7 \times 10^{-10}$ for the quadrupole transition and $V = (4.48\text{Å})^3$, so that $C_{\mathbf{q}} = 42.45$ μeV$\sqrt{E_{\mathbf{q}}/\hbar\omega_{\mathbf{q}}}$. In what follows, we fix the total exciton number as $N = 10^{10}$, which gives a critical temperature of $T_c \approx 1.5$ K.

Figure 1 compares our results for the density distribution of the non-condensed ($T = 2$ K, $\mu - E_g = 231$ μeV) and condensed systems ($T = 1$ K, $\mu - E_g = 314$ μeV), with the latter exhibiting a condensate fraction of $N_c/N = 0.5$.

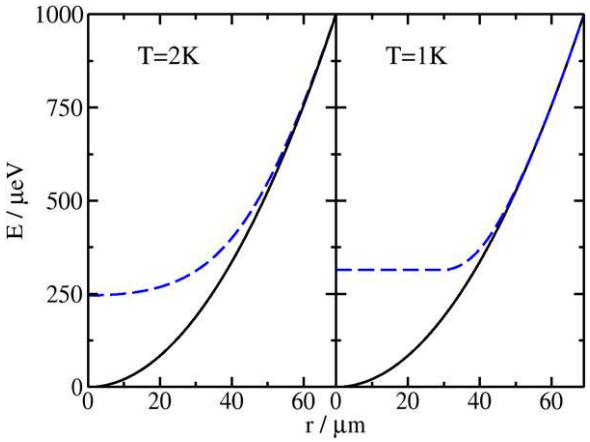

Figure 2 Minimal excitation energy $E = E_0(r) - E_g - V_0 + \mu$ of bogolons (blue dashed lines), compared to the external potential $V_{\rm ext}(r) - V_0 - E_g$ (black lines). Left panel: non-condensed situation with $T = 2$ K and $\mu - E_g = 231$ μeV. Right panel: condensed situation with $T = 1$ K, $\mu - E_g = 314$ μeV and $N_c = N_T = 5 \times 10^9$.

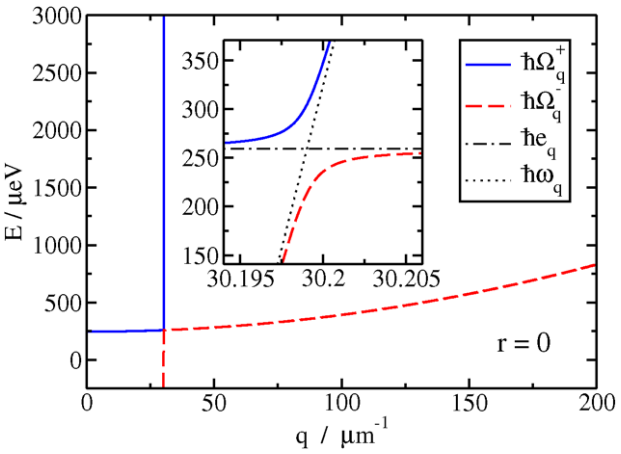

Figure 3 Upper and lower bogolariton spectrum $E = \hbar\Omega_q^{\pm} - E_g - V_0 + \mu$ as a function of q, for $r = 0$ and $T = 2$ K. The inset magnifies the (avoided) crossing region of the free photon and bogolon dispersions.

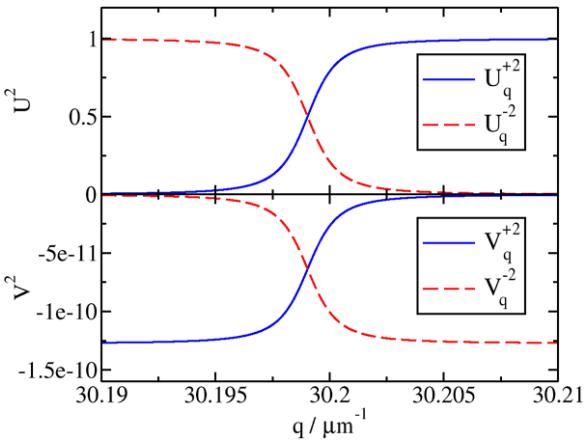

Figure 4 Spectral weights of the upper and lower bogolariton spectrum, in dependence on q, for $r = 0$ and $T = 2$ K.

Figure 2 displays the corresponding minimal excitation energies E_0(r), compared to the external potential $V_{\rm ext}$(r). In the non-condensed case, the thermal exciton cloud has an extension of about 70μm. The mean-field interaction causes a considerable flattening of the disperison curve when compared to the external potential. In the condensed system, the thermal excitons get pushed aside by the condensed exciton cloud. The two phases still mix, however, since the paraexciton interaction is too weak for a complete phase separation [23]. The cusp in the thermal density profile is an artefact of the Thomas–Fermi approximation for the condensate density which becomes invalid near the edge of the condensate cloud. The solution of the full Gross–Pitaevskii equation would yield a smooth course of the condensate and thermal density curves. Note that the quasiparticle spectrum exhibits a flat bottom wherever $n_c > 0$.

Now we switch on the bogolon-photon interaction. Figure 3 shows the resulting positive upper and lower branches of the new quasiparticle spectrum $\hbar\Omega_{\mathbf{q}}^{\pm}$ as a function of q for $r = 0$. Here, $\hbar\Omega_0^+$ corresponds to the minimal bogolon energy $E_0(r = 0)$ in Fig. 2. Varying r will simply shift the minimum $\hbar\Omega_0^+$ according to Fig. 2, so that in the following, we will keep $r = 0$ fixed. The inset of Fiq. 3 shows a zoom in on the crossing point of the uncoupled photon and bogolon dispersions. As expected, we find a gap with a width of $2C_{\mathbf{q}} \approx 90$ μeV.

Figure 4 gives the q-dependence of the spectral weights $U_{\mathbf{q}}^{\pm\,2}$ and $V_{\mathbf{q}}^{\pm\,2}$ contributing to the photonic spectral function in Eq. (37). As a matter of course, far from the gap, the weights $U_{\mathbf{q}}^{\pm\,2}$ equal one or zero, representing the undisturbed photon states. Near the gap, they smoothly switch roles, whereby their sum remains constant. The weights of the mirror branches are smaller by ten orders of magnitude, and they will be ignored in the following. We note, however, that the $V_{\mathbf{q}}^{\pm}$ are finite even for $n_c = 0$. In contrast, the bogolon mirror branch in Eq. (11) only exists in the presence of a condensate ($v_{\mathbf{q}} = 0$ for $n_c = 0$); a result which has formerly been declared a footprint of exciton condensation [22, 23].

Combining our results for the dispersions and weights, Fig. 5 presents the photon spectral function $A_{aa}(q, E)$ in the vicinity of the gap (with a slight broadening of the delta peaks, for visibility). The photon

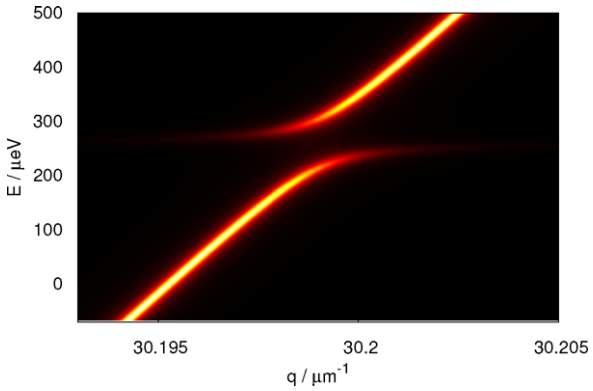

Figure 5 Photonic spectral function A_{aa} as a function of q and $E = \hbar\omega - E_g - V_0 + \mu$ in the avoided crossing region, for $r = 0$ and $T = 2$ K.

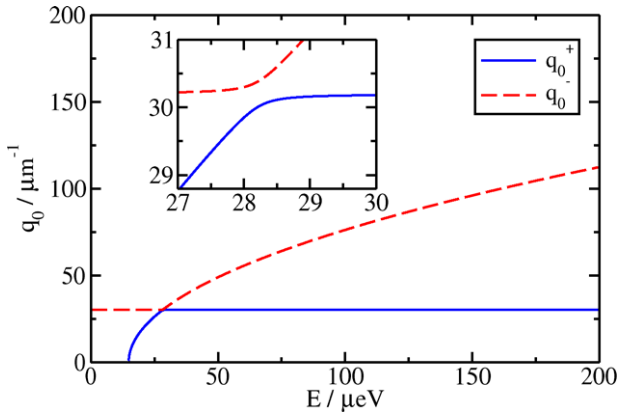

Figure 6 Critical wave vectors $q_0^{\pm}$ as a function of $E = \hbar\omega - E_g - V_0 + \mu$, for $r = 0$ and $T = 2$ K.

dispersion is considerably renormalised, with a hockey stick like structure at the gap.

As a consequence, the luminescence at a given energy will now depend on the bogolariton density of states at two critical wave numbers $q_0^{\pm}$. This is in contrast to earlier works [8, 9, 22, 23], where the intensity signal was given by the coupling strength and bogolon density of states at the fixed value $q_0 = 30.2\ \mu\text{m}^{-1}$ at the intersection of the free bogolon and photon dispersions (cf. inset of Fig. 3). We numerically determine the wave numbers $q_0^{\pm}$ so that $E = \hbar\Omega_q^{\pm}$ for fixed r. Figure 6 presents $q_0^{\pm}$ as a funtion of E at $r = 0$. For small E, we find $q_0^- \sim q_0$, and the wave number q_0^+ is undetermined as long as $E < \hbar\Omega_q^+$. After E crosses the gap position, we find $q_0^+ \sim q_0$, while q_0^- grows due to the q^2-dependence of the bogolon dispersion. We note that the smallest difference between q_0^+ and q_0^- is found at the gap: $q_0^- - q_0^+ = 0.38\ \mu\text{m}^{-1}$.

6 Conclusion and outlook

To summarise, this work presents the first results of a real-time Green's function based theory for the luminescent zero-phonon decay of condensed semiconductor excitons. Motivated by the long lifetime of the paraexcitons in cuprous oxide, our approach adopts a two-step picture: the excitons reach their own thermodynamic quasi-equilibrium (and possibly a condensate) before any interaction with the photonic states takes place. The exciton luminescence is then understood as a steady-state decay of bogolon quasiparticles via polariton-like transient states, while the corresponding photon correlation function determines the luminescence intensity.

We find that the photonic spectrum shows a characteristic gap around the former crossing point of free photons and bogolons. The gap's position is dependent on the spatial profile of the bogolon dispersion within the trap. Due to the anomalous terms in the coupling Hamiltonian, mirror branches contribute to the luminescence even without a condensate. Their weight, however, is extremely small.

The present theory can be extended in several directions. The most pressing task is the calculation of the photonic correlation function which not only contains the spectrum but also the steady-state occupation of the bogolariton states. Of course, the most striking signature for BEC would be the coherence of the emitted light. Therefore, the first and second order coherence functions (the former also contained in the field–field correlation function) would be highly desirable to calculate. Moreover, the phonon-assisted decay of orthoexcitons, in principle, can be accounted for in our scheme by introducing a corresponding self-energy term in the Keldysh formalism.

Acknowledgements. We would like to thank P. Grünwald (Rostock) and K. W. Becker (Dresden) for many fruitful discussions. This work was supported by the Deutsche Forschungsgemeinschaft via Collaborative Research Center SFB 652, project B14.

Key words. Excitons, Bose–Einstein condensation, luminescence spectra, cuprous oxide.

References

[1] J. M. Blatt, K. W. Böer, and W. Brandt, *Phys. Rev.* **126**, 1691 (1962).
[2] S. A. Moskalenko, *Fiz. Tverd. Tela* **4**, 276 (1962).
[3] D. Snoke and G. M. Kavoulakis, *Rep. Prog. Phys.* **77**, 116501 (2014).

[4] R. Schwartz, N. Naka, F. Kieseling, and H. Stolz, *New J. Phys.* **14**, 023054 (2012).
[5] H. Stolz, R. Schwartz, F. Kieseling, S. Som, M. Kaupsch, S. Sobkowiak, D. Semkat, N. Naka, Th. Koch, and H. Fehske, *New J. Phys.* **14**, 105007 (2012).
[6] K. Kamida and T. Ogawa, *Phys. Rev. B* **83**, 165319 (2011).
[7] V.-N. Phan, K. W. Becker, and H. Fehske, *Phys. Rev. B* **93**, 075138 (2016).
[8] H. Haug and H. Kranz, *Z. Phys. B* **53**, 151 (1983).
[9] H. Shi, G. Verechaka, and A. Griffin, *Phys. Rev. B* **50**, 1119 (1994).
[10] S. Sobkowiak, D. Semkat, and H. Stolz, *Phys. Rev. B* **90**, 075206 (2014).
[11] S. Sobkowiak, D. Semkat, and H. Stolz, *Phys. Rev. B* **91**, 075209 (2015).
[12] T. Bergeman, D. L. Feder, N. L. Balazs, and B. I. Schneider, *Phys. Rev. A* **61**, 063605 (2000).
[13] D. Gerace and L. C. Andreani, *Phys. Rev. B* **75**, 235325 (2007).
[14] L. C. Andreani, in: Strong Light-Matter Coupling, From Atoms to Solid-State Systems, edited by A. Auffèves, D. Gerace, M. Richard, S. Portolan, M. F. Santos, L. C. Kwek, and C. Miniatura (World Scientific, Singapore, 2014).
[15] R. J. Glauber, *Phys. Rev.* **130**, 2529 (1963).
[16] L. V. Keldysh, *Zh. Eksp. Teor. Fiz.* **47**, 1515 (1964).
[17] A. L. Fetter and J. D. Walecka, Quantum Theory of Many-Particle Systems (McGraw-Hill, New York, 1971).
[18] D. Kremp, M. Schlanges, and W.-D. Kraeft, Quantum Statistics of Nonideal Plasmas (Springer, Berlin, 2005).
[19] D. C. Langreth, in: Linear and Nonlinear Electron Transport in Solids, edited by J. T. Devreese and E. Dorenvan (Plenum, New York, 1976).
[20] J. J. Hopfield, *Phys. Rev.* **112**, 1555 (1958).
[21] J. Shumway and D. M. Ceperley, *Phys. Rev. B* **63**, 165209 (2001).
[22] H. Stolz and D. Semkat, *Phys. Rev. B* **81**, 081302(R) (2010).
[23] S. Sobkowiak, D. Semkat, H. Stolz, Th. Koch, and H. Fehske, *Phys. Rev. B* **82**, 064505 (2010).

Danksagung

An dieser Stelle möchte ich mich bei allen bedanken, die mich auf meinem wissenschaftlichen Werdegang begleitet und somit die Abfassung dieser Habilitationsschrift ermöglicht haben.

Als erstes möchte ich hier Dietrich Kremp danken, der mich nicht nur als Hochschullehrer für die Theoretische Physik begeistert und als Doktorvater betreut, sondern später auch meine ersten Schritte auf dem Gebiet der Halbleiterphysik begleitet hat.

Mein besonderer Dank gilt ebenso Heinrich Stolz, dem Spiritus rector der Rostocker Suche nach dem Bose–Einstein–Kondensat, der mich mit Optimismus und nie versiegendem Elan durch die Untiefen der Halbleiterphysik gelotst hat.

Ganz herzlich danken möchte ich zudem Wolf-Dietrich Kraeft und Thomas Bornath, an deren Erfahrungsschatz ich in ungezählten Diskussionen teilhaben konnte und kann.

Mein großer Dank gilt jenen Kollegen, die meine Lehrer waren und sind. Neben den bereits Genannten sind das auf dem Gebiet der Plasmaphysik Michael Bonitz, Manfred Schlanges und Ronald Redmer, auf dem Gebiet der Festkörperphysik Klaus Henneberger und Günter Manzke.

Eine besonders enge und fruchtbare Zusammenarbeit, aus der auch ein Großteil der in dieser Arbeit zusammengefaßten Artikel hervorgegangen sind, verbindet mich neben Letzteren zudem mit Felix Richter, Siegfried Sobkowiak, Thomas Koch und Holger Fehske, desweiteren mit Florian Schöne, wobei ich darüber hinaus das große Vergnügen hatte, Siegfried und Florian bei ihren ersten Schritten in der physikalischen Forschung in Form ihrer Diplom- bzw. Bachelor- und Masterarbeiten zu betreuen.

Ein unschätzbarer Vorteil für beide Seiten ist die enge Zusammenarbeit zwischen

Theorie und Experiment. Hier möchte ich insbesondere Rico Schwartz und Maria Dietl danken.

Stefan Scheel gilt mein Dank nicht nur für die räumliche Aufnahme in seiner Arbeitsgruppe, sondern auch für viele interessante Diskussionen zur brandaktuellen Forschung. In diesem Zusammenhang möchte ich auch Peter Grünwald danken.

Nicht zuletzt gilt mein Dank auch allen bisher nicht genannten Kollegen der Arbeitsgruppen, in denen ich längere oder kürzere Phasen meines bisherigen Arbeitslebens verbrachte – die AG Kremp, Redmer, Henneberger, Stolz und Scheel in Rostock, AG Schlanges und Fehske in Greifswald und AG Bonitz in Kiel – für die angenehme Zusammenarbeit und das für die wissenschaftliche Arbeit so wichtige und unerläßliche gute Arbeitsklima.

Diese Danksagung wäre unvollständig, würde nicht eine Institution erwähnt, in der die zuletzt genannten Punkte quasi ihren kondensierten Ausdruck finden – die tägliche Kaffeerunde, die den physikalischen Horizont genauso erweitert wie den der Allgemeinbildung.

Und schließlich ist physikalische Forschung ohne einen institutionellen Rahmen nicht denkbar, der hier in Rostock nicht nur durch das Institut für Physik gebildet wird, sondern auch durch den Sonderforschungsbereich 652 „Starke Korrelationen und kollektive Phänomene im Strahlungsfeld – Coulombsysteme, Cluster und Partikel“. Ich möchte allen daran beteiligten Kollegen und besonders seinem Sprecher Karl-Heinz Meiwes-Broer danken.

Lebenslauf

Persönliche Angaben

Name:	Dirk Semkat
Anschrift:	Am Bahnhof 2
	18292 Krakow am See
Geburtsdatum:	16. Juli 1973
Geburtsort:	Güstrow
Familienstand:	verheiratet
Staatsangehörigkeit:	Deutsch

Schulausbildung

1979 – 1989	Polytechnische Oberschule “Wilhelm Pieck” in Schwerin
1989 – 1991	Erweiterte Oberschule “Johann Wolfgang v. Goethe”
	in Schwerin
	Abschluß: Abitur (Durchschnitt 1,0)

Studium

1991 – 1996	Studium der Physik an der Universität Rostock
	Abschluß: Diplom (Prädikat “Mit Auszeichnung”)

Beruflicher Werdegang

01.09.1996 – 31.08.2001	Wissenschaftlicher Mitarbeiter am Fachbereich Physik der Universität Rostock, Arbeitsgruppe “Statistische Physik” (Prof. Dr. D. Kremp) Promotion auf dem Gebiet der Quantenstatistik von Vielteilchensystemen im Nichtgleichgewicht
01.09.2001 – 31.03.2002	Wissenschaftlicher Mitarbeiter am Institut für Physik der Ernst–Moritz–Arndt–Universität Greifswald, Arbeitsgruppe “Theorie dichter Plasmen” (Prof. Dr. M. Schlanges)
14.11.2001	Verteidigung der Dissertation Thema: “Kurzzeitkinetik und Anfangskorrelationen in nichtidealen Vielteilchensystemen” Prädikat: *summa cum laude*
01.04.2002 – 31.12.2004	Wissenschaftlicher Mitarbeiter am Fachbereich Physik der Universität Rostock, Arbeitsgruppe von Prof. Dr. D. Kremp
01.01.2005 – 31.03.2005	Wissenschaftlicher Mitarbeiter am Institut für Theoretische Physik und Astrophysik der Christian–Albrechts–Universität zu Kiel, Arbeitsgruppe “Statistische Physik und Plasmatheorie” (Prof. Dr. M. Bonitz)
01.04.2005 – 31.12.2005	Wissenschaftlicher Mitarbeiter am Institut für Physik der Universität Rostock, Arbeitsgruppe “Statistische Physik” (Prof. Dr. R. Redmer)
01.01.2006 – 30.06.2009	Wissenschaftlicher Mitarbeiter am Institut für Physik der Universität Rostock, Arbeitsgruppe “Festkörpertheorie” (Prof. Dr. K. Henneberger)

01.07.2009 – 30.09.2009	Wissenschaftlicher Mitarbeiter am Institut für Physik der Universität Rostock, Arbeitsgruppe “Halbleiterphysik” (Prof. Dr. H. Stolz)
01.10.2009 – 30.11.2009	Vorbereitung eines Projekts am Institut für Physik der Universität Rostock, Arbeitsgruppe “Halbleiterphysik”
01.12.2009 – 31.12.2009	Wissenschaftlicher Mitarbeiter am Institut für Physik der Ernst–Moritz–Arndt–Universität Greifswald, Arbeitsgruppe “Komplexe Quantensysteme” (Prof. Dr. H. Fehske)
seit 01.01.2010	Wissenschaftlicher Mitarbeiter am Institut für Physik der Universität Rostock, Arbeitsgruppe “Halbleiterphysik” (Prof. Dr. H. Stolz)

Weitere berufliche Erfahrungen

Mitorganisation der internationalen Tagungen
International Workshop “Kadanoff–Baym Equations – Progress and Perspectives for Many-Body Physics”,
20.–24.09.1999, Rostock;
International Workshop “Progress in Nonequilibrium Green’s Functions”,
19.–23.08.2002, Dresden

Mitherausgabe der Bücher
Introduction to Computational Methods in Many-Body Physics,
M. Bonitz and D. Semkat (Eds.), Rinton Press, Paramus, New Jersey (2005);
Progress in Nonequilibrium Green’s Functions II,
M. Bonitz and D. Semkat (Eds.), World Scientific Publ., Singapore (2003)

Betreuung von Diplom-, Master- und Bachelorarbeiten

Selbständigkeitserklärung

Hiermit versichere ich an Eides statt, daß ich die vorliegende Arbeit selbständig angefertigt und ohne fremde Hilfe verfaßt, keine außer den von mir angegebenen Hilfsmitteln und Quellen dazu verwendet und die den benutzten Werken inhaltlich und wörtlich entnommenen Stellen als solche kenntlich gemacht habe.

Dirk Semkat
Rostock, den 21.02.2017